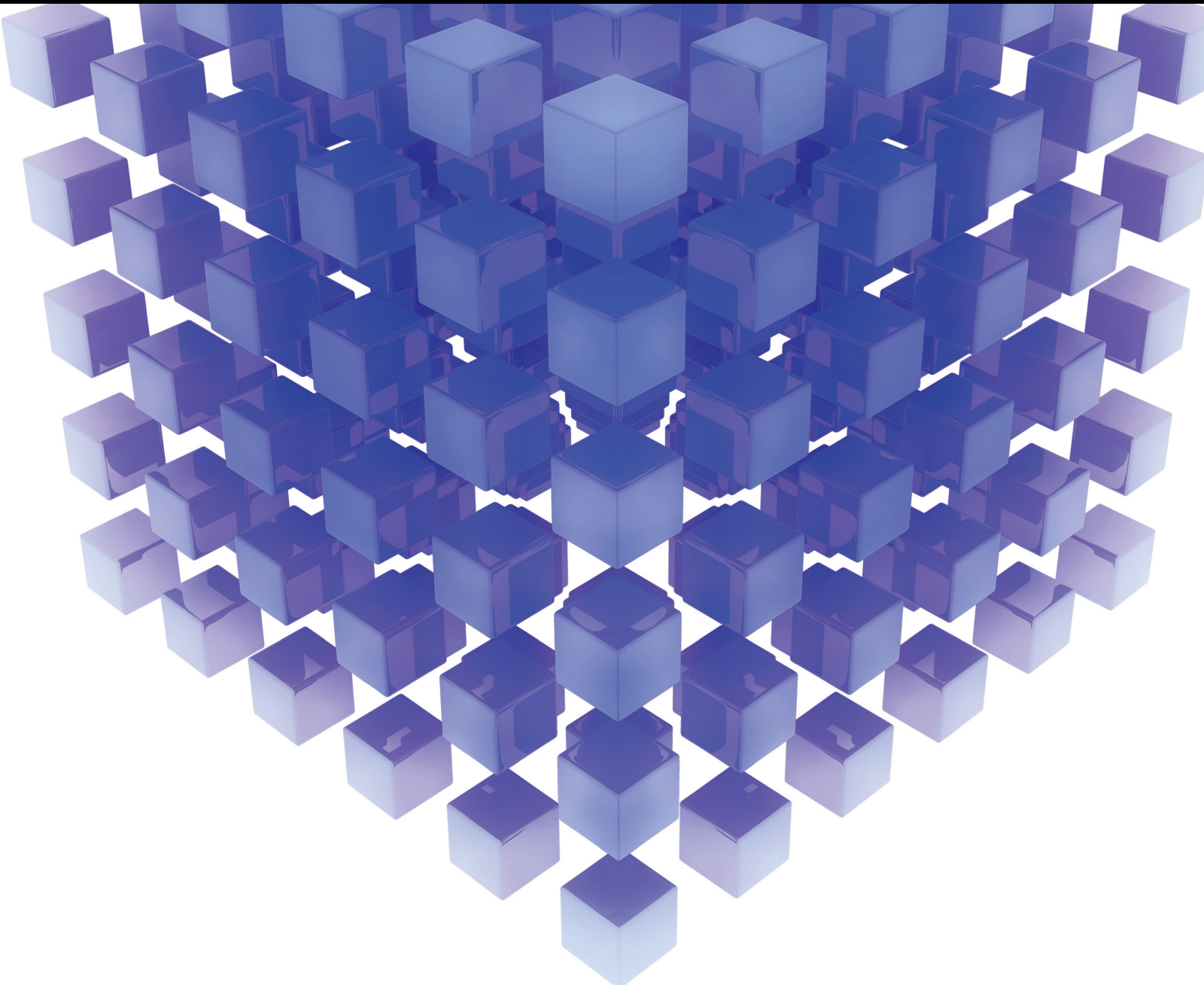# Modelling and Characterization of Infrastructure Materials

Lead Guest Editor: Bowen Guan
Guest Editors: Haibin Li, Guanyuan Zhao, Fulu Wei, Rui Xiong, and Dongyu Niu

Modelling and Characterization of Infrastructure Materials

Modelling and Characterization of Infrastructure Materials

Lead Guest Editor: Bowen Guan
Guest Editors: Haibin Li, Guanyuan Zhao, Fulu Wei, Rui Xiong, and Dongyu Niu

José António Fonseca De Oliveira Correia, Portugal
Jose Renato De Sousa, Brazil
Michael Defoort, France
Alessandro Della Corte, Italy
Laurent Dewasme, Belgium
Sanku Dey, India
Gianpaolo Di Bona, Italy
Roberta Di Pace, Italy
Francesca Di Puccio, Italy
Ramón I. Diego, Spain
Yannis Dimakopoulos, Greece
Hasan Dinçer, Turkey
José M. Domínguez, Spain
Georgios Dounias, Greece
Bo Du, China
Emil Dumic, Croatia
Madalina Dumitriu, United Kingdom
Premraj Durairaj, India
Saeed Eftekhar Azam, USA
Said El Kafhali, Morocco
Antonio Elipe, Spain
R. Emre Erkmen, Canada
John Escobar, Colombia
Leandro F. F. Miguel, Brazil
FRANCESCO FOTI, Italy
Andrea L. Facci, Italy
Shahla Faisal, Pakistan
Giovanni Falsone, Italy
Hua Fan, China
Jianguang Fang, Australia
Nicholas Fantuzzi, Italy
Muhammad Shahid Farid, Pakistan
Hamed Faroqi, Iran
Yann Favennec, France
Fiorenzo A. Fazzolari, United Kingdom
Giuseppe Fedele, Italy
Roberto Fedele, Italy
Baowei Feng, China
Mohammad Ferdows, Bangladesh
Arturo J. Fernández, Spain
Jesus M. Fernandez Oro, Spain
Francesco Ferrise, Italy
Eric Feulvarch, France
Thierry Floquet, France

Eric Florentin, France
Gerardo Flores, Mexico
Antonio Forcina, Italy
Alessandro Formisano, Italy
Francesco Franco, Italy
Elisa Francomano, Italy
Juan Frausto-Solis, Mexico
Shujun Fu, China
Juan C. G. Prada, Spain
HECTOR GOMEZ, Chile
Matteo Gaeta, Italy
Mauro Gaggero, Italy
Zoran Gajic, USA
Jaime Gallardo-Alvarado, Mexico
Mosè Gallo, Italy
Akemi Gálvez, Spain
Maria L. Gandarias, Spain
Hao Gao, Hong Kong
Xingbao Gao, China
Yan Gao, China
Zhiwei Gao, United Kingdom
Giovanni Garcea, Italy
José García, Chile
Harish Garg, India
Alessandro Gasparetto, Italy
Stylianos Georgantzinos, Greece
Fotios Georgiades, India
Parviz Ghadimi, Iran
Ştefan Cristian Gherghina, Romania
Georgios I. Giannopoulos, Greece
Agathoklis Giaralis, United Kingdom
Anna M. Gil-Lafuente, Spain
Ivan Giorgio, Italy
Gaetano Giunta, Luxembourg
Jefferson L.M.A. Gomes, United Kingdom
Emilio Gómez-Déniz, Spain
Antonio M. Gonçalves de Lima, Brazil
Qunxi Gong, China
Chris Goodrich, USA
Rama S. R. Gorla, USA
Veena Goswami, India
Xunjie Gou, Spain
Jakub Grabski, Poland

Bekir Sahin, Turkey
Laxminarayan Sahoo, India
John S. Sakellariou, Greece
Michael Sakellariou, Greece
Salvatore Salamone, USA
Jose Vicente Salcedo, Spain
Alejandro Salcido, Mexico
Alejandro Salcido, Mexico
Nunzio Salerno, Italy
Rohit Salgotra, India
Miguel A. Salido, Spain
Sinan Salih, Iraq
Alessandro Salvini, Italy
Abdus Samad, India
Sovan Samanta, India
Nikolaos Samaras, Greece
Ramon Sancibrian, Spain
Giuseppe Sanfilippo, Italy
Omar-Jacobo Santos, Mexico
J Santos-Reyes, Mexico
José A. Sanz-Herrera, Spain
Musavarah Sarwar, Pakistan
Shahzad Sarwar, Saudi Arabia
Marcelo A. Savi, Brazil
Andrey V. Savkin, Australia
Tadeusz Sawik, Poland
Roberta Sburlati, Italy
Gustavo Scaglia, Argentina
Thomas Schuster, Germany
Hamid M. Sedighi, Iran
Mijanur Rahaman Seikh, India
Tapan Senapati, China
Lotfi Senhadji, France
Junwon Seo, USA
Michele Serpilli, Italy
Silvestar Šesnić, Croatia
Gerardo Severino, Italy
Ruben Sevilla, United Kingdom
Stefano Sfarra, Italy
Dr. Ismail Shah, Pakistan
Leonid Shaikhet, Israel
Vimal Shanmuganathan, India
Prayas Sharma, India
Bo Shen, Germany
Hang Shen, China

Xin Pu Shen, China
Dimitri O. Shepelsky, Ukraine
Jian Shi, China
Amin Shokrollahi, Australia
Suzanne M. Shontz, USA
Babak Shotorban, USA
Zhan Shu, Canada
Angelo Sifaleras, Greece
Nuno Simões, Portugal
Mehakpreet Singh, Ireland
Piyush Pratap Singh, India
Rajiv Singh, India
Seralathan Sivamani, India
S. Sivasankaran, Malaysia
Christos H. Skiadas, Greece
Konstantina Skouri, Greece
Neale R. Smith, Mexico
Bogdan Smolka, Poland
Delfim Soares Jr., Brazil
Alba Sofi, Italy
Francesco Soldovieri, Italy
Raffaele Solimene, Italy
Yang Song, Norway
Jussi Sopanen, Finland
Marco Spadini, Italy
Paolo Spagnolo, Italy
Ruben Specogna, Italy
Vasilios Spitas, Greece
Ivanka Stamova, USA
Rafał Stanisławski, Poland
Miladin Stefanović, Serbia
Salvatore Strano, Italy
Yakov Strelniker, Israel
Kangkang Sun, China
Qiuqin Sun, China
Shuaishuai Sun, Australia
Yanchao Sun, China
Zong-Yao Sun, China
Kumarasamy Suresh, India
Sergey A. Suslov, Australia
D.L. Suthar, Ethiopia
D.L. Suthar, Ethiopia
Andrzej Swierniak, Poland
Andras Szekrenyes, Hungary
Kumar K. Tamma, USA

Zaoli Yang, China
Jun Ye, China
Min Ye, China
Luis J. Yebra, Spain
Peng-Yeng Yin, Taiwan
Muhammad Haroon Yousaf, Pakistan
Yuan Yuan, United Kingdom
Qin Yuming, China
Elena Zaitseva, Slovakia
Arkadiusz Zak, Poland
Mohammad Zakwan, India
Ernesto Zambrano-Serrano, Mexico
Francesco Zammori, Italy
Jessica Zangari, Italy
Rafal Zdunek, Poland
Ibrahim Zeid, USA
Nianyin Zeng, China
Junyong Zhai, China
Hao Zhang, China
Haopeng Zhang, USA
Jian Zhang, China
Kai Zhang, China
Lingfan Zhang, China
Mingjie Zhang, Norway
Qian Zhang, China
Tianwei Zhang, China
Tongqian Zhang, China
Wenyu Zhang, China
Xianming Zhang, Australia
Xuping Zhang, Denmark
Yinyan Zhang, China
Yifan Zhao, United Kingdom
Debao Zhou, USA
Heng Zhou, China
Jian G. Zhou, United Kingdom
Junyong Zhou, China
Xueqian Zhou, United Kingdom
Zhe Zhou, China
Wu-Le Zhu, China
Gaetano Zizzo, Italy
Mingcheng Zuo, China

Contents

Research Article

Evaluation of Freeze-Thaw Durability of Silica Fume Concrete with Spraying Inorganic Coating Using Ultrasonic Testing

Wujian Yan [1,2,3] **Fuhang Niu,**[3] **and Xinxin Tian**[1]

[1]*Key Laboratory of Loess Earthquake Engineering, China Earthquake Administration, 450 Donggang West Road, Lanzhou 730000, China*
[2]*Key Laboratory of Earthquake Engineering and Engineering Vibration, Institute of Engineering Mechanics, China Earthquake Administration, 29 Xuefu Road, Harbin 150080, China*
[3]*State Key Laboratory of Frozen Soil Engineering, Northwest Institute of Eco-Environment and Resources, Chinese Academy of Sciences, 382 Donggang West Road, Lanzhou 730000, China*

Correspondence should be addressed to Wujian Yan; yanwj1980@126.com

To study the antifreezing durability of internal coating silicon fume concrete with different external coatings, fast freeze-thaw (FT) cycle testing was performed for three types of external coatings applied to the internal coatings of silicon fume concrete. Using ultrasonic testing and compressive strength tests, we analysed the relationships between the ultrasonic pulse velocity and the mechanical and physical properties of concrete under freeze-thaw action. The results show that the compressive strength and pulse velocity of the studied concrete changed little before the first 100 FT cycles but varied significantly after being subjected to 100 FT cycles and diminished linearly with increasing FT cycles. The dynamic elastic parameters of the concrete were inferred using pulse velocity calculations, and the dependence on FT cycles was very similar to that of ultrasonic pulse velocity. The concrete strength was strongly and positively correlated with ultrasonic pulse velocity. The linear regression model of between ultrasonic pulse velocity, kinetic coefficient, and compressive strength of concrete was also established. The damage incurred to the external coating material (XT-HPA + XT-SS and XT-HPS) was small, and the good performance of the concrete with the added inorganic coating after freeze-thaw cycles indicates good frost resistance.

1. Introduction

Concrete is currently one of the most widely used materials in civil engineering. It is composed of cement, aggregate, sand, and water. Its strength comes from the chemical reaction in which binders and water form a gel, hardening the aggregates and combining them together. Owing to the increasing use of concrete in construction projects, the durability of concrete structures has become an important research topic in the field of engineering materials and structures; thus, it is important to develop new methods for improving the concrete durability [1]. In the report that describes the progress of concrete durability studies over the span of the last 50 years, Mehta [2] pointed out that, at

present, there are three main causes of concrete failure in the world: (1) steel bar corrosion, (2) freeze-thaw damage, and (3) physicochemical action owing to the presence of erosive environments.

In the northern hemisphere at mid- to high latitudes, the damage to reinforced concrete structures caused by freeze-thaw cycles has attracted much attention for the past decades [3]. In America, many reinforced concrete structures were built in extremely cold areas and the FT process critically affects the mechanical behaviour of concrete [4]. In Canada, infrastructure has been rapidly deteriorating as a result of the cold weather conditions, such as FT cycles, deicing salt, and persistent cold weather [5]. In the cold areas of China, such as on the Tibetan Plateau, in Southwest China, and in

Xinjiang, concrete structures of reinforced concrete are subjected to freezing-thawing for long periods of time, and the daytime-night temperature variations are significant, which constitutes natural conditions for freeze-thaw cycles. China spans a vast territory, seasonal permafrost covers about 53% of China's area, and permafrost accounts for ~21.5% [6], where the permafrost is mainly distributed in the low- and midlatitude regions, known as the third pole of the world on the Qinghai-Tibet Plateau; thus, freeze-thaw cycles significantly contribute to the destruction of concrete. Freeze-thaw damage of concrete is mainly assessed according to the currently applicable durability codes. The degree of damage is quantified based on indices such as mass damage, compressive strength, and relative dynamic modulus of elasticity after freeze-thaw cycles [7, 8].

The quality of a concrete structure is closely related to its mechanical and physical properties. Among the physical properties of concrete, concrete strength is generally considered to be the most important characteristic. Many techniques have been proposed for evaluating concrete strength, but those traditional nondestructive testing methods cannot provide a full and reliable concrete strength evaluation. The ultrasonic pulse velocity method is widely used for studying the physical properties of concrete [9–17], which is used for assessing concrete strength, presence and nature of defects in concrete, and the concrete thickness, by observing the propagation speed of ultrasonic impulses, reflected pulses, and shock pulses through the concrete [18]. These methods are usually based on observing the pulse propagation speed, which is closely related to the physical properties and elastic modulus of concrete.

The method of ultrasonic pulse velocity is a method of measuring concrete strength. Because of its obvious advantage as a nondestructive testing (NDT) method, the ultrasonic pulse velocity method is widely used for studying the integrity and physical properties of concrete structures [9, 15, 17]. At the same time, the ultrasonic pulse velocity technology is one of the most commonly used NDT for determining the performance of concrete.

Antonaci studied the behaviour of the existing interfaces using the nonlinear ultrasonic nondestructive testing method and revealed the effectiveness of specimens with a discontinuity surface under a compression load in describing the mechanical evolution of concrete [19]. Dynamic modulus of elasticity (DME) is an indispensable and important factor for assessing the quality and performance of concrete structures [20, 21]. Ultrasonic pulse velocity is an available parameter for estimating the Poisson ratio and dynamic modulus of elasticity (DME) [22]. Wen and Li studied the dynamic modulus of elasticity (DME) of concrete using the compressive pulse velocity method [23]. Mardani-Aghabaglou et al. evaluated the frost resistance of high-content fly fume concrete and found that dynamic modulus of elasticity (DME) corresponds to the percentage of mass change during freeze-thaw cycles [24]. Trtnik et al. analysed the parameters affecting ultrasonic pulse speed-strength relationship in concrete and analysed the relationships between ultrasonic pulse speed, static and dynamic Young's moduli, and shear modulus [25]. Lei et al. measured

the thickness of the surface damage layer and the relative dynamic modulus of elasticity (RDME) of concrete using the ultrasonic pulse velocity method and effectively estimated the deterioration degree of concrete [26]. Yan predicted the service life of concrete under freeze-thaw action using ultrasonic pulse velocity [27].

NDT method of concrete with the P-pulse velocity method has been popular owing to its simplicity and low cost. Most countries have developed standardised testing procedures [28], where the concrete strength is evaluated using the pulse speed method, and a national standard is used for NDT of concrete [28]. Examples include the British 4408 standard [29]. In general, these tests nondestructively estimate the concrete strength, but other nondestructive testing methods are also used.

Considering the influence of prolonged FT cycles on the concrete project on Qinghai-Tibet Plateau, the impacts of three methods of protective inorganic coating of silica fume concrete mixed with high-permeability inorganic crystallisation water-repelling agents were studied in this work. The ultrasonic test and compressive strength test of concrete under FT cycles were conducted, and for all studied types of concrete, the dynamic elastic mechanical parameters of the concrete subjected to freeze-thaw treatment were inferred from the ultrasonic pulse velocity calculation. The mechanical properties and damage patterns of the three concrete types subjected to freeze-thaw treatment were obtained. These studies indicated inner-doped high-permeability inorganic crystalline waterproof agent silica-ash concrete with better antifreezing durability.

2. Materials Preparation and Methodology

2.1. Materials

2.1.1. Cement.
Portland 42.5R cement with a specific gravity of 3.15 g/cm³ and a specific surface area of 345 m²/kg was used and its chemical composition is shown in Table 1.

2.1.2. Natural Aggregate.
The fine aggregate is natural river sand of Tao River, with mud content less than 0.2%, and the coarse aggregate is hammer crushed stone of limestone quality, with a grain size of 5–20 mm.

2.1.3. Silica Fume (SF) and Plasticiser.
Silica fume with the average particle size of 0.10μm was used, whose chemical composition is listed in Table 2. The plasticiser of polycarboxylic acid high-efficiency water-reducing agent was used.

2.1.4. External Inorganic Coating Materials and Methods.
External inorganic coating materials are as follows: (1) XT-HPA environmental protection type high-permeability inorganic crystalline waterproofing agent (permeable type): it can penetrate into the concrete interior, forming a hydrophobic coating, making the concrete hydrophobic, and stopping the erosive media such as chloride ions and sulfate ions brought in by water; (2) XT-SS environmental surface sealer (sealing type): it can form a physical barrier to protect the concrete and effectively prevent the infiltration of various chloride ions, sulfate

TABLE 1: Chemical composition of cement (%).

Composition	CaO	SiO$_2$	Fe$_2$O$_3$	Al$_2$O$_3$	SO$_3$	MgO	K$_2$O
Cement (%)	62.28	21.08	3.96	5.47	2.63	1.73	0.80

TABLE 2: Chemical composition of SF (%).

Composition	SiO$_2$	Fe$_2$O$_3$	Al$_2$O$_3$	SO$_3$	MgO	K$_2$O	CaO
Cement (%)	93.70	0.80	0.30	0.50	0.20	0.30	0.20

ions, and other aggressive media brought in by water into the concrete; (3) XT-HPS environmental protection type high-permeability enhanced sealant (composite type): it can form both a dense coating on the surface and a hydrophobic coating in the infiltrated concrete; because this coating has both a physical barrier and a hydrophobic coating of dual protection, it has an excellent effect on preventing the entry of water and its corrosive media brought in.

The spraying method of inorganic coatings applied to concrete with polypropylene fibers is as follows: concrete specimens in the water after 28 days of natural maintenance are removed from the water to clean the surface impurities and natural drying after 24 hours, the use of water-filled pneumatic spray cans will be wet concrete surface, pay attention to the surface of concrete specimens which cannot have bright water, spray the entire concrete surface once XT-HPA environmental protection type high-permeability inorganic crystalline waterproofing agent, after the surface of concrete specimens dry, spray them again (Figure 1(a)). After an interval of 24 hours, the surface of concrete specimens were cleaned with water and sprayed with XT-SS environmental surface sealer once, and after the concrete specimens were naturally dried for 24 hours, various strength tests were conducted on them (Figure 1(b)). After all strength tests were completed, the concrete specimens will continue to be tested in the FT cycles and were in a water-filled condition during the FT cycles.

2.1.5. Other Materials. Lanzhou drinking water was used. The design parameters and external coating materials of concrete are listed in Table 3.

2.2. Freeze-Thaw Testing Process of Concrete. The freeze-thaw resistance of each group of concrete was tested according to GB/T50082-2009 [30]. Three $100\,mm \times 100\,mm \times 400\,mm$ specimens and twenty-seven standard cubic briquettes with a side length of 100 mm were prepared for each mix design. After 28 days in water, all specimens were inserted into the freeze-thaw testing machine, and the FT temperature was in the range from $-17 \pm 2°C$ to $8 \pm 2°C$. The average RDME and mass loss rates were detected every 50 cycles up to mass loss rate arrived at 5% or three hundred cycles.

2.3. NDT Using Ultrasonic Testing

2.3.1. The Device and the Principle of Ultrasonic Testing. The ultrasonic testing device was based on an RSM-SY5 (T) type nonmetallic sound pulse detector developed by Wuhan Geotechnical Institute of the Chinese Academy of Sciences, which was composed of a wire, an acoustic detector, a receiving transducer, and a transmitting transducer. The frequency of the compressive pulse transducer is 50 kHz, and the frequency of the shear pulse transducer is 200 kHz. The sampling interval was in the $0.1–200\,\mu s$ range, the recording length was in the 0.5–1 kμs range, the transmission voltage was 500 V/1000 V, the amplification gain was 100 dB, the transmission pulse width was in the $0.1–100\,\mu s$ range and was continuously adjustable, and the bandwidth of the frequency band was in the 0.3–300 kHz range. To make the test results comparable, the parameters of the acoustic detector were consistent throughout the entire test process. Compared with previously used instruments, the transducer frequency of the new ultrasonic detector RSM-SY5 (T) was lower and the pulse could penetrate thicker samples. Therefore, the samples were not subjected to slicing, the disturbance of the samples was smaller, the obtained data were more accurate, and the nondestructive testing results for the concrete samples and the comparison of the test result in terms of mechanical and physical properties of the concrete samples were facilitated.

The ultrasonic detector generated repetitive electric pulses and stimulated the emission transducer. The ultrasonic pulses emitted by the transmitting transducer were coupled to the tested sample, propagated in the sample, and then detected and converted into electrical signals by the receiving transducer. The electric signals were sent to the ultrasonic instrument and the waveforms were drawn and recorded by the instrument. Ultrasonic pulse propagation time in the sample is determined by the ultrasonic pulse propagation speed. To measure ultrasonic pulse propagation time correctly, it was necessary to correct the time of the sound propagation, to identify the type of the pulses, and to determine the first pulse.

The sound propagation time was calculated according to the following formula:

$$t = t_i - t_0 - t', \tag{1}$$

where t is the time of the sound propagation after correcting the measuring point (μs), t_i is the time of the sound propagation of the P-pulse and S-pulse before correcting the measuring point (μs), t_0 is the system delay time (μs), and t' is the correction for the time of the sound propagation (μs).

Therefore, the equations for determining the velocities of the P-pulse and shear pulse were as follows, respectively:

$$V_P = \frac{L}{t_P - t_0 - t'},$$
$$V_S = \frac{L}{t_S - t_0 - t'}, \tag{2}$$

where V_P is compressive pulse velocity (km/s), V_S is shear pulse velocity (km/s), L is test-piece length (mm), t_p is the sound propagation time of compressive pulse before correcting the measuring point (μs), and t_s is the time of the sound propagation of the S-pulse before correcting the measuring point (μs).

TABLE 3: Concrete mix proportions.

Strength grade	Sample	Cement (kg/m³)	Limestone (kg/m³)	Sand (kg/m³)	Water (kg/m³)	Silica fume (kg/m³)	Water-reducing agent (kg/m³)	XT-HPA material (kg/m³)	Water-binder ratio	External inorganic coating materials
C40	C40-A1-NCTC	418	999	785	176	22	2.2	2.2	0.4	XT-HPA + XT-SS
C40	C40-A2-NCTC	418	999	785	176	22	2.2	2.2	0.4	None
C40	C40-A3-NCTC	418	999	785	176	22	2.2	2.2	0.4	XT-HPS

FIGURE 1: Inorganic coating spraying of concrete. (a) Concrete samples and coating material; (b) concrete surface morphology after inorganic coating spraying.

2.3.2. Ultrasonic Testing Method. The propagation speed of ultrasonic pulses in the studied concrete samples was measured using an RSM-SY5 (T) nonmetallic acoustic detector, as shown in Figure 2. Because the attenuation of concrete is greater than that of other nonmetallic materials, the frequencies were in the 20–100 kHz range. The test procedure was as follows:

(1) Vaseline was used as a coupling medium to ensure good contact between concrete and sensors.

(2) The instrument parameters were set as follows. For the ultrasonic P-pulse velocity test, the sampling interval was 1 μs, the sampling length was 512 μs, the transmitted pulse width was 50 μs, and the emission voltage was low. For the ultrasonic S-pulse velocity test, the sampling interval was 0.5 μs, the sampling length was 512 μs, the transmitted pulse width was 50 μs, and the emission voltage was low. The calibration values of the instruments were set, respectively.

(3) When sampling, the transmitting transducer and the receiving transducer were pressed and stored when the waveform was stable, so that shear pulse velocity and compressive pulse velocity of concrete specimens with different mix ratios could be measured.

2.4. Compressive Strength Test. Cubic briquettes with 100 mm side lengths were used for concrete compressive strength testing, and there were three briquettes in each group. The test was conducted using a 2000-kN electrohydraulic servo-pressure testing machine (Figure 3); a detailed description can be found in "Standard of Test Methods for Mechanical Properties of Ordinary Concrete (GB/T50081-2002)" [31]. The loading speed was 0.20 MPa/s to the failure.

After 50 freeze-thaw cycles, a set of concrete briquettes was taken for measuring the compressive strength, and its average value (over the briquettes) was calculated.

3. Results and Discussion

3.1. Characteristics of Variation of Ultrasonic Pulse Velocity of Concrete during FT Cycles

3.1.1. The Decay Rate of Ultrasonic Compressive Pulse Velocity. We used the ultrasonic detector RSM-SY5 (T) to measure the ultrasonic compressive pulse velocity of the concrete specimens for different numbers of FT cycles, for calculating the decay of the compressive pulse velocity.

After every 50 FT cycles, the surface moisture was wiped from the tested concrete specimens, and ultrasonic compressive pulse velocity was measured according to the above-described method. Equation (3) was used for calculating the decay rate of the compressive pulse velocity of the concrete samples:

$$P_v = \frac{V_{P_0} - V_{P_n}}{V_{P_0}} \times 100\%, \qquad (3)$$

where P_v is the decay rate of compressive pulse velocity of concrete, V_{P_n} is the velocity of the compressive pulse after FT cycles (km/s), and V_{P_0} is the velocity of the compressive pulse before freeze-thaw cycles (km/s).

Figure 4 shows the variation of the compressive pulse velocity and its decay rate during 300 FT cycles for the tested concrete samples coated using three different methods as described above. As can be seen from Figure 4(a), the trends of the compressive pulse velocity for the three groups of tested concrete specimens (C40-A1-NCTC, C40-A2-NCTC, and C40-A3-NCTC (number of three groups of concrete mix ratio)) subjected to FT cycles were similar. In general,

(a)   (b)

FIGURE 2: Photograph of ultrasonic velocity tests. (a) Ultrasonic compressive pulse velocity test; (b) ultrasonic shear pulse velocity test.

FIGURE 3: MATEST digital display pressure tester.

(a)   (b)
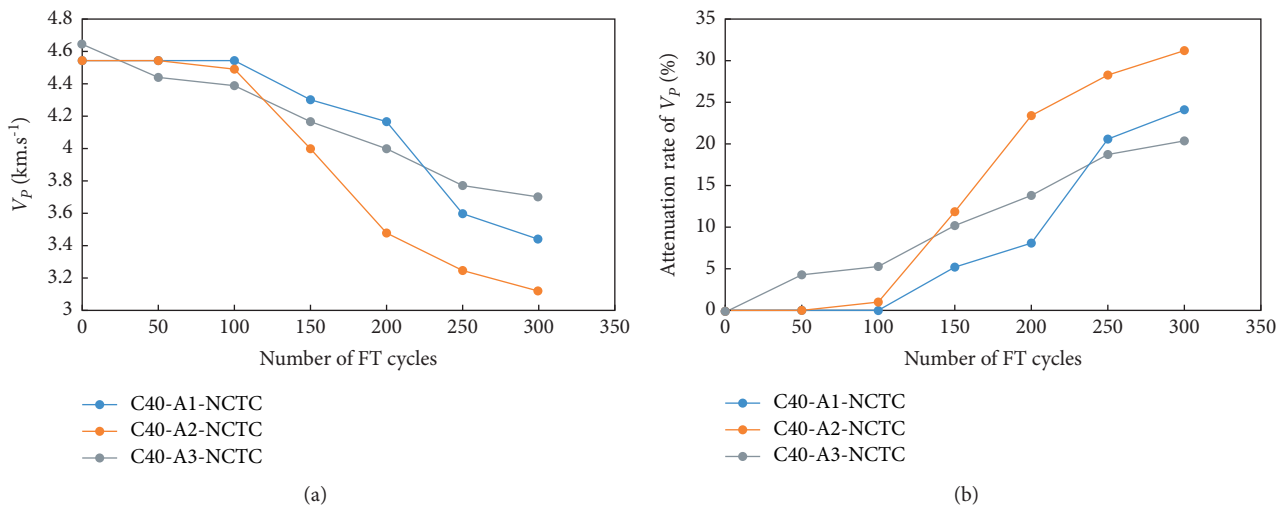
FIGURE 4: Variation characteristic of ultrasonic compressive pulse velocity and its decay rate of three kinds of concrete over 300 FT cycles. (a) Variation characteristic of ultrasonic compressive pulse velocity; (b) decay rate of ultrasonic compressive pulse velocity.

the compressive pulse velocity tended to decrease; the rate of attenuation was relatively slow during the first 100 FT cycles but then increased rapidly. The compressive pulse velocity and the attenuation rate during the FT cycles are shown in Figure 4(b) and Table 4.

From Figure 4(b) and Table 4, the initial P-pulse velocities for the three types of tested concrete samples are similar for no FT cycles, but the decay rates become different after 300 FT cycles. The concrete sample sprayed with the XT-HPA inorganic coating and the XT-SS inorganic coating

(C40-A1-NCTC) and concrete specimens sprayed with the XT-HPA inorganic coating (C40-A3-NCTC) exhibit smaller ultrasonic pulse velocity decay than unsprayed inorganic coated concrete specimens (C40-A2-NCTC), whose specific parameters are listed in Table 5.

The compressive pulse velocities for the three kinds of concrete specimens were close to those of the three groups of concrete samples before the FT treatment. Nevertheless, after 300 FT cycles, the compressive pulse velocities for group A (C40-A1-NCTC to C40-A3-NCTC) were 3.45 km/s, 3.13 km/s,

TABLE 4: Parameters of linear relationship between ultrasonic compressive pulse velocity and shear pulse velocity.

Specimen	a	b	Determination coefficient
All samples	0.6102	0.0713	0.9936
C40-A1-NCTC	0.6044	0.0977	0.9984
C40-A2-NCTC	0.6108	0.0692	0.9993
C40-A3-NCTC	0.6182	0.036	0.9679

TABLE 5: Variation characteristic in the ultrasonic compressive pulse velocity of three kinds of concrete under FT cycles.

Specimen	V_P at 0 FT cycles (km/s)	V_P at 300 FT cycles (km/s)	Decay rate of V_P (%)
C40-A1-NCTC	4.55	3.45	24.14
C40-A2-NCTC	4.55	3.13	31.24
C40-A3-NCTC	4.65	3.70	20.36

and 3.70 km/s, respectively. The decay rates of the compressive pulse velocities were 24.14%, 31.24%, and 20.36%, respectively, which was very different from the values for the other spraying methods. These results show that the external inorganic coating of concrete improves the antifreezing performance.

3.1.2. The Decay Rate of Ultrasonic Shear Pulse Velocity.
The ultrasonic detector RSM-SY5 (T) was used for measuring the ultrasonic shear pulse velocity of the tested concrete specimens, for different numbers of FT cycles.

After every 50 FT cycles, the surface moisture was wiped from the tested concrete samples, and the ultrasonic shear pulse velocity was measured according to the above-described test method. Equation (4) was used for calculating the attenuation rate of shear pulse velocity of concrete specimens:

$$S_v = \frac{V_{S_0} - V_{S_n}}{V_{S_0}} \times 100\%, \qquad (4)$$

where S_v is the decay rate of shear pulse velocity of a concrete specimen, V_{S_n} is shear pulse velocity after an FT cycle (km/s), and V_{S_0} is shear pulse velocity before the freeze-thaw cycle (km/s).

Figure 5 shows the variation of the shear pulse velocity and its attenuation rate during 300 FT cycles, to concrete specimens coated using three different methods. According to Figure 5(a), shear pulse velocity variations during the FT cycles are similar for three types of concrete (C40-A1-NCTC to C40-A3-NCTC) and all exhibit decreasing trends. The pulse velocity decay is slow in the first 100 FT cycles but decays rapidly after the first 100 FT cycles. Shear pulse velocities and decay rates during freeze-thaw cycles are shown in Figure 5(b) and Table 6.

From Figure 5(b) and Table 6, the initial shear pulse velocities of concrete with inorganic coatings are similar when no FT cycles are applied. After 300 FT cycles, the attenuation patterns of shear pulse velocity for three kinds of concrete become distinctly different. The concrete specimen sprayed with the XT-HPA inorganic coating and XT-SS inorganic coating with surface sealant (C40-A1-NCTC) and concrete specimen sprayed with the XT-HPA inorganic coating (C40-A3-NCTC) exhibit smaller shear pulse velocity decay than unsprayed inorganic concrete specimen (C40-A2-NCTC) with inorganic coating, whose specific parameters are listed in Table 6.

The variation of shear pulse velocities for three kinds of concrete is similar to that of compressive pulse velocities. The values are close for three kinds of concrete before FT treatment; however, after 300 FT cycles, shear pulse velocities for three types of concrete (C40-A1-NCTC to C40-A3-NCTC) are 2.18 km/s, 1.97 km/s, and 2.31 km/s, respectively, and the decay rates of shear pulse velocities are 23.33%, 30.49%, and 19.29%, respectively, which is very different from the values for other spraying methods. These results show that the external coating of inorganic coating improves the frost resistance of concrete.

3.2. Variation of the Kinetic Coefficient of Concrete during Freeze-Thaw Cycles

3.2.1. The Standard Method of Kinetic Parameters.
The dynamic elastic modulus E, the dynamic shear modulus G, and the Poisson ratio μ of concrete define its basic mechanical properties. At present, the methods for quantifying these three dynamic parameters mainly include the resonance column method, the pulse velocity method, and the dynamic three (single) test method. Compared with other methods, the pulse velocity method is simple, nondestructive, and fast; as a result, it is widely used for nondestructive testing of concrete. However, the existing pulse velocity method is mainly used for simple determination of the pulse velocity, but the dynamic elastic modulus, the dynamic shear modulus, and the pulse velocity ratio of concrete are less commonly quantified using the pulse velocity method. Based on the elastic theory, the measured P-pulse velocity V_P, the shear pulse velocity V_S, and the sample density ρ are used for determining these quantities of interest. The equations for computing the above three quantities are as follows:

$$E = \frac{\rho V_S^2 \left(3V_P^2 - 4V_S^2\right)}{V_P^2 - V_S^2}, \qquad (5)$$

$$G = \rho V_S^2, \qquad (6)$$

$$\mu = \frac{V_P^2 - 2V_S^2}{2\left(V_P^2 - V_S^2\right)}, \qquad (7)$$

where ρ is the tested sample's density (g/cm³).

(a)

(b)
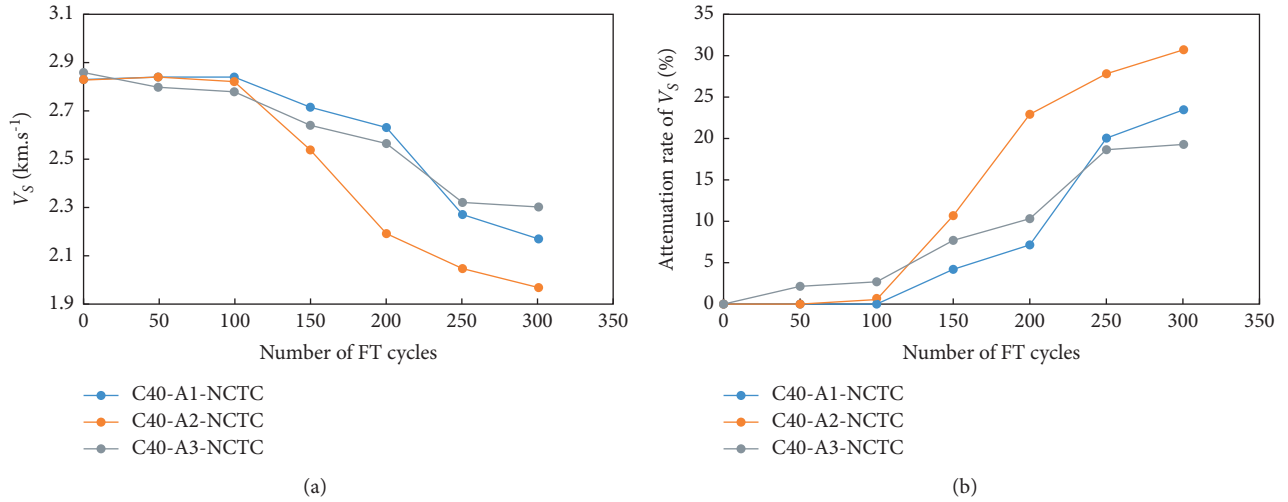
Figure 5: Variation characteristic of ultrasonic shear pulse velocity and its decay rate of three kinds of concrete over 300 FT cycles. (a) Variation characteristic of ultrasonic shear pulse velocity; (b) decay rate of ultrasonic shear pulse velocity.

Table 6: Variation characteristic in the ultrasonic shear pulse velocity of three kinds of concrete under FT cycles.

Specimen	V_S at 0 FT cycles (km/s)	V_S at 300 FT cycles (km/s)	Decay rate of V_S (%)
C40-A1-NCTC	2.84	2.18	23.33
C40-A2-NCTC	2.84	1.97	30.49
C40-A3-NCTC	2.86	2.31	19.29

The relationships between dynamic modulus of elasticity (DME) E, dynamic shear modulus (DSM) G, Poisson's ratio μ, and the number of FT cycles are shown in Figure 6. From Figure 6, the variation trends of DME E and DSM G of concrete with FT cycles are similar to ultrasonic pulse velocity under FT cycles; these quantities decrease with increasing FT cycles, and these trends become very clear after 100 FT cycles.

Figures 6(a) and 6(b) show the variation characteristics of DME and DSM, computed using ultrasonic pulse velocity method (equations (5) and (6)), for the three kinds of concrete specimens, during 300 FT cycles. Figure 6(c) shows the changes in the Poisson ratio for the three types of concrete specimens, during 300 FT cycles.

From Figure 6(a), DME for three types of concrete decrease relatively slowly during the first 100 freeze-thaw cycles, but the rate of attenuation increases after the first 100 freeze-thaw cycles. After 300 FT cycles, DME for three types of concrete (C40-A1-NCTC to C40-A3-NCTC) are 27.262 GPa, 22.458 GPa, and 31.541 GPa. Relative dynamic moduli of elasticity (RDME) are 57.81%, 46.22%, and 64.37%, respectively, which shows that both of the three concrete types reached the failure criterion; overall, the two types of concrete demonstrate poor antifreezing.

From Figures 6(a) and 6(b), variation characteristics of DME and DSM of concrete types during FT treatment are similar. The dynamic shear moduli for three kinds of concrete (C40-A1-NCTC to C40-A3-NCTC) decrease relatively slowly during the first 100 FT cycles, but the rate of attenuation is much higher after the first 100 FT cycles. After 300 FT cycles, the dynamic shear moduli for three concrete types (C40-A1-NCTC to C40-A3-NCTC) are 11.66 GPa, 9.61 GPa, and 13.32 GPa, respectively. The respective relative dynamic shear moduli are 59.18%, 48.18%, and 66.18%.

For three kinds of concrete, the Poisson ratio during FT treatment gradually decreases (Figure 6(c)).

3.2.2. Damage Amount. The damage amount D can describe the damage and performance degradation of concrete [32, 33], and the following equation is obtained using the dynamic elastic modulus concept:

$$D = \frac{E_0 - E_t}{E_0}, \tag{8}$$

where E_0 is initial DME (GPa) and E_t is DME after FT treatment (GPa).

Figure 7 shows the relationship between the number of FT cycles and the damage amount, for the three types of concrete. From Figure 7, the relationship between the number of FT cycles and the amount of damage to the concrete differs depending on the type of concrete coating. During the first 100 FT cycles, the damage amount for the three types of concrete is small, and the amount of damage actually decreases for two of three kinds (C40-A1-NCTC and C40-A2-NCTC), which suggests that a small number of FT cycles can increase the strength of concrete. Beyond 100 FT cycles, the damage amount for the three groups of samples increases rapidly, and the damage amount for C40-A2-NCTC is the greatest.

After 300 FT cycles, the damage amount for three kinds of concrete samples is as follows: C40-A1-NCTC < C40-A3-NCTC < C40-A2-NCTC.

(a)

(b)

(c)
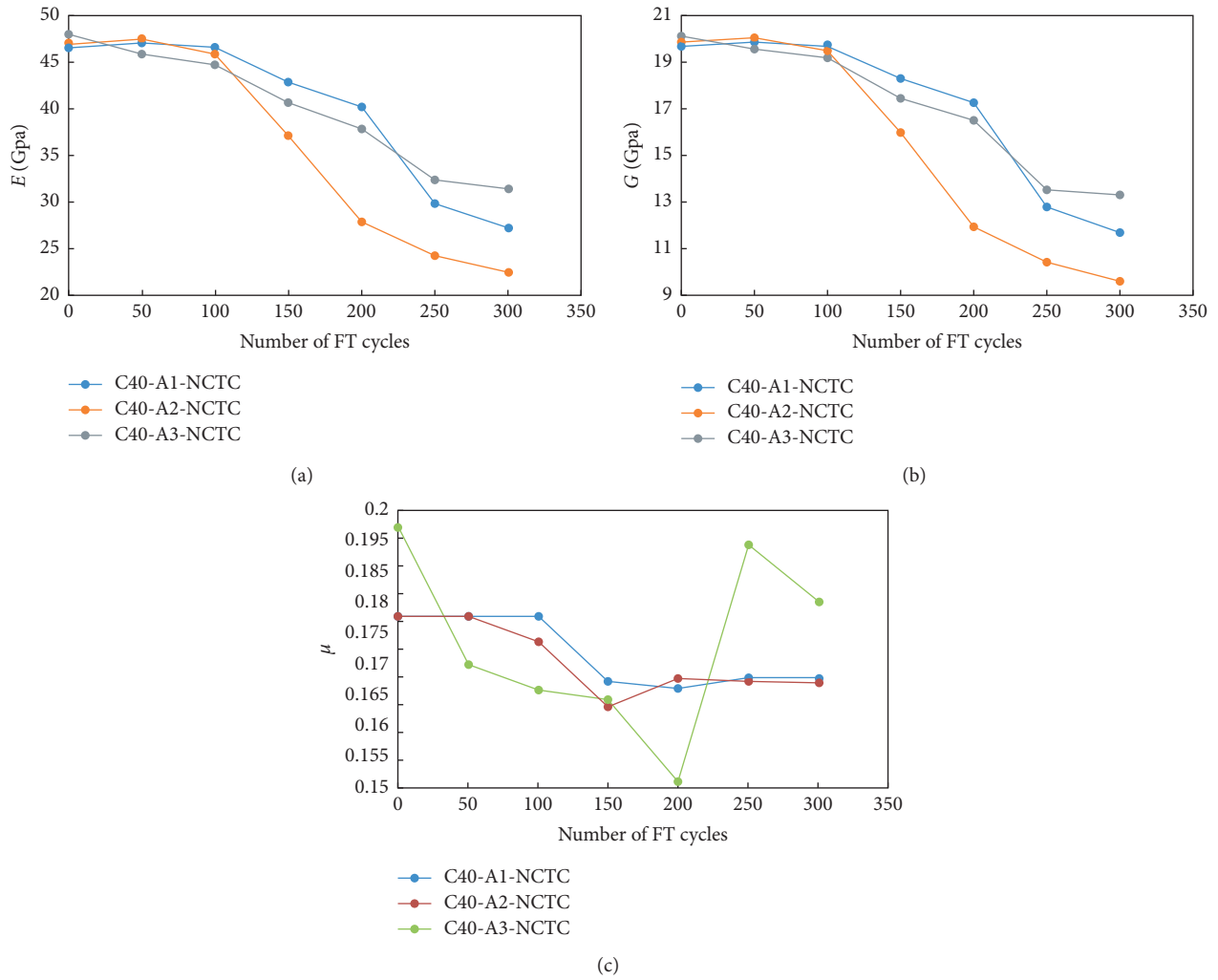
Figure 6: Variation characteristic of DME, DSM, and Poisson's ratio of three kinds of concrete over 300 FT cycles. (a) Variation characteristic of DME; (b) variation characteristic of DSM; (c) variation characteristic of Poisson's ratio.
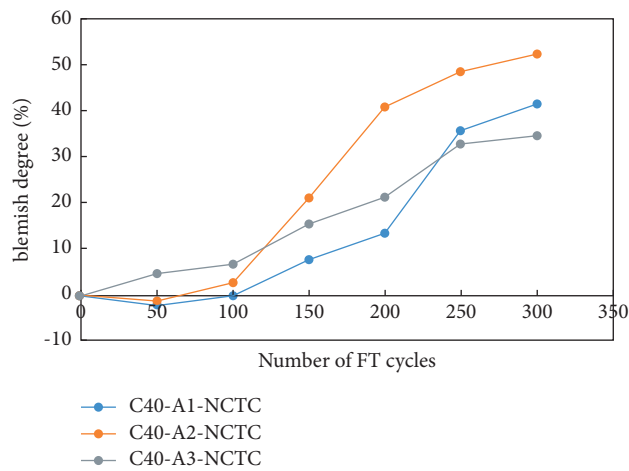
Figure 7: The relationship curve between the damage amount of three kinds of concrete and the number of FT cycles.

3.3. Mass Loss of Concrete with External Inorganic Coating during FT Treatment.

Figure 8 indicates variation characteristics of mass loss for concrete subjected to the freeze-thaw treatment. From Figure 8, during the first 100 FT cycles, the mass loss of concrete is small. Nevertheless, after the first 100 FT cycles, loss rate of mass becomes much smaller, with mass loss rates for the three types of concrete being 1.73% (for C40-A1-NCTC), 1.47% (for C40-A2-NCTC), and 0.44% (for C40-A3-NCTC). The trends of the mass loss and the damage amount were similar for the three types of concrete. However, the failure standard of GB/T 50082-2009 has not been met for the mass loss [30], which suggests that coating enhances the bonding properties of concrete to a certain extent, helping to reduce its mass loss.

3.4. Loss Rate of Compressive Strength.

According to GB/T 50082-2009 [30], the compressive strength per 50 FT cycles was tested for three kinds of concrete. The formula for calculating the loss rate p of the concrete compressive strength was

$$p = \frac{f_0 - f}{f_0} \times 100\%, \tag{9}$$

where p is the loss rate of the compressive strength of concrete, f is the compressive strength of concrete after the freeze-thaw treatment (MPa), and f_0 is the initial compressive strength of concrete without the freeze-thaw treatment (MPa).

Figures 9 (a) and 9(b) show variations in the compressive strength and the loss rate of the compressive strength for three kinds of concrete subjected to FT treatment. These figures show that, for the three types of concrete subjected to the freeze-thaw treatment, the loss rate of the compressive strength of concrete is similar to that of damage amount and attenuation rate of ultrasonic pulse velocity, which shows that the loss rate of the compressive strength of concrete increases linearly with increasing the number of freeze-thaw cycles. The loss rates of the compressive strengths for the two types of concrete (C40-A1-NCTC and C40-A2-NCTC) decrease somewhat during the first 150 FT cycles and then increase sharply. After 300 FT cycles, the compressive strengths for the three types of concrete (C40-A1-NCTC to C40-A3-NCTC) were 52.37 MPa, 50.00 MPa, and 54.24 MPa, respectively. The respective loss rates of the compressive strength were 21.66%, 25.02%, and 19.11%.

Figure 9(c) shows an example image of concrete failure following the compressive strength test after 300 FT cycles, which shows good cementing performance.

After 300 FT cycles, the relative dynamic moduli of elasticity for two of the three concrete types are below 60%, which meets the national standard of failure, for which the loss rate of the concrete compressive strength should be above 19.00%. However, the compressive strength was still above 50.00 MPa, which is much higher than the national standard for C40 concrete. This observation shows that concrete with inorganic coating has good frost resistance, and it also suggests that there are some limitations on the standard of the relative dynamic elastic moduli under 60%.
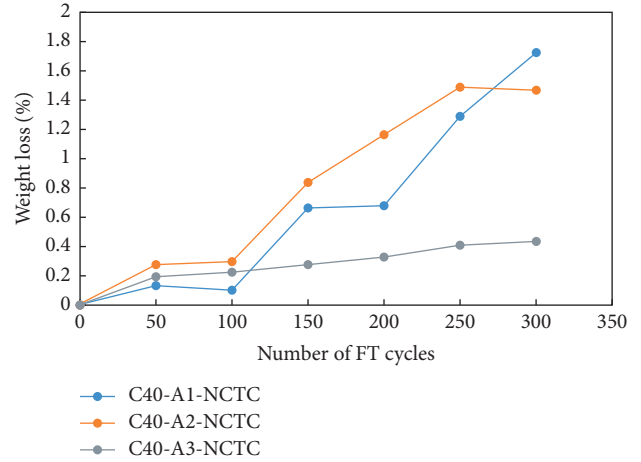
FIGURE 8: Weight loss of three kinds of concrete specimens under FT cycles.

3.5. Relationship between the Ultrasonic Shear Pulse Velocity, Dynamic Coefficient, Compressive Strength, and Ultrasonic Compressive Pulse Velocity for Concrete Subjected to the Freeze-Thaw Treatment.

The relationships between the ultrasonic shear pulse velocities, the dynamic coefficients, the compressive strengths, and the ultrasonic compressive pulse velocities for the three kinds of concrete subjected to FT treatment were gained using the linear regression analysis. The relationships were modelled as follows:

$$\begin{aligned} V_S &= aV_P + b, \\ E &= a'V_P + b', \\ G &= AV_P + B, \\ f &= A'V_P + B', \end{aligned} \tag{10}$$

where a, b, a', b', A, B, A', and B' are correlation coefficients, which are related to the mixing proportions of concrete materials. In this test, the values of the concrete correlation coefficients (a, b, a', b', A, B, A', and B') for three kinds of concrete subjected to FT treatment are listed in Tables 4, 7–9, respectively.

The results in Tables 4 and 7–9 show that the linear regression model linking ultrasonic pulse velocity, dynamic coefficient, compressive strength, and ultrasonic pulse velocity of concrete yields the determination coefficient above 0.90. This suggests a good correlation between the ultrasonic pulse velocity and the dynamic elastic modulus and provides the basis for further studies on the relationship between the strength of concrete estimated using the ultrasonic method and FT cycles.

Figure 10(a) shows the ratio of ultrasonic shear pulse velocity V_S to compressive pulse velocity V_P, for 21 concrete specimens subjected to FT treatment. The ratio of ultrasonic shear pulse velocity V_S to compressive pulse velocity V_P for concrete subjected to FT treatment is mainly distributed between 0.61 and 0.63.

Figure 10(b) shows the ratio of dynamic shear modulus G to dynamic elastic modulus E, for 21 concrete samples subjected to the FT treatment. The ratio of dynamic shear

(a)

(b)

(c)

(c)
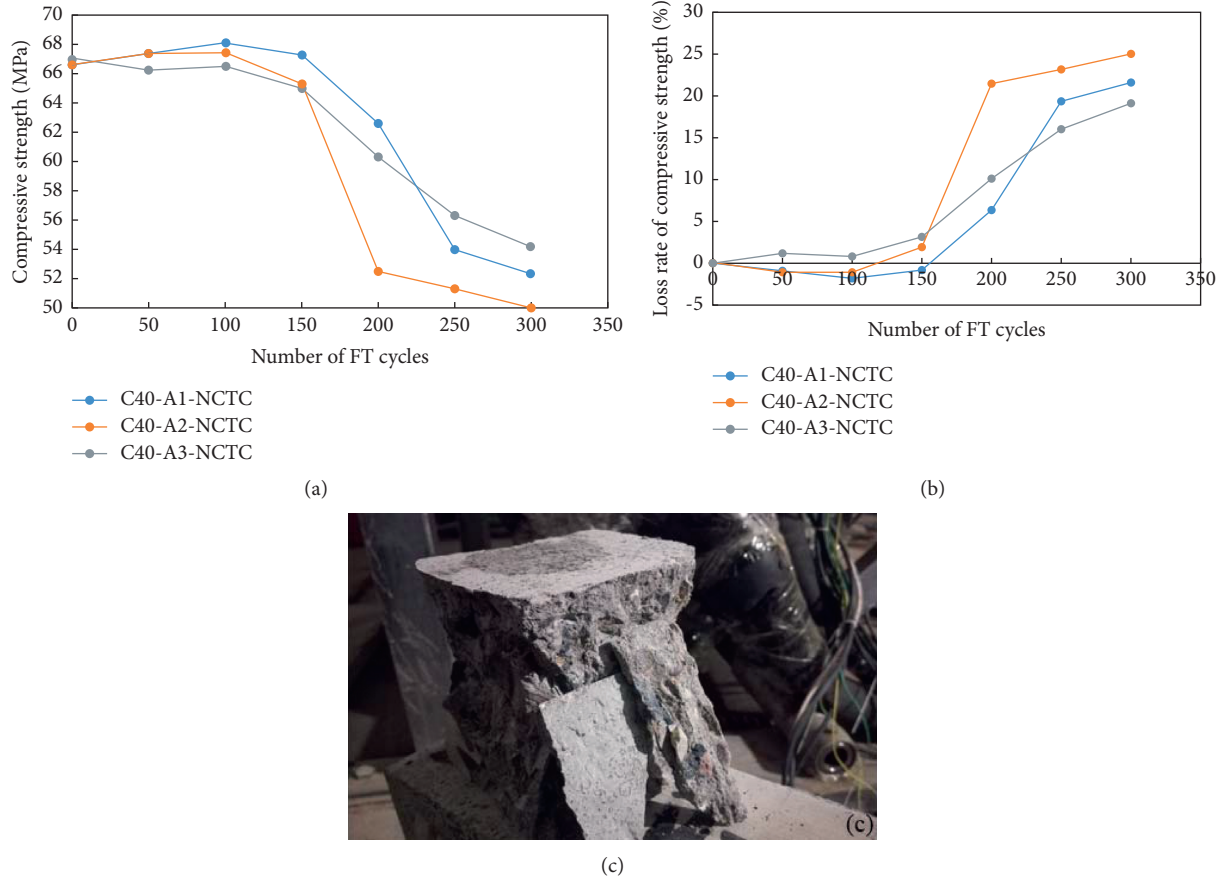
FIGURE 9: Variation curve of compressive strength and the loss rate of compressive strength of three kinds of concrete during FT cycles. (a) Variation characteristics of compressive strength; (b) loss rate of compressive strength; (c) failure image of concrete after compressive strength test.

TABLE 7: Parameters of linear relationship between ultrasonic compressive pulse velocity and dynamic modulus of elasticity.

Specimen	a'	b'	Determination coefficient
All samples	17.775	−33.762	0.9969
C40-A1-NCTC	17.913	−34.501	0.9988
C40-A2-NCTC	17.594	−32.909	0.9991
C40-A3-NCTC	18.435	−36.495	0.9894

TABLE 8: Parameters of linear relationship between ultrasonic compressive pulse velocity and dynamic shear modulus.

Specimen	A	B	Determination coefficient
All samples	7.4618	−13.95	0.9924
C40-A1-NCTC	7.4878	−14.118	0.9975
C40-A2-NCTC	7.3929	−13.626	0.9994
C40-A3-NCTC	7.7563	−15.169	0.9656

TABLE 9: Parameters of linear relationship between ultrasonic compressive pulse velocity and compressive strength.

Specimen	A'	B'	Determination coefficient
All samples	13.269	7.515	0.9359
C40-A1-NCTC	14.361	2.8576	0.9636
C40-A2-NCTC	12.814	9.8827	0.9408
C40-A3-NCTC	14.169	3.2907	0.9084

(a)

(b)

(c)
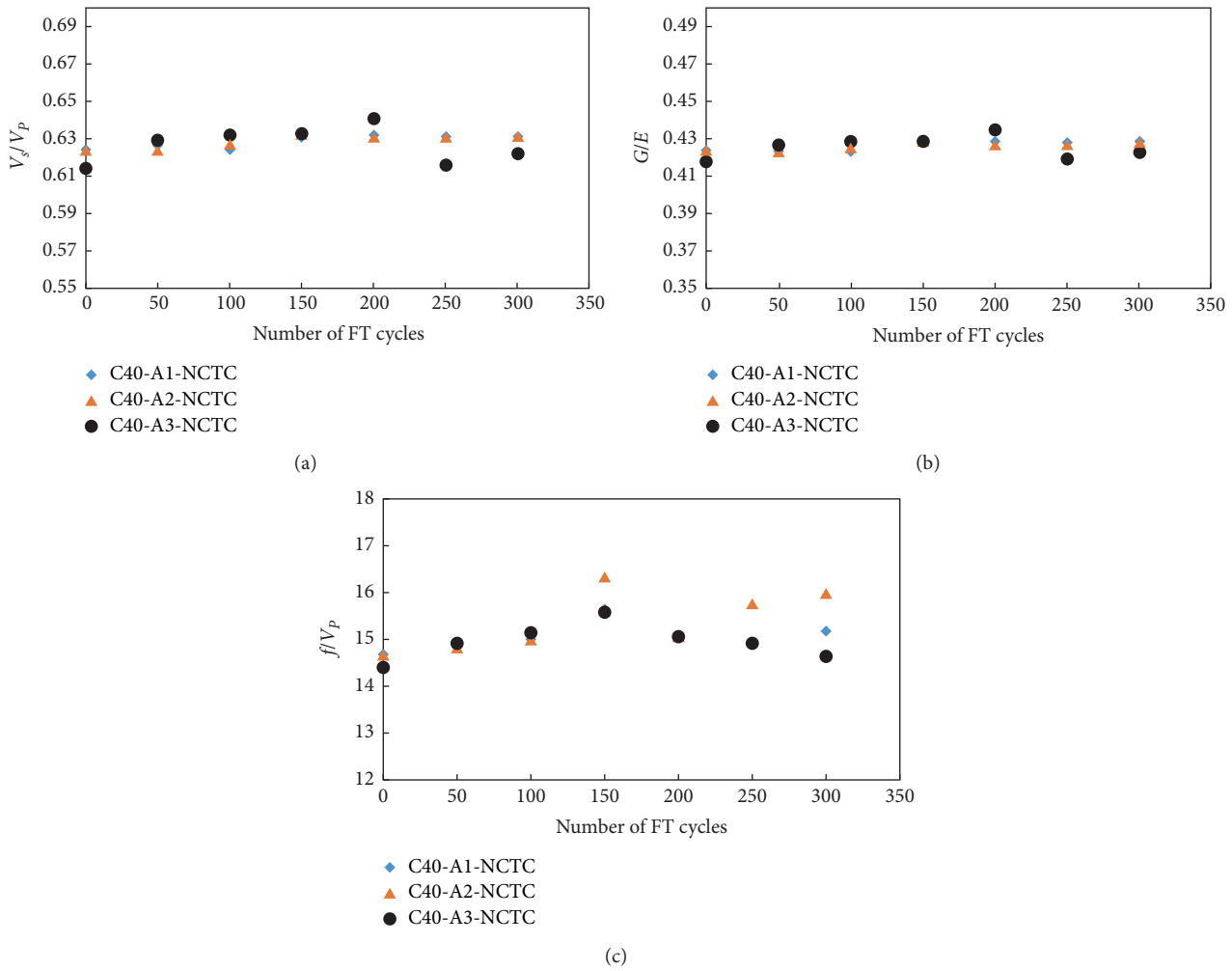
FIGURE 10: The ratio of dynamic strength to compressive pulse velocity of concrete under FT cycles. (a) V_S/V_P; (b) G/E; (c) f/V_P.

modulus G to dynamic elastic modulus E for concrete subjected to the freeze-thaw treatment is mainly distributed between 0.42 and 0.43.

Figure 10(c) shows the ratio of concrete compressive strength f to compressive pulse velocity V_P, for 21 concrete samples subjected to FT treatment. The ratio of the compressive strength f to the compressive pulse velocity V_P for concrete subjected to FT treatment is mainly distributed between 14.6 and 16.0. There is significant discreteness, which indicates that individual briquette characteristics significantly affect the compressive strength, but there is still a good correlation between the concrete compressive strength and its compressive pulse velocity.

3.6. Strength Attenuation Mechanisation of Concrete under FT Cycles. Frost damage is due to several pore pressures caused by ice formation, that is, hydraulic pore pressure due to ice volume expansion and crystallisation and low-temperature water absorption pressure due to thermodynamic equilibrium between ice crystals and thawing water. It has also been observed that only highly saturated concrete can be damaged by frost. It can be found that the strength of concrete attenuates with the increase of freeze-thaw times, especially after 100 FT cycles. Because the freeze-thaw cycle adversely affects the strength of concrete decreasing with the increase of freeze-thaw cycles, the ultrasonic pulse velocity and compressive pulse velocity of concrete decrease with the increase of the number of freeze-thaw cycles. As for the slow attenuation of strength before 100 FT cycles, it should be that the concrete is still hydrated in the early freeze-thaw cycle, so the strength also increases. However, after 100 hydration reactions, freezing and thawing lead to a rapid decrease in strength.

4. Conclusions

In this study, the rapid freeze-thaw cycle test of internal coating silicon fume concrete with different external coatings was carried out, the strength evolution law of concrete with different external inorganic coatings was analysed by ultrasonic testing and compressive strength, and the correlation between ultrasonic pulse velocity and physical mechanics was analysed. The following conclusions were obtained in this study through theoretical derivation and experimental examinations:

(1) The compressive strength and ultrasonic velocity of the studied concrete samples decreased gradually with increasing the number of freeze-thaw cycles, especially after the first 100 FT cycles. As for the slow attenuation of strength before 100 FT cycles, it should be that the concrete is still hydrated in the early FT cycle, so the strength also increases. But after 100 hydration reactions, freezing and thawing lead to a rapid decrease in strength.

(2) The trends for dynamic elastic modulus E and dynamic shear modulus G versus the number of FT cycles were similar to that of ultrasonic pulse velocity. Both moduli decreased with increasing FT cycles and also decreased dramatically after the first 100 FT cycles. For the three types of concrete, the Poisson ratios gradually decreased with increasing FT cycles.

(3) The amount of damage to the three types of concrete samples was small during the first 100 FT cycles, but after the first 100 FT cycles, the amount of damage increased rapidly. The amount of damage to the concrete samples without external coating increased sharply after the first 100 FT cycles. The damage amount to the external coating material (XT-HPA plus XT-SS and XT-HPS) of concrete was small, and the performance of the concrete samples after the freeze-thaw treatment was good, which shows good frost resistance durability. After 300 FT cycles, the damage amount for three kinds of concrete was as follows: C40-A1-NCTC < C40-A3-NCTC < C40-A2-NCTC. The respective relative dynamic elastic moduli (C40-A1-NCTC, C40-A2-5NCTC, and C40-A1-NCTC) are 57.81%, 46.22%, and 64.37%, which shows that two of the three concrete types reached the failure criterion; overall, the two types of concrete demonstrate poor antifreezing.

(4) Following the freeze-thaw treatment, the ratio of the pulse velocity V_S to the P-pulse velocity V_P of the concrete samples was mainly between 0.61 and 0.63. The ratio of the dynamic shear modulus G to the dynamic elastic modulus E was mainly distributed between 0.42 and 0.43. The ratio of the compressive strength f to the P-pulse velocity V_P of concrete subjected to the freeze-thaw treatment was mainly distributed between 14.6 and 16.0. There was a good correlation between these quantities.

(5) The relationship between ultrasonic pulse velocity and intensity of concrete was well-described by a linear function, and the coefficient of determination of the linear regression fit was above 0.90, indicating a good correlation between the ultrasonic pulse velocity and concrete intensity. Thus, the strength of concrete can be estimated by measuring its ultrasonic pulse velocity.

Data Availability

The underlying data supporting the results of this study are included within this article.

Conflicts of Interest

The authors declare that they have no conflicts of interest.

References

[1] D. Gui-Zhen and F. Cong-Qi, "Research progress and new thinking of destruction of concrete due to freeze-thaw cycles," *Concrete*, vol. 12, no. 5, pp. 16–20, 2013, in Chinese.

[2] P. K. Mehta, "Concrete durability-fifty year's progress," in *Proceedings of the 2nd International Conference on Concrete Durability, ACI*, pp. 11–31, Montreal , Canada, August 1991.

[3] R. Terje Finnerup, "Freeze-thaw resistance of concrete effect of curing conditions, moisture exchange and materials," PhD dissertation, Trondheim: Norwegian Institute of Technology, Trondheim, Norway, 2001.

[4] Y. Frank, "Damage assessment, characterization, and modeling for enhanced design of concrete bridge decks in cold regions," PhD dissertation, Department of Civil and Environmental Engineering, North Dakota State University, Fargo, ND, USA, 2015.

[5] G. Mark, J. S. Dent Aaron, and A. Bisby Luke, "Effect of freeze-thaw cycling on the behavior of reinforced concrete beams strengthened in flexure with fiber reinforced polymer sheets," *Canadian Journal of Civil Engineering*, vol. 30, no. 6, pp. 1081–1088, 2011.

[6] Y. Zhou, "Frozen Soil in China," Science Publishing House, New York City, NY, USA, 2000.

[7] X. X. Wang, X. D. Shen, H. L. Wang, and C. Gao, "Nuclear magnetic resonance analysis of concrete-lined channel freeze-thaw damage," *Ceramic Society of Japan*, vol. 123, pp. 43–51, 2015.

[8] X. Wang, Y. Wu, X. Shen, H. Wang, S. Liu, and C. Yan, "An experimental study of a freeze-thaw damage model of natural pumice concrete," *Powder Technology*, vol. 339, pp. 651–658, 2018.

[9] R. S. Ravindrarajah, "Strength evaluation of high-strength concrete by ultrasonic pulse velocity method," *NDT & E International*, vol. 30, no. 4, pp. 262–275, 1997.

[10] A. Galan, "Estimate of concrete strength by ultrasonic pulse velocity and damping constant," *ACI Journals*, vol. 64, no. 10, pp. 678–684, 1967.

[11] R. Solís-Carcaño and E. I. Moreno, "Evaluation of concrete made with crushed limestone aggregate based on ultrasonic pulse velocity," *Construction and Building Materials*, vol. 22, no. 6, pp. 1225–1231, 2008.

[12] ACI 228.2R-98. Nondestructive test methods of evaluation of concrete in structures. ACI Committee 228.

[13] M. Sansalone and W. B. Streett, *Impact-echo Nondestructive Evaluation of Concrete and Masonry*, Bullbrier Press, Ithaca, NY, USA, 1997.

[14] W. F. Price and J. P. Haynes, "In situ strength testing of high strength concrete," *Magazine of Concrete Research*, vol. 48, no. 176, pp. 189–197, 1997.

[15] S. Nazarian, M. Baker, and K. Crain, "Assessing quality of concrete with wave propagation techniques," *ACI Materials Journal*, vol. 94, no. 35, pp. 296–305, 1997.

[16] Y. Wu-Jian, N. Fu-Jun, W. Zhi-Jian, N. Fuhang, L. Zhanju, and N. Zuojun, "Mechanical property of polypropylene fiber reinforced concrete under freezing-thawing cycle effect," *Journal of Traffic and Transportation Engineering*, vol. 16, no. 4, pp. 37–44, 2016.

[17] P. Turgut, "Research into the correlation between concrete strength and UPV values," *Non-Destructive Testing*, vol. 12, no. 12, pp. 56–63, 2004.

[18] A. Iwatake, "Nondestructive testing on concrete pavements by ultrasonic wave," in *Proceedings of the 3rd International Conference on NDT*, Tokyo, Japan, 1960.

[19] P. Antonaci, C. L. E. Bruno, P. G. Bocca, M. Scalerandi, and A. S. Gliozzi, "Nonlinear ultrasonic evaluation of load effects on discontinuities in concrete," *Cement and Concrete Research*, vol. 40, no. 2, pp. 340–346, 2010.

[20] A. Kar, U. B. Halabe, I. Ray, and A. Unnikrishnan, "Nondestructive characterizations of alkali activated fly ash and/or slag concrete," *European Scientific Journal*, vol. 9, no. 24, pp. 187–195, 2013.

[21] G. Singh and R. Siddique, "Effect of waste foundry sand (WFS) as partial replacement of sand on the strength, ultrasonic pulse velocity and permeability of concrete," *Construction and Building Materials*, vol. 26, no. 1, pp. 416–422, 2012.

[22] L. Qixian and J. H. Bungey, "Using compression wave ultrasonic transducers to measure the velocity of surface waves and hence determine dynamic modulus of elasticity for concrete," *Construction and Building Materials*, vol. 10, no. 4, pp. 237–242, 1996.

[23] S.-Y. Wen and X.-B. Li, "Experimental study on Young's modulus of concrete," *Journal of Central South University of Technology*, vol. 7, no. 1, pp. 43–45, 2000.

[24] A. Mardani-Aghabaglou, Ö. Andiç-Çakir, and K. Ramyar, "Freeze-thaw resistance and transport properties of high-volume fly ash roller compacted concrete designed by maximum density method," *Cement and Concrete Composites*, vol. 37, pp. 259–266, 2013.

[25] G. Trtnik, F. Kavčič, and G. Turk, "Prediction of concrete strength using ultrasonic pulse velocity and artificial neural networks," *Ultrasonics*, vol. 49, no. 1, pp. 53–60, 2009.

[26] J. Lei, N. Di-Tao, S. Ying-Zhao, and F. Qian-Nan, "Ultrasonic testing and microscopic analysis on concrete under sulfate attack and cyclic environment," *Journal of Central South University*, vol. 21, pp. 4723–4731, 2014.

[27] W. Yan, Z. Wu, F. Niu, T. Wan, and H. Zheng, "Study on the service life prediction of freeze–thaw damaged concrete with high permeability and inorganic crystal waterproof agent additions based on ultrasonic velocity," *Construction and Building Materials*, vol. 259, pp. 1–13, 2020.

[28] K. Komlos, S. Popovics, T. Nu¨rnbergerova´, B. Babál, and J. Popovics, "Ultrasonic pulse velocity test of concrete properties as specified in national standards," *Cement and Concrete Composites*, vol. 18, pp. 357–364, 1996.

[29] BS 4408, *Non-destructive Methods of Test for Concrete Measurement of the Ultrasonic Pulses Velocity in Concrete*, British Standard Institute, London, UK, 1970.

[30] Ministry of Housing and Urban-Rural Development of the People's Republic of China, GB/T 50082–2009, *Standard for Test Methods of Long-Term Performance and Durability of Ordinary Concrete*, China Construction Industry Press, Beijing, China, 2009, in Chinese.

[31] Ministry of Housing and Urban-Rural Development of the People's Republic of China, GB/T 50081–2002, *Standard of Test Methods for Mechanical Properties of Ordinary Concrete*, China Construction Industry Press, Beijing, China, 2002, in Chinese.

[32] Z. Lixiang, W. Shichao, and Z. Zaodong, "Analysis of reliability confidence limits of fatigue damage strength of concrete," *Engineering Mechanics*, vol. 21, no. 4, pp. 139–143, 2004, in Chinese.

[33] Y. Tianqing and Q. Jicheng, *The Theory and Application of Blemish*, National Defense Industry Press, Beijing, China, 1991, in Chinese.

Research Article

Study on the Performance and Adhesion Behavior of Ultrathin Wearing Course Using Calcined Bauxite as Aggregate

Yanping Sheng [iD],[1] **Runzhi Wang,**[1] **Haichuan Jia** [iD],[1] **Wenli Qiu,**[2] **Lei Feng,**[2] **Shaobo Zhang,**[2] **Shian Cui,**[1] **and Xiaorui Zhao**[1]

[1]*School of Material Science and Engineering, Chang'an University, Xi'an 710064, China*
[2]*Hebei Xiong'an Jingde Expressway Co., Ltd., Xiong'an, Hebei 071700, China*

Correspondence should be addressed to Yanping Sheng; shengyanping2003@163.com and Haichuan Jia; hcjia1117@163.com

An ultrathin wearing course is an effective maintenance treatment for prolonging the service life of asphalt pavements, which have been widely used in the field of pavement construction and road maintenance. However, the repeated vehicle load and wear results in a decreased durability of ultrathin wear course cover pavement. Hence, the gradation of ultrathin wear course was designed using calcined bauxite in this study, and the water stability, low-temperature properties, resistance to permanent deformation, and salt erosion were investigated through a laboratory test. Results indicated that the addition of a nonammonia antistripping agent significantly improves the water stability of the asphalt mixture with calcined bauxite and its ability to resist salt erosion as well as improve its low-temperature deformation ability. At the same time, polyphosphoric acid improves the adhesion between asphalt and calcined bauxite aggregate and the high-temperature performance of asphalt mixture but has limited improvement in water stability and resistance to salt erosion. This research is conducive to the widespread use of calcined bauxite aggregates in road pavements and is of great significance for improving the durability of ultrathin wear course asphalt pavements.

1. Introduction

The ultrathin wear course is suitable for the maintenance and transformation of various asphalt pavement, cement pavement, bridge deck, and tunnel. The unique structure of the ultrathin wear course could be directly overlaid onto the pavement without milling, while hardly having a significant impact on the auxiliary structure and drainage of the asphalt pavement [1–3]. At the same time, the weight of the wear course mixture was reduced due to the ultrathin course structure, and the weight increase of the wear course mixture for bridge load was negligible when used for bridging deck overlays. The application of ultrathin course in road pavement has many advantages, such as improving the smoothness of the road surface, increasing the antiskid performance of the road surface, and reducing the driving noise. The surface abrasion courses, as a structural course directly in contact with passing vehicles and the natural environment, require sufficient structural strength, stability,

durability, surface smoothness, and surface antiskid performance. Ultrathin wear course is a satisfactory method in highway preventive maintenance, which affects driving safety and comfort during road service [4–6]. However, as the influence of load, light, precipitation, and climate changes, its durability decreases, and its service life dropped to less than ten years. Moreover, the current service level of the ultrathin wear course during the service period is low, such as poor flatness, fast antiskid attenuation, and loud driving noise, which not only reduces driving comfort but also increases noise pollution and traffic safety [7–11]. Therefore, it should not only meet the structural performance requirements but also have sufficient flatness, antiskid performance, wear resistance, low noise, and other functional properties.

Wan et al. [12] proposed that steel slag was used to design an ultrathin wear course for road maintenance with the function of melting ice and snow. The effect of steel slag was characterized by measuring the corresponding

induction temperature rise and effective induction heating depth. The results showed that steel slag improved the induction heating performance of the pavement friction course. Compared with the hot mix mixture, the steel slag-based mixture has sufficient volume and durability. At the same time, the addition of steel slag also improved the ice and snow melting efficiency of the road friction course. Hu et al. [13] showed that the porous ultrathin wear course is an effective preventive maintenance measure that can improve road performance and extend service life. Due to the high porosity of the porous asphalt mixture, it provides high drainage capacity and reduces noise, water skiing, water splashing, and spraying. However, the high porosity of this mixture also results in a decrease in strength and looseness resistance compared to densely graded wear courses. Deng et al. [14] developed an ultrathin wear course with high slip resistance and wear resistance using polyurethane as a bonding agent. Experiments and molecular dynamics simulation methods were used to study the properties and nanoadhesion behavior of polyurethane cardboard. The grey correlation method was used to further analyze the relationship between the mechanical properties of aggregates and the antiskid performance of the pavement. The results showed that cemented carbide pavement bricks using emery with a particle size of 2-3 mm as aggregate exhibit better wear resistance and slip resistance, as well as higher structural stability. Yu et al. [15] proposed a new type of ultrathin asphalt overlay design program, "high-toughness ultrathin friction course." The material properties were optimized and construction technology was designed through laboratory and field tests to evaluate the mechanical and functional properties. The results showed that the high-toughness ultrathin friction course exhibits excellent antislip and noise reduction functions. In addition, the enhancement of the coarse aggregate interlocking and the increase of the asphalt film made it more resistant to fatigue cracking. Amel et al. [16] added nanomontmorillonite materials to asphalt binder, improving the resistance to permanent deformation of asphalt pavements. The test results showed that the asphalt mixture prepared by asphalt containing 3% nanomontmorillonite has the best resistance to permanent deformation. However, the ultrathin wear course also has some technical defects that need to be solved urgently. The reduction in the thickness of the structure leads to the tensile stress at the bottom of the asphalt surface layer, the fatigue damage rate of the structure course, and the increase in the interlayer shear force. The traditional wear course is more prone to fatigue cracking, rolling, peeling, and other diseases [17–20].

The objective of this paper is to study the performance and adhesion behavior of ultrathin wear course using calcined bauxite as aggregate. In this paper, the calcined bauxite ultrathin wear course was designed, and then the high-temperature stability, crack resistance, water stability, and interlayer adhesion of the bauxite antiskid wear course were investigated using the rutting test, low-temperature bending test, water stability test, salt spray erosion test, salt spray-dynamic water flushing test, oblique shear test, and pullout test. The result showed that the water stability, low-

temperature deformation ability, and ability to resist salt erosion were improved by adding calcined bauxite with nonammonia antistripping agent and polyphosphoric acid. This study provides the widespread use of calcined bauxite aggregates in road pavements, improving the durability of ultrathin wear course asphalt pavements.

2. Materials and Methods

2.1. Materials

2.1.1. Asphalt and Aggregate. SK-90 matrix asphalt was used in this study, and its technical indicators are shown in Table 1. Bauxite aggregates, granite, and limestone aggregates are also used, with their chemical compositions shown in Table 2. The physical technical indicators of 90# calcined bauxite are shown in Table 3, and finely ground limestone powder was used as mineral powder. According to the SMA-5 gradation requirements, the required ratio of aggregates for each grade was determined. The synthetic gradation of the three aggregates meets the requirements.

2.1.2. Fiber Stabilizer and Admixture. Fiber stabilizer has a very significant effect on the performance of SMA asphalt mixture, choosing high-quality lignin fiber is of great significance to the design of SMA asphalt mixture, and its technical indicators are shown in Table 4. The selected additives are nonammonia antistripping agents and polyphosphoric acids. SBS adopts a YH-791 (1301) modifier produced by Sinopec Baling Petrochemical, and the mixing amount is 4% when modifying asphalt. The rubber powder modifier used waste heavy-duty vehicle tires as raw materials and was pulverized at room temperature to prepare the rubber powder. The dose of ammonia antistripping agent was 2.0% and the dose of polyphosphoric acid was 1.5%.

2.2. Methods

2.2.1. Rutting Test. The high-temperature stability of asphalt mixture is defined as the ability of asphalt mixture to resist high-temperature diseases such as rutting, waves, shifting, and crowding under long-term vehicle load under the condition of high road temperature (above 60°C). The rutting test is used to evaluate the high-temperature stability of the asphalt mixture. The test time is about 1 h, and the rut depth reaches 25 mm. Record the rut deformation d_1 and d_2 at 45 min and 60 min, respectively, to an accuracy of 0.01 mm. The dynamic stability of asphalt mixture is calculated according to formula (1):

$$\mathrm{DS} = \frac{(t_2 - t_1) \times N}{d_2 - d_1} \times C_1 \times C_2, \tag{1}$$

where DS is the dynamic stability of asphalt mixture (times/mm); d_1 is the amount of deformation with loading time t_1; d_2 is the amount of deformation with loading time t_2; C_1 is the type coefficient of testing machine; C_2 is the specimen coefficient; N is the return rolling speed of test wheel.

TABLE 1: Technical properties of SK-90# asphalt binder.

Item		Unit	Result	Technical requirements	Specification
Penetration (25°C, 100 g, 5 s)		0.1 mm	92	80 ~ 100	ASTM D5-97
Ductility (10°C)		cm	>100	≥45	ASTM D113-99
Softening point		°C	48.3	≥45	ASTM D36-06
Density (15°C)		g/cm³	0.981	—	ASTM D70-76
RTFOR (163°C, 75 min)	Penetration ratio (25°C)	%	71.3	≥57	ASTM D5-97
	Mass loss	%	−0.26	≤±0.8	ASTM D2872-04
	Ductility (10°C)	%	14	≥8	ASTM D113-99

TABLE 2: Chemical composition of aggregate.

Aggregate	The content of component (%)										
	SiO_2	TiO_2	Al_2O_3	TFe_2O_3	MnO	MgO	CaO	Na_2O	K_2O	P_2O_5	LOI
Calcined bauxite	6.74	3.21	86.48	1.55	0.01	0.12	0.72	<0.01	0.15	0.23	0.55
Granite	66.64	0.38	15.94	2.7	0.16	0.05	3.71	4.41	1.86	0.11	0.01
Limestone	6.65	0.038	0.68	0.21	0.004	0.71	51.1	0.03	0.15	0.013	0.01

TABLE 3: Technical indexes of bauxite aggregate.

Item	Unit	Technical requirements	Result	Specification
Crush value, ≯	%	26	7.74	T0316
Los Angeles wear value, ≯	%	28	10.61	T0317
Apparent density, ≮	—	2.60	3.28	T0304
Water content, ≯	%	2.0	1.463	T0304
Needle flake content, <	%	1	0.54	T0310

TABLE 4: Technical indexes of fiber.

Item	Ash content (%)	PH value	Oil absorption	Water content
Requirements	18 ± 5	7.5 ± 1.0	—	<5
Result	16.8	7.5	5.6	3.1

2.2.2. Low-Temperature Bending Test. Asphalt mixtures with strong ultimate deformability under low-temperature conditions have good low-temperature viscosity and plasticity. The ultimate flexural strain at low temperatures can be used to evaluate the low-temperature performance of asphalt mixtures. The low-temperature bending test is used to evaluate the low-temperature crack resistance of the SMA-5 calcined bauxite asphalt mixture, and the bending tensile stress, strain, and stiffness modulus are calculated by formulae (2)–(4).

$$\sigma_0 = \frac{3LF_0}{2bh^2} \times 10^{-6}, \tag{2}$$

$$\varepsilon = \frac{6h \, d}{L^2}, \tag{3}$$

$$\varepsilon = \frac{6h \, d}{L^2}, \tag{4}$$

where L is the span, mm; b and h are the width and height of the trabeculae; d is the deformation at failure (deflection in the middle of the span), mm; F_0 is the failure load, N.

2.2.3. Water Stability Test. Moisture damage is one of the main damage methods of asphalt pavements. Under the action of the vehicle's dynamic load, the water entering the gap of the pavement produces hydrodynamic pressure and the repeated action of vacuum suction and the freeze-thaw cycle. The speed of the aggregate interface causes the asphalt film to peel off the surface of the stone, forming potholes, crowding and deformation, and other damage phenomena on the asphalt pavement. The water stability of the SMA-5 calcined bauxite asphalt mixture was evaluated by the water immersion Marshall test and freeze-thaw splitting test.

2.2.4. Salt Spray Erosion Test. The salt spray erosion is used to simulate the chloride salt corrosion of the test specimen in the outdoor environment. The salt spray test box is used and the corrosion medium is clean water and a 5% NaCl solution. Put the Marshall specimens into the test box, and perform the water immersion Marshall test and freeze-thaw splitting test after 3 days, 6 days, and 9 days of erosion.

2.2.5. Salt Spray-Dynamic Water Flushing Test. The salt spray erosion is used to simulate the chloride salt corrosion of the test specimen in the environment. The salt spray test box is used and the corrosion medium is clean water and a 5% NaCl solution. Marshall specimens were put into the test box and erode for 3 days, 6 days, and 9 days. When the dynamic water scouring test is carried out, the scouring medium is clean water. Pour the above-configured solution into the bucket and make the water surface cover the test piece. The water temperature and hydrodynamic pressures were set to 30°C and 0.2 MPa, respectively, because a large number of studies showed that the hydrodynamic pressure is closely related to the speed of the vehicle. As the speed of the vehicle increases, the hydrodynamic pressure also rises geometrically. When the vehicle travels at a speed of 60 km/h, the hydrodynamic pressure generates approximately 0.2 MPa. The number of scouring specimens was set to 6000 times, and each group included five parallel test specimens. After different times of scouring, the Marshall specimen was taken out, the splitting strength and Marshall stability were measured, and the ratios of splitting strength and Marshall stability before and after scouring were calculated.

2.2.6. Oblique Shear Test and Pullout Test. The thickness of the ultrathin wear course is 1.5~2.5 cm. The construction was carried out after the ordinary asphalt mixture surface course was laid. Therefore, due to the insufficient interlayer adhesion performance under the load and shear of the vehicle, the interlayer slippage or even slippage will be caused. Studies have shown that the maximum tensile stress of the ultrathin wear course is the transverse tensile stress, and the maximum shear stress is the transverse shear stress, which mainly occurs at the bottom of the ultrathin wear course. The interlayer oblique shear test and the interlayer pullout test were used to evaluate the interlayer bonding performance of the ultrathin wearing course and the asphalt pavement.

For the failure load of the oblique shear test, the shear strength of the specimen can be calculated according to

$$\tau = \frac{P}{A} \sin \alpha, \tag{5}$$

where τ is the shear strength of the specimen (MPa); P is the failure load (kN); A is the shear surface area (m^2); α is the shear angle (°).

3. Results and Discussion

3.1. High-Temperature Performance. The results of the high-temperature rutting test are shown in Table 5. The high-temperature dynamic stability of the SMA-5 calcined bauxite asphalt mixture is much higher than the specified index, because the high-temperature stability of the asphalt mixture mainly comes from the cohesiveness and adhesion of the asphalt binder. SMA-5 has a dense skeleton structure, and with interembedded skeletons in the mixture and since calcined bauxite aggregates are broken aggregates and are more likely to form good intercalation, SMA-5 calcined

bauxite asphalt mixture has excellent resistance to load deformation. Moreover, under high-temperature conditions, the stiffness of asphalt mastic reduces the framework structure and can also improve the supporting effect, so it has excellent high-temperature resistance to rutting. The slight difference in dynamic stability is due to the fact that the nonammonia antistripping agent belongs to the organic solution, which would cause the asphalt to soften, resulting in the decrease of the high-temperature stability of the asphalt mixture. The addition of polyphosphoric acid would increase the viscosity of the asphalt and cause the asphalt to harden it, so the dynamic stability is improved.

3.2. Low-Temperature Performance. The low-temperature crack resistance test results are shown in Table 6, showing that the SMA-5 calcined bauxite asphalt mixture has excellent low-temperature crack resistance, because the low-temperature crack resistance of the asphalt mixture depends on the tensile strength of the asphalt binder. The selected SBS-modified asphalt has excellent tensile deformation ability, and the grading design of SMA ensures that the mixture of aggregates is filled with rich asphalt mastic, which is fully on the surface of mineral aggregates. Meanwhile, when the temperature drops, the asphalt mixture shrinks and deforms and causes aggregate separation, but the SBS asphalt mastic still has strong bonding ability, so the asphalt mixture as a result has excellent low-temperature crack resistance performance. The addition of nonammonia antistripping will cause the asphalt to soften, so the deformability is enhanced and the addition of polyphosphoric acid would increase the modulus of the asphalt, so the deformability would decrease.

3.3. Water Stability Test. The water stability test results of the SMA-5 calcined bauxite asphalt mixture using the water immersion Marshall test and freeze-thaw splitting test are shown in Table 7. The results show that the SMA-5 calcined bauxite asphalt mixture is water stable. The performance is also better due to two main reasons. The first is that the SBS-modified asphalt and 90# calcined bauxite aggregate have better adhesion and water damage resistance. The second is that the SMA asphalt mixture has a very small void ratio and poor water permeability, so the mixture is less affected by water. Furthermore, after adding the nonammonia antistripping agent, the water stability was greatly improved. Because the nonammonia antistripping agent is a surface modifier, which can better improve the adhesion of the asphalt and the calcined bauxite aggregate, it resists moisture damage. Also, when polyphosphoric acid is added, the water stability is much more improved, and the addition of polyphosphoric acid could promote the conversion of asphaltene, increase the polarity of the asphalt, and make polar aggregates absorption on the surface easier. It can be seen from the results that the quality of the aggregate itself is good, as well as the reasonable selection and mix ratio design of the asphalt, and as a result, the high-temperature performance, low-temperature performance, and water stability

TABLE 5: Results of rutting test.

Item	Dynamic stability	Deformation (45 min)	Deformation (60 min)
Without antistripping agent	6951	1.19	1.40
Antistripping agent	6872	1.21	1.43
Polyphosphoric acid	7104	1.17	1.37

TABLE 6: Results of trabecular bending test.

Item	Flexural tensile strength (MPa)	Maximum bending strain ($\times 10^{-6}$)	Modulus of flexural stiffness (MPa)
Without antistripping agent	11.51	5702	2018
Antistripping agent	11.26	5873	1917
Polyphosphoric acid	11.76	5507	2135

TABLE 7: Results of water stability test.

Item	TSR (%)	MS_0 (%)
Without antistripping agent	86.3	85.6
Antistripping agent	90.4	91.2
Polyphosphoric acid	87.7	86.9

of the SMA-5 ultrathin wear course asphalt mixture are excellent.

The salt spray erosion is used to simulate the chloride salt corrosion of the test piece in the outdoor environment. The salt spray test box is used with the corrosion medium being clean water and a 5% NaCl solution. The Marshall specimens were put into the test box, water immersion Marshall and freeze-thaw splitting tests were performed after 3 days, 6 days, and 9 days of erosion, and the relationship between salt spray erosion time and water stability test is shown in Figure 1. The freeze-thaw splitting strength ratio and the water-immersed Marshall strength ratio of the calcined bauxite both decrease with the extension of the salt spray erosion time, which is due to the salt spray erosion destroying the bonding interface between the asphalt and the calcined bauxite aggregate, thereby showing that it can improve the water stability of calcined bauxite asphalt mixture.

The relationship between the water stability test results and the water immersion tensile strength loss rate is shown in Figure 2. It can be seen that the water immersion tensile strength loss rate has a good correlation with the water stability of the asphalt mixture, because the deterioration of the mechanical properties of the asphalt mixture is mainly caused by the damage of the asphalt and bonding interface between the asphalt and the calcined bauxite aggregate under the conditions of water immersion and the softening of the asphalt. It is similar to the reduction mechanism of the tensile strength of asphalt and calcined bauxite aggregate under water immersion.

The salt spray erosion is used to simulate the chloride salt corrosion of the test piece in the field environment. The salt spray test box is used, and the corrosion medium is clean water and a 5% NaCl solution. The Marshall specimens were put into the test box and erode for 3 days, 6 days, and 9 days. When the dynamic water scouring test is carried out, the scouring medium is clean water. The standard Marshall specimens of the SMA-5 calcined bauxite were fixed with 50

times of double-sided compaction according to the above grading and curing for 24 hours at room temperature on the mold, and the above-mentioned solution was poured into the barrel ensuring that the water surface was just over the test specimens. The water temperature was set to 30°C and the hydrodynamic pressure was set to 0.2 MPa, because a large number of studies have shown that the hydrodynamic pressure is closely related to the speed of the vehicle. As the vehicle speed increases, the hydrodynamic pressure also rises geometrically. When the vehicle travels at a speed of 60 km/h, the hydrodynamic pressure generated is approximately 0.2 MPa. The number of scouring specimens was set to 6000 times, and each group included five parallel test specimens. After different times of scouring, the Marshall specimens were taken out, the splitting strength and Marshall stability were measured, and the splitting strength ratio before and after scouring as well as the Marshall stability ratio was calculated.

The relationship between salt spray erosion time and dynamic water erosion test results is shown in Figure 3. It can be seen from the results that, compared to the water stability test, the dynamic stability and split strength ratio of the calcined bauxite Marshall specimens after being washed by dynamic water show a greater decrease, and the drop rate is greater than that under clean water conditions. It was found that the addition of a nonammonia antistripping agent and polyphosphoric acid can significantly improve the ability of the calcined bauxite asphalt mixture to resist erosion and erosion by dynamic water. Furthermore, the improvement of the resistance to dynamic water erosion in the calcined bauxite asphalt mixture is greater with the addition of nonammonia antistripping agent than with the addition of polyphosphoric acid.

The relationship between the results of the scouring test and the loss of pullout strength in water is shown in Figure 4. It can be seen that the loss rate of pullout strength in water has a poor correlation with the results of the dynamic water scour test of asphalt mixture. This is because, during the
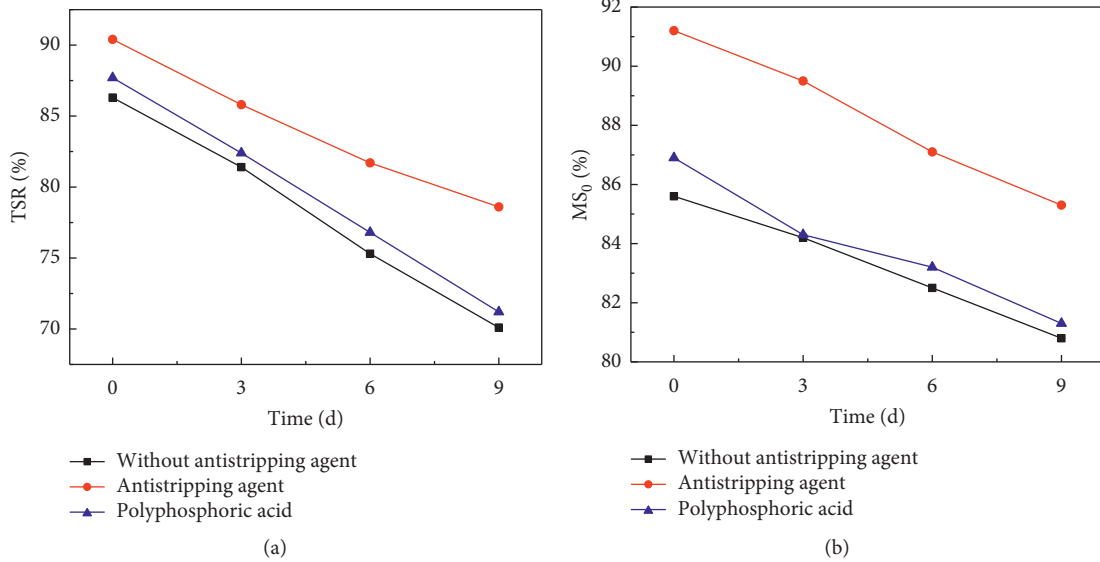
FIGURE 1: Relationship between salt spray erosion time and water stability test results. (a) TSR. (b) MS_0.
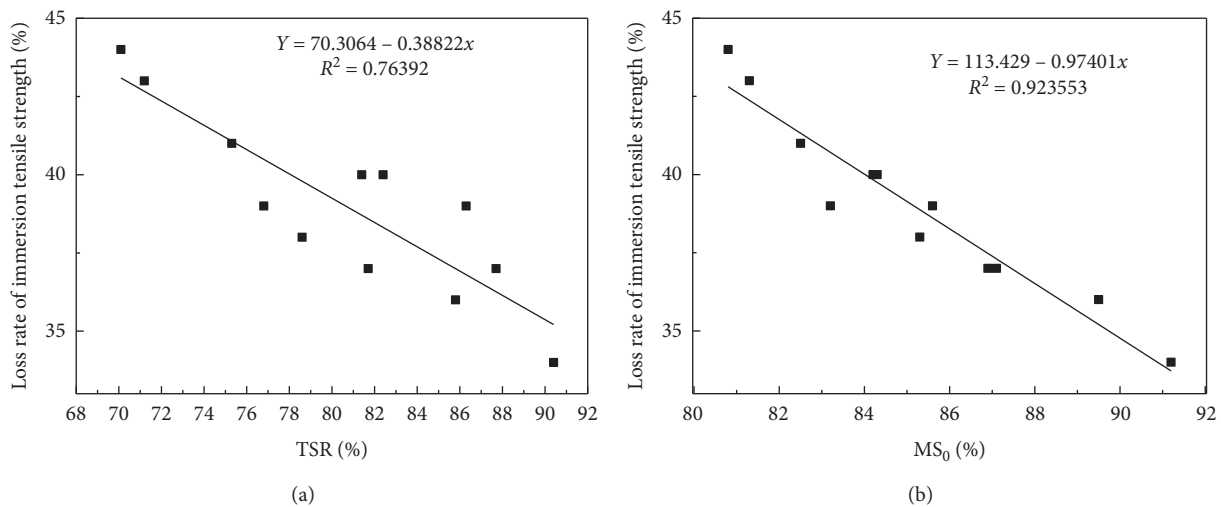
FIGURE 2: Relationship between water stability test results and water immersion tensile strength loss rate. (a) TSR. (b) MS_0.

process of dynamic water scour, there is not only water erosion and displacement but also dynamic water pressure scour. The joint action aggravated the destruction of the bonding interface between the asphalt and the calcined bauxite aggregate, while the water immersion pullout test only simulated the erosion under static water conditions, so the correlation between the two test results was poor.

3.4. Adhesion between Layer Tests. The results of the interlayer shear test are shown in Table 8. The results indicated that the use of different emulsified asphalt spreads between layers has a greater impact on the interlayer shear strength. SBS modified asphalt was used as the adhesive layer material to increase the shear strength of the layer frame is clear, because SBS-emulsified modified asphalt has higher

viscosity than base-emulsified asphalt, stronger tensile properties, and better interlayer bonding effect. The addition of admixtures to the asphalt mixture has little effect on the interlayer shear strength because the most important factors affecting the interlayer shear performance are the type and amount of emulsified asphalt. During the service of asphalt pavement, the contact state of the surface layer would change under the action of driving load, which would cause the stress redistribution of the internal structure of the pavement and may convert the compressive stress into tensile stress. Therefore, it is necessary to evaluate the pullout strength of the surface layer frame during the design of the ultrathin wear course. The results of the interlayer shear test are shown in Table 9. Similar to the layer frame shear strength, the use of SBS-emulsified modified asphalt could significantly improve the interlayer pullout strength, but the
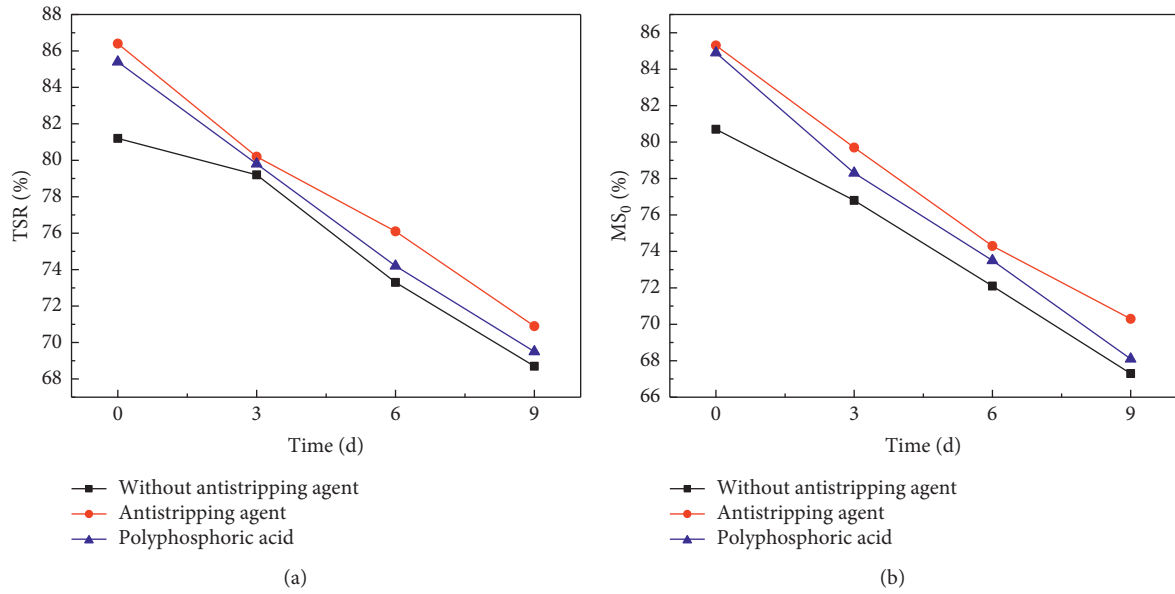
FIGURE 3: Relationship between salt spray erosion time and dynamic water erosion test results. (a) TSR. (b) MS_0.
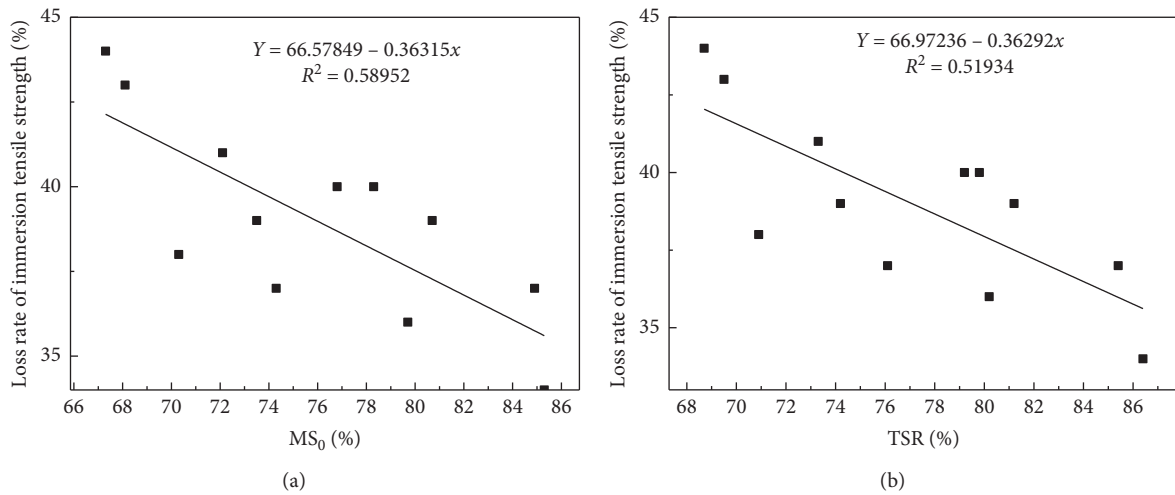
FIGURE 4: Relationship between the results of dynamic water scour test and the loss of tensile strength. (a) MS_o. (b) TSR.

TABLE 8: Results of interlayer shear test.

Item	Shear strength between layers (MPa)	
	Base-emulsified asphalt	SBS-emulsified asphalt
Without antistripping agent	2.21	2.65
Antistripping agent	2.17	2.69
Polyphosphoric acid	2.10	2.73

TABLE 9: Results of interlayer pullout test.

Item	Pullout strength between layers (MPa)	
	Base-emulsified asphalt	SBS-emulsified asphalt
Without antistripping agent	1.16	1.57
Antistripping agent	1.17	1.55
Polyphosphoric acid	1.12	1.52

interlayer pullout strength is much smaller than the interlayer shear strength, because in the shear failure process, the emulsified asphalt does have not only a cohesive effect but also an intermixing effect.

4. Conclusions

In this paper, the gradation design of the calcined bauxite asphalt mixture was carried out, subsequently, its road performance was tested, and the conclusions are as follows:

(1) Calcined bauxite asphalt mixture without an antistripping agent has good high-temperature stability, low-temperature crack resistance, and water stability, as well as good interlayer adhesion. It is recommended to use polyphosphoric acid to improve the adhesion between asphalt and calcined bauxite aggregate in high temperature, drought, and heavy traffic areas.

(2) The addition of a nonammonia antistripping agent can significantly improve the water stability of the calcined bauxite asphalt mixture and its ability to resist salt erosion and can soften the asphalt and improve its low-temperature deformation ability. The addition of polyphosphoric acid can improve the adhesion between asphalt and calcined bauxite aggregate and the high-temperature performance of asphalt calcined bauxite asphalt mixture but has limited effects in improving its water stability and resistance to salt erosion.

(3) The tensile strength loss rate of asphalt and calcined bauxite in water has a good correlation with the water stability of Marshall specimens at water immersion conditions. The tensile strength of the water immersion pull test can be used to evaluate the relationship between asphalt and aggregate adhesion. The water stability of the asphalt mixture is predicted by the loss rate of pullout strength in water.

(4) The bauxite can be used in asphalt mixtures instead of aggregates and has excellent performance, which is conducive to improving the durability of pavements. However, economics needs to be further considered to reduce costs.

Data Availability

The data used to support the findings of this study are included within the article.

Conflicts of Interest

The authors declare that they have no conflicts of interest.

Acknowledgments

References

[1] L. Geng, T. Ma, J. Zhang et al., "Research on performance of a dense graded ultra-thin wearing course mixture," *Applied Sciences*, vol. 7, no. 8, 2017.

[2] W. Cui, K. Wu, X. Cai et al., "Optimizing gradation design for ultra-thin wearing course asphalt," *Materials*, vol. 13, no. 1, 2020.

[3] H. Li, W. Wang, W. Li, A. Taoum, G. Zhao, and P. Guo, "Replacement of limestone with volcanic stone in asphalt mastic used for road pavement," *Arabian Journal for Science and Engineering*, vol. 44, no. 10, pp. 8629–8644, 2019.

[4] L. Cong, T. Wang, L. Tan, J. Yuan, and J. Shi, "Laboratory evaluation on performance of porous polyurethane mixtures and OGFC," *Construction and Building Materials*, vol. 169, pp. 436–442, 2018.

[5] F. Yang, H. Li, G. Zhao, P. Guo, and W. Li, "Mechanical performance and durability evaluation of sandstone concrete," *Advances in Materials Science and Engineering*, vol. 2020, no. 13, 10 pages, Article ID 241749, 2020.

[6] K. Krummenauer and J. J. de Oliveira Andrade, "Incorporation of chromium-tanned leather residue to asphalt microsurface layer," *Construction and Building Materials*, vol. 23, no. 1, pp. 574–581, 2009.

[7] Z. Qian and Q. Lu, "Design and laboratory evaluation of small particle porous epoxy asphalt surface mixture for roadway pavements," *Construction and Building Materials*, vol. 77, pp. 110–116, 2015.

[8] A. Vaitkus, T. Andriejauskas, V. Vorobjovas, A. Jagniatinskis, B. Fiks, and E. Zofka, "Asphalt wearing course optimization for road traffic noise reduction," *Construction and Building Materials*, vol. 152, pp. 345–356, 2017.

[9] Y. Sheng, H. Jia, H. Lv et al., "Study on mesoscopic mechanics of recycled asphalt mixture in the indirect tensile test," *Mathematical Problems in Engineering*, vol. 2020, Article ID 6621275, 12 pages, 2020.

[10] H. Li, F. Zhang, Z. Feng et al., "Study on waste engine oil and waste cooking oil on performance improvement of aged asphalt and application in reclaimed asphalt mixture," *Construction and Building Materials*, vol. 276, Article ID 122138, 2021.

[11] H. Ziari, A. Moniri, P. Bahri, and Y. Saghafi, "The effect of rejuvenators on the aging resistance of recycled asphalt mixtures," *Construction and Building Materials*, vol. 224, pp. 89–98, 2019.

[12] J. Wan, S. Wu, Y. Xiao et al., "Enhanced ice and snow melting efficiency of steel slag based ultra-thin friction courses with steel fiber," *Journal of Cleaner Production*, vol. 236, 2019.

[13] M. Hu, L. Li, and F. Peng, "Laboratory investigation of OGFC-5 porous asphalt ultra-thin wearing course," *Construction and Building Materials*, vol. 219, pp. 101–110, 2019.

[14] M. Deng, Y. Ding, Z. He et al., "Investigation on performance and nano-adhesion behavior of ultra-thin wearing course using polyurethane as binder," *Construction and Building Materials*, vol. 278, 2021.

[15] J. Yu, F. Chen, W. Deng et al., "Design and performance of high-toughness ultra-thin friction course in south China," *Construction and Building Materials*, vol. 246, 2020.

[16] A. Ameli, R. Babagoli, M. Khabooshani et al., "Permanent deformation performance of binders and stone mastic asphalt mixtures modified by SBS/montmorillonite nanocomposite," *Construction and Building Materials*, vol. 239, 2020.

[17] A. Ongel, K. Erwin, Q. Lu et al., "Comparison of surface characteristics and pavement/tire noise of various thin asphalt overlays," *Road Materials and Pavement Design*, vol. 9, no. 2, 2008.

[18] X. Hu, Y. Lei, H. Wang, P. Jiang, X. Yang, and Z. You, "Effect of tack coat dosage and temperature on the interface shear properties of asphalt layers bonded with emulsified asphalt binders," *Construction and Building Materials*, vol. 141, pp. 86–93, 2017.

[19] G. G. Al-Khateeb and A. Shenoy, "Mixture-property-independent asphalt film thickness model," *Materials Today Communications*, vol. 19, pp. 482–486, 2019.

[20] K. Sobban and M. Mashnad, "Tensile strength and toughness of soil-cement-fly-ash composite reinforced with recycled high-density polyethylene strips," *Journal of Materials in Civil Engineering*, vol. 14, no. 2, pp. 177–184, 2002.

Research Article

Study on the Mechanical Properties of Chlorine Saline Soil under the Interaction of Multiple Factors

Anhua Xu,[1] Pengcheng Wang [ID],[2] and Jianhong Fang[3]

[1]*Qinghai Communication Technical College, Xining, Qinghai 810003, China*
[2]*School of Civil Engineering, Qinghai University, Xining, Qinghai 810016, China*
[3]*Qinghai Research Institute of Transportation, Xining, Qinghai 810016, China*

Correspondence should be addressed to Pengcheng Wang; wpc0423@qq.com

The distribution of chlorine saline soils is extensive in Haixi region of Qinghai Province in Northwest China. Its natural and geographical conditions are unique, and the external environment varies greatly. To study the effects of variable external environment on the mechanical characteristics of chlorine saline soils, a number of unconsolidated undrained (UU) dynamic triaxial tests under different confining pressure, moisture content, and loading frequency were carried out. The dynamic stress–dynamic strain, failure strength, dynamic elastic modulus, and parameter of shear strength were analyzed. The triaxial test results demonstrated that the stress–strain curves of the soil were strain-hardening. The failure strength and dynamic elastic modulus increased with the increasing of confining pressure; the law with moisture content and loading frequency were inconsistent. The dynamic cohesion and dynamic friction angle increased with the increasing of loading frequency, but decreased with the increasing of moisture content. Besides, the significance analysis theory was used to analyze the effect degree of different factors. It found that the effects of confining pressure, loading frequency, and the interaction between confining pressure and frequency on mechanical characteristics were significant, but the moisture content had less effect.

1. Introduction

Saline soil is a special type of soil that distributes to various degrees in many countries and regions. Similarly, saline soil is also widely distributed in China which covers approximately a total area of 36.9 million ha, accounting for 4.88% of Chinese available land area [1]. Nearly 69.03% of saline soil is mainly distributed in Xinjiang, Shaanxi, Ningxia, Inner Mongolia, Gansu, and Qinghai. The saline soil in Qinghai is mainly distributed in the west of the extremely arid Qaidam Basin, the mid-lower reaches of the Huangshui River Basin to the east of Xining, and the Pingchuan Plain area [2].

In recent years, many studies have been performed to investigate the engineering characteristics of saline soil. The shear strength of saline soil increases with increasing salt content due to the presence of salt crystals in soil [3, 4]. Fang et al. [5] established a formula to describe salt expansion in soil containing sodium chloride and sodium sulfate through a combination of theory, salt swelling, and microscopic test. Zhang et al. [6] found that the shear stress–strain curve of the soil with high salinity showed stronger expansion and strain-softening behaviour due to an obvious change of temperature. Bing et al. [7] conducted a study on the influence of freeze–thaw cycles on the physical and mechanical properties of saline soil and showed that the samples had plastic failure after freeze–thaw cycles. Han et al. [8] studied the influence of the freeze–thaw cycle on the shear strength of saline soil in cold regions by triaxial compression test and proposed a reliable mathematical equation to describe the effect of interaction between freeze–thaw cycle and salt content on the maximum shear strength. Although the chloride salt does not chemically react with lime, its presence would increase the number of coarse particles in the soil and reduced the total surface area of the soil [9]. Liu et al. [10] demonstrated that the addition of lime in carbonate soil

would result in a strong exchange between anion and cation, and the structure of soil particles and pores would change. The unconfined compressive strength increased with the increase of lime content. Zhang et al. [11] performed a mass of unconsolidated undrained triaxial tests that indicated that the shear strength of saline soil decreased with increasing salt content, and the sustaining deterioration of the strength was due to the freeze–thaw cycle destroying the soil grain structure through microscopic analysis. Some studies have shown that the incorporation of fly ash and other materials would have a certain effect on the strength characteristics of saline soil [12, 13]. Lai et al. [14] and Lai et al. [15] studied, respectively, the effect of cooling rate on salt crystallzation and crystallzation deformation of saline soil under freezing and thawing, which would not only describe the effect of cooling rate on initial crystallization and expansion of salt, but also propose a dynamic model considering nucleation, molecular diffusion, and crystal growth. Zhang et al. [16] demonstrated that adding slaked lime and other materials could not only effectively reduce the amount of salt expansion, but also reduced the sensitivity of salt expansion, and the feasibility and rationality of improving coarse sulfate saline soil with inorganic binder were clarified. Al-Amoudi et al. [17] found the reason why the arid saline soil had stronger collapsibility, which was that the soluble salt in the soil was dissolved. Mishra et al. [18] analyzed the influence of salinity on soil shrinkage characteristic curve. The dynamic strength criterion of frozen sulfate silty clay under cyclic loading was proposed, and the method for determining the dynamic strength parameter was given by Zhao et al. [19]. The effects of temperature, loading frequency, and other factors on the dynamic strength and microstructure of saline soils were analyzed [20, 21].

The research results on the mechanical characteristics of saline soil are mostly concentrated on static conditions. But the saline soil of the roadbed not only bears the influence of changes in external factors such as temperature, but also sustains tens of thousands of traffic loading. Therefore, UU triaxial dynamic tests were developed on chlorine saline soil with different factors, and SPSS software was used for the significance test. The effect of single factor and interaction between factors on the mechanical characteristics of chlorine saline soil was analyzed. The results provided a useful reference for the engineering construction in the area of over-chlorine saline soil.

2. Materials and Methods

2.1. Materials of Chlorine Saline soil.

The chlorine saline soil for the test was taken from a highway in the Qarhan Salt Lake area of Qinghai Province, China. The area has a typical plateau continental climate. There is little precipitation, the rain and heat are in the same season, and the precipitation varies greatly with the spatial distribution in this area. The basic physical test was measured according to Test Methods of Soils for Highway Engineering [22], the particle-size grading curve was obtained by the sieving method, and the basic physical properties are shown, respectively, in Figure 1 and Table 1. A negative liquidity index indicated that the
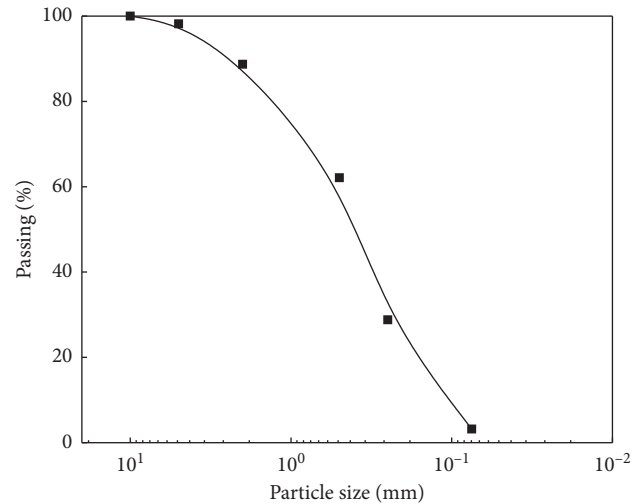
Figure 1: Particle-size curve of chlorine saline soil.

presence of crystalline salt in the soil makes the soil harder. The chemical composition analysis of chlorine saline soil was analyzed by ion chromatography, and the result is shown in Table 2. According to the Standard for Soil Test Method [23] and Specifications for Design of Highway Subgrades [24], the soil was characterized as a silty clay and over-chlorine saline soil, respectively.

2.1.1. Testing Equipment.

The test was completed by a dynamic triaxial test system of Global Digital Systems, shown in Figure 2, including three modules of advanced loading, dynamic loading, and triaxial acquisition. It can realize the control of various conditions, such as different confining pressure, frequency, and wave. The test data can be collected automatically with higher test precision.

2.1.2. Sample Preparation and Testing Method.

The saline soil sample needed to be dried and passed through a 2 mm sieve. The soil sample with the target moisture content was prepared according to the test requirements and stuffed for more than 12 h. The reshaped triaxial samples with a compacting degree of 95%, a diameter of 39.1 mm, and a height of 80 mm were prepared by 5-layer compaction with a three-part mold. The sinusoidal wave was applied to simulate traffic cyclic load through the stress control single-stage loading method, shown in Figure 3. The loading was terminated when the axial strain of the sample reaches 5% or the number of vibrations reaches 5000 [25]. Based on the analysis of the influencing factors of saline soil, the confining pressure, frequency, and moisture content were mainly considered in the test. The confining pressure was controlled at 200 kPa, 300 kPa, and 400 kPa. The frequency was controlled at 0.5 Hz, 1.0 Hz, and 2.0 Hz. The moisture content was controlled at 3.2%, 5.2%, and 7.2%. 20 kPa was taken as a dynamic stress amplitude according to the previous study [26]. The specific test plan design is shown in Table 3.

TABLE 1: Basic physical parameters of chlorine saline soil.

Liquid limit ω_L (%)	Plastic limit ω_P (%)	Plastic index IP	Liquid index I_L	Maximum dry density $\rho_{d\max}$ (g·cm^{-3})	Optimum moisture content ω_{opt} (%)
20.47	7.44	13.03	<0	1.81	5.20

TABLE 2: Chemical composition analysis of chlorine saline soil.

Anion (C) (%)				Cation (C) (%)			
Cl$^-$	SO$_4^{2-}$	CO$_3^{2-}$	HCO$_3^-$	Na$^+$	K$^+$	Ca^{2+}	Mg^{2+}
17.950	0.320	0.010	0.049	11.160	0.061	0.22	0.20
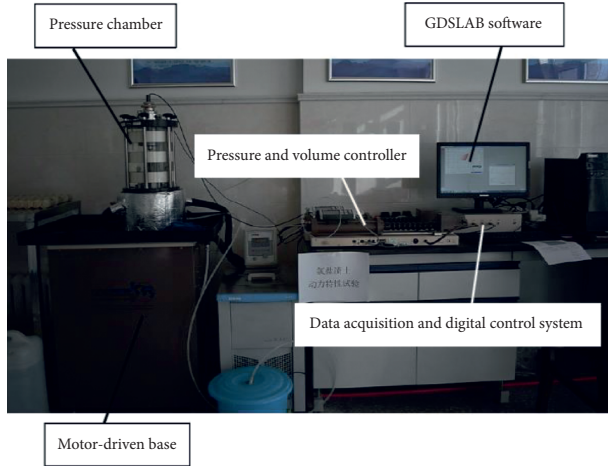
FIGURE 2: GDS dynamic triaxial test system.
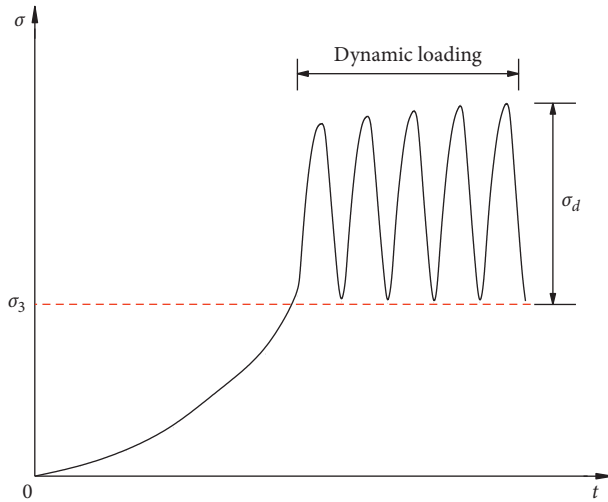
FIGURE 3: The curve of axial single-stage loading.

TABLE 3: Test plan design.

Confining pressure (kPa)	Moisture content (%)	Frequency (Hz)
200	3.2	0.5
300	5.2	1.0
400	7.2	2.0

2.1.3. Principle of Significance Test considering the Interaction between Factors. For saline soils with high salinity, the analysis of mechanical characteristics should not only take into account the particularity of the soil itself, but also the effect of moisture content, frequency, confining pressure, and other factors. In addition, the interaction between multiple factors should not be completely ignored. If there is no interaction between the influencing factors, the effect of a single factor can be studied separately and then superimposed. But if the interaction between multiple factors is obvious, the comprehensive effect of the interaction should be considered. The significance test can be used to study the influence of different factors on the mechanical characteristics of high-salinity soil. In other words, the F test is performed on mechanical parameters under a certain degree of confidence, so as to judge whether single-factor and multifactor interaction have a greater effect on mechanical characteristics in the test [27].

For the three factors A, B, and C, there are m, n, and r levels of each factor, respectively. An experiment is performed at each combined level (A_i, B_j, and C_k); the observed value of the test index can be obtained as x_{ijk}. The computational method of symbols is expressed in the following equations:

$$R = \sum_{i=}^{m} \sum_{j=1}^{n} \sum_{k=1}^{r} x_{ijk}^2, \tag{1a}$$

$$CT = \frac{1}{mnr} \left(\sum_{i=}^{m} \sum_{j=1}^{n} \sum_{k=1}^{r} x_{ijk} \right)^2, \tag{1b}$$

$$Q_A = \frac{1}{nr} \sum_{i=1}^{m} \left(\sum_{j=1}^{n} \sum_{k=1}^{r} x_{ijk} \right)^2, \tag{1c}$$

$$Q_B = \frac{1}{mr} \sum_{j=1}^{n} \left(\sum_{i=1}^{m} \sum_{k=1}^{r} x_{ijk} \right)^2, \tag{1d}$$

$$Q_C = \frac{1}{mn} \sum_{k=1}^{r} \left(\sum_{i=1}^{m} \sum_{j=1}^{n} x_{ijk} \right)^2. \tag{1e}$$

The sum of squares of the total variance is obtained by the following equation:

$$S_T = Q_T - CT. \tag{2}$$

The sum of squares of the variance of factors A, B, and C and error E are, respectively, calculated by the following equations:

$$S_A = Q_A - CT, \tag{3a}$$

$$S_B = Q_B - CT, \tag{3b}$$

$$S_C = Q_C - CT, \tag{3c}$$

$$S_E = S_T - S_A - S_B. \tag{3d}$$

The estimated variances F_A, F_B, and F_C of factors A, B, and C can be, respectively, expressed as follows:

$$F_A = \frac{S_A/f_A}{S_E/f_E}, \tag{4a}$$

$$F_B = \frac{S_B/f_B}{S_E/f_E}, \tag{4b}$$

$$F_C = \frac{S_C/f_C}{S_E/f_E}, \tag{4c}$$

where f_A, f_B, f_C, and f_E are, respectively, the degree of freedom of factors A, B, and C and error E. For a significant level α, if $F_A \geq F_\alpha(f_A, f_\alpha)$, then it can be seen that the effect of factor A on the index is significant; otherwise, it is not significant. The same method can be used to judge the significance of factors B and C.

As for the significant study of three factors, the interaction between $A \times B \times C$ is generally weak, so it is not considered in practice, and only the interaction between two factors is considered. Then, the computational method is denoted by the following equations:

$$Q_{AB} = \frac{1}{r} \sum_{i=1}^{m} \sum_{j=1}^{n} \left(\sum_{k=1}^{r} x_{ijk} \right)^2, \tag{5a}$$

$$Q_{AC} = \frac{1}{n} \sum_{i=1}^{m} \sum_{k=1}^{r} \left(\sum_{j=1}^{n} x_{ijk} \right)^2, \tag{5b}$$

$$Q_{BC} = \frac{1}{m} \sum_{j=1}^{n} \sum_{k=1}^{r} \left(\sum_{i=1}^{m} x_{ijk} \right)^2. \tag{5c}$$

Further, the sum of squares of the variance of interaction effect of factors A and B, factors A and C, and factors B and C can be indicated by the following equations:

$$S_{AB} = Q_{AB} - Q_A - Q_B + CT, \tag{6a}$$

$$S_{AC} = Q_{AC} - Q_A - Q_C + CT, \tag{6b}$$

$$S_{BC} = Q_{BC} - Q_B - Q_C + CT, \tag{6c}$$

And the significance analysis method of the interaction between factors is the same as that of single-factor analysis. $F_\alpha(f_1, f_2)$ was the critical value of F test, shown in Table 4. The evaluation of the significant effect was specified as follows: if $\alpha < 0.001$, its significance is I; if $0.001 \leq \alpha < 0.01$, its

TABLE 4: F test critical values $F_\alpha(f_1, f_2)$.

Significant level α	0.1	0.05	0.025	0.01	0.005	0.001
$f_1 = 2, f_2 = 4$	4.32	6.94	10.65	18.00	26.28	61.25
$f_1 = 2, f_2 = 8$	3.11	4.46	6.06	8.65	11.04	18.49
$f_1 = 4, f_2 = 8$	2.81	3.84	5.05	7.01	8.81	14.39

significance is II; if $0.01 \leq \alpha < 0.1$, its significance is III; and if $\alpha \geq 0.1$, its significance is IV.

3. Results and Discussion

3.1. Dynamic Stress–Strain Curves. The maximum dynamic stress and maximum dynamic strain (the vertices of each stress–strain hysteresis loop, Figure 4) could be drawn under different dynamic stress cycles to obtain the dynamic stress–strain backbone curve (Figure 5), which was adequate evidence that the curves performed a strain-hardening behaviour for all samples [28].

The effects of different confining pressures, moisture content, and frequency on stress–strain curves were compared and analyzed. As shown in Figure 5(a) and 5(b), it was evident that the dynamic stress increased with the increase of confining pressure and frequency under the same other conditions. But the failure strength was the maximum at the best moisture content under the same confining pressure and frequency.

The hyperbolic model of equation (7) used to fit the dynamic stress–strain curve was proposed by Konder as early as 1963 [29]. After analysis and fitting, it is found that the dynamic stress–strain curves of chlorine saline soil with high salinity under dynamic load were difficult to be described by equation (7). Therefore, equation (8) [30] was used to fit the dynamic stress–strain curves:

$$\sigma_d = \frac{\varepsilon_d}{a + b\varepsilon_d}, \tag{7}$$

$$\sigma_d = \frac{a\varepsilon_d^b}{1 + c\varepsilon_d^b}, \tag{8}$$

where σ_d and ε_d are dynamic stress and dynamic strain and a, b, and c are parameters related to the test conditions and the physical properties of the soil.

Furthermore, equation (9) was obtained from the special conditions using $\varepsilon_d \longrightarrow +\infty$ in equation (8) as follows:

$$\sigma_{d\max} = \sigma_d \big|_{\varepsilon_d \longrightarrow +\infty} = \frac{a}{c}. \tag{9}$$

The results of the related fitting parameters in the experiment were a, b, c, and $\sigma_{d\max}$, as shown in Table 5.

According to the different types of dynamic stress–strain curves, the principles for determining the failure strength of soil are also different. From the achieved stress–strain curves, the average value of the dynamic stress after the stress–strain curve stabilizes is taken as the failure strength.

The change curves of failure strength under different influencing factors obtained from the test results were shown in Figure 6. The effects of different confining pressures,
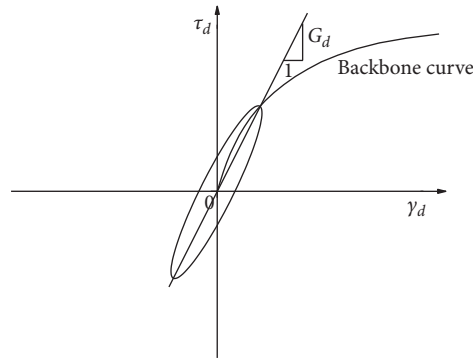
FIGURE 4: Hysteresis curve and backbone curve.
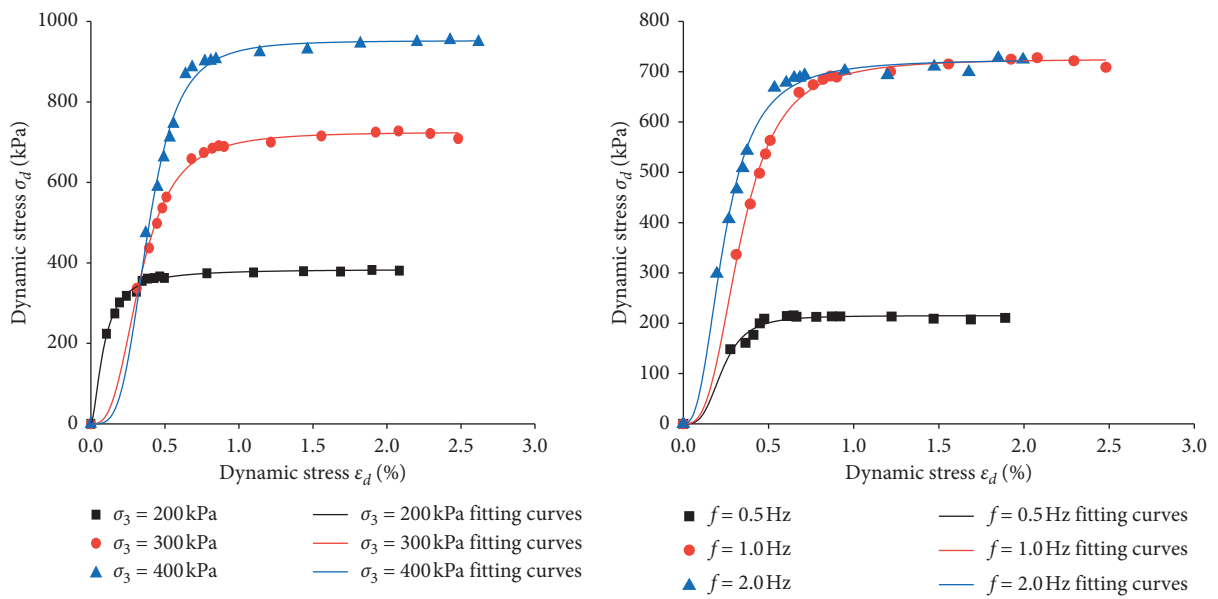
(a)

(b)
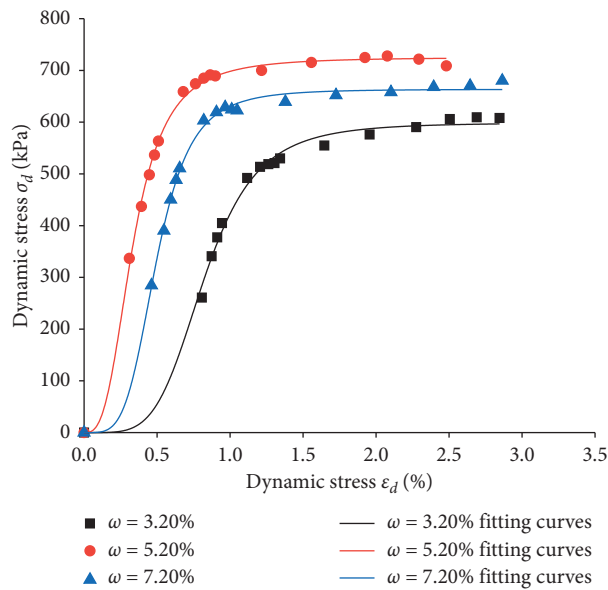
(c)

FIGURE 5: Dynamic stress–dynamic strain relationship curves. (a) $f = 1.0$ Hz, $\omega = 5.20\%$, (b) $\omega = 5.20\%$, $\sigma_3 = 300$ kPa, and (c) $f = 1.0$ Hz, $\sigma_3 = 300$ kPa.

TABLE 5: Chlorine saline soil test conditions and the fitting values of backbone curve parameters.

Test group	σ_3 (MPa)	f (Hz)	ω (%)	a	b	c	$\sigma_{d\max}$ (MPa)	R^2
	0.2	1.0	5.2	20786.65	1.65	54.07	0.38	0.997
BYZ1	0.3			18695.38	2.97	25.78	0.73	0.997
	0.4			34231.06	3.75	35.95	0.95	0.992
	0.3	0.5	5.2	30981.62	3.38	143.98	0.22	0.977
BYZ2		1.0		18695.38	2.97	25.78	0.73	0.998
		2.0		28604.87	2.57	39.48	0.72	0.994
	0.3	1.0	3.2	1441.33	4.57	2.41	0.60	0.993
BYZ3			5.2	18695.38	2.97	25.78	0.73	0.998
			7.2	12695.06	4.21	19.13	0.67	0.997
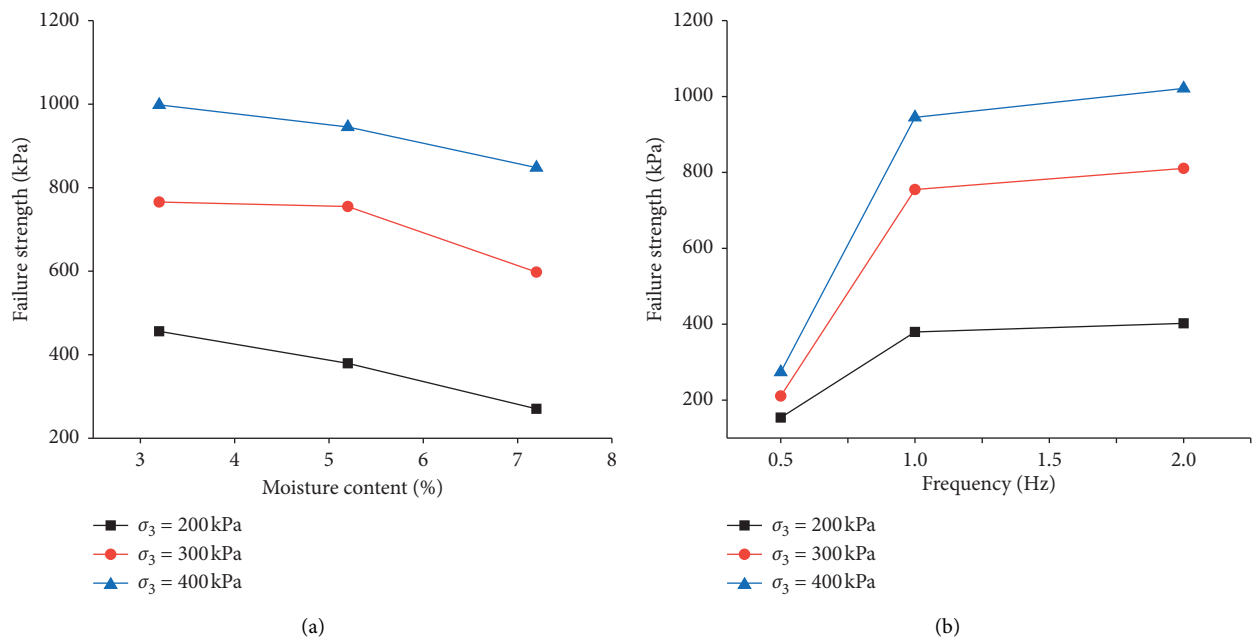
FIGURE 6: Variety regularity of failure strength with moisture content and frequency. (a) f = 1.0 Hz. (b) ω = 5.20%.

moisture content, and frequency on the failure strength were compared and discussed.

As shown in Figure 6, it was evident that the failure strength of chlorine saline soil increased significantly with the increase of confining pressures. Under higher confining pressure, the porosity of the soil decreased. Soil particles were filled with each other to form a tighter framework structure, the friction and uneven occlusion between soil particles were enhanced, and the ability to resist external deformation heightens. Therefore, the failure strength increased with the increase of confining pressure.

Figure 6(a) showed the failure strength of chlorine saline soil decreases gradually with the increase of moisture content. Under the condition of certain salinity, with the increase of moisture content, on one hand, the presence of pore water weakened the interaction between particles. On the other hand, it also reduced the bonding force between soil particles and leads to the decrease of soil strength. Therefore, the failure strength decreased with the increase of moisture content.

Figure 6(b) showed that the failure strength of chlorine saline soil increases with the increase of frequency. The

frequency changed from 0.5 Hz to 1.0 Hz, and the failure strength changed notably. The frequency indirectly reflected the speed of driving. The smaller the frequency, the longer the cyclic loading acts on the soil, and the greater the effect on the soil. On the contrary, the frequency had a smaller effect on the bite force and bonding force between soil particles. The soil still had a stronger ability to resist deformation, and the failure strength increased with the increase of frequency.

Taking confining pressure, moisture content, and frequency, respectively, as factors A, B, and C, there were 3 levels of each factor. The significance of the failure strength under the interaction between factors was studied, and the computational results were shown in Table 6.

According to the significant levels given in Table 4, the effect of confining pressure and frequency on the failure strength was significant while the effect of moisture content was not significant. In addition, the interaction between confining pressure and frequency had a significant effect on the failure strength of chlorine saline soil. The interaction between confining pressure and moisture content and that between frequency and moisture content were significant

TABLE 6: Significance test of failure strength considering interactions.

Source of variance	Sum of squares	Degree of freedom	F value	Significance
Confining pressure A	682595.48	2	133.48	I
Moisture content B	367.00	2	0.07	IV
Frequency C	1328069.81	2	259.71	I
$A \times B$	19176.49	4	1.88	IV
$A \times C$	165960.64	4	16.23	I
$B \times C$	21128.29	4	2.07	IV
Errors	20454.99	8		
Sums	2237752.70	26		

when the significant level α was greater than or equal to 0.100. It was clear from Table 6 that the significance of the effect of each single factor and the interaction between multiple factors on the failure strength was frequency C, confining pressure A, $A \times C$, $B \times C$, $A \times B$, and moisture content B in order.

3.1.1. Effects of the Different Factor on the Dynamic Elastic Modulus.

The elastic modulus is a key parameter to describe the properties of soil, and it also plays an important role in deformation and stability analysis in geotechnical engineering; then, it is usually acquired in smaller strain. The computational methods of static elastic modulus and dynamic elastic modulus are different. Lee et al. [31] took the ratio of the deviant stress increment corresponding to 1.5% of strain to the axial strain increment as the static elastic modulus of soil, and Wang [32] choose the tangent modulus as the static elastic modulus of soil. However, the computational method of dynamic elastic modulus is as shown in equation (10a):

$$E_d = \frac{\sigma_d}{\varepsilon_d}, \tag{10a}$$

$$\sigma_d = \frac{(\sigma_{d\,max} - \sigma_{d\,min})}{2}, \tag{10b}$$

$$\varepsilon_d = \frac{(\varepsilon_{d\,max} - \varepsilon_{d\,min})}{2}, \tag{10c}$$

where E_d is dynamic elastic modulus, σ_d and ε_d are, respectively, axial dynamic stress and axial dynamic strain; the computational method is as shown in equations (10b) and (10c).

Figure 7 shows the dynamic elastic modulus changes of chlorine saline soil with different moisture content, frequency, and confining pressure. It could be seen that dynamic elastic modulus was increasing with confining pressure. In addition, the dynamic elastic modulus increased at the beginning and then decreased with the increase of moisture content, but there was an exception when the confining pressure was 200 kPa, which was considered to be caused by the test error. However, the change of dynamic elastic modulus with frequency was not explicit.

Table 7 shows the significance analysis results of the effect of confining pressure, moisture content, and frequency on dynamic elastic modulus. According to the significant levels given in Table 4, the effect of confining pressure and frequency on dynamic elastic modulus was significant. Furthermore, the effect of moisture content and the interaction between confining pressure and moisture content was significant when significant level α was larger than or equal to 0.005; the effect of the interaction between confining pressure and moisture content and the interaction between confining pressure and frequency were significant when significant level α was greater than or equal to 0.01. As could be seen from Table 5, the significance of the effect of each single factor and the interaction between multiple factors on dynamic elastic modulus followed the order of confining pressure A, frequency C, moisture content B, and confining pressure A, $B \times C$, $A \times C$, and $A \times B$ (from greatest to least).

3.1.2. Effect of Different Factors on Shear Strength Parameters.

The properties of soil are extremely complex, so the strength of soil should not be simply considered as the strength of mineral particles, but the interaction effect between particles must be considered. Similarly, the shear strength of soil also depends on many factors, which are generally divided into two categories. One is the properties of the soil itself, such as physical properties; the other is the external conditions of the soil, such as stress and strain conditions. In the practical application, the most common theory of shear strength is the Mohr–Coulomb strength criterion with only two parameters: cohesion c and friction angle φ.

The cohesion is mainly provided by physical and chemical forces such as electrostatic force and Van der Waals' force and is affected by ion concentration, ion valence, and the mineral composition of particles. The friction angle can reflect the mutual movement and bite between particles, such as friction caused by sliding between particles.

According to the results of the unconsolidated undrained triaxial test, take $(\sigma_1 + \sigma_3)/2$ and $(\sigma_1 - \sigma_3)/2$ as the center of the circle and the radius, draw the stress circle under different test conditions and the common tangent of the circle, and obtain the inclination angle and longitudinal intercept from the strength envelope, that is, to obtain the required dynamic cohesion c_d and dynamic friction angle φ_d.

Figure 8 shows the relationship between dynamic friction angle and dynamic cohesion with the moisture content of chlorine saline soil under different loading frequencies. It could be seen that the dynamic cohesion and dynamic friction angle decrease with the increase of moisture content.

(a)

(b)
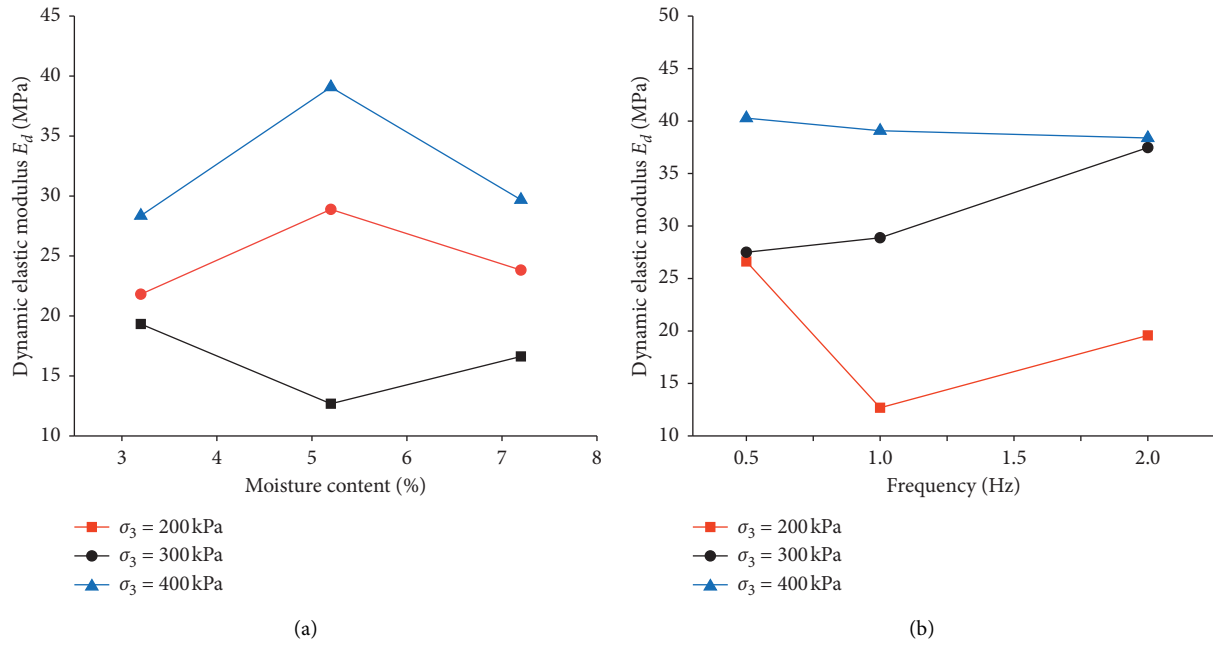
FIGURE 7: Variety regularity of dynamic elastic modulus with moisture content and frequency. (a) $(f) = 1.0$ Hz. (b) $\omega = 5.20\%$.

TABLE 7: Significance test of dynamic elastic modulus.

Source of variance	Sum of squares	Degree of freedom	F value	Significance
Confining pressure A	1852.77	2	36.38	I
Moisture content B	371.96	2	10.95	II
Frequency C	1123.09	2	33.08	I
$A \times B$	201.41	4	2.97	III
$A \times C$	302.18	4	4.45	III
$B \times C$	657.07	4	9.68	II
Errors	118.85	8		
Sums	3855.02	26		

(a)

(b)
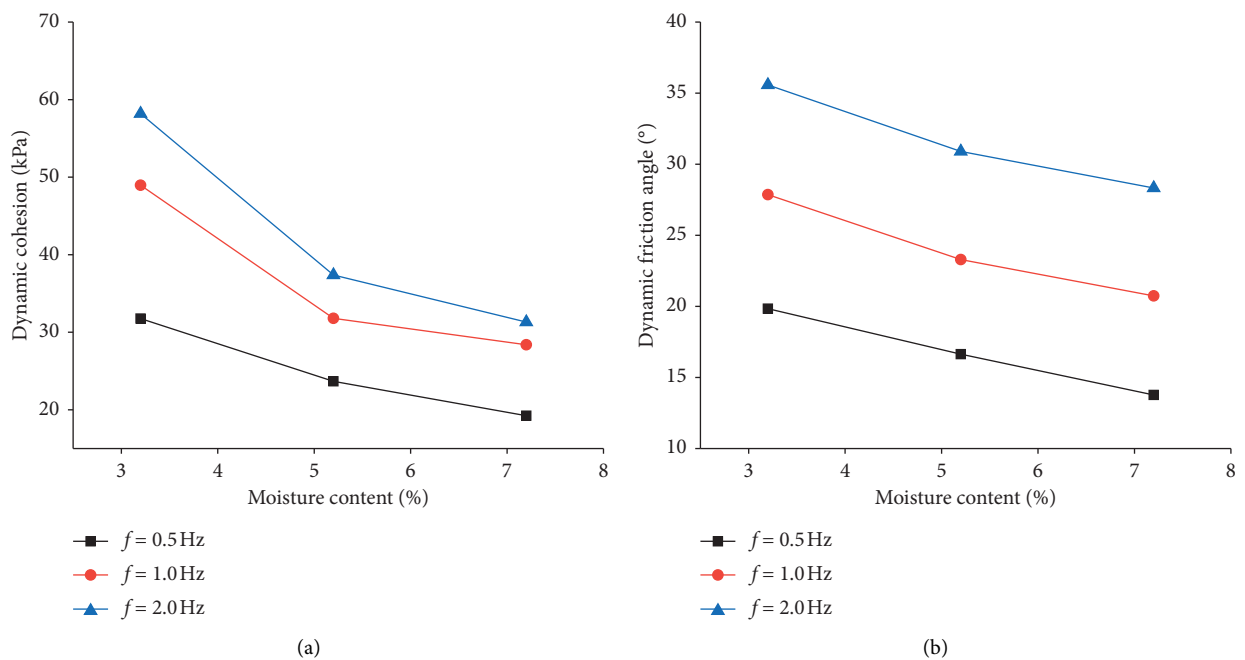
FIGURE 8: Variety regularity of shear strength parameter with water content and frequency. (a) Dynamic cohesion. (b) Dynamic friction angle.

TABLE 8: Significant test of cohesion of influencing factors.

Source of variance	Sum of squares	Degree of freedom	F value	Significance
Moisture content B	887.44	2	4.10	IV
Frequency C	701.97	2	3.24	I
Errors	432.83	4		
Sums	2022.23	8		

TABLE 9: Significant test of the friction angle of influencing factors.

Source of variance	Sum of squares	Degree of freedom	F value	Significance
Moisture content B	87.85	2	2.00	IV
Frequency C	623.97	2	14.21	I
Errors	87.83	4		
Sums	799.65	8		

When the frequency was 1.0 Hz, the dynamic cohesion decreased dramatically from 48.96 kPa to 31.80 kPa and the dynamic friction angle decreased quickly from 27.86° to 20.74° as moisture content increased from 3.2% to 5.2%. So, the dynamic cohesion and dynamic friction angle increased with the increase of frequency. When the moisture content was 5.2%, the dynamic cohesion increased rapidly from 23.66 kPa to 31.80 kPa and the dynamic friction angle increased obviously from 16.64° to 23.29° as frequency increased from 0.5 Hz to 1.0 Hz. In summary, the higher the loading frequency and the lower the moisture content might be obtained, the larger the dynamic cohesion and dynamic friction angle.

With the increase of moisture content, the pore water filled between soil particles would increase, the electrostatic attraction, Van der Waals' force and the ion concentration in the soil would decrease, and the electrokinetic potential of the colloid in the soil would increase, resulting in the enhancement of the mutual interaction between the colloids. And the thickness of hydration film on the surface of soil particles increased with the increasing of moisture content. Besides, the salt solution acted as a lubricant in the soil and weakened the bonding force between soil particles. Therefore, the dynamic friction angle and dynamic cohesion of chlorine saline soil decrease with the increase of moisture content, and shear strength also decreased. If loading frequency was too high, the effect of cyclic loading would be inadequate on the soil, and it would have little effect on the biting force and bonding force between soil particles. The soil could resist external deformation. Therefore, the shear strength increased with the increase of loading frequency.

The significance analysis results of the effect of moisture content and frequency on the dynamic cohesion and dynamic friction angle of chlorine saline soil are indicated in Tables 8 and 9, respectively.

According to the significance test level given in Table 4, it could be judged that the effect of frequency on dynamic cohesion and dynamic friction angle was significant, while the effect of moisture content was not significant.

Based on the above analysis, it could be seen that not only single factors such as confining pressure, moisture content, and frequency had a certain effect on the mechanical characteristics of chlorine saline soil, but also the effect of the interaction of multiple factors might be significant. Therefore, it was necessary to consider the effect of a single factor and the interaction between multiple factors on the mechanical characteristics of soil comprehensively, instead of analyzing the independent influence of each single factor only.

4. Conclusions

The mechanical characteristics of chlorine saline soil affected by a number of factors were studied, and the following conclusions have been drawn:

(1) The dynamic stress–dynamic strain curve of chlorine saline soil was strain-hardening. Although the hyperbolic model was not well fitted, the power function model achieved a quite good fit of over 97%.

(2) The confining pressure, frequency, and the interaction between confining pressure and frequency could significantly affect the failure strength and dynamic elastic modulus. Some discrepancies in the changes of the failure strength and dynamic elastic modulus with factors were observed.

(3) The effect of frequency on dynamic cohesion and dynamic friction angle was more significant, which increased with the increase of frequency. While moisture content had a weaker effect, dynamic cohesion and dynamic friction angle decreased as moisture content increased.

(4) Based on the significance test theory, the effect of confining pressure and frequency on the mechanical properties of chlorine saline soil was significant, but the effect of moisture content was weaker. It could be obtained that the effect of interaction between confining pressure and frequency was significant simultaneously. Therefore, when studying the mechanical characteristics of soil, the interaction between multiple factors needs to be taken into consideration.

Data Availability

The data used in the paper have been uploaded on the Baidu Netdisk (https://pan.baidu.com/s/1Xjw1k7QZ9LbYq6znsGZ4aQ); extract code: 0i96. These data are automatically collected by GDS.

Conflicts of Interest

The authors declare that they have no conflicts of interest regarding the publication of this paper.

Acknowledgments

References

[1] J. S. Yang, "Development and prospect of the research on salt-affected soils in China," *Acta Pedol Sin*, vol. 45, no. 5, pp. 837–845, 2008.

[2] Z. Q. Wang, S. Q. Zhu, and R. P. Yu, *Chinese Saline Soils*, Science Press, Beijing, China, 1993.

[3] H. J. Wang and Y. Y. Zhao, "Engineering geological characteristics of superchlorinated saline soil," *Hydrogeology and Engineering Geology*, vol. 1, pp. 39-40, 1981.

[4] X. S. Yang, J. Q. Dang, and L. L. Wang, "Experimental research on the shear strength characteristics of saturated chlorine saline soil," *Geotechnical Investigation & Surveying*, vol. 232, no. 11, pp. 6–9, 2008.

[5] J. Fang, X. Li, J. Liu, C. Liu, Z. Liu, and Y. Ji, "The crystallization and salt expansion characteristics of a silty clay," *Cold Regions Science and Technology*, vol. 154, no. 10, pp. 63–73, 2018.

[6] Y. Zhang, Z. Yang, J. Liu, and J. Fang, "Impact of cooling on shear strength of high salinity soils," *Cold Regions Science and Technology*, vol. 141, no. 6, pp. 122–130, 2017.

[7] H. Bing and P. He, "Influence of freeze-thaw cycles on physical and mechanical properties of salty soil," *Chinese Journal of Geotechnical Engineering*, vol. 31, no. 12, pp. 1958–1962, 2009.

[8] Y. Han, Q. Wang, N. Wang et al., "Effect of freeze-thaw cycles on shear strength of saline soil," *Cold Regions Science and Technology*, vol. 154, no. 2, pp. 42–53, 2018.

[9] M. Li, S. Chai, H. Du, and C. Wang, "Effect of chlorine salt on the physical and mechanical properties of inshore saline soil treated with lime," *Soils and Foundations*, vol. 56, no. 3, pp. 327–335, 2016.

[10] Y. Liu, Q. Wang, S. Liu et al., "Experimental investigation of the geotechnical properties and microstructure of lime-stabilized saline soils under freeze-thaw cycling," *Cold Regions Science and Technology*, vol. 161, no. 3, pp. 32–42, 2019.

[11] W. Zhang, J. Ma, and L. Tang, "Experimental study on shear strength characteristics of sulfate saline soil in Ningxia region under long-term freeze-thaw cycles," *Cold Regions Science and Technology*, vol. 160, no. 8, pp. 48–57, 2019.

[12] X. S. Yang, J. Q. Liu, and J. Q. Dang, "Experimental research on the engineering property of chlorine saline soil improved by fly ash," *Chinese Journal of Geotechnical Engineering*, vol. 29, no. 11, pp. 82–86, 2012.

[13] Z. Y. Zhang, Y. C. J. Luo, and X. J. Pei, "Engineering characteristic of reinforcement chlorine saline soil in Coastal," *Journal of Civil Engineering and Management*, vol. 34, no. 04, pp. 59–63, 2017.

[14] Y. Lai, X. Wan, and M. Zhang, "An experimental study on the influence of cooling rates on salt expansion in sodium sulfate soils," *Cold Regions Science and Technology*, vol. 124, pp. 67–76, 2016.

[15] Y. Lai, D. Wu, and M. Zhang, "Crystallization deformation of a saline soil during freezing and thawing processes," *Applied Thermal Engineering*, vol. 120, pp. 463–473, 2017.

[16] S. Zhang, X. Yang, S. Xie, and P. Yin, "Experimental study on improving the engineering properties of coarse grain sulphate saline soils with inorganic materials," *Cold Regions Science and Technology*, vol. 170, Article ID 102909, 2020.

[17] O. S. B. Al-Amoudi and S. N. Abduljauwad, "Compressibility and collapse characteristics of arid saline sabkha soils," *Engineering Geology*, vol. 39, no. 3-4, pp. 185–202, 1995.

[18] P. N. Mishra, A. Scheuermann, T. Bore et al., "Salinity effects on soil shrinkage characteristic curves of fine-grained geomaterials," *Journal of Rock Mechanics and Geotechnical Engineering*, vol. 11, no. 01, pp. 185–195, 2019.

[19] Y. Zhao, Y. Lai, J. Zhang, and M. Liao, "A dynamic strength criterion for frozen sulfate saline silty clay under cyclic loading," *Cold Regions Science and Technology*, vol. 173, Article ID 103026, 2020.

[20] F. T. Zhao, L. J. Chang, and W. Y. Zhang, "Experimental study on dynamic strength characteristics of frozen saline soil under stepped cyclic loading," *Journal of Glaciology and Geocryology*, vol. 41, no. 06, pp. 1397–1405, 2019.

[21] F. T. Zhao, L. J. Chang, and W. Y. Zhang, "Analysis on the influence of cyclic stress ratio and vibration frequency on microstructure of saline soil," *Journal of Glaciology and Geocryology*, vol. 42, no. 03, pp. 854–864, 2020.

[22] JTG E40-2007, *Test Methods of Soils for Highway Engineering*, China Communications Press, Beijing, China, 2007.

[23] GB/T 50123-2019, *Standard for Soil Test Method*, China Planning Press, Beijing, China, 2019.

[24] JTG D30-2015, *Specifications for Design of Highway Subgrades*, China Communications Press Co., Ltd., Beijing, China, 2015.

[25] D. Y. Xie, *Soil Dynamics*, Higher Education Press, Beijing, China, 2011.

[26] Z. F. Huang, *Experimental Study on Properties of Traffic Silt Embankment under Cyclic Dynamic Loading*, Tianjin University, Tianjin, China, 2011.

[27] S. Q. Li, L. X. Gao, and S. X. Chai, "Significance and interaction of factors on mechanical properties of frozen soil," *Rock Soil Mechanics*, vol. 33, no. 4, pp. 1173–1177, 2012.

[28] J. Liu, D. Chang, and Q. Yu, "Influence of freeze-thaw cycles on mechanical properties of a silty sand," *Engineering Geology*, vol. 210, pp. 23–32, 2016.

[29] G. X. Li, *Advanced Soil Mechanics*, Tsinghua University Press, Beijing, China, Second edition, 2016.

[30] Y. Zhang, L. W. Kong, A. G. Guo et al., "Cumulative plastic strain of saturated soft clay under cyclic loading," *Rock Soil Mechanics*, vol. 30, no. 06, pp. 1542–1548, 2009.

[31] W. Lee, N. C. Bohra, A. G. Altschaeffl, and T. D. White, "Resilient modulus of cohesive soils and the effect of freeze-thaw," *Canadian Geotechnical Journal*, vol. 32, no. 4, pp. 559–568, 1995.

[32] J. Wang, *Research on the Mechanical Properties of Subgrade Soil after Several Freeze Thaw Cycles in Seasonally Frozen Soil Region and Microscopic Mechanism Analysis*, Jilin University, Changchun, China, 2012.

Research Article

Laboratory Investigation on the Interface Bonding between Portland Cement Concrete Pavement and Asphalt Overlay

Fulu Wei [ID],[1] **Jianfeng Cao** [ID],[2] **Hongduo Zhao** [ID],[3] **and Bingye Han** [ID][4]

[1]*China Construction Eighth Engineering Division Co., Ltd., Shanghai 200122, China*
[2]*China Harbour Engineering Co. Ltd., Beijing, China*
[3]*The Key Laboratory of Road and Traffic Engineering, Ministry of Education, Tongji University, Shanghai 201804, China*
[4]*School of Civil and Transportation Engineering, Beijing University of Civil Engineering and Architecture,*
 No. 1 Zhanlanguan Road, Xicheng District, Beijing 100044, China

Correspondence should be addressed to Bingye Han; hanbingye@bucea.edu.cn

The interface bonding between Portland cement concrete (PCC) pavement and hot-mix asphalt (HMA) overlay plays an important role in the performance of the composite pavement. This research conducted a series of comprehensive laboratory studies to investigate the influence factors of the interface bonding strength using a self-designed direct shear test apparatus that can simultaneously apply normal stress and shear stress on a specimen. Four kinds of commonly used tack coat materials were systematically tested and compared under various combinations of normal stress and temperature. Then, coupling effects of the normal stress and temperature on the interface bonding between PCC and HMA were analyzed. The test results show that temperature has a significant impact on the adhesion of the tack coat. Emulsified asphalt was considered the optimal tack coat material because of its simple construction method. In addition, it was found that a damaged interface could still provide considerable bonding strength. Normal stress generated by traffic loads was beneficial to the interface bonding strength, especially at lower temperatures. The temperature had a significant effect on interface bonding and played a leading role in the failure mode of interface bonding.

1. Introduction

The interface bonding between Portland cement concrete (PCC) pavement and hot-mix asphalt (HMA) overlay is widely recognized as one of the most critical influence factors on mechanical responses of composite pavement as well as its long-term performance [1–3]. Several studies have revealed that a weak interface bonding strength will undoubtedly cause higher bending stress, shear stress, and deflection in the composite pavement, resulting in some unexpected pavement distresses [3, 4]. In the worst case, the HMA overlay might encounter problems such as slippage cracking, delamination, or severe rutting [5–10]. These facts highlight the important role of interface bonding in composite pavement. So far, most studies have focused on the influence factors of interface bonding and experimental test

methods or equipment. Nevertheless, these studies have not been widely accepted by researchers and engineers due to lack of sufficient supporting data [11–14].

In the past few decades, many equipment and methods have been developed for studying the interface boding, including direct shear test, pull-off test, and torsional shear test [15, 16]. The direct shear test is one of the most used methods to investigate the interfacial adhesive properties of multilayer materials or structures. Generally, in terms of the stress field applied during the test, the direct shear test includes pure direct shear test and direct shear test with normal stress. The pure direct shear test only applies shear force to the interface of specimen without normal stress, such as Superpave shear tester [17], Leutner shear test [14], Laboratory Bond Interface Strength device [18], and Florida Department of Transportation shear tester [19]. However,

there is almost no pure shear stress state in the interface of composite pavement. Considering the influence of normal stress, it is more in line with the actual situation. Uzan et al. [11] designed a direct shear box that can apply both normal and shear loads on the interface of the double-layered prismatic specimen to measure the stiffness K under different test conditions. Donovan et al. [20] developed a device to determine the optimum dosage of tack coat for a PCC bridge deck overlaid with geomembrane and HMA layer. Al-Qadi et al. [15] modified a direct shear tester that can apply normal load in the horizontal direction and shear load in the vertical direction. Arulrajah et al. [21] evaluated the interface shear strength through a large-scaled direct shear apparatus. The American Association of State Highway and Transportation Officials (AASHTO) standard also recommended a method using Louisiana Interlayer Shear Strength Tester to test the interlayer shear strength between asphalt pavement layers [22]. In the above equipment, it is recommended to use a device that can apply both normal load and direct shearing force since it can obtain the interface bonding strength of the specimen under a more realistic stress state.

It has been widely accepted that the mixture type, PCC surface texture, tack coat material, application rate of tack coat, normal stress on the interface, and temperature are the main influence factors affecting the interface bonding strength between HMA overlay and PCC layer [23–25]. For instance, a study pointed out that the interfacial shear strength at 25°C is about five times that of high temperature at 55°C. Ge et al. [26] conducted a series of orthogonal experiments using the shear test method to evaluate the impact of temperature, bonding material, and confining pressure, but the study mainly investigated the benefits of glass fiber reinforced asphalt membrane. Leng et al. [23] used a direct shear tester to study several influence factors, including HMA type, tack coat type, tack coat application rate, PCC surface texture, and temperature. The investigation concluded that SS-1hP asphalt emulsion shows a better performance than RC-70 cutback asphalt, and the optimum application rate of tack coat is $0.27\,\text{L/m}^2$. Moreover, compared with high temperature, the lower temperature is beneficial to interface bonding strength. Later, an accelerated pavement testing (APT) was conducted in 2008 to verify some of these findings [24]. However, these two investigations have some limitations. Firstly, only two kinds of HMA mixtures and tack coat materials were included in the test, which limited the distribution of these findings. Secondly, the studies ignored the effects of normal stress on interface bonding, but the normal stress was so important that it could not be ignored, which made the conclusions unconvincing. Finally, the coupling effect of normal stress and temperature were also not considered. The authors believe that more efforts are needed to focus on more influence factors affecting interface bonding. It is also of great significance to investigate the interfacial bonding strength between HMA overlay and PCC pavement.

The objective of this study is to investigate the influence factors that affect interface bonding strength between HMA overlay and PCC layer through a series of laboratory tests. To fulfill this purpose, a self-designed direct shear tester was developed, and both normal load and shear force could be applied to the specimen at the same time. Four types of tack coat materials, five different test temperatures, and four different normal stresses were considered, and the coupling effect of temperature and normal stress was further analyzed.

2. Methodology

2.1. Test Apparatus. Considering the effects of normal stress on interface bonding between HMA overlay and PCC layer, an upgraded direct shear test apparatus was developed, and more details about the device can be found in the previous research [25]. The equipment is able to apply normal stress in a horizontal direction through a hydraulic actuator, and the magnitude of normal stress can be obtained by a built-in stress sensor, as shown in Figure 1(a). However, the direct shear tester itself cannot apply the shear force to the specimen. Therefore, a material testing system (MTS) is employed to apply the shear force on the loading plate under a displacement control mode with a constant shearing rate of 2.5 mm/min in accordance with the AASHTO standard [22]. Specimen slot is designed for a double-layer specimen whose size is 150 mm in diameter and 100 mm in height. The MTS's environment cabinet was used to control test temperature.

2.2. Material and Specimen Preparation. In this study, four types of tack coat were investigated, including cutback asphalt, anionic emulsified asphalt, rubber asphalt, and virgin asphalt. Table 1 lists the properties of the four tack coats. This study adopted the manufacturer-recommended optimal application rate of tack coat (i.e., $0.33\,\text{L/m}^2$ for cutback asphalt, $0.31\,\text{L/m}^2$ for emulsified asphalt, and $0.27\,\text{L/m}^2$ for the rests). Commonly, the curing time of cutback asphalt and emulsified asphalt was two hours and half an hour, respectively.

As mentioned above, the specimen used for the direct shear test is composed of two layers of materials, PCC and HMA, as shown in Figure 1(b). Firstly, a concrete core sample was drilled from a 50 mm thick PCC slab with a smooth surface. Then, the hot-mix asphalt mixture was compacted on the surface of the concrete core sample using a Superpave Gyratory Compactor (SGC). Figure 2 shows the aggregate gradation of the HMA mixture. According to the Marshall design method, the optimum binder content was 4.5% when using the virgin asphalt.

2.3. Data and Parameters. The pretest result shows that there were two typical shear stress-displacement curves for the direct shear test, which represented brittle failure and plastic failure, respectively. As shown in Figure 3, the shear stress reduced dramatically after reaching its peak value for the brittle-failure curve. In contrast, the shear stress of plastic failure did not show a clear decrease trend during the whole test. To describe the characteristics of interface bonding thoroughly, this study used four parameters, including shear strength, interface bonding coefficient (IBC), residual strength, and residual ratio.
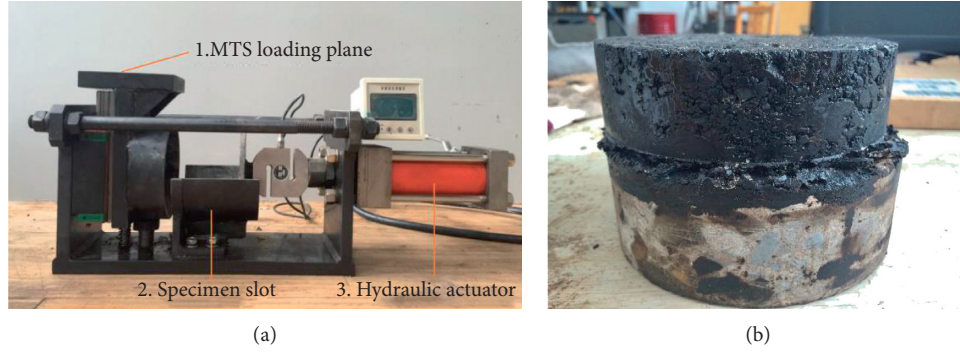
FIGURE 1: The test setup. (a) The shear test apparatus. (b) Specimen.

TABLE 1: Properties of tack coats.

Tack coat type	Penetration at 25°C (0.1 mm)	Ductility (cm)	Viscosity at 135°C (Pa·s)	Softening point (°C)
Rubber asphalt	53.2	35.5	2.23	72.6
Virgin asphalt	62.4	123	0.56	48.3
Emulsified asphalt	67.8	57.7	0.7	-
Cutback asphalt	65.1	129	0.6	-
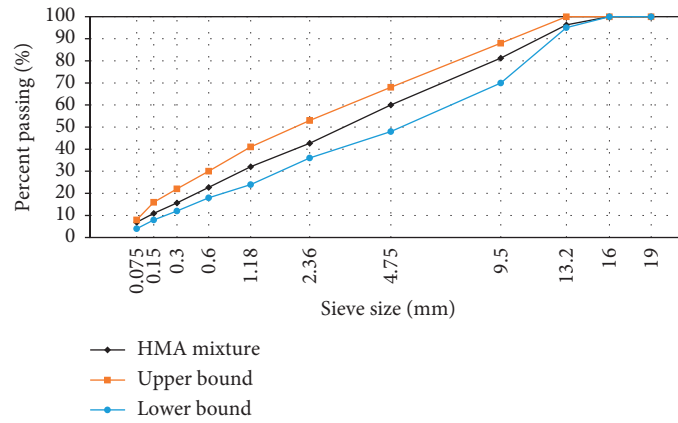
FIGURE 2: Aggregate gradation of HMA mixture.

2.3.1. Shear Strength. Shear strength is the peak shear stress in the direct shear test, which can be determined from equations (1) and (2). For the brittle-failure curve, it is easy to obtain the peak shear stress. However, it is complex to get the peak value in the plastic failure curve due to a lack of evident peak value. After in-depth inspection and analysis of most plastic failure curves, the authors found that it is reasonable to use the shear stress at the shear displacement of 5 mm as its shear strength. Therefore, the shear strength for the plastic failure curve is determined according to equation (2):

$$\tau = \frac{F}{A}, \tag{1}$$

$$\tau_{max} = \begin{cases} \max(\tau), & \text{Brittle failure,} \\ \tau(\text{displacement} = 5\,\text{mm}), & \text{Plastic failure,} \end{cases} \tag{2}$$

where τ is shear stress, MPa; τ_{max} is shear strength, MPa; F is shear force applied by MTS, N; and A is the cross section area of the specimen, mm^2.

2.3.2. Interface Bonding Coefficient. Interface bonding coefficient (IBC) is a parameter introduced in the Goodman contact model [27], as defined in equation (3). In 1978, Uzan et al. [11] firstly adopted IBC to evaluate the interface contact issue. IBC is the shear stiffness of interface bonding. A higher IBC value indicates that the interface bonding tends to brittle failure, while a lower IBC implies that the interface bonding is prone to plastic failure:

$$K = 1000 \times \frac{\tau_{max}}{\Delta\mu}, \tag{3}$$
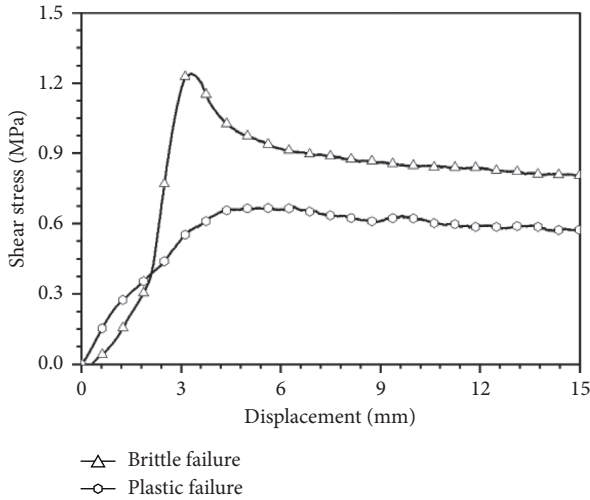
FIGURE 3: Two typical shear stress-displacement curves from the direct shear test.

where K is interface bonding coefficient, N/cm^3; $\tau_{\max}$ is shear strength, MPa; and $\Delta\mu$ is the displacement corresponding with its shear strength, mm.

2.3.3. Residual Strength and Residual Ratio.

As shown in Figure 3, the interface bonding of the specimen does not completely lose its strength after reaching the peak shear stress. Actually, the residual strength of the interface bonding is still high, especially for plastic failure specimen, which suggests that the interface bonding strength between HMA overlay and PCC layer might be still good enough, even if suffering damage. Therefore, it is meaningful to study the residual strength's properties. In this investigation, the residual strength is empirically defined as the shear stress at a displacement of 10 mm. Consequently, the residual ratio can be calculated by equation (4). In most cases, R is less than 1, but R can also be greater than 1 in terms of its definition. It should be noted that the residual ratio of the brittle-failure curve is quite different from that of the plastic failure curve:

$$R = \frac{\tau_R}{\tau_{\max}}, \tag{4}$$

where R is residual ratio; τ_R is residual strength, MPa; and $\tau_{\max}$ is shear strength, MPa.

2.4. Test Plan.

The laboratory investigation roughly includes two steps. The first step was aiming at further studying the influence of tack coat on interface bonding. Four types of tack coat materials, virgin asphalt, rubber asphalt, anionic emulsified asphalt, and cutback asphalt, were tested at 15°C and 45°C under 1.5 MPa normal stress. Each test included three replicates. The second step was attempting to figure out the coupling effects of normal stress and temperature on the interface bonding by implementing a multifactorial experiment. Several different test temperatures between 0 and 60°C, with an interval of 15°C, were selected to represent actual high and low environmental temperatures in the East China area. Test temperature included 0°C, 15°C, 30°C, 45°C, and 60°C, and the normal stresses contained 0 MPa, 0.5 MPa, 1.0 MPa, and 1.5 MPa.

3. Results and Discussion

In this section, the shear strength, IBC, residual strength, and residual ratio were calculated based on laboratory test results. Both analysis of variance (ANOVA) and data analysis were employed to figure out the significant influence factors and internal mechanism of interface bonding between HMA overlay and PCC pavement.

3.1. Determining the Optimal Tack Coat Material.

Figure 4 illustrates the typical shear stress-displacement curves for various tack coat materials at two different temperatures. All tests in this section were implemented under 1.5 MPa normal stress. It is obvious that the failure of interface bonding was tightly related to the test temperature. Low temperature was prone to lead to brittle failure and higher shear strength, while the high temperature was likely to cause plastic failure and lower shear strength. However, when cutback asphalt was used, no matter at 15°C or 45°C, the interface bonding exhibited plastic failure. The possible reason was that the adhesion of cutback asphalt was weaker, and its plastic deformation was better. In this situation, the interface bonding was likely to form rolling friction.

It can be also found in Figure 4 that the test temperature had significant effects on the bonding performance of the tack coat. The adhesive ability ranking of tack coat based on the shear strength at 15°C was emulsified asphalt > rubber asphalt > virgin asphalt > cutback asphalt. It should be noted that the shear strength of cutback asphalt was significantly lower than that of others. In contrast, the adhesive ability ranking at 45°C was virgin asphalt > cutback asphalt > rubber asphalt > emulsified asphalt, which was quite different from the results at 15°C.

Figure 5 illustrates the test results of various tack coat materials grouped by four interface bonding parameters. As shown in Figure 5(a), emulsified asphalt showed the highest shear strength at low temperature (i.e., 15°C), following by rubber asphalt and then virgin asphalt. In contrast, the shear strength from cutback asphalt was significantly lower than others. However, the shear strength of emulsified asphalt and rubber asphalt became smaller at high temperature (i.e., 45°C), while the virgin asphalt and cutback asphalt produced a higher shear strength. These facts indicated that temperature played an important role in the adhesive properties of tack coat, and the tack coat owning a high shear strength at low temperature might not provide similar bonding performance at high temperature. Therefore, considering the influence of temperature could be helpful to choose the proper tack coat material in engineering practice. In addition, the bonding properties of emulsified asphalt and rubber asphalt were more sensitive to temperature change.

Figure 5(b) shows the results of interface bonding coefficient (IBC) from different tack coat materials. Like the shear strength, emulsified asphalt, rubber asphalt, and virgin

(a)   (b)
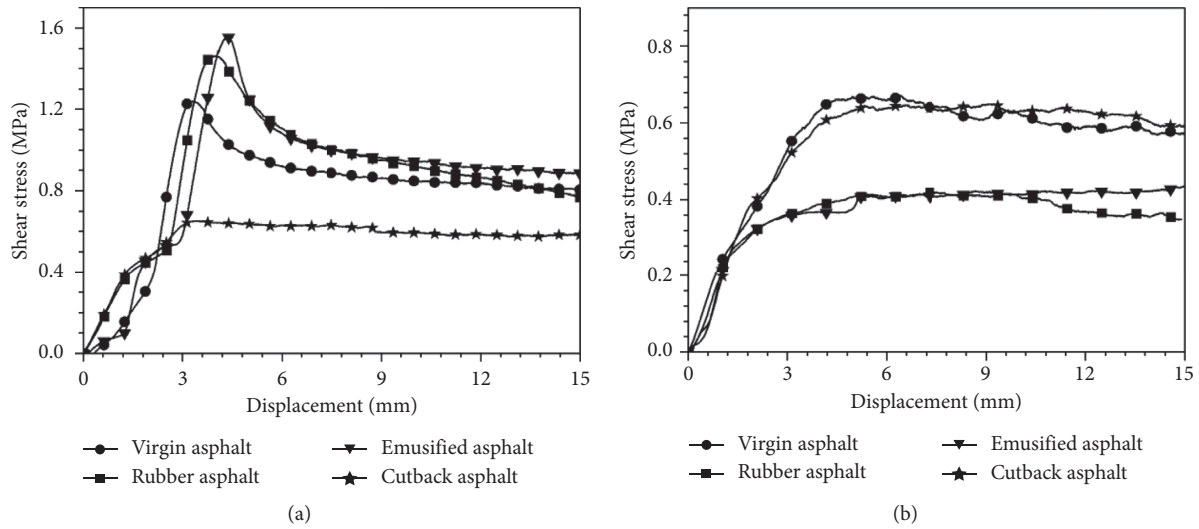
FIGURE 4: Shear stress-displacement curves at two different temperatures: (a) At 15°C. (b) At 45°C.

asphalt had higher IBC when the test temperature was at 15°C. However, all IBC decreased significantly at 45°C. Further study revealed that the brittle-failure specimens had higher IBC than plastic failure specimens. The IBC gap between brittle-failure specimens and plastic failure specimens suggested that the IBC of plastic failure might be less than a certain threshold value. Unfortunately, this study could not determine that value, and more tests were needed in the future.

The residual strength was used to characterize whether the interface bonding could still provide a certain strength after the interface bonding was damaged. Roughly, a specimen with higher shear strength was likely to have higher residual strength according to Figure 5(c), which meant that all residual ratios were at a high level. Residual ratios presented in Figure 5(d) were able to prove the above inference. The minimum residual ratio at 15°C and 45°C was 52.6% and 85%, respectively. In other words, the interface bonding between HMA overlay and PCC layer could still provide good adhesive ability after failure (that was when it encountered a large relative displacement).

Based on the above analysis, it is clear that temperature will affect the adhesive ability of the tack coat, and the interface bonding between HMA overlay and PCC layer can still provide considerable bonding strength after failure. The shear strength and IBC results indicate that emulsified asphalt, rubber asphalt, and virgin asphalt are the three suitable tack coat materials. Considering the different procedures and difficulty of construction, this study recommends the emulsified asphalt as the optimal tack coat material.

3.2. Coupling Effects of Normal Stress and Temperature on Interface Bonding.

This section tried to study the coupling effects of normal stress and temperature on interface bonding. In the recommended tack coat, emulsified asphalt was adopted. Table 2 lists the main test conditions and average test results. The results under 1.5 MPa and at 0°C

were not listed in the table because the shear force was too high and exceeded the MTS range used in this study. It is concluded from Table 2 that lower temperature and higher normal stress were beneficial for interface bonding.

3.2.1. The Influence of Normal Stress.

Further analysis was conducted to study the relationship between interface bonding strength and normal stress at different test temperatures. From Figure 6(a), it is obvious that the shear strength increased with the increase of normal stress at 0°C. According to the test results, when the normal stress was 1.5 MPa, the shear force was higher than 100 kN, the maximum applied load of the MTS. Consequently, the interface bonding was very strong at 0°C, so it could meet the adhesive requirements in most cases.

At 15°C, the influence of normal stress was more significant. For example, the shear strength was increased by 50% when normal stress was changed from 0.5 MPa to 1.0 MPa, as shown in Figure 6(b). In addition, the shear strength was increased by 48.6% when normal stress was changed from 1.0 MPa to 1.5 MPa. However, the enhancement effect of normal stress on the interface bonding strength was weakened as the temperature increased. As shown in Figure 6(e), the normal stress had a very limited influence on the shear strength when it was less than 0.5 MPa.

Figure 7 illustrates the relationship between normal stress and other interface bonding parameters at 30°C, including the shear strength, residual strength, interface bonding coefficient, and residual ratio. It can be found from Figure 7(a) that both shear strength and residual strength were positively correlated with normal stress, even though the increase rate of shear strength and residual ratio gradually slowed down. When normal stress increased from 0 to 1.5 MPa, the shear strength increased from 0.3 to 0.9 MPa, and the residual strength increased from 0.07 to 0.7 MPa. However, the growth trend of IBC was not consistent with the increase of normal stress, which reduced at first and then

(a)

(b)

(c)

(d)
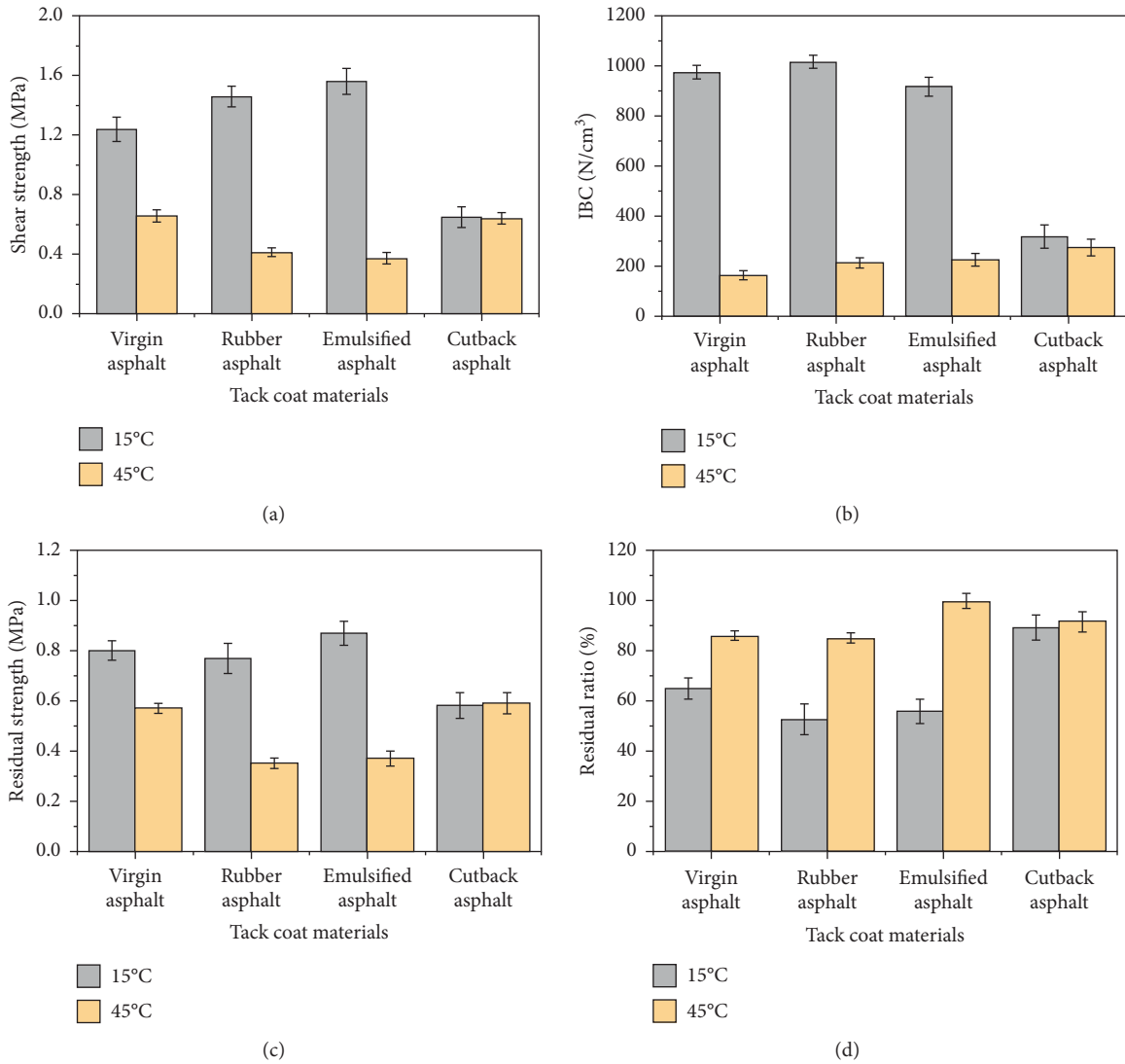
Figure 5: Test results of various tack coat materials. (a) Shear strength. (b) Interface bonding coefficient. (c) Residual strength. (d) Residual ratio.

Table 2: Test results from different combinations of normal stress and temperatures.

Temperature (°C)	Normal stress (MPa)	Shear strength (MPa)	IBC (N/cm^3)	Residual strength (MPa)	Residual ratio (%)
0	0	2.35	1445.33	0.00	0.00
	0.5	3.11	1368.16	0.35	11.41
	1.0	4.16	1415.66	0.80	19.35
15	0	0.77	518.21	0.07	9.12
	0.5	0.69	271.38	0.41	58.66
	1.0	1.04	448.46	0.43	41.78
	1.5	1.55	859.79	0.88	56.79
30	0	0.28	161.46	0.14	48.19
	0.5	0.36	158.37	0.30	82.61
	1.0	0.93	417.43	0.71	75.65
	1.5	1.15	343.00	1.01	87.20
45	0	0.12	33.67	0.06	49.42
	0.5	0.31	98.07	0.27	87.51
	1.0	0.57	152.09	0.61	106.28
	1.5	0.58	144.27	0.59	101.97
60	0	0.05	17.78	0.03	56.87
	0.5	0.39	100.75	0.33	83.60
	1.0	0.38	445.05	0.41	106.22
	1.5	0.37	223.72	0.37	99.79

(a)

(b)

(c)

(d)

(e)
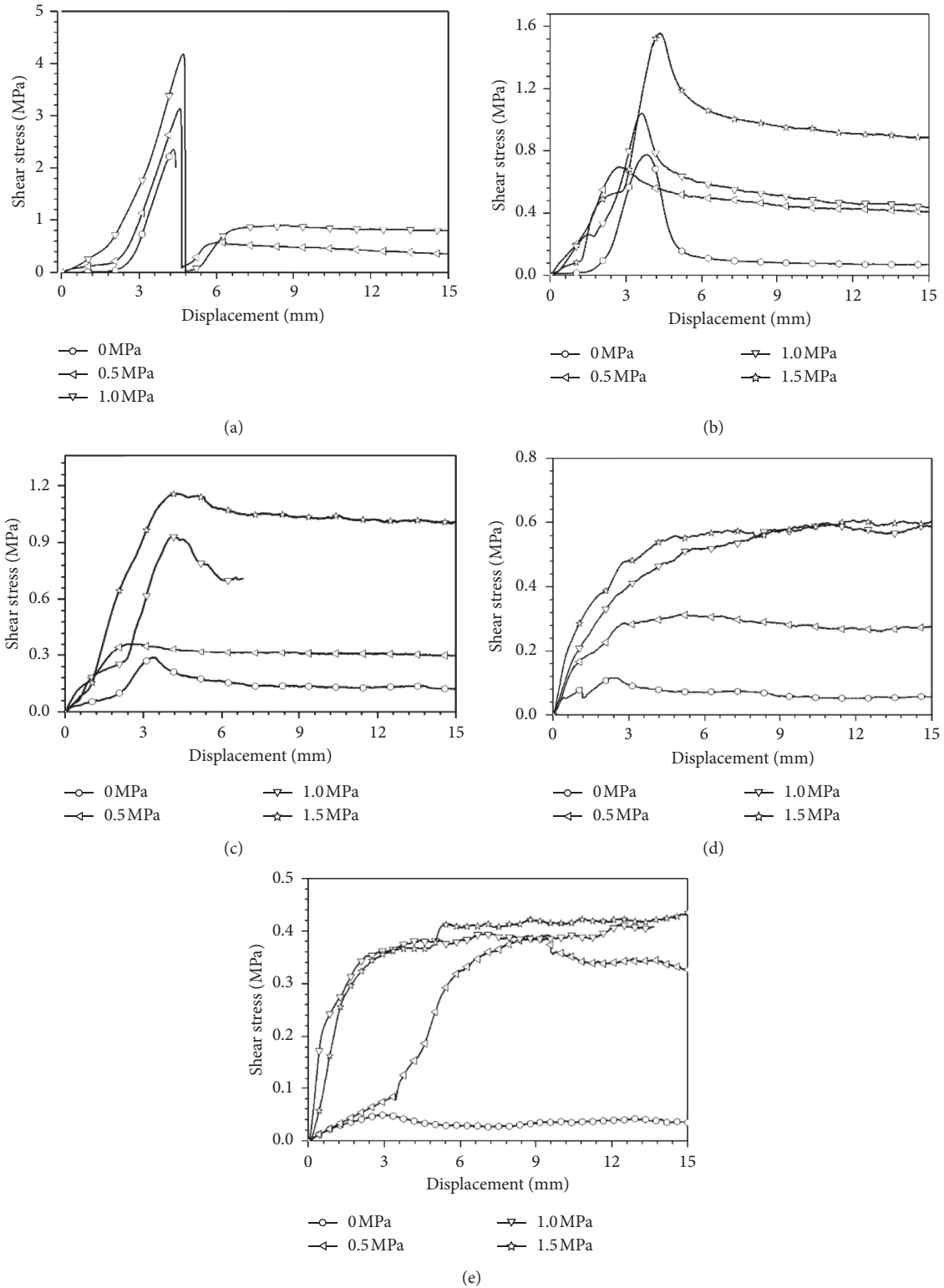
FIGURE 6: Shear stress-displacement curves under various normal stress. (a) At 0°C. (b) At 15°C. (c) At 30°C. (d) At 45°C. (e) At 60°C.
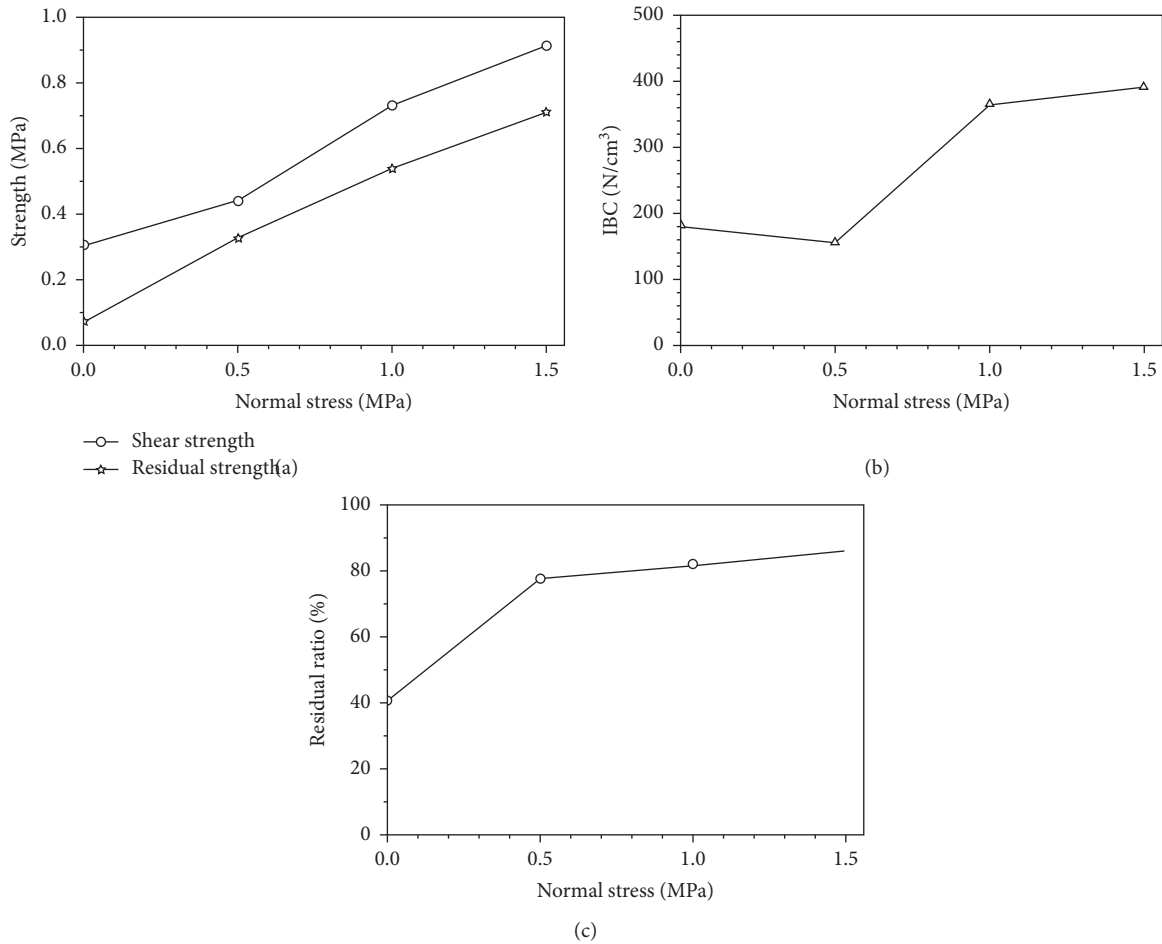
—○— Shear strength
—⋆— Residual strength(a)

(b)

(c)

FIGURE 7: Relationship between normal stress and other interface bonding parameters. (a) Shear strength and residual strength. (b) Interface bonding coefficient. (c) Residual ratio.

increased. In addition, the residual ratio also had positive correlation with normal stress. As shown in Figure 7(c), the residual ratio rapidly increased from 40.9% to 78.1% when the normal stress increased from 0 to 0.5 MPa, and then the increase ratio reduced significantly.

In conclusion, the normal stress benefited interface bonding strength, especially at a lower temperature. Higher normal stress can increase both residual strength and residual ratio, but it usually had a very limited influence on the failure mode of interface bonding.

3.2.2. The Influence of Temperature. To study the effects of temperature on the interface bonding, the shear strength-displacement curves were redrawn according to normal stress. As shown in Figure 8, as the temperature increased, the hump of the curves disappeared gradually. It was obvious that the temperature was related to the failure mode (i.e., plastic failure or brittle failure) of interface bonding, and low temperature tended to cause brittle failure. In contrast, only plastic failure would occur when the test temperature was not less than 45°C in this study. Additionally, the high

temperature would significantly decrease the shear strength, no matter what the normal stress was.

The relationships between temperature and other interface bonding parameters under 1.0 MPa normal stress are illustrated in Figure 9. Despite some slight fluctuations, both shear strength and IBC were negatively correlated with. However, the residual strength did not show any significant change when the temperature rose from 0 to 60°C, which indicated that the temperature might not influence the residual strength. It was interesting that the residual ratio was positively related to the temperature because plastic failure was easier to occur at a high temperature, which would usually result in a higher residual rate.

In summary, temperature had a significant effect on interface bonding, and higher temperature would undoubtedly reduce the shear strength and interface bonding coefficient. Moreover, temperature played a dominant role in the failure mode of interface bonding. Specifically, interface bonding was more prone to plastic failure at high temperature but trended to encounter brittle failure at low temperature.
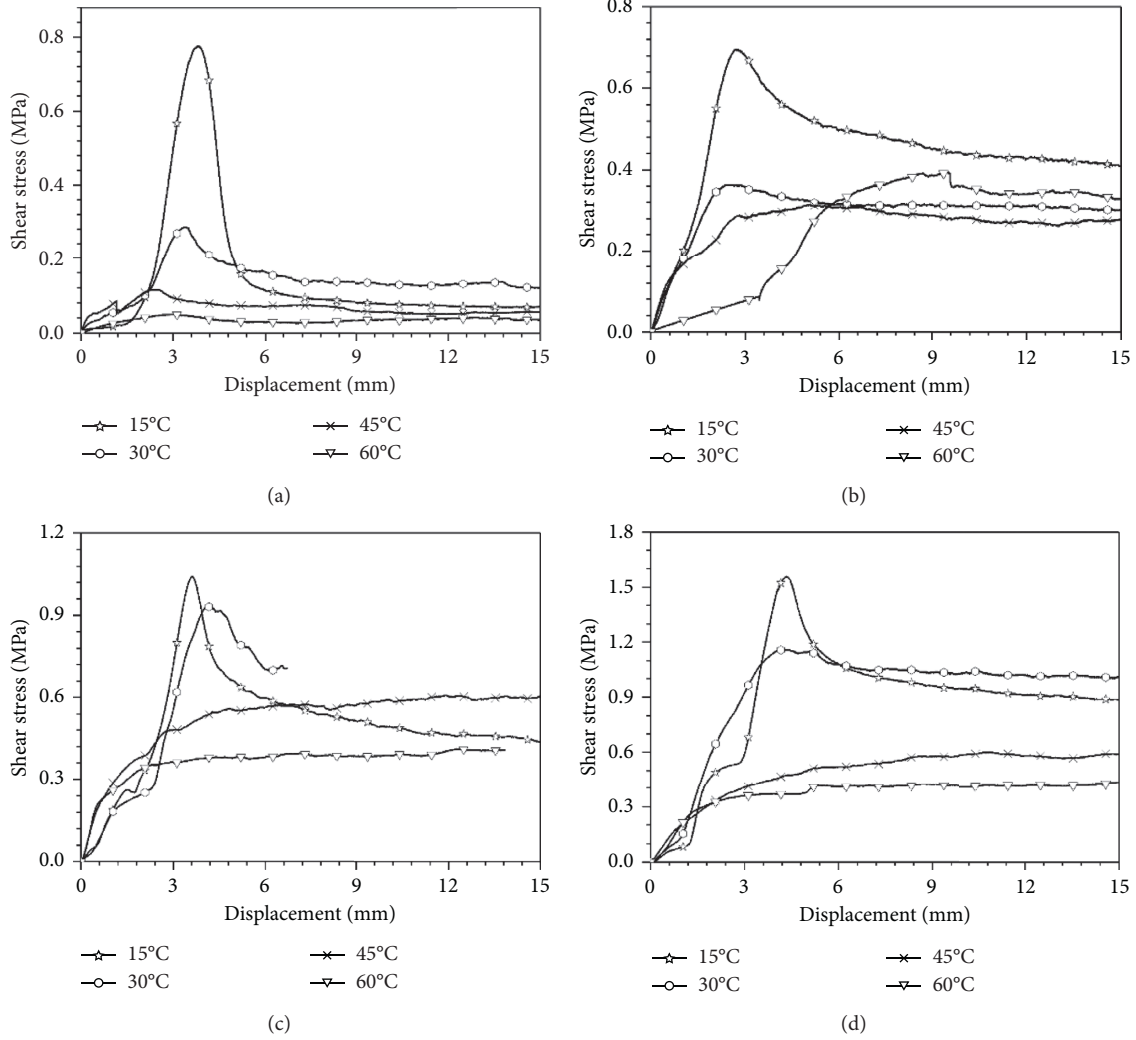
Figure 8: Shear stress-displacement curves at different temperatures. (a) 0 MPa, (b) 0.5 MPa, (c) 1.0 MPa, and (d) 1.5 MPa.

Figure 9: Continued.

(c)
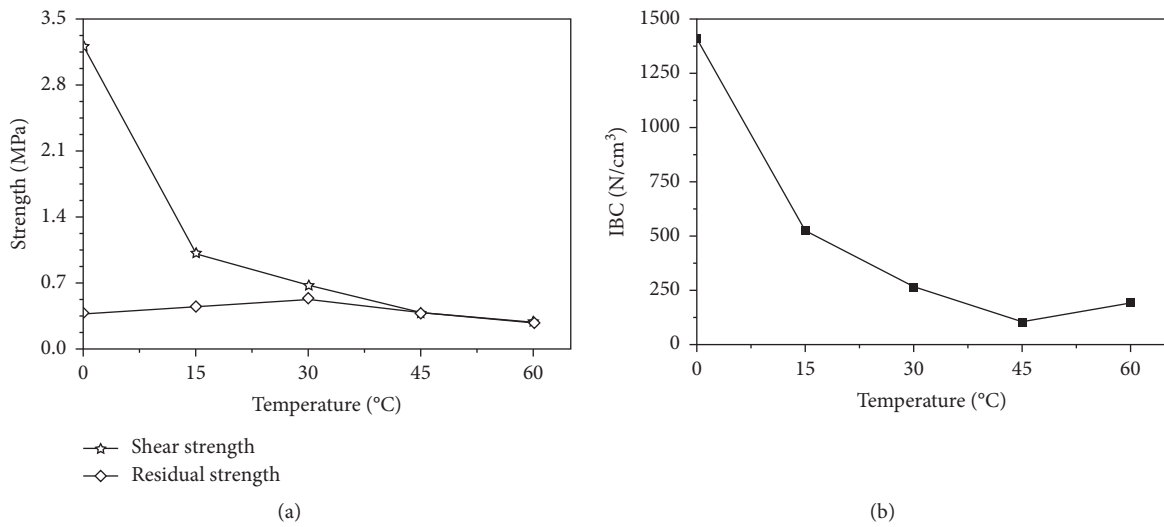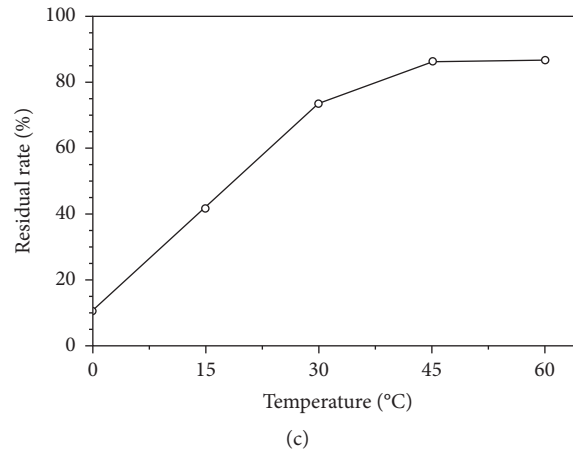
FIGURE 9: Relationship between temperature and other interface bonding parameters. (a) Shear strength and residual strength. (b) Interface bonding coefficient. (c) Residual ratio.

4. Conclusions

To study the characteristics of interface bonding comprehensively, a series of laboratory tests were conducted based on a self-designed direct shear test apparatus that can simultaneously apply shear force and normal stress on a specimen. Four kinds of tack coat materials were investigated under four different normal stresses and five temperatures. This research tried to analyze the coupling effects of normal stress and temperature on interface bonding. The key findings or conclusions were summarized as follows.

Temperature had a significant influence on the adhesive ability of the tack coat. A tack coat that had high shear strength at low temperature might not provide similar interface bonding strength at high temperature. Although emulsified asphalt, rubber asphalt, and virgin asphalt had a similar adhesive ability, the emulsified asphalt was recommended because of its simple construction method.

The interface between HMA overlay and PCC layer was still able to provide considerable bonding strength after failure, indicating that the damaged interface could still function. The interface bonding coefficient could be selected as an indicator to distinguish the failure mode of interface bonding.

Normal stress benefited interface bonding strength, especially at a lower temperature. Higher normal stress can increase both residual strength and residual ratio, but it usually had very limited impacts on the failure mode of interface bonding.

Temperature had a significant effect on interface bonding and played a dominant role in the failure mode of interface bonding. Specifically, the interface bonding was more prone to plastic failure at a high temperature, while it trended to encounter brittle failure at a low temperature.

Data Availability

The data used to support the findings of this study are available from the corresponding author upon request.

Additional Points

Highlights. A special direct shear test device was designed and manufactured to apply both normal stress and shear stress on the specimen. Different tack coat materials were tested and compared, and the optimal tack coat material was determined. The coupling effects of normal stress and temperature on interface bonding between Portland cement concrete and hot-mix asphalt mixture were analyzed.

Conflicts of Interest

The authors declare that they have no conflicts of interest.

Acknowledgments

References

[1] S. Chun, K. Kim, J. Greene, and B. Choubane, "Evaluation of interlayer bonding condition on structural response characteristics of asphalt pavement using finite element analysis and full-scale field tests," *Construction and Building Materials*, vol. 96, pp. 307–318, 2015.

[2] D. Fordyce and K. Khweir, "Influence of layer bonding on the prediction of pavement life," in *Proceedings of the ICE-Transport*, vol. 156, no. 2, pp. 73–83, 2003.

[3] J. Ling, F. Wei, H. Zhao, Y. Tian, B. Han, and Z. A. Chen, "Analysis of airfield composite pavement responses using full-scale accelerated pavement testing and finite element method," *Construction and Building Materials*, vol. 212, pp. 596–606, 2019.

[4] A. Mateos, J. Harvey, J. Paniagua, F. Paniagua, and F. Liu, "Mechanical characterisation of concrete-asphalt interface in bonded concrete overlays of asphalt pavements," *European Journal of Environmental and Civil Engineering*, vol. 81, no. 89, pp. 1–11, 2012.

[5] S. Romanoschi and J. Metcalf, "Characterization of asphalt concrete layer interfaces," *Transportation Research Record:*

Journal of the Transportation Research Board, vol. 1778, no. 1, pp. 132–139, 2011.

[6] D. Fordyce and K. Khweir, "Influence of layer bonding on the prediction of pavement life," *Transport*, vol. 156, no. 2, pp. 73–83, 2003.

[7] H. Ozer, I. L. Al-Qadi, H. Wang, and Z. Leng, "Characterisation of interface bonding between hot-mix asphalt overlay and concrete pavements: modelling and in-situ response to accelerated loading," *International Journal of Pavement Engineering*, vol. 13, no. 2, pp. 1–16, 2012.

[8] K. Liu, F. Wang, and X. Wang, *Research on Interlaminar Instability Failure of Asphalt Overlay on Old Cement Pavement*, The Annual Meeting of Transportation Research Board, Washington, DC, USA, 2012.

[9] M. Saghebfar and Y. M. Najjar, *Evaluation of Interface Bond Strength of Asphalt Pavements*, The Annual Meeting of Transportation Research Board, Washington, DC, USA, 2014.

[10] J. P. Zaniewski, S. F. Knihtila, and H. N. Rashidi, *Evaluation of the Bond Strength of Asphalt Overlays* International Airfield and Highway Pavements Conference, Washington, DC, USA, 2015.

[11] J. Uzan, M. Livneh, and Y. Eshed, *Investigation of Adhesion Properties Between Asphaltic-Concrete Layers* Association of Asphalt Paving Technologists Proc, Washington, DC, USA, 1978.

[12] A. A. Molenaar, J. P. Heerkens, and J. M. Verhoeven, *Effects of Stress Absorbing Membrane Interlayers* Vol. 55, Association of Asphalt Paving Technologists Proc, Washington, DC, USA, 1986.

[13] D. Mrawira and D. J. Damude, "Revisiting the Effectiveness of Tack Coats in HMA Overlays: The Shear Strength of Tack Coats in Young Overlays," in *Proceedings of the Annual Conference-Canadian Technical Asphalt Association*, pp. 115–130, Ontario, Canada, December 1999.

[14] C. Sangiorgi, N. H. Thom, and A. C. Collop, "Assesment of bond condition using the Leutner shear test," *Transport*, vol. 156, no. 4, pp. 211–217, 2003.

[15] I. L. Alqadi, *Tack Coat Optimization for HMA Overlays: Laboratory Testing*, Civil Engineering Studies Illinois Center for Transportation, Illinois, USA, 2008.

[16] B. Han, J. Ling, X. Shu et al., "Resilient interface shear modulus for characterizing shear properties of pavement base materials," *Journal of Materials in Civil Engineering*, vol. 30, no. 12, Article ID 04018333, 2018.

[17] B. Han, J. Ling, X. Shu et al., "Quantifying the effects of geogrid reinforcement in unbound granular base," *Geotextiles and Geomembranes*, vol. 47, no. 3, pp. 369–376, 2019.

[18] M. S. Buchanan and M. E. Woods, *Field Tack Coat Evaluator. Emulsions*, 2004.

[19] A. T. Papagiannakis, L. Tashman, and K. Nam, *Evaluation of the Influence of Tack Coat Construction Factors on the Bond Strength between Pavement Layers*, Milling, Washington, DC, USA, 2006.

[20] E. P. Donovan, I. L. Al-Qadi, and A. Loulizi, "Optimization of tack coat application rate for geocomposite membrane on bridge decks," *Transportation Research Record: Journal of the Transportation Research Board*, vol. 1740, no. 1, pp. 143–150, 2000.

[21] A. Arulrajah, M. A. Rahman, J. Piratheepan, M. W. Bo, and M. A. Imteaz, "Evaluation of interface shear strength properties of geogrid-reinforced construction and demolition materials using a modified large scale direct shear testing apparatus," *Journal of Materials in Civil Engineering*, vol. 26, no. 5, pp. 1–9, 2013.

[22] AASHTO, *Standard Method of Test for Determining the Interlayer Shear Strength (ISS) of Asphalt Pavement Layers*, AASHTO, Washington, D.C, 2015.

[23] Z. Leng, H. Ozer, I. L. Al-Qadi, and S. H. Carpenter, "Interface bonding between hot-mix asphalt and various Portland cement concrete surfaces," *Transportation Research Record: Journal of the Transportation Research Board*, vol. 2057, no. 1, pp. 46–53, 2008.

[24] Z. Leng, I. L. Al-Qadi, S. Carpenter, and H. Ozer, "Interface bonding between hot-mix asphalt and various Portland cement concrete surfaces," *Transportation Research Record: Journal of the Transportation Research Board*, vol. 2127, no. 2127, pp. 20–28, 2009.

[25] H. Zhao, J. Cao, and Y. Zheng, "Investigation of the interface bonding between concrete slab and asphalt overlay," *Road Materials and Pavement Design*, vol. 2, pp. 1–10, 2017.

[26] Z. Ge, H. Wang, Q. Zhang, and C. Xiong, "Glass fiber reinforced asphalt membrane for interlayer bonding between asphalt overlay and concrete pavement," *Construction and Building Materials*, vol. 101, pp. 918–925, 2015.

[27] L. A. Goodman, "Statistical methods for the mover-stayer model," *Journal of the American Statistical Association*, vol. 56, no. 296, pp. 841–8, 1961.

Research Article

Assessment of Freeze-Thaw Cycles Impact on Flexural Tensile Characteristics of Asphalt Mixture in Cold Regions

Cidan Duojie,[1] Wei Si ⓘ,[1] Biao Ma,[1] Yongping Hu,[1] Xue Liu,[2] and Xintong Wang[3]

[1]*Key Laboratory for Special Area Highway Engineering of Ministry of Education, Chang'an University, Xi'an 710064, China*
[2]*School of Data and Computer Science, Sun Yat-sen University, Guangzhou 510275, China*
[3]*School of Humanities and Social Science, Hong Kong University of Science and Technology, Clear Water Bay, Kowloon,
  Hong Kong 999077, China*

Correspondence should be addressed to Wei Si; siwei@chd.edu.cn

Low average temperature, large temperature difference, and continual freeze-thaw cycles have significant impacts on mechanical property of asphalt pavement. Bending test was applied to illustrate the mixtures' flexural tensile properties under freeze-thaw (F-T) conditions. Experiment results showed that the flexural tensile strength and strain declined as F-T cycles increased; the deterioration of flexural tensile properties decreased sharply during initial F-T cycles but turned smooth after 15–21 F-T cycles. ANOVA showed that F-T cycles, asphalt-aggregate ratio, and gradation had obvious influence on flexural tensile characteristics. Flexural characteristics of AC-13 behaved better than the other gradations. It turned out that the mixtures' low-temperature bending characteristics were improved when 5.5% optimum asphalt-aggregation ratio or slightly larger AC-13 gradation was applied.

1. Introduction

Qinghai-Tibet Plateau (QTP), located in the southwest of China, has an average altitude over 4000 m. It is the largest plateau in China with permafrost widely distributed. QTP has capricious climates and complex geological conditions, which are different from other ordinary regions [1–3]. In QTP, the mean annual air temperature is under 0°C: a transient period as temperature goes over 0°C from July to August, under 0°C from November to the following March, and changeable around 0°C in the remaining days, during which period the temperature gap between day and night is sharp, with a maximum temperature gap up to 26°C [4–6]. Additionally, the solar radiation is higher than 3600 KJ/m². Cooling and heating rates are rapid; thus, the asphalt pavement in this area suffers more frequent freeze-thaw (F-T) cycles compared with other regions.

Qinghai-Tibet Highway (QTH) passes through the QTP from north to south, of which the pavement is semirigid base asphalt concrete (AC) and the general structure is 4 cm AC-13 + 6 cm AC-16 + 20 cm cement stabilized macadam base. QTH suffers from the severe environment conditions such as low annual average temperature, large difference in temperature, rapid cooling rate, and frequent and violent F-T cycles [7–10]. All these adverse weather conditions have evident influences on mechanical property and durability of asphalt pavement [11].

Asphalt is a thermoplastic material with asphalt concrete mixtures, property of which is sensitive as temperature changes, with viscoelastic characteristic. Distresses in cold regions are more complex and serious than those in normal areas. Distresses like settlement, nonuniform deformation, and thermal cracks are critical for highway in cold regions, especially in QTH [12–14]. Numerous studies have found that distresses of highway have significant relationships with local special climate and environment conditions as well as loads.

By investigating the operation and distress of QTH, researchers found that there were serious distresses and damages, especially various cracks along the highway. As

shown in Figure 1, there are many serious longitudinal and transverse cracks in the highway pavement and trends to form map cracking. It is known that transverse cracks in cold regions are generally caused by lower temperature and rapid cooling, that is, F-T cycles effect. F-T effect has obvious impacts on asphalt pavement performance as well as the pavement lifecycle [15, 16].

Asphalt pavement is exposed in atmosphere; when temperature falls rapidly or there is continuous low temperature, thermal stress in asphalt pavement forms. If the stress relaxation of asphalt pavement is larger than comprehensive stress growth (including temperature stress and load stress), there is no obvious distress in the appearance, but the interior microdamage of pavement will be accumulated. When there is comprehensive stress over the ultimate tensile strength of asphalt mixture, cracks and other distresses will arise [17]. Moreover, when pavement is in moisture environment, hydrodynamic pressure and vacuum constriction will appear in the surface layer under repeatable loads. This leads to the surface AC stripping aggravation and voids increase. Finally, the asphalt mixture becomes loose and cracks are formed from initial tiny damage, which is caused by the complicated effects including the migration, accumulation, and freezing of water in asphalt mixture and displacement of water in asphalt film [18, 19]. Consequently, the increasing of F-T cycles or continuous low temperature will speed up the damage and become more harmful to AC structures.

Asphalt pavement suffered from the impact of F-T in cold regions worldwide, and how to precisely evaluate the influence of F-T cycles on flexural characteristics has become one of the daunting tasks [20]. To solve this problem, low-temperature bending property of asphalt mixture under different F-T cycles had been applied in this research, and the influences of aggregate ratio and gradation were also analyzed.

The objectives of this research are to analyze the flexural tensile characteristics of AC under F-T cycles and to evaluate the impact factors on asphalt-aggregate ratio, gradation, and F-T cycles. The results provided a good reference for asphalt mixture design, distress prevention, and some scientific guidelines for highway construction and maintenance in cold regions.

2. Materials and Experimental Methods

2.1. Materials Used.
The materials used in this study are listed below. The type of asphalt used was styrene butadiene rubber (SBR) modified asphalt supplied by Jinshi in Xinjiang, China, which is frequently used in QTP. Test results are presented in Table 1. Aggregates and mineral powders were obtained from lime-stone Haihong rock quarry in Tibet, China.

Asphalt mixtures used in this research were AC-10, AC-13, and AC-16, and gradation composition of aggregates mixture recommended by specification of Ministry of Transportation of China was given in Table 2.

The optimum asphalt content of the asphalt mixture was obtained by Marshall Test [21]. On the basis of Marshall Test and considering the special climate and traffic condition in cold QTP, the final optimum asphalt contents (OAC) of the three asphalt mixtures AC-10, AC-13, and AC-16 are 5.0%, 5.5%, and 6.0%, respectively.

2.2. F-T Cycle Test.
At first, F-T cycle test used in civil engineering is to evaluate the impact of F-T cycles on the performance of cement concrete [22] and soil [23, 24]. As the application of flexural pavement increases in cold regions and the unusual distresses appear, some researchers noticed that asphalt pavement also suffered from F-T cycles influence. There is a big difference between viscoelastic characteristics of asphalt concrete and cement concrete elastic property. Some researches have been conducted on the F-T performance of asphalt mixtures [25].

In terms of AC F-T cycle test, there is no standard due to the differences in climate among different cold areas. In AASHTO 283 testing procedure, each vacuum saturated specimen was tightly covered with plastic wrap and placed in a plastic bag with approximately 10 ± 0.5 mL of water and then sealed; the plastic bags were placed in a freezer at $-18 \pm 3°C$ for 24 h and then removed to a water bath at $60 \pm 1°C$ for 24 h and finally placed in a water bath at $25 \pm 0.5°C$ for $2 h \pm 10$ min to achieve room temperature [26]. In one research, the samples were soaked in water for 12 h at room temperature; then each was covered with plastic wrap, sealed in a plastic bag, and placed in an environmental chamber for 12 h at $-17.8°C$. The conditioned samples were exposed to seven 24 h cycles [27]. In another research, the specimens were firstly water-conditioned by vacuum saturation for 15 min and then subjected to 8 successive cycles of freezing and thawing. Each cycle was consisted of freezing at $-20°C$ for 8 h followed by soaking in water at $60°C$ for 4 h [28].

Meteorological data in QTH show that annual average lowest temperature is among $-14.5°C$ to $-17.4°C$, annual average highest temperature is $6.8°C$ to $8.1°C$, and the maximum temperature difference between day and night can reach a range between $23°C$ and $26°C$, which indicates that it has a rapid cooling and heating rate. Considering present F-T test, a modified F-T test was proposed according to the practical climate conditions of QTH in this paper. The test uses plastic bag to seal up each specimen and injects 30 ml water to the plastic bag when freezes. Freezing temperature is $-25 \pm 1°C$ and freezing lasts 12 h; then the specimens are put in a water bath to be thawed at $25 \pm 1°C$ and the thawing lasts 12 h. The freezer and water bath are used to simulate the F-T cycles.

Fresh mixed asphalt mixtures are shaped up by Wheel Grinding Method into slabs that are 300 mm in length and width and 50 mm in height. The slabs are then cut into prism beam that is 250 mm $\pm$ 2.0 mm in length, 30 mm $\pm$ 2.0 mm in width, and 35 mm $\pm$ 2.0 mm in height by cutter. The mixture flexural tensile laboratory test was carried out by Universal Material Tester System (UMTS) performed by three-point bending test, and the loads and deformations were automatically measured by computer. The UMTS is a computer-controlled system that can operate automatically. Loads and

Figure 1: Crack distresses in Qinghai-Tibet Highway.

Table 1: Test results of asphalt parameters.

Asphalt state	Test item		Results
Original sample	Penetration/0.1 mm	15°C	51
		25°C	123
	Softening point (R&B)/°C		47.6
	Ductility/cm	5°C	>150
	Density/g·cm^{-3}		1.023
	Flashing point/°C		>260
	Solubility/%		99.6
After aging	Mass loss/%		0.2
	Vestigial penetration ratio/%	15°C	65.3
		25°C	58.1
	Ductility/cm	5°C	>150

deflection of specimen were measured by load cells and linear variable differential transducers (LVDTs), respectively. UMTS was equipped with environment chamber with an accuracy of ±0.1 °C, and loading speed could be chosen according to the needs of the experiment. The purpose of flexural tensile under F-T cycles testing is to evaluate asphalt mixture's bending failure property, temperature, and moisture susceptibility.

When three-point bending test under low temperature was conducted, −10 ± 0.5°C and 50 mm/min were applied as test temperature and load speed, respectively. After samples were tested by bending test under F-T cycles, the bending performance of asphalt mixture was evaluated by failure flexural strength and failure flexural strain, which are calculated by the following formulas [21]:

$$R_B = \frac{3 \times L \times P_B}{2 \times b \times h^2},$$

$$\xi_B = \frac{6 \times h \times d}{L^2},$$

(1)

where R_B is the failure flexural strength (MPa), L is distance between beam supports (200 mm), P_B is the ultimate loading at failure (N), b is width of beam specimen (30 mm), h is height of beam specimen (35 mm), ξ_B is the failure flexural strain ($\mu\xi$), and d is the mid-span deflection at the specimen failure (mm). Average value of three-specimen failure (mm) and average value of three specimens for each F-T cycle condition test were applied to analyze the flexural tensile characteristics in this paper.

3. Results and Discussion

3.1. Impact of F-T Cycles. In order to explain F-T cycles' impact on mixture flexural characteristics, AC-13 asphalt mixture with OAC 5.5% was taken for test. After 30 F-T cycles, the tendencies of flexural tensile strength and flexural tensile strain are shown in Figure 2.

Figure 2 shows that flexural tensile strength and tensile strain tend to decline with F-T cycles increasing. In initial F-T cycles, flexural characteristics drop significantly; after 9 F-T cycles, the decline of flexural tensile characteristics becomes gentle. Through 15 to 21 F-T cycles, the degradation tendency is gradually stable. After 30 F-T cycles, the flexural tensile strength reduces nearly 4 MPa compared with unconditioned (no F-T cycle) performance, the attenuation reaches 27%, and the flexural tensile strain attenuates 12.6%.

Under the repetitive F-T cycles, mixture internal pores and air voids are increased. Water enters into the asphalt membrane easily and decreases the bond force between asphalt membrane and aggregate, which leads the mixture to be easily broken. When AC is in moisture environment, especially in saturated condition, its air voids will be filled with water. This water turns into ice in freezing cycles, causing the ice volume expansion. The internal of the mixture generates expansion force and results in micro-damage to mixture [28]. During the thaw cycles, with the filled ice melting, more water will permeate through air voids and internal pores, and the bonding between asphalt membrane and aggregates decreases as the water erodes [27, 29]. The bond force declines rapidly after repetitive F-T cycles. Results indicate that F-T cycles in the early years have obvious influence on asphalt mixture flexural performance. So, the early damage of asphalt pavement in cold regions is more frequent and serious than in other regions.

Due to the uneven distribution of aggregate, defects of internal structure, and increment of F-T cycles, the mixture's internal damage gradually increases and finally fractures in the loading test. Therefore, the mixture's flexural tensile strength is related to mixture porosity, coarse aggregate distribution, and internal structure defects.

Figure 3 illustrates that mixture performance attenuated with F-T cycles increasing. However, there are still some abnormal points, which decrease sharply in a certain F-T cycles performance and inversely increase in the next F-T cycle. In terms of this phenomenon, the uneven aggregate

TABLE 2: Gradation composition of aggregates mixture.

Gradation	Passing rate (%) of sieve size (mm)										
	19	16	13.2	9.5	4.75	2.36	1.18	0.6	0.3	0.15	0.075
AC-10	-	-	100	95	60	44	33	22.5	16	11	6
AC-13	-	100	95	76.5	53	37	26.5	19	13.5	10	6
AC-16	100	95	81	70	48	34	24.5	17.5	12.5	9.5	6
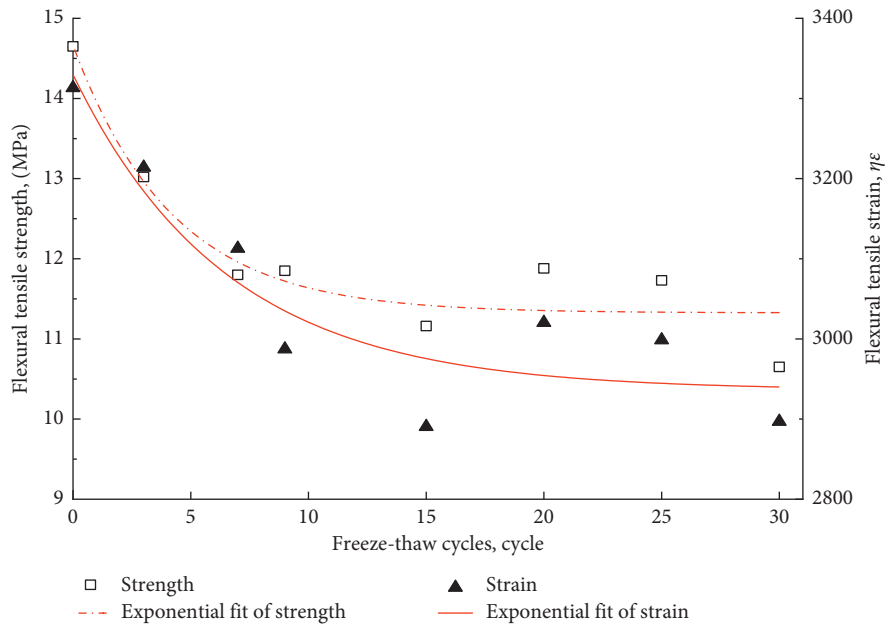
FIGURE 2: Relationship of flexural tensile characters and F-T cycles.
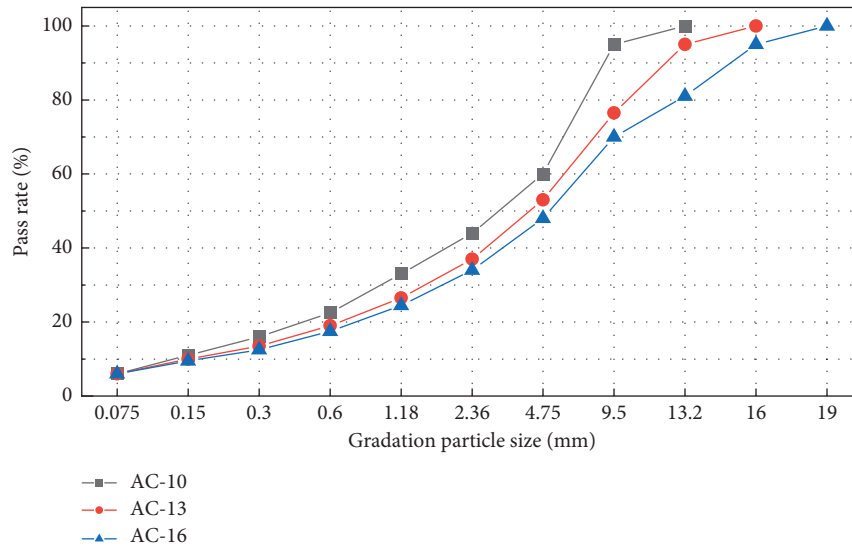
FIGURE 3: Grading curve.

distribution (differences between the cut beams) may take main responsibility.

3.2. Exponential Model Fitting.

Curves of flexural tensile strength and flexural tensile strain versus F-T cycles in Figure 2 present nonlinear variation, and the curves can be simulated by exponent or logarithm function. The exponential model is chosen to fit the flexural tensile characteristics variation in this paper. The formula used is as follows [24, 25]:

$$y = a + b \cdot e^{c \times x} + \varepsilon, \quad \varepsilon \sim N(0, \delta^2), \tag{2}$$

where a is the constant term, which means the initial value of flexural tensile characteristics; b is coefficient, which refers to the degradation speed; c is coefficient, which refers to curvature of curves; x is the explanatory variable, denoting F-T cycles here; y is explained variable, representing flexural tensile characteristics (MPa); and ε is the error term.

In this model, the error term is supposed to be approximately normally distributed. The variance of the error term δ^2 is independent, homoscedastic, and identical across observations. The least-square method has been applied to parameter estimation, due to the ε subjects to normal distribution; Chi-square has been used to assess the goodness of fit (GOF) of the exponential model. The equation is as follows [24, 25]:

$$\chi^2 = \sum_{i=1}^{n} w_i (y_i - \widehat{y}_i)^2, \tag{3}$$

where w_i is the weighting coefficient, which can be calculated by $w_i = (1/(\sigma_i^2))$; y_i is the experimental data point and $\widehat{y}_i$ is the theoretical point; n is the experimental number. This paper considers the measurement errors as unknown; σ_i is set to 1 for all i and the curve fitting is performed without weighting.

R^2 represents the fitting quality of models, which increases with adding variables to the model without enough information. Adjusted R_{adj}^2 (adj. R-square) is preferable as it has the advantage that it only increases if the added variable reduces the mean square error of the model.

Fitting results are shown in Table 3. Results show that the exponential model well reflects the variation of flexural tensile strength and flexural tensile strain with F-T cycles; the adj. R-square reaches 0.866 and 0.823, respectively. The ANOVA method is used to analyze the fitting significance. The results are listed in Table 4. The ANOVA results indicate that, at the 0.01 level, tensile characteristics and regression model have good relationship, and the exponential model can be used to simulate the mixture degradation under F-T cycles.

Impact of asphalt-aggregate ratio.

AC-13 was used as an example to illustrate the influence of asphalt-aggregate ratio on flexural characteristics under F-T cycles, with asphalt-aggregate ratio of 4.5%, 5.0%, 5.5%, 6.0%, and 6.5%, respectively. Test results are shown in Figures 4(a) and 4(b).

Figure 4 shows that flexural tensile characteristics present as parabolic variation as the asphalt content increases. Tensile strength has more obvious parabolic variation than tensile stain; at the OAC (5.5%), both tensile strength and stain attain the peak value. When asphalt-aggregate ratio exceeds OAC, tensile strength declines more sharply compared with tensile strain.

After 30 F-T cycles, the flexural tensile strength of asphalt-aggregate ratio with 4.5% and 6.5% reduces by 3.2 MPa and 1.1 MPa, respectively. For unconditioned mixture, the flexural tensile performance is significantly greater than others, and their performance decreases gradually with F-T cycles increasing. Compared with lower asphalt-aggregate ratio (4.5% and 5.0%), the mixture's attenuation tendency of tensile strain is smaller with higher asphalt-aggregate ratio (6.0%, 6.5%) under F-T cycles. Under the F-T cycle, compared with the lower asphalt-aggregate ratio (4.5% and 5.0%), the higher the asphalt-aggregate ratio (6.0% and 6.5%) is, the slower the tensile strain attenuation of the mixture will be.

Asphalt-aggregate ratio is closely related to the mixtures' porosity. The larger the asphalt-aggregate ratio is, the smaller mixture porosity is. Air voids and internal pores will expand as the filled water freezes in F-T cycles. Icy water in the pore causes a huge expansion force, which leads to the mixture internal structure deterioration and destruction.

If asphalt-aggregate ratio is too small, it is hard to form the thin asphalt membrane to bind aggregate particles. The bond force between asphalt and aggregate is not intense. Under temperature gradient, loading stress, and F-T cycles, the mixture structure becomes loose, which leads to decline of flexural characteristics. With asphalt-aggregate ratio increasing, the structure asphalt forms gradually. Each particle has been packed by asphalt and formulates cohesive force between asphalt and aggregate. The cohesive force increases with asphalt content increasing. Flexural characteristics reach the peak value in OAC of 5.5%. Experiencing several F-T cycles, the flexural characteristics still are the best at the OAC compared with other asphalt-aggregate ratios.

With asphalt-aggregate ratio continually increasing, there is no more extra porosity to fill the asphalt and formed surplus asphalt. Compared with structure asphalt, surplus asphalt becomes free asphalt and lubricant. Aggregate particles will be "pushed away" and slide under the loading condition [29, 30]. This leads to the flexural tensile strength reducing fiercely; however, flexural tensile strain decreases slowly.

If pores of mixture are too small, once water enters into the internal pores, it is hard to remove. Due to capillary action, when the water in the pores begins to freeze, its volume increases with the freezing of water, which produces water pressure. The water pressure makes the water in the pores continuously gather on the freezing peak surface under F-T cycles, which leads to the intensification of freezing effect. After several F-T cycles, porosity constantly increases with the accumulation of freezing impact. Flexural characteristics are reduced. The reduction extent of flexural characteristics is smaller at high asphalt content compared with the lower asphalt content.

TABLE 3: Fitting results of the exponential model.

	a		b		c		Statistics	
	Value	Error	Value	Error	Value	Error	Reduced χ^2	R^2_{adj}
Tensile strength	11.38	0.23	4.46	0.89	−0.32	0.12	0.20	0.866
Tensile strain	2943	40	460	87	−0.19	0.08	3954	0.823

TABLE 4: ANOVA results of exponential model.

		Df	Sum of squares	Mean square	F value	Prob $> F$
Tensile strength	Regression	3	1179.481	393.1603	1927.163	$6.04E - 08$
	Residual	5	1.02005	0.20401		
	Uncorrected total	8	1180.501			
	Corrected total	7	10.67235			
Tensile strain	Regression	3	$7.48E + 07$	$2.49E + 07$	6303.609	$3.13E - 09$
	Residual	5	19767.54	3953.507		
	Uncorrected total	8	$7.48E + 07$			
	Corrected total	7	156315.9			
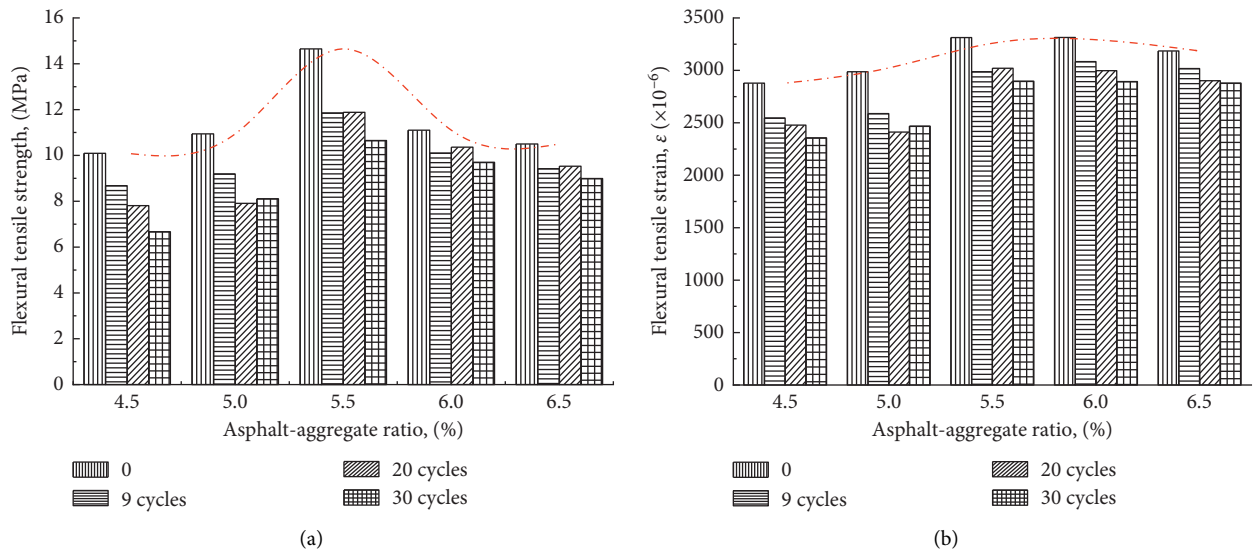
FIGURE 4: Relationship of flexural tensile characteristics and asphalt-aggregate ratio. (a) Flexural tensile strength. (b) Flexural tensile strain.

From the laboratory test data analysis, it is known that F-T cycles and asphalt-aggregate ratio have influence on flexural tensile characteristics. ANOVA with a 0.05 level significance from statistic view is applied to illustrate the impacts of F-T cycles and asphalt-aggregate ratio. For F-T cycle factor, it has eight levels as shown in Figure 2; and asphalt-aggregate ratio has five levels as shown in Figure 4. For the same gradation and different asphalt-aggregate ratio mixture, results of ANOVA are shown in Table 5.

Table 5 shows that asphalt-aggregate ratio and F-T cycles have obvious influence on flexural tensile characteristics, respectively. More results imply that the interaction of asphalt-aggregate ratio and F-T cycles also has significant influence on flexural tensile characteristics. Results indicate that asphalt-aggregate ratio and F-T cycle are both important parameters, which impact on the performance of mixture. Therefore, the proper asphalt-aggregate ratio can be

designed and got based on laboratory test, which can be used to limit the damage of F-T cycles.

3.2.1. Impact of Gradation.

This paper chooses AC-10, AC-13, and AC-16 to analyze the gradation impact on mixture flexural characteristics under F-T cycles.

As depicted in Figure 5, flexural characteristics of different gradations all show a declining trend as F-T cycles increase. In addition to the F-T cycles, the flexural characteristics of asphalt mixture are affected by many other factors, such as porosity, compaction, and uneven aggregate distribution, which inevitably cause some abnormal data in the flexural characteristics. However, after the F-T cycles, the overall trend of attenuation of the flexural characteristics remains unchanged. Flexural tensile characteristics of AC-13 are evident higher than the other two gradations. The

TABLE 5: Two-factor ANOVA about F-T cycle and asphalt-aggregate ratio.

Sources of variation	SS	Df	MS	P value	F-crit
Asphalt-aggregate ratio	197.10	4	49.27	$4.05E-63$	2.49
F-T cycles	76.29	7	10.90	$1.9E-45$	2.13
Interaction	24.29	28	0.87	$2.51E-20$	1.62
Interior	5.08	80	0.06		
Amount	302.75	119			
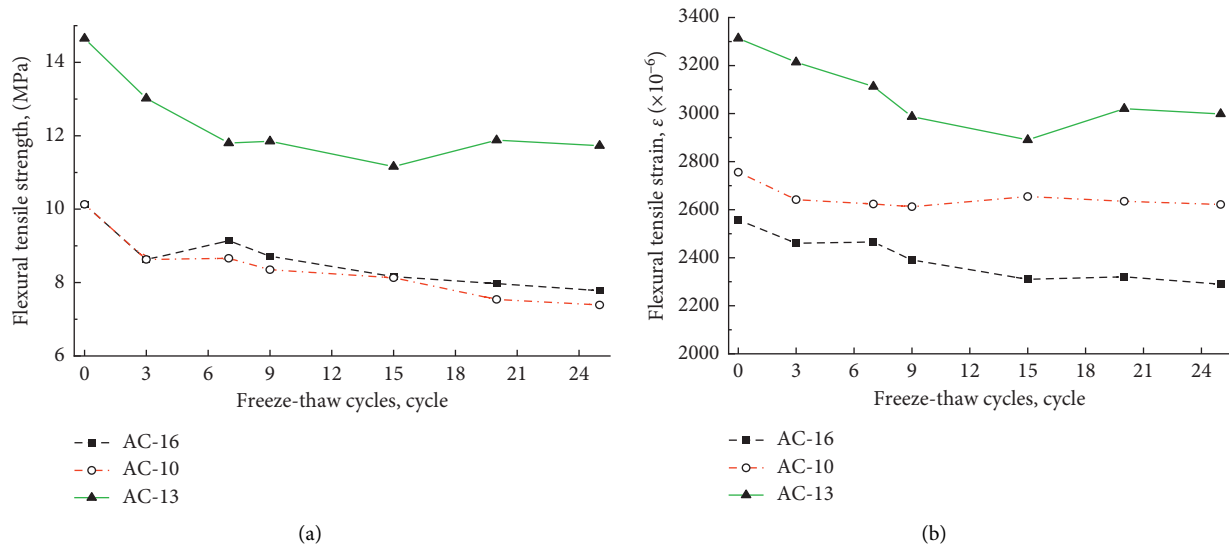
FIGURE 5: Flexural tensile characteristics and asphalt-aggregate ratio under different gradations. (a) Flexural tensile strength. (b) Flexural tensile strain.

difference of flexural tensile strength between AC-10 and AC-16 is small, and the change curves of flexural tensile strength have the same trend. For the flexural tensile strain between AC-10 and AC-16, the difference is small in the initial F-T cycles. With F-T cycles increasing, AC-10 tends to be stable, while AC-16 continually decreases, hence enlarging the difference between them.

Under loading conditions, loads are mainly transmitted along the aggregate particles, especially in large size particles; coarse aggregate plays an important role in bearing load. Under low-temperature loading, the strength of asphalt mixture mainly comes from coarse aggregate skeleton support. Asphalt binder effects are relatively reduced. With the maximum diameter decreasing, asphalt mixture becomes denser, and the resistance of low-temperature crack is improved to a certain extent. Additionally, the mixture defects are reduced. However, if the size of coarse aggregate is too small and the content of fine aggregate is too large, the strength of the mixture will also decrease. For AC-13 asphalt mixture, its nominal maximum aggregate size is between AC-10 and AC-16. Because AC-13 has high skeleton strength, high density of its mixture, and superior comprehensive performance, its flexural tensile strength and flexural tensile strain are superior to the other two gradations' mixture under F-T cycles.

The ANOVA method was applied to analyze the significance of F-T cycles and gradation change to flexural tensile strength characteristics. There are three levels of

aggregate gradation, AC-10, AC-13, and AC-16. There are seven levels of F-T cycle factors: no F-T cycles, 3 cycles, 7 cycles, 9 cycles, 15 cycles, 20 cycles, and 25 cycles.

Flexural tensile characteristics were statistically analyzed with a level of significance of 0.05. Results are shown in Table 6.

Gradation and F-T cycle have significant influence on flexural tension properties. The influence of gradation is greater than that of F-T cycles, which indicates that gradation is a major factor to determine the flexural tension properties of asphalt mixture.

ANOVA presents that all the F-T cycle, asphalt-aggregate ratio, gradation, and their interaction have significant influence on the flexural tensile properties of asphalt mixture. Flexural performance decreases evidently as the F-T cycles increase. Therefore, in cold regions, F-T cycle is another critical factor to determine the pavement durability and suitability besides the vehicle loads. Attention should be paid to F-T and other environment factors. Furthermore, appropriate asphalt-aggregate ratio and gradation can reduce the negative influence of F-T cycles on AC. In other words, they improve the resistance ability against complex climate.

3.2.2. Loss Ratio of Flexural Tensile Characteristics. As described before, flexural tensile characteristics of AC decline with the F-T cycles increasing. However, how to assess this

TABLE 6: ANOVA about gradation and F-T cycle.

Sources of variation	SS	Df	MS	P value	F-crit
F-T cycles	15.15	6	2.53	$5.48E - 05$	3.00
Gradation	66.66	2	33.33	$5.84E - 10$	3.89
Error	1.98	12	0.17		
Amount	83.79	20			

TABLE 7: Fitting results of the logistic model.

	a		b		x_0		p		Statistics	
	Value	Error	Value	Error	Value	Error	Value	Error	Reduced χ^2	R^2_{adj}
Tensile strength	-0.11582	0.48	0.24	0.06	1.86	4.25	1.21	1.75	0.001	0.843
Tensile strain	$3.25E - 04$	0.03	0.11	0.02	5.24	2.04	2.36	1.87	$4.36E - 04$	0.786
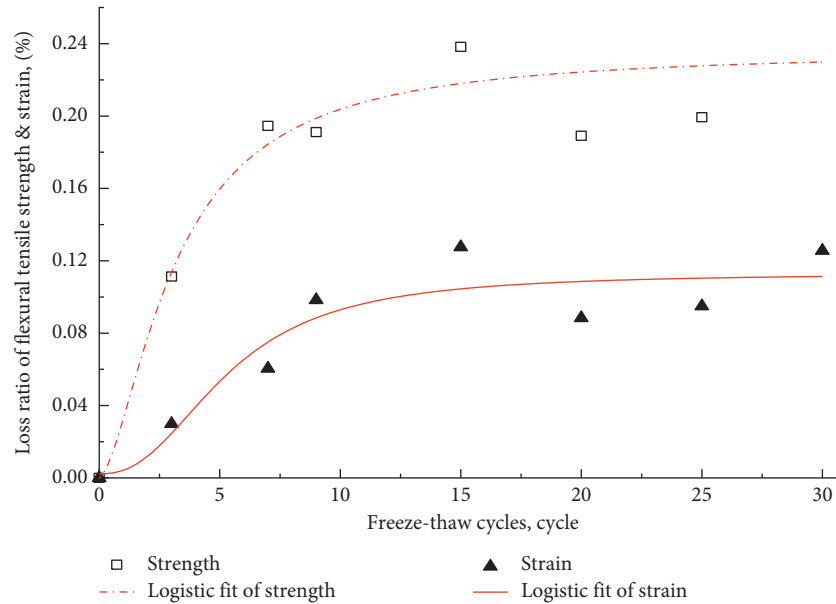
FIGURE 6: Relationship between loss ratio and F-T cycles.

variation effectively and conveniently is still a problem. The first pavement performance model was developed based on the data provided by the AASHO Road Test. The AASHO equation estimates deterioration based on a dimensionless parameter g referred to as damage. The damage parameter was defined as the loss in serviceability at any given time.

$$g_t = \frac{p_0 - p_t}{p_0 - p_f} = \left(\frac{N_t}{\rho}\right)^b. \tag{4}$$

The recursive model is another popular model to simulate the performance deterioration. The following equation is applied from the beginning of the experiment:

$$p_t = p_0 + \alpha \sum_{s=0}^{s=t-1} N_s^\sigma \Delta N_{s+1}, \tag{5}$$

where g_t is a dimensionless damage parameter; p_0 is initial service ability at time $t = 0$; p_t is serviceability index at time t

(or load frequency, load variation); p_f is terminal serviceability index; N_t is cumulative number of equivalent 80 KN single-axle loads applied until time t; N_s is the deterioration; ΔN_{s+1} is the increment of deterioration; and ρ, b, α, σ are parameters or functions to be estimated. Another general and flexible deterioration model is shown as follows:

$$y = f(x) = a + bx^c, \tag{6}$$

where y is a variable representing a measure of material quality; x is a variable representing a measure of load (or traffic); a is a parameter or a function that represents the initial condition; b is a parameter or a function that represents the rate at which quality deteriorates with load frequency (or time, traffic); and c is a parameter that represents the curvature of the function.

Performance deterioration functions (5) to (7) can be combined to predict the variation of performance. Based on these three functions, loss ratio has been applied to get the

relationship of flexural tensile characteristics and F-T cycles; loss ratio formula is as follows:

$$L_i = 1 - \left(\frac{y_i}{y_0}\right), \tag{7}$$

where L_i is loss ratio of flexural tensile characteristics, y_0 represents the unconditioned flexural tensile characteristics, y_i represents the flexural tensile characteristics that change with F-T cycles, and subscript i represents the F-T cycles, from 0 to 30 in this research. Flexural tensile characteristics y_i can be indicated by regression function (6).

Logistic model is a common sigmoid function; it is in relation to population growth. The logistic model is widely applied in neural networks, biology, probability, statistics, sociology, political science, and economics [12, 13]. Considering that the deterioration of loss ratio presents logistic curve with the increasing of F-T cycles, where deterioration is approximately exponential in initial stage, as saturation begins, the deterioration slows, and, at maturity, deterioration stops. Therefore, this paper uses modified logistic model to fit the deterioration trend, and the function is

$$y = \frac{a - b}{1 + (x/x_0)^p} + b, \tag{8}$$

where y represents loss ratio flexural tensile characteristics; x_0, a, b, and p are estimated parameters, x_0 is the center value, a is the initial value, b is the terminal value, and p is the power and it is greater than zero. The estimation method of the logistic model is similar to that of the exponential model, applying the χ^2 method to minimize the residual sum.

AC-13 of OAC of 5.5% is taken as an example to illustrate the loss ratio about flexural tensile strength and flexural tensile strain under different F-T cycles. The fitting results are shown in Table 7, and the variation tendency is depicted in Figure 6.

Figure 6 illustrates that the logistic model and the loss ratio well reflect the deterioration of flexural tensile characteristics with the increasing of F-T cycles. The variation of deterioration is corresponding with the changes of flexural tensile characteristics.

The variation of loss ratio of flexural tensile strength is more intense than flexural tensile strain as F-T cycles increase, which implies that the flexural tensile strength of AC is more sensitive under F-T conditions. Previous research has indicated that the tensile strength of AC is related to fatigue cracking, moisture susceptibility, and the ability of resistance of thermal stress cracks. A higher tensile strength means that asphalt pavement can tolerate higher strains before failing (i.e., cracking). Therefore, this can explain why there are more cracks in cold regions, especially in frequent F-T cycles of cold plateau regions.

4. Conclusions

This work was conducted to explore the effect of F-T cycle on flexural tensile characteristics of asphalt mixture in laboratory. The main conclusions drawn from this study are summarized as follows.

When asphalt mixture suffered F-T impacts, the flexural tensile strength and flexural tensile strain will decline. Flexural tensile performance keeps declining as F-T cycles increase, which declines rapidly in the initial F-T cycles and then becomes gentle after 15–21 cycles.

Both asphalt content and gradation have an obvious influence on the flexural characteristics of asphalt mixture. In general, the higher asphalt content is, the slower degradation will be under F-T cycle. AC-13 has better flexural performance than AC-10 and AC-16, which indicates that AC-13 has better durable ability in low temperature and F-T conditions.

The flexural tensile properties get to peak value at the optimum asphalt content and obtain the slowest degradation correspondingly under F-T test.

The ANOVA results show that asphalt content, gradation, F-T cycles, and their interaction have significant impact on flexural tensile characteristics with a 0.05 level of significance from statistic view.

For the Qinghai-Tibet Plateau with severe weather conditions, it will improve the performance against low temperature if skeleton close-grained gradation of AC-13 and 5.5% or a little higher asphalt content is applied. Therefore, proper high asphalt content can reduce thermal cracks and moisture distress in cold regions, especially in high-frequency F-T zones.

Data Availability

All the data used to support the findings of this study are available from the corresponding author upon request.

Conflicts of Interest

The authors declare that they have no conflicts of interest.

Acknowledgments

References

[1] Z. Zhang, Q. Wu, G. Jiang, S. Gao, J. Chen, and Y. Liu, "Changes in the permafrost temperatures from 2003 to 2015 in the Qinghai-Tibet plateau," *Cold Regions Science and Technology*, vol. 169, Article ID 102904, 2020.

[2] S. Wang, J. Chen, J. Zhang, and Z. Li, "Development of highway constructing technology in the permafrost region on the Qinghai-Tibet plateau," *Science in China Series E: Technological Sciences*, vol. 52, no. 2, pp. 497–506, 2009.

[3] G. Cheng and T. Wu, "Responses of permafrost to climate change and their environmental significance, Qinghai-Tibet Plateau," *Journal of Geophysical Research*, vol. 112, 2007.

[4] G. Jiang, L. Wang, H. Yun, S. Gao, and Q. Wu, "Thermal influences of road engineering on permafrost underneath different surface condition in the Qinghai-Tibet Plateau," *Cold Regions Science and Technology*, vol. 173, Article ID 103028, 2020.

[5] W. Si, B. Tang, Y. Hu, B. Ma, Q. Ren, and S. Ge, "Variation and quantification of meteorological parameters along with the Qinghai-Tibet highway," *China Sciencepaper*, vol. 13, no. 07, pp. 727–731+736, 2018.

[6] L. Quan, B. Tian, K.-M. Niu, J.-D. Xie, Z. He, and Y.-H. Zhang, "Temperature variation properties of pavements and subgrades for high-grade roads on Qinghai-Tibet Plateau," *Journal of Traffic and Transportation Engineering (China)*, vol. 17, no. 2, pp. 21–30, 2017.

[7] Q. B. Wu, Y. Sheng, Q. H. Yu, J. Chen, and W. Ma, "Engineering in the rugged permafrost terrain on the roof of the world under a warming climate," *Permafrost Periglacial Process*, vol. 12, 2020.

[8] J. Yuan, X. Pei, Q. Cheng, G. Zhang, and J. Chen, "Analysis on temperature variation regularity and slope temperature field-deformation along sichuan-tibet expressway," *Journal of Highway and Transportation Research and Development*, vol. 36, no. 10, p. 33, 2019.

[9] K. Yang, Y. Mu, W. Ma, G. Bi, G. Li, and Y. Mao, "The evolution law of ground temperature field in permafrost roadbed of the Qinghai-Tibet plateau under climate warming," *China Earthquake Engineering Journal*, vol. 40, no. 4, pp. 734–744, 2018.

[10] W. Si, N. Li, B. Ma, J. Ren, H. Wang, and J. Hu, "Impact of freeze-thaw cycles on compressive characteristics of asphalt mixture in cold regions," *Journal of Wuhan University of Technology (materials science) editorial department*, vol. 30, no. 4, pp. 703–709, 2015.

[11] M. T. Chai, Y. H. Mu, J. M. Zhang, W. Ma, G. Liu, and J. B. Chen, "Characteristics of asphalt pavement damage in degrading permafrost regions: case study of the qinghai-tibet highway, China," *Journal of Cold Regions Engineering*, vol. 32, no. 2, p. 11, 2018.

[12] W. Ke, H. Chen, and Y. Lei, "Mechanical response of high-grade highway asphalt pavement in cold and high altitude area in Qinghai-Tibet Plateau," *Journal of Chang'An University. Natural Science Edition*, vol. 39, no. 1, pp. 34–43, 2019.

[13] B. Ma, X. Zhou, W. Si, N. Li, and S. Peng, "Study of the water stability and high temperature performance of asphalt mixtures in Qinghai-Tibet cold regions," *Journal of Glaciology and Geocryology*, vol. 37, no. 01, pp. 175–182, 2015.

[14] N. Li, W. Si, B. Ma, X. Zhou, and Y. Tian, "Impact of freeze-thaw cycles on flexural tensile characteristics of asphalt mixture in cold plateau regions," *Journal of Jiangsu University (Natural Science Edition)*, vol. 36, no. 05, pp. 610–614, 2015.

[15] B. Teltayev, C. O. Rossi, G. Izmailova, and E. Amirbayev, "Effect of freeze-thaw cycles on mechanical characteristics of bitumens and stone mastic asphalts," *Applied Sciences*, vol. 9, no. 3, p. 458, 2019.

[16] Z. Li, Y. Tan, S. Wu, and F. Yang, "The effects of the freeze-thaw cycle on the mechanical properties of the asphalt mixture," *Journal of Harbin Engineering University*, vol. 35, no. 03, pp. 378–382, 2014.

[17] P. Kettil, G. Engström, and N.-E. Wiberg, "Coupled hydro-mechanical wave propagation in road structures," *Computers & Structures*, vol. 83, no. 21-22, pp. 1719–1729, 2005.

[18] H. Xu, H. Shi, H. Zhang, H. Li, Z. Leng, and Y. Tan, "Evolution of dynamic flow behavior in asphalt mixtures exposed to freeze-thaw cycles," *Construction and Building Materials*, vol. 255, p. 119320, 2020.

[19] H. Xu, W. Guo, and Y. Tan, "Permeability of asphalt mixtures exposed to freeze-thaw cycles," *Cold Regions Science and Technology*, vol. 123, pp. 99–106, 2016.

[20] H. Wu, P. Li, T. Nian, G. Zhang, T. He, and X. Wei, "Evaluation of asphalt and asphalt mixtures' water stability method under multiple freeze-thaw cycles," *Construction and Building Materials*, vol. 228, p. 117089, 2019.

[21] JTG-E20-2011, *Standard Test Material of Bitumen and Bituminous Mixtures for Highway Engineering*, China Ministry of Transport, Beijing, China, 2011.

[22] L. X. Hua, F. P. Xiao, Y. T. Li et al., "A potential damage mechanism of rubberized cement under freeze-thaw cycle," *Construction and Building Materials*, vol. 252, p. 12, 2020.

[23] X. Zhang, M. Zhang, J. Lu, W. Pei, and Z. Yan, "Effect of hydro-thermal behavior on the frost heave of a saturated silty clay under different applied pressures," *Applied Thermal Engineering*, vol. 117, pp. 462–467, 2017.

[24] Y. Ji, G. Zhou, and M. R. Hall, "Frost heave and frost heaving-induced pressure under various restraints and thermal gradients during the coupled thermal-hydro processes in freezing soil," *Bulletin of Engineering Geology and the Environment*, vol. 78, no. 5, pp. 3671–3683, 2019.

[25] G. Xu, Y. Yu, D. Cai, G. Xie, X. Chen, and J. Yang, "Multi-scale damage characterization of asphalt mixture subject to freeze-thaw cycles," *Construction and Building Materials*, vol. 240, p. 117947, 2020.

[26] AASHTO, *Resistance of Compacted Asphalt Mixtures to Moisture-Induced Damage*, Vol. 283, AASHTO T, Washington, DC, USA, 2014.

[27] S. W. Goh, M. Akin, Z. You, and X. Shi, "Effect of deicing solutions on the tensile strength of micro- or nano-modified asphalt mixture," *Construction and Building Materials*, vol. 25, no. 1, pp. 195–200, 2011.

[28] D. Feng, J. Yi, D. Wang, and L. Chen, "Impact of salt and freeze-thaw cycles on performance of asphalt mixtures in coastal frozen region of China," *Cold Regions Science and Technology*, vol. 62, no. 1, pp. 34–41, 2010.

[29] X. Gong, P. Romero, Z. Dong, and D. S. Sudbury, "The effect of freeze-thaw cycle on the low-temperature properties of asphalt fine aggregate matrix utilizing bending beam rheometer," *Cold Regions Science and Technology*, vol. 125, pp. 101–107, 2016.

[30] S. Wu, J. Yang, R. Yang, J. Zhu, S. Liu, and C. Wang, "Investigation of microscopic air void structure of anti-freezing asphalt pavement with X-ray CT and MIP," *Construction and Building Materials*, vol. 178, pp. 473–483, 2018.

Research Article

Swelling and Degradation Characteristics of Crumb Rubber Modified Asphalt during Processing

Caiyun Xia,[1] Mingyuan Chen [ID],[2] Jiuguang Geng,[2] Xiaofeng Liao,[1] and Zhongda Chen[1]

[1]*School of Highway, Chang'an University, Xi'an, China*
[2]*School of Materials Science and Engineering, Chang'an University, Xi'an, China*

Correspondence should be addressed to Mingyuan Chen; chenmy@chd.edu.cn

The existence of cross-linked structure in crumb rubber modified asphalt (CRMA) leads to the complexity of its system. According to the preparation test of CRMA under different processing technology, the influence of processing temperature and time on the properties and cross-linking structure of CRMA was analyzed. By analyzing the volume expansion rate of the rubber powder after swelling and the toluene insoluble content attenuation rate, the formation conditions of the macro-level cross-linked structure were determined, and the relationship model between the cross-linked structure and the rubber asphalt performance was established. The results show that the rubber particles can form a continuous phase structure after swelling. At this time, the expansion ratio of the swollen rubber powder was 1.76–2.14. Too high temperature (above 200°C) and too long time (above 60 min) caused serious degradation of rubber. The suitable processing technology was stirring at 180–190°C for 45–60 min.

1. Introduction

Crumb rubber modified asphalt (CRMA) is highly concerned by the road industry for its good temperature resistance, fatigue and skid resistance, reduction of road noise and road construction costs, and environmental advantages of waste recycling [1, 2]. Waste tire rubber powder (vulcanized rubber) contains natural rubber, synthetic rubber, sulfur, carbon black, anti-aging agents, and other ingredients. These ingredients help to improve the quality of CRMA, including increasing the softening point, reducing penetration, increasing ductility, and improving the elastic recovery of CRMA [3]. However, crumb rubber (CR) is an inert polymer material. In the production process of modified asphalt, it needs strong stirring or mechanical shearing to be dispersed in the asphalt at high temperature. The current preparation process conditions are mainly determined with reference to engineering experience, and there is still a lack of theoretical basis for the interaction between rubber powder and asphalt. Many scholars have carried out research on the performance and engineering application of CRMA. A large number of research results

have been obtained in the process conditions such as the preparation temperature and time of CRMA, as well as particle size and amount of rubber powder [4–8]. The reaction process of CRMA was closely related to the asphalt medium, reaction temperature, and reaction time, and the deeply degraded rubber powder can be quickly dispersed in the asphalt [9, 10].

The swelling and degradation behavior of CR in the asphalt greatly affects the modification effect and road performance of CRMA. In order to obtain high-performance CRMA, researchers have gradually begun to study the physical-chemical behavior and microscopic mechanism of CR and asphalt. Abdelrahman et al. [11] pointed out that there were rubber powder swelling and degradation behavior in CRMA. Frantzis et al. [12] and Cong et al. [13] used scanning electron microscope (SEM) to describe the swelling of rubber powder in hot asphalt. At the high temperature, the rubber powder absorbed the light components of the asphalt and expanded. The rubber powder particles contacted each other and were connected by the gel film to form a semi-solid continuous structure, which restricted the movement of the free asphalt and formed a continuous interlocking phase [14]. Cui et al. [6]

and Dong et al. [15] used infrared spectroscopy (IR), thermogravimetry, and x-ray photoelectron spectroscopy (XPS) to analyze the impact of the microstructure of CR powder on the properties of CRMA and found that the swelling of rubber in the asphalt started from a rapid growth process and then tended to balance. Excessive temperature or time caused excessive degradation and agglomeration of rubber powder, or asphalt aging behavior, which would change the physical and chemical state of CRMA, resulting in performance degradation [16]. Besides, Wang et al. [17] and Ji et al. [18] used finite element model and Crank diffusion model to predict the expansion behavior of rubber in asphalt and proposed two swelling parameters-swelling coefficient and final swelling amount. However, the swelling and degradation characteristics of rubber powder in asphalt still lack rapid and intuitive analysis and evaluation. The physical and chemical properties and modification behavior of CRMA still need to be further studied.

In the paper, the changes in the cross-linking structure of CRMA during processing were evaluated quickly and intuitively from a macro perspective. CRMA was prepared by different processing temperature and time. Through penetration, softening point, ductility, viscosity, and resilience, the physical properties of CRMA under different processing temperature and time conditions were studied. In addition, the swelling and degradation of CRMA during processing were evaluated by the volume and mass of toluene insoluble matter. Besides, the correlation analysis of the applicability of the cross-linked structure test methods was carried out to determine the appropriate processing temperature and time from the perspective of rubber swelling and degradation in the CRMA. Finally, SEM was used for intuitive verification.

2. Materials and Methods

2.1. Raw Materials.
The performance of base asphalt will directly affect the performance of crumb rubber modified asphalt (CRMA). The main properties of Shell-70 are shown in Table 1. The 40-mesh crumb rubber (CR) was produced in Sichuan Province, China. The basic physical properties of CR are shown in Table 2.

2.2. Preparation of CRMA.
Prior to mixing, crumb rubber was preserved in the oven at 60°C for 30 min to remove residual water. Then, the dried crumb rubber (16% by the weight of base asphalt) was added to the heated asphalt. This blend was mixed at designated mixing temperature (160°C, 180°C, 200°C, 220°C, and 240°C) and mixing time (30 min, 45 min, 60 min, and 75 min) using a high-speed shear mixer at a constant shearing speed of 5000 r/min. Finally, the CRMA was stirred manually for 5 min to exhaust air.

2.3. Research Approach.
The purpose of this study was to analyze the influence of different processing temperatures and times on the performance of CRMA with polynomial correlation. At the same time, the process of swelling and degradation of CRMA was judged from the macroscopic and

microscopic perspectives. The material preparation and testing performed in this study are shown in Figure 1. Details are introduced in the following subsections.

2.3.1. Physical Properties.
The physical properties of asphalt, including penetration at 25°C, softening point, ductility at 5°C, viscosity at 180°C, and resilience at 25°C, were tested in accordance with ASTM D5, ASTM D36, ASTM D113, ASTM D2196, and ASTM D5329, respectively.

2.3.2. Degradation and Swelling of Crumb Rubber.
Crumb rubber would continue to swell and degrade during processing. Vulcanized rubber powder is basically insoluble in toluene, and the soluble part increases after desulfurization (S–S/C–S). The swelling and degradation of rubber can be evaluated by quantitatively analyzing the volume and mass loss of toluene insoluble matter (TIM) [19, 20]. During CRMA processing, after reaching the specified time each time, without affecting the stirring, the CRMA with a certain mass (M_0) was directly weighed out twice: Part a and Part b. Among them, Part a and Part b were used for swelling test and degradation test of crumb rubber, respectively. Next, an appropriate amount of toluene at 50–60°C was added and stirred until the asphalt and other soluble matter were completely dissolved in toluene. Then, the solution was poured into a sand core funnel with filter paper and washed with toluene to obtain CR powder until the filtrate was colorless.

After that, Part a, the rubber with filter paper was put into a measuring cylinder with a known volume of water (V_0), and the increased volume (V_2) was recorded. Simultaneously, the same operation on the pure CR was performed and the volume (V_1) in the measuring cylinder was recorded. Part b, the washed CR powder was placed in a vacuum drying oven with a temperature of $60 \pm 1°C$ and a vacuum of $93\,kPa \pm 1\,kPa$ to a constant weight, and the mass (M_1) was recorded. Expansion ratio of TIM (E), the TIM content (K), and attenuation rate of TIM content (Q) were calculated using equations (1)–(3), respectively:

$$E = \frac{V_2 - V_0}{V_1 - V_0}, \tag{1}$$

$$K = \frac{M_1}{c \times M_0} \times 100\%, \tag{2}$$

$$Q = \frac{K_0 - K}{K_0} \times 100\%, \tag{3}$$

where c is CR powder content (16%) and K_0 is the content of TIM in pure CR powder in the experiment (0.945%).

2.3.3. SEM.
SEM has high resolution and can observe the microscopic morphology, structure, and distribution of modified asphalt [21, 22]. The samples in the system were scanned under 20,000x magnification by Hitachi S-4800.

TABLE 1: Physical properties of base asphalt.

Properties	Softening point (°C)	Penetration (25°C, 0.1 mm)	Ductility (15°C, cm)
Shell-70	47.5	72	>100

TABLE 2: Physical properties of crumb rubber.

Test methods	Relative density	Water content (%)	Fiber content (%)	Metal content (%)
Test value	1.08	0.31	0.25	0.03
Screening test				
Sieve size (mm)	0.6	0.3	0.15	0.075
Trough rate (%)	98.3	63.4	2.4	0.5

FIGURE 1: Experimental design.

3. Results and Discussion

3.1. The Influence of Processing Temperature on CRMA. Processing temperature is an important condition that affects the preparation process of CRMA. The higher the temperature, the better the reaction speed and degree of CR desulfurization and swelling, but too high temperature would easily lead to aging of the base asphalt and rapid CR degradation. Generally, when selecting the preparation temperature, the CR should be fully swelled and uniformly dispersed during the process. The control of specific temperature should be determined comprehensively according to the characteristics of base asphalt and rubber powder and their interaction. The influence of processing temperature on CRMA's performance is shown in Figure 2.

As the temperature increased, the penetration of CRMA basically showed an increasing trend (Figure 2(a)), because high temperature intensified the desulfurization and degradation of CR, and the cross-linking reaction between CR and asphalt accelerated. Simultaneously, with the effective

CR particles decreasing, the soluble components in the asphalt increased, and the light components participating in the swelling reaction returned to the asphalt, resulting in more light components in the CRMA system at high temperatures than that at low temperatures, so the penetration degree increased with the increase of temperature.

From the data in Figure 2(b), as the processing temperature increased, the softening point decreased. The decreasing trend was not obvious between 180°C and 200°C. Under this temperature range, the light components absorbed by the swelling reaction in CRMA, and part of CR underwent desulfurization and degradation reactions "freed" out soluble components; thus, they were in equilibrium. However, an inflection point occurred at 200°C; that is, the softening point was greatly reduced. A qualitative change has occurred in CR interior at 200°C. Desulfurization and degradation reactions began to replace swelling reactions and gradually dominate [23]. Therefore, when the preparation temperature was too high, the high-temperature stability of CRMA would decrease.

(a)

(b)

(c)

(d)

(e)

FIGURE 2: The influence of processing temperature on CRMA's performance. (a) Penetration. (b) Softening point. (c) Ductility. (d) Viscosity. (e) Resilience.

The ductility of CRMA kept increasing within 200°C, and basically tended to be stable after 200°C (Figure 2(c)). With the increase of temperature, the swelling rate of CR in asphalt gradually increased, and the volume of CR particles expanded rapidly. At the same time, the desulfurization and degradation effects increased the soluble composition of CR, which improved the low-temperature flexibility of CRMA. But when the temperature was higher than 200°C, the asphalt began to age, and the light components were volatilized, while the degree of CR degradation also increased. Under the combined action, the trend of ductility was basically stable. After the temperature continued to rise, the rubber powder degraded seriously and lost the effect of improving the low-temperature performance of CRMA.

It can be seen from Figure 2(d) that the viscosity of CRMA first increased and then decreased. The swelling reaction rate of the rubber powder absorbing the light components in the asphalt increased, which enhanced the cross-linking between the CR particles, and finally increased the viscosity. After the temperature exceeded 200°C, the desulfurization and degradation effects reduced the volume of the rubber powder. When the volume was small to a certain extent, the cross-linking between the CR particles weakened, thereby reducing the viscosity of CRMA.

The change trend of the elastic recovery of CRMA was shown to increase slowly and then decrease. At the beginning, the temperature rose, the swelling reaction rate increased, and CRMA formed a good micro-network structure, which enhanced the resistance to deformation. After the temperature reached 200°C, the volatilization of light components intensified, and the micro-network structure was destroyed; thus, the elastic recovery decreased.

3.2. The Influence of Processing Time on CRMA. In the preparation process of CRMA, the processing temperature and processing time influence and restrict each other. Therefore, it is important to choose the right processing temperature and time. From Figure 3(a)–3(c), it can be seen that, with the extension of processing time, the penetration and ductility of CRMA basically showed an upward trend, while the softening point showed a downward trend. At the beginning of processing, CR mainly swelled in the asphalt, absorbed the light components, and formed a microscopic network structure with the asphalt. As the preparation time continued to extend, the swelling reaction reached the upper limit, and the desulfurization degradation of CR began to dominate. In the CRMA system, the effective rubber content decreased, so the penetration increased and the softening point decreased. The desulfurization and degradation reactions accelerated the generation of rubber's molecular chain segment.

The viscosity of CRMA showed a tendency to increase first and then decrease (Figure 3(d)), because the CR had poor swelling effect, small volume ratio, and discontinuous particles at the initial stage of preparation. After that, the continuous swelling reaction enhanced the mutual cross-linking between CR particles, resulting in an increase in viscosity. When the time was too long, the desulfurization

and degradation would decrease the volume of the rubber particles and the effective rubber content. When the volume was small to a certain extent, the cross-linking between the CR particles would weaken, thus making the viscosity of CRMA decrease.

The resilience of CRMA gradually increased as a whole, and then its growth trend gradually slowed down. The volume of CR absorbed light components increased, and the elastic effect of rubber particles was enhanced, so that the resilience ability of CRMA was developed. After CR swelling reaction was sufficient, the elastic effect of CR particles was fully used, and the resilience of CRMA would slowly level off.

In general, when the processing temperature is too low or the mixing time is too short, the consistency of CRMA is relatively large, and the rubber powder cannot be fully dispersed in the asphalt, which is not conducive to the swelling reaction. Besides, too high temperature or too long time will cause excessive aging of asphalt and rapid degradation of rubber powder. In order to prevent excessive desulfurization and degradation of rubber powder, the final suitable processing technology determined according to the materials used is high-speed stirring at a temperature range of 180–190°C for 45–60 min.

3.3. Degradation Analysis. During CRMA processing, due to the combined action of high-speed shear, high temperature, and time, rubber would swell, desulfurize, and degrade. The vulcanized rubber contained in the CR powder is insoluble and becomes soluble in toluene after desulfurization and degradation. The greater the attenuation rate (Q value) of toluene insoluble content, the more serious the desulfurization and degradation of CR powder. According to the test results in Figure 4, the Q value went up with time. At the same time, the higher the processing temperature of CRMA, the greater the Q value. It shows that the degree of desulfurization and degradation of rubber powder under high-temperature conditions was serious. With the extension of time, the degree of desulfurization and degradation continued to increase. The initial growth was relatively fast, but the later reaction gradually slowed down. Therefore, the reaction temperature should be strictly controlled in the CRMA processing. The low temperature and the insufficient swelling were not conducive to the desulfurization and degradation reaction. The insufficient sol content caused the improvement of the flexibility of the asphalt to be limited. This corresponded to the conventional physical properties of CRMA. However, too high temperature would cause excessive decomposition of rubber powder, so the processing temperature should not be too high, and the storage time under high temperature should not be too long.

3.4. Swelling Analysis. Crumb rubber would absorb the light components in asphalt and swell. It can be seen from Figure 5 that at low temperatures, as time increased, the expansion ratio gradually climbed and then tended to be flat. Due to the complex structure and large molecular volume of the saturated and aromatic components in asphalt, the content of light oil is limited, and it is also enveloped by gums and asphaltenes [24].

(a)

(b)

(c)

(d)

(e)
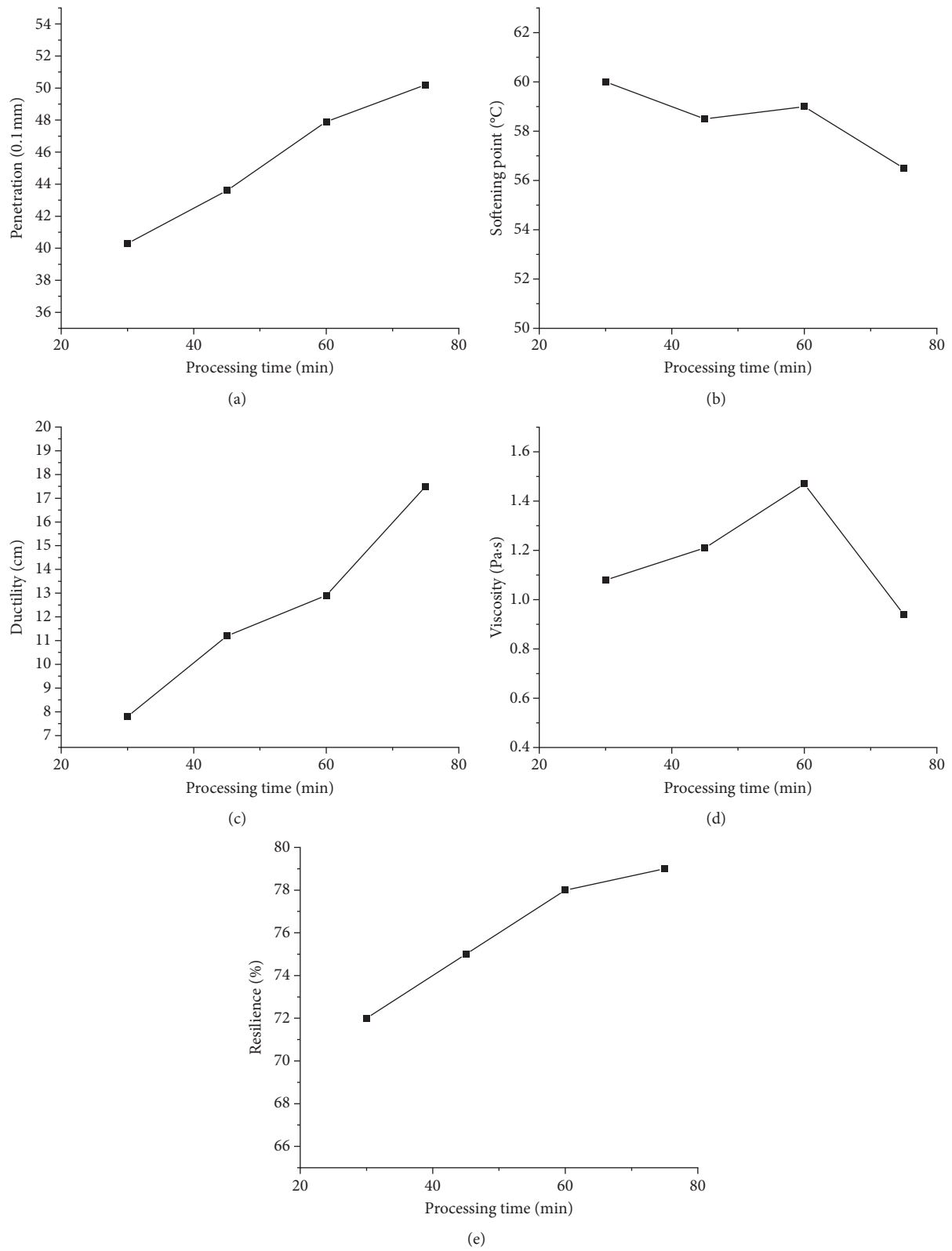
Figure 3: The influence of processing time on CRMA's performance. (a) Penetration. (b) Softening point. (c) Ductility. (d) Viscosity. (e) Resilience.
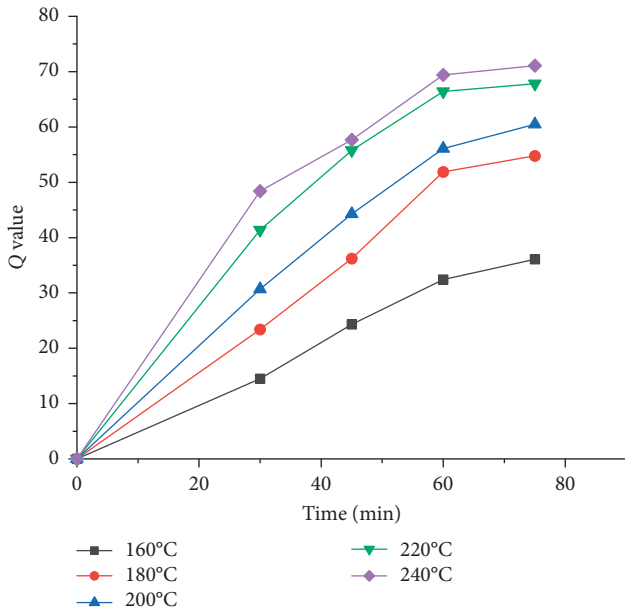
Figure 4: The changing law of toluene insoluble content attenuation rate.
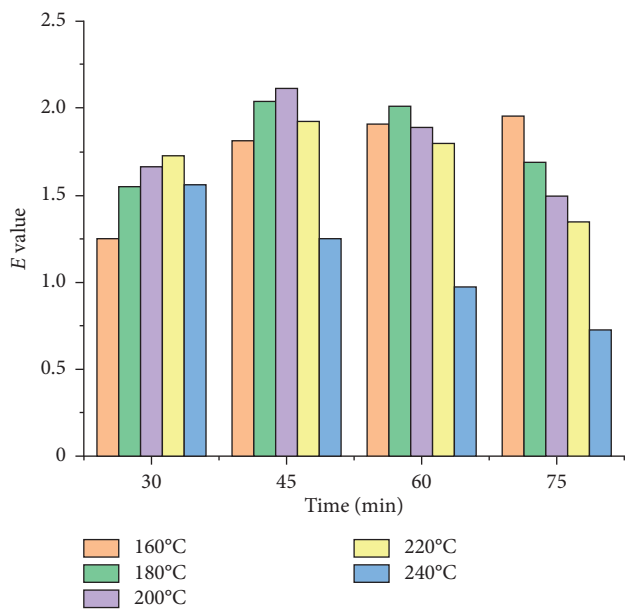
Figure 5: The expansion ratio of CRMA.

As the processing temperature increased, the speed of rubber swelling in asphalt rose. But if it is processed for a long time, the balance between swelling and desulfurization degradation would be broken. Evaluation by the volume of toluene insoluble matter shows that the expansion ratio of CRMA has decreased. When the temperature was too high, the speed of desulfurization and degradation was faster than that of swelling, which reduced the toluene insoluble matter, and the measured expansion ratio continued to decrease. Considering the large content of CR powder, the volume of CR powder after swelling in the asphalt was greatly increased, and because part

of the light oil in the asphalt was absorbed by the CR powder, the total volume of the asphalt was reduced. The proportion of expanded rubber powder will account for 40% or more of the total volume of CRMA. The particles of rubber powder gradually change from the dispersed phase to the continuous phase, which leads to a large change in the properties of the asphalt.

3.5. Correlation Analysis of Swelling and Degradation. At this stage, the correlation between the swelling and degradation of CRMA at different temperature and time was analyzed, and the results are shown in Figure 6. At the same time, polynomial regression fitting on the data was performed, seen in Tables 3 and 4 for the fitting parameters. The closer the coefficient of determination (R^2) value is to 1, the better the fit of the regression line to the observed value; on the contrary, the smaller the value of R^2, the worse the fit of the regression line to the observed value. Due to the use of toluene insolubles to test the volume and content of vulcanizates, although there was slight error, the regularity was certain. For different processing times, when processing for 30 min and 75 min, the correlation between the swelling and degradation of CRMA was better, and R^2 was above 0.90. Since the swelling rate of CRMA was higher than that of degradation in a short time, and the opposite law appeared when the time is too long, the correlation is better. At 45 min and 60 min, the balance of swelling and degradation of CRMA has been fluctuating; R^2 was only 0.64–0.72. In addition, under different processing temperature conditions, the correlation of the swelling and degradation of CRMA at 160°C, 180°C, 200°C, and 240°C was good; R^2 reached above 0.88. Simultaneously, it can be predicted from the fitting curve that, at 180°C, the swelling rate is slightly faster than the degradation rate, while the degradation rate is faster than the degradation rate at 220°C.

3.6. SEM. The morphology of the rubber powder particles was observed by SEM, and the results are shown in Figure 7, where (a) is the pure rubber powder particles, (b) is the observation of the rubber powder after washing with toluene, and (c) is observation that the rubber powder in CRMA was washed with toluene.

It can be seen from Figure 7(a) that the surface of the pure rubber powder particles was uneven, with many wrinkles and a small amount of carbon black on the surface of the particles, which was approximately a network structure, resulting in easily adsorbing the light components in the asphalt. After being soaked and dissolved in toluene (Figure 7(b)), the CR powder particles were not completely dissolved, but no obvious changes were observed under the naked eye. SEM observations showed that the surface of CR particles had a small amount of change, surface wrinkles were more obvious, and carbon black particles increased. It indicates that some substances were dissolved under the action of toluene, making some carbon black particles exposed. After the CR powder was fully reacted in the asphalt (Figure 7(c)), the surface was more uneven and the exposed carbon black particles were more obvious. Under the action

(a)

(b)
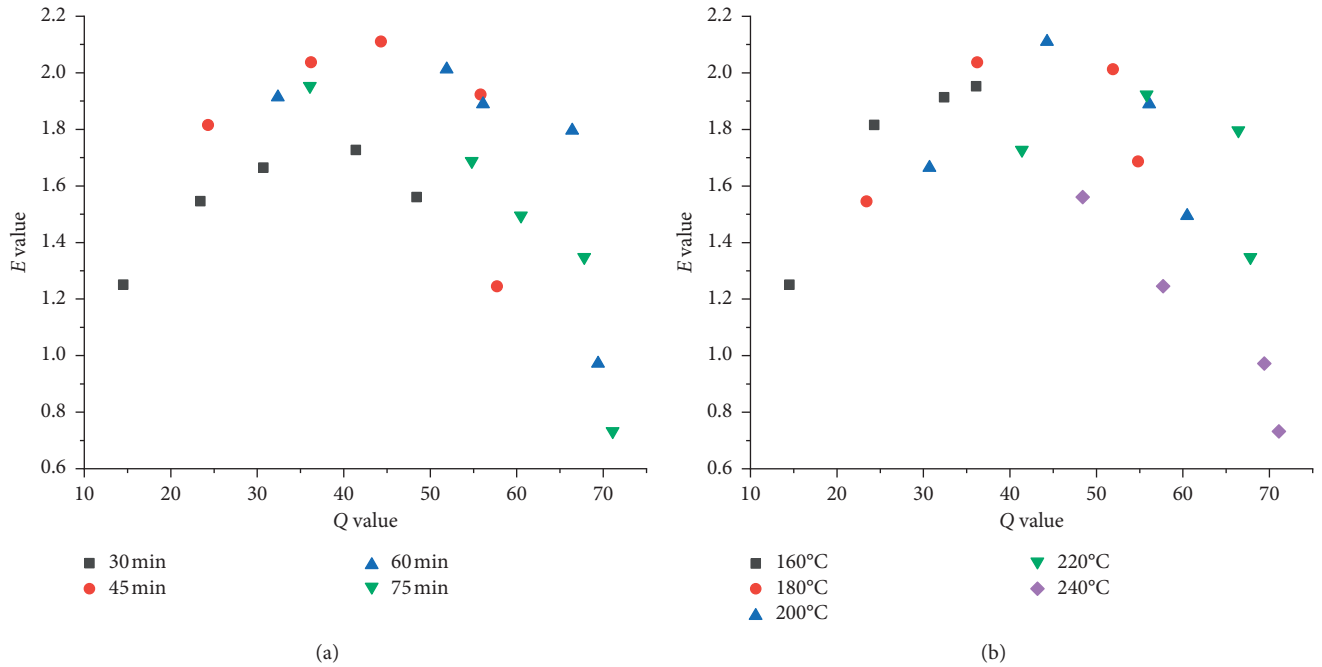
FIGURE 6: The relationship between Q value and E value. (a) Different time. (b) Different temperature.

TABLE 3: The fitting value of Q value and E value at different time.

Equation	$y_2 = A + B_1 * x + B_2 * x^2$			
Time	30 min	45 min	60 min	75 min
A	0.41709 ± 0.10752	-0.47394 ± 1.76446	-0.92246 ± 2.3433	-0.05313 ± 1.94987
B_1	0.0713 ± 0.00752	0.13537 ± 0.0905	0.13604 ± 0.09693	0.09845 ± 0.07659
B_2	$-9.77807E - 4 \pm 1.17461E - 4$	-0.00175 ± 0.00108	$-0.00151 \pm 9.49146E - 4$	$-0.0012 \pm 7.16878E - 4$
R^2	0.98564	0.64699	0.72062	0.90059

TABLE 4: The fitting value of Q value and E value at different temperature.

Equation	$y_1 = A + B_1 * x + B_2 * x^2$				
Temperature	160°C	180°C	200°C	220°C	240°C
A	-0.24772 ± 0.27814	-1.0352 ± 1.05358	-2.78019 ± 0.87009	-3.73591 ± 5.3311	2.41475 ± 4.52155
B_1	0.13284 ± 0.02408	0.15342 ± 0.0584	0.21996 ± 0.04037	0.21701 ± 0.20182	-0.00781 ± 0.15374
B_2	$-0.00201 \pm 4.75419E - 4$	$-0.00187 \pm 7.37085E - 4$	$-0.00246 \pm 4.42059E - 4$	-0.00206 ± 0.00184	$-2.07267E - 4 \pm 0.00128$
R^2	0.99331	0.88453	0.96963	0.62527	0.95613

(a)

(b)
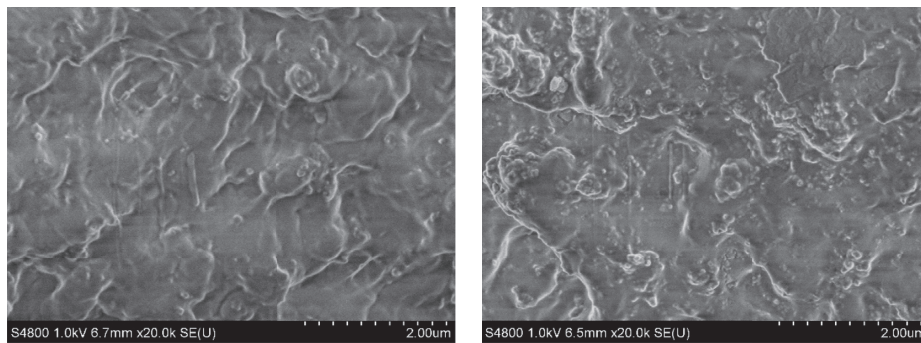
FIGURE 7: Continued.
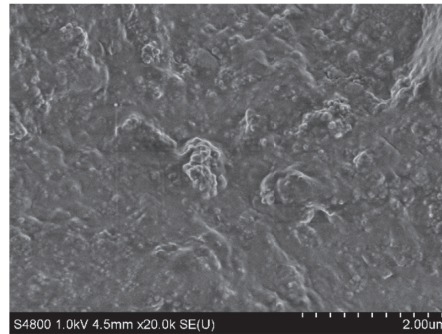
(c)

Figure 7: Observation results of rubber powder particle morphology. (a) Pure rubber. (b) Rubber after toluene rinse. (c) Rubber in the CRMA.

of high temperature and high-speed shear, part of the rubber particles desulfurized and degraded, showing off from the rubber powder, changing the original surface state [13].

4. Conclusion

(1) The processing temperature and time of CRMA should not be excessive; otherwise, they would lead to accelerated degradation of rubber and aging of asphalt and have a bad influence on the physical properties of CRMA. The final suitable processing technology was the temperature range of 180–190°C and the stirring time of 45–60 min.

(2) With the increase of processing time and temperature, the attenuation rate of toluene insoluble matter went up, indicating that the rubber in CRMA was seriously degraded.

(3) For the swelling of rubber, at low temperature, the expansion rate increased as the time increased. But due to the effect of degradation at high temperature, the expansion rate decreased gradually with the increase of time.

(4) The expansion ratio of rubber and the attenuation rate of toluene insoluble matter showed a certain polynomial regression correlation at different processing temperature and time. Most of the correlation coefficients were above 0.88.

(5) It can be seen from the SEM that excessive processing exposed the carbon black and accelerated the desulfurization and degradation of rubber in the CRMA.

Data Availability

Some of the data required to reproduce these findings cannot be shared at this time as the data also form part of an ongoing study.

Conflicts of Interest

The authors declare that they have no conflicts of interest regarding this work.

Acknowledgments

References

[1] W. Huang and Y. Zhang, "The technical criteria frame of pavement used asphalt rubber in China," *Journal of Central South Highway Engineering*, vol. 32, no. 1, pp. 111–114, 2007.

[2] M. A. Mull, K. Stuart, and A. Yehia, "Fracture resistance characterization of chemically modified crumb rubber asphalt pavement," *Journal of Materials Science*, vol. 37, no. 3, pp. 557–566, 2002.

[3] Y. Yang, H. Yuan, and M. A. Tao, "Swelling principle and pavement performance of desulfurized rubber asphalt," *Journal of Highway and Transportation Research and Development*, vol. 29, no. 2, pp. 35–39, 2012.

[4] K. Baha Vural, M. Yilmaz, and A. Geçkil, "Evaluation of the low temperature and elastic properties of crumb rubber and SBS modified asphalt and mixtures," *Journal of Materials in Civil Engineering*, vol. 25, no. 2, pp. 257–265, 2013.

[5] Z. Ding and L. I. Pei-Long, "Research on influence factors and prediction model of viscosity of crumb rubber modified asphalt," *Highway*, no. 7, pp. 213–216, 2012.

[6] Y.-N. Cui, Y.-M. Xing, L. Wang et al., "Improvement mechanism of crumb rubber-modified asphalt," *Journal of Building Materials*, vol. 14, no. 5, pp. 634–638, 2014.

[7] H. Liu, G. Luo, X. Wang et al., "Effects of preparation process on performance of rubber modified asphalt," *IOP Conf. Series: Materials Science and Engineering*, vol. 87, Article ID 012008, 2015.

[8] T. Wang, R. Yang, A. Li et al., "Effects of sasobit and its adding process on the performance of rubber asphalt," *Chemical Engineering Transactions*, vol. 51, pp. 181–185, 2016.

[9] F. Ye, S. Yang, X. Wu et al., "Rheological property of highly degraded rubber modified asphalt," *Journal of Building Materials*, vol. 19, no. 5, pp. 945–949, 2016.

[10] Y. Liu, C. Liu, and Y. Zhang, "Reaction rules of crumb rubber modified asphalt," *Journal of China University of Petroleum*, vol. 41, no. 3, pp. 154–160, 2017.

[11] A. Magdy and C. Samuel, "Mechanism of interaction of asphalt cement with crumb rubber modifier," *Transportation Research Record: Journal of the Transportation Research Board*, vol. 5, pp. 106–113, 1999.

[12] F. J. López-Moro, M. C. Moro, F. Hernández-Olivares, B. Witoszek-Schultz, and M. Alonso-Fernández, "Microscopic analysis of the interaction between crumb rubber and bitumen in asphalt mixtures using the dry process," *Construction and Building Materials*, vol. 48, pp. 691–699, 2013.

[13] P. Cong, P. Xun, M. Xing, and S. Chen, "Investigation of asphalt binder containing various crumb rubbers and asphalts," *Construction and Building Materials*, vol. 40, pp. 632–641, 2013.

[14] A. Ignacio and A. Khalid Hussain, "Diffusion kinetics of asphalt into waste tyre rubber (with discussion)," *Association of Asphalt Paving Technologists*, vol. 75, pp. 133–164, 2006.

[15] D. Dong, X. Huang, X. Li, and L. Zhang, "Swelling process of rubber in asphalt and its effect on the structure and properties of rubber and asphalt," *Construction and Building Materials*, vol. 29, pp. 316–322, 2012.

[16] P. Li, Z. Ding, and C. Chong, "Analysis of swelling and degradation characteristics of crumb rubber in hot asphalt," *Journal of South China University of Technology (Natural Science Edition)*, vol. 44, no. 12, pp. 97–103, 2016.

[17] H. Wang, X. Liu, P. Apostolidis, S. Erkens, and T. Scarpas, "Numerical investigation of rubber swelling in bitumen," *Construction and Building Materials*, vol. 214, pp. 506–515, 2019.

[18] X. Ji, Y. Hou, and W. Han, "Establishment of swelling model and determination of swelling parameters between rubber and asphalt," *China Synthetic Rubber Industry*, vol. 33, no. 3, pp. 191–193, 2010.

[19] W. Zhang and K. Müllen, "Analyzing solid fossil-fuel pitches by a combination of Soxhlet extraction and Fourier transform ion cyclotron resonance mass spectrometry," *Carbon*, vol. 167, pp. 414–421, 2020.

[20] B. F. Bowers, B. Huang, and X. Shu, "New method for detecting asphalt contamination within fine aggregate medium through chemical testing," *Journal of Materials in Civil Engineering*, vol. 25, no. 2, pp. 252–256, 2013.

[21] H. Hong, H. Zhang, and L. Huang, "Study progress of characterization of asphalt materials by nuclear magnetic resonance, thermal analysis and scanning electron microscopy," *Journal of Highway and Transportation Research and Development*, vol. 36, no. 12, pp. 15–28, 2019.

[22] M. Mithil, R. Ahmed, A. Ahmed et al., "SEM and ESEM techniques used for analysis of asphalt binder and mixture: a state of the art review," *Construction and Building Materials*, vol. 186, pp. 313–329, 2018.

[23] L. He, T. Ling, Y. Ma et al., "Research on asphalt rubber aging performance and characteristics," *Journal of Building Materials*, vol. 18, no. 4, pp. 565–571, 2015.

[24] R. Dong, J. Yang, and M. Zhao, *Research on New Component Analysis Method for Pyrolytic Crumb Rubber Modified Asphalt*, Transportation Research Congress, Hangzhou, China, 2017.

Research Article

Grey Prediction Model for Drying Shrinkage of Cement Concrete Made from Recycled Coarse Aggregate Containing Superabsorbent Polymers

Jinbao Zhang [1], **Song Li** [2], **and Jiahui Zhai** [3]

[1]*Qinghai Transportation Holding Group Co., Ltd., Xining 810001, China*
[2]*School of Transportation, Wuhan University of Technology, Wuhan 430070, China*
[3]*School of Materials Science and Engineering, Northwestern Polytechnical University, Xi'an 710072, China*

Correspondence should be addressed to Jiahui Zhai; 2020261122@mail.nwpu.edu.cn

The aim of this paper is to investigate the effect of superabsorbent polymers (SAPs) on the drying shrinkage of the recycled concrete (RC). The natural aggregate (NA) was replaced by recycled aggregate at three replacement ratios (0%, 50%, and 100%). Then, the recycled concrete (RC) with different SAP contents was prepared. The performance of recycled concrete with different SAP content was analyzed with slump test, compressive strength test, and drying shrinkage test. GM (1, N) grey prediction model was utilized to predict the drying shrinkage of recycled concrete containing SAP. The results show that the strength and durability of concrete are decreased by the addition of recycled aggregate. With the increase of the dosage of SAP, the strength and durability also raise. The prediction GM (1, N) model for the drying shrinkage of recycled concrete with SAP is in good agreement with the actual drying shrinkage.

1. Introduction

Due to low cost, convenience, simple production process, and excellent mechanical and durability properties, natural concrete (NC) materials are widely utilized in building construction, road engineering, and bridge engineering [1–4]. With the rapid development of the economy, the huge demand for concrete materials is increasing. The cement concrete is composed of cement, aggregate, sand, and some admixtures. The main source of the coarse aggregate is crushed natural rocks obtained from natural mountains [5]. This has consumed the amount of natural rock of nonrenewable resources and caused the higher price of natural aggregates. On the other hand, according to the statistics of China, the production of concrete reached 1.8 billion tons in 2020, and construction waste such as waste concrete from the demolition of abandoned buildings was approximately 134×10^8 tons [6–8]. Meanwhile, the construction and demolition waste (CDW) in China has shown an increasing trend.

Many studies have shown that the utilization of recycled coarse aggregate to prepare cement concrete not only saves 60% natural aggregate resource but also consumes a large amount of CDW and reduces 20% emission of CO_2 [9, 10]. However, replacing natural aggregates with recycled aggregates will result in a decrease in the durability of concrete. Recycled aggregate is composed of natural aggregate and old mortar. There are a lot of pores in the old mortar and interfacial transition zone (ITZ). Therefore, RA showed higher porosity and water absorption compared with natural aggregate [11]. Concrete made of RA is easy to shrink and crack, resulting in the insufficient durability of concrete. Therefore, it is necessary to investigate the shrinkage of recycled concrete. The factor that affects shrinkage is complex, including wind speed, constituents, temperature, curing time, and pore size distribution [12]. The loss of water of the calcium silicate hydrates (CSHs) caused by a low relative humidity environment usually leads to the volume reduction of concrete. This phenomenon is called drying

shrinkage [13]. The models that are widely utilized to predict shrinkage including the EC2-08 [14], ACI 209R [15], the Bažant-Baweja B3 [16], the CEB Model Code 99 [17], and the GL2000 [18] have been improved. Haejin et al. [19] investigated dry shrinkage of crushed returned concrete aggregate, evaluated the validity of the ACI 209 model, and found that the ACI 209 model is not suitable for the mixture that is beyond the standard conditions. Therefore, a new model was established to evaluate the drying shrinkage of the concrete made from the crushed returned concrete aggregate. Al-Manaseer et al. [20] estimated the shrinkage prediction capabilities of models based on the RILEM database [21, 22] and found that the Bažant-Baweja B3 and GL2000 models convey the best predictions for the shrinkage strain. Zhang et al. [23] proposed a prediction model for early-age shrinkage of cement paste considering the influence of wind speed. Li et al. [24] established some prediction equations by analyzing the relationship between pore structure and shrinkage of cement-based materials. Wang et al. [25] established a theoretical drying shrinkage model for RC considering the properties of the concrete, including its service time and strength. Compared with the empirical statistical regression method, autoregressive moving average model, and adaptive control Markov model, the grey model is more used due to the high prediction accuracy [26]. Wang et al. [27] used GM (1, 1) model to predict the drying shrinkage of crumb rubber concrete. Tang et al. [28] established the monthly attenuation prediction for asphalt pavement performance by using GM (1, 1) model. Shrinkage is one of the important factors that affect the durability of recycled concrete, which is closely related to time. However, there are few studies on the grey prediction model for shrinkage of concrete made from recycled aggregates.

The internal curing material maintains the relative humidity inside the concrete by releasing water, and it was used in cement concrete to solve the problem of shrinkage and cracking. As a highly effective internal curing material, superabsorbent polymers (SAPs) can significantly decrease the shrinkage of concrete. Kong et al. [29] analyzed the influence of presoaked SAP on the shrinkage of high-performance concrete (HPC) and found that the addition of SAP decreased the drying shrinkage of high-performance cement-based materials under the same water-cement ratio. Ma et al. gained a similar result.

In this study, NA is replaced by RA with 0%, 50%, and 100% replacement rates. Recycled aggregate concretes with 0.3%, 0.5%, and 0.7% SAP were prepared. The workability, mechanical properties, and shrinkage of concrete made from recycled coarse aggregate containing were analyzed, respectively. GM (1, N) grey prediction model was established to predict the drying shrinkage of recycled concrete with SAP.

2. Materials and Methods

2.1. Raw Materials.
Ordinary Portland cement was utilized in this paper and its physical properties are shown in Table 1. Recycled coarse aggregate was used in the experiments with the grain size of 4.75–9.5 mm, 9.5–19 mm, and 19–31.5 mm.

The physical properties of recycled coarse aggregate are shown in Table 2. River sand was used as fine aggregate, and its properties are shown in Table 3. Superplasticizer was supplied by Shandong Gaoqiang Co., Ltd., and its solid content was 37%. The performance of SAP is shown in Table 4.

2.2. Preparation of Recycled Concrete with SAP.
The recycled aggregate was adopted by weight of natural aggregate at 0%, 50%, and 100%. The proportions of recycled concretes are shown in Table 5. The content of SAP is set as 0%, 0.3%, 0.5%, and 0.7% by mass of concrete.

2.3. GM (1, N) Grey Prediction Model.
The grey theory is a kind of prediction method that can predict, make decision, or control using incompleteness of information. As the system is whitened by many effective messages around its forecast origin, the predicted series is fairly good.

Pairs of observations $\left\{ x_1^{(0)}(1), x_1^{(0)}(2), \ldots, x_1^{(0)}(n) \right\}$ from a certain dynamic system with $n - 1$ inputs $\left\{ X_2^{(0)}, X_3^{(0)}, \ldots, X_n^{(0)} \right\}$ and an output $X_1^{(0)}$ are supposed to be available at an equispaced interval of time. Consider the original series, it can be obtained that

$$X_1^{(0)} = \left\{ x_1^{(0)}(1), x_1^{(0)}(2), \ldots, x_1^{(0)}(n) \right\}, \tag{1}$$

$$X_2^{(0)} = \left\{ x_2^{(0)}(1), x_2^{(0)}(2), \ldots, x_2^{(0)}(n) \right\}, \tag{2}$$

$$X_N^{(0)} = \left\{ x_N^{(0)}(1), x_N^{(0)}(2), \ldots, x_N^{(0)}(n) \right\}. \tag{3}$$

$X_i^{(1)}$ are the 1-AGO series of $X_i^{(0)}$, $i = 1, 2, \ldots, N$, respectively. In addition, $Z_1^{(1)}$ is the adjacent generated serial of $X_1^{(1)}$, and then

$$x_1^{(0)}(k) + a z_1^{(1)}(k) = \sum_{i=2}^{N} x_i^{(1)}(k) \tag{4}$$

is called the grey differential equation of GM (1, N) model, where 1 stands for the first-order derivative of 1-AGO series of $X_1^{(0)}$ (called the predicted series) and n stands for there being $n - 1$ relative series (called the associated series) of the system.

Define $\widehat{\alpha} = \begin{bmatrix} a & b_2 & \cdots & b_N \end{bmatrix}^T$ as the parameter series of the grey differential equation of GM (1, N) model, and then according to the least square method (LSM), it can be obtained that

$$\widehat{\alpha} = \left(B^T B \right)^{-1} B^T Y, \tag{5}$$

where

$$B = \begin{bmatrix} -z_1^{(1)}(2) & x_2^{(1)}(2) & \cdots & x_N^{(1)}(2) \\ -z_1^{(1)}(3) & x_2^{(1)}(3) & \cdots & x_N^{(1)}(3) \\ \cdots & & \cdots & \\ -z_1^{(1)}(n) & x_2^{(1)}(n) & \cdots & x_N^{(1)}(n) \end{bmatrix}, \tag{6}$$

and

TABLE 1: Physical properties of cement.

Indicators	Fineness (%)	Setting time (min)		Volume stability (mm)	Compressive strength (MPa)		Flexural strength (MPa)	
		Initial setting	Final setting		3 d	28 d	3 d	28 d
Value	2.3	165	260	1.5	18.5	46.8	4.7	7.0

TABLE 2: Physical properties of recycled aggregate.

Grain size (mm)	Apparent relative density (kg/m^3)	Water absorption (%)	Flakiness and elongation (%)	Crushing value (%)	Dust content (%)	Impurity content (%)
4.75–9.5	2660	5.80	4.5	—	0.3	0.2
9.5–19	2636	4.41	4.3	24.5	0.2	0.4
19–31.5	2625	3.20	3.2	—	0.2	0.3

TABLE 3: Properties of fine aggregate.

Fineness modulus	Grade	Packing density (kg/m^3)	Apparent density (kg/m^3)	Voidage (%)	Powder content (%)	Content of soil (%)	Crushing value (%)
2.4	Medium sand	1447	2583	40	1.0	0.7	13

TABLE 4: Properties of superabsorbent polymers.

Water absorption rate	Deionized water absorption (g·g^{-1})	Tap water absorption (g·g^{-1})
600	≥600	≥300

TABLE 5: Mix proportions of recycled concretes.

	RA (%)	Cement (kg/m^3)	Water (kg/m^3)	Additional water consumption (kg/m^3)	Free water-cement ratio	Sand (kg/m^3)	Coarse aggregate (kg/m^3)	Addition agent (kg/m^3)
NC	0	367	180	0	0.49	735	1058	5.14
RC1	50	367	180	30.7	0.57	735	1058	5.14
RC2	100	367	180	61.4	0.65	735	1058	5.14

$$Y = \left[x_1^{(0)}(2) \ \ x_1^{(0)}(3) \ \cdots \ x_1^{(0)}(n) \right]^T. \tag{7}$$

Then

$$\frac{dx_1^{(1)}}{dt} + a x_1^{(1)} = b_2 x_2^{(1)} + b_3 x_3^{(1)} + \cdots + b_N x_N^{(1)} \tag{8}$$

is the albinism differential equation or silhouette equation of equation (4). From equation (8), the modeling value can be derived as

$$x_1^{(1)}(t) = e^{-at} \left[\sum_{i=2}^{N} \int b_i x_i^{(1)}(t) e^{at} dt + x_1^{(1)}(0) - \sum_{i=2}^{N} \int b_i x_i^{(1)}(0) dt \right]$$

$$= e^{-at} \left[x_1^{(1)}(0) - t \sum_{t=2}^{N} b_i x_i^{(1)}(0) + \sum_{i=2}^{N} \int b_i x_i^{(1)}(t) e^{at} dt \right]. \tag{9}$$

When the rangeability of $X_i^{(1)}$ ($i = 1, 2, ..., N$) is small, the value of $\sum_{i=2}^{N} b_i x_i^{(1)}(k)$ can be deemed as a grey constant. Therefore, the approximate time response equation of equation (4) can be derived as

$$\widehat{x}_1^{(1)}(k+1) = \left[x_1^{(1)}(0) - \frac{1}{a} \sum_{i=2}^{N} b_i x_i^{(1)}(k+1) \right] e^{-ak} + \frac{1}{a} \sum_{i=2}^{N} b_i x_i^{(1)}(k+1), \tag{10}$$

where $x_1^{(1)}(0)$ is equal to $x_1^{(0)}(1)$. Then

$$\widehat{x}_1^{(0)}(k+1) = \widehat{x}_1^{(1)}(k+1) - \widehat{x}_1^{(1)}(k). \tag{11}$$

2.4. Test Procedure

2.4.1. Slump Test. Slump test was widely utilized to estimate the fluidity and working performance of concrete, and the operation was in accordance with specification (GB/T50081-2002, 2002; ASTM C143–C143M-15a, 2015).

2.4.2. Compressive Strength Test. According to the specification (GB/T50081-2002, 2002; ASTM C39/C39M-18, 2018a), the universal testing machine (UTM) was carried out to examine the compressive strength of 3 days, 7 days, and 28 days at the loading speed of 0.8 MPa/s.

2.4.3. Drying Shrinkage. The drying shrinkage samples of RC with 100 mm × 100 mm × 400 mm were prepared. After took away the model, the sample was stored in a dry room under the condition of 20°C and 50% relative humidity (RH). The change of length at 1, 3, 7, 14, 28, 56, and 90 days was estimated by shrinkage measuring instrument. Every type of concrete should be prepared as three samples, and the average value is reported as the results.

3. Results and Discussions

3.1. Slump of Concrete. The slump and expansion of fresh concrete are shown in Figure 1. When the SAP content is 0%, the slump and expansion of concretes decrease with the increase of the replacement proportion of RA. This is because the RA contained many inherent defects and microcracks and was covered by old mortar. The old mortar causes the increase of water absorption of RA and reduces the slump and expansion of recycled concrete. When the replacement proportion of RA is the same, the slump and extension of recycled aggregate increase with the increase of SAP dosage. A possible explanation for this might be that SAP is a microsphere, which can reduce the friction resistance among aggregates and improve the expansion and slump of the recycled concrete.

3.2. Compressive Strength. Figure 2 shows the influence of SAP on the compressive strength of recycled concrete. It can be seen that the compressive strength of concrete decreases with the increase of the replacement proportion of RA. When the replacement proportion of RA is 100%, the compressive strength (7 d and 28 d) of recycled concrete with SAP decreases. However, the reduction value of compressive strength of recycled concrete with SAP is smaller than that without SAP. This indicates that the addition of SAP can improve the mechanical properties of recycled concrete. Meanwhile, with the rise of SAP content, the compressive strength of recycled concrete becomes higher.

The RA contained many inherent defects and microcracks and was covered by old mortar, which leads to the decrease of modulus of elasticity. When added to recycled aggregate concrete, the SAP can reduce the amount of mixing water and the water-cement ratio. This is one reason that SAP can enhance the strength of concrete.

In addition, when the hydration process of cement consumes internal water of concrete, SAP will release the water that is absorbed to promote the hydration process of cement-based materials. Therefore, the hydration time of recycled concrete incorporation with SAP is longer than that without SAP, so its mechanical property is improved.

3.3. Shrinkage of Concrete. Figure 3 shows the effect of SAP content on the drying shrinkage of recycled concrete. It can be seen that the drying shrinkage of recycled concrete develops rapidly in the early stage and grows slowly in
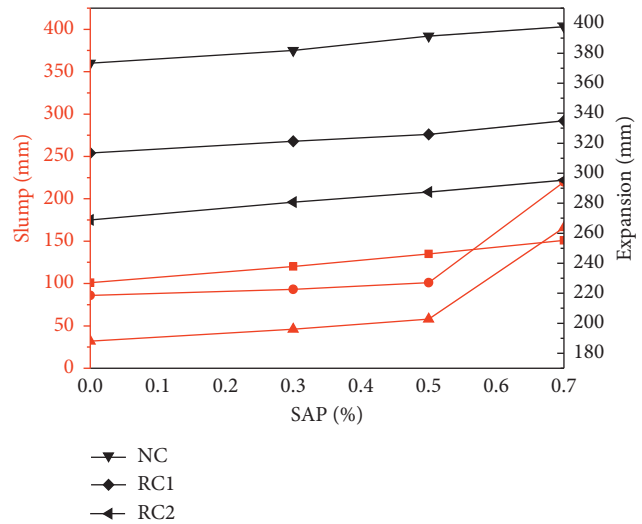
FIGURE 1: Influence of SAP on the workability of recycled concrete.

the later stage. With the rise of the replacement amount of RA, the drying shrinkage of concrete also raises. Under the condition of the same age and replacement amount of RA, the shrinkage rate of the recycled concrete with different dosages of SAP is lower than that without SAP, demonstrating that the addition of SAP can effectively reduce the drying shrinkage of the recycled concrete.

The higher water absorption of RA is the reason that causes the bigger drying shrinkage of recycled aggregate. To meet the workability of recycled concrete, more water will be added. However, the mixing water could not be completely consumed by the hydration process. After hardened, the evaporation of water will leave the pore and cause the shrinkage of concrete. The SAP acts as a "reservoir" in recycling concrete. After the water evaporation, the inside of the concrete is relatively dry, and SAP will release the water that is absorbed to promote the further hydration of cement-based material.

SAP continuously supplements the evaporated water of recycled concrete. This reduces the drying shrinkage of concrete and promotes the completion of hydration of concrete. The increase of hydration products can improve the density of concrete and reduce the drying shrinkage of concrete.

4. Prediction of Recycled Concrete Shrinkage Containing SAP Based on the Grey Prediction Model

The grey prediction model is mainly aimed at the processing of equidistant data. To obtain the data with equal spacing, the dry shrinkage rate (Y) is fitted linearly. However, due to the larger value of the dry shrinkage rate (Y), it is not convenient for calculation, so the dry shrinkage rate (Y) is normalized. Then the normalization interval is adjusted to a positive value, and the dry shrinkage (Y) that suffered the above process is finally used for grey prediction. Similarly,
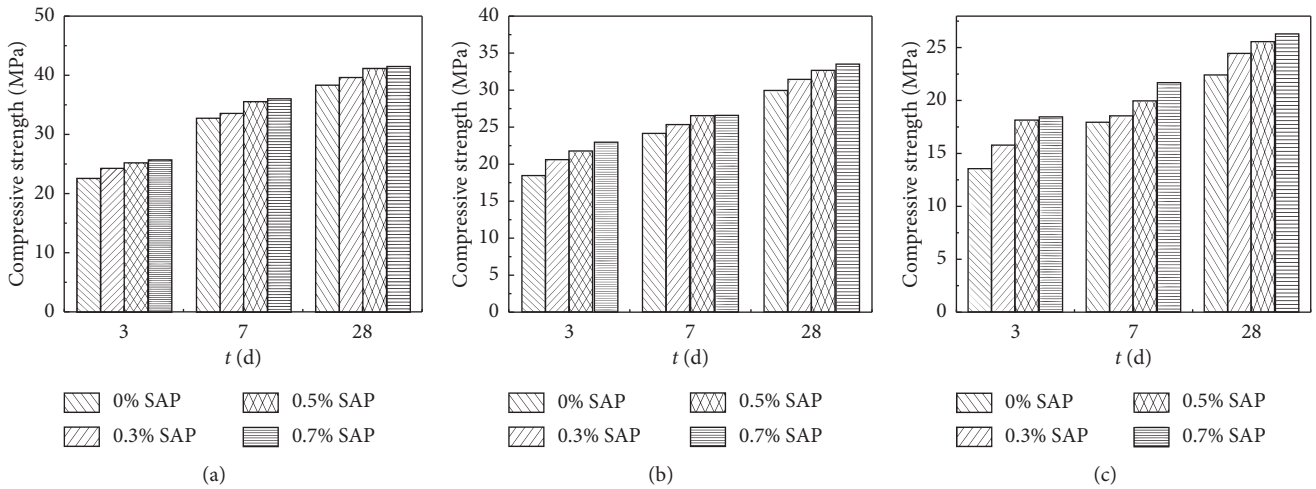
FIGURE 2: Influence of SAP on mechanical properties of reclaimed aggregate concrete. (a) 0% RA. (b) 50% RA. (c) 100% RA.
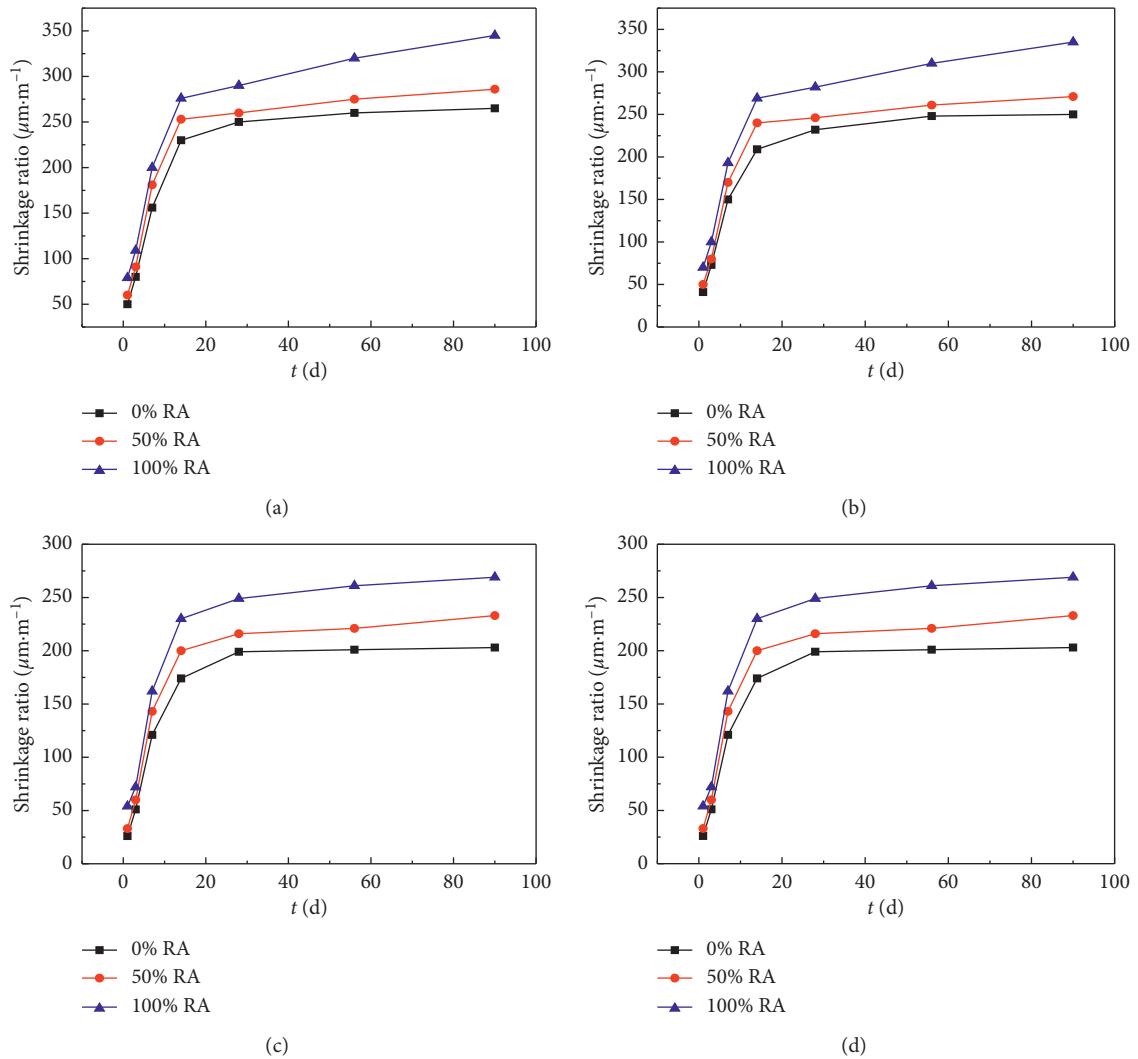
FIGURE 3: Influence of SAP content on drying shrinkage of recycled concrete. (a) 0% SAP, (b) 0.3% SAP, (c) 0.5% SAP, and (d) 0.7% SAP.
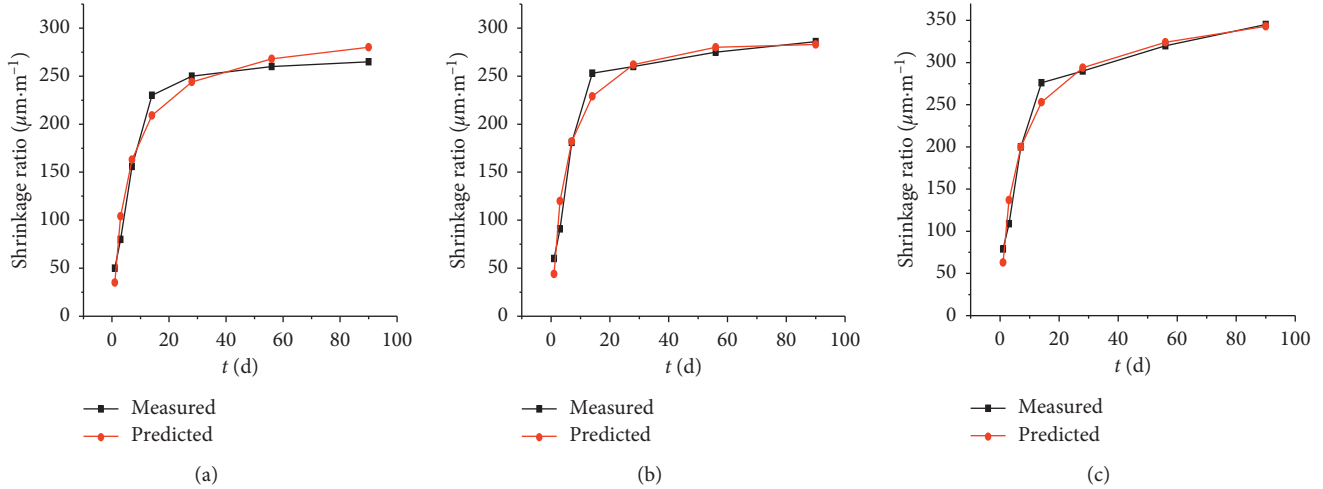
FIGURE 4: The test and predicted results of concrete shrinkage without SAP. (a) NC, (b) RC1, and (c) RC2.
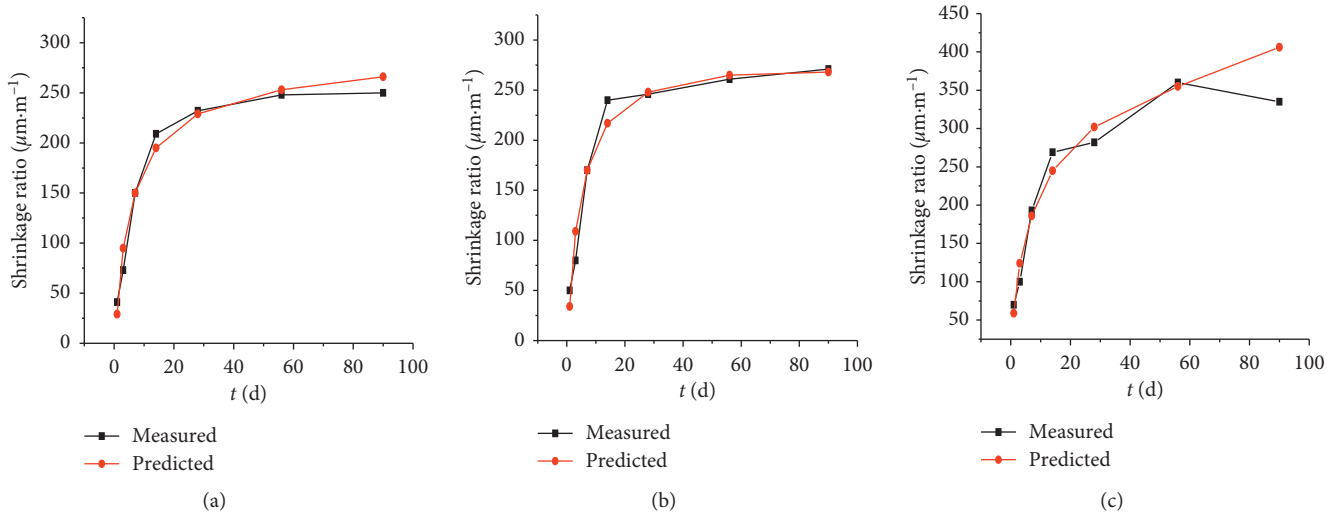
FIGURE 5: The test and predicted results of concrete shrinkage with 0.3%SAP. (a) NC, (b) RC1, and (c) RC2.

this operation is also performed for time (X) to obtain the time (X) that can be used in the grey prediction model. After the simulation, the predicted data can be inversely processed.

The shrinkage of recycled aggregate concrete containing SAP is predicted by the grey prediction model. 1, 3, 7, 14, 28, 56, and 90 d shrinkage results are used as the original data for the prediction. The results indicate that the maximum dry shrinkage occurs about 90 d.

Figures 4–7 show the test and predicted results of drying shrinkage. The results demonstrate that the 90 d shrinkage of RC decreases with the increase of SAP content. This indicates that the addition of SAP is beneficial to the durability of concrete.

The relative error, correlation, mean square deviation ratio, and probability of small error are usually used to evaluate the accuracy of the grey prediction model. In this study, the C is utilized to estimate the accuracy of the model and it can be calculated by equations (12)–(15):

$$\overline{x} = \frac{1}{n} \sum_{k=0}^{n} x(k), \tag{12}$$

$$S_1^2 = \frac{1}{n} \sum_{k=0}^{n} [x(k) - \overline{x}]^2, \tag{13}$$

$$S_2^2 = \frac{1}{n} \sum_{k=0}^{n} [\zeta(k) - \overline{\zeta}]^2, \tag{14}$$

$$C = \frac{S_2}{S_1}. \tag{15}$$

The elevated indicators of the accuracy of the grey prediction model are listed in Table 6.

The grade of (C)-mean square deviation ratio can be divided into four grades. All C values in this test are less than 0.1. According to Table 6, the grade is one, indicating the model owns best accuracy.
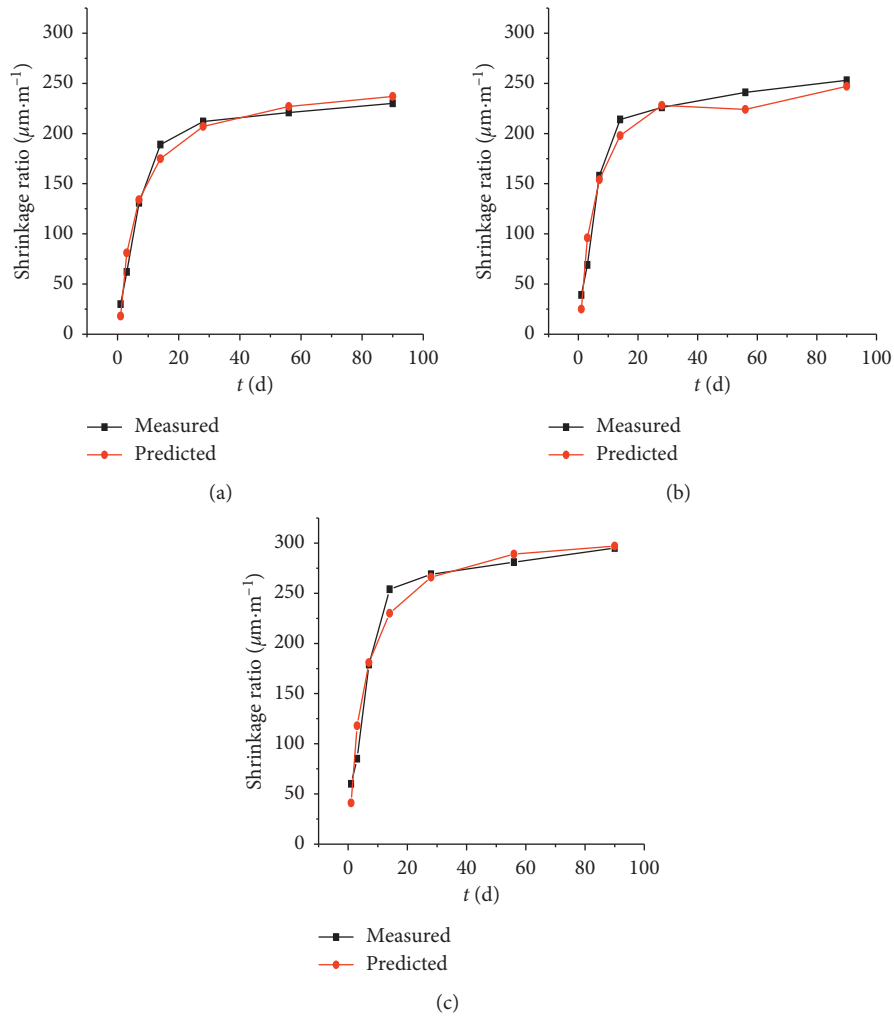
FIGURE 6: The test and predicted results of concrete shrinkage with 0.5% SAP. (a) NC, (b) RC1, and (c) RC2.
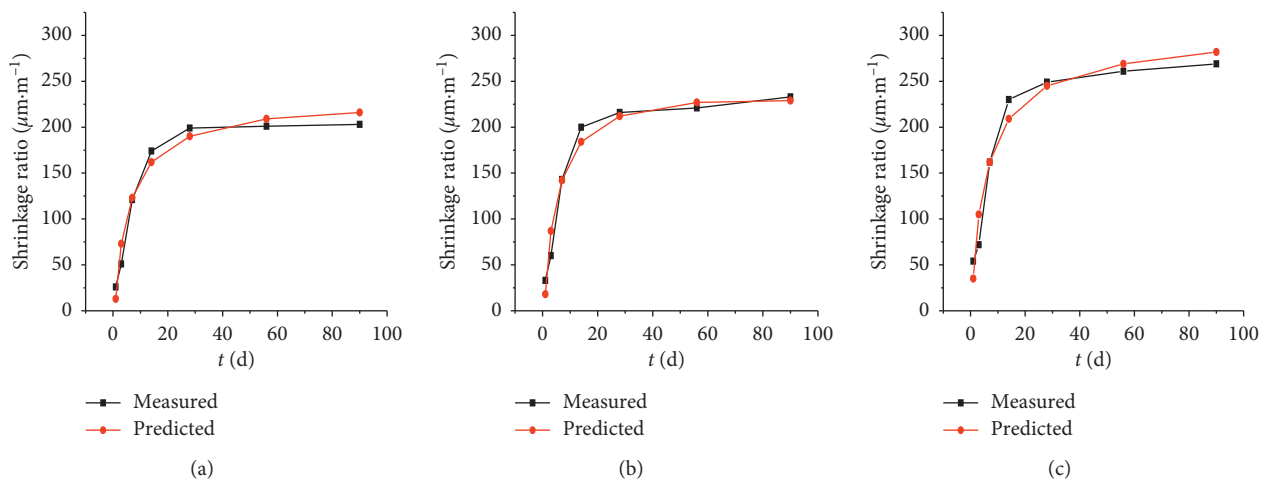
FIGURE 7: The test and predicted results of concrete shrinkage with 0.7% SAP. (a) NC, (b) RC1, and (c) RC2.

Table 6: The elevated indicators of the accuracy of the grey prediction model.

Grade	Indicators			
	Relative error	Correlation	(C)-mean square deviation ratio	Probability of small error
One	0.01	0.90	0.35	0.95
Two	0.05	0.80	0.50	0.80
Three	0.10	0.70	0.65	0.70
Four	0.20	0.60	0.80	0.60

5. Conclusions

In this paper, the natural aggregate (NA) was replaced by recycled aggregate at three replacement ratios (0%, 50%, and 100%). Then, the recycled concrete (RC) with different SAP contents was prepared. The performance of recycled concrete with different SAP contents was analyzed by slump test, compressive strength test, and drying shrinkage test. GM (1, N) grey prediction model was utilized to predict the drying shrinkage of recycled concrete containing SAP.

(1) The replacement of natural coarse aggregate with recycled aggregate has a negative influence on the workability, mechanical properties, and shrinkage of concrete.

(2) With the increase of the dosage of SAP, the strength and durability of recycled concrete also raise. The proper dosage of SAP is 0.7%.

(3) The prediction GM (1, N) model for the drying shrinkage of recycled concrete with SAP is in good agreement with the actual drying shrinkage. This indicates that the grey system theory is feasible to predict the drying shrinkage of recycled concrete with SAP.

(4) The GM prediction model provides a new and effective way of predicting the shrinkage of concrete. In addition, more factors such as the change of climate should be considered in this model in the future study.

Data Availability

The authors would like to declare that all the data in the manuscript were obtained by experiment and the data are true and effective in the manuscript.

Conflicts of Interest

The authors declare that they have no conflicts of interest.

Acknowledgments

References

[1] S. Sun, X. Yu, B. Han, and J. Ou, "In situ growth of carbon nanotubes/carbon nanofibers on cement/mineral admixture particles: a review," *Construction and Building Materials*, vol. 49, pp. 835–840, 2013.

[2] Z. Li, S. Ding, X. Yu, B. Han, and J. Ou, "Multifunctional cementitious composites modified with nano titanium dioxide: a review," *Composites Part A: Applied Science and Manufacturing*, vol. 111, pp. 115–137, 2018.

[3] A. Nobili, L. Lanzoni, and A. M. Tarantino, "Experimental investigation and monitoring of a polypropylene-based fiber reinforced concrete road pavement," *Construction and Building Materials*, vol. 47, pp. 888–895, 2013.

[4] S. Freyne, C. Ramseyer, and J. Giebler, "High-performance concrete designed to enhance durability of bridge decks: Oklahoma experience," *Journal of Materials in Civil Engineering*, vol. 24, no. 7, pp. 933–936, 2012.

[5] Y. Jiao, Y. Zhang, M. Guo, L. Zhang, H. Ning, and S. Liu, "Mechanical and fracture properties of ultra-high performance concrete (UHPC) containing waste glass sand as partial replacement material," *Journal of Cleaner Production*, vol. 277, Article ID 123501, 2020.

[6] H. Duan, T. R. Miller, G. Liu, and V. W. Y. Tam, "Construction debris becomes growing concern of growing cities," *Waste Management*, vol. 83, pp. 1–5, 2019.

[7] J. De Brito and N. Saikia, *Recycled Aggregate in Concrete Use of Industrial, Construction and Demolition Waste*, Springer, Berlin, Germany, 2013.

[8] J. Xie, J. Li, Z. Lu et al., "Combination effects of rubber and silica fume on the fracture behaviour of steel-fibre recycled aggregate concrete," *Construction and Building Materials*, vol. 203, pp. 164–173, 2019.

[9] J. Sainz-Aja, J. Pombo, D. Tholken et al., "Dynamic calibration of slab track models for railway applications using full-scale testing," *Computers & Structures*, vol. 228, Article ID 106180, 2020.

[10] J. A. Sainz-Aja, I. A. Carrascal, J. A. Polanco et al., "Determination of the optimum amount of superplasticizer additive for self-compacting concrete," *Applied Sciences*, vol. 10, no. 9, p. 3096, 2020.

[11] C. Carloni and K. V. Subramaniam, "Investigation of subcritical fatigue crack growth in FRP/concrete cohesive interface using digital image analysis," *Composites Part B: Engineering*, vol. 51, pp. 35–43, 2013.

[12] V. W. Y. Tam and C. M. Tam, "Assessment of durability of recycled aggregate concrete produced by two-stage mixing approach," *Journal of Materials Science*, vol. 42, no. 10, pp. 3592–3602, 2007.

[13] A. M. Neville and J. J. Brooks, *Concrete Technology*, Pearson, London, United Kingdom, 2nd edition, 2010.

[14] EN-1992-1-1, *Eurocode 2–Design of Concrete Structures*, Comité Européen De Normalisation (CEN), Brussels, Belgium, 2008.

[15] ACI-209, *Guide for Modeling and Calculating Shrinkage and Creep in Hardened Concrete*, Vol. 48, American Concrete Institute, Farmington Hills, MI, USA, 2008.

[16] Z. P. Bažant and S. Baweja, "Creep and shrinkage prediction model for analysis and design of concrete structures–model B3," *Materials and Structure*, vol. 28, no. 6, pp. 357–365, 1995.

[17] CEB-FIP, *Model Code for Concrete Structures*, Comité Euro-International Du Béton, Lausanne, Switzerland, 1990.

[18] N. J. Gardner and M. J. Lockman, "Design provisions for drying shrinkage and creep of normal-strength concrete," *ACI Materials Journal*, vol. 98, no. 2, pp. 159–167, 2001.

[19] H. Kim and D. G. Goulias, "Shrinkage behavior of sustainable concrete with crushed returned concrete aggregate," *Journal of Materials in Civil Engineering*, vol. 27, no. 7, Article ID 04014204, 2015.

[20] A. Al-Manaseer and J. P. Lam, "Statistical evaluation of shrinkage and creep models," *ACI Materials Journal*, vol. 102, no. 3, pp. 170–176, 2005.

[21] RILEM-TC-107, "Guidelines for characterizing concrete creep and shrinkage in structural design codes or recommendations," *Materials and Structure*, vol. 28, no. 1, pp. 52–55, 1995.

[22] Z. P. Bažant and G. H. Li, "Comprehensive database on concrete creep and shrinkage," *ACI Materials Journal*, vol. 105, pp. 635–637, 2008.

[23] L. Zhang, X. Qian, J. Lai, K. Qian, and M. Fang, "Effect of different wind speeds and sealed curing time on early-age shrinkage of cement paste," *Construction and Building Materials*, vol. 255, Article ID 119366, 2020.

[24] Y. Li, J. Bao, and Y. Guo, "The relationship between autogenous shrinkage and pore structure of cement paste with mineral admixtures," *Construction and Building Materials*, vol. 24, no. 10, pp. 1855–1860, 2010.

[25] Y. Liu, T. Tafsirojjaman, A. U. R. Dogar, and A. Hückler, "Shrinkage behavior enhancement of infra-lightweight concrete through FRP grid reinforcement and development of their shrinkage prediction models," *Construction and Building Materials*, vol. 258, Article ID 119649, 2020.

[26] J. Ofosu-Adarkwa, N. Xie, and S. A. Javed, "Forecasting CO_2 emissions of China's cement industry using a hybrid Verhulst-GM $(1, N)$ model and emissions' technical conversion," *Renewable and Sustainable Energy Reviews*, vol. 130, Article ID 109945, 2020.

[27] M. Wang, X. M. Sui, Z. X. Han, and Y. Li, "Grey prediction of drying shrinkage of crumb rubber concrete based on GM $(1, 1)$," *Journal of Building Materials*, vol. 6, pp. 653–656, 2008.

[28] L. M. Tang and D. Y. Xiao, "Monthly attenuation prediction for asphalt pavement performance by using GM $(1, 1)$ model," *Advances in Civil Engineering*, vol. 2019, Article ID 9274653, , 2019.

[29] X.-M. Kong, Z.-L. Zhang, and Z.-C. Lu, "Effect of pre-soaked superabsorbent polymer on shrinkage of high-strength concrete," *Materials and Structures*, vol. 48, no. 9, pp. 2741–2758, 2014.

Research Article

Rapid Identification and Quantitative Analysis of Polycarboxylate Superplasticizers Using ATR-FTIR Spectroscopy Combined with Chemometric Methods

Zhiwei Li [iD],[1] **Bo Li** [iD],[1] **Zhizhong Zhao** [iD],[2] **Weizhong Ma** [iD],[3] **Wenju Li** [iD],[1] **and Jiadong Wang** [iD][1]

[1]*National and Provincial Joint Engineering Laboratory of Road & Bridge Disaster Prevention and Control, Lanzhou Jiaotong University, Lanzhou 730070, China*
[2]*Gansu Highway Construction Management Group Co., Ltd., Lanzhou, China*
[3]*Key Laboratory of Highway Net Monitoring in Gansu Province, Gansu Hengda Road and Bridge Group Co., Ltd., Lanzhou, China*

Correspondence should be addressed to Bo Li; 8857807@qq.com

Although the quality inspection method of polycarboxylate superplasticizers (PCE) based on macroperformance is still widely used, it has the drawbacks of time-consuming and low precision. This study aims to develop a practicable alternative method for quality inspection of PCE. For this, spectra collection, feature extraction, and cluster analysis were performed up on the PCE samples to demonstrate the feasibility of the method. Also, a new similarity calculation method was introduced in this work. Results show that the solid PCE sample for spectrum collection can be prepared using the simple heating method. High-quality spectra can be rapidly collected by infrared spectrometer combined with ATR accessory. Meanwhile, the accuracy of classification and clustering is high, suggesting that the feature extraction method based on principal component analysis (PCA) is effective. In addition, compared with conventional similarity calculation methods of cosine angle and correlation coefficient, the new similarity calculation method achieves better classification results and better generalization ability. This work provides a method of quantitative analysis and rapid identification of PCE for the construction site.

1. Introduction

As an important concrete admixture, the water-reducing agent has been widely used in improving concrete performance. They can improve the compressive strength by reducing the amount of water required [1]. Lignosulfonate was the first plasticizer used in concrete, which is a derivative of lignin in pulp industry. Then, poly melamine sulfonates and poly naphthalene sulfonates were developed and applied. However, these plasticizers have limited water-reducing effect and may bring potential problems to the concrete hardening process [2]. The new generation is polycarboxylate superplasticizer (PCE). These superplasticizers are widely used in the construction site and studied in the academic field. Take China as an example, the consumption of PCE in China was 7.23 million tons in 2017, which was about 77.6% of all water-reducing agents used in the year [3]. Therefore, choosing PCE accurately and reasonably is a major concern for industry personnel.

Authenticity is a very important quality criterion for PCEs because there is a big difference among different types of PCE products [4, 5]. However, determination of authenticity for PCEs is traditionally a time-consuming and laborious process, typically using dispersion effect, adsorption amount, and setting times to characterize PCEs [6, 7]. Although these methods can reflect the macroperformance and ensure the engineering performance of PCEs to some extent, they have some drawbacks.

On the one hand, the relevant methods require a huge amount of PCE sample and high operating skills of the test personnel, which may bring potential impact on accuracy [8]. On the other hand, macroperformance test results mainly reflect construction control index, but cannot characterize the relationship between molecular structure and performance of PCE. For example, different PCEs with same or similar macroperformance may exhibit distinct-different in-site performance, with regard of durability, strength, and workability of concrete due to molecular composition of PCE, resulting in structure diseases after long-term use [9].

Moreover, the molecular structure of PCE can be readily adjusted to provide desirable features in order to improve the performance of concrete, such as adaptability to different temperatures and compatibility with different types of cements [10]. Just because the molecular structure is different, the physical and chemical composition of PCE is unique [11]. This uniqueness is similar to human fingerprint, which can be called fingerprint information of PCE. In addition, due to the fingerprint information of PCE, it is feasible to identify PCE in theory.

Recently, fingerprint identification technology has been widely applied in material analysis [12, 13]. Several techniques have been used to describe and determine the quality of the test sample, including colorimetric methods, Gel Permeation Chromatography (GPC), Nuclear Magnetic Resonance Hydrogen Spectrum (NMR), and Gas Chromatography Mass spectrometry. Although these methods can identify the unique fingerprint information of samples, they have the disadvantages of time-consuming, expensive, or cumbersome operation. Compared with the conventional methods, Fourier transform infrared (FTIR) spectroscopy has become one of the most useful analytical means because of its merits including rapid detection, easy operation, and cost saving. Combined with attenuated total reflection (ATR) accessory, a small amount of samples can be analyzed in a short time without sample preparation. ATR-FTIR spectroscopy measures the sample at a depth of 0.5–5 μm from the surface of the internal reflection element. ATR-FTIR schematic diagram is shown in Figure 1, which usually employs a diamond, and collects information from the layer of the sample adjacent to the surface of the internal reflection element. In particular, the development of chemometric technology linked with ATR-FTIR spectral data provides an effective way to determine the physical and chemical properties of materials. Mahsa Mohammadi proposed a new analytical method using ATR-FTIR spectroscopy associated with chemometric methods for addressing regression and classification tasks for crude oil analysis based on API gravity values [14]. Hannah Tiernan applied ATR-FTIR spectroscopy to determining protein content and protein secondary structure composition [15]. Li Zhihui employed ATR-FTIR spectra coupling with SVM classifier to identify graded asphalt [16]. Xiting Sun proposed a rapid and expedient method to determine asphalt properties, including content, softening point, and penetration [17]. Christian Schramm studied the curing process of the impregnated and dried cotton samples by using ATR-FTIR spectroscopy [18].
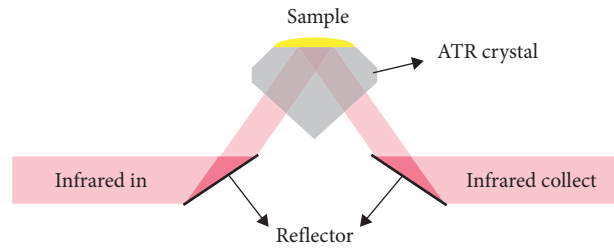
Figure 1: The schematic diagram of ATR-FTIR technology.

Currently, the combination of ATR-FTIR and chemometrics has been widely used in the evaluation of petroleum, flocculant, and wood. However, there is no work that has treated the properties of PCE by direct spectroscopic methods according to literature index. This work uses ATR-FTIR combined with chemometrics to identify and quantitatively analyze PCE. The method of obtaining high-quality spectrum of PCE is firstly explored. The feature extraction and classification were carried out by chemometrics. In addition, different PCEs were compared by the similarity calculation formula, and acceptance threshold was established for each PCE. The results provide a rapid, accurate, and nondestructive method for quality control of PCE.

2. Materials and Methods

2.1. Materials. The selected PCEs for this study are commonly used by contractors on construction projects in Gansu Province, China. Four kinds of PCEs are selected from four different manufacturers, denoted here as A, B, C, and D. The corresponding batches are denoted here as A1, A2, A3, A4, B1, B2, B3, B4, C1, C2, C3, C4, D1, D2, D3, and D4. The acronym A1 represents manufacturer A and batch 1, as indicated in Table 1. All PCE samples are sealed in the sample tank before testing to avoid long time connection with air and stored in a shady and cool place.

2.2. Sample Preparation. All the PCE collected in this research are liquid samples, and the samples contain water. Water can interfere with the quality of infrared spectrum, so it is crucial to eliminate the impact of water. Some researchers achieve this goal by organic solvent extraction. In Standard ASTM C494/C494M-13, a drying method is adopted, that is, the diluted PCE sample is weighed and dried at $105 \pm 3°C$ for $17 \pm ¼$ h [19]. After cooling, infrared spectra of dried residue are studied by the KBr method. However, this method is complex and time-consuming, so it is not suitable for field test. Casale et al. III exploded the feasibility of reducing the drying time to 10 h [5]. Part of the study content, especially the spectral sampling method, is different from this study. Therefore, it is necessary to explore the feasibility of reducing drying time in this study.

This study refers to the test procedure outlined by the ASTM Standard above. In order to study the feasibility of reducing drying time, weigh 3 ± 0.1 g PCE sample, put it in an evaporation dish, and dry it in an oven at $105 \pm 3°C$ for 30, 60, 90, 120, 150, and 180 minutes until the weight does not

TABLE 1: Detailed information of PCEs used in this paper.

PCE	Manufacturer	Batch	Water-reducing rate (%)	Bleeding rate (%)	Setting time difference (min)		Compressive strength ratio (%)	
					Initial setting	Final setting	7 d	28 d
A1		1	31	9	−10	+35	194	168
A2		2	32	18	+65	+5	194	167
A3	A	3	29	9	−25	−65	186	164
A4		4	28	12	−20	−55	165	142
B1		1	35	52	+120	+120	197	173
B2		2	27	12	+100	—	163	149
B3	B	3	26	22	+105	—	153	147
B4		4	26	35	+120	—	192	174
C1		1	27	27	+95	+70	198	169
C2		2	29	42	+100	+60	190	165
C3	C	3	32	12	+95	+105	194	168
C4		4	28	15	+95	+40	190	169
D1		1	35	50	+120	+120	178	173
D2		2	27	60	+120	—	160	146
D3	D	3	28	20	+80	+70	161	155
D4		4	27	15	+100	—	158	147
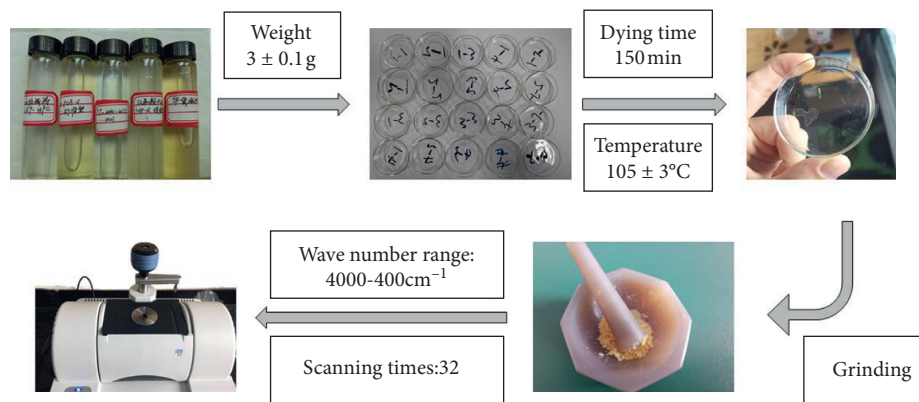
FIGURE 2: The sample preparation process and ATR-FTIR spectrum collection.

change. The time is recorded and used as drying time. The flow chart of sample preparation is shown in Figure 2.

2.3. FTIR Measurements.
ATR-FTIR spectra were obtained using Thermo Fisher Scientific® NicoletiS5 Fourier Transform Infrared Spectrometer combined with iD5 ATR accessory, with an instrument parameter of 32 scans in 4000–400 cm^{-1} range and a resolution of 4 cm^{-1}. To collect infrared spectra, the dried residue of PCE was directly put on the diamond ATR crystal, and the torque knob was tightened to ensure that the sample is in close contact with the diamond ATR crystal. Analyses were carried out at room temperature (25°C). The background collected before every sample was measured. The diamond ATR crystal was cleaned by kerosene. In order to solve the problem that PCE samples are small, a reasonable method is to repeat the number of spectral for each sample. Based on the word reported by Yang et al., three scans were performed and saved in a database for each PCE in each batch [4]. Please note that each scan saved is the average of

four scans, and 48 scans were utilized for chemometric analysis.

2.4. Data Pretreatment and Outlier Detection.
Before using the chemometric method for the next calculation, raw data obtained should be preprocessed. Baseline correction was performed by using OMINIC software. Then, the data were smoothed using the Savitzky–Golay method. Also, in order to increase the calculation accuracy, it is necessary to detect and eliminate outliers. To this end, according to the method provided by Mahsa Mohamadi's paper, the PCA model and Hotelling T^2 statistical plot are used to detect outliers [20]. Outliers can be eliminated from the original dataset, and the original dataset were loaded in the Unscrambler V-10.5 software (CAMO Analytics) for outlier detection by using the Hotelling T^2 statistical method. Data processing and PCA were further performed with MATLAB software (MathWorks).

2.5. Multivariate Analysis: Chemometrics.
Infrared spectrum data is a high-dimensional vector composed of

absorbance corresponding to different wave numbers. Along with the development of spectral detection technology, the characteristic variables of spectral data become larger and larger. One of the major drawbacks of high-dimensional data analysis is the curse of dimensionality. However, a related fact is that hyperspace is essentially sparse, causing the phenomenon of empty space [21]. A natural way to mitigate this problem is to significantly reduce the dimension of original data. It has been shown that principal component analysis (PCA) is an effective multivariate statistical approach for both dimension reduction and information retention. Therefore, all ATR-FTIR spectra data were analyzed by principal component analysis (PCA) to determine the characteristic band. In this way, the redundant information can be filtered effectively. Then, the band selection method is verified by support vector machine (SVM) and cluster analysis [22]. As a new algorithm for classification, SVM has been widely used to nonlinear separation problems [23]. SVM represents the samples as points in space. The samples are separated by plane or line vectors after mapping. The new sample data is first mapped to the same space, and the category is determined based on which side of the vector they fall. A set of 108 samples were used to construct the calibration model, and 36 samples were used for the prediction model.

In addition, similarity calculation was used for calculating the spectral difference and similarity threshold for each PCE was determined. Spectral similarity analysis is an effective method to characterize spectral difference [24]. According to the similarity results, the quality fluctuation of PCE can be determined or the types of PCE can be distinguished. In the process of infrastructure construction, IR spectrum can be considered when the sample is completely known, and the material composition and quality are required to confirm. However, based on the favorable comparison between the infrared spectrum and original sample spectrum, the interpretation of the results is qualitative. The New Jersey Department of Transportation (NJDOT) uses correlation coefficient-based quantitative assessment of infrared scanning to accept or reject field sample. The NJDOT determined an acceptable correlation coefficient threshold of 97.5% [5]. However, the objective fact is that the thresholds for each material may be different. In addition, the quality control method for quantitative evaluation of concrete admixtures using the correlation coefficient has not been established. Therefore, it is necessary to establish the correlation between the sample to be tested and the original sample and to establish the acceptable threshold. This helps to visually verify whether the PCE received at the construction site is acceptable using the quantitative method. Most researchers believe that similarity is an effective parameter to distinguish different spectra [25–27]. After literature retrieval, there are many methods to calculate the similarity, among which the angle cosine formula and

correlation coefficient formula are more commonly used, which can be evaluated by

$$\cos \alpha = \frac{\sum_{i=1}^{n} a_i b_i}{\sqrt{\sum_{i=1}^{n} a_i^2} \sqrt{\sum_{i=1}^{n} b_i^2}},$$

$$S = \frac{\sum_{i=1}^{n} (a_i - \overline{a})(b_i - \overline{b})}{\sqrt{\sum_{i=1}^{n} (a_i - \overline{a})^2 \sum_{i=1}^{n} (b_i - \overline{b})^2}},$$

(1)

where $\cos \alpha$ means angle cosine value, a_i means absorbance values of the measured PCE sample, b_i means absorbance values of the standard PCE sample, $\overline{a}$ means average of absorbance value of the measured PCE sample, and $\overline{b}$ means average of absorbance value of the standard PCE sample. The detailed flowchart is illustrated in Figure 3.

3. Results and Discussion

3.1. Drying Time. ASTM C494/C494M-13 Sect.18.1.1 requires that dry conditions are $17\pm\frac{1}{4}$ h at $105 \pm 3°C$ [19]. This method belongs to the existing uniformity and equivalence tests, so the quality of PCEs can be unchanged by high temperature in theory. However, considering that this method needs to dilute the PCE first and the drying time is too long, this study explored the feasibility of shortening the drying time.

Figure 4 illustrates typical variation curves of weight of PCEs with drying time. The drying time at the temperature of $105 \pm 3°C$ was 0, 30, 60, 90, 120, 150, and 180 min, respectively. As shown in Figure 4, the weight of four different PCEs decreases with the increase of drying time. The observation can be attributed to the evaporation of water in PCEs. Furthermore, after evaporation for 30 minutes, the weight of PCEs decreases sharply and then decreases slowly with drying time. At 150 minutes, the weight of four PCEs was kept stable. Therefore, the drying time of all samples is determined to be 150 minutes.

3.2. Spectral Characteristics of PCE. The ATR-FTIR spectra of evaporated residue of different PCEs are shown in Figure 5. PCEs are composed of different types of hydrocarbons and oxygen containing compounds. As shown in Figure 5, the spectra of all PCE samples are basically the same. The intensity and position of some absorption peaks are slightly different, which indicates that the composition of different PCEs is different [28, 29]. The peak location provides the structural information of the sample, and the peak intensity corresponds to the information of molecular concentration in the sample. In addition, the width of the peak is easily affected by the pH value and hydrogen bond [30]. The characteristic absorption peaks of all PCE spectral range from 3700 to 700 cm^{-1} and are especially concentrated between 1700 and 700 cm^{-1}, that is, the fingerprint region. The band observed at 3400–3200 cm^{-1} corresponds
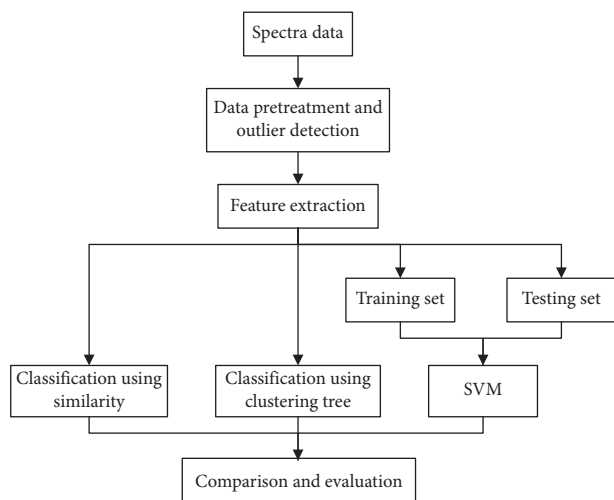
FIGURE 3: The flowchart of the chemometric analysis for determination and classification of PCEs.
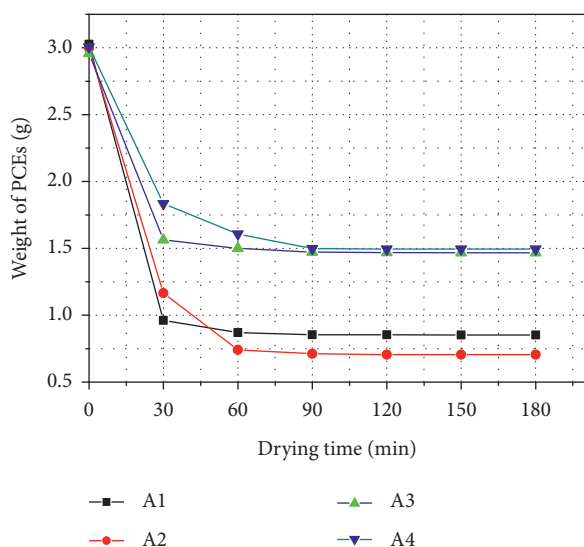
FIGURE 4: Variation in weight of PCEs at different drying times: temperature = 105°C.

to O-H stretching vibrations in PCE. The absorption peaks around 2865 and 2950 cm^{-1} are attributed to aliphatic C-H symmetric and asymmetric stretching vibrations, respectively. Moreover, the band at 1635–1750 indicates the existing of C＝O stretching vibrations. The band around 1130–1070 corresponds to C-O stretching vibrations. The spectral characteristics measured are consistent with the results of literature, indicating that the sample preparation method is reasonable [31].

In addition to the absorption peaks described above, there are some nonobvious peaks in infrared spectra of PCEs. In order to determine which absorption peak can represent the difference of different PCEs, all spectra need to be further processed and analyzed by the chemometric method.

3.3. Data Preprocessing and Outlier Detection.

Figure 6(a) is the overview of PCA using the Unscrambler software. In the score chart, 85% of total variance was presented by the first two principal components (PC-1 and PC-2). Outliers can also be detected by Hotelling's T^2 statistic plot, as shown in Figure 6(c). It is noteworthy to see that no outlier is detected. Therefore, all spectral data can be utilized for further calculation.

3.4. Spectral Feature Selection.

A total of 48 spectral data of 4 different PCEs were imported into MATLAB software to establish the PCA model. Table 2 shows the results of principal component analysis. It can be seen from Table 2 that there were three principal components: PC1, PC2, and PC3, with an eigenvalue of 0.2 or more. The eigenvalue of the first principal component was large with 0.542, as shown in Figure 7, and the contribution rate of variance of the first four principal components is 98.47%. Therefore, it can be concluded that most of the information of the original data has been retained by the first four principal components [24].

PCA results consist of the score plot and loading plot. Among them, the score plot represents the relationship between different samples, while the loading plot represents the relationship between variables. The loading plot can help to determine which variables carry useful information. Figure 8 shows the distribution of the load factor with the wave number. The relationship between spectra variables becomes clear. The absorption peak around 1730 cm^{-1} has a higher influence on the PCA model in the negative direction of X-axis, which corresponds to C＝O stretching vibrations, indicating this absorption peak of different PCEs is obviously different. Similarly, the wave number around 3287, 2859, 1573, 1466, 1409, 1342, 1278, 1241, 1093, 961, and 839 cm^{-1} also have high influence on the PCE model. In addition, compared with PC1, PC2, and PC3, the loading factor distribution of PC4 is more balanced. This is because the variance of PC4 is less than that of PC1, PC2, and PC3, that is to say, PC4 contains less difference among sample classes. Therefore, PC4 basically does not contain valid variables.

In addition, according to the rotation component matrix, the absorbance at the wave number of 3287, 2859, 1730, 1573, 1466, 1409, 1342, 1278, 1241, 1093, 961, and 839 has a large load. It is noteworthy that these 12 bands correspond to the corresponding absorption peaks of ATR-FTIR spectrum of PCE, indicating that the difference between PCEs is mainly near these 12 peaks, as shown in Table 3. It should be noted that the O-H hydroxyl absorption peak around 3287 cm^{-1} fluctuates greatly and is not suitable for modeling. Therefore, the 11 absorption peak wavelengths can be selected for further calculation, as shown in Table 3.

3.5. Support Vector Machine (SVM) Model.

The present work proposed a model of classification based on SVM. In order to expand the sample, sample preparation was performed, and 36 spectral data were collected for each PCE sample. A total of 144 spectral data were collected. Among them, a set of 108 samples were used to construct the calibration model, and 36
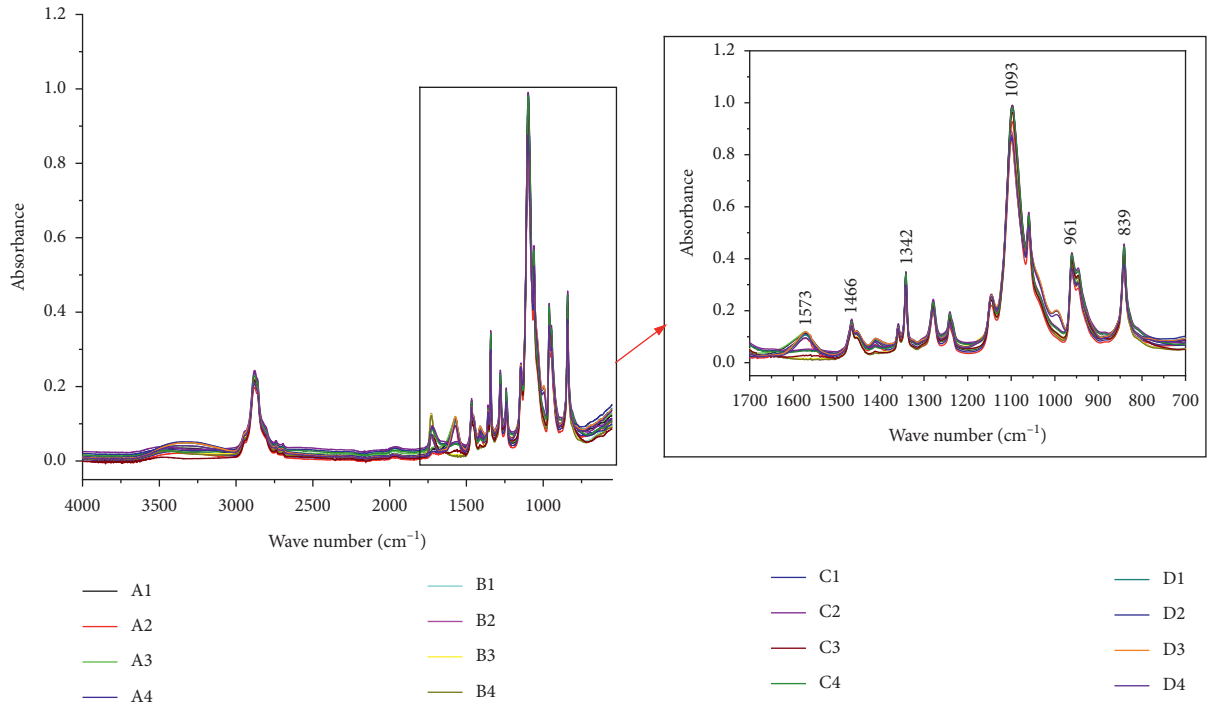
FIGURE 5: Full-wave band and local band spectral of PCE without any pretreatment.
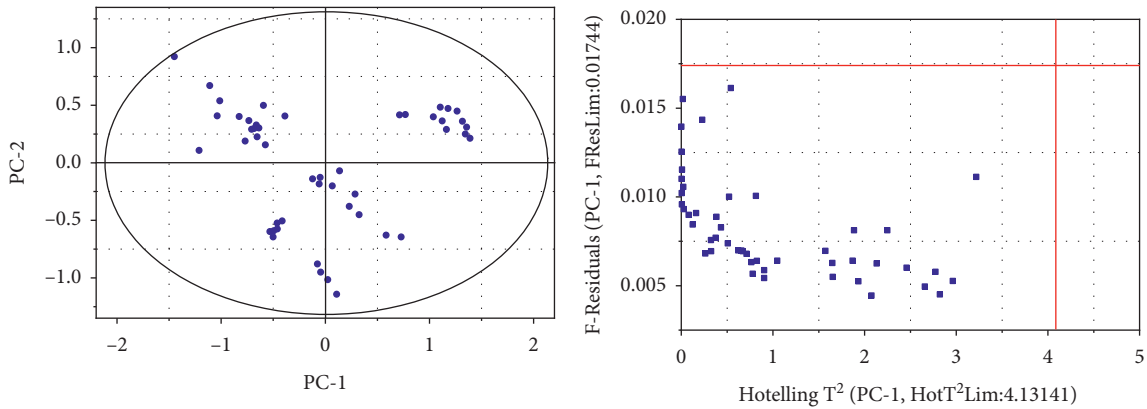
(a)

(b)
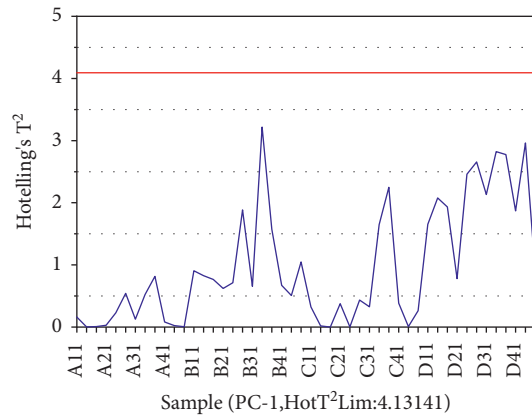
(c)

FIGURE 6: (a) Score plot. (b) Residual plot on ATR-FTIR of PCEs. (c) Hotelling's T2 statistic plot.

TABLE 2: Results of principal component analysis.

Number of principal components	Eigenvalue	Variance contribution (%)	Cumulative variance contribution (%)
1	0.6521	0.5426	0.5426
2	0.2556	0.2127	0.7553
3	0.2413	0.2008	0.9561
4	0.0343	0.0286	0.9847
5	0.0076	0.0063	0.9910
6	0.0063	0.0053	0.9963
7	0.0013	0.0011	0.9974
8	0.0008	0.0007	0.9981
9	0.0004	0.0004	0.9984
10	0.0004	0.0003	0.9988
11	0.0003	0.0003	0.9990
12	0.0002	0.0002	0.9992
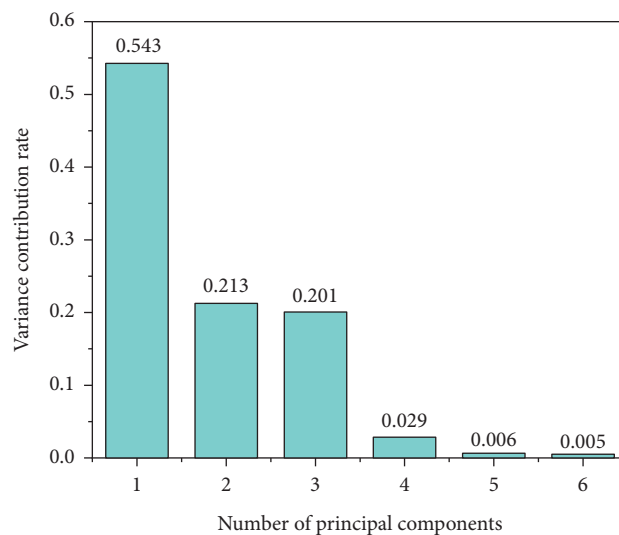
FIGURE 7: The scoring diagram of the first six principal components.

samples were used for the prediction model. By using the SVM classifier, the accuracy rate of total verifying samples stood at up to 100%, as shown in Figure 9. Figure 10 shows the prediction accuracy of four PCE samples. The diagonal part is the proportion accurately predicted, while the other part is the proportion misjudged as other classes. As shown, the four PCEs used in this work were found with an accuracy of 100%, 100%, 100%, and 100%. It means it was 100% correctly classified, whereas none were misclassified. Similarly, PCE-A, PCE-B, and PCE-C were 100% correctly classified. Therefore, the type of PCE can be rapidly identified by using the SVM classifier. In addition, characterized bands selected are effective and suggested for further calculation.

3.6. Systematic Clustering Analysis. Figure 11 shows the results for systematic clustering analysis, and the data used for analysis were the characteristic bands of ATR-FTIR spectra of four PCEs. The abscissa represents the sample number, and the ordinate represents the rescaled distance cluster combine.

It can be seen that the spectra of all samples are classified into four categories, and the result was consistent with the number of PCE samples used in this study. Among them, one cluster was A1-1, A1-2, A1-3, A2-1, A2-2, A2-3, A3-1, A3-2, A3-3, A4-1, A4-2, and A4-3. The second cluster was B1-1, B1-2, B1-3, B2-1, A2-2, A2-3, B3-1, B3-2, B3-3, B4-1, B4-2, B4-3, and C3-2. The third cluster was C1-1, C1-2, C1-3, C2-1, C2-2, A2-3, C3-1, C3-3, C4-1, C4-2, and C4-3, while D1-1, D1-2, D1-3, D2-1, D2-2, D2-3, D3-1, D3-2, D3-3, D4-1, D4-2, and D4-3 belong to another cluster. The PCE spectra are clustered well according to their types except that C3-2 is incorrectly clustered. The potential reason is that the spectrum was not operated properly during collection. PCEs have different molecular structure, so the intensity and location of infrared absorption peaks are slightly different. Therefore, the PCEs can also be classified effectively by the cluster method. This further shows that the feature selection method based PCE can effectively highlight the difference between different water-reducing agents.

3.7. Similarity Analysis of ATR-FTIR Spectra of PCE Samples. Figures 12 and 13 show similarity calculation results by using the angle cosine formula and correlation coefficient formula, respectively. To establish the correlation between different PCE samples, the similarities of infrared

(a)

(b)

(c)

(d)
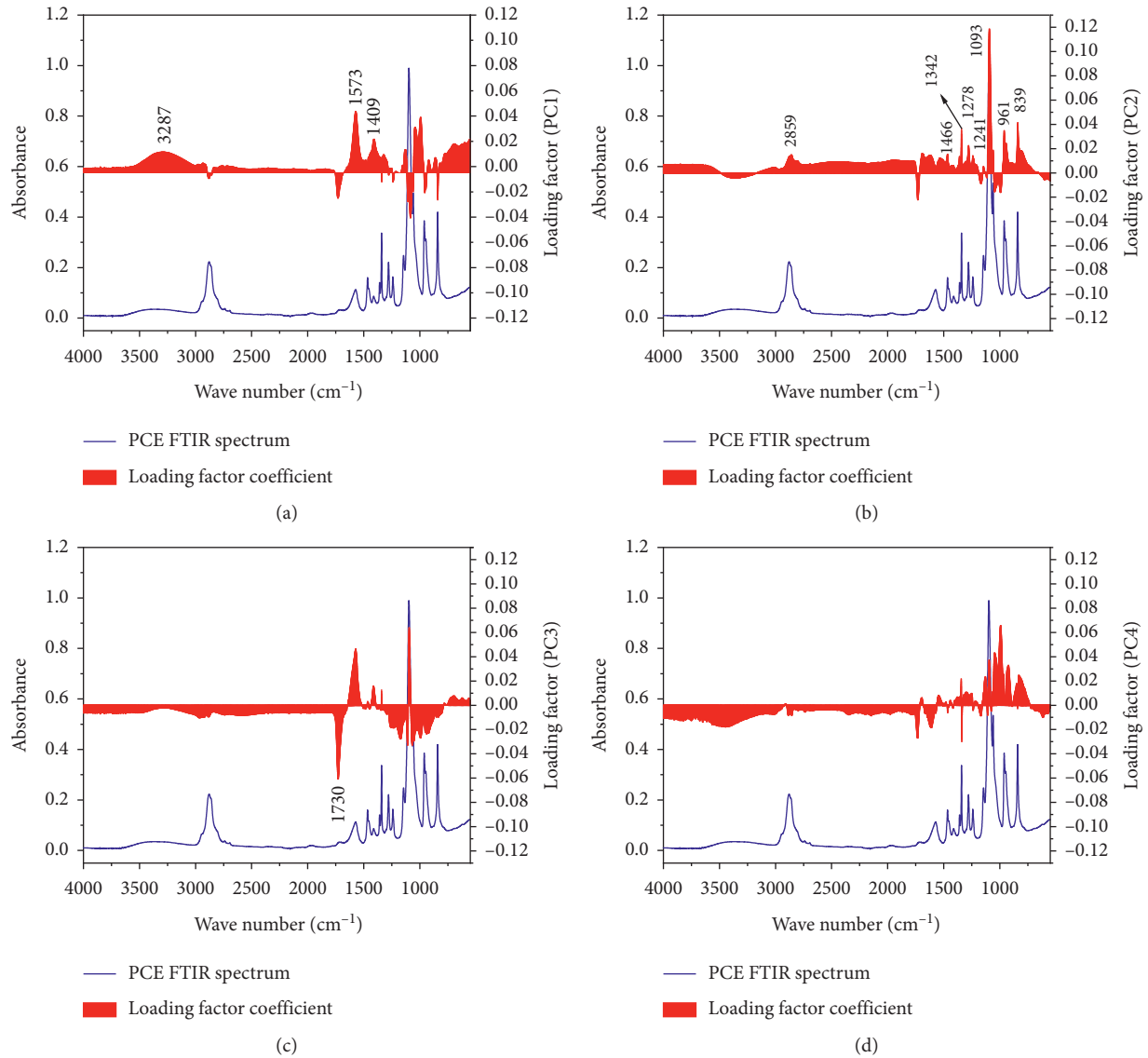
FIGURE 8: Distribution of the load factor with the wave number: (a) PC1, (b) PC2, (c) PC3, and (d) PC4.

TABLE 3: Rotating principal component factor score.

No.	Wave number (cm^{-1})	Factor 1	Factor 2	Factor 3	Factor 4	Upper bound (cm^{-1})	Lower bound (cm^{-1})
1	2859	−0.002	**0.015**	−0.006	−0.006	2755	3000
2	1730	−0.020	−0.022	**−0.060**	−0.025	1681	1754
3	1573	**0.047**	0.005	0.046	−0.006	1504	1652
4	1466	0.005	**0.015**	0.003	−0.005	1428	1504
5	1409	**0.026**	0.005	0.014	0.002	1385	1427
6	1342	−0.002	**0.036**	0.013	0.001	1318	1353
7	1278	−0.002	**0.022**	-0.005	0.005	1263	1298
8	1241	−0.006	**0.014**	−0.016	−0.002	1223	1258
9	1093	−0.019	**0.118**	0.062	0.036	1067	1132
10	961	−0.008	**0.035**	−0.006	0.013	982	1032
11	839	−0.021	**0.041**	−0.006	−0.001	895	979

spectrum of each PCE sample from all batches were evaluated.

As shown in Figures 12 and 13, the similarities (correlation coefficient value) of all 16 samples were all greater than 0.98. In addition, the results show that the similarity of the same PCE, even from different batches, is close to 1 as expected, indicating that the chemical composition is basically the same. However, the PCE cannot be accurately
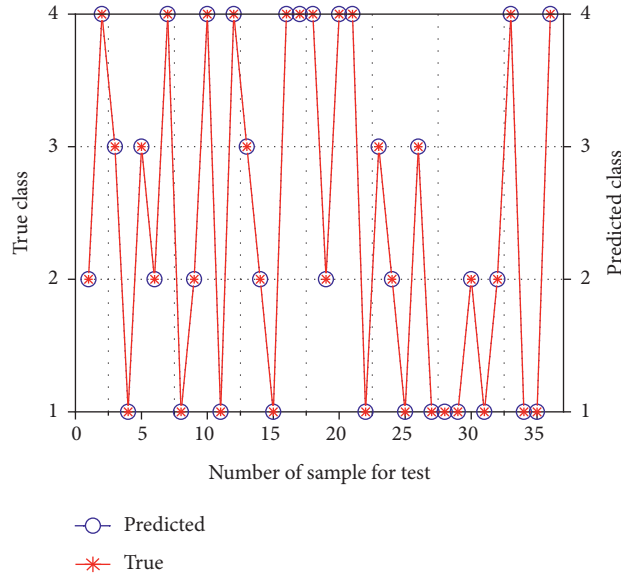
FIGURE 9: Comparison of the test set and SVM prediction results (RBF kernel function).
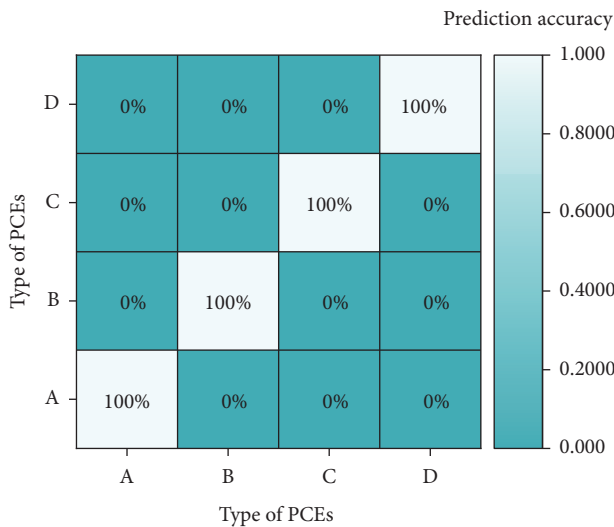
FIGURE 10: SVM matrix results of individual class in percentage.

matched by the above two formulas. For example, the similarity between D3 and D4 (0.998) from the same manufacturer is the same as C1 and D3 (0.998) from different manufacturers by using the angle cosine formula. Similar results are also found in the calculation results using the correlation coefficient formula. This is because the two formulas have some limitations, that is, they are not sensitive to the concentration. For this reason, other similarity calculation methods are needed to be introduced.

In order to improve the sensitivity to the concentration and increase the discrimination between different samples, a new similarity calculation method is introduced in this work, which is shown as

$$S = 1 - \frac{\sum_{i=1}^{n} \left| (X_i - Y_i) / (X_i + Y_i) \right|}{\left(n \left(\sum_{i=1}^{n} X_i + \sum_{i=1}^{n} Y_i \right) \right)^k}, \tag{2}$$

where S means similarity between measured PCE spectral and standard PCE spectral, X_i means peak area of the measured PCE sample, Y_i means peak area of the standard PCE sample, n means total absorption peak number of the standard sample spectrum, and k means shape parameter, $k = 0.3$ in this work, specifically.

In PCA analysis, the characteristic bands of the PCE spectra were extracted, and the bands correspond to the absorption peaks in PCE spectra, indicating the difference between different PCEs. Therefore, the area under the absorption peak corresponding to the characteristic band is substituted into equation (2). On this basis, similarity calculation results are shown in Figure 14. As expected, the similarity between PCEs from the same manufacturer is basically greater than 0.9, whereas PCEs from different manufacturers is less than 0.8, which shows that the new similarity calculation formula has better distinguishing ability. When the PCE product received by the construction site changes, the new formula can choose to reject the product according to the change of some absorption peak area.

The similarity analysis should have an upper and lower bound, making it transferable between dataset and methods [32]. As mentioned earlier, NJDOT currently uses 0.975 as the acceptance standard threshold for concrete admixtures. However, the fluctuation of each PCE is different, and the specific threshold should be determined for each PCE. In this work, the three sigma method is used to establish target threshold, as shown in

$$AT = \mu - 3\sigma, \tag{3}$$
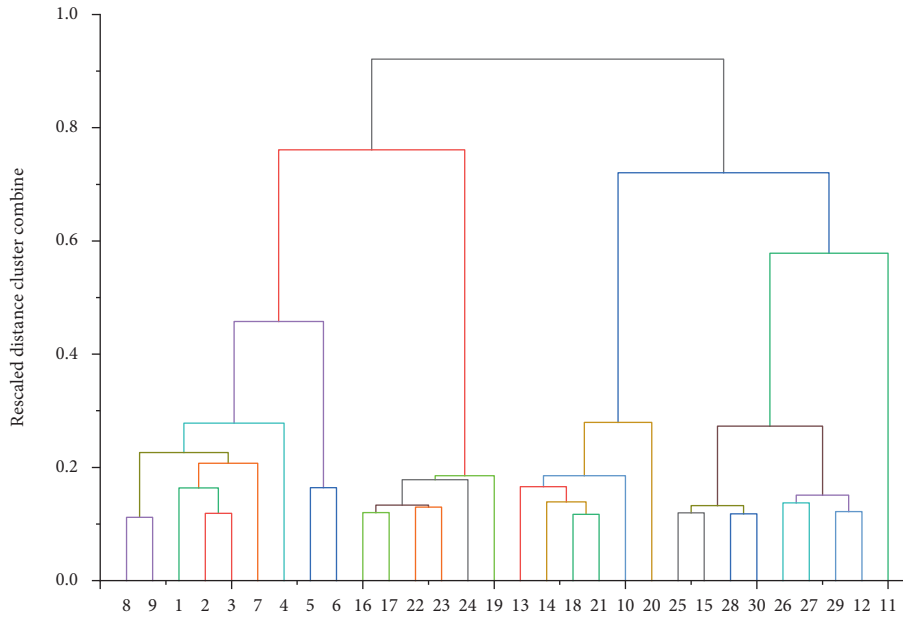
FIGURE 11: Dendrogram of PCEs based on selected variables.
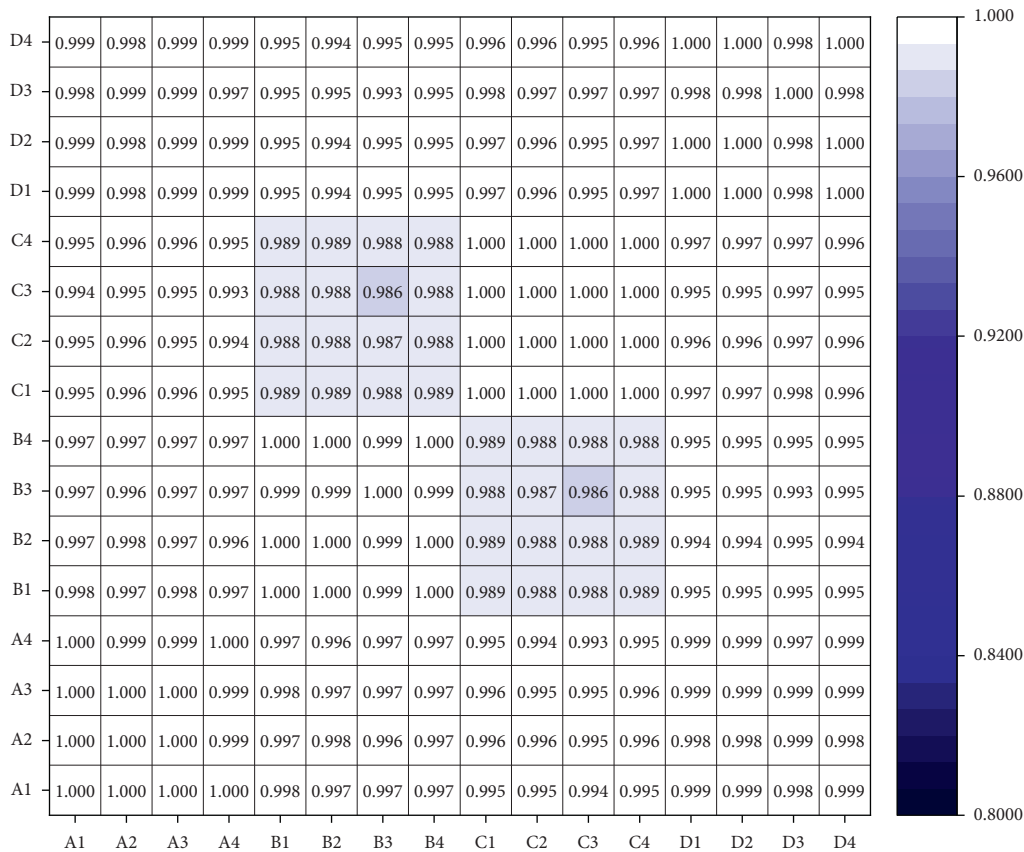
FIGURE 12: Similarity calculation results using the angle cosine formula.

where μ means the average of similarities and σ means standard deviation of similarities involved in calculation.

Therefore, the Acceptance Threshold (AT) corresponding to each PCE is given in Table 4. In this case, the AT of PCE-D is 0.883, indicating the quality fluctuation of this product is large. In addition, the AT of PCE-A, PCE-B, and PCE-C is 0.965, 0.942, and 0.928, respectively. Therefore, it is more accurate to determine a specific AT for each PCE.
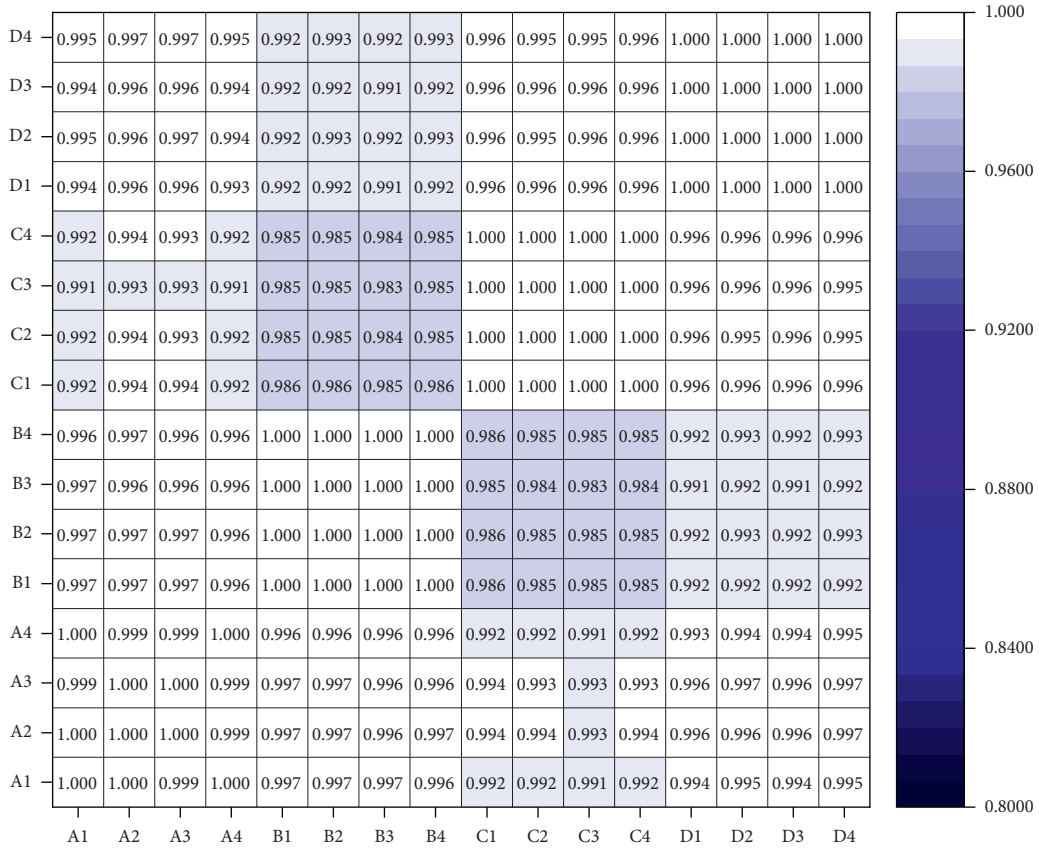
FIGURE 13: Similarity calculation results using the correlation coefficient formula.
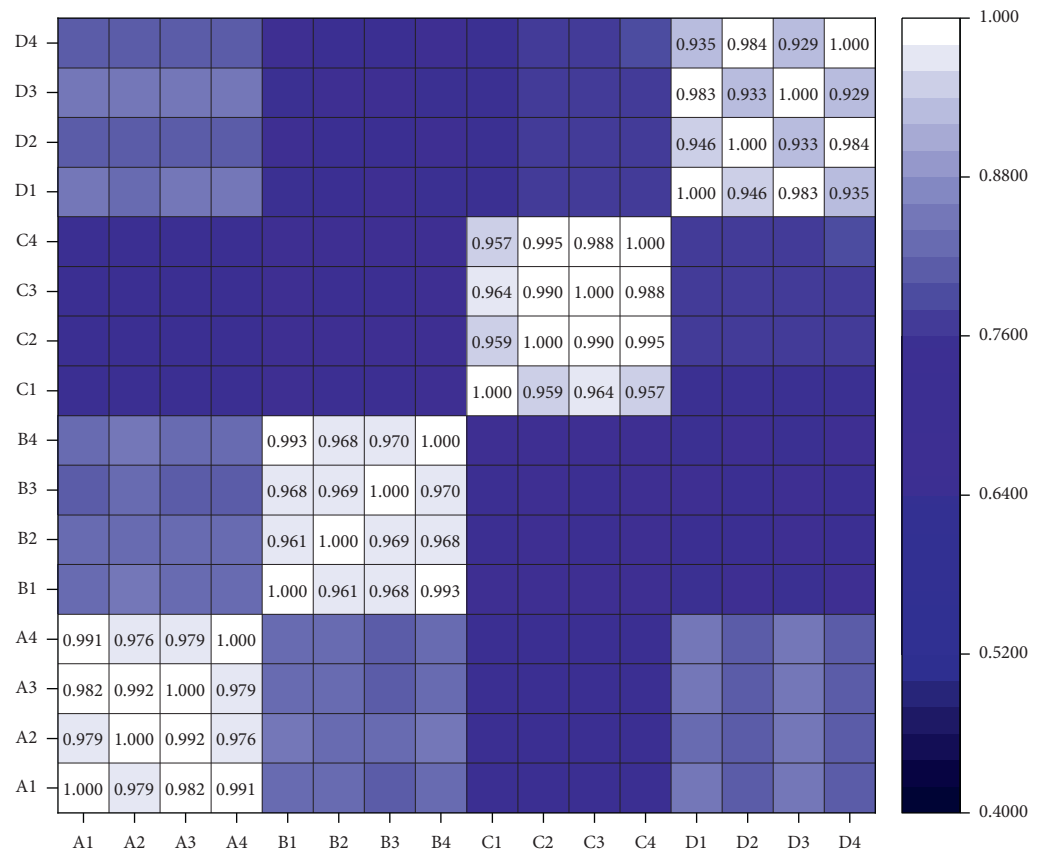
FIGURE 14: Similarity calculation results utilization.

TABLE 4: The AT corresponding to each PCE.

Type of PCE	μ	σ	AT
A	0.983	0.006	0.965
B	0.972	0.010	0.942
C	0.976	0.016	0.928
D	0.952	0.023	0.883

4. Conclusions

This study developed a practicable alternative method for quality inspection of PCE. Specifically, the methods of spectra collection, feature extraction, and cluster analysis were discussed in this study. Moreover, the specific operation steps of PCE quality inspection were also proposed. Based on the experimental result and analysis, the following conclusions can be drawn:

(i) FTIR analysis indicated that a simple heating method can be used to prepare samples for collecting high-quality PCE spectra.

(ii) The feature extraction method based on PCA can effectively reserve significant information bands while reducing the load of calculation. The SVM and cluster analysis results further confirm the validity of the feature extraction method and optimization method.

(iii) Similarity calculation results indicated that the new similarity calculation method not only has better classification performance but also has good generalization ability compared with the conventional method.

(iv) The acceptance threshold determination method based on the 3σ principle determined the specific threshold for each PCE rather than unified threshold, which is much more rational and in accordance with the actual conditions.

(v) It should be noted that it is not enough to establish the acceptance threshold only by 4 batches. In practical application, the correlation between sample number and acceptance threshold should be further explored. In addition, concrete admixtures are not limited to PCE. Future research studies should further verify the feasibility of applying this method to air entraining agent, retarder, and other concrete admixtures.

Data Availability

The PCE spectra data used to support the findings of this study are available from the corresponding author upon request.

Conflicts of Interest

The authors declare that they have no conflicts of interest regarding the publication of this paper.

References

[1] A. Tramaux, N. Azéma, Y. El Bitouri et al., "Synthesis of phosphonated comb-like copolymers and evaluation of their dispersion efficiency on CaCO$_3$ suspensions part II: effect of macromolecular structure and ionic strength," *Powder Technology*, vol. 334, pp. 163–172, 2018.

[2] A. Colombo, M. R. Geiker, H. Justnes, R. A. Lauten, and K. De Weerdt, "On the effect of calcium lignosulfonate on the rheology and setting time of cement paste," *Cement and Concrete Research*, vol. 100, pp. 435–444, 2017.

[3] J. Liu, C. Yu, X. Shu, Q. Ran, and Y. Yang, "Recent advance of chemical admixtures in concrete," *Cement and Concrete Research*, vol. 124, pp. 105–834, 2019.

[4] Y. Hong, J. Irudayaraj, and M. M. Paradkar, "Discriminant analysis of edible oils and fats by FTIR, FT-NIR and FT-Raman spectroscopy," *Food Chemistry*, vol. 93, no. 1, pp. 25–32, 2005.

[5] A. J. Casale, J. Doukakis, H. Najm, and K. Davis, "Quantitative assessment of infrared analysis of concrete admixtures," *International Journal of Concrete Structures and Materials*, vol. 7, no. 3, pp. 203–214, 2013.

[6] S. Tong, Z. Yuqi, and W. Qiang, "Recent advances in chemical admixtures for improving the workability of alkali-activated slag-based material systems," *Construction and Building Materials*, vol. 124, 2020.

[7] Y. Ma, C. Shi, L. Lei et al., "Research progress on polycarboxylate based superplasticizers with tolerance to clays - a review," *Construction and Building Materials*, vol. 255, 2020.

[8] H. Tian, X. Kong, Y. Cui, Q. Wang, and D. Wang, "Effects of polycarboxylate superplasticizers on fluidity and early hydration in sulfoaluminate cement system," *Construction and Building Materials*, vol. 228, 2019.

[9] S. Sha, M. Wang, C. Shi, and Y. Xiao, "Influence of the structures of polycarboxylate superplasticizer on its performance in cement-based materials-a review," *Construction and Building Materials*, vol. 233, 2020.

[10] X. Lin, H. Pang, D. Wei, M. Lu, and B. Liao, "Effect of the cross-linker structure of cross-linked polycarboxylate superplasticizers on the behavior of cementitious mixtures," *Colloids and Surfaces A: Physicochemical and Engineering Aspects*, vol. 608, 2020.

[11] F. Autelitano, "The odour fingerprint of bitumen," *Road Materials & Pavement Design*, vol. 18, no. Suppl.2, pp. 1–11, 2017.

[12] F. S. Hashemi-Nasab and H. Parastar, "Pattern recognition analysis of gas chromatographic and infrared spectroscopic fingerprints of crude oil for source identification," *Microchemical Journal*, vol. 153, pp. 104–326, 2020.

[13] N. Shekari, M. Vosough, and K. Tabar Heidar, "Chromatographic fingerprinting through chemometric techniques for

herbal slimming pills: a way of adulterant identification," *Forensic Science International*, vol. 286, pp. 213–222, 2018.

[14] M. Mohammadi, M. K. Khorrami, A. Vatani et al., "Genetic algorithm based support vector machine regression for prediction of SARA analysis in crude oil samples using ATR-FTIR spectroscopy," *Spectrochimica Acta Part A: Molecular and Biomolecular Spectroscopy*, vol. 245, 2020.

[15] H. Tiernan, B. Byrne, S. G. Kazarian et al., "ATR-FTIR spectroscopy and spectroscopic imaging for the analysis of biopharmaceuticals," *Spectrochimica Acta Part A: Molecular and Biomolecular Spectroscopy*, vol. 241, pp. 118–636, 2020.

[16] L. Zhihui, Z. Rui, Z. Yonghua, C. Qian, and Q. Weijun, "Discriminating wavenumbers selection of ATR-FTIR spectra for identifying graded asphalt," *Construction and Building Materials*, vol. 214, pp. 565–573, 2019.

[17] X. Sun, H. Yuan, C. Song et al., "Rapid and simultaneous determination of physical and chemical properties of asphalt by ATR-FTIR spectroscopy combined with a novel calibration-free method," *Construction and Building Materials*, vol. 230, 2020.

[18] C. Schramm, "High temperature ATR-FTIR characterization of the interaction of polycarboxylic acids and organo-trialkoxysilanes with cellulosic material," *Spectrochimica Acta Part A: Molecular and Biomolecular Spectroscopy*, vol. 243, 2020.

[19] American Standard Test Methods, *Standard Specification for Chemical Admixtures for Concrete*, ASTM C494/C494M-13, West Conshohocken, PA, USA, 2013.

[20] M. Mohammadi, M. K. Khorrami, A. Vatani et al., "Rapid determination and classification of crude oils by ATR-FTIR spectroscopy and chemometric methods," *Spectrochimica Acta Part A: Molecular and Biomolecular Spectroscopy*, vol. 232, pp. 118–157, 2020.

[21] V. Pestov, "Is the k-NN classifier in high dimensions affected by the curse of dimensionality?" *Computers & Mathematics with Applications*, vol. 65, no. 10, pp. 1427–1437, 2013.

[22] H. Guttmann-Beck, R. Rozen, and M. Stern, "Vertices removal for feasibility of clustered spanning trees," *Discrete Applied Mathematics*, vol. 2020, pp. 1–17, 2020.

[23] H. Ling, C. Qian, W. Kang, C. Liang, and H. Chen, "Combination of support vector machine and K-fold cross validation to predict compressive strength of concrete in marine environment," *Construction and Building Materials*, vol. 206, pp. 355–363, 2019.

[24] R. Ren, K. Han, P. Zhao et al., "Identification of asphalt fingerprints based on ATR-FTIR spectroscopy and principal component-linear discriminant analysis," *Construction and Building Materials*, vol. 198, pp. 662–668, 2019.

[25] M. A. Dritschel, D. Estévez, and D. Yakubovich, "Resolvent criteria for similarity to a normal operator with spectrum on a curve," *Journal of Mathematical Analysis and Applications*, vol. 463, no. 1, pp. 345–364, 2018.

[26] N. M. O'Boyle and R. A. Sayle, "Comparing structural fingerprints using a literature-based similarity benchmark," *Journal of Cheminformatics*, vol. 8, no. 1, p. 36, 2016.

[27] K. Wang, L. Cheng, and B. Yong, "Spectral-similarity-based kernel of SVM for hyperspectral image classification," *Remote Sensing*, vol. 12, no. 13, p. 2154, 2020.

[28] M. Xu, Y. Zhang, P. Zhao, and C. Liu, "Study on aging behavior and prediction of SBS modified asphalt with various contents based on PCA and PLS analysis," *Construction and Building Materials*, vol. 265, 2020.

[29] S. Chen, S. Sun, X. Chen et al., "Effects of core-shell polycarboxylate superplasticizer on the fluidity and hydration behavior of cement paste," *Colloids and Surfaces A: Physicochemical and Engineering Aspects*, vol. 590, 2020.

[30] M. Lopes, V. Mouillet, L. Bernucci, and T. Gabet, "The potential of attenuated total reflection imaging in the mid-infrared for the study of recycled asphalt mixtures," *Construction and Building Materials*, vol. 124, pp. 1120–1131, 2016.

[31] X. Lin, B. Liao, J. Zhang, S. Li, J. Huang, and H. Pang, "Synthesis and characterization of high-performance cross-linked polycarboxylate superplasticizers," *Construction and Building Materials*, vol. 210, pp. 162–171, 2019.

[32] E. Källman, M. G. Delcey, M. Guo, R. Lindh, and M. Lundberg, "Quantifying similarity for spectra with a large number of overlapping transitions: examples from soft X-ray spectroscopy," *Chemical Physics*, vol. 535, 2020.

Research Article

Cleaning of Graphite Particles Embedded in the Surface of Ductile Iron by Using a Novel Method

Baoshen Jia, Xinxiang Miao, Yilan Jiang, Hongping Tang, and Caizhen Yao [ID]

Laser Fusion Research Center, Chinese Academy of Engineering Physics, Mianyang 621900, China

Correspondence should be addressed to Caizhen Yao; yaocaizhen2008@126.com

Ductile iron has unique mechanical property and has been widely used in many industrial applications, e.g., engine cylinder covers, crank axles, and machine tool beds and cams. The welding performance of ductile iron is normally influenced by graphite particles in the surface of ductile iron, which needs to be removed before welding. In this article, laser cleaning technique was developed to remove graphite particles implanted in the surface of ductile iron. Laser cleaning parameters and the damage threshold value of the substrate were investigated by using a pulsed Nd: YAG laser. The optimized laser cleaning parameters were obtained to achieve high-quality cleaning effect and avoid the formation of the oxide layer. Surface morphologies and elemental compositions of specimens before and after laser cleaning were characterized by scanning electron microscopy and energy-dispersive X-ray spectroscopy. Results indicated that graphite particles implanted in the surface of ductile iron were removed completely and efficiently by using the pulsed laser without the protection of inert gas atmosphere, and surface oxidation was not observed during the laser cleaning process.

1. Introduction

Ductile cast iron is used extensively in different industrial fields for the manufacturing of engine cylinder covers, crank axles, machine tool beds and cams, and so on. It is a potential replacement of steel in some applications due to its excellent casting performance, extraordinary abrasive resistance, outstanding corrosion resistance, and the well combination of toughness and strength [1–4]. Phase compositions of ductile cast iron are pearlite, ferrite, and graphite phases, with ferrite as the matrix. However, graphite particles implanted in the surface of ductile iron could affect the quality of coating, reduce the welding performance, and short the service life of the workpiece. Those particles need to be removed completely before welding [5]. Techniques have been developed by researchers to remove graphite particles, in which the sand-blasting method is the most commonly used. Sand blasting [6] is an efficient and effective technique for the cleaning of the large surface area. However, it is time and energy consuming for the cleaning of small workparts of ductile iron. Chemical etching [7] is not suitable for the

removal of graphite particles due to their chemical stability. Recently, laser cleaning technique has been developed as a novel method to remove surface contaminants [8–11]. Comparing with traditional surface treatment techniques, laser cleaning is environmentally friendly for direct removal of contaminants without altering or affecting properties of matrix.

Different from continuous lasers for cutting, welding, and cladding, pulsed laser source was employed for laser cleaning. Laser cleaning is a multifactor process with mechanism of evaporation, ablation, acoustic effect, and impact effect (Figure 1) [12]. Intensity and spatiotemporal characteristics of radiation play the main role during laser cleaning process. Cleaning effect is also related to the absorbing ability of the material, which strongly depends on temperature, thermal conductivity, and other factors.

When laser irradiates on metal surface, the metal partially absorbs the laser radiation, and it will be heated, melted, partially evaporated, and ionized. A rigorous mathematical description of the interaction taking into account all participating physical processes is complex.
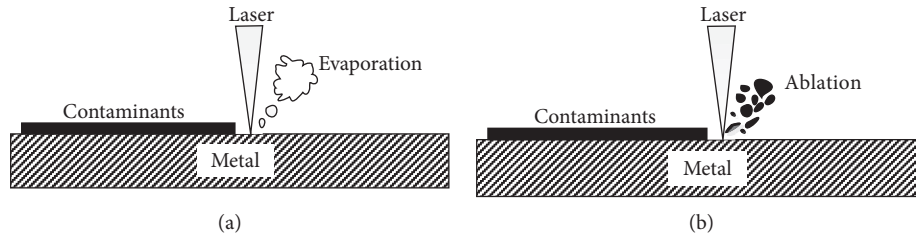
FIGURE 1: Mechanism of destruction of contaminants on metal's surface: (a) evaporation and (b) impact ablation [12].

Depending on the power density of the radiation impacting the surface, laser cleaning can be implemented by evaporation process, impact process, or acoustic and thermoplastic forces [12, 13]. Evaluations indicate that effective cleaning due to evaporation for most materials (Figure 1(a)) is achieved at the power density of 10^7–10^8 W/cm^2. A low threshold thermal-chemical impact ablation mechanism of the film can be implemented under the effect of pulsed laser radiation with power density lower than 10^7 W/cm^2 [12, 14] (Figure 1(b)). Laser cleaning technique has been successfully applied to removal of paint and oxide layer on metal surfaces, cleaning of optical and electronic elements, and conservation of cultural heritage [15–22]. However, few research studies have been carried out on laser cleaning of ductile iron.

Inspired by the effectiveness of the laser cleaning technique for the removal of surface contaminants, in this work, the infrared high-repetition nanosecond pulsed laser was employed to remove graphite particles implanted in the surface of ductile iron. The technical details of laser cleaning and removal possibilities of graphite particles with different implantation forms were discussed. Cleaning effects of different laser parameters were investigated. Surfaces before and after laser treatments were characterized by scanning electron microscopy (SEM) and energy-dispersive X-ray spectroscopy (EDS). The optimized cleaning parameters and the damage threshold value of the substrate were obtained. Results indicated that laser cleaning is an effective and environmentally friendly technique for the removal of graphite particles, which will not lead to degradation of essential performance of the ferrite matrix.

2. Materials and Methods

2.1. Sample Preparation. Different from the contaminants adhered to the surface of substrate, for ductile iron, graphite particles are embedded in the ferrite matrix, and it is technically more difficult to be removed. The cleaning process and laser parameters are different from those for cleaning of the dusts, rubber particles, and paints from the substrate. If the shape of graphite particles is assumed as a regular sphere, the implanted particles have 4 forms in the iron substrate as shown in Figure 2.

It is obvious that shallowly embedded particles can be removed easily. Particles A and B in Figure 2 can be removed by laser ablation. However, for particle C, evaporation should be the main mechanism. A few particles like D, because of their small exposed area, are difficult to be

removed completely by laser cleaning or sand blasting. Furthermore, it is difficult to calculate the adhere force between graphite particles and matrix, which is necessary to decide laser parameters when ablation is the main mechanism in a cleaning process. In this case, evaporation mechanism is more suitable for ductile iron cleaning. The boiling point of graphite is higher than that of iron, and it is much higher than melting point of iron; therefore, iron substrate would melt and gasify during laser cleaning process. Melting and gasification of iron substrate are acceptable phenomenon. If a power intensity higher than 10^8 W/cm^2 is used during laser cleaning process, oxidation may be induced, which is not acceptable for further treatment of iron substrate. Iron oxide will be formed quickly in atmosphere when the temperature is higher than 5000°C.

In this work, a ductile iron club was chosen as the research target, and it was cut into small specimens with a dimension of ϕ20 mm × 8 mm. Specimens were cleaned by using alcohol to remove particulate and organic contaminants from the surface.

2.2. Experimental Setup. The schematic diagram of the laser cleaning system is shown in Figure 3. Specimens were fixed on a platform moving along Y-axis controlled by a computer. Laser beam movement on surfaces of specimens was controlled by a directional control system in X-axis, and its movement in Y-axis was achieved by the movable platform. High power densities were guaranteed by an F-θ lens, which focused the laser beam on the surface of specimen with a spot diameter of 500 μm at focal plane. Values of fluence were adjusted by varying the output power while keeping the repetition rate and pulse duration the same. To obtain the threshold fluence, several fluence values were chosen to determine the optimal condition for the graphite removal. Surfaces were cleaned several times to remove the implanted graphite particles completely. Inert gas was not applied to the irradiated area during the laser cleaning process.

A Q-switched Nd:YAG laser system with a maximum power of 400 W, repetition rate of 5–100 kHz, and pulse duration of 60–100 ns was employed in laser cleaning experiments. The diameter of laser spot at focal plane was 500 μm. During the experiment, the repetition rate of the laser was much higher than the scanning rate, ensuring the complete surface coverage during cleaning process. Meanwhile, the scanning rate was matched to the repetition rate, ensuring a small overlap rate (20%) to reduce the influence of energy accumulation.
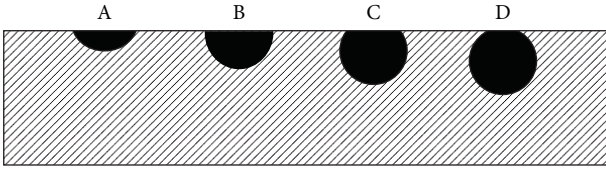
FIGURE 2: Schematic diagram of graphite particles embedded in the ferrite substrate.
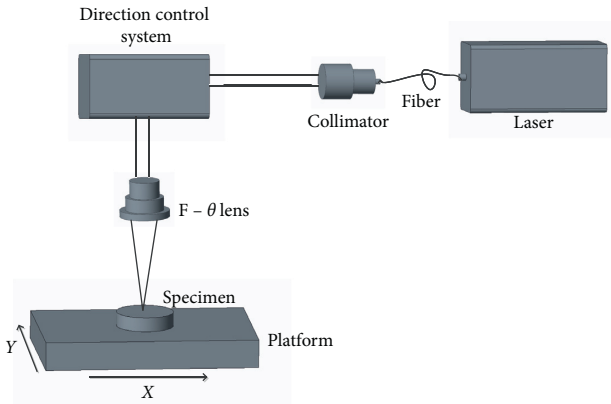
FIGURE 3: Schematic diagram of the laser cleaning setup.

3. Results and Discussion

3.1. Theoretical Calculation. Considering that the radiation is absorbed in the near-surface metal layer, while parameters such as diffusivity α_t and thermal conductivity K are constant, the heat conduction equation can be written as follows [12]:

$$T(z,t) = T_0 + \frac{2P(1-R)}{KS}\left\{\sqrt{\alpha_t t} * \text{ierfc}\left(\frac{z}{2\sqrt{\alpha_t t}}\right)\right\}, \quad (1)$$

where $T(z,t)$ is the temperature of the material at depth z after time t, P is the power of a single pulse, S is the area of spot, T_0 is room temperature, R is reflection of ductile iron, and ierfc () is the error function. The value of ierfc () varies with values of depth z and time t. Critical density of the radiation flux to attain the boiling point on the surface of the material can be determined by the temperature field. Critical temperature of Fe substrate can be obtained by using equation (1), and calculated results are shown in Figure 4. Thermal parameters of substrate are given in Table 1.

Because inert gas is not applied, cleaning parameters especially oxidation threshold of laser power intensity should be obtained and optimized. According to the calculated results in Figure 4, oxidation threshold of laser power intensity is about 10 J/cm^2.

3.2. Experimental Demonstration. According to equation (1), a high temperature is needed to completely remove graphite particles. Thus, a high laser power intensity is required. There are two routes to increase the power intensity,

one is to increase the output laser power and the other is to decrease the spot area. Increasing output power is much easier in comparison with decreasing the spot area. In this research, the average power was increased while maintaining other experimental parameters the same as shown in Table 2. The repetition rate was 15 kHz, the pulse duration was 100 ns, and the scanning velocity was 3200 mm/s. The surface of the specimen was placed at the focal plane of the laser beam. The cleaning passes were carefully chosen. Cleaned specimens were judged by their appearance first and then evaluated by the combination of SEM and EDS analysis.

Based on previous analysis and the conclusion of reference [14], initial testing experiment on S0 is performed with a laser radiation power density of 6.79×10^7 W/cm^2 (6.79 J/cm^2). As shown in Figure 5, region A is the surface before cleaning and region B is the surface after cleaning. The color of cleaned surface is silver white, much brighter than that of original surface, and is approaching to the color of iron. It seems that the expected appearance has been achieved by only one-step laser cleaning.

Figure 6 shows detailed views of surface morphologies of initial (Figure 6(a)) and laser cleaned (Figure 6(b)) specimens. As previously mentioned, different from particulate contaminants adhere to the surface, Figure 6(a) shows that graphite particles (black area, e.g., C) with diameters ranging from 10 μm to 50 μm embedded in the matrix of ductile iron (gray area, e.g., D). Figure 6(b) indicates that graphite particles with diameters less than 10 μm were completely removed (e.g., site 1), leaving implanted holes. Deeply embedded particles with diameters between 10~50 μm were not completely removed (e.g., site 3). Shallowly implanted large particles were also completely removed (e.g., site 2). Comparing with Figure 6(a), it can be seen that the ferrite matrix melted due to the high laser radiation power density, which is in agreement with our previous analysis. In this case, evaporation is the main mechanism for ductile iron cleaning. The boiling point of graphite (4830°C) is higher than that of iron (2750°C), and it is much higher than melting point of iron (1535°C); therefore, iron substrate melt and be gasified during laser cleaning process. Melting and gasification of iron substrate are acceptable for further welding treatment of ductile iron.

EDS analysis was employed for further investigation of the oxidation process during laser cleaning. Figure 7 shows the EDS results of regions C and D of initial specimen (Figure 6(a)) and region E of the cleaned specimen (Figure 6(b)). It can be seen from Figure 7(a) that the main elements of region C (graphite particle) and D (ductile iron substrate) are carbon and iron, respectively, which are consistent with the composition of ductile iron. Comparing with Figure 7(a), Figure 7(b) shows that the composition of iron substrate after laser cleaning is similar to that of the initial status, which demonstrates that oxidation does not occur on iron substrate during laser cleaning process. The result indicates that laser cleaning is a promising method to remove graphite particles implanted in ductile iron while preserving the mechanical property of the substrate.
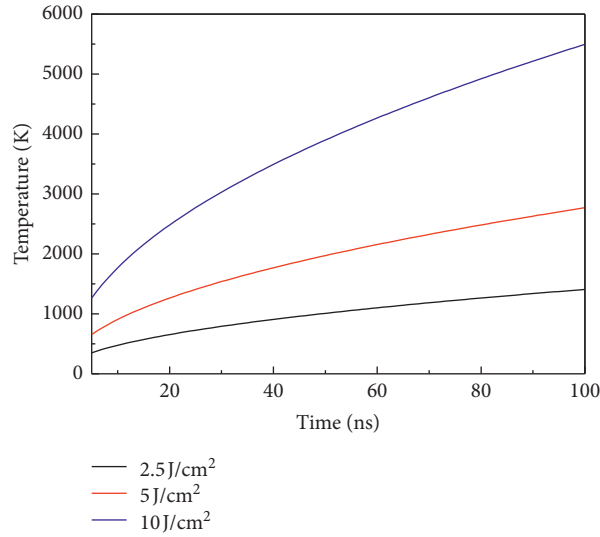
FIGURE 4: Time-temperature curves of the top surface at different energy intensities.

TABLE 1: Thermal parameters of Fe substrate.

Thermal properties	Thermal conductivity ($W \cdot m^{-1} \cdot K^{-1}$)	Density (kg$\cdot m^{-3}$)	Specific heat ($J \cdot kg^{-1} \cdot K^{-1}$)	Absorptivity
Fe substrate	55	7.86×10^3	0.60×10^3	0.18

TABLE 2: Designed laser cleaning parameters.

Nominated name	Power (W)	Repetition rate(kHz)	Diameter of spot(mm)	Scanning rate(mms^{-1})	Pulse duration (ns)	Pass
S0	200	15	0.5	3200	100	1
S1	220	15	0.5	3200	100	1
S2	240	15	0.5	3200	100	1
S3	260	15	0.5	3200	100	1
S4	280	15	0.5	3200	100	1
S5	290	15	0.5	3200	100	1
S6	290	15	0.5	3200	100	3
S7	290	15	0.5	3200	100	5
S8	300	15	0.5	3200	100	1
S9	320	15	0.5	3200	100	1
S10	320	15	0.5	3200	100	3
S11	340	15	0.5	3200	100	1

FIGURE 5: Comparison of the appearance of S0. Region A is the surface before cleaning, and region B is the surface after cleaning (200 (W).

(a)

(b)
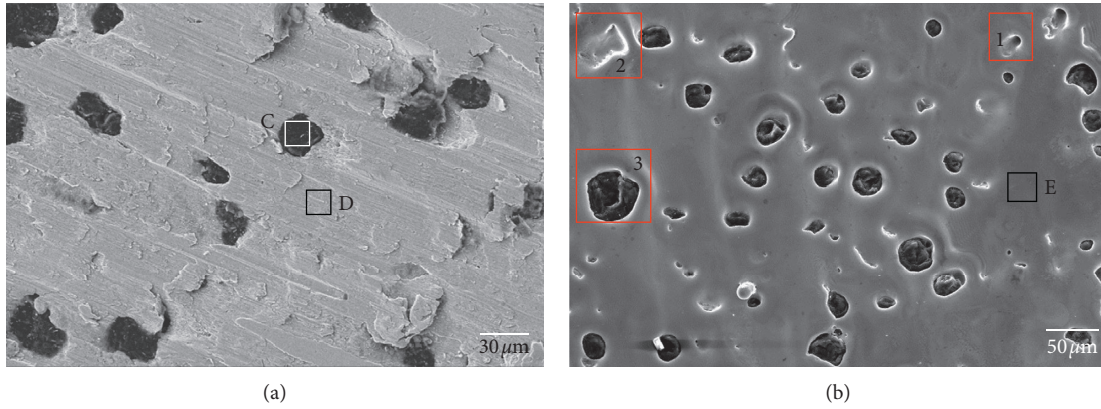
FIGURE 6: Surface morphologies of initial (a) and 200 W laser cleaned (b) specimens.

Region C
Fe 94.90 Si 5.10 % Atomic

Region D
C 98.75 Fe1.25 % Atomic

(a)

Element	Atomic%
Fe	95.79
Si	4.21

(b)
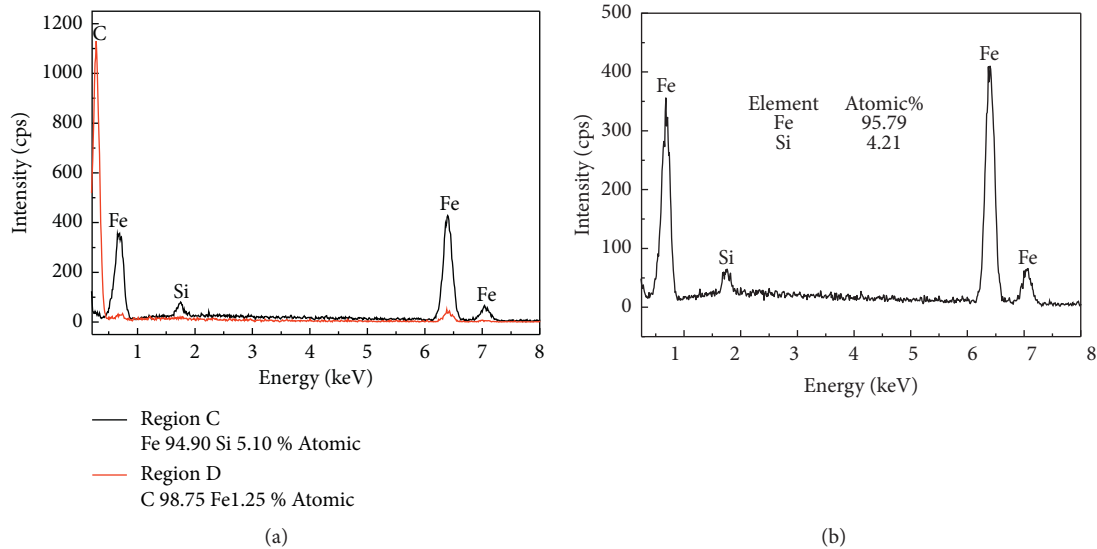
FIGURE 7: EDS results of regions C and D of initial specimen (a) and region E of the cleaned specimen (b) in Figure 6.

However, deeply embedded graphite particles still exist after laser cleaning. In following experiments, laser cleaning parameters will be optimized to improve the remove efficiency.

Figure 8(a) is the specimen cleaned by using the laser with the power of 340 W (region F) and 320 W (region H). Damage is observed on the surface of the specimen cleaned by using the 340 W laser. SEM/EDS analysis of the circled part of region F was performed, and its results are shown in Figure 8(b). It can be seen that the atomic ratio of O is 58.08%, of O is 58.08 at.%, demonstrating that oxidation occurred during 340 W laser cleaning process. The SEM image in Figure 8(b) reveals that graphite particles were removed but the appearance of the substrate also changed. Some loose materials formed on the surface such as region I could be iron oxide. The appearance of region H is similar to that of region B in Figure 5. The SEM image of region H is shown in

Figure 8(c). It can be observed that there are still many residual graphite particles. The number of removed particles is more than that of the specimen in Figure 6(b), demonstrating that increasing power intensity to a certain value below damage threshold is a proper way to obtain a better cleaning performance. According to above results, it can be concluded that the safe power intensity for the cleaning of ductile iron substrate is about 320 W, corresponding to 10.86 J/cm^2 (1.086×10^8 W/cm^2), which is close to the calculated result. According to literatures [10, 23–25], the thick surface layer can be completely removed by increasing cleaning times. Thus, in following experiments, average laser power is adjusted to 320 W and other parameters are kept the same with prior experiments. The number of laser passes will be increased and tested to improve the cleaning efficiency.

Figure 9(a) is the SEM image of a specimen cleaned 3 times by using the 320 W laser with 60 s time gap.

(a)

(b)

(c)
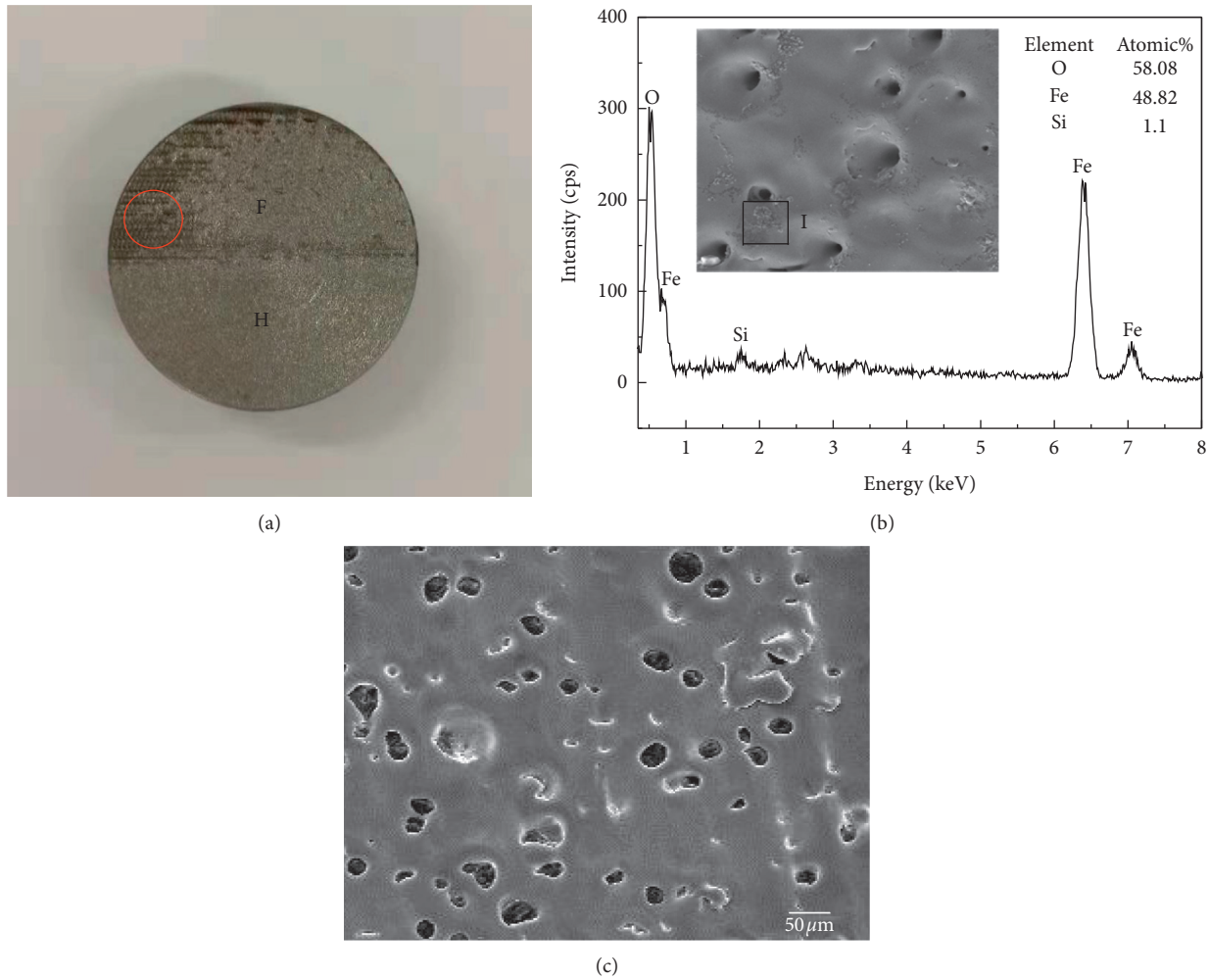
FIGURE 8: Specimen cleaned by using the laser with power 340 W (region (F) and 320 W (region (H) (a); the SEM/EDS analysis of the circled area of region F (b); the SEM image of region H (c).

Comparing with Figure 8(c), it can be seen that most of graphite particles were removed except those with large diameters or deeply embedded ones. The increasing of cleaning times is a feasible way to obtain an excellent cleaning result. Figure 9(b) shows EDS analysis of the surface after the third pass. The ingredients of substrate (region J) are similar to those of the initial status (Figure 7(a)). However, the ingredients of the graphite area (region K) are different from those of the initial surface (Figure 7(a)), indicating that surface graphite particles were efficiently removed. Oxidation was not observed during laser cleaning process. Therefore, the power intensity of 1.087×10^8 W/cm^2 is a safe parameter for the cleaning of ductile iron substrate. Time duration more than 60 s between cleaning passes is necessary. Figure 9(c) shows the SEM image of a specimen cleaned 3 times by using the 320 W laser but without time gap, which is similar to the image inset in Figure 8(b). Loose materials (e.g., region L) are observed on the surface of ductile iron. It can be concluded that oxidation occurred during laser cleaning process without time gap.

Decreasing the output power is extremely important for the real application of laser cleaning technique, which may save power, shorten the cleaning time, and decrease the oxidation rate during continuous laser cleaning process without time gap. Thus, in following experiment, the output power was decreased to 290 W (9.85×10^7 W/cm^2) and cleaning processes were increased to 5 times without time gap between passes. Other experimental parameters were kept the same. The SEM image of the cleaned specimen is shown in Figure 10. Results showed that most of graphite particles were removed, and no region like region L in Figure 9(c) was observed. It can be concluded that more passes should be performed at a lower output power to optimize laser cleaning effect.

(a)

Region I
Fe 98.54 Si 1.16 Atomic%
Region K
Fe 97.27 Si 1.73 Atomic%

(b)

(c)
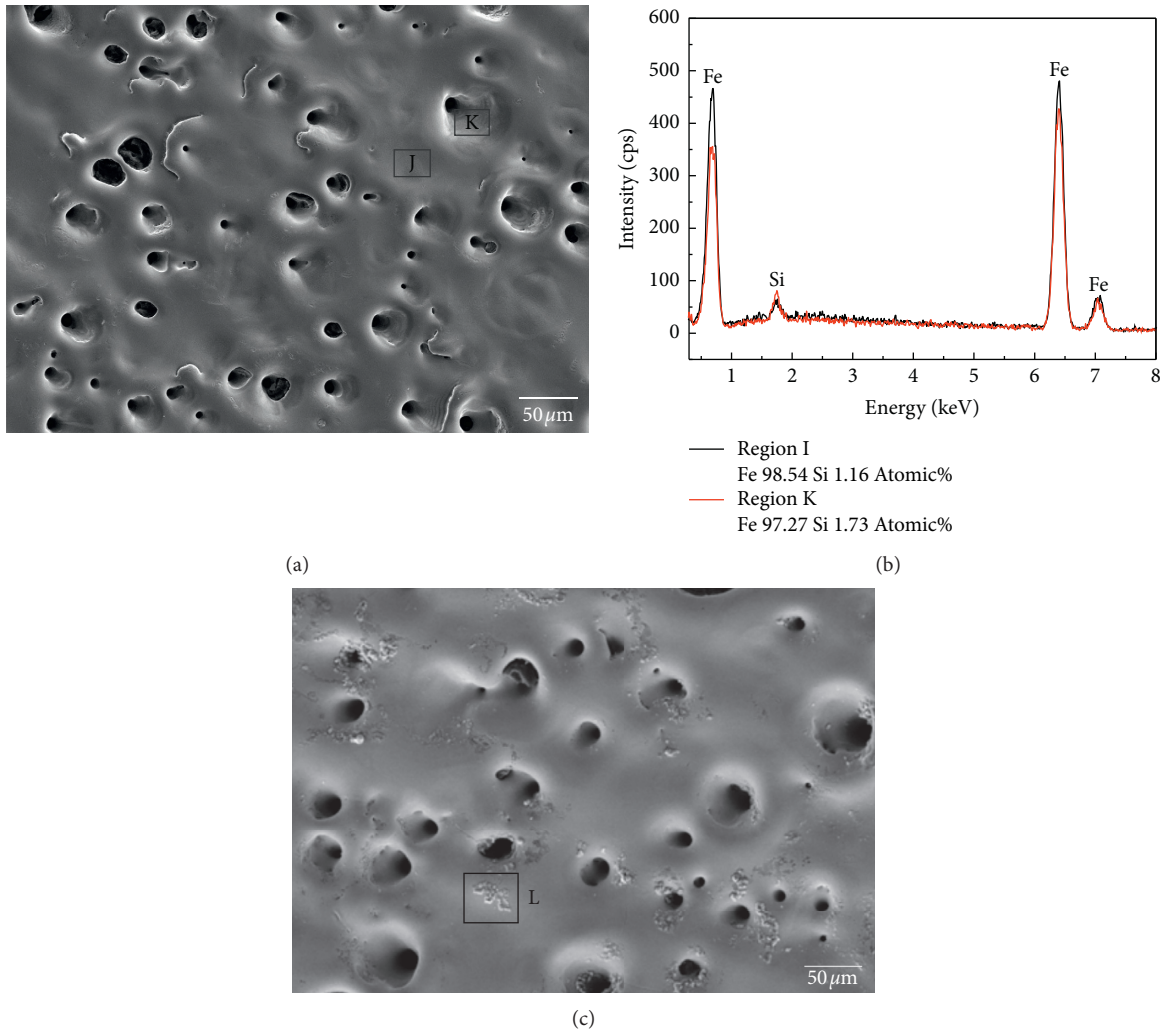
FIGURE 9: (a) The SEM image of a specimen cleaned 3 times by using the 320 W laser with 60 s time gap; (b) EDS analysis of a specimen cleaned 3 times by using the 320 W laser with 60 s time gap; (c) the SEM image of a specimen cleaned 3 times by using the 320 W laser without time gap.
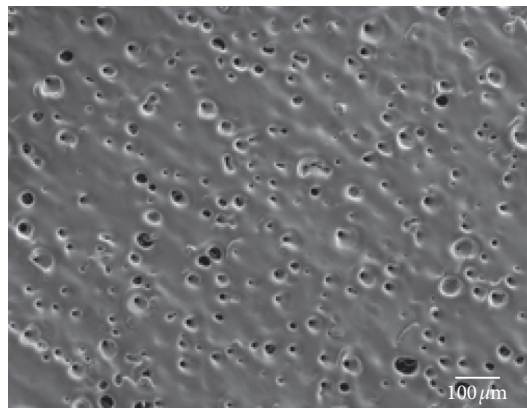
FIGURE 10: The SEM image of a specimen cleaned 5 times by using the 290 W laser.

4. Conclusions

In this article, a novel and environmental friendly method is developed to remove graphite particles embedded in the surface of ductile iron to improve its welding performance. Oxidation threshold of laser power intensity of 10 J/cm^2 was obtained by calculation. Graphite particles implanted in the surface of ductile iron were removed effectively by using proposed laser technique. Experimental results showed that oxidation of substrate occurred during laser cleaning process when power intensity of single pulse is higher than 1.087×10^8 W/cm^2. Most graphite particles were removed after three laser scanning passes with a power intensity of single pulse of 1.087×10^8 W/cm^2. The time gap between passes is necessary in this case due to the occurrence of oxidation. The optimize power intensity of single pulse is 9.85×10^7 W/cm^2, and cleaning process is 5 times with continuous laser scanning without time gap. This investigation contributes to the improvement of welding performance of ductile iron.

Data Availability

The data used to support the findings of this study are included within the article.

Conflicts of Interest

The authors declare that they have no conflicts of interest regarding the publication of this paper.

Acknowledgments

References

[1] Y. Li, S. Dong, S. Yan, X. Liu, P. He, and B. Xu, "Microstructure evolution during laser cladding Fe-Cr alloy coatings on ductile cast iron," *Optics & Laser Technology*, vol. 108, pp. 255–264, 2018.

[2] V. Dakre, D. R. Peshwe, S. U. Pathak, and A. Likhite, "Effect of austenitization temperature on microstructure and mechanical properties of low-carbon-equivalent carbidic austempered ductile iron," *International Journal of Minerals, Metallurgy, and Materials*, vol. 25, no. 7, pp. 770–778, 2018.

[3] J. O. Olawale, S. A. Ibitoye, K. M. Oluwasegun, M. D. Shittu, and A. P. I. Popoola, "Forced-air cooling quenching: a novel technique for austempered ductile iron production," *International Journal of Metalcasting*, vol. 11, no. 3, pp. 568–580, 2017.

[4] M. Polajnar, M. Kalin, I. Thorbjornsson, J. T. Thorgrimsson, N. Valle, and A. Botor-Probierz, "Friction and wear performance of functionally graded ductile iron for brake pads," *Wear*, vol. 382-383, pp. 85–94, 2017.

[5] M. Gagne, S. Leclerc, S. Helgee, N. Stenbacka, and J. Tani, "The continentalization of science," *Modern Casting*, vol. 97, pp. 30–34, 2007.

[6] I. Grubova, T. Priamushko, M. Surmeneva et al., "Conference Series," *Journal of Physics*, vol. 830, Article ID 012109, 2017.

[7] S. M. A. Boutorabi and J. Campbell, "An etching technique for primary austenite dendrites in ductile cast iron," *Materials Characterization*, vol. 31, no. 3, pp. 127–132, 1993.

[8] M. Grupp in *Proceedings of the 16th International Conference Laser Optics*, Burbach, Germany, 2014.

[9] Y. Ye, B. Jia, J. Chen et al., "Laser cleaning of the contaminations on the surface of tire mould," *International Journal of Modern Physics B*, vol. 31, no. 16-19, Article ID 1744100, 2017.

[10] L. Zhu, B. Sun, Z. Li, X. Pan, Y. Chen, and Y. Cao, "The weld quality improvement via laser cleaning pre-treatment for laser butt welding of the HSLA steel plates," *Welding in the World*, vol. 64, no. 10, pp. 1715–1723, 2020.

[11] C. Zhou, H. Li, G. Chen, G. Wang, and Z. Shan, "Effect of single pulsed picosecond and 100 nanosecond laser cleaning on surface morphology and welding quality of aluminium alloy," *Optics & Laser Technology*, vol. 127, Article ID 106197, 2020.

[12] A. P. Kuznetsov, A. S. Alexandrova, O. I. Buzhinsky et al., "Fiber laser cleaning of metal mirror surfaces for optical diagnostic systems of the ITER," *Physics of Atomic Nuclei*, vol. 78, no. 10, pp. 1155–1163, 2015.

[13] T. Schwarz-Selinger, F. Genoese, C. Hopf, and W. Jacob, "Carbon removal from tile gap structures with oxygen glow discharges," *Journal of Nuclear Materials*, vol. 390-391, pp. 602–605, 2009.

[14] W. M. Steen and J. Mazumder, *Laser Material Processing*, Springer, London. UK, 2010.

[15] Z. Zhang, J. Zhang, Y. Wang et al., "Optical humidity detection based on tunable diode laser absorption spectroscopy," in *Proceedings of the Second International Conference on Photonics and Optical Engineering*, p. 116114, Aveiro, Portugal, February 2017.

[16] G. Zhang, X. Hua, Y. Huang et al., "A promising material for microwave absorption," *Applied Surface Science*, vol. 359, pp. 1–9, 2019.

[17] B. Rauh, S. Kreling, M. Kolb et al., "UV-laser cleaning and surface characterization of an aerospace carbon fibre reinforced polymer," *International Journal of Adhesion and Adhesives*, vol. 82, pp. 50–59, 2018.

[18] Q. H. Tang, D. Zhou, Y. L. Wang, and G. F. Liu, "Laser cleaning of sulfide scale on compressor impeller blade," *Applied Surface Science*, vol. 355, pp. 334–340, 2015.

[19] R. Li, J. Yue, X. Shao, C. Wang, F. Yan, and X. Hu, "A study of thick plate ultra-narrow-gap multi-pass multi-layer laser welding technology combined with laser cleaning," *The International Journal of Advanced Manufacturing Technology*, vol. 81, no. 1-4, pp. 113–127, 2015.

[20] S. Arif, S. Bushuk, A. Kouzmouk, H. Tatur, S. Batishche, and W. Kautek, "Middle-ultraviolet laser cleaning of particulates from sized ground wood cellulose and pure cellulose paper," *Journal of Cultural Heritage*, vol. 15, no. 6, pp. 602–608, 2014.

[21] A. Kumar and D. J. Biswas, "Particulate size and shape effects in laser cleaning of heavy metal oxide loose contamination off clad surface," *Optics & Laser Technology*, vol. 106, pp. 286–293, 2018.

[22] X. Li, T. Huang, A. W. Chong, R. Zhou, and Y. S. Choo, "Target Setting in Tournaments: Theory and Evidence from China," *Opto-Electronic Engineering*, vol. 44, pp. 341–344, 2017.

[23] C. Zhou, H. Li, G. Chen, G. Wang, and Z. Shan, "Effect of single pulsed picosecond and 100 nanosecond laser cleaning

on surface morphology and welding quality of aluminium alloy," *Optics & Laser Technology*, vol. 127, pp. 1–9, 2020.

[24] D. S. Prokuratov et al., "Laser cleaning of archaeologically corroded iron objects with inlays," *Optical and Quantum Electronics*, vol. 52, pp. 13–125, 2020.

[25] J.-E. Kim, M.-S. Han, and J.-D. Kim, "Removal characteristics of shop-primer paint by laser energy density in Q-switching fiber laser cleaning," *Modern Physics Letters B*, vol. 34, no. 07n09, p. 2040042, 2020.

Research Article

Effects of Sudden Temperature Drop on Stress at Rapidly Repaired Bonding Interface of Pavement

Le-fan Wang ⬦,[1] **Weng Xing-zhong,**[1] **Ye Li,**[2] **Le Liang,**[1] **and Wan Li**[1]

[1]*Department of Airport Engineering and Architecture, Air Force Engineering University, Xi'an 710038, China*
[2]*School of Economics and Management, Chang'an University, Xi'an 710064, Shaanxi, China*

Correspondence should be addressed to Le-fan Wang; 329873077@qq.com

The numerical simulations were employed to establish an edge-corner repair model with magnesium phosphate cement (MPC) concrete as the repair material and ordinary Portland cement concrete as the old pavement. After the simulation of repair construction by using MPC concrete with different coarse aggregates, the effect of sudden temperature drop during the stable stage of hydration reaction on the stress distribution at each bonding interface was analyzed. The numerical calculations indicate that the sudden temperature drop led to temperature-induced stress on the bonding interfaces. The stress distribution at each bonding interface was obtained and the maximum principal stress at each bonding interface was at the intersection angle of three bonding interfaces. The relationship between the temperature and stress at each bonding interface was found when different coarse aggregates were used to prepare the repairing material. Also, the effect of different coarse aggregates on the bonding interface of the repairing material was obtained when basalt was the coarse aggregate of old concrete. The stability of bonding surface from best to worst was as follows: basalt > limestone > granite > conglomerate > sandstone > quartzite.

1. Introduction

In recent years, owing to its high rigidity, good stability, and convenient construction, cement concrete has been extensively used in the runway projects of airports [1]. However, apart from these advantages, cement concrete has prominent disadvantages. As a relatively brittle material, cement concrete has relatively poor tensile deformation, and its flexural, tensile, and fatigue properties are also relatively low. Especially in areas with large variations in temperature and humidity in day and night, or within four seasons, the concrete pavement is more prone to damage due to continuous impact of natural environment and repeated load [2]. For a concrete pavement, the weakest areas are the edges and corners. Hence, it is necessary to repair the damaged areas in time, which can not only prevent further expansion of damage but also extend the working life of concrete pavement [3].

Magnesium phosphate cement (MPC) is a relatively novel type of rapid-repair material for the concrete

pavement. It has several advantages such as short setting time, high strength, remarkable wear resistance, strong temperature adaptability, and excellent volume stability [4, 5]. In the early stage of repair with magnesium phosphate cement, the hydration reaction as neutralization reaction releases a large amount of heat and heat further accelerates the hydration reaction. Hence, in a short time, the repair concrete achieves decent early-stage mechanical properties [6, 7]. However, due to thermal expansion and contraction, microexpansion and deformation occur on the repair concrete in the early hydration process. All the interfaces of the repair concrete impose compressive stress on the old concrete, which is favorable for the interfacial bonding between the repair concrete and old concrete. When the repair construction is completed and most of the hydration heat has been released, the repair concrete slowly cools down until it reaches the ambient temperature.

At this time, the strength and bonding strength of the repair concrete continue to increase slowly. Hence, the interfacial stress between the repair concrete and old

concrete pavement is close to zero. If the ambient temperature is constant, the strength and bonding strength of the repair concrete continue to increase until they reach a certain level. Therefore, the bond strength becomes significantly greater than the temperature stress caused by the changes induced by the external environment, and the repair interface becomes stable. However, in practical applications, the temperature is not constant and some areas have larger temperature variation between day and night. The large temperature variation causes a certain tensile stress between the new and old concrete parts. When the tensile stress is greater than the current interfacial bonding strength, it causes damage of the bonding interface that is in the strength-growth period [8, 9]. Therefore, in the rapid-repair project under extreme weather conditions, it is essential to study the effect of temperature load on the stress distribution of the repaired bonding interface.

At present, the research on the effect of temperature on concrete is mostly focused on the cracking caused by the high internal temperature of the newly poured large-scale concrete [10], on the variations of the bonding interface between the two reinforced concretes due to temperature variation [11], on the bonding conditions between the concrete and the in-concrete rebar under high temperature [12], on the effect of high temperature on the bonding performance of concrete after repairing [13, 14], and so forth. However, there are few studies on the stress distribution of bonding interface between the new and old concretes under the conditions of drastic drop in temperature. Therefore, this paper discusses the repair of the ordinary Portland cement concrete pavement using the MPC concrete. When the hydration becomes stable and the strength continues to increase, the stress distribution is adopted as the research object and the effect of environmental temperature change on the stress distribution of each bonding interface is investigated. The study provides a theoretical basis for the applications of magnesium phosphate cement concrete in the repairing engineering under extreme climate conditions.

2. Theory

In the rapid-repair project, the cracking of repaired bonding interface occurs due to large external temperature variation. The fundamental reason is that different linear expansion coefficients of the two materials lead to the inconsistency in the deformation between the rapid-repair material and the old concrete material when the external environment temperature changes greatly [15]. Therefore, with regard to the repaired concrete pavement, it is necessary to study the linear expansion coefficients of rapid-repair materials and old concrete material. The linear expansion coefficient of concrete is primarily determined by that of the coarse aggregates. When the new and old concrete coarse aggregates are the same, the temperature variation leads to the consistent volume change of the two concretes, and hence there is no interfacial stress. When the two concrete coarse aggregates are different, the stress is induced at the interface with the variation of temperature. Therefore, to analyze the

bonding interface between the repair concrete and the old concrete, the temperature variation and the linear expansion coefficient of the old and new concretes need to be considered. The relationship between the linear expansion coefficients (α_l), the temperature (t), the length at $t°C$ (l_t), and the length at $0°C$ (l_0) is as follows:

$$\alpha_l = \frac{l_t - l_0}{l_0 t}, \tag{1}$$

Therefore, herein, ordinary Portland cement concrete is selected as the old concrete, basalt as coarse aggregate, and magnesium phosphate cement concrete as the fast-repair material. Different coarse aggregates were used to prepare the systems consisting of the old concrete pavement and repair concrete. The effect of temperature drop on the stress distribution of the repaired bonding interface was studied after the hydration heat release tended to stabilize.

3. Establishment of Repair Model

In the actual use of concrete pavement of airport, owing to various influencing factors in the early pouring and later use, the edges and corners are the weakest areas of the pavement. In other words, the edges and corners are most likely to be damaged under normal circumstances. Based on this phenomenon, the pavement corner was designed as the damaged position of the concrete pavement (see Figure 1). The dimension of the old concrete pavement was $5 m \times 5 m \times 0.3 m$, while the dimension of the repair concrete was $0.7 m \times 0.7 m \times 0.07 m$. There were three bonding interfaces between the repair concrete and the old concrete pavement: two vertical bonding interfaces A and B and one horizontal bonding interface C.

After the rapid-repair construction was completed, the hydration reaction tended to stabilize. In this stage, the established model primarily considered the impact of sudden temperature drop on the bonding interface between the new and old concretes. Based on the above requirements, the ABAQUS simulation software was selected for simulation and finite element calculation. This is because ABAQUS software has certain advantages for thermodynamic simulations, in particular the simulation of heat conduction, thermocouple analysis, and rock and soil mechanics analysis. Furthermore, ABAQUS has higher precision than ANSYS.

The model structure was mainly divided into two regions, namely, the concrete pavement and the repair concrete. Based on the overall model of the concrete pavement, three sections were set at its corners: two vertical sections and one horizontal section. The intersection of the three interfaces was replaced with repair concrete, as shown in structure in Figure 2. The white overall is the old concrete pavement, while the red frame indicates the location of the repair concrete.

The old concrete pavement material was 42.5 R ordinary Portland cement concrete, while the repair concrete was MPC concrete. Because the hydration and coagulation process of MPC concrete are extremely rapid, decent
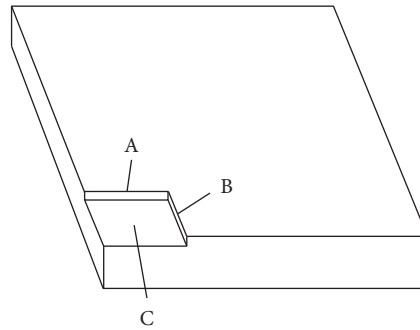
FIGURE 1: Schematic diagram of repairing corner of airport pavement.
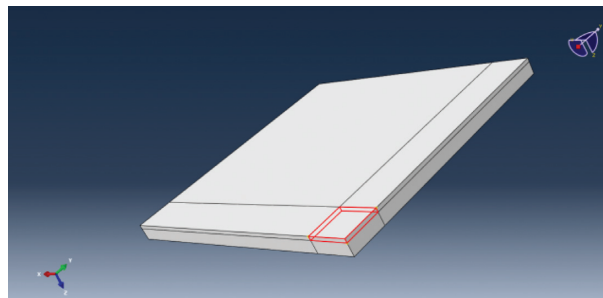
FIGURE 2: Model of repaired concrete.

strength was achieved at 1 d age under 20°C. The hydration stabilized, so the indexes in test at age of 1d were used as the experimental parameters of the material.

The elastic moduli of two concretes were obtained from the experiments, where the old cement concrete and repair concrete had a modulus of 32.5 GPa and 39.4 GPa, respectively. Because the concretes use the same fine aggregates and coarse aggregates except for cement, their thermal conductivity and specific heat capacity were relatively close. The common mean thermal conductivity and specific heat capacity of concrete as per the reference data are 1.28 W/m·K and 0.97 J/g·K, respectively. The test indicates that the masses of two concretes were similar when the concrete was small beam with dimensions of 100 mm × 100 mm × 400 mm. Therefore, the calculation was performed under the following parameters: the density was 2500 kg/m^3; the coarse aggregate in old cement concrete was basalt; and the linear expansion coefficient was 0.86×10^{-5}°C. As shown in Table 1, the coarse aggregate of repair concrete was selected from different materials. "a" is linear expansion coefficient in Table 1.

The environmental temperature was set to drop from 20°C to 10°C, 0°C, −10°C, −20°C, and −30°C. The air convection coefficient on the surface of the concrete model was set to 15 W/(m^2·K) and the initial ambient temperature was maintained at 20°C. Five temperature models and five stress models were established for calculations. To show the temperature and stress distributions on each bonding interface more clearly, only the modules of repair concrete were selected and the position of each bonding interface is shown in Figure 3. The longitudinal bonding interface A was

perpendicular to the x-axis, the longitudinal bonding interface B was perpendicular to the y-axis, and the horizontal bonding interface C was perpendicular to the z-axis.

4. Effect of Different Ambient Temperatures on Stress at Bonding Interfaces

Using quartzite as the repair material and the temperature to drop to 0°C as example, the stress distribution cloud chart of three interfaces of repair material is presented in Figure 4.

As shown in Figure 4, since $L_A = L_B$, (L_A and L_B are the lengths of the vertical bonding interfaces A and B) when the ambient temperature dropped, the stress on the bonding interface was symmetrically distributed, and maximum principal stresses reached the positions close to the intersection of the three bonding interfaces. Therefore, the most unfavorable position for pavement repair is at the intersection of the three bonding interfaces, where the stress is tensile stress. To understand the distribution of each axial stress when each bonding interface was subjected to maximum stress, stress analysis was performed on each bonding interface (see Figures 5 and 6).

As per Figure 5(a), the stresses on the vertical bonding interface A and along the x-axis direction were all tensile stresses. Closer to the intersection angle of the three bonding interfaces, the tensile stress was greater with the maximum value of 1.243 MPa. Figure 5(b) shows the shear stresses on the vertical bonding interface A and along the y-axis. The shear stress direction in the upper area was the positive direction of the y-axis, while that in the lower area was the negative direction of the y-axis. Figure 5(c) displays the shear

TABLE 1: Linear expansion coefficient of different coarse aggregates.

Coarse aggregate	Limestone	Basalt	Granite	Conglomerate	Sandstone	Quartzite
A $(10^{-5}/°C)$	0.68	0.86	0.95	1.08	1.17	1.19
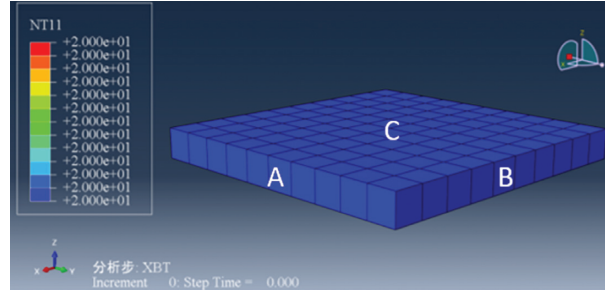
FIGURE 3: Schematic diagram of positions of bonding interfaces.
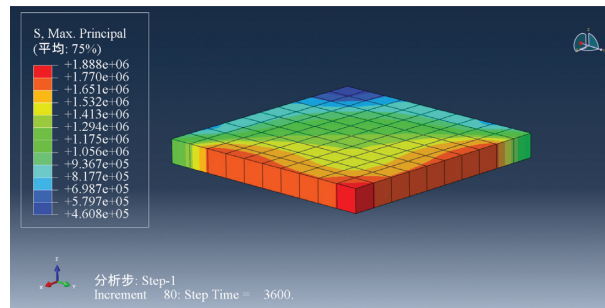
FIGURE 4: Cloud chart of maximum principal stress on three bonding interfaces.

stress along the z-axis direction and on vertical bonding interface A. The shear stress direction at each point on the surface was the positive direction of z-axis, with the magnitude increasing from top to bottom.

As $L_A = L_B$, the vertical bonding interface A and vertical bonding interface B were symmetrical in stress conditions and had the same dimensions; therefore, the vertical bonding interface B was not analyzed.

As per Figure 6(a), along the z-axis direction, the center and edge areas of horizontal bonding interface were both subjected to tensile stresses. Four corners of the horizontal bonding interface were subjected to higher tensile stresses and there was a circle of compression-stressed areas between the two tensile-stressed areas. Figure 6(b) shows that, along the x-axis, the stress on horizontal bonding interface was shear stress: the left half reflects the shear stress along the negative x-axis, while the right half reflects the shear stress along the positive x-axis. The two shear stresses acted on the horizontal bonding interface together. Figure 6(c) demonstrates that the stress along the y-axis of horizontal bonding interface was shear stress and the upper half was the shear stress along the positive direction of the y-axis, while the lower half was the shear stress along the negative direction of the y-axis. The two shear stresses acted together on the horizontal bonding interface. Therefore, when the temperature dropped sharply, the vertical and horizontal bonding

interfaces of MPC concrete were simultaneously subjected to the combined action of tensile stress and shear stress along different directions.

For maximum principal stress on the bonding interface of MPC concrete as the repair material with different coarse aggregates, the results under different ambient temperatures were calculated (see Figure 7). The positive values denote tensile stress, while negative values denote compressive stress.

As shown in Figure 7, after the hydration of MPC as repair concrete was completed, the set ambient temperature was 20°C. Hence, irrespective of which coarse aggregate was used to prepare the MPC concrete, the interfacial stresses were all 0 at 20°C. When the ambient temperature dropped sharply, the concrete shrank. Accordingly, stress occurred on each bonding interface because different coarse aggregates have different linear expansion coefficients. At this time, the stress was induced on the bonding interface between the old concrete and the MPC concrete prepared with different coarse aggregates. When the expansion coefficient of the coarse aggregate of old concrete was greater than that of the MPC concrete, that is, when limestone was used as the coarse aggregate of repairing concrete, the maximum principal stress at the intersection angle of the three bonding interfaces was the compressive stress and the compressive stress increases with the decrease in temperature. When the
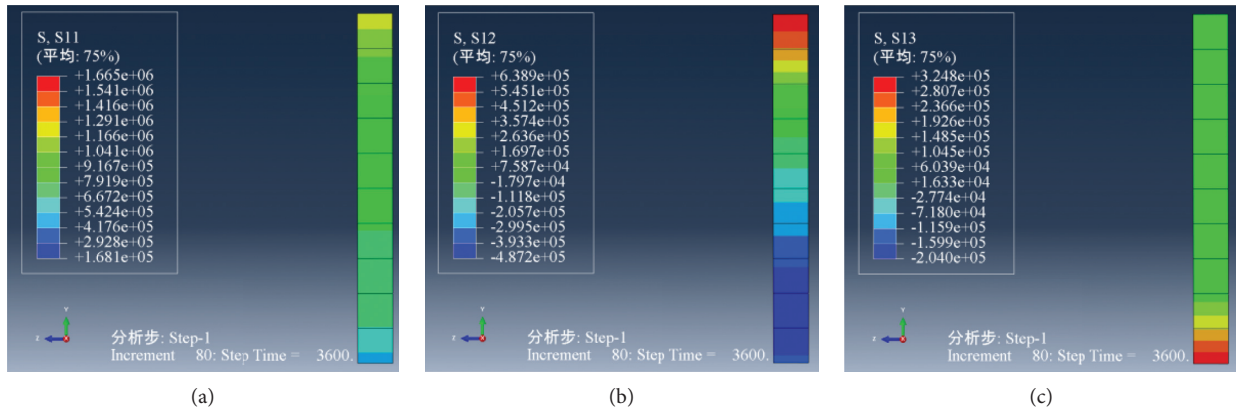
FIGURE 5: Cloud chart of stress on vertical bonding interface A. (a) Normal stress along x-axis (σ_x). (b) Shear stress along y-axis (τ_{xy}). (c) Shear stress along z-axis (τ_{xz}).
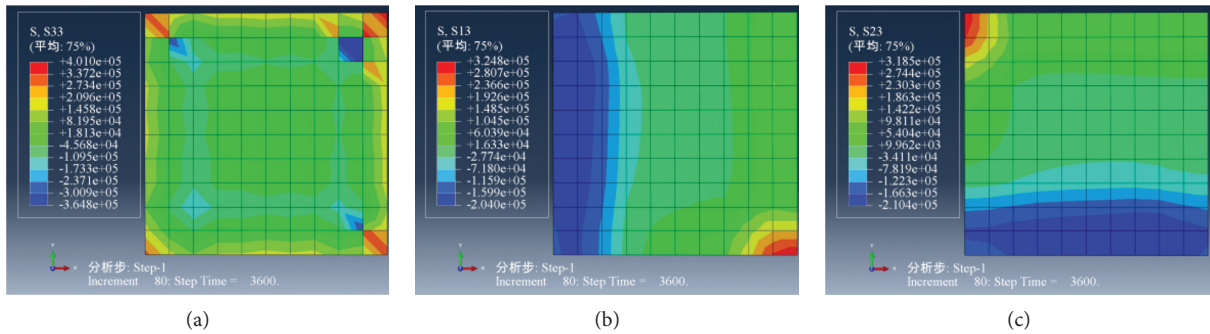
FIGURE 6: Cloud chart of stress on horizontal bonding interface. (a) Normal stress along z-axis (σ_z). (b) Shear stress along x-axis (τ_{zx}). (c) Shear stress along y-axis (τ_{zy}).
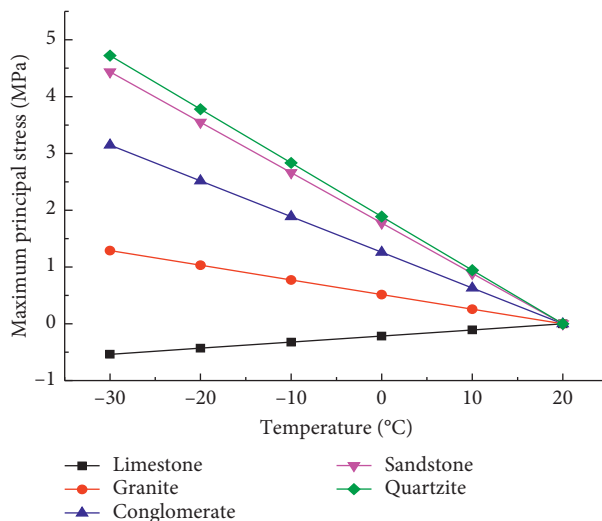
FIGURE 7: Relationship between maximum principal stress and temperatures on bonding interface of repair concrete with different coarse aggregates.

expansion coefficient of the coarse aggregate of old concrete was less than that of the MPC concrete, the maximum principal stress at the intersection of the three bonding interfaces was the tensile stress, which increases with the decrease in temperature. As per the calculation results, when the coarse aggregate of old pavement concrete was basalt, the influencing sequence of coarse aggregate in MPC concrete on the bonding interface from best to worst was as follows:

basalt > limestone > granite > conglomerate > sandstone > quartzite.

5. Conclusions

Herein, MPC repair materials with different coarse aggregates were prepared, which can be used in the rapid-repair project of airport pavement. After the repair was completed and when the hydration reaction entered a stable stage, the effect of sudden temperature drop on the stress distribution of each bonding interface was investigated. The conclusions are as follows:

(1) When the repair material was different from the coarse aggregates of old concrete, the sudden temperature drop causes a temperature stress on the repaired bonding interface. The magnitude of the temperature stress corresponds to the magnitude of temperature drop and the type of coarse aggregates.

(2) As the ambient temperature drops, the stress of the repaired bonding interface is symmetrically distributed and the maximum principal stress of each bonding interface was located at the intersection angle of the three bonding interfaces.

(3) When the linear expansion coefficient of the old concrete coarse aggregate was greater than that of the MPC as repair concrete, the maximum principal stress was located at the intersection angle of the three bonding interfaces. This stress is the compressive stress and its magnitude increases with the decrease in temperature. When the expansion coefficient of the coarse aggregate in old concrete was smaller than that in the MPC as repair concrete, the maximum principal stress was located at the intersection angle of the three bonding interfaces. The maximum principal stress is tensile stress and its magnitude increases with the decrease in temperature.

(4) When the coarse aggregate of the old concrete pavement was basalt, the influencing sequence of coarse aggregate of MPC concrete as repair concrete on the bonding interface from best to worst was as follows: basalt > limestone > granite > conglomerate > sandstone > quartz rock.

Therefore, in the repair project, as much as possible, coarse aggregate in MPC concrete should be selected as close to that in the old concrete. In the absence of consistent coarse aggregates, the one with less stress under temperature drop should be selected for the preparation of repair concrete and the bonding strength of repair concrete should be higher than the maximum shear stress on the horizontal bonding interface and the maximum tensile stress on the vertical bonding interface. The above requirements for material and strength can ensure that the repair material would not crack under temperature drop.

Data Availability

The data used to support the findings of this study are included within the article.

Conflicts of Interest

The authors declare that they have no conflicts of interest.

References

[1] T. Guo, Y. Xie, and X. Weng, "Evaluation of the bond strength of a novel concrete for rapid patch repair of pavements," *Construction and Building Materials*, vol. 186, pp. 790–800, 2018.

[2] A. Bieliatynskyi, E. Krayushkina, and A. Skrypchenko, "Modern technologies and materials for cement concrete pavement's repair," *Procedia Engineering*, vol. 134, pp. 344–347, 2016.

[3] T. Guo, X. Weng, C. Liu, Q. Yu, C. Zhang, and Y. Li, "Evaluation of the bonding and fatigue properties of an innovative rapid repair structure for concrete pavement," *Construction and Building Materials*, vol. 235, Article ID 117484, 2020.

[4] B. Xu, H. Ma, and Z. Li, "Influence of magnesia-to-phosphate molar ratio on microstructures, mechanical properties and thermal conductivity of magnesium potassium phosphate cement paste with large water-to-solid ratio," *Cement and Concrete Research*, vol. 68, pp. 1–9, 2015.

[5] J. Li, W. Zhang, and Y. Cao, "Laboratory evaluation of magnesium phosphate cement paste and mortar for rapid repair of cement concrete pavement," *Construction and Building Materials*, vol. 58, pp. 122–128, 2014.

[6] Y. Xie, X. Lin, X. Pan, and T. Ji, "Preliminary investigation of the hydration mechanism of MgO-SiO2-K2HPO4 cement," *Construction and Building Materials*, vol. 235, Article ID 117471, 2020.

[7] Y. Jianming, W. Luming, and Z. Jie, "Experimental study on the deformation characteristics of magnesium potassium phosphate cement paste at early hydration ages," *Cement and Concrete Composites*, vol. 103, pp. 175–182, 2019.

[8] Y. Jung, W. Lin, H. Hao, and Y.-H. Cho, "Interface behavior of partial depth repair for airport concrete pavement subjected to differential volume change," *Construction and Building Materials*, vol. 143, pp. 515–521, 2017.

[9] X. Jia, J. Li, P. Wang, J. Qian, and M. Tang, "Preparation and mechanical properties of magnesium phosphate cement for rapid construction repair in ice and snow," *Construction and Building Materials*, vol. 229, p. 116927, 2019.

[10] Y. Li, L. Nie, and B. Wang, "A numerical simulation of the temperature cracking propagation process when pouring mass concrete," *Automation in Construction*, vol. 37, pp. 203–210, 2014.

[11] A. Borosnyói, "Influence of service temperature and strain rate on the bond performance of CFRP reinforcement in concrete," *Composite Structures*, vol. 127, pp. 18–27, 2015.

[12] V. Carvelli, M. A. Pisani, and C. Poggi, "High temperature effects on concrete members reinforced with GFRP rebars," *Composites Part B: Engineering*, vol. 54, pp. 125–132, 2013.

[13] A. Sharma, J. Bošnjak, and S. Bessert, "Experimental investigations on residual bond performance in concrete subjected to elevated temperature," *Engineering Structures*, vol. 187, pp. 384–395, 2019.

[14] A. Albidah, A. Abadel, F. Alrshoudi, A. Altheeb, H. Abbas, and Y. Al-Salloum, "Bond strength between concrete substrate and metakaolin geopolymer repair mortars at ambient and elevated temperatures," *Journal of Materials Research and Technology*, vol. 9, no. 5, pp. 10732–10745, 2020.

[15] B. P. Gautam, D. K. Panesar, S. A. Sheikh, and F. J. Vecchio, "Effect of coarse aggregate grading on the ASR expansion and damage of concrete," *Cement and Concrete Research*, vol. 95, pp. 75–83, 2017.

Research Article

Research on Creep Characteristics and Influencing Factors of Cement Asphalt Composite Binder

Yimin Li,[1] Mulbah Yombah,[2] Ahmed Abdulakeem Temitope,[2] Xiaolong Zou,[2] Fayong Yang ![ORCID],[2] Wenbo Li,[2] and Hongjun Jing ![ORCID][2]

[1]*Ankang City Traffic Construction Quality Supervision Station of Shaanxi Province, Ankang 725000, China*
[2]*School of Architecture and Civil Engineering, Xi'an University of Science and Technology, Xi'an 710064, China*

Correspondence should be addressed to Hongjun Jing; jinghongjun@xust.edu.cn

Cement emulsified asphalt composite material (CA composite cement) has the excellent properties of cement and emulsified asphalt cement. As a composite cementing material, cement emulsified asphalt concrete can be one of the choices of road paving materials. However, under the effect of temperature and wheel load, the performance of it may get worse; especially, the creep behavior of CA composite cement has an important influence on the stability of pavement structure. This paper mainly focuses on the research on the creep and creep recovery performance of CA composite cement, determines the raw materials and proportions of CA composite cement, and formulates experimental research programs such as creep and creep recovery tests and stress scanning tests. The creep and creep recovery test research of CA composite cement was carried out, and the influence of creep and creep recovery characteristics, temperature, and A/C on the creep mechanical properties of CA composite cement was analyzed. The results show that the creep compliance of CA composite cement decreases with the increase of aging degree, the static mechanical properties tend to be elastic as a whole, and different factors such as temperature and A/C have different effects on the viscoelastic-plastic mechanical properties of the material.

1. Introduction

Cement emulsified asphalt concrete is a road paving material formed by using cement and emulsified asphalt as a cementing material, and together with suitable grading aggregates through cold mixing, cold laying, and rolling. Obviously, cement emulsified asphalt concrete has achieved the goal of significantly reducing energy consumption and pollutant emissions in the production and construction process. At the same time, it uses the characteristics of the emulsified asphalt in the material system to release water during demulsification and the water requirement during cement hydration to promote the strength development of composite materials, which will absorb the flexibility of asphalt concrete and the rigid characteristics of cement concrete, and has outstanding advantages such as energy-saving and emission reduction, complementary performance, and strong constructability [1–7]. As a cementing material, cement emulsified asphalt composite material does not have similar normative indicators such as penetration, ductility, and softening point to evaluate its performance. Therefore, there is a lack of appropriate method indicators when preparing cement emulsified asphalt composite materials to characterize and judge the rationality of its material composition [8–13]. When the composition ratio of cement and emulsified asphalt changes within a certain range, the cement emulsified asphalt composite material behaves as a viscoelastic material, especially with different material compositions and different ages, and the viscoelastic properties of the composite material have obvious changes [14–16].

Ji [17] determined the various index parameters, initial mix ratio, and construction mix ratio of CA mortar filling layer through the research and analysis of the raw material selection principle of CA mortar raw materials. From the perspective of construction technology and material

selection, some performance suggestions have been improved. Song et al. [18] studied the characteristics of the durability, stability, and mechanical properties of CA mortar based on the typical material selection and material ratio of CA mortar, analyzed its main influencing factors, and described the structure formation and the microlevel evolution mechanism provides technical support for the operation and maintenance of the CA mortar layer of the slab ballastless track. Fu et al. [19] presented the results of observations of scanning electron microscope micro/macrocrack development and simultaneous measurements of temperature-dependent stress-strain relations of hardened cement pastes and mortar under a steady thermal state and a displacement-controlled loading process. Lucas et al. [20] and others comprehensively analyzed the damage development process and mechanism of asphalt mixture, combined with the principle of viscoelasticity, established the damage model of asphalt mixture, and obtained the model parameters by fitting the results of the uniaxial creep test. Saber et al. [21] analyzed and studied various creep damage development rules and their mechanisms and clarified the way of creep damage development and changes from a microscopic point of view and the basic rules of changes over time. Xu and Wang [22] put forward a digital simulation modeling and test method for viscoelastic mechanical properties of CA mortar by comparing the results of the creep test and digital simulation experiment of CA mortar.

At present, the research on the creep performance and creep damage development law of CA composite cement has achieved certain results and has laid a solid foundation for the study of the viscoelastic mechanical behavior of the material. However, the different influence on viscoelastic plastic has not been studied systemically. This article mainly studies the creep and recovery characteristics of CA composite cement, analyzes the influence of aging on its creep performance, discusses the influence of different factors such as temperature and A/C on its viscoelastic mechanical properties, and will further supplement the cement research on related fields of asphalt composite cement.

2. Materials and Methods

2.1. Materials

2.1.1. Cement and Emulsified Asphalt. The cement used in this paper is Portland Ordinary Cement No. 42.5 produced by Baoji, Shaanxi. The properties of the cement were tested in accordance with JTG E30—2005, and the results are shown in Table 1. The emulsified bitumen must be cationic emulsified bitumen, and the demulsification speed should not be too fast to facilitate the full mixing of the internal components; that is, the emulsified bitumen with slow cracking or medium cracking should be selected. The properties of slow-cracking emulsified asphalt are shown in Table 2. In order to reduce the difficulty of mixing and comprehensively consider the requirements of the mix ratio [23], additional water is needed to control the water-cement ratio during the material mixing process, and the water-cement ratio is determined to be 0.8.

2.1.2. Additives. The additives used in CA composite cement mainly include defoamers, water reducers, and thickeners. Due to the cement hydration process and mixing process, it is easy to produce more air bubbles in the mixed fluid. If it cannot be discharged in time, the molded test piece will have a larger porosity, which will affect the various mechanical properties of the test piece. It will have a greater impact [24]. The purpose of adding defoamers is to reduce the content of bubbles during the molding process of the specimen. The basic properties of defoamers are shown in Table 3. In order to ensure that the CA composite cement has a certain viscosity during mixing and avoid material segregation, a thickener needs to be added to increase the viscosity. The thickener is diluted to 25 times with water at a ratio of $1:24$ during use. The basic properties of the thickener are shown in Table 4. The main purpose of the water reducing agent is to reduce water consumption while ensuring the fluidity and workability of the cement. It can reduce the water-cement ratio to a certain extent and improve the bonding performance of the CA composite cement. The basic properties of water reducing agent are shown in Table 5.

2.2. Material Mix Design and Ultraviolet Aging Test

2.2.1. Mix Design. In order to study the effect of material ratio on the mechanical properties of CA composite cement, the material ratio of CA composite cement was determined as shown in Table 6. The water content of the emulsified asphalt in the mixing ratio design in the table is 45%. When the mass ratio of different asphalt to cement is changed, the ratio of the water-cement ratio was controlled to be $1:0.8$.

2.2.2. Ultraviolet (UV) Aging Test. The UV aging test was carried out in an ultraviolet aging box. After the actual measurement, the ultraviolet radiation intensity on the surface of the specimen under the stable working state of the aging box was $13.85 \, mW/cm^2$. The aging time of this study was $12 \, h$.

2.3. Creep and Creep Recovery Test Plan. The dynamic shear rheometer (DSR) shown in Figure 1 was used to carry out the mechanical performance test of CA composite cement, including the creep and creep recovery test [25]. Based on the existing theoretical results, when the complex modulus of the specimen changes from 100% to 90% during the stress scanning process, the materials were all within the online viscoelastic range. The scanning stress range was set from 100 Pa to 1,200,000 Pa, and the stress scanning test was performed on the CA composite cement specimens with different mix ratios. Use the vernier caliper to measure the length, width, and thickness of the test piece, input the size parameters, then fix the test piece on the fixture, and use the dynamic rheological shear instrument to carry out the stress scanning test. During the test, the change of the complex modulus was observed in real time.

Table 1: Basic properties of cement.

Specific surface area (m²/kg)	Initial setting time (min)	Final setting time (min)	3D intensity (MPa)	Ignition loss (%)
300	50	560	17	5

Table 2: Basic properties of emulsified asphalt.

| Cement adaptibility | Evaporation residue | | | | Demulsification speed |
	Content (%)	Penetration (25°C, 0.01 mm)	Ductility (cm)	Softening point (°C)	
Qualified	54	70	125	47	Slow cracking

Table 3: Basic properties of defoamers.

Type of defoamers	Active ingredients (%)	pH value	Valid period (d)	Stability
Silicone defoamers	11 ± 3	6.5~7.5	360	No stratification

Table 4: Basic properties of thickener.

Variety	Thickening performance	Durability	Solid content (%)	pH	Viscosity (MPa·s)
Cylin	Excellent	Good	30	3.5	42

Table 5: Basic properties of water reducing agent.

Density (g/cm³)	pH	Solid content (%)	Sodium sulfate content (%)	Chloride (%)	Total alkali (%)
1.07	8.8	21.32	0.93	0	1.3

Table 6: Material ratio.

Mix ratio	Cement	Asphalt	Water	Water reducing agent	Thickener	Defoamers
0.3	1.0	0.3	0.548	0.015	0.075	0.003
0.6	1.0	0.6	0.458	0.015	0.075	0.003
0.9	1.0	0.9	0.368	0.015	0.075	0.003
1.2	1.0	1.2	0.278	0.015	0.075	0.003
1.5	1.0	1.5	0.188	0.015	0.075	0.003

Figure 1: Dynamic shear rheometer.

2.4. Stress Scanning Analysis. In order to analyze the influence of stress level on the creep and creep recovery performance of CA composite cement, six different stress levels were selected. The stress levels are different. During the creep test, CA composite cement will produce different degrees of creep. The damage will affect its creep behavior and creep recovery behavior. To this end, it is necessary to conduct a stress scanning test in advance to determine the creep stress corresponding to different stress levels. During the stress scanning process, the complex modulus of the material decreases as the scanning stress increases. When the complex modulus decreases not more than 10% of the initial value, the material properties are considered to be within the linear viscoelastic range. The stress levels are, respectively, selected from the benchmark of 50%, 100%, and 150%, and 200% used as creep loads in this paper, and the test temperatures were 30°C, 45°C, and 60°C, respectively. The stress scanning test obtains the corresponding stress when the complex modulus drops to 90% of the initial value, and then the creep stress corresponding to different stress levels can be obtained. The creep load is shown in Table 7.

3. Results and Discussion

3.1. Creep and Creep Recovery Characteristics of CA Composite Cement. According to the aforementioned CA composite cement's creep and creep recovery test plan, creep and creep recovery tests at different temperatures and different stress levels were conducted. According to the test results, the creep and creep recovery compliances are shown in Figures 2–6.

TABLE 7: Creep stress table.

A/C	Temperature (°C)	Stress level (%)			
		50	100	150	200
0.3	30	0.15	0.30	0.45	0.60
	45	0.07	0.14	0.21	0.28
	60	0.05	0.09	0.14	0.18
0.6	30	0.14	0.27	0.41	0.54
	45	0.09	0.18	0.27	0.36
	60	0.04	0.07	0.11	0.14
0.9	30	0.10	0.20	0.30	0.40
	45	0.05	0.10	0.15	0.20
	60	0.09	0.17	0.26	0.34
1.2	30	0.09	0.17	0.26	0.34
	45	0.03	0.06	0.09	0.12
	60	0.02	0.03	0.05	0.06
1.5	30	0.08	0.16	0.24	0.32
	45	0.03	0.06	0.09	0.12
	60	0.01	0.02	0.03	0.04
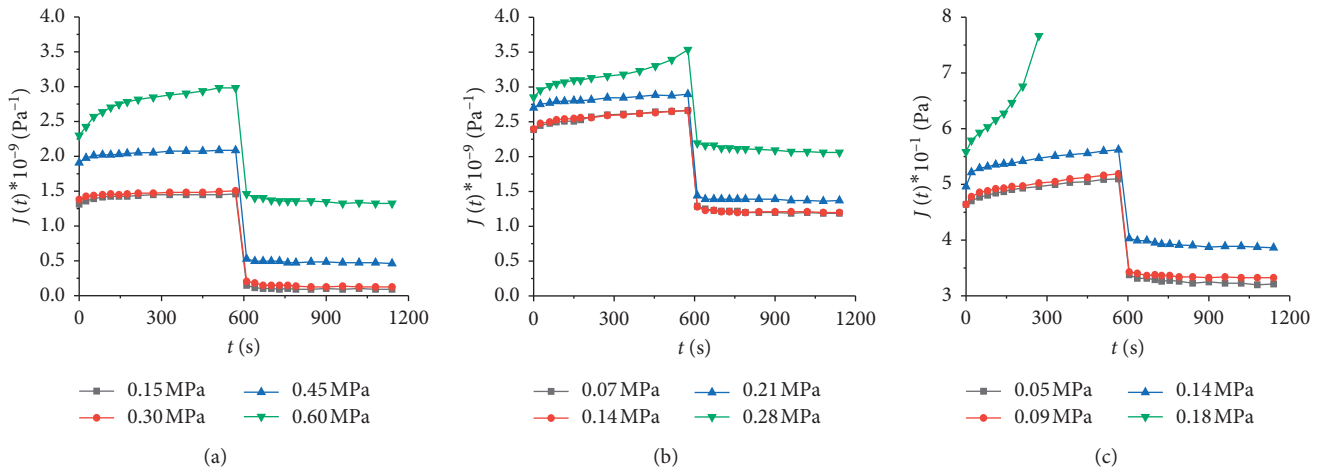
FIGURE 2: A/C = 0.3 creep and creep recovery compliance curve. (a) 30°C. (b) 45°C. (c) 60°C.

It can be seen from Figures 2–6 that at the moment $t = 0$, that is, the moment of stress loading, the CA composite cement will produce instantaneous deformation, and the magnitude of instantaneous deformation closely related to the stress level. As the stress level increases, the instantaneous deformation also increases. This part of the instantaneous deformation includes instantaneous elastic deformation and instantaneous plastic deformation. As the stress level increases, when the stress exceeds a certain value, plastic deformation will occur instantaneously at the moment of loading, and this part of the deformation cannot be recovered. After instantaneous deformation occurs at the moment of loading, it then enters the deceleration creep stage. In this stage, the creep rate gradually decreases and then enters the constant velocity creep stage. In the constant velocity creep stage, the compliance rate is basically constant. For CA composite cement with different proportions, the creep stress has a significant effect on its creep behavior. When the creep stress is small, in the 600s creep time, the creep curve only includes two stages of deceleration creep and constant velocity creep. When the creep stress is large, as the creep stress increases, the creep rate in the deceleration and constant velocity phases increases, and it quickly enters the accelerated creep phase. In some cases, due to the creep in the accelerated creep phase, the rate of change is relatively large, and the creep damage occurs within $t = 600$ s, but the subsequent creep recovery phase is not entered. From the comparison of the curves of the creep recovery stage after $t = 600$ s, it can be seen that with the increase of the creep stress, the creep recovery compliance increases, and with the increase of the creep stress, the deformation recovery ability of the CA composite adhesive decreases. The residual strain of the material increases.

It can also be seen from the figure that the creep compliance and creep recovery compliance of CA composite cement basically coincide under low-stress levels, which is in line with the physical characteristics of creep compliance and creep recovery compliance. Within the range of online viscoelasticity, creep compliance and creep recovery compliance as the basic material parameters of viscoelastic materials have nothing to do with the stress level. Creep compliance and creep recovery compliance are determined by the nature of
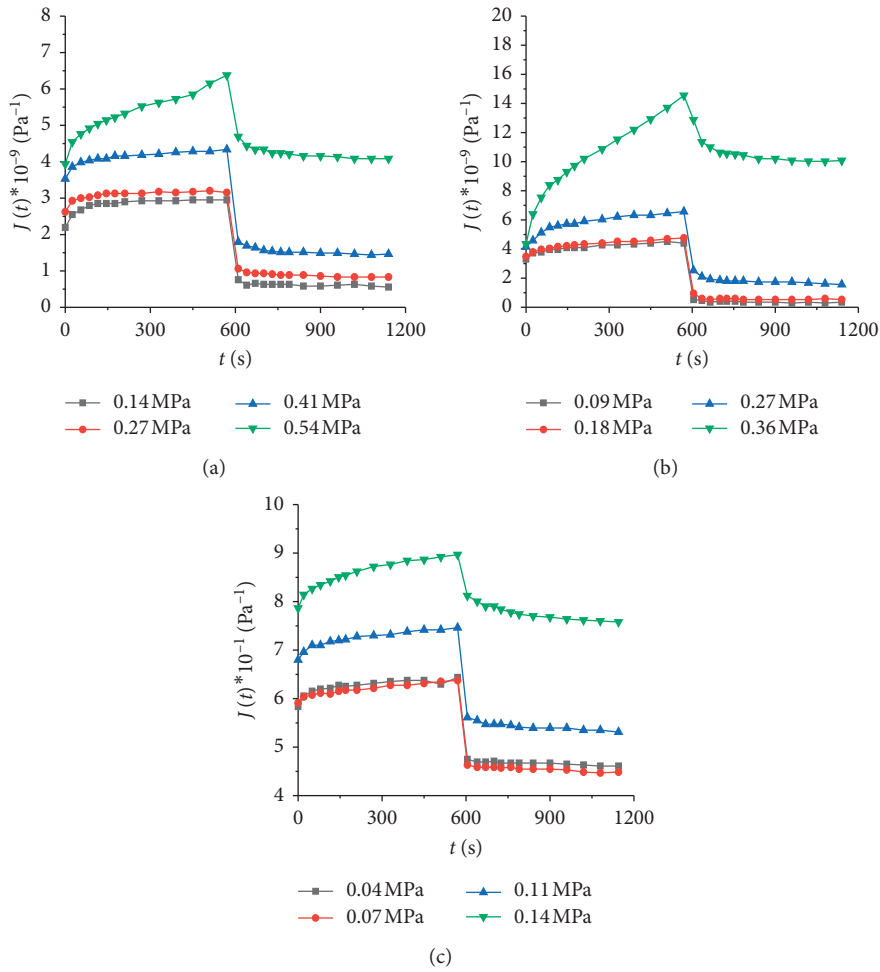
Figure 3: A/C = 0.6 creep and creep recovery compliance curve. (a) 30°C. (b) 45°C. (c) 60°C.
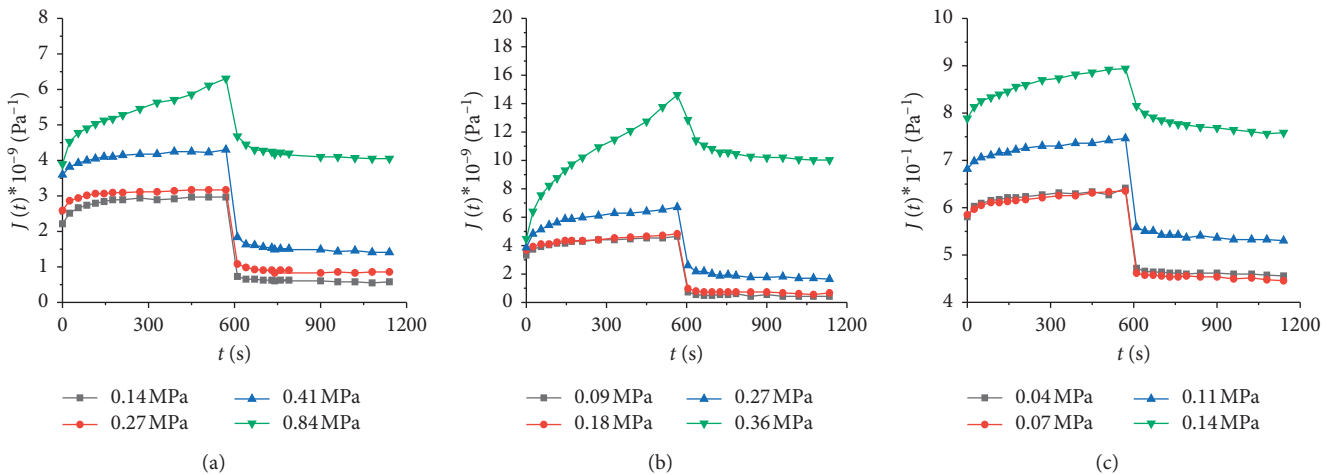
Figure 4: A/C = 0.9 creep and creep recovery compliance curve. (a) 30°C. (b) 45°C. (c) 60°C.

the material itself and its external loads. However, under the condition of high-stress level, during the creep test process, the material has large creep damage, which causes the creep deformation of the material to increase, so its creep and creep recovery compliance increase accordingly.

3.2. Effect of Aging on Creep Properties of CA Binder. The indoor ultraviolet accelerated aging test is used to simulate the aging of cement asphalt composite material in the actual use environment. The aging time is 150 h, 300 h, 600 h, and 900 h and the test results are shown in Figure 7. It can be seen
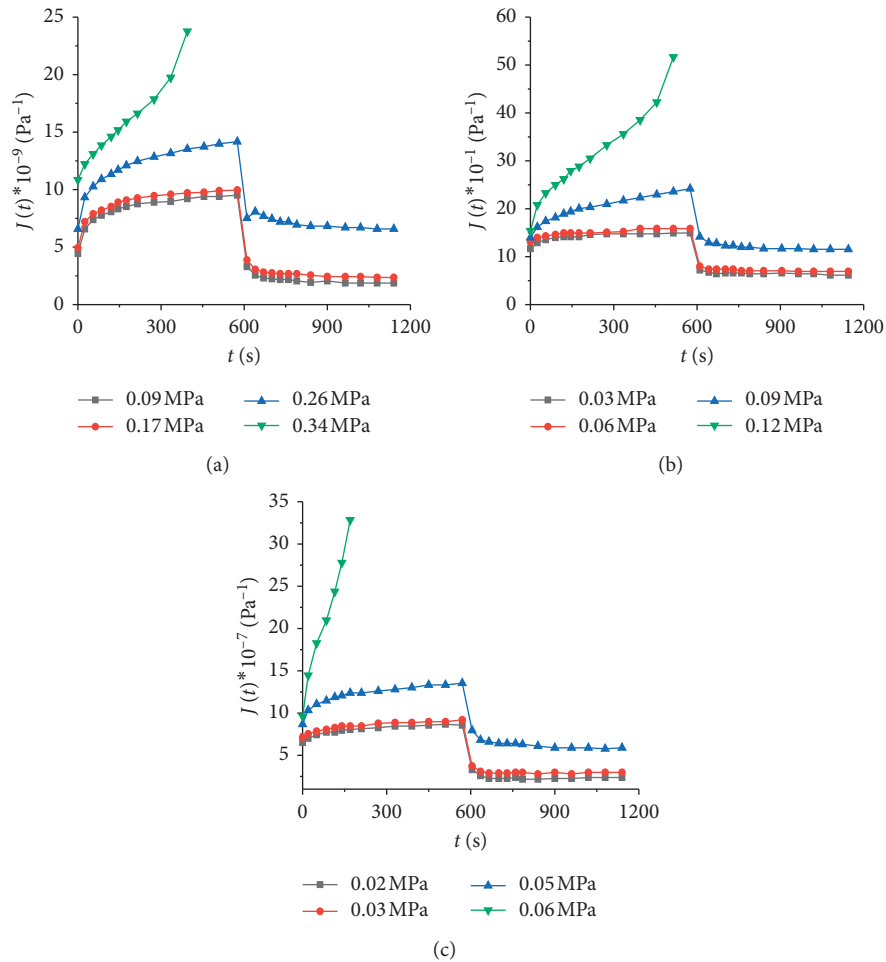
FIGURE 5: A/C = 1.2 creep and creep recovery compliance curve. (a) 30°C. (b) 45°C. (c) 60°C.

from Figure 7 that, as the degree of aging increases, the creep compliance of the CA cement with the same raw material ratio in the creep recovery phase and the absolute value of the incremental compliance increase in the deceleration recovery phase decrease, while the creep compliance of the gap between the curves gradually stabilizes as the recovery time increases. The above shows that the instantaneous elasticity, delayed elasticity, and viscous flow deformability of CA cement all weaken as the degree of aging increases, which is the same as the conclusion obtained from the creep test. As the degree of aging deepens, the deceleration creep and deceleration recovery phases of the CA cement are gradually shortened. When the aging time is 900 h, the deceleration creep and deceleration recovery phases of the CA cement of each ratio tend to disappear. As the degree deepens, the CA cement will gradually change from viscoelastic body to elastomer and tend to be hard and brittle.

In the initial period of aging, the asphalt component in CA binder is rapidly oxidized by UV, and the light component in the system decreases rapidly, which leads to the rapid decline of the flexibility and deformation ability of the material. With the aging process, the active light components easy to react in asphalt decrease, and the aging speed of asphalt slows down, which results in the change of

viscoelastic deformation capacity of the material. When the aging time is long enough, the creep deformation capacity of CA binder will tend to be stable and will not change with the aging time.

3.3. Influence of Temperature on Viscoelastic-Plastic Mechanical Properties. The changes of J_K (600)/J (600), J_K (600)/J_H (600), and J_1 (600)/J (0) with temperature are shown in Figures 7–11. From the subfigure (a) in Figures 8–12, it can be seen that, under the same stress level conditions, J_K (600)/J (600) increases with increasing temperature; that is, the ratio of viscoplastic strain to total strain increases, indicating that the temperature increases and the viscoplastic deformation of CA composite cement increases. It can be seen from subfigure (b) in Figures 8–12 that, under the same stress level conditions, J_K (600)/J_H (600) increases with increasing temperature; that is, the ratio of plastic strain to recoverable strain gradually increases to large, indicating that the temperature rises and the proportion of residual deformation gradually increases; from subfigure (c), it can be seen that, under the same stress level, J_1 (600)/J (0) decreases with the increase of temperature. That is, the ratio of elastic strain to elastic-plastic

(a)

(b)

(c)
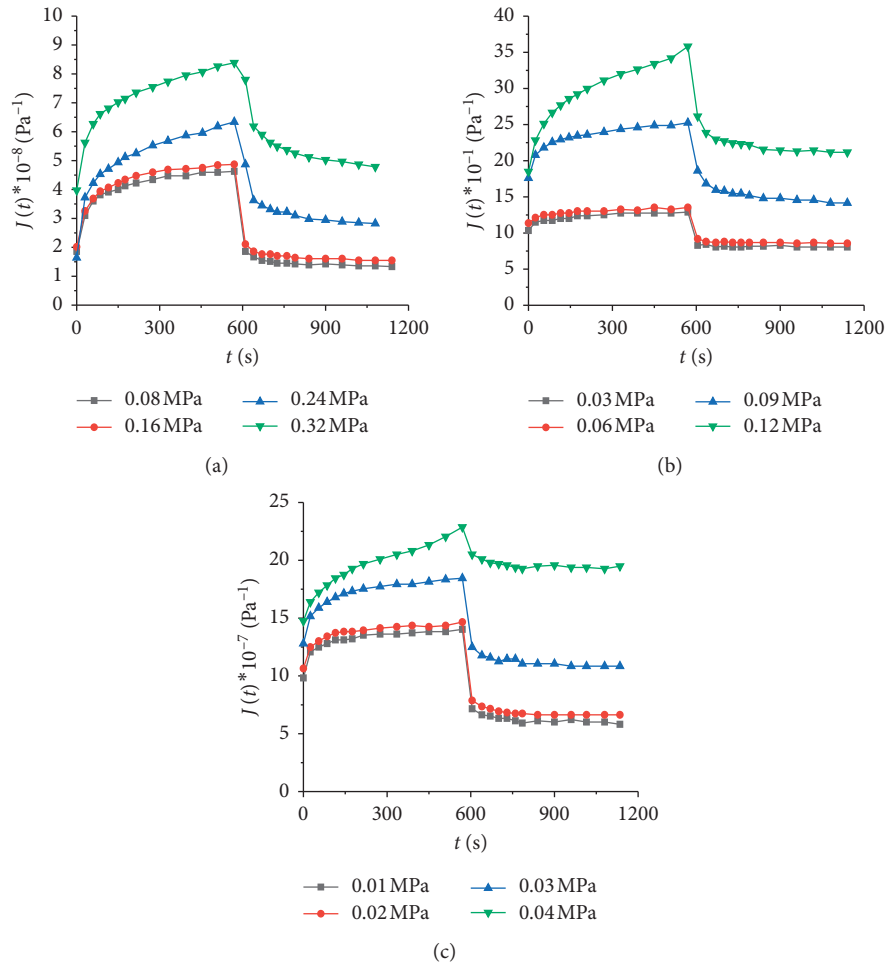
Figure 6: A/C = 1.5 creep and creep recovery compliance curve. (a) 30°C. (b) 45°C. (c) 60°C.

(a)

(b)

Figure 7: Continued.

(c)
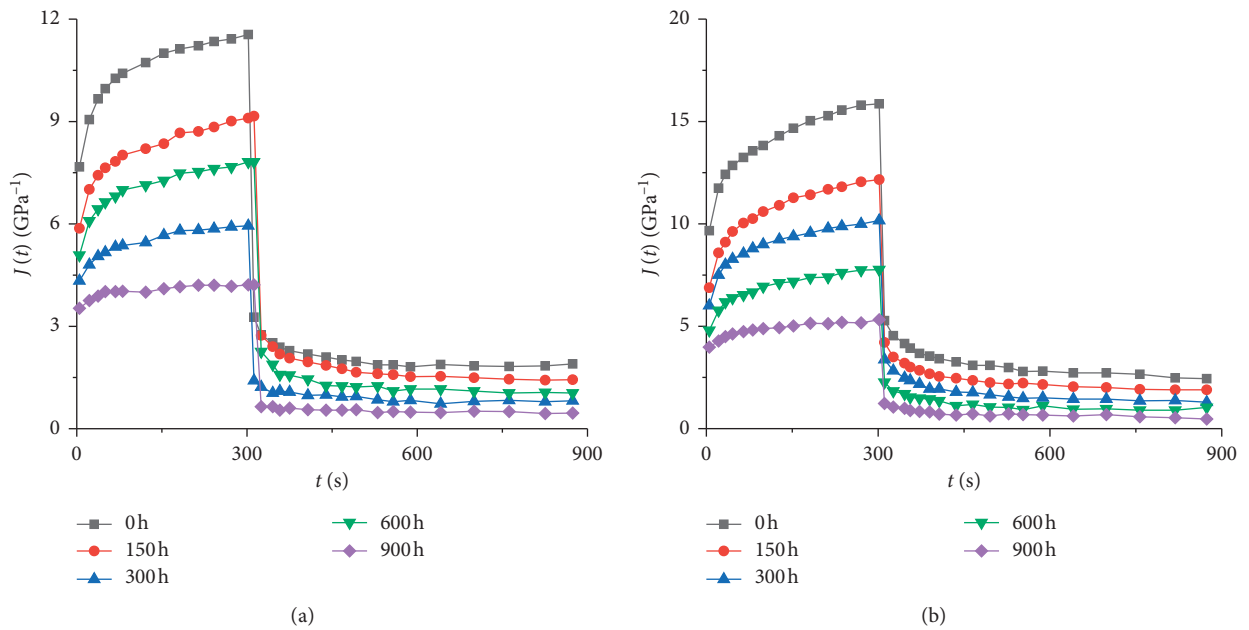
(d)
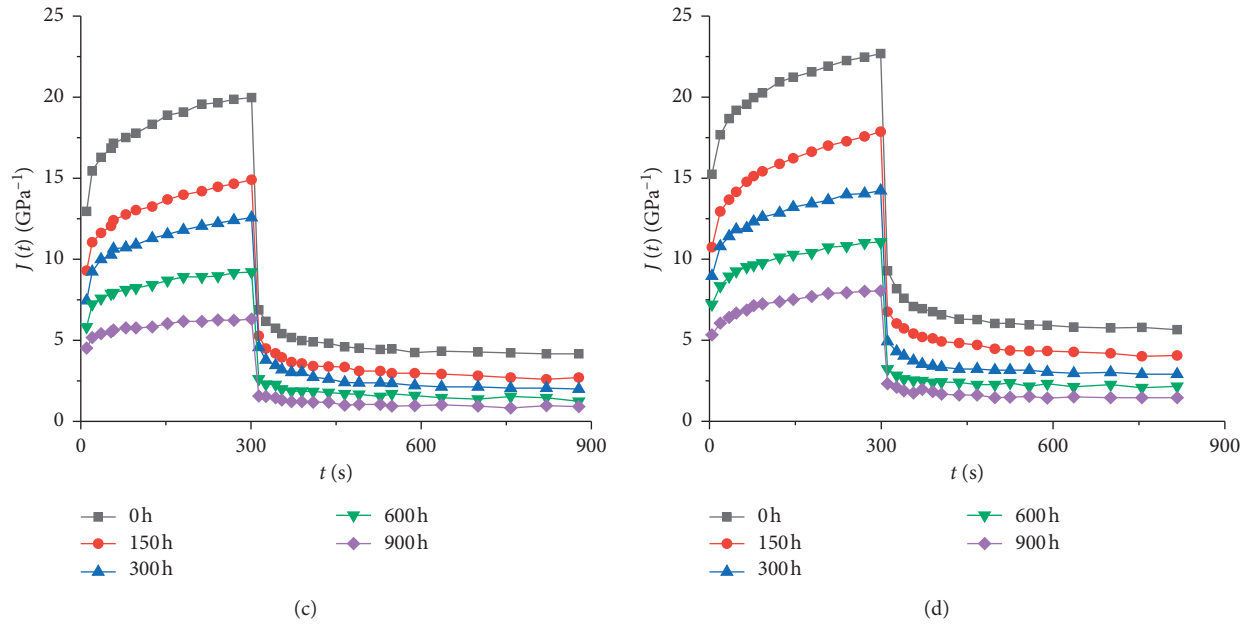
FIGURE 7: Creep compliance curve of creep recovery test of CA cement with different aging times. (a) A/C = 0.6. (b) A/C = 0.8. (c) A/C = 1.0. (d) A/C = 1.2.

strain decreases, indicating that the temperature rises and the deformation recovery ability gradually weakens. The above analysis shows that, as the temperature increases, the proportion of recoverable deformation of CA composite cement decreases, the proportion of nonrecoverable deformation of viscosity and plasticity increases, and the ability of CA composite cement to resist deformation and deformation recovery ability decreases. This is consistent with the influence law of stress level. In the material composition of CA composite cement, the temperature sensitivity of asphalt is greater while the temperature sensitivity of cement is lower. When the temperature rises, the asphalt material softens and fluidity increases, resulting in a gradual increase in the proportion of viscoplastic deformation. At the same time, as the temperature increases, the elastic properties of CA composite cement decrease, resulting in a gradual decrease in the ratio of elasticity and viscoelastic deformation.

3.4. Influence of A/C on Viscoelastic-Plastic Mechanical Properties.

The viscoelastic and plastic mechanical properties of CA composite cement are mainly determined by the interaction of cement hydration products, asphalt, and asphalt and cement hydration products. Among them, cement hydration products mainly affect its elastic properties, and asphalt mainly affects its viscosity properties. As well as plastic properties, the interaction of asphalt and cement hydration products affects its delayed elastic properties. Therefore, it is necessary to analyze the influence of the composition material ratio of CA composite cement on its viscoelastic-plastic mechanical properties. The changes of parameters $J_K(600)/J(600)$, $J_K(600)/J_H(600)$, and $J_1(600)/J(0)$ with A/C are shown in Figures 13–15. It

can be seen from subfigure (a) that, under the corresponding force level condition, $J_K(600)/J(600)$ increases with the increase of A/C; that is, the ratio of viscoplastic strain to total strain increases, indicating that with A/C increases, the proportion of viscoplastic deformation of the specimen increases; as can be seen from subfigure (b), $J_K(600)/J_H(600)$ increases with the increase of A/C, and the strain and plasticity can be restored. The strain ratio gradually decreases, indicating that as A/C increases, the deformation recovery capacity gradually decreases; as can be seen from subfigure (c), $J_1(600)/J(0)$ shows a decreasing trend as A/C increases; that is, the ratio of elastic strain to elastic-plastic strain decreases, indicating that A/C increases and elastic deformation recovery capacity decreases.

The above analysis shows that, with the increase of the CA composite cement A/C, that is, the increase in the amount of asphalt, the elastic performance of the CA composite cement weakens and the proportion of viscous deformation and plastic deformation increases. The viscous component in the CA composite cement increases with the proportion of elastic components increasing. The elastic performance of CA composite cement mainly depends on the hydration products of cement, while the viscoplastic performance mainly depends on asphalt. Therefore, as the amount of asphalt increases, that is, the greater the A/C, the elastic performance of CA composite cement decreases and flows. The deformation ability is enhanced, and the material's ability to resist deformation and deformation recovery is weakened. In addition, in the law of $J_1(600)/J(0)$ changing with A/C, when A/C = 0.9, there is a fluctuation, which is mainly caused by the microstructure composition and material ratio of CA composite cement. Performance changes are related.
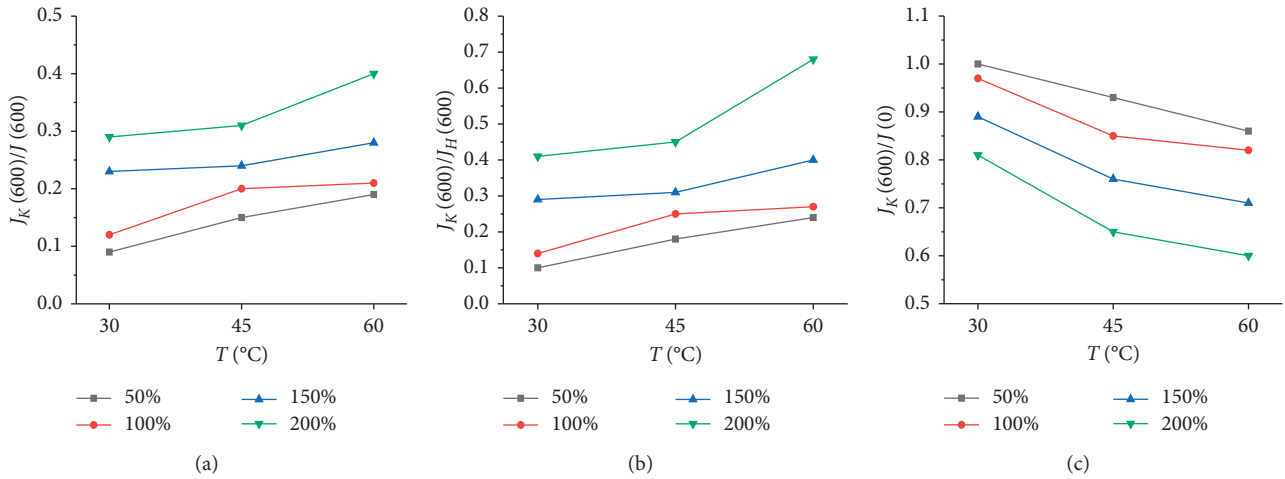
FIGURE 8: A/C = 0.3 creep compliance data curve. (a) $J_K(600)/J(600)$. (b) $J_K(600)/J_H(600)$. (c) $J_1(600)/J(0)$.
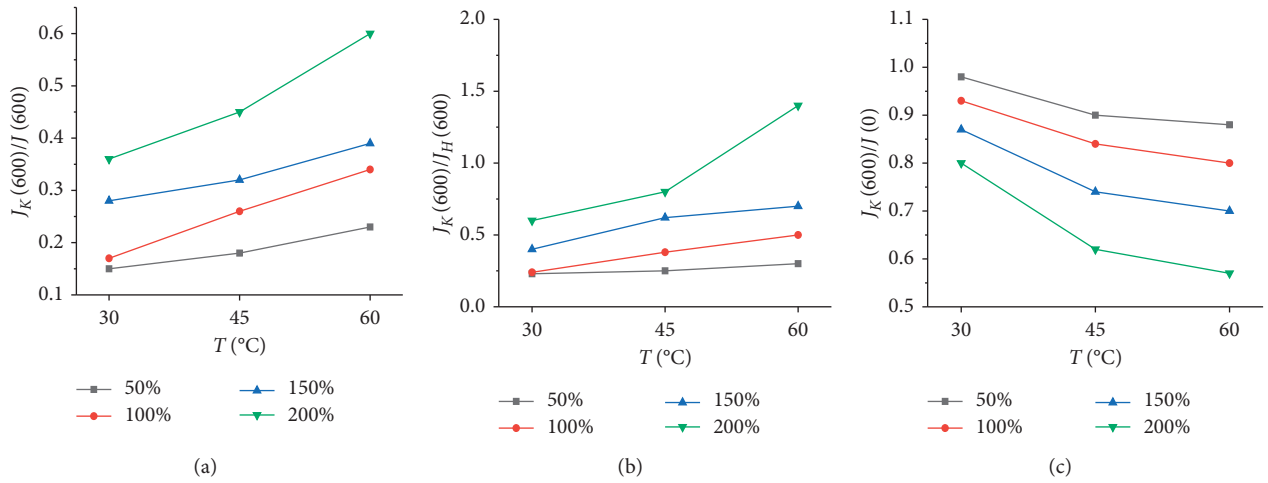
FIGURE 9: A/C = 0.6 creep compliance data curve. (a) $J_K(600)/J(600)$. (b) $J_K(600)/J_H(600)$. (c) $J_1(600)/J(0)$.
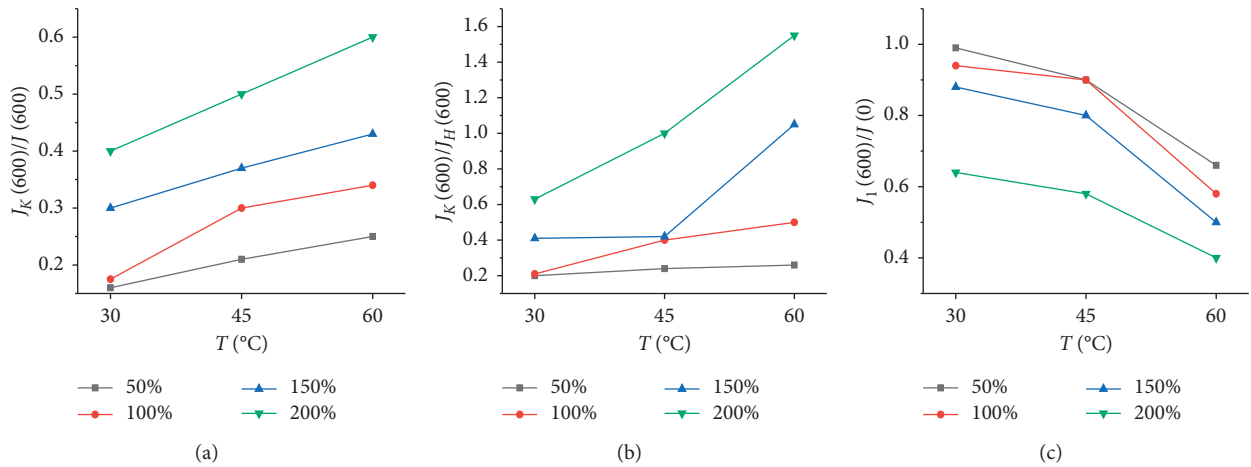
FIGURE 10: A/C = 0.9 creep compliance data curve. (a) $J_K(600)/J(600)$. (b) $J_K(600)/J_H(600)$. (c) $J_1(600)/J(0)$.
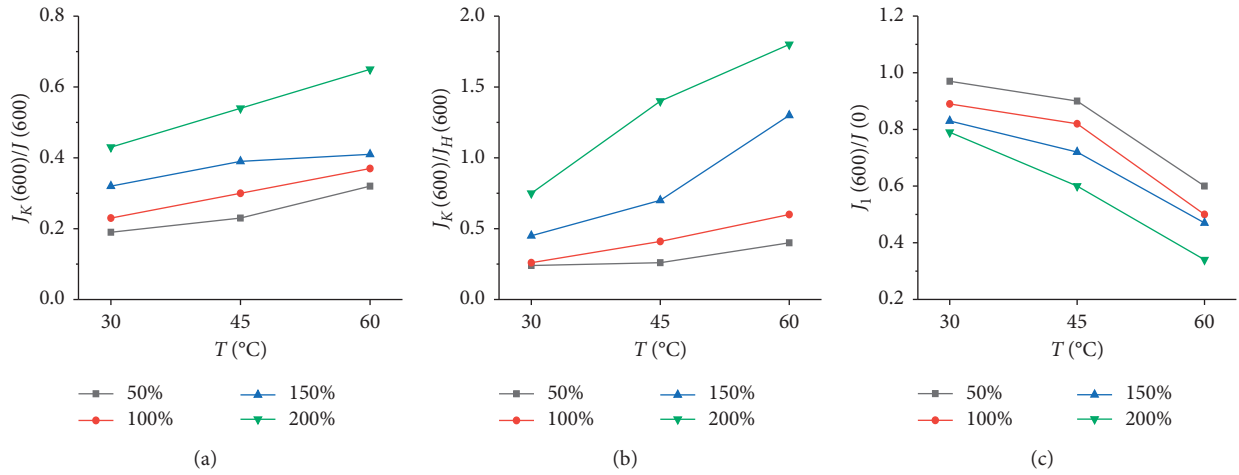
FIGURE 11: A/C = 1.2 creep compliance data curve. (a) $J_K(600)/J(600)$. (b) $J_K(600)/J_H(600)$. (c) $J_1(600)/J(0)$.
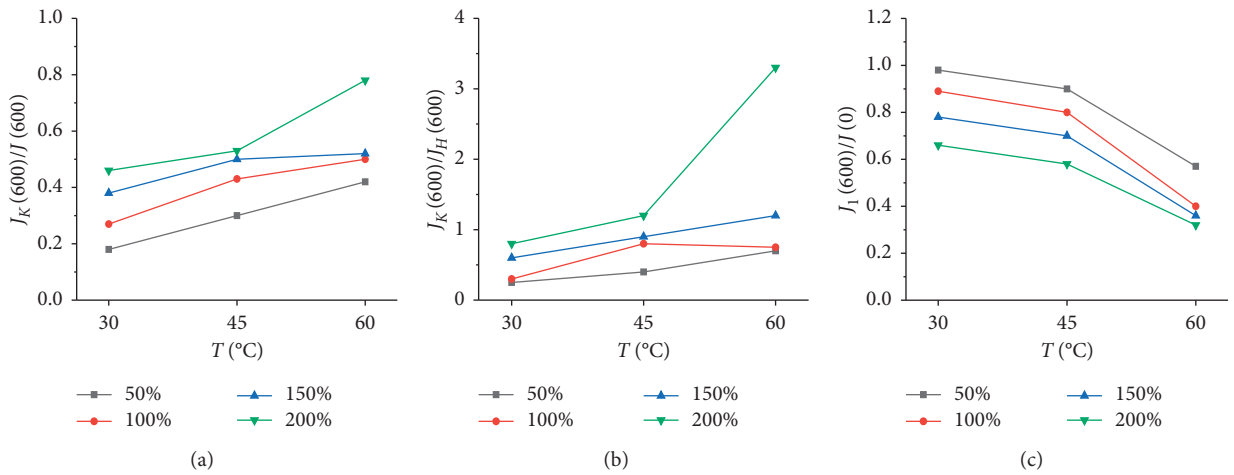
FIGURE 12: A/C = 1.5 creep compliance data curve. (a) $J_K(600)/J(600)$. (b) $J_K(600)/J_H(600)$. (c) $J_1(600)/J(0)$.
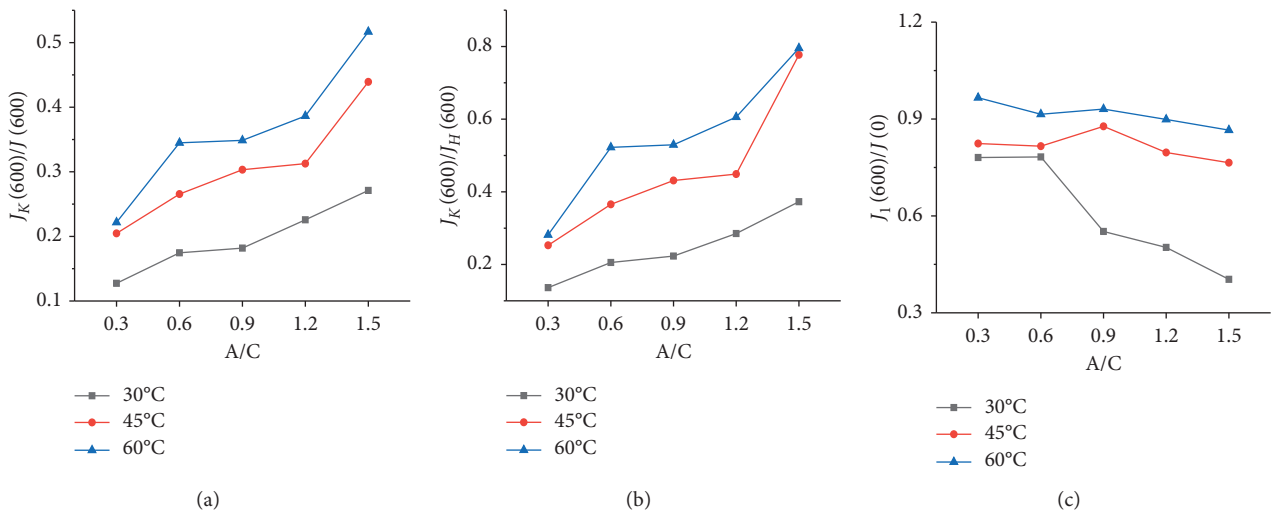
FIGURE 13: Creep compliance data curve at 100% stress level. (a) $J_K(600)/J(600)$. (b) $J_K(600)/J_H(600)$. (c) $J_1(600)/J(0)$.
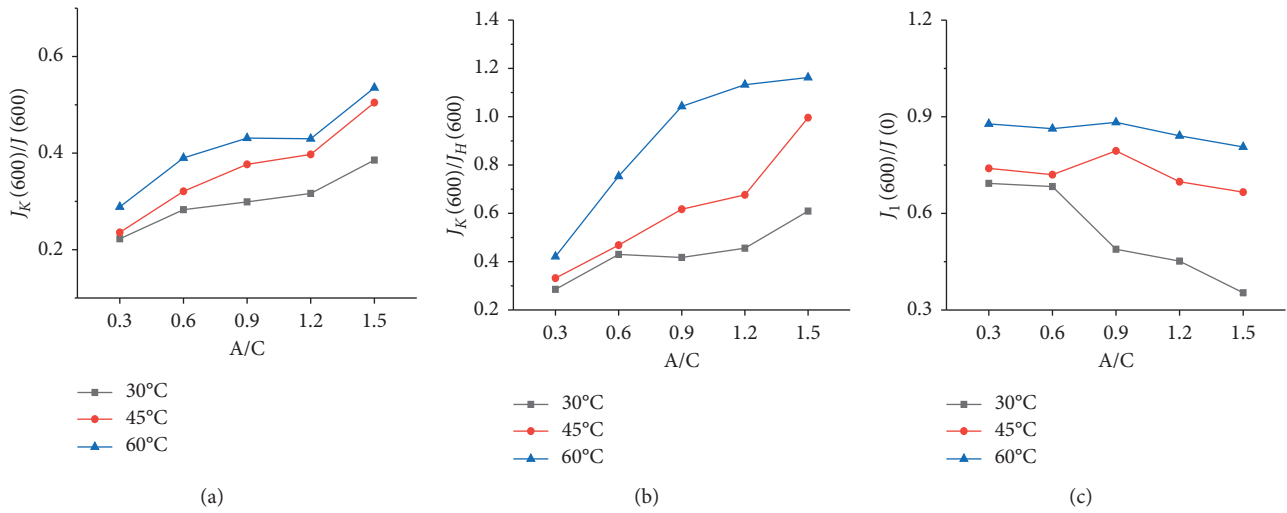
FIGURE 14: Creep compliance data curve at 150% stress level. (a) $J_K(600)/J(600)$. (b) $J_K(600)/J_H(600)$. (c) $J_1(600)/J(0)$.
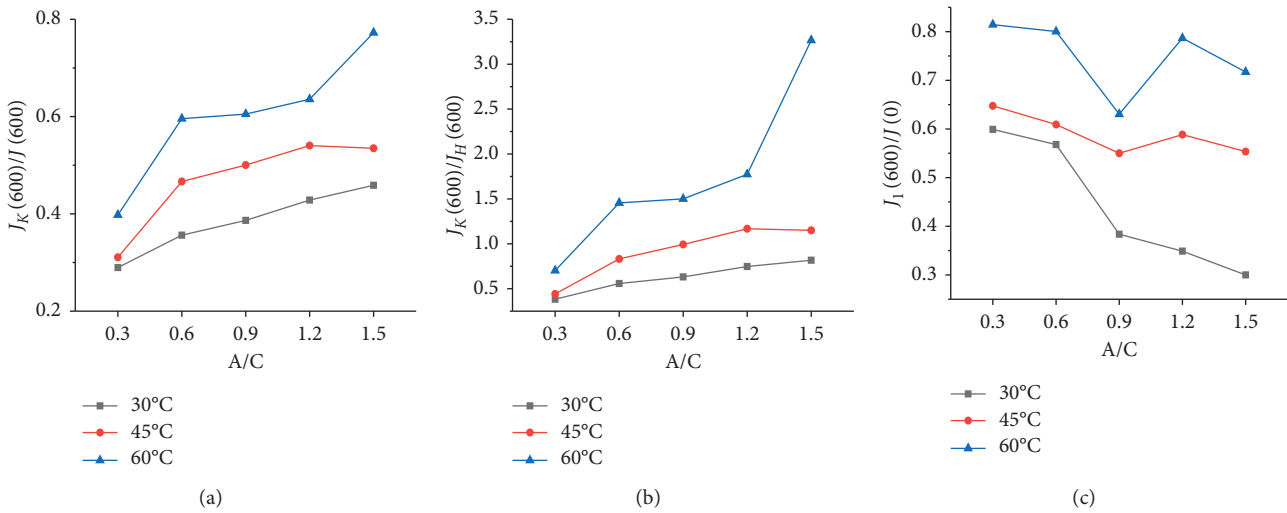
FIGURE 15: Creep compliance data curve at 200% stress level. (a) $J_K(600)/J(600)$. (b) $J_K(600)/J_H(600)$. (c) $J_1(600)/J(0)$.

In summary, it can be seen that the stress level, temperature, and A/C have a greater impact on the viscoelastic-plastic mechanical properties of CA composite cement. When the stress level is high, the material is prone to damage, and the greater the stress level, the greater the creep damage, resulting in a significant change in the material's viscoelastic and plastic mechanical properties; temperature and A/C mainly affect the ratio of viscous and elastic components in the material relationship, and temperature and A/C changes will lead to changes in the relative proportions of viscous components and elastic components in the material, leading to changes in the deformability of CA composite cement. With the increase of temperature and A/C, the ratio of viscoplastic deformation of CA composite cement increases, and the ability to resist deformation and the ability to recover from deformation are weakened.

4. Conclusion

In this paper, the creep and creep recovery tests of CA composite cement are carried out. Based on the results of creep and creep recovery tests, the creep and creep recovery characteristics of CA composite cement and the effects of aging on their creep properties are analyzed. The effects of temperature and material ratio on the viscoelastoplastic mechanical properties of CA composite cement are studied, and the conclusions are as follows:

(1) As the degree of aging increases, the creep compliance of CA cement decreases, the creep deformation ability decreases, the proportion of creep recovery deformation increases, the proportion of residual deformation decreases, and the deceleration creep and deceleration creep recovery stages tend to

disappear, and the overall static mechanical properties of the material tend to be elastic.

(2) With the increase of temperature, the proportion of recoverable deformation of CA composite cement decreases, the proportion of nonrecoverable deformation of viscosity and plasticity increases, and the ability of CA composite cement to resist deformation and deformation recovery ability decreases.

(3) The elastic performance of CA composite cement mainly depends on the hydration products of cement, while the viscoplastic performance mainly depends on asphalt. Therefore, as the amount of asphalt increases, that is, the greater the A/C, the elastic performance of the CA composite cement decreases and increases the flow deformation ability, and the material resistance to deformation and deformation recovery ability is reduced.

Data Availability

No data were used to support this study.

Conflicts of Interest

The authors declare that they have no conflicts of interest.

Acknowledgments

References

[1] R. Chang and H. Peiwen, "Rheological properties and aging mechanism of crumb rubber/ret modified asphalt before and after aging," *Journal of Building Materials*, vol. 6, no. 20, pp. 914–920, 2017.

[2] T. Wang, H. Jia, and H. Li, "Rheological properties of CRTs I cement emulsified asphalt mortar," *Journal of Civil Engineering and Management*, vol. 1, no. 35, pp. 48–53, 2018.

[3] H. Li, W. Wang, W. Li, A. Taoum, G. Zhao, and P. Guo, "Replacement of limestone with volcanic stone in asphalt mastic used for road pavement," *Arabian Journal for Science and Engineering*, vol. 44, no. 10, pp. 8629–8644, 2019.

[4] Y. Li, Y. Liu, Ji Lun et al., "Influence of aging on dynamic mechanical properties of cement emulsified asphalt binder," *Journal of Composite Materials*, vol. 7, no. 35, pp. 299–306, 2018.

[5] H. Li, G. Liu, B. Dong et al., "Research on the development and regeneration performance of asphalt rejuvenator based on the mixed waste engine oil and waste cooking oil," *International Journal of Pavement Research and Technology*, vol. 12, no. 3, pp. 336–346, 2019.

[6] X. Zhou, Y. Xie, K. Zheng et al., "Quality change and volume stability of cement emulsified asphalt mortar under dry wet cycle," *Acta Silicate Sinica*, vol. 7, no. 46, pp. 895–904, 2018.

[7] C. Zhang, X. Cao, S. Jiao et al., "Viscoelastic plastic compaction characteristics of cement emulsified asphalt mixture based on Bodner partom model," *Acta Highway Sinica*, vol. 7, no. 32, 2019.

[8] F. Yang, H. Li, G. Zhao et al., "Mechanical performance and durability evaluation of sandstone concrete," *Advances in Materials Science and Engineering*, vol. 2020, Article ID 2417496, 2020.

[9] X.. Bao, "Study on the influence of emulsified asphalt content on the performance of super early strength CAEM," *Highway*, vol. 3, no. 64, pp. 246–250, 2019.

[10] H. Li, B. Dong, W. Wang et al., "Effect of waste engine oil and waste cooking oil on performance improvement of aged asphalt," *Applied Sciences*, vol. 9, no. 9, 2019.

[11] J. Ouyang, H. Li, and B. Han, "The rheological properties and mechanisms of cement asphalt emulsion paste with different charge types of emulsion," *Construction and Building Materials*, vol. 147, pp. 566–575, 2017.

[12] H. Gengren, W. Huang, J. Yuan et al., "Effect of aging on chemical and rheological properties of SBS modified asphalt with different compositions," *Construction and Building Materials*, vol. 156, pp. 902–910, 2017.

[13] H. Li, W. Li, A. A. Temitope et al., "Analysis of the influence of production method, crumb rubber content and stabilizer on the performance of asphalt rubber," *Applied Sciences*, vol. 10, no. 16, 2020.

[14] P. Li, Z. Ding, L. x. Ma, and Z. g. Feng, "Analysis of viscous flow properties of asphalt in aging process," *Construction and Building Materials*, vol. 124, pp. 631–638, 2016.

[15] A. Rasouli, A. Kavussi, M. J. Qazizadeh, and A. H. Taghikhani, "Evaluating the effect of laboratory aging on fatigue behavior of asphalt mixtures containing hydrated lime," *Construction and Building Materials*, vol. 164, pp. 655–662, 2018.

[16] A. Chen, G. Liu, Y. Zhao, J. Li, Y. Pan, and J. Zhou, "Research on the aging and rejuvenation mechanisms of asphalt using atomic force microscopy," *Construction and Building Materials*, vol. 167, pp. 177–184, 2018.

[17] Y. Ji, *Study on Cement Emulsified Asphalt Mortar for Ballastless Track of High Speed Railway*, Chang'an University, Xi'an, China, 2011.

[18] H. Song, Y. Xie, and G. long, "Research progress of cement emulsified asphalt mortar," *Materials Guide*, vol. 5, no. 32, pp. 836–846, 2018.

[19] Y. F. Fu, Y. L. Wong, C. S. Poon et al., "Experimental study of micro/macro crack development and stress–strain relations of cement-based composite materials at elevated temperatures," *Cement and Concrete Research*, vol. 5, no. 34, pp. 789–797, 2004.

[20] F. de A. L. B. Lucas, S. F. Jorge Luis, J. B. Soares et al., "Aging-effect incorporation into the fatigue-damage modeling of asphalt mixtures using the S-VECD model," *Journal of Materials in Civil Engineering*, vol. 12, no. 28, 2016.

[21] M. Saber, W. Sun, and T. H. Hyde, "Numerical study of the effects of crack location on creep crack growth in weldment," *Engineering Fracture Mechanics*, vol. 154, pp. 72–82, 2016.

[22] H. Xu and P. Wang, "Effects of strain rate and stress level on dynamic compressive property of CA mortar," *Journal of Building Materials*, vol. 6, no. 18, pp. 1084–1088, 2015.

[23] H. Li, B. Dong, D. Zhao, P. Guo, and J. Zhang, "Physical, rheological and stability properties of desulfurized rubber asphalt and crumb rubber asphalt," *Arabian Journal for Science and Engineering*, vol. 44, no. 5, pp. 5043–5056, 2019.

[24] H. song, X. Zeng, Y. Xie et al., "Creep characteristics of cement emulsified asphalt mortar under long-term load," *Journal of Building Materials*, vol. 2, no. 23, pp. 271–278, 2020.

[25] D. S. Seo and H. B. Choi, "Effects of the old cement mortar attached to the recycled aggregate surface on the bond characteristics between aggregate and cement mortar," *Construction and Building Materials*, vol. 59, pp. 72–77, 2014.

Research Article

Study on Mesoscopic Mechanics of Recycled Asphalt Mixture in the Indirect Tensile Test

Yanping Sheng,[1] Haichuan Jia [ID],[1] Hongli Lv,[2] Huaxin Chen [ID],[1] Xiaorui Zhao,[1] Runzhi Wang,[1] and Jiandang Meng[2]

[1]*School of Material Science and Engineering, Chang'an University, Xi'an 710064, China*
[2]*Management Office of Puyang to Hebi Highway Section, Division of Highway, Henan Department of Transportation, Henan 410902, China*

Correspondence should be addressed to Haichuan Jia; hcjia1117@163.com and Huaxin Chen; hxchen@chd.edu.cn

Reclaimed asphalt pavement (RAP) mainly contains asphalt binder and aggregates, and the RAP materials used in paving roads could save virgin materials. This paper studied the following: asphalt mixture with different RAP material contents was prepared; then the indirect tensile test was carried out, and the mesoscopic model of the recycled asphalt mixture was reconstructed digitally. Discrete element method (DEM) of indirect tensile test was carried out to analyze the mechanical properties of recycled asphalt mixture in mesoscopic perspective. The results showed that there were some gaps between the simulation result of the digital specimen model and the test value of the recycled asphalt mixture, but the velocity vector and the law of force chain development of the recycled asphalt mixture could be explained in mesoscopic perspective. It proved that the virtual simulation test of the mechanical test was effective. The damage process of recycled asphalt mixture was analyzed in mesoscopic perspective, and the unification of mechanical response and macroscopic appearance was completed. Meanwhile, the simulation method of mesoscopic mechanics was an effective supplement to traditional tests, and guided tests method theoretically.

1. Introduction

Asphalt pavement is used widely in the construction of highways in the world because of its excellent performance [1]. However, the service life of asphalt pavement could be affected by severe climate and overload [2–4]. The environmental condition and repeated load lead to pavement distress such as fatigue cracking, permanent deformation, low-temperature cracking, and moisture damage. Then, the damaged asphalt pavements are discarded, resulting in a lot of waste of resources. The resource conservation and environmental problems attracted attention and became the focus in more research [5, 6]. Recycled asphalt and aggregate are used in asphalt pavement, saving the use of aggregate and asphalt in paving roads. RAP materials from damaged asphalt pavements contain asphalt and aggregate. Moreover, the use of RAP materials in asphalt pavement reduces the consumption of raw materials (asphalt and aggregate) and

saves resources. The fatigue and cracking properties of recycled asphalt mixtures decline compared with hot mix asphalt (HMA) because of aged bitumen and reduction in brittleness of the mixtures containing high RAP contents. Additionally, aging in asphalt and secondary aging of RAP materials may happen due to excessive construction temperature [7–12]. Hence, the RAP material contents used in recycled asphalt mixtures are generally less than 30%. Furthermore, the tensile strength, resistance to rutting, low-temperature cracking, and fatigue cracking of recycled asphalt mixture should be concerned.

Montanez [13] studied the rheological properties, mechanical properties, and moisture damage of fine aggregates from different RAP material sources and evaluated the differences between RAP materials. The results showed that the single source of RAP materials or the homogenization process between different RAP material sources was significant for manufacturing HMA. Goli [14] used indirect

tensile strength, indirect tensile fatigue failure, semicircular bending, and dynamic creep tests to study the effect of moisture damage on the performance of asphalt mixtures. The results showed that the warm mix asphalt containing RAP materials has hydrophilicity, moisture sensitivity, and aging properties but has an inhibitory effect on the influence of moisture performance. Rathore [15] evaluated the asphalt mixing parameters (mixing temperature, mixing time, and equipment) of recycled asphalt mixture with high RAP content using the indirect tensile strength and the stiffness modulus test. The results showed that mixing and heating temperature were important parameters in producing recycled asphalt mixture. Zhu [16] examined the performance of high modulus asphalt mixture containing RAP materials including high-temperature performance, low-temperature performance, and moisture susceptibility. The fatigue and crack behavior of recycled asphalt mixture are significant design indexes, which affects the use of pavement. In previous studies, the long-term life of recycled asphalt pavement was considered through indirect tensile strength test, fatigue failure test, semicircular bending test, and modulus tests. Scientists and engineers studied that the mechanical properties of recycled asphalt mixtures were affected by the use of regenerants, the content of RAP materials, and environmental conditions. Furthermore, the indirect tensile test obtains the failure strength and deformation parameters to evaluate the mechanical properties of the material. However, the composition structure of the recycled asphalt mixture is more complex and uneven compared with HMA [17]. Thus, the indirect tensile test is difficult to define the internal damage law of the asphalt mixture accurately.

Meanwhile, the mesoscopic mechanics method provides the way for the study of the mechanical behavior of asphalt mixtures. Numerical simulation is an effective method to research the occurrence and development of cracking in asphalt mixtures. At present, there are two different numerical methods used extensively for such investigations: finite element method (FEM) and discrete element method (DEM). The FEM represents discrete elements in the actual continuous domain and was widely used to study the cracking behavior of homogeneous materials using the continuum mechanics theory [18]. However, asphalt mixtures are discontinuous in material distribution and mechanical parameters. Therefore, the microcracking of asphalt mixture is difficult to simulate based on the FEM accurately. DEM uses explicit difference algorithms for mechanical research in mesoscopic perspective, which is suitable for studying the force of granular mixture. It decomposes the asphalt mixture into spherical elements or disks elements of unit thickness, which quantify the internal stress of the asphalt mixture during loading [19, 20]. Moreover, it reflects the particle properties and discontinuous characteristics of asphalt mixtures. Compared with continuum mechanics, DEM is a simulation method to research asphalt mixture with heterogeneous and particulate characteristics [21–23].

Wu [24] modified asphalt mixtures with styrene-butadiene-styrene (SBS) and established the DEM model of AC-16 asphalt mixture. During the grinding process, the

asphalt mixture was avoided from being broken into large pieces considering reducing the damage of the aggregate. Ma [25] researched the air void of the asphalt mixture during the compaction process and the characteristics of the mesoscopic structure changes. DEM was used to establish a numerical simulation method for compaction considering critical particle size and boundary effects in the study. Wang [26] researched that the simplified viscoelastic continuum damage model was used to characterize the recycled asphalt pavement according to the material properties, traffic load, and climatic conditions, and the result showed that the theoretical performance predictions matched the field performance. Qian [27] investigated the Marshall impact compaction and static compaction methods by using DEM simulation to evaluate the compacting effects of the compaction process. In the compaction process, the size distribution of particles was unevenly distributed in a horizontal direction due to the large size particles (>16 mm) being difficult to move in the dense specimen. Yu [28] studied that the DEM was used to investigate the effect of aggregate size and angularity distribution on dynamic modulus, which evaluates the aggregate effect on fatigue and rutting performance and provides the guide to improve the mixing design. Researches showed that DEM is used to simulate the compaction of the specimen and then simulate the performance test. The method is scientific and could complete experimental conditions that cannot be achieved in the laboratory.

As the heterogeneous and particulate mixture, recycled asphalt mixture is the discontinuous medium material with complex components. Many scholars researched the traditional properties of recycled asphalt mixtures, but there is little research on the analysis of the mesoscopic damage evolution of recycled asphalt mixtures based on the DEM. In this study, the indirect tensile tests of recycled asphalt mixture with different RAP material contents were conducted, then the mesoscopic model of the recycled asphalt mixture was reconstructed digitally based on DEM, and the simulation method was used to research the mesoscopic damage of recycled asphalt mixture. The objective of this paper is to research the damage process of recycled asphalt mixture in mesoscopic perspective and carry out the unification of mechanical behavior and macroscopic appearance to supplement the traditional tests effectively. The flow chart of research is presented in Figure 1.

2. Materials

2.1. Asphalt Binder and Aggregate. SK-90# asphalt was used in the test, and its properties are shown in Table 1. The penetration (25°C), specific gravity (15°C), ductility (15°C), softening point, and residual penetration ratio (25°C) test were conducted according to the Standard Test Methods of Bituminous Mixtures for Highway Engineering of China (JTG E20-2011) [29]. Additionally, the aggregate with the nominal maximum aggregate size (NMAS) of 16 mm was selected, and the indexes are shown in Table 2.
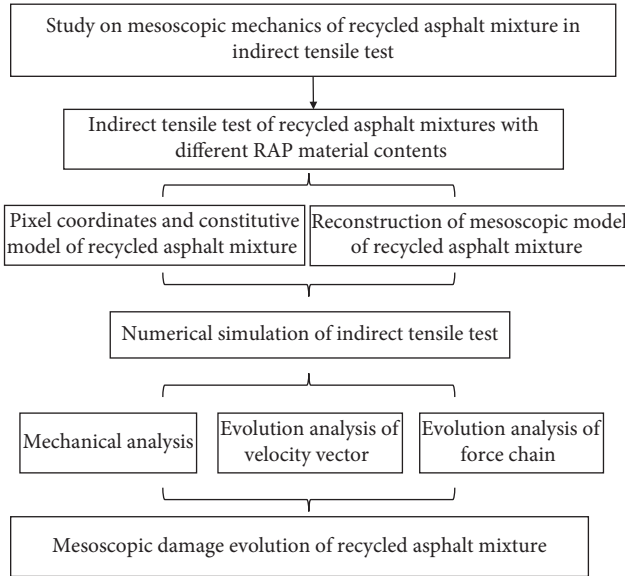
FIGURE 1: The research plan chart.

TABLE 1: Technical properties of SK-90# asphalt binder.

Test	Unit	Result	Standard
Penetration test (25℃, 5s, 100g)	0.1 mm	95	T0604
Ductility test (15℃)	cm	>100	T0605
Softening point (℃)	℃	44.5	T0606
Solubility	%	99.62	T0607
Specific gravity (15℃)	g/cm^3	1.030	T0603
RTFOT	Mass loss	%	0.4	T0609
	Residual penetration ratio (25℃)	%	57.8	T0604
	Ductility (10℃)	cm	12	T0605

TABLE 2: Technical properties of Aggregate.

Test	Unit	Result	Standard
Coarse aggregate specific gravity	g/cm^3	2.758	T0304
Fine aggregate specific gravity	g/cm^3	2.746	T0328
Water absorption	%	1.02	T0304
Crush value	%	19.8	T0316
Los Angeles abrasion value	%	19.1	T0317
Flakiness	%	2.6	T0312
Sand equivalent	%	1	T0310

2.2. RAP Materials and Rejuvenator. The RAP materials of Gonghe-Yushu Expressway in Qinghai Province were separated by centrifugal separation, and the asphalt content was 5.13%. Meanwhile, the trichloroethylene solvent extraction method was used to collect the aggregates. The sieving results of RAP materials are shown in Table 3. The RAP material contents of 0%, 15%, 30%, 45%, and 60% in recycled asphalt mixture corresponded to the optimum asphalt content of 4.72%, 4.87%, 4.81%, and 4.71%, respectively. And the optimum rejuvenator content was 0.2% of RAP material contents. The Marshall design method was used for grading design, and the aggregate grading is shown in Figure 2.

3. Numerical Simulation in Discrete Element Method

The two-dimensional particle flow code (PFC2D) is mainly based on numerical methods, using circular particle elements to simulate the motion and interaction of the particle medium to perform numerical simulation analysis, then the simulation results of local elements are used to research the constitutive model of overall material calculation [30]. Furthermore, the explicit difference algorithm and the mesoscopic mechanics in the discrete element theory were used to analyze the overall mechanical properties of the materials. In this paper, the digital model for the indirect tensile test of recycled asphalt mixtures was established, and the servo mechanism was used to control the load application of the digital specimen, then the mesoscopic damage changes of the specimen were tracked during the loading process. The difference between the numerical simulation and the experimental results was compared, and the feasibility of the DEM was verified [31–34]. A binary image of the cross section of specimen was obtained as the numerical simulation object of the indirect tensile test and is shown in Figure 3. The pixel coordinates of the aggregates, reclaimed aggregates, and asphalt mortar were extracted, and the coordinate reading of the mesoscopic model was completed. Then, the coordinates of each component were imported into the discrete element software to generate a two-dimensional digital sample of the recycled asphalt mixture. The coordinated results of aggregates, reclaimed aggregates, and asphalt mortar are shown in Figure 4.

3.1. Constitutive Model. In Figure 5, the constitutive models in PFC2D include stiffness model, sliding model, and bonding model. Moreover, the stiffness model is the relationship between contact force and relative displacement, the sliding model is the relationship between tangential and normal contact forces (two contacting particles may relatively slide), and the bonding model imposes constraints on the contacting particles. What is more, the mesoscopic model included an internal contact of aggregate, aggregate-aggregate contact, reclaimed asphalt mortar-aggregate contact, and internal contact of reclaimed asphalt mortar. Burger's model is used to describe the viscous behavior of the asphalt mixtures, which is the combination of Kelvin model (spring and dashpot in parallel) and Maxwell model (spring and dashpot in series). The Kelvin model describes creep and creep recovery behavior, and the Maxwell model describes the mechanical behavior of stress relaxation. After the two models are connected in series, the creep and stress relaxation characteristics of the material could be described, which is suitable for the force analysis of viscoelastic materials. Additionally, the aggregates and reclaimed aggregates are regarded as elastic materials, and their constitutive mechanical properties are characterized by the spring model [35, 36]. The contact inside the aggregate and between adjacent aggregates is described by a linear contact model, which is characterized by two springs connected in series, as

Size (mm)	16	13.2	9.5	4.75	2.36	1.18	0.6	0.3	0.15	0.075
Passing (%)	100.00	94.43	77.20	43.82	28.54	21.19	15.70	11.54	7.91	4.61
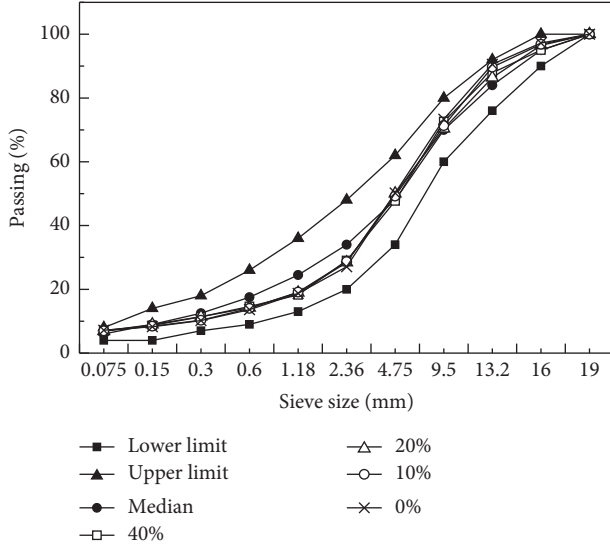
FIGURE 2: The aggregate grading of asphalt mixture.

FIGURE 3: Binary image.

shown in Figure 5(c). What is more, the stiffness model at the contact point of the reclaimed asphalt mortar is described by the Burgers model in the normal and shear directions, as shown in Figure 5(a). The stiffness model of the contact between the aggregate and the reclaimed asphalt mortar is made up of the spring element and the Burgers model in series, as shown in Figure 5(b). Meanwhile, the aggregates and reclaimed aggregates were represented by spring element, and the reclaimed asphalt mortar was represented by the Burgers model. The sliding model at all contact points is expressed by the friction coefficient μ, and the bonding model is expressed by the tensile strength and the shear strength.

3.2. Model Reconstruction in DEM Simulation.

In the mesoscopic model, the irregular aggregates and reclaimed asphalt mortar are composed of disks with single particle size. For example, in the cross section of the recycled asphalt mixture with 40% RAP materials, the cross section of the digital sample was composed of 11277 disks discrete element particles. The number of basic units constituting the aggregate was 5026, the number of basic units of the reclaimed aggregate was 1989, and the number of basic units of the reclaimed asphalt mortar was 4262. The generated two-dimensional digital specimen of the recycled asphalt mixture is shown in Figure 6.

With the mesoscopic structure of the recycled asphalt mixture, the mesoscopic parameters of the two-dimensional digital specimen model of the recycled asphalt mixture were set up, as shown in Tables 4 and 5. According to the two-dimensional digital model, the bond strength of the digital specimens was 4%. The bonding stiffness of digital specimens with 0%, 10%, 20%, and 40% RAP material was selected as 4, 1, 0.5, and 1, respectively. And the friction coefficients μ were 0.5, 0.3, 0.1, and 0.1, respectively. The indirect tensile test of asphalt mixture is to apply load to the cylindrical specimen of a specified size at the loading speed. And a dial indicator is used to measure the vertical and horizontal deformation of the specimen until the specimen is split and destroyed. The indirect tensile test of the two-dimensional digital specimen of recycled asphalt mixture was carried out by controlling the loading plate to load at 1 mm/min rate. The FISH language functions were used for secondary program development, and the servo mechanism control load application was carried out, tracking and monitoring the development of stress-strain, velocity vector, and force chain. The sample model after setting the loading plate is shown in Figure 7.

The constitutive relationship of Burger's contact model is expressed by

$$
\begin{aligned}
f_n &= C_{mn}\dot{u_{mn}} = u_k K_{kn} + \dot{u_k} C_{kn} = K_{mn} u_{mk}, \\
f_s &= C_{ms}\dot{\delta_{mc}} = \delta_k K_{ks} + \dot{\delta_k} C_{ks} = K_{ms} \delta_{mk}, \\
u_n &= u_k + u_{mk} + u_{mc}, \\
u_s &= \delta_k + \delta_{mk} + \delta_{mc},
\end{aligned}
\tag{1}
$$

where $C_{mn}, C_{ms}, C_{kn}, C_{ks}$—dashpot viscosity; $K_{kn}, K_{ks}, K_{mn}, K_{ms}$—spring stiffness; u_{mk}, δ_{mk}—the spring displacement of Maxwell model element in normal and shear direction; u_{mc}, δ_{mc}—the dashpot displacement of Maxwell model element in normal and shear direction; f_n, f_s—normal and shear force at the contact point; u_n, u_s—normal and shear displacement at the contact point; u_k, δ_k—the displacement of Kelvin model element in normal and shear direction.
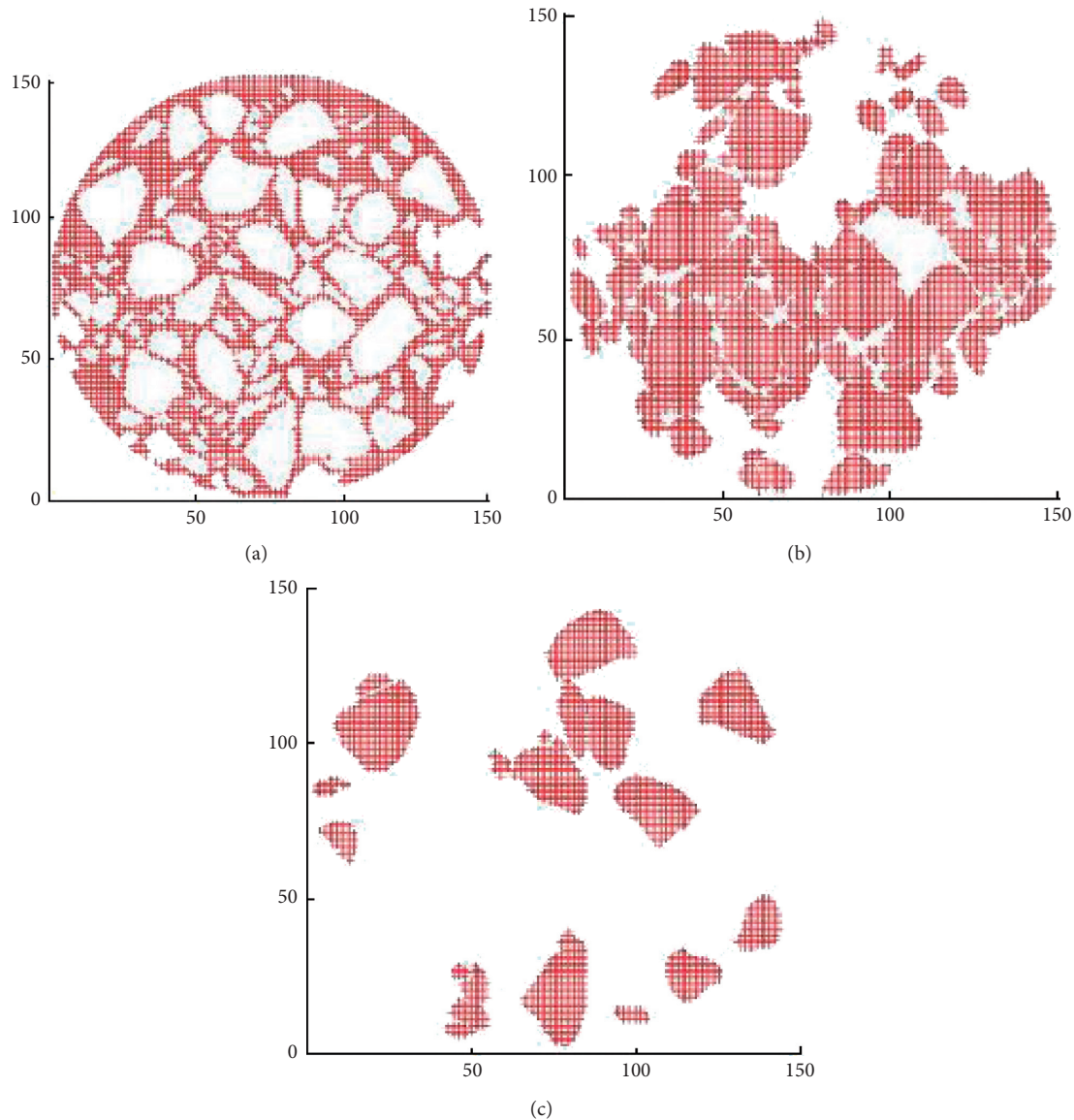
Figure 4: The coordinates of each component. (a) Asphalt mortar. (b) Aggregate. (c) Recycled aggregate.

4. Results and Discussion

4.1. Verification of the Discrete Element Model. As illustrated in Figure 8, there are differences between the discrete element simulation test and the test results. Because the parameters in the two-dimensional mechanical model were greatly simplified, resulting in a low consistency between the virtual model and test sample. What is more, in the mesoscopic model constructed by the DEM, the air void in the model was different from the test specimen. The components of the recycled asphalt mixture were complex, and the mesoscopic composition of structure was not clear, and the recognition of particle edge, binarization, and the co-ordinate reading of each component resulted in the loss of particle image information in the image processing. However, the overall simulation reflected the splitting strength value of the numerical specimens of recycled asphalt

mixture, which showed that the discrete element simulation of splitting strength test was feasible under certain conditions.

4.2. Velocity Vector Evolution Analysis. The indirect tensile test of the two-dimensional digital specimen was carried out by controlling the moving speed of the loading plate. The internal damage of the digital specimens with different RAP materials at the initial and completion loading was measured, respectively, which performed the failure process under the virtual test.

In Figure 9, the deformation of the digital specimen at the initial loading is mainly void compression. The voids were compressed during the initial loading, and the specimens reached the dense state. It showed that the mesoscopic performance of the digital specimens was consistent with the
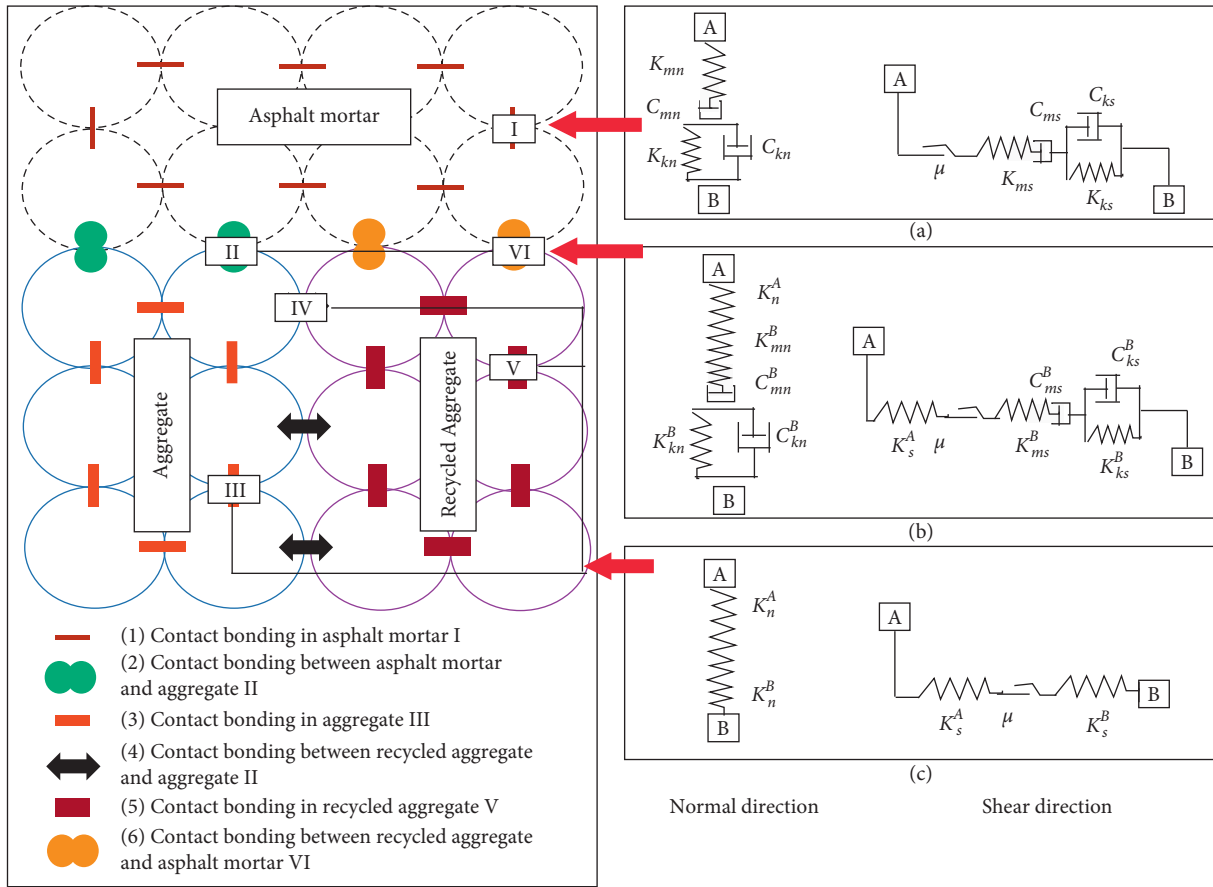
Figure 5: Constitutive model of recycled asphalt mixture.

macroscopic phenomenon. Furthermore, the compactness of digital specimens with different RAP material contents is different after initial loading. When the initial loading of specimen was completed, the color of the velocity vector area with the HMA was obviously lighter than that of others. On the other hand, the color of the specimen with 40% RAP materials was the darkest, and the sample had been deformed. During the simulation loading process, the HMA reached the dense state at the latest, but the compaction of digital specimen mixed with different RAP material contents was relatively faster. It showed that the digital specimen with higher RAP material contents could reach the compact state easily in the simulation test. At the same loading time step, when the compaction of specimen was faster, the pressure-bearing time would be longer, and the occurrence of cracks would be easier. Therefore, the addition of RAP materials to the asphalt mixture had an impact on the compactness. What is more, the crack resistance of the mixture decreased as the content of RAP materials increased.

Figure 10 shows that the specimens with different RAP material contents all have shear failure, and the shear surface has been marked in red in the figure. The digital specimens suffered shear failure when the load plate pressure reached the peak. Moreover, the shear failure surface was roughly divided into four directions and far away from the moving loading plate. And the failure surface was also shown as shear failure along a certain angle. The sample test and the

mesoscopic characterization of numerical model were almost coincident, which verified the reliability of the DEM. When the loading was completed, parts of the particles were scattered of the digital specimens with 0%, 10%, and 20% RAP materials, while more particles in the specimens with 40% RAP materials were scattered in the model area, and the damage was obvious. Because the specimen with 40% RAP materials had already been damaged before the stop node was controlled by the loading plate, the loading plate still applied load after failure, which caused the particles to rearrange and bear pressure randomly.

4.3. Evolutionary Law of the Force Chain.

Figure 11 shows the contact force chain gradually running through the entire specimen as the load time increased. Below the loading plate, its force chain was mainly manifested as a pressure force chain, which extended in the vertical direction. In addition, the force chain on the outer edge of the specimen was mainly manifested as a tensile force chain distributed along the edge of the test specimen. At the same time, the particles contacted and transferred the load, and the internal pressure of the specimen was kept in a synchronized state. The edge area of tensile stress of the digital specimen with 40% RAP materials was obviously more than that of others in the initial loading, and the internal compressive stress area of the specimen had the wider influence range. It indicated that the
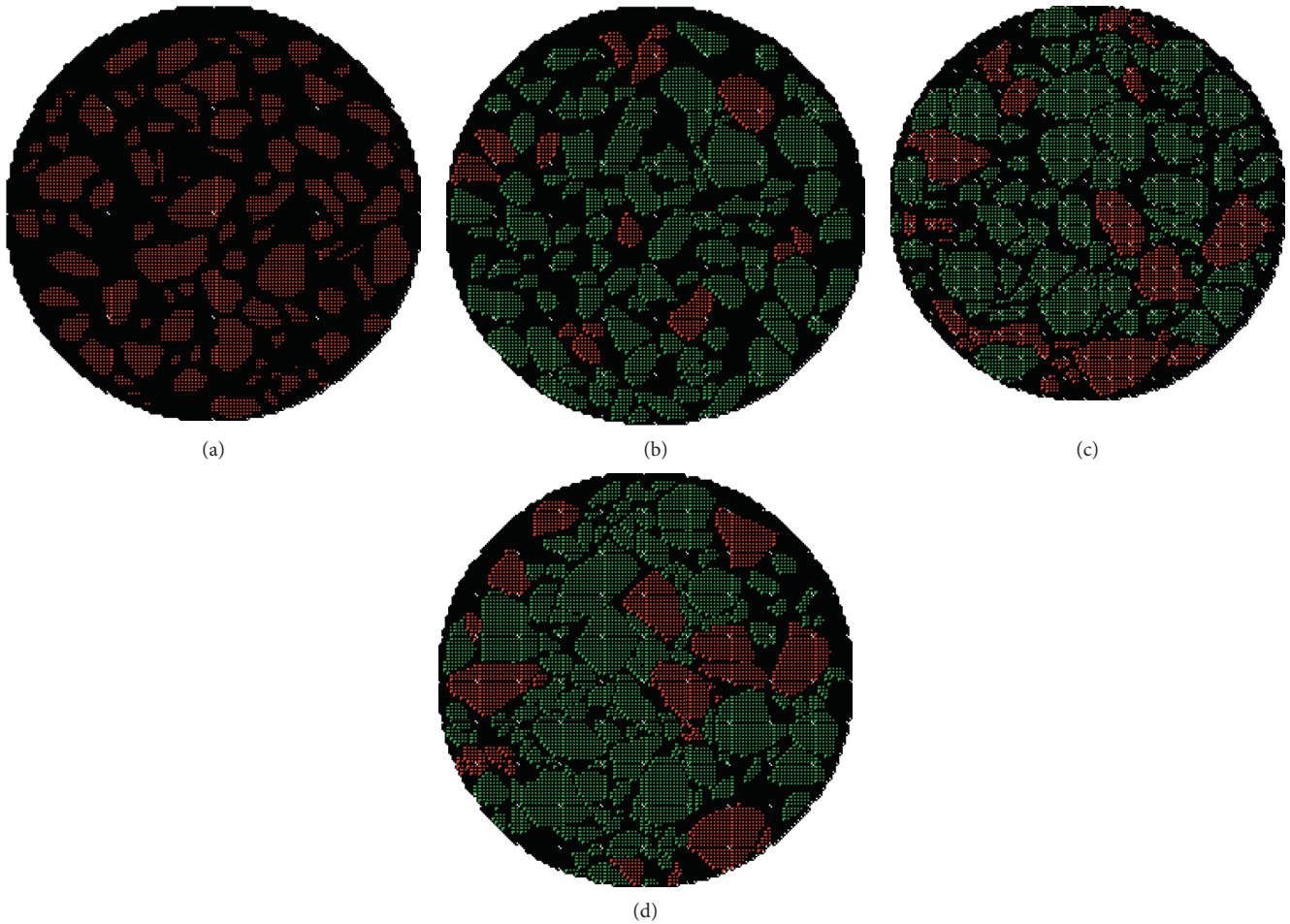
FIGURE 6: The two-dimensional digital specimen of the recycled asphalt mixture. (a) 0% RAP. (b) 10% RAP. (c) 20% RAP. (d) 40% RAP.

TABLE 4: Aggregate particle parameters.

Parameters	Density	Normal stiffness (particle)	Shear stiffness (particle)	Normal stiffness (contact)	Shear stiffness (contact)
Unit	kg/m^3	10^9N/m	10^9N/m	10^9N/m	10^9N/m
Value	2650	2.0	2.0	1.0	1.0

TABLE 5: Parameter values of Burger's model.

Parameters		Value
Maxwell	Normal stiffness (10^9N/m)	70.0
	Normal viscosity (Pa·s)	6.0
	Shear stiffness (10^9N/m)	25.0
	Shear viscosity (Pa·s)	2.0
Kelvin	Normal stiffness (10^9N/m)	4.0
	Normal viscosity (Pa·s)	0.5
	Shear stiffness (10^9N/m)	1.5
	Shear viscosity (Pa·s)	0.1
	Coefficient of friction	0.5
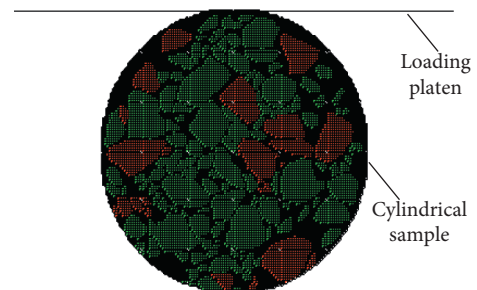
FIGURE 7: Loading model with specimen.

crack resistance of the digital specimen with 40% RAP materials was poor. The edge force chain of the HMA was tensile force, and the internal pressure force chain was mainly distributed. It was obviously better than the digital specimen mixed with RAP materials, indicating that the crack resistance of the HMA was better than that of the recycled asphalt mixture. Therefore, the force chain distribution diagram showed the mechanical response of the
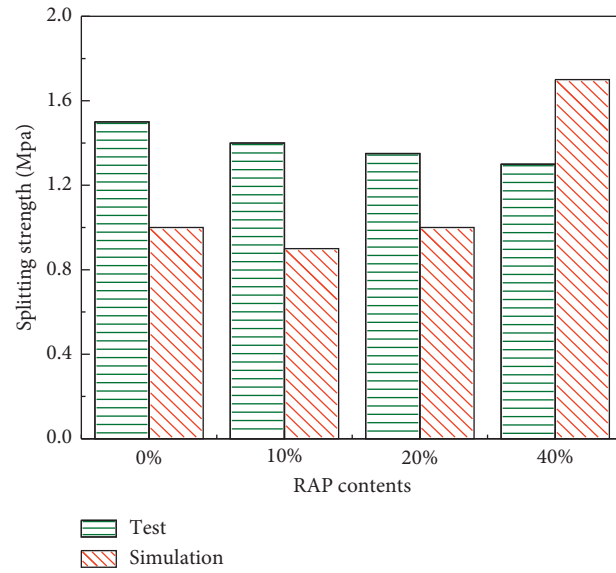
FIGURE 8: The discrete element simulation and experimental results.
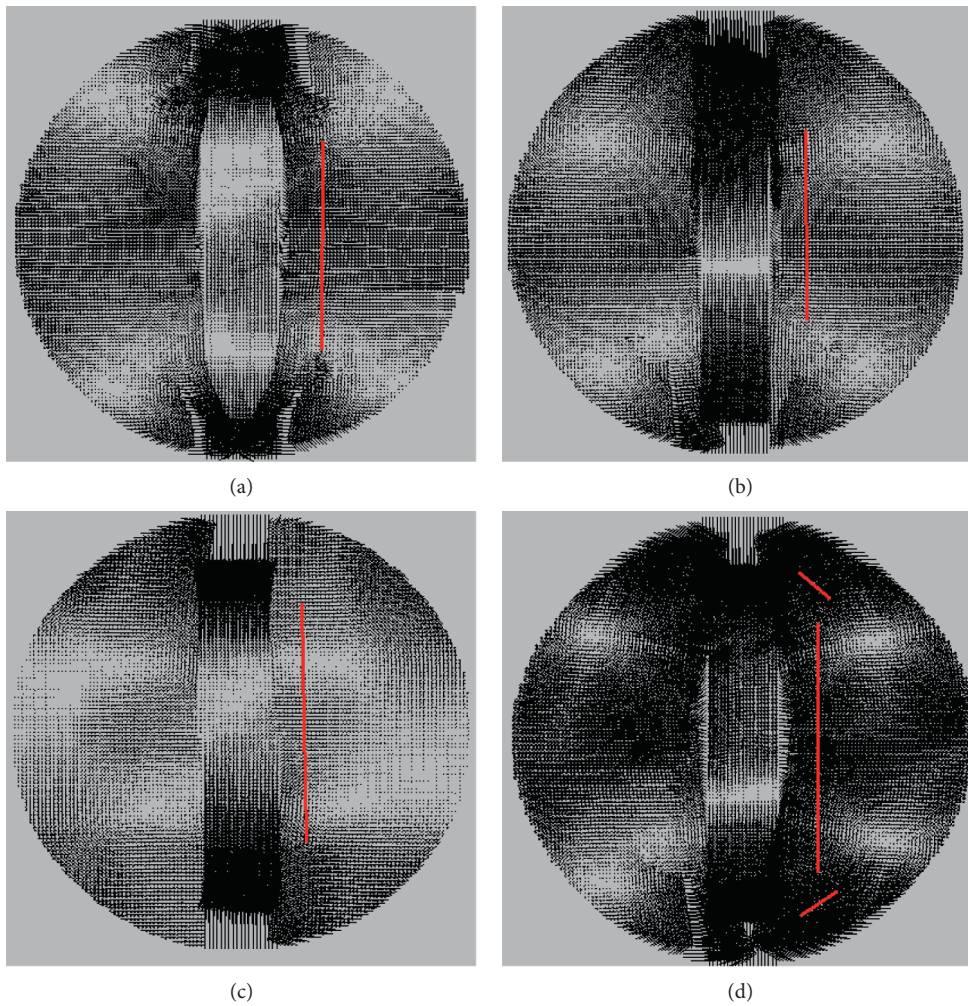
FIGURE 9: The vector diagram of specimens with different RAP content at the initial loading speed. (a) 0% RAP. (b) 10% RAP. (c) 20% RAP. (d) 40% RAP.

(a)

(b)

(c)

(d)
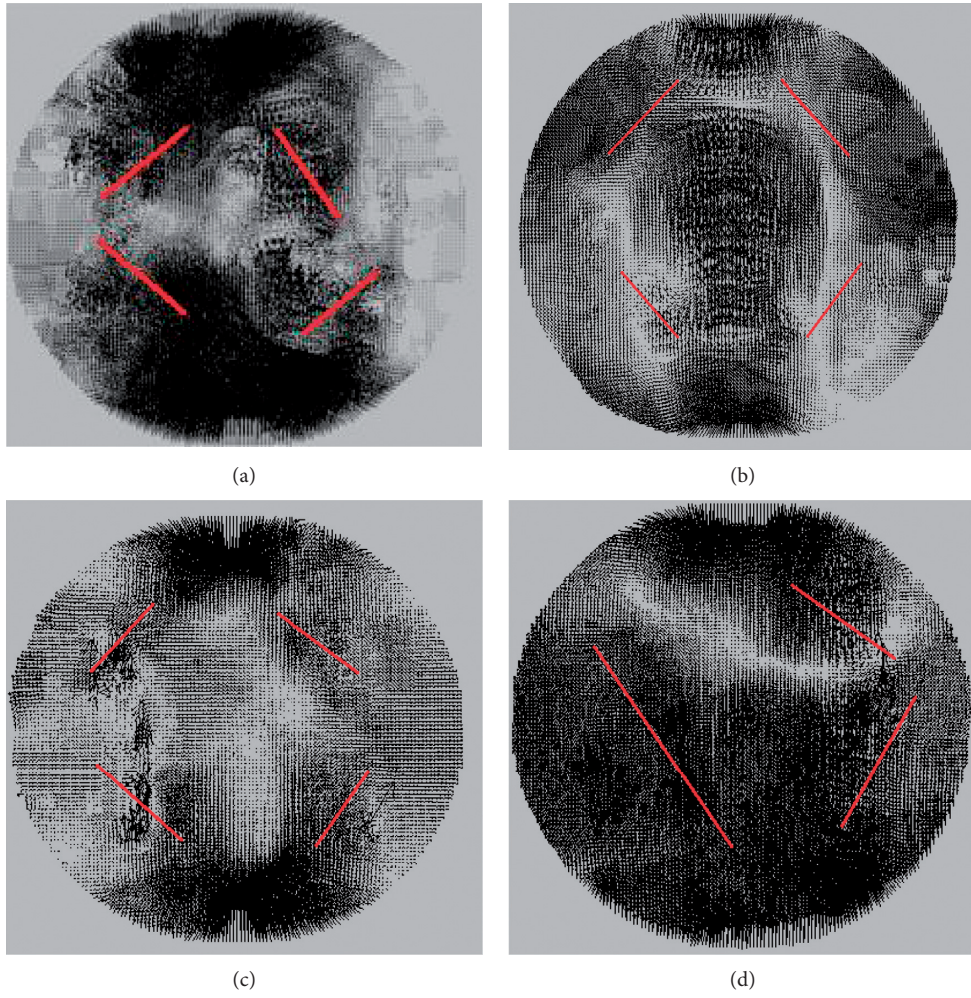
Figure 10: The vector diagram of specimens with different RAP material contents at the completed loading speed. (a) 0% RAP. (b) 10% RAP. (c) 20% RAP. (d) 40% RAP.

(a)

(b)
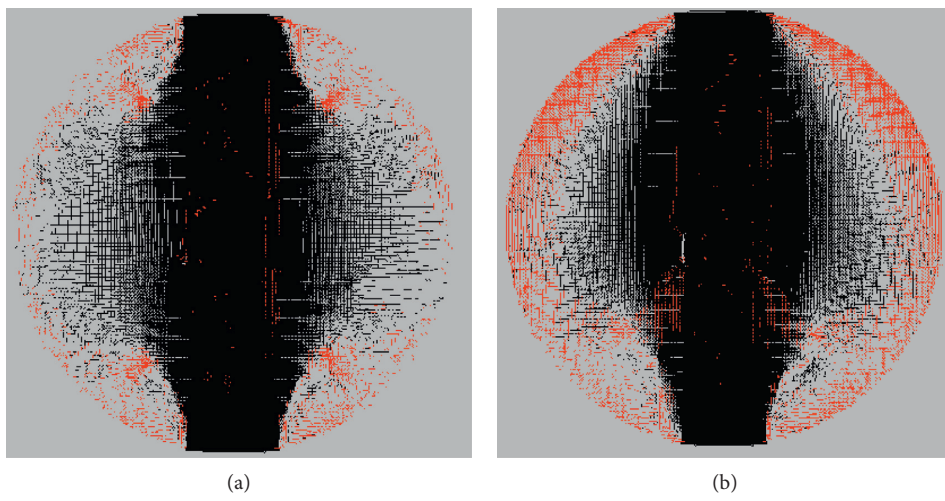
Figure 11: Continued.

(c)   (d)
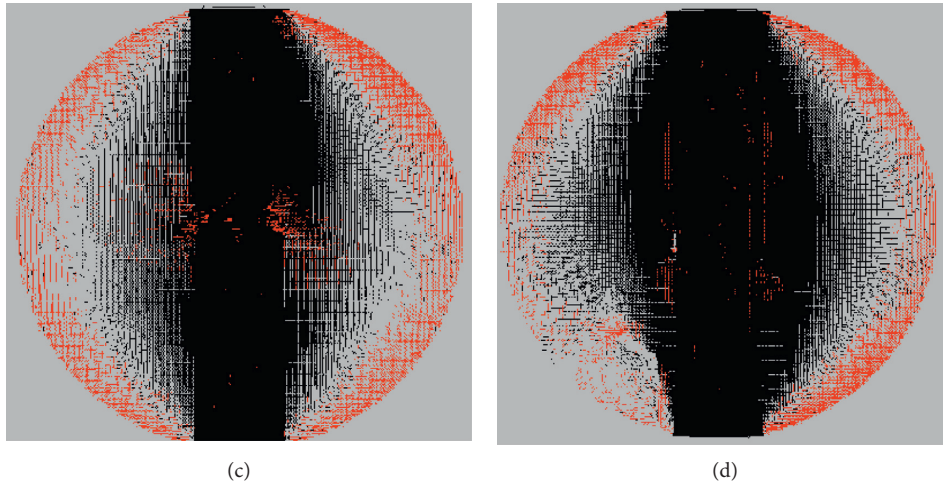
FIGURE 11: The force chain distribution diagram of specimens with different RAP material contents at the initial loading speed. (a) 0% RAP. (b) 10% RAP. (c) 20% RAP. (d) 40% RAP.

(a)   (b)

(c)   (d)
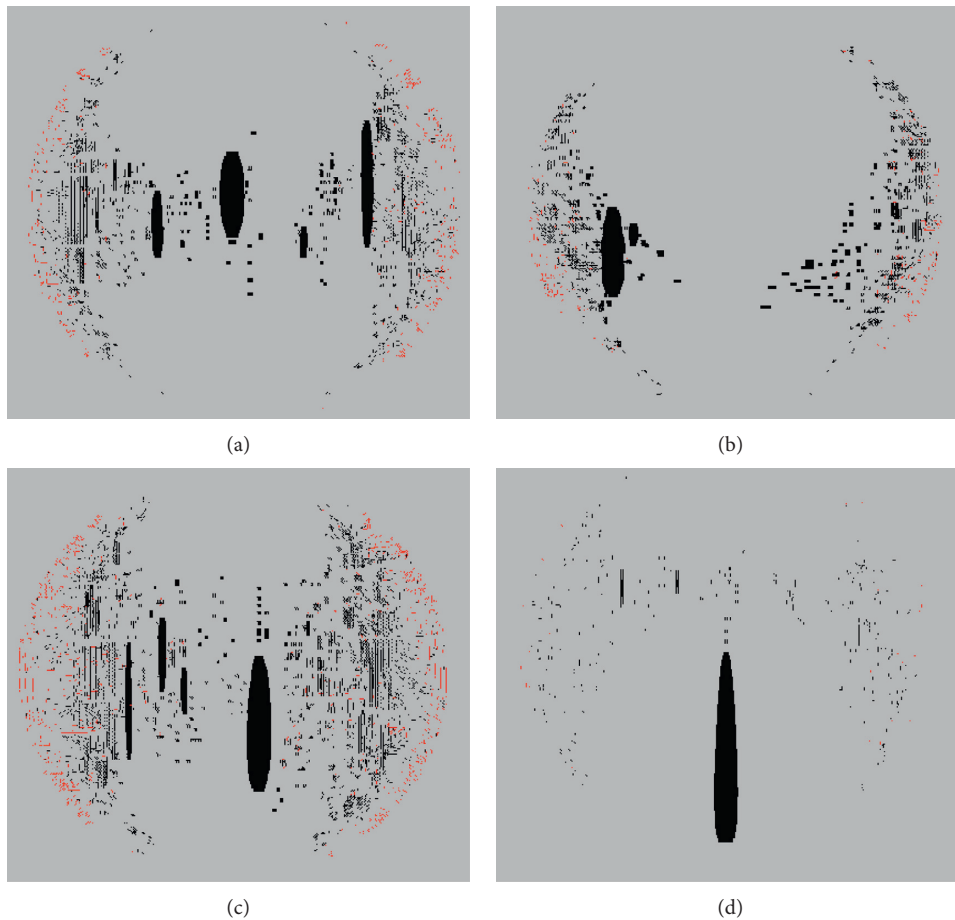
FIGURE 12: The force chain distribution diagram of specimens with different RAP material contents at the completed loading speed. (a) 0% RAP (b) 10% RAP. (c) 20% RAP. (d) 40% RAP.

indirect tensile test in mesoscopic perspective. Meanwhile, it explained the mesoscopic evolution rule of the indirect tensile test and was consistent with the macroscopic results.

As shown in Figure 12, when the test specimen is loaded completed, the digital test specimen all occurs shear failure. The contact force between the particles in

each test specimen gradually weakened, the particles separated under the loading, and the particles were rearranged randomly under the external loading. It could be shown that the internal particle contact force of the specimen with 40% RAP materials was more damaged than other specimens when the loading was completed. Furthermore, the disk units of the model were scattered around, parts of the aggregate particles were obviously broken, and the contact force chain disappeared. The macroscopic appearance of the indirect tensile test was that the specimen partially cracked at the initial loading. As the load increased, the cracks rapidly expanded to penetration, and the specimen eventually failed.

5. Conclusion

The indirect tensile simulation test explained internal damage law from mesoscopic perspective. It verified the feasibility of the DEM and provided the mesoscopic study of the traditional test method. The main conclusions are as follows:

(i) The two-dimensional digital image reconstruction in DEM was carried out, and the model parameter was selected to complete the virtual mechanical test simulation of the digital reconstruction specimen.

(ii) The indirect tensile simulation test results showed that there is still a certain gap with the laboratory test after the comparison of mesoscopic parameters. However, the simulation results could reflect the split strength of the numerical specimens.

(iii) When the loading was completed, the specimen with 40% RAP materials was damaged more than other specimens. Meanwhile, more particles in the specimens with 40% RAP materials were scattered. The high RAP material contents in recycled materials will have a negative impact on the crack resistance of the mixture.

(iv) The indirect tensile simulation test of recycled asphalt mixture explained the internal damage law in the mesoscopic perspective and provided a mesoscopic method of the traditional laboratory test method of recycled asphalt mixture.

Data Availability

The data used to support the findings of this study are included within the article.

Conflicts of Interest

The authors declare that they have no conflicts of interest.

Acknowledgments

References

[1] L.-s. Gao, H.-c. Dan, and L. Li, "Response analysis of asphalt pavement under dynamic loadings: loading equivalence," *Mathematical Problems in Engineering*, vol. 2017, Article ID 7020298, 15 pages, 2019.

[2] S. Sun, P. Li, J. Akhtar, J. Su, and C. Dong, "Analysis of deformation behavior and microscopic characteristics of asphalt mixture based on interface contact-slip test," *Construction and Building Materials*, vol. 257, 2020.

[3] S. Lv, L. Hu, C. Xia et al., "Development of fatigue damage model of asphalt mixtures based on small-scale accelerated pavement test," *Construction and Building Materials*, vol. 260, 2020.

[4] X. Ji, Y. Jiang, H. Zou, F. Cao, and Y. Hou, "Application of numerical simulation method to improve shear strength and rutting resistance of asphalt mixture," *International Journal of Pavement Engineering*, vol. 21, no. 1, pp. 112–121, 2018.

[5] F. Yang, H. Li, G. Zhao, P. Guo, and W. Li, "Mechanical performance and durability evaluation of sandstone concrete," *Advances in Materials Science and Engineering*, vol. 2020, Article ID 2417496, 10 pages, 2020.

[6] H. Li, W. Wang, W. Li, A. Taoum, G. Zhao, and P. Guo, "Replacement of limestone with volcanic stone in asphalt mastic used for road pavement," *Arabian Journal for Science and Engineering*, vol. 44, no. 10, pp. 8629–8644, 2019.

[7] X. Zhu, Y. Sun, C. Du, W. Wang, J. Liu, and J. Chen, "Rutting and fatigue performance evaluation of warm mix asphalt mastic containing high percentage of artificial RAP binder," *Construction and Building Materials*, vol. 240, 2020.

[8] Z. Xie, H. Rizvi, C. Purdy, A. Ali, and Y. Mehta, "Effect of rejuvenator types and mixing procedures on volumetric properties of asphalt mixtures with 50% RAP," *Construction and Building Materials*, vol. 218, pp. 457–464, 2019.

[9] S. Mo, Y. Wang, F. Xiong, C. Ai, D. Wang, and G. Y. A. Tan, "Changes of asphalt fumes in hot-mix asphalt pavement recycling," *Journal of Cleaner Production*, vol. 258, 2020.

[10] L. Gaillard, J. C. Quezada, C. Chazallon, and P. Hornych, "Resilient modulus prediction of RAP using the contact dynamics method," *Transportation Geotechnics*, vol. 24, 2020.

[11] Y. Yan, R. Roque, C. Cocconcelli, M. Bekoe, and G. Lopp, "Evaluation of cracking performance for polymer-modified asphalt mixtures with high RAP content," *Road Materials and Pavement Design*, vol. 18, no. sup1, pp. 450–470, 2017.

[12] Y. Yan, R. Roque, D. Hernando, and S. Chun, "Cracking performance characterisation of asphalt mixtures containing reclaimed asphalt pavement with hybrid binder," *Road Materials and Pavement Design*, vol. 20, no. 2, pp. 347–366, 2019.

[13] J. Montañez, S. Caro, D. Carrizosa, A. Calvo, and X. Sánchez, "Variability of the mechanical properties of Reclaimed Asphalt Pavement (RAP) obtained from different sources," *Construction and Building Materials*, vol. 230, 2020.

[14] H. Goli and M. Latifi, "Evaluation of the effect of moisture on behavior of warm mix asphalt (WMA) mixtures containing recycled asphalt pavement (RAP)," *Construction and Building Materials*, vol. 247, 2020.

[15] M. Rathore and M. Zaumanis, "Impact of laboratory mixing procedure on the properties of reclaimed asphalt pavement mixtures," *Construction and Building Materials*, vol. 264, 2020.

[16] J. Zhu, T. Ma, J. Fan, Z. Fang, T. Chen, and Y. Zhou, "Experimental study of high modulus asphalt mixture containing reclaimed asphalt pavement," *Journal of Cleaner Production*, vol. 263, 2020.

[17] H. Ziari, A. Moniri, P. Bahri, and Y. Saghafi, "The effect of rejuvenators on the aging resistance of recycled asphalt mixtures," *Construction and Building Materials*, vol. 224, pp. 89–98, 2019.

[18] D. Zhang, S. Hou, J. Bian, and L. He, "Investigation of the micro-cracking behavior of asphalt mixtures in the indirect tensile test," *Engineering Fracture Mechanics*, vol. 163, pp. 416–425, 2016.

[19] F. Gong, Y. Liu, X. Zhou, and Z. You, "Lab assessment and discrete element modeling of asphalt mixture during compaction with elongated and flat coarse aggregates," *Construction and Building Materials*, vol. 182, pp. 573–579, 2018.

[20] H. Feng, M. Pettinari, B. Hofko, and H. Stang, "Study of the internal mechanical response of an asphalt mixture by 3-D discrete element modeling," *Construction and Building Materials*, vol. 77, pp. 187–196, 2015.

[21] F. Masi, I. Stefanou, V. Maffi-Berthier, and P. Vannucci, "A Discrete Element Method based-approach for arched masonry structures under blast loads," *Engineering Structures*, vol. 216, 2020.

[22] Y. Wang, D. Zhang, L. Yang, T. Cui, H. Jing, and X. Zhong, "Modeling the interaction of soil and a vibrating subsoiler using the discrete element method," *Computers and Electronics in Agriculture*, vol. 174, 2020.

[23] B. Owen, A. M. A. Nasar, A. R. G. Harwood, S. Hewitt, N. Bojdo, and B. Keavney, "Vector-based discrete element method for solid elastic materials," *Computer Physics Communications*, vol. 254, 2020.

[24] J. Wu, D. Li, B. Zhu, and C. Wu, "Milling process simulation of old asphalt mixture by discrete element," *Construction and Building Materials*, vol. 186, pp. 996–1004, 2018.

[25] T. Ma, Y. Zhang, D. Zhang, J. Yan, and Q. Ye, "Influences by air voids on fatigue life of asphalt mixture based on discrete element method," *Construction and Building Materials*, vol. 126, pp. 785–799, 2016.

[26] Y. D. Wang, B. Keshavarzi, and Y. R. Kim, "Fatigue performance analysis of pavements with RAP using viscoelastic continuum damage theory," *KSCE Journal of Civil Engineering*, vol. 22, no. 6, pp. 2118–2125, 2018.

[27] K. H. G. Qian, J. Li, X. Bai, and N. Li, "Compaction process tracking for asphalt mixture using discrete element method," *Construction and Building Materials*, vol. 235, 2020.

[28] H. Yu and S. Shen, "Impact of aggregate packing on dynamic modulus of hot mix asphalt mixtures using three-dimensional discrete element method," *Construction and Building Materials*, vol. 26, no. 1, pp. 302–309, 2012.

[29] JTG E20-2011, *Standard Test Methods of Bituminous Mixtures for Highway Engineering of China*, Ministry of Transport, Beijing, China, 2011.

[30] Z. Zhang, W. Gao, K. Li, and B. Li, "Numerical simulation of rock mass blasting using particle flow code and particle expansion loading algorithm," *Simulation Modelling Practice and Theory*, vol. 104, 2020.

[31] M. Baqersad, A. Hamedi, M. Mohammadafzali, and H. Ali, "Asphalt mixture segregation detection: digital image processing approach," *Advances in Materials Science and Engineering*, vol. 2017, pp. 1–6, 2017.

[32] S. Chen, Z. You, S.-L. Yang, A. Garcia, and L. Rose, "Influence of air void structures on the coefficient of permeability of asphalt mixtures," *Powder Technology*, vol. 377, pp. 1–9, 2021.

[33] C. Nie, J. Li, and S. Wang, "Modeling the effect of spending on cyber security by using surplus process," *Mathematical Problems in Engineering*, vol. 2020, pp. 1–10, 2020.

[34] P. K. Das, N. Kringos, and B. Birgisson, "Numerical study on the effect of mixture morphology on long-term asphalt mixture ageing," *International Journal of Pavement Engineering*, vol. 16, no. 8, pp. 710–720, 2014.

[35] J. Zhang, Z. Li, H. Chu, and J. Lu, "A viscoelastic damage constitutive model for asphalt mixture under the cyclic loading," *Construction and Building Materials*, vol. 227, 2019.

[36] H. Feng, M. Pettinari, and H. Stang, "Study of normal and shear material properties for viscoelastic model of asphalt mixture by discrete element method," *Construction and Building Materials*, vol. 98, pp. 366–375, 2015.

Research Article

Laboratory Investigation on the Performance of Cement Stabilized Recycled Aggregate with the Vibration Mixing Process

Yongliang Wang [1], **Jinbao Zhang**,[1] **Xuetao Wang**,[1] **and Zhi Zhang**[2]

[1]*Qinghai Transportation Holding Group Co., Ltd., Xining 810001, China*
[2]*Qinghai Provincial Traffic Engineering Technology Service Center, Xining 810001, China*

Correspondence should be addressed to Yongliang Wang; wangyongliang2013@163.com

The objective of this article is to investigate the effect of the vibration mixing process (VMP) on the performance of cement stabilized recycled aggregate (CSRA). The ordinary mixing process (OMP) was also used for comparative analysis with the VMP. The performance of CSRA with different cement content was tested and comprehensively analyzed by the unconfined compressive strength test, dry shrinkage test, and temperature shrinkage test. The results showed that compared with OMP, VMP can greatly improve the compressive strength, dry shrinkage, and temperature shrinkage properties of CSRA. The optimum parameters of vibration time and vibration frequency in VMP were 30 s and 40 Hz, respectively. The reason why VMP can improve the performance of CSRA was that VMP strengthened the aggregate and interface transition zone and introduced microbubbles to optimize the pore structure.

1. Introduction

Because China's economy has developed rapidly in recent years, the existing transportation infrastructure cannot meet the increasing demand for transportation. Therefore, many roads and bridges need to be rebuilt and expanded, which will result in producing a huge amount of waste concrete. Due to the fact that the disposal of waste concrete by landfill will occupy precious land resources and damage the environment seriously, most of the waste concrete was used to produce recycled aggregate that can be directly utilized in road construction. The recycled aggregates are obtained by crushed, sieved, washed, and dried process from the demolished concrete structures. Old mortar is attached to the surface of natural aggregates, which leads to the poor performance of recycled aggregate. Compared to natural aggregate, recycled aggregate has a lower density, higher porosity, and higher water absorption. Therefore, recycled aggregates are only utilized in the low-grade road construction for road bases and surface layer of concrete in China. Cement stabilized recycled aggregate (CSRA)

generally has insufficient strength and shrinkage cracking problems, which limit its application in high-grade road engineering. Currently, the recycled aggregates are strengthened before the mixing process to improve the performance of CSRA. Physical and chemical methods were proposed: (I) removing adhered mortar of coarse recycled aggregates by machine milling or soaking in acid solution and (II) filling surface pores of coarse recycled aggregates by soaking in pozzolan slurry including fly ash and silica fume. Many studies have shown that the strength process of recycled aggregate can greatly improve the mechanical properties of CSRA and improve shrinkage properties. Al-Bayati et al. [1] found that the water absorption of recycled aggregate was reduced by 27% with combined treatment of heat process at 350°C and mechanical process for 60 s. Shaban et al. [2] soaked recycled aggregate in 40% fly ash and 3% nanosilica fume mixed slurries for 4 h finding that water absorption of recycled aggregate was lower by 50–55% than before and particle densities increased by 10–11%. However, the strength process will greatly increase the cost and time of the production of CSRA.

In the process of the production of CSRA, mixing is an indispensable and important process. Different mix parameters resulted in various performances of CSRA [3–5]. Han and Ferron [6] studied the relationship between mixing speed and hydration of cement pastes and found that higher speed mixing can increase the rate of cement hydration resulting in larger agglomerates. Chang and Peng [3] prepared high-performance concrete by six mixing processes and found that workability can be improved by adding all superplasticizers in water during the mixing process. Yao et al. [5] showed that the compress strength of concrete prepared by the double-blade mixer was higher than that prepared by the ordinary biaxial mixer. Feng [7] found that the vibration mixing process can make the mixture more uniform and improve the quality of the mixture. The performance of cement stabilized gravel is closely related to the degree of mixing, and the type of mixer has an important influence on the performance of the mixture [8, 9]. Zhang et al. [10] developed a new vibrating mixing instrument for cement stabilized crushed stone, and the strength of cement stabilized crushed stone prepared by vibration mixing increased by 12.8%. Li et al. [11] found that when the strength of cement stabilized gravel was the same, the cement content of cement stabilized crushed stone prepared by vibrating mixing process was lower than that of cement stabilized gravel prepared by the ordinary mixing process. Zhao et al. [12] analyzed the curve of the compressive strength of cement stabilized gravel prepared by VMP under different vibration parameters. The results showed that compared with ordinary mixing, the compressive strength of the cement stabilized gravel prepared by vibrating mixing increased and the coefficient of variation decreased. Dong et al. [13] showed that compared with ordinary mixing, vibrating mixing can improve strength, reduce water loss, and reduce shrinkage strain and the coefficient of shrinkage of cement stabilized crushed stone. These studies have shown that vibration mixing can significantly improve the performance of cement concrete. These studies show that optimization of the mixing process can significantly improve the performance of cement concrete. Compared with the traditional mixing process, vibration mixing is accompanied by mechanical vibration during mixing, which reduces the viscosity and internal friction between cementitious material and the aggregate greatly. Cement paste is easy to enter the voids and cracks on the surface of recycled aggregate and enhance the bonding force between cement paste and aggregates. It can be inferred that the cement paste can completely wrap the recycled aggregate with VMP, which will repair surface defects of recycled aggregate, such as cracks and large voids. The performance of CSRA, such as strength and shrinkage, also may be enhanced by the mixing process with vibration. However, few studies reported this.

The objective of this article is to investigate the effect of VMP on the performance of CSRA. The ordinary mixing process (OMP) was also used for comparative analysis with the vibration mixing process (VMP). Three groups of specimens with different water–cement ratios were prepared with VMP and OMP. The compressive strength, dry shrinkage, and temperature shrinkage were tested and comprehensively analyzed. The optimal parameters of VMP for CSRA were obtained by systematic analysis of experimental data. The mechanism for improving the performance of CSRA with VMP was also discussed.

2. Materials and Testing Methods

2.1. Materials

2.1.1. Cement.
P.C 32.5R cement from Qinghai Qilianshan Cement Co., Ltd., was selected, and physical properties of cement were tested according to "Test Methods of Cement and Concrete for Highway Engineering" (JTG E30-2005) [14]. The test results are shown in Table 1.

2.1.2. Aggregate.
Recycled coarse aggregates were provided by Huashan Road and Bridge Recycling Co., Ltd. Physical properties of coarse recycled aggregates are shown in Table 2. Natural fine aggregates were produced by the China Railway 17th Bureau Group Co., Ltd. Physical properties of fine natural aggregates are shown in Table 3.

2.1.3. Aggregate Gradation.
According to "Technical Guidelines for Construction of Highway Roadbases" (JTG F20-2015) [15], the aggregate gradation of the CSRA is given in Figure 1.

2.2. Sample Preparation.
Recycled coarse aggregates were used to completely replace natural coarse aggregates for preparing CSRA. According to "Test Method of Materials Stabilized with Inorganic Binders for Highway Engineering" (JTG E51-2009) [16], the optimum water content and maximum dry density of CSRA with a cement content of 3%, 4%, and 5% were tested and obtained. The experimental results of the optimum water content and maximum dry density are shown in Table 4.

The preparation of CSRA specimens was divided into four steps. At first, the quality of each component in the CSRA was weighed, including cement, coarse and fine aggregates, and the optimal content of water. Secondly, the cement, coarse and fine aggregates, and water were poured into the mixer and mixed for 2 minutes. The mixture was mixed by the double horizontal shaft vibration mixer produced by Henan Wanli Transportation Technology Group Co., Ltd. The appearance and structure of the mixer are shown in Figure 2. Vibration time and vibration frequency were considered to be important technical parameters that affect the performance of the mixture. The range of vibration time was 20~60 s. The range of vibration frequency was 20~60 Hz. In the third step, the mixture was poured into the mold. The mold was placed on the press machine and subjected to a pressure loaded at a speed of 1 mm/min. In the fourth step, after demolding, the samples were placed in a curing chamber with a relative humidity greater than 95% at 20°C for 7 days.

TABLE 1: Physical properties of cement.

Fineness (%)	Setting time (min)		Volume stability (mm)	Compressive strength (MPa)		Flexural strength (MPa)	
	Initial setting time	Final setting time		3 d	28 d	3 d	28 d
4.1	221	383	1.5	22.9	34.3	4.3	6.4

TABLE 2: Physical properties of coarse aggregates.

Particle size (mm)	Specific gravity (g/cm^3)	Water absorption rate (%)	Needle-like content (%)	Crushed value (%)	Mud content (%)
5–10	2.660	4.20	4.5	—	0.3
10–20	2.636	2.17	4.3	24.5	0.2
20–30	2.625	2.20	3.2	—	0.2

TABLE 3: Physical properties of fine aggregates.

Apparent relative density	Fineness modulus	Angularity (%)
2.688	2.73	34.9
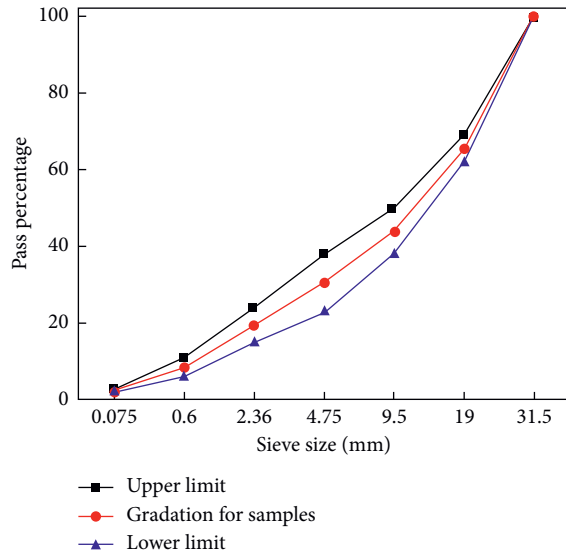
FIGURE 1: Gradation of CSRA.

TABLE 4: Optimum water content and maximum dry density of CSRA.

Cement content (%)	Optimum water content (%)	Maximum dry density (g/cm^3)
3	6.3	2.236
4	6.5	2.254
5	6.8	2.269

2.3. Test Methods

2.3.1. Unconfined Compressive Strength.
JTG E51-2009 T0805-1994 was followed to test the unconfined compressive strength of CSRA. The mixture was molded in a standard specimen of $\Phi150\,mm \times 150\,mm$ and cured with a temperature of $20 \pm 2°C$ and 95% relative humidity (RH) for 7 days. At the given curing age, the sample was loaded at a constant loading speed of 1 mm/min until failure. The test results were representative values of three repeated samples for each specific combination.

2.3.2. Drying Shrinkage.
JTG E51-2009 T0854-2009 was followed to test the dry shrinkage of CSRA. The test sample for the drying shrinkage test was a prism measuring $100\,mm \times 100\,mm \times 400\,mm$. The specimens were maintained in a standard curing room at a temperature of $20°C \pm 2°C$ and relative humidity above 95% for 7 days. Then, the drying shrinkage of each specimen was measured every day in the first week. After the first week, the drying shrinkage of the specimens was measured every two days. After 30 days, the drying shrinkage was recorded at 60 d, 90 d, 120 d, 150 d, and 180 d. Each result was the average obtained from the testing of three specimens per mixture.

The evaluation parameter of drying shrinkage performance can be calculated as follows:

$$
\begin{aligned}
\omega_i &= \frac{(m_i - m_{i+1})}{m_p}, \\[6pt]
\delta_i &= \frac{\left(\sum_{j=1}^{4} X_{i,j} - \sum_{j=1}^{4} X_{i+1,j}\right)}{2}, \\[6pt]
\varepsilon_i &= \frac{\delta_i}{l}, \\[6pt]
\alpha_{di} &= \frac{\varepsilon_i}{\omega_i}, \\[6pt]
\alpha_d &= \frac{\sum \varepsilon_i}{\sum \omega_i},
\end{aligned}
\tag{1}
$$

where ω_i is water loss rate by test time i, %; δ_i is drying shrinkage by test time i, mm; ε_i is dry shrinkage strain by test time i, %; α_{di} is dry shrinkage coefficient by test time i, %; α_d is total dry shrinkage coefficient, %; m_i is weight of specimen by test time i, g; $X_{i,j}$ is the reading value of jth dial indicator by test time i; l is the length of the standard test specimen, mm; and m_p is the weight of standard test specimen after being dried, g.

2.3.3. Temperature Shrinkage Test.
JTG E51-2009 T0855-2009 was followed to test the temperature shrinkage of CSRA. The temperature shrinkage test equipment was the same as the drying shrinkage test equipment. After being cured for 7 days, the sample was dried in a 105°C oven for 10 to 12 hours until a constant quality. The test temperature range was 40°C to −10°C, and every 10°C increase was used as an interval level, placing the sample in the curing chamber at

(a)

(b)
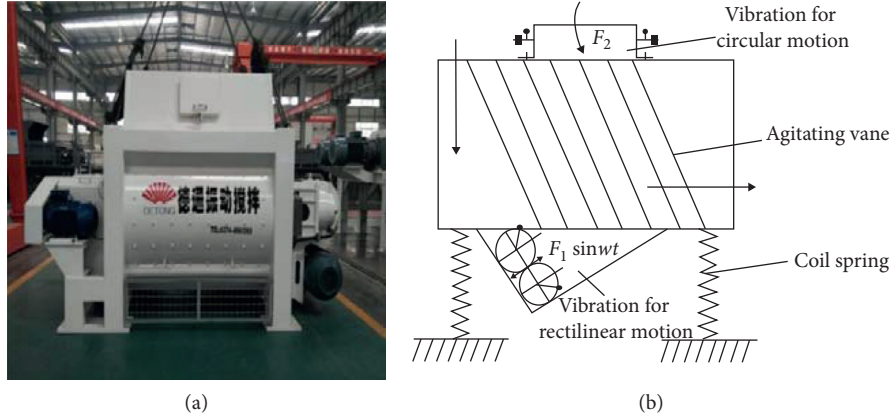
FIGURE 2: The appearance and the structure of the mixer. (a) The appearance of the mixer. (b) The structure of the mixer.

the set temperature for 5 hours and then measuring the temperature shrinkage of the specimen.

The temperature shrinkage coefficient can be calculated as follows:

$$\varepsilon_i = \frac{l_i - l_{i+1}}{L_0},$$
$$\alpha_t = \frac{\varepsilon_i}{t_i - t_{i+1}}, \tag{2}$$

where l_i is the average reading value of dial indicator at the ith temperature interval, mm; t_i is the ith temperature interval, °C; L_0 is the initial length of the specimen, mm; ε_i is the average temperature shrinkage strain at the ith temperature, %; and α_t is the temperature shrinkage coefficient.

2.3.4. Microstructure Characteristic.
The microstructure and pore structure of concrete prepared by OMP and VMP were examined. The samples were broken into small pieces and coated in gold; then, the environmental scanning electron microscope (ESEM) was used to obtain the interfacial transition zone (ITZ) of the concrete. The pore structure parameters of the concrete were determined by mercury intrusion porosimeter (MIP) at a pressure range of 135 kPa to 415 MPa.

3. Results and Discussion

3.1. Effect of Vibration Mixing Parameters on the Strength of CSRA

3.1.1. Vibration Time.
The unconfined compressive strength of the specimen was tested after 7 days of curing. The test results of CSRA with different cement content prepared with a vibration frequency of 40 Hz and vibration times of 20 s, 30 s, 40 s, 50 s, and 60 s are shown in Figure 3. As Figure 3 depicted, the cement content determines the compressive strength of CSRA. The unconfined compressive strength of CSRA increases with the increase of cement content. VMP was beneficial to improve the mechanical strength of CSRA. As the vibration time increases, the compressive strength increases. From the relationship curve between vibration time and compressive strength, it is found that there is an

optimal vibration time. When the vibration time is 30 s, the compressive strength has a significant increase. When the vibration time is 30 s and the vibration frequency is 40 Hz, the unconfined compressive strength of CSRA with 3% cement content is 3.0 MPa. It meets the road base strength requirements for medium and light traffic in China.

3.1.2. Vibration Frequency.
The unconfined compressive strength of CSRA with different cement content prepared with vibration time of 30 s and vibration frequency of 20 Hz, 30 Hz, 40 Hz, 50 Hz, and 60 Hz are shown in Figure 4. It is demonstrated in Figure 4 that the cement content determines the compress strength of CSRA, which is consistent with the conclusion of Section 3.1.1. As the vibration frequency increases, the unconfined compressive strength first increases and then decreases. From the relationship curve between vibration frequency and compressive strength, it is found that 40 Hz is the optimal vibration frequency. When the vibration time is 30 s and the vibration frequency is 40 Hz, the unconfined compressive strength of CSRA with 5% cement content is 4.2 MPa. It meets the road base strength requirements for medium and light traffic in China.

3.2. Effect of VMP on the Performance of CSRA

3.2.1. Compressive Strength.
The compressive strength of CSRA prepared by VMP was tested to compare with the compressive strength of CSRA prepared by OMP. Figure 5 shows the compressive strength of CSRA prepared by VMP and OMP at different ages. It can be seen from Figure 5 that compared with OMP, the compressive strength of CSRA was improved by VMP. When the cement content is 3%, 7-day compressive strength and 28-day compressive strength increase by 15.4% and 9.7%, respectively. When the cement content is 4%, the compressive strength of 7 days and 28 days increases by 16.2% and 9.6%, respectively. However, when the cement content is 5%, the compressive strength of 7 days and 28 days only increases by 4.5% and 5.1%. It indicates that the additional energy of vibration can destroy the cement agglomeration structure, and the cement is evenly dispersed into smaller cement particles, resulting in cement hydration
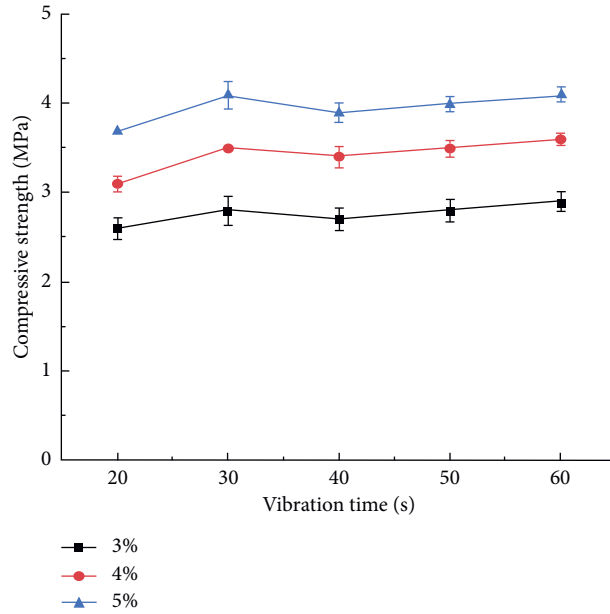
FIGURE 3: Seven-day compressive strength of CSRA with different vibration times.
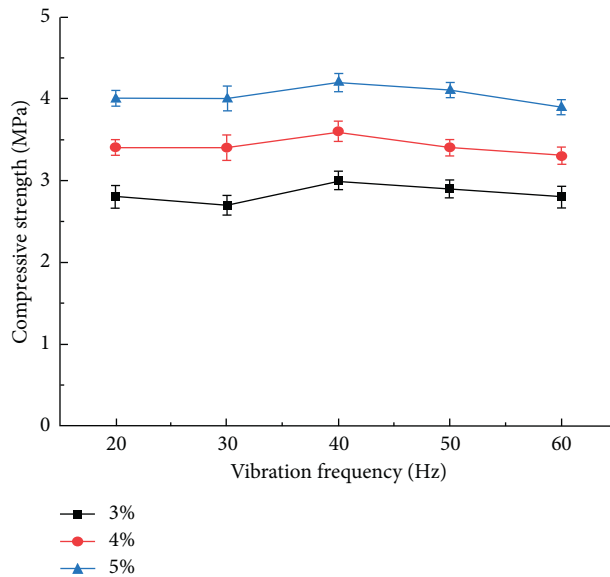
FIGURE 4: Seven-day unconfined compressive strength of CSRA with different vibration frequencies.

reaction more sufficient [17]. The smaller the cement content in CSRA, the more obvious this improvement effect of VMP. Figure 6 shows the micromorphology of the interface transition zone CSRA prepared by OMP and VMP. Compared with the specimen prepared by nonvibration mixing, the specimen prepared by vibrating mixing has a tighter bond and higher bonding strength between cement paste and recycle aggregate. Better interface transition zone results in higher compressive strength of cement stabilized recycle aggregate [18]. During the VMP, the collision of recycled aggregates will also strengthen the recycled aggregates, which is also beneficial to the improvement of the compressive strength of CSRA.

3.2.2. Drying Shrinkage. The drying shrinkage of CSRA prepared by VMP and OMP at different ages are shown in Figures 7–9. As shown from Figures 7–9 with the two mixing methods, as the age increases, the cumulative water loss rate and dry shrinkage strain of CSRA increase for all specimens. When the cement dosage is the same, the cumulative water loss rate, dry shrinkage strain, and dry shrinkage coefficient of vibration mixed CSRA are lower than those of ordinary mixed CSRA. As cement content increases, the drying shrinkage coefficient of CSRA increases. Although the increase in cement content is good for compressive strength, it is not good for shrinkage performance. It is worth noting that both strength and the drying shrinkage can be improved by VMP.

(a)

(b)

(c)
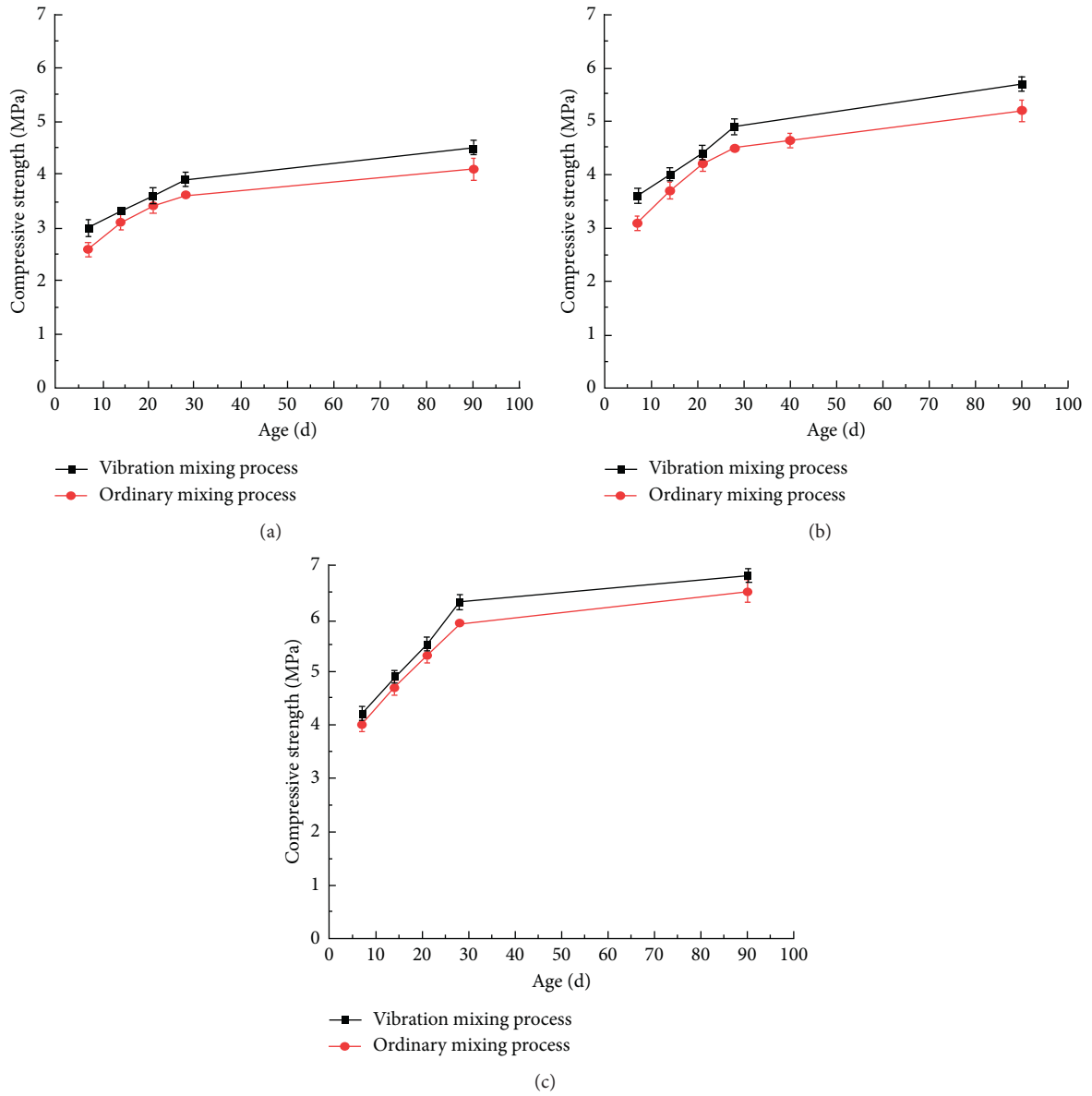
Figure 5: Compressive strength of CSRA with different cement contents. (a) 3%. (b) 4%. (c) 5%.

(a)

(b)
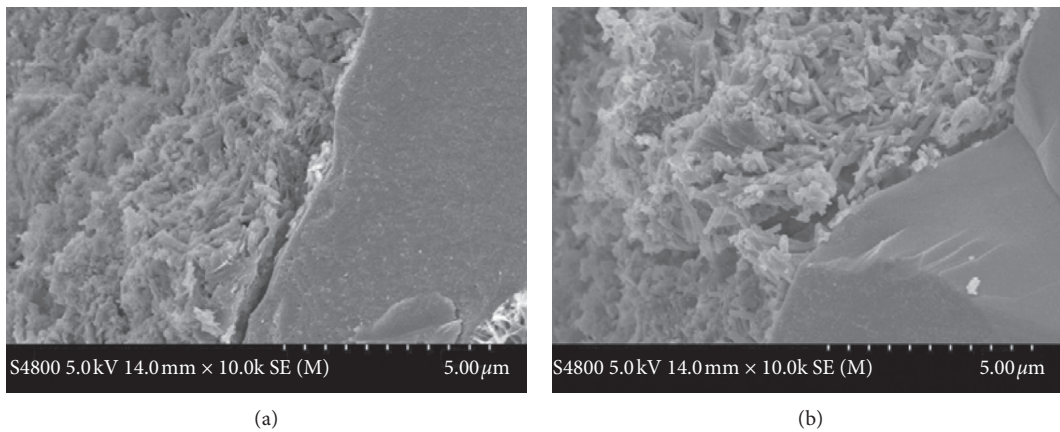
Figure 6: Micromorphology of the interface transition zone of CSRA. (a) OMP. (b) VMP.

(a)

(b)

(c)
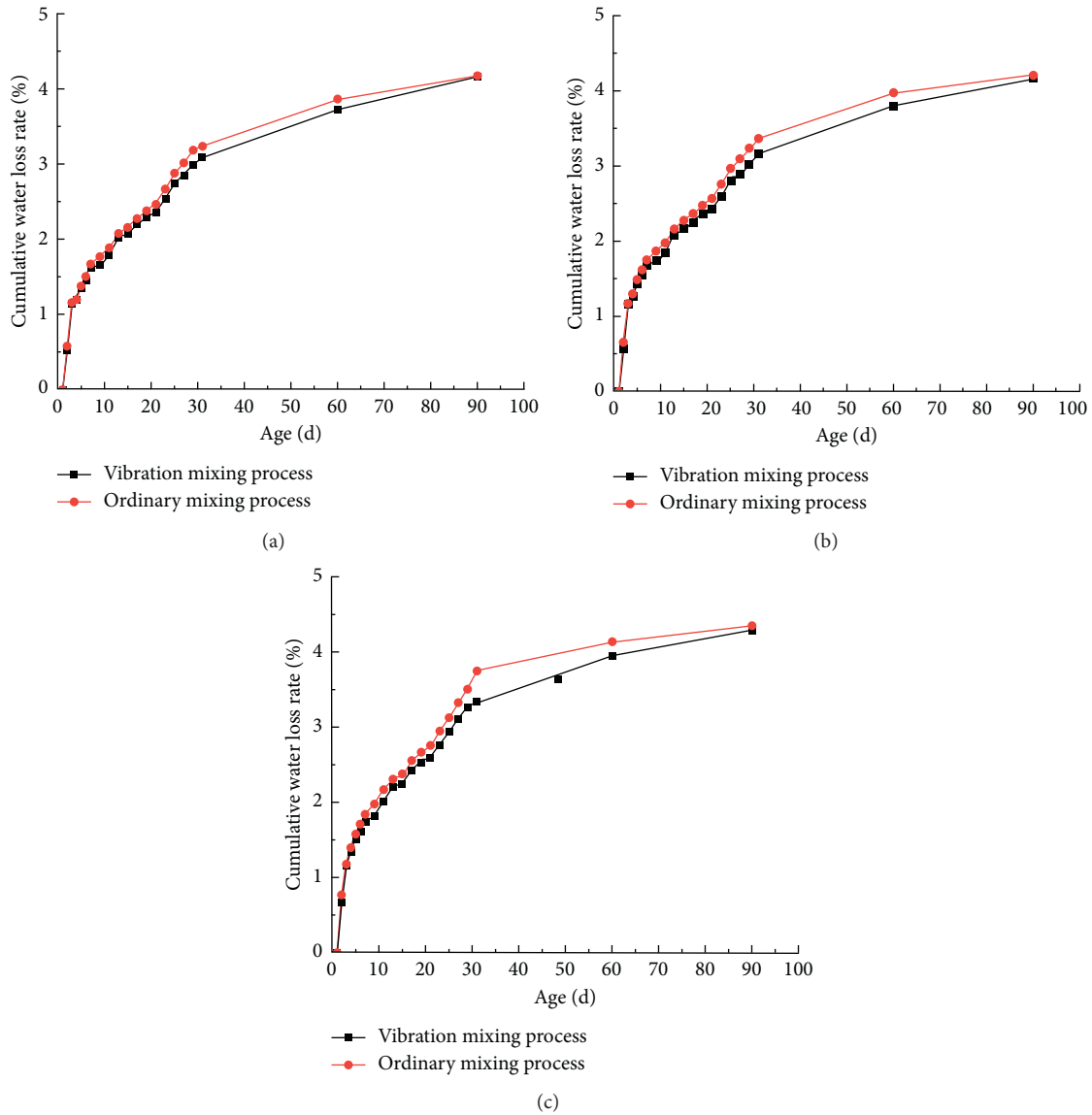
Figure 7: Cumulative water loss rate of CSRA with different cement contents. (a) 3%. (b) 4%. (c) 5%.

Table 5 shows the pore structure parameters of CSRA with 4% cement content prepared by OMP and VMP. The values of pore structure parameters including pore surface area, area median aperture, average aperture, and porosity of the CSRA with vibration mixing are all smaller than those of the CSRA without vibration mixing. This shows that vibration mixing can reduce the number of large pores, reduce the pore size, and optimize the structure of the pores. The increase of porosity indicates that the vibration mixing process has a proper air-entraining effect. When the CSRA is mixed with vibration, the water film on the surface of the aggregate and the cement particles is broken, so that more air can be introduced. At the same time, the large bubbles are broken due to the vibration, which optimizes the pore structure of CSRA [19]. Loss of capillary water will cause dry shrinkage of the CSRA, which will lead to increased tensile stress. The VMP introduces a large number of tiny

bubbles to close the capillary structure to prevent the evaporation of water and improve the shrinkage performance of CSRA.

3.2.3. Temperature Shrinkage. The temperature shrinkage test results of CSRA with different cement content are shown in Figure 10. As Figure 10 depicts, compared with OMP, VMP can improve the temperature shrinkage of CSRA greatly. At the same cement content, the temperature shrinkage coefficient of CSRA prepared by VMP is lower than that of CSRA prepared by OMP. Similar to the development curve of drying shrinkage, the temperature shrinkage coefficient increases with the increase of cement content. Compared with OMP, when the temperature range is 30°C~20°C and the cement content is 5%, the temperature shrinkage coefficient of the stabilized recycled aggregate of vibration mixing cement is reduced by about 27%. The

(a)

(b)

(c)
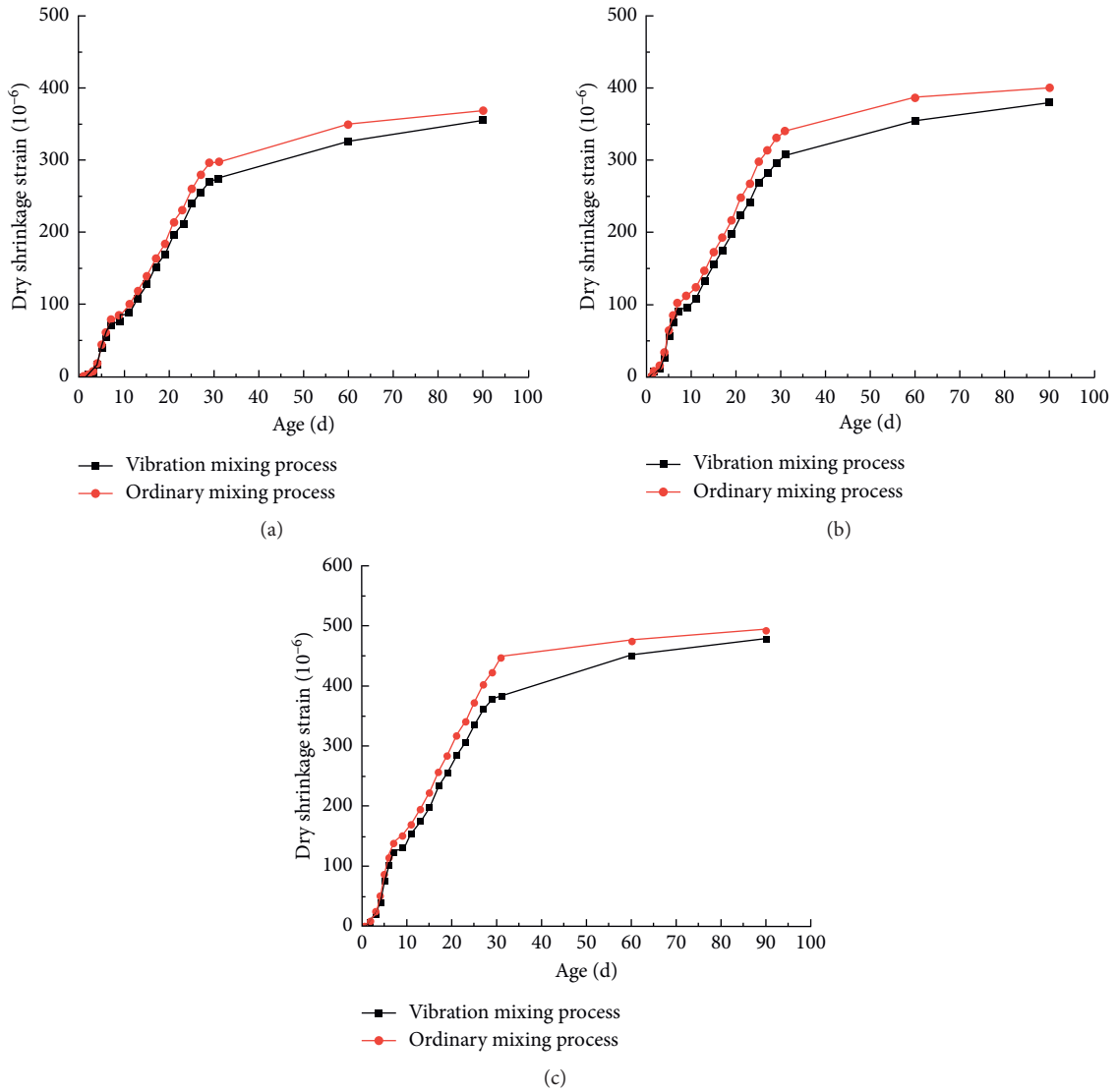
FIGURE 8: Dry shrinkage strain of CSRA with different cement contents. (a) 3%. (b) 4%. (c) 5%.

(a)

(b)

FIGURE 9: Continued.

(c)
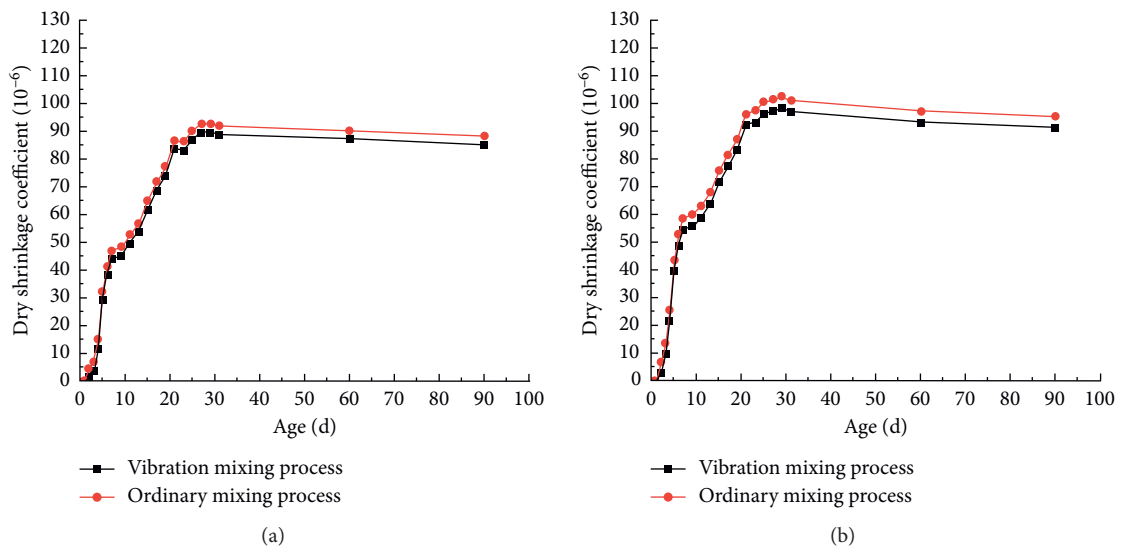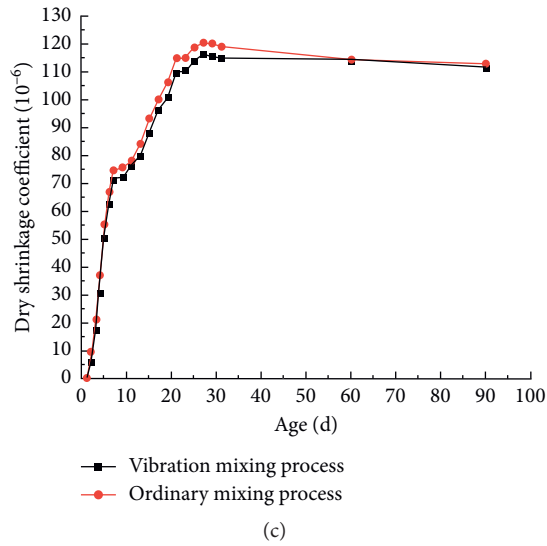
FIGURE 9: Dry shrinkage coefficient of CSRA with different cement contents. (a) 3%. (b) 4%. (c) 5%.

TABLE 5: The pore structure parameters of CSRA with 4% cement content.

Parameters	Vibration mixing process	Ordinary mixing process
Pore surface area (m^2/g)	2.712	4.359
Area median aperture (μm)	0.315	0.454
Average aperture (μm)	0.048	0.059
Porosity (%)	16.01	12.21

(a)

(b)
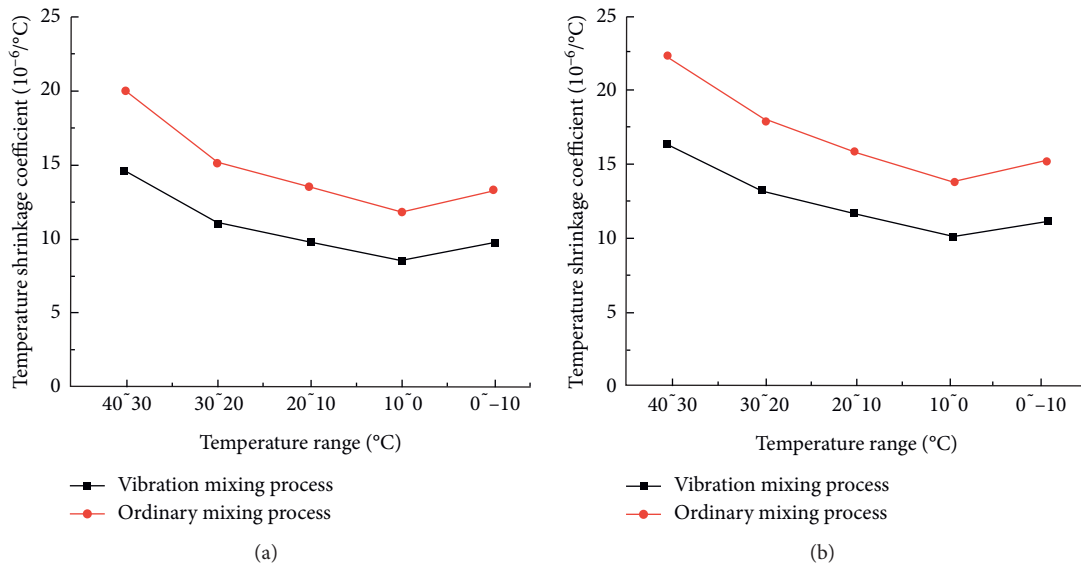
FIGURE 10: Continued.

(c)
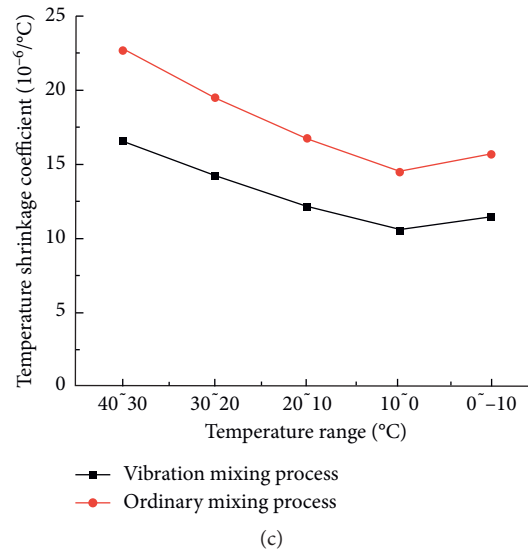
FIGURE 10: Temperature shrinkage coefficient of CSRA with different cement contents. (a) 3%. (b) 4%. (c) 5%.

temperature shrinkage cracks of CSRA refer to the cracks caused by the volume shrinkage caused by the distance between the molecules of the internal structure of the mixture as the temperature changes. Through VMP, the homogeneity of the mixture is improved and the interface transition zone leads to the improvement of temperature shrinkage performance [20].

4. Conclusions

(1) Compared with OMP, VMP can greatly improve the compressive strength, dry shrinkage, and temperature shrinkage properties of CSRA.

(2) Considering the road performance and economic benefits, the optimum parameters of vibration time and vibration frequency in VMP were 30 s and 40 Hz, respectively.

(3) The reason why VMP can improve the performance of CSRA was that VMP strengthened the aggregate and interface transition area and introduced microbubbles to optimize the pore structure.

Data Availability

The data used to support the findings of this study are included within the article.

Conflicts of Interest

The authors declare that they have no conflicts of interest.

Acknowledgments

References

[1] H. K. A. Al-Bayati, P. K. Das, S. L. Tighe, and H. Baaj, "Evaluation of various treatment methods for enhancing the physical and morphological properties of coarse recycled concrete aggregate," *Construction and Building Materials*, vol. 112, pp. 284–298, 2016.

[2] W. M. Shaban, J. Yang, H. Su et al., "Properties of recycled concrete aggregates strengthened by different types of pozzolan slurry," *Construction and Building Materials*, vol. 216, pp. 632–647, 2019.

[3] P.-K. Chang and Y.-N. Peng, "Influence of mixing techniques on properties of high performance concrete," *Cement and Concrete Research*, vol. 31, no. 1, pp. 87–95, 2001.

[4] T. Hemalatha, K. R. Ram Sundar, A. R. Murthy, and N. R. Iyer, "Influence of mixing protocol on fresh and hardened properties of self-compacting concrete," *Construction and Building Materials*, vol. 98, pp. 119–127, 2015.

[5] Y. Yao, Z. Feng, S. Chen, B. Li, L. Zhao, and W. Zhao, "A double-blade mixer for concrete with improved mixing quality," *Arabian Journal for Science and Engineering*, vol. 41, pp. 4809–4816, 2016.

[6] D. Han and R. D. Ferron, "Influence of high mixing intensity on rheology, hydration, and microstructure of fresh state cement paste," *Cement and Concrete Research*, vol. 84, pp. 95–106, 2016.

[7] Z. Feng, W. Wang, L. Zhao et al., "Test research on concrete vibratory mixing techniques," in *Proceedings of the 2006 Xi'an International Conference of Architecture and Technology*, pp. 825–830, Lodz, Poland, April 2006.

[8] C. F. Ferraris, "Concrete mixing methods and concrete mixers: state of the art," *Journal of Research of the National Institute of Standards and Technology*, vol. 106, no. 2, pp. 391–399, 2001.

[9] J. Dils, G. De Schutter, and V. Boel, "Influence of mixing procedure and mixer type on fresh and hardened properties of concrete: a review," *Materials and Structures*, vol. 45, no. 11, pp. 1673–1683, 2012.

[10] H. Zhang, S. Liang, H. Yang, and L. Yul, "Research on performance of cement stabilized crushed stone based on indoor

vibration stirring," *Journal of China Highway*, vol. 31, pp. 58–65, 2018.

[11] R. Li, S. Luo, H. Wang, Z. Guang, and M. Liu, "Comparative study on the strength performance of vibrating agitated cement stabilized gravel," *Journal of Chongqing Jiaotong University (Natural Science Edition)*, vol. 36, pp. 33–36, 2017.

[12] L. Zhao, W. Jiang, J. Hou, Z. Feng, and S. Xue, "Influence of mixing methods on performance of compressive strength for cement stabilized Macadam mixture," *Journal of China Highway*, vol. 31, pp. 151–158, 2018.

[13] W. Dong, S. Xie, L. Zhao, and Z. Feng, "Influence of vibration on mixing process of cement stabilized Macadam and its performance," *Journal of China Highway*, vol. 32, pp. 181–190, 2019.

[14] JTG E30-2005, *Highway Engineering Cement and Cement Concrete Test Specification*, China Communication Press, Beijing, China, 2005.

[15] JTG F20-2015, *Technical Guidelines for Construction of Highway Roadbases*, China Communication Press, Beijing, China, 2015.

[16] JTG E51-2009, *Test Methods of Materials Stabilized with Inorganic Binders for Highway Engineering*, China Communication Press, Beijing, China, 2009.

[17] G. Xiong, C. Wang, S. Zhou et al., "Preparation of high strength lightweight aggregate concrete with the vibration mixing process," *Construction and Building Materials*, vol. 229, p. 116936, 2019.

[18] P. Vargas, O. Restrepo-Baena, and J. I. Tobón, "Microstructural analysis of interfacial transition zone (ITZ) and its impact on the compressive strength of lightweight concretes," *Construction and Building Materials*, vol. 137, pp. 381–389, 2017.

[19] J. Zhang, X. Gao, and L. Yu, "Improvement of viscosity-modifying agents on air-void system of vibrated concrete," *Construction and Building Materials*, vol. 239, Article ID 117843, 2020.

[20] V. Collin and P.-H. Jézéquel, "Mixing of concrete or mortars: distributive aspects," *Cement and Concrete Research*, vol. 39, no. 8, pp. 678–686, 2009.

Research Article

Effect of Diatomite and Basalt Fibers on Pavement Performance and Vibration Attenuation of Waste Tires Rubber-Modified Asphalt Mixtures

Chunli Wu,[1] Liding Li [ID],[1] Yongchun Cheng,[1] Zhengwei Gu [ID],[1] Zehua Lv,[2] Renbing Wang,[3] and Baigeng Guan[3]

[1]*College of Transportation, Jilin University, Changchun 130022, China*
[2]*Hebei Provincial Communications Planning and Design Institute, Shijiazhuang 050011, China*
[3]*Jilin Shengda Highway & Bridge Construction Co., Ltd., Jilin 132200, China*

Correspondence should be addressed to Zhengwei Gu; gzw@jlu.edu.cn

As an eco-friendly pavement material, waste tires rubber-modified asphalt mixtures (WRMs) have been applied in pavement engineering widely. To further improve the performance and adaptability of WRM, diatomite and basalt fibers are, respectively, added to WRM. Subsequently, the Marshall tests, the rutting tests, the low-temperature splitting tests, the freeze-thaw splitting tests, and the vibration attenuation tests are conducted to study the effect of diatomite and basalt fibers on pavement properties of WRM. Furthermore, the correlation degree between the content of diatomite, basalt fibers, asphalt, and the pavement properties of WRM is analysed by the grey correlation grade analysis (GCGA). The results show that the addition of diatomite and basalt fibers can significantly improve the pavement and vibration attenuation properties of WRM. The improvement of high-temperature permanent deformation resistance, low-temperature cracking resistance, and water damage resistance of WRM is mainly attributed to diatomite, basalt fibers, and asphalt-aggregate ratio, respectively. The improvement of the vibration attenuation of WRM by diatomite and basalt fibers is mainly attributed to the increase of waste tires rubber-modified asphalt (WRA) content caused by adding diatomite and basalt fibers.

1. Introduction

With the increase of global car ownership, a large number of waste tires have been produced, which seriously pollutes the natural environment and occupies a large number of land resources. Recycling these waste tires is an urgent problem to be solved. Notably, it has become an effective method to deal with waste tires by using them in road engineering materials [1–4]. Using waste tires rubber (WR) in road engineering materials can not only protect the environment and save resources but also improve the mechanical properties of pavement materials and reduce vibration and noise on the road [2, 5–9]. Some studies pointed out that the addition of WR to the asphalt mixtures could improve the performance of antideformation at high temperature and anticrack at low temperature [6, 10–12]. And WR also enhanced the high-temperature performance of desulphurization gypsum residues modified asphalt mixtures [12]. In addition, the fatigue performance of WR modified asphalt mixtures (WRM) had been studied by using the semicircular bending tests and flexure beam tests, and the results showed that the WRM exhibited better fatigue performance compared to the nonreinforced mixtures [7, 13–15]. Moreover, WRM exhibited more excellent recoverable strain than the styrene-butadiene-styrene modified asphalt mixtures [16].

The application of WR in road engineering materials not only improves the engineering performance of asphalt mixtures but also has good environmental and economic benefits. In order to further improve the performance and adaptability of WRM and WR modified asphalt (WRA),

many researchers had proposed some feasible solutions. Chen et al. [9] applied the reacted and activated WR to enhance the engineering performance of asphalt mixtures, and the results showed that, compared to the polymer modified asphalt mixtures, the reacted and activated WRM exhibited excellent low-temperature cracking resistance, high-temperature rutting resistance, fatigue cracking resistance, moisture susceptibility, and noise reduction. Gong et al. [17] reported that cement coated rubber aggregate had better bonding performance with asphalt and higher mechanical strength than untreated rubber aggregate. Liu et al. [18] introduced that the diatomite and WR compound modified asphalt exhibited better performance in short-term aging resistance than the diatomite modified asphalt and WRA. Maharaj et al. [19] claimed that the WR and polyethylene terephthalate compound modified asphalt presented excellent mechanical properties. Zhang et al. [5] pointed out that the WR and plastic compound modified asphalt mixtures had excellent fatigue resistance and rutting resistance. It can be concluded that, at present, many studies focused on adding organic and inorganic materials to enhance the performance of WRA and WRM. However, the addition of some organic modifiers raises the mixing and compaction temperature of WRM, thereby increasing the release of toxic gases such as xylene and toluene [20].

Therefore, in this paper, the diatomite and basalt fibers, two inorganic and eco-friendly reinforced materials, were used to enhance the performance of WRM. Subsequently, the effects of diatomite and basalt fibers' contents on the high-temperature permanent deformation resistance, low-temperature cracking resistance, and water damage resistance of WRM were studied. Considering that rubber is an excellent damping material, it can be used to improve the vibration attenuation of asphalt mixtures. Accordingly, the effects of diatomite and basalt fibers' contents on the vibration attenuation of WRM were also studied and analysed by the vibration attenuation tests of the rutting plates and the tire.

In addition, the accelerometer was widely used to evaluate the performance of asphalt mixtures. Polaczyk et al. [21] used accelerometers to study the Marshall compaction process of asphalt mixtures. Real et al. [22] used the impact hammer excitation technology to evaluate the damping characteristics of asphalt mixtures. Biligiri [23] analysed the damping characteristics of asphalt mixture based on the data collected by accelerometer based on vibroacoustic technology and evaluated the noise reduction performance of asphalt mixture.

Furthermore, to analyse the internal cause of the effect of diatomite and basalt fibers on the pavement performance and vibration attenuation of WRM, the grey correlation degree analysis (GCGA) was performed to quantitatively calculate the correlation degree between the diatomite content, basalt fibers content, as well as asphalt-aggregate ratio (ratio of asphalt to mineral aggregate) and volume of air voids (VV), voids in the mineral aggregate (VMA), voids filled with asphalt (VFA), the pavement performance, and the vibration attenuation of WRM. This work can provide some references for the practical application and performance enhancement of WRM, and it can also help protect the natural environment and promote the development of sustainable technology.

2. Materials and Methods

2.1. Materials. In this paper, WRA was used as the binder to fabricate the asphalt mixtures. The WRA was prepared as the following processes. Firstly, the base asphalt A-90# supplied by Panjin Petrochemical Industry was heated to 150–160°C. Subsequently, the tire rubber powders with 40 mesh (particle size: 0.4 mm) and 20 wt.% (weight ratio) of asphalt were added to the base asphalt at the temperature of 180°C for 30 min at a shear speed of 5000 rpm [24–26]. The physical properties of the base asphalt and WRA were tested, and the test results are shown in Table 1. The diatomite and the basalt fibers originated from Changbai Mountain and the Jiuxin Basalt Industry Co., Ltd., respectively. Their properties are shown in Tables 2 and 3. The basalt aggregate with nominal maximum aggregate size 13.2 mm, as shown in Table 4, was used to fabricate WRM, diatomite reinforced WRM (DWRM), and basalt fibers reinforced WRM (BWRM) according to Standard Test Methods of Bitumen and Bituminous Mixtures for Highway Engineering (JTG E20-2011) [27].

2.2. Experimental Methods

2.2.1. Asphalt Mixtures Preparation. In this study, three types of asphalt mixtures were prepared, namely, WRM, DWRM, and BWRM. The three types of asphalt mixtures were divided into seven groups: WRM, DWRM with 5 wt.% diatomite, 7.5 wt.% diatomite, and 10 wt.% diatomite, BWRM with 0.2 wt.% basalt fibers, 0.3 wt.% basalt fibers, and 0.4 wt.% basalt fibers, and the specific preparation scheme is shown in Table 5. The content of diatomite and basalt fibers is determined by the previous research [28–30]. According to Table 5, the diatomite (added in substitution to mineral filler), basalt fiber (relative to mineral mass ratio), WRA, and aggregate were mixed to prepare the standard Marshall specimens ($\phi101.6 \, mm \times 63.5 \, mm$) and the rutting specimens (300 mm × 300 mm × 50 mm) for subsequent testing. All the samples were formed under the asphalt-aggregate ratio in the research. All the samples were fabricated with the optimum asphalt-aggregate ratio in the research [28].

2.2.2. Volume and Mechanical Properties Tests. According to JTG E20-2011, VV, VMA, VFA, Marshall stability (MS), flow value (FL), and pavement properties indexes of 7 groups of asphalt mixtures were tested and calculated [31]. The test processes are shown in Figure 1. The pavement properties of asphalt mixtures mainly include permanent deformation resistance at high temperature, crack resistance at low temperature, and water damage resistance. The high-temperature permanent deformation resistance is usually characterized by the value of dynamic

TABLE 1: Physical properties of asphalt.

Properties	A-90# asphalt		WRA	
	Standard	Value	Standard	Value
Density (15°C, g/cm^3)	—	1.016	—	1.025
Penetration (25°C, 0.1 mm)	80–100	91.6	60–100	62.6
Softening point $T_{R\&B}$ (°C)	≥45	46.9	>50	66.5
Ductility (cm)	≥100 (25°C)	>150 (25°C)	≥10 (5°C)	20.9 (5°C)
Elastic recovery (%)	—	—	≥50	74.3

TABLE 2: Properties of basalt fibers.

Properties	Diameter (μm)	Length (mm)	Water content (%)	Combustible content (%)	Tensile strength (MPa)	Tensile modulus of elasticity (GPa)	Elongation at break (%)
Value	10–13	6	0.030	0.56	2320	86.3	2.84

TABLE 3: Properties of diatomite.

Properties	Particle size	Density	Bulk density	Color	pH
Value	<0.075 mm	2.34 g/cm^3	0.34–0.41 g/cm^3	White	9.0

TABLE 4: Aggregate gradation of AC-13.

Sieve size (mm)	0.075	0.15	0.3	0.6	1.18	2.36	4.75	9.5	13.2	16
Percent passing	4.8	8.3	12.2	18.6	25.8	33.9	54.8	80.9	94.8	100

TABLE 5: The mix proportion scheme of seven groups of asphalt mixtures.

Mixtures	WRM	DWRM			BWRM		
Diatomite content (%)	0	5	7.5	10	0	0	0
Basalt fibers content (%)	0	0	0	0	0.2	0.3	0.4
Asphalt-aggregate ratio (%)	5.10	5.25	5.35	5.45	5.27	5.38	5.50

stability (DS), and the higher the value, the better the resistance permanent deformation at high temperature. The DS can be calculated according to equation (1) [27]. The resistance cracking at low temperature is usually reflected by the splitting tensile strain at −10°C (ε_T). A greater ε_T means that there is a better resistance cracking at low temperature. ε_T can be calculated by equation (2) [27]. And equations (3) and (4) show the calculated method of splitting tensile strength (R_T) and failure stiffness modulus (S_T) at low temperature, respectively. The water damage resistance is usually characterized by the tensile strength ratio (TSR). A greater TSR means better water damage resistance. The TSR can be calculated by equation (5) [27]:

$$\text{DS} = \frac{(t_2 - t_1) \times N}{d_2 - d_1}, \tag{1}$$

where N is wheel moving speed, 42 times/min, and d_1 and d_2 are the tracking depth at t_1 (45 min) and t_2 (60 min), respectively, mm:

$$\varepsilon_T = \frac{Y_T \times (0.0307 + 0.0936 \times \mu)}{(17.94 - 0.314 \times \mu)},$$

$$R_T = \frac{0.006287 \times P_T}{h}, \tag{2}$$

$$S_T = \frac{P_T \times (3.588 - 0.0628 \times \mu)}{h \times Y_T}.$$

where Y_T (mm) is the total vertical deformation corresponding to the maximum breaking load P_T (N); μ is Poisson's ratio, which is 0.25; and h is the height of Marshall specimens, mm:

$$TSR = \frac{R_{T2}}{R_{T1}} \times 100, \tag{3}$$

where R_{T1} and R_{T2} are the average tensile strength of frozen-thawed specimens and original specimens respectively, MPa.

2.2.3. Vibration Attenuation Tests of the Rutting Plates.

The vibration attenuation tests of the rutting plates (300 mm × 300 mm × 50 mm) made of WRM, DWRM, and BWRM are shown in Figure 2. The test processes are as follows [22]. Firstly, the acceleration sensor was bonded to the center of the back of the rutting plate with the epoxy resin, and the other end of the acceleration sensor was well connected to DH5922 dynamic signal test and analysis system. Subsequently, the rutting plate with the acceleration sensor was bonded on two concrete blocks with the epoxy
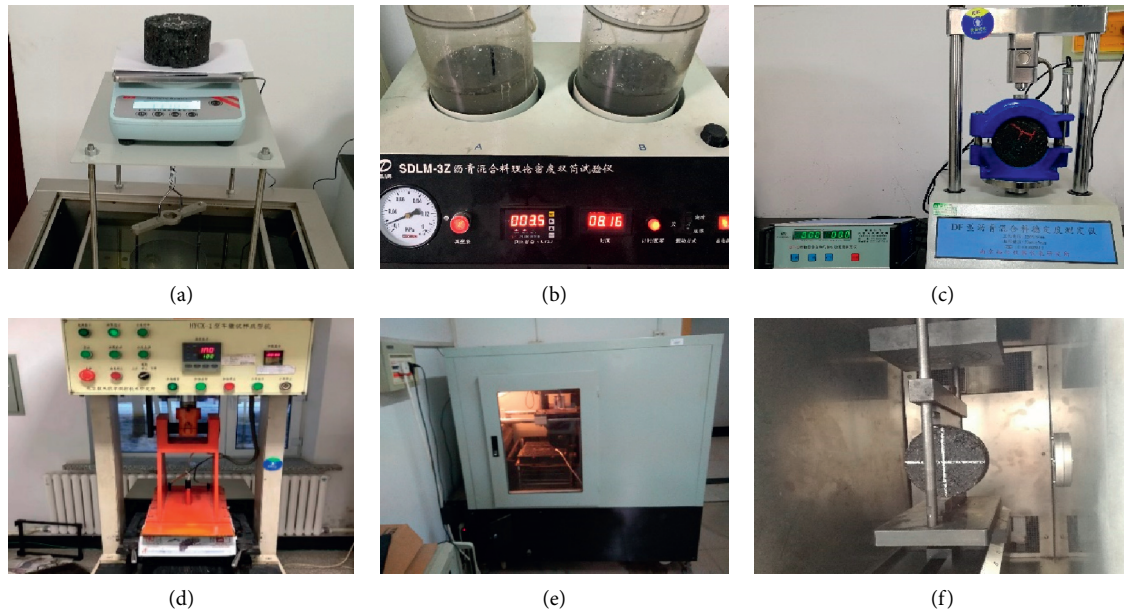
FIGURE 1: WRM performance tests: (a) bulk volume density tests; (b) theoretical maximum density tests; (c) Marshall stability tests; (d) rutting plate compaction; (e) rutting tests; (f) splitting strength tests.
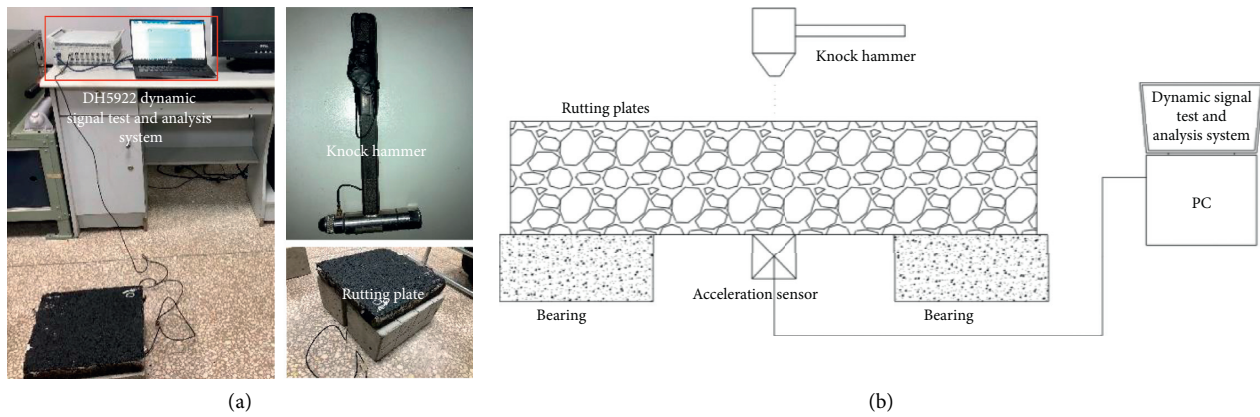
FIGURE 2: Vibration attenuation tests of the rutting plate: (a) factual picture and (b) schematic diagram.

resin and the movement of the rutting plate in the x, y, and z directions restricted. Finally, the knock hammer with rubber head shown in Figure 2 was used to hit the center position of the front of the rutting plate, and the vibration attenuation signal of the rutting plate was collected by the acceleration sensor with a frequency of 2 kHz and analysed by the DH5922 dynamic signal test and analysis system.

2.2.4. Free Vibration Attenuation Tests of Tire.

The tire free vibration attenuation tests are shown in Figure 3. The vibration attenuation of tire on the asphalt mixtures was tested as the following processes [23]. Firstly, the acceleration sensor was connected with DH5922 dynamic signal test and analysis system, and the sensor was fixed on the Michelin tire (250 kPa, 195/60R14) so that the sensor could measure the vertical acceleration of the tire. Subsequently, the tire with

the acceleration sensor was placed 3 cm above the center of the standard rutting plate specimens bonded tightly with the rigid ground. Finally, the tire fell freely and vertically onto the rutting plate, and the vibration attenuation signal of the tire was collected by the acceleration sensor and analysed by the DH5922 dynamic signal test and analysis system.

2.3. Vibration Attenuation Model.

To evaluate the vibration attenuation properties of the asphalt specimen and the tire on the asphalt specimen, the pavement and the tire are simplified as the tire-pavement vibration model as shown in Figure 4. When the impact load is applied on the asphalt pavement and the tire, displacement x, velocity $\dot{x}$, and acceleration $\ddot{x}$ of vibration of the asphalt pavement and the tire conform to the relationship as shown in the following equation [22, 23, 32, 33]:
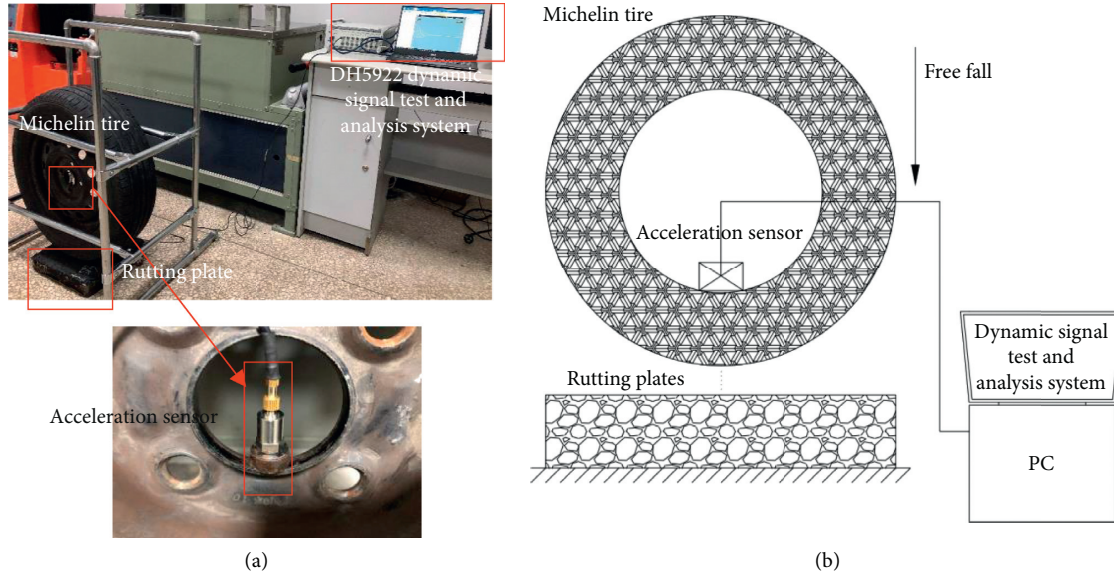
FIGURE 3: Tire free vibration attenuation test of asphalt mixtures: (a) factual picture and (b) schematic diagram.
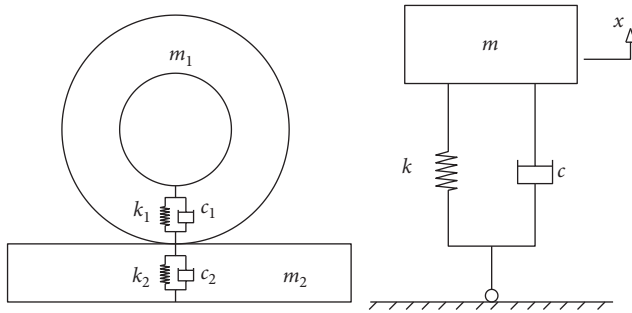
FIGURE 4: Tire and rutting plate vibration model.

$$m\ddot{x} + c\dot{x} + kx = 0, \tag{4}$$

where m, c, and k are the equivalent vibration mass, stiffness, and viscosity coefficient of the asphalt pavement or the tire, respectively. Let $\omega_n^2 = k/m$ and $\xi^2 = c^2/4mk$, equation (4) can be written as the following equation:

$$\ddot{x} + 2\xi\omega_n\dot{x} + \omega_n^2 x = 0, \tag{5}$$

where ω_n is the circular frequency of system vibration and ξ is the damping ratio of system vibration. It can be seen that the previous equation is the second-order linear homogeneous differential equation, and its characteristic roots are shown in equation (4).

$$s = \omega_n\left(-\xi \pm \sqrt{\xi^2 - 1}\right). \tag{6}$$

Since the vibration attenuation of the tire and pavement is underdamped, $0 < \xi < 1$ can be obtained. Letting $\omega_d = \omega_n\sqrt{1 - \xi^2}$, equation (6) can be further expressed as the following equation:

$$s = -\xi\omega_n \pm i\omega_d. \tag{7}$$

Therefore, the solution of equation (5) is expressed as the following equation:

$$\begin{aligned} x(t) &= G_1 e^{-\xi\omega_n t + i\omega_d t} + G_2 e^{-\xi\omega_n t - i\omega_d t} \\ &= e^{-\xi\omega_n t}\left(G_1 e^{i\omega_d t} + G_2 e^{-i\omega_d t}\right). \end{aligned} \tag{8}$$

According to the Euler equation (equation (9)), equation (8) can be written as equation (10):

$$e^{\pm i\omega t} = \cos\omega t \pm i\sin\omega t, \tag{9}$$

$$\begin{aligned} x(t) &= e^{-\xi\omega_n t}\left(A_1 \sin\omega_d t + A_2 \cos\omega_d t\right) \\ &= A e^{-\varepsilon t}\cos\left(\omega_d t + \varphi\right), \end{aligned} \tag{10}$$

where A and φ are the parameters determined by the initial conditions and ε is the exponential decay rate. It can be found that the envelope of vibration attenuation of the pavement and tire conform to the relationship as shown in equation (11). The vibration attenuation equation for the pavement and tire is in the form of exponential decay. By calculating the second derivative of equation (11), the envelope of acceleration attenuation of the tire and pavement vibration can be obtained as shown in the following equation [22]:

$$x(t) = A e^{-\varepsilon t}, \tag{11}$$

$$a = \ddot{x}(t) = A\varepsilon^2 e^{-\varepsilon t}. \tag{12}$$

2.4. GCGA Method. In order to study the effect of diatomite content, basalt fibers content, and WRA content on the basic volume indexes, the pavement performance, and the vibration attenuation performance of WRM, the GCGA, a

mathematical analysis method, is used to quantitatively analyse these experimental data [34–37]. Since different physical indicators have different physical meanings, it is necessary for all physical indicators to perform normalization processing before the GCGA. The normalization method is as the following equation:

$$x_i = \frac{f_i - \min(f_1, f_2, \ldots, f_7)}{\max(f_1, f_2, \ldots, f_7) - \min(f_1, f_2, \ldots, f_7)}, \quad (13)$$

where x_i is the normalization results of the experimental data ($i = 1, 2, \ldots, 7$) and f_i is the experimental data of the group i asphalt mixture. A grey correlation coefficient between the reference sequence $x_0 = (x_0(1), x_0(2), \ldots, x_0(7))$ and comparative sequences $x_j = (x_j(1), x_j(2), \ldots, x_j(7))$, γ_j, is defined as the following equation:

$$\gamma_j = \frac{1}{N} \sum_{k=1}^{N} \lambda_j(k), \quad (14)$$

where $N = 7$ and $\lambda_j(k)$ can be calculated with the following equation:

$$\lambda_j(k) = \frac{\min_j \min_k |x_0(k) - x_j(k)| + 0.5 \max_j \max_k |x_0(k) - x_j(k)|}{|x_0(k) - x_j(k)| + 0.5 \max_j \max_k |x_0(k) - x_j(k)|}. \quad (15)$$

3. Results and Discussion

3.1. Marshall Indexes of the Three Types of Asphalt Mixtures.
According to JTG E20-2011, the VV, VMA, VFA, MS, and FL of seven groups of asphalt mixtures were tested and calculated. The calculated test results are shown in Table 6. It can be seen from Table 6 that the addition of diatomite can reduce the VV of asphalt mixture, while the addition of basalt fiber increases the VV of asphalt mixture. And the VMA, VFA, and MS of asphalt mixture can be increased by adding diatomite and basalt fiber. In addition, with the increase of diatomite content, VV of DWRM decreases gradually, and, with the increase of basalt fibers content, VV of BWRM increases gradually. The addition of diatomite increases the content of WRA, thus the colloid composed of asphalt and diatomite can occupy more space between the aggregates, which raises VFA of asphalt mixtures, thus reducing VV of asphalt mixtures. Different from this, the addition of basalt fibers increases the WRA content but hinders the compaction of the aggregate [38, 39], which raises VMA of asphalt mixtures; thus it can increase VV of asphalt mixtures. Furthermore, the addition of diatomite and basalt fibers can improve the Marshall stability of WRM, but the excessive basalt fibers content can have a negative impact on the stability of WRM.

3.2. Pavement Performance of Asphalt Mixtures.
Table 7 shows the test results of the permanent deformation resistance at high temperature, cracking resistance at low temperature, and water damage resistance of the seven groups of asphalt mixtures, and three samples from each group were tested. It can be concluded and calculated from Table 7 that the

values of the DS, ε_T, and TSR of DWRM and BWRM is larger than those of WRM. For DWRM, DS, ε_T, and TSR have increased by 53.84%, 33.02%, and 5.31% in maximal, respectively. And the basalt fibers maximally increase those indexes by 17.65%, 28.15%, and 8.93%, respectively, which means that diatomite and basalt fibers can significantly improve the high- and low-temperature performance and moisture susceptibility of WRM. In addition, it can be inferred that diatomite is superior to basalt fibers in improving high- and low-temperature performance of WRM; however, basalt fibers are superior to diatomite in improving moisture susceptibility of WRM. Moreover, it can be also found that the excessive diatomite content has a negative effect on the high- and low-temperature performance of WRM, and the excessive basalt fibers content has a negative impact on the high-temperature performance and moisture susceptibility of WRM.

3.3. Vibration Attenuation Analysis of WRM.
According to the method described in Section 2.2.3, the vibration attenuation properties of the rutting plate specimens made of seven groups of asphalt mixtures were tested. Figure 5 shows the vibration acceleration reduction curves of these rutting plate specimens after impact loading. It can be seen from Figure 5 that the amplitude of the vibration acceleration of these rutting plates is continuously decreasing with the increase of time after the impact load is applied. This is because the asphalt mixture is a viscoelastic material. After the impact loading, the amplitude of the vibration acceleration of these rutting plates continuously reduces due to the viscous damping of these asphalt mixtures.

Further, equation (12) is used to fit the envelope curves of vibration acceleration attenuation. The fitting results are also shown in Figure 5, and Figure 5(h) shows the variation of the exponential decay rate (damping coefficient ε_r) with the content of diatomite and basalt fibers. As can be seen from Figure 5, the correlation coefficients R^2 of exponential equation (12) for fitting the envelopes of vibration acceleration attenuation of seven groups of WRM are greater than 0.97, which shows that the exponential equation can well characterize the vibration attenuation of these asphalt mixtures. According to the fitting results of the damping coefficients ε_r, it can be calculated that, compared with WRM, the damping coefficient ε_r of DWRM with 5 wt.%, 7.5 wt.%, and 10 wt.% diatomite and BWRM with 0.2 wt.%, 0.3 wt.%, and 0.4 wt.% basalt fibers increases by 40.22%, 104.37%, 152.01%, 101.21%, 183.14%, and 216.02%, respectively. It can be found that the addition of diatomite and basalt fibers can significantly improve the vibration attenuation properties of WRM, and with the increase of the content of diatomite and basalt fibers, the improvement is more significant. In addition, it can be also concluded that the basalt fibers are superior to diatomite in improving the vibration attenuation properties of WRM.

3.4. Vibration Attenuation Analysis of Tires on WRM.
According to the method described in Section 2.2.4, the vibration attenuation properties of the tire on the rutting plate specimens made of these asphalt mixtures were tested.

TABLE 6: Test results of Marshall indexes for seven groups of asphalt mixtures.

Mixtures	Content (%)	VV (%)	VMA (%)	VFA (%)	MS (kN)	FL (mm)
WRM	0	3.6	14.1	75.0	14.28	3.26
DWRM	5	3.6	14.7	75.5	14.49	3.1
	7.5	3.2	14.2	77.4	14.98	3.98
	10	2.5	13.9	82.4	16.50	3.32
BWRM	0.2	3.1	14.2	78.6	15.23	3.1
	0.3	3.6	14.5	75.2	15.41	3.69
	0.4	3.8	15.2	75.0	14.79	3.12

TABLE 7: Test results of pavement properties for seven groups of asphalt mixtures.

Mixtures	Content (%)	High-temperature performance			Low-temperature performance			Moisture susceptibility		
		d_1 (mm)	d_2 (mm)	DS (times/min)	R_T (MPa)	$\varepsilon_T (\mu\varepsilon)$	S_T (MPa)	R_{T1} (MPa)	R_{T2} (MPa)	TSR (%)
WRM	0	2.810	3.010	3150	3.8	2732	2376	14.34	12.69	88.5
DWRM	5	2.300	2.440	4500	4.1	3478	2537	14.49	13.07	90.2
	7.5	2.670	2.800	4846	4.0	3634	2133	14.98	13.65	91.1
	10	2.040	2.180	4500	4.0	2804	2673	15.96	14.88	93.2
BWRM	0.2	2.460	2.630	3706	3.9	3436	2348	15.23	14.40	94.6
	0.3	2.540	2.710	3706	4.4	3490	2199	15.41	14.86	96.4
	0.4	2.640	2.830	3316	4.1	3501	2110	14.79	14.05	95.0

(a)

(b)

FIGURE 5: Continued.

(c)

(d)

(e)

(f)

(g)

(h)
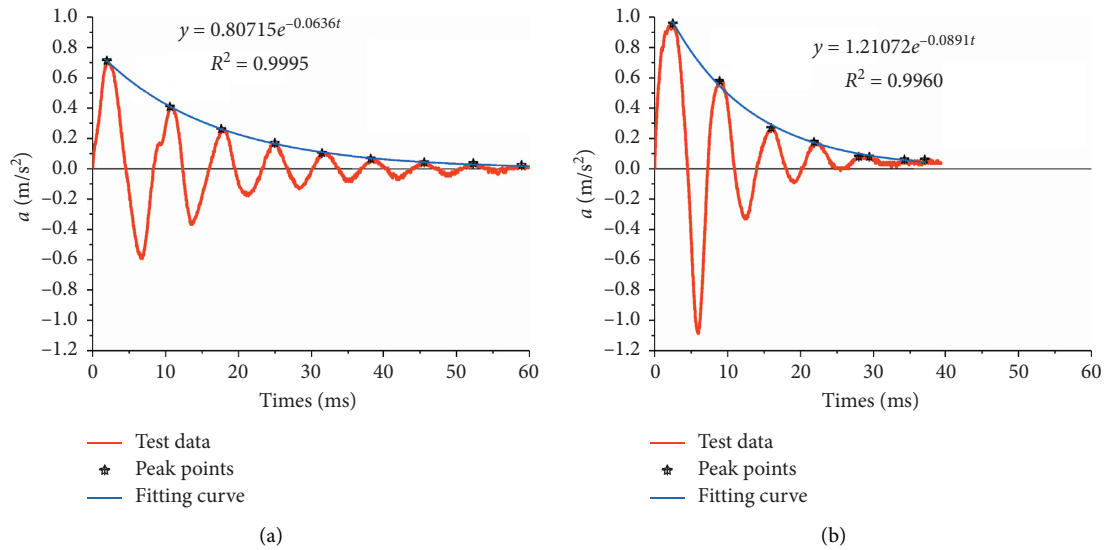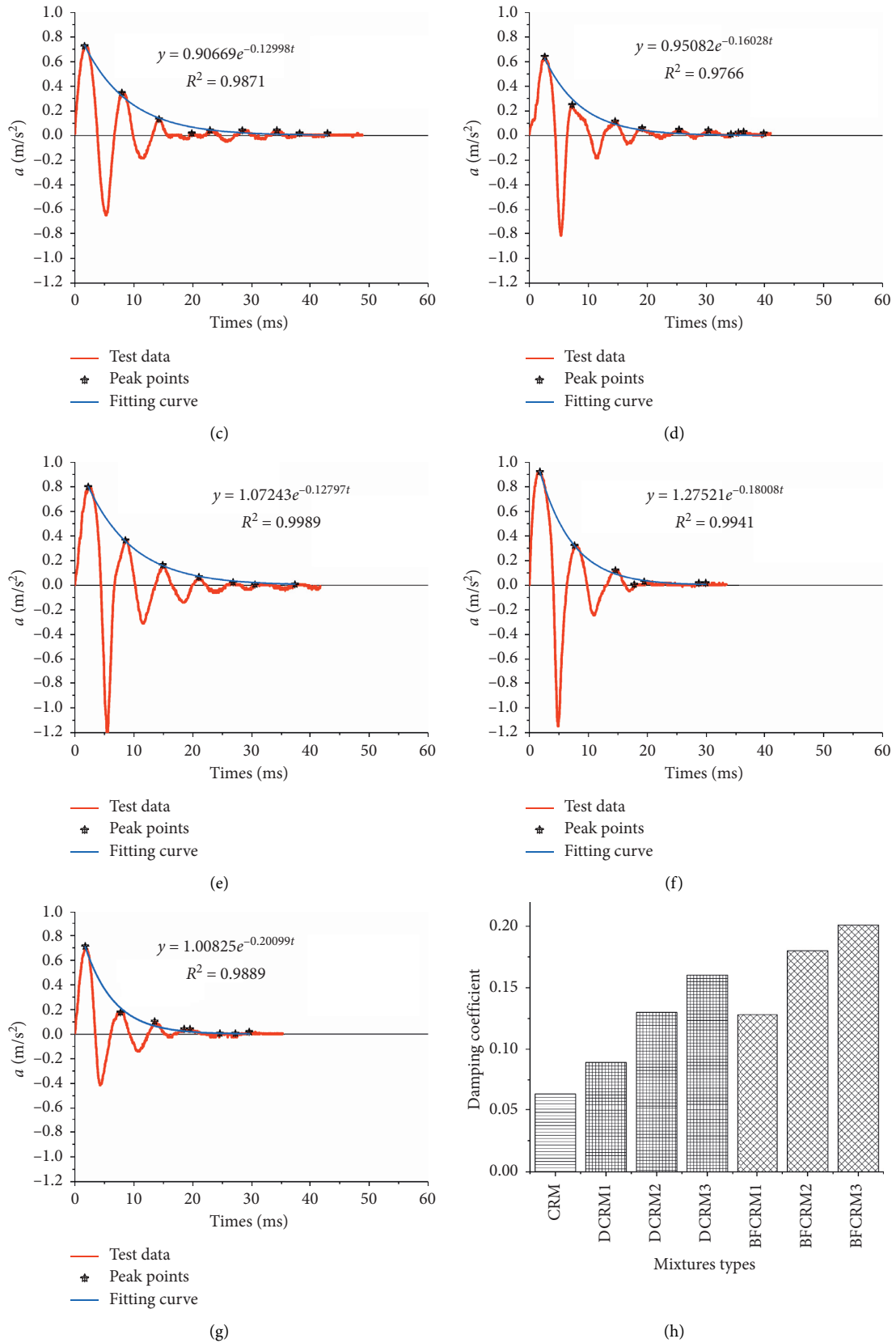
FIGURE 5: Vibration attenuation curves and damping coefficient of the rutting plates: (a) WRM; (b) DWRM with 5 wt.% diatomite; (c) DWRM with 7.5 wt.% diatomite; (d) DWRM with 10 wt.% diatomite; (e) BWRM with 0.2 wt.% basalt fibers; (f) BWRM with 0.3 wt.% basalt fibers; (g) BWRM with 0.4 wt.% basalt fibers; and (h) damping coefficient of the rutting plates.

(a)

(b)

(c)

(d)

(e)

(f)
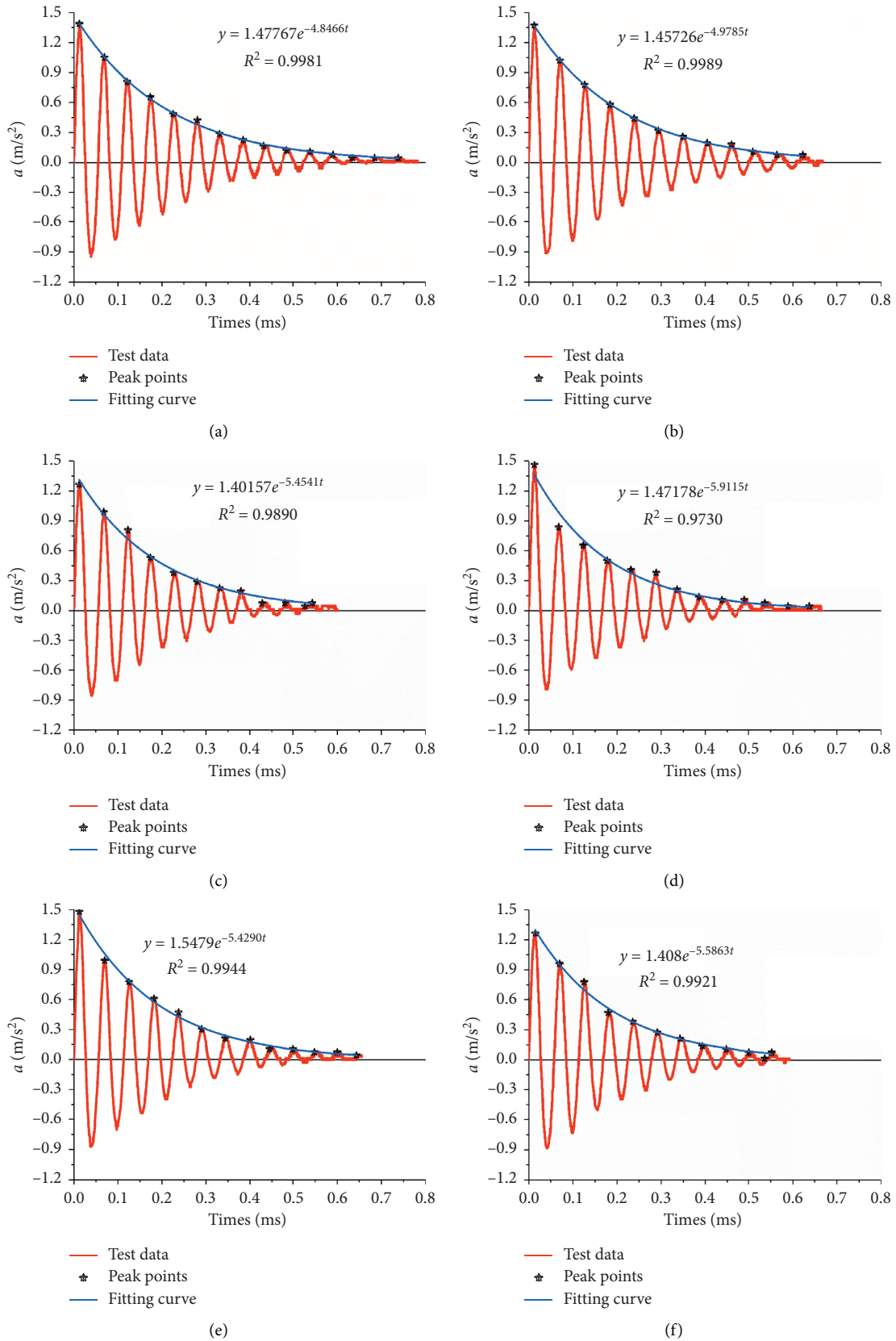
FIGURE 6: Continued.

(g)

(h)
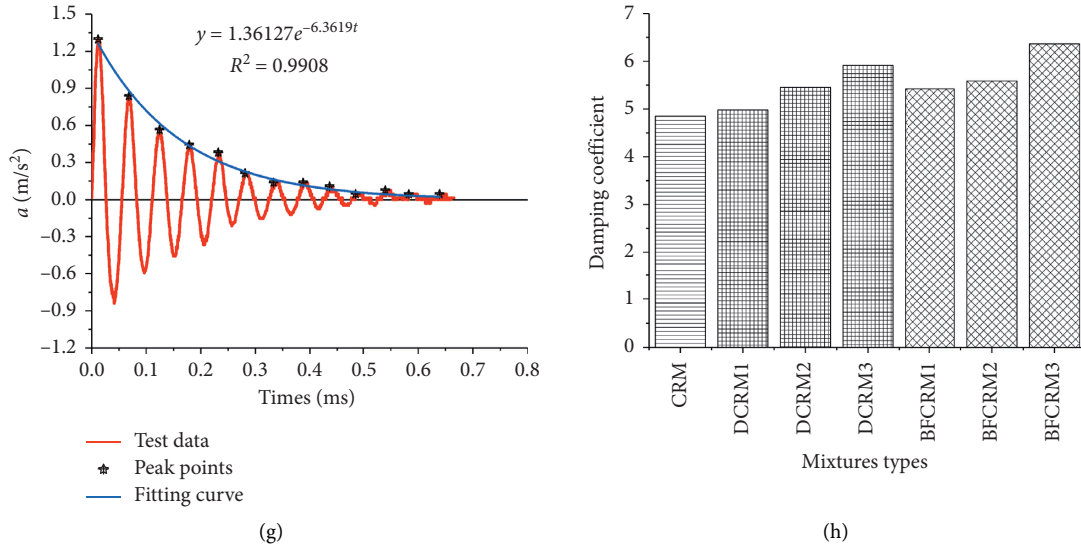
Figure 6: Vibration attenuation and damping coefficient of tire on the rutting plates: (a) WRM; (b) DWRM with 5 wt.% diatomite; (c) DWRM with 7.5 wt.% diatomite; (d) DWRM with 10 wt.% diatomite; (e) BWRM with 0.2 wt.% basalt fibers; (f) BWRM with 0.3 wt.% basalt fibers; (g) BWRM with 0.4 wt.% basalt fibers; and (h) damping coefficient of the tire.

Figures 6(a)–6(g) show the vibration attenuation curves of the tire on these rutting plate specimens after impact loading. Just as the vibration attenuation variation of the rutting plates, it can be seen from Figures 6(a)–6(g) that the amplitude of the vibration acceleration of the tire on these rutting plates is continuously decreasing with the increase of time after loading due to the damping of the tire and these asphalt mixtures.

Again, equation (12) is used to fit the envelope curves of the vibration acceleration attenuation of the tire. The fitting results are also shown in Figure 6, and Figure 6(h) shows the trend of the exponential decay rate (damping coefficient ε_t) with the content of diatomite and basalt fibers. It can be also found from Figure 6 that exponential equation (12) can well reflect the vibration attenuation characteristics of the tire on these asphalt mixtures.

According to the fitting results, it can be found that the damping coefficient ε_t of the asphalt mixture can be increased by adding diatomite and basalt fiber. 10% diatomite and 20% basalt fiber can increase the damping coefficient ε_t of asphalt mixture by 21.97% and 31.27%, respectively. It be concluded that the addition of diatomite and basalt fibers can significantly improve the vibration attenuation properties of the tire on WRM. And with the increase of the content of diatomite and basalt fibers, the damping coefficient increases continuously, and the vibration attenuation properties of the tire on the WRM are also continuously enhanced. In addition, it can be also seen that the basalt fibers are superior to diatomite in improving vibration attenuation properties of the tire on the WRM. This means that the vehicle will be more comfortable on the road made of DWRM and BWRM and will produce less road noise.

3.5. Correlation Analysis. It can be seen from the above that the addition of diatomite and basalt fibers can significantly improve the high-temperature stability, low-temperature

cracking resistance, water damage resistance, and vibration damping performance of WRM. However, whether these improvements in road performance and vibration attenuation of WRM are caused by the addition of diatomite and basalt fibers or by the changes of asphalt-aggregate ratio remains to be further studied. The correlation degree between the basalt fibers content, diatomite content, as well as asphalt-aggregate ratio and the volume indexes, the pavement performance, and the vibration attenuation of WRM also needs to be further calculated and analysed. Therefore, the GCGA method is used to quantitatively calculate the correlation degree between them and analyse the internal cause of improvement of the pavement performance and the vibration attenuation for DWRM and BWRM. The dimensionless processing of these indexes is needed before GCGA. The dimensionless results of all indicators are shown in Table 8 according to equation (13). Subsequently, according to equation (14) and equation (15), the grey correlation degree γ_j is calculated as shown in Table 9.

From Table 9, it can be seen that there is a large difference in the correlation degree between the basalt fibers content, diatomite content, as well as asphalt-aggregate ratio and the volume indexes, the pavement performance, and the vibration attenuation of WRM. Compared with diatomite content and asphalt-aggregate ratio, basalt fiber content has a higher correlation with the VV and VMA of WRM. However, the correlation between diatomite content and VFA is higher than that between basalt fiber content and asphalt-aggregate ratio and VFA. This means that the VV and VMA of WRM are closely related to the basalt fibers content, and the addition of basalt fibers can hinder the compaction movement of aggregate in WRM and then increase VV and VMA of WRM. And the increase of the VFA of WRM is mainly caused by the increase of diatomite content and WRA content. The colloid formed by the fine

TABLE 8: The dimensionless results of the test indexes.

Groups	D	B	A	VV	VMA	VFA	MS	DS	ε_T	TSR	ε_r	ε_t
1	0	0	0	0.846	0.154	0	0	0	0	0	0	0
2	0.5	0	0.375	0.846	0.615	0.068	0.095	0.796	0.827	0.215	0.186	0.087
3	0.75	0	0.625	0.538	0.231	0.324	0.315	1	1	0.329	0.483	0.401
4	1	0	0.875	0	0	1	1	0.796	0.08	0.595	0.704	0.703
5	0	0.5	0.425	0.462	0.231	0.486	0.428	0.328	0.78	0.772	0.469	0.378
6	0	0.75	0.7	0.846	0.462	0.027	0.509	0.328	0.84	1	0.848	0.488
7	0	1	1	1	1	0	0.23	0.098	0.853	0.823	1	1

Note. D: diatomite content; B: basalt fibers content; A: asphalt-aggregate ratio.

TABLE 9: The grey correlation degree of the test indexes.

Factors	VV	VMA	VFA	MS	DS	ε_T	TSR	ε_r	ε_t
D	0.460	0.563	0.790	0.687	0.721	0.537	0.548	0.588	0.596
B	0.713	0.740	0.648	0.676	0.535	0.690	0.687	0.776	0.755
A	0.687	0.680	0.671	0.739	0.678	0.660	0.712	0.849	0.812

Note. D: diatomite content; B: basalt fibers content; A: asphalt-aggregate ratio.

diatomite adsorbing a large amount of free WRA fills the gap between the aggregates and increases VFA of WRM.

For the engineering properties of WRM, the correlation degree with MS of WRM: asphalt-aggregate ratio > diatomite content > basalt fibers content. Compared with the asphalt-aggregate ratio or basalt fibers content, diatomite content has a higher correlation with the DS of WRM. However, the correlation between basalt fibers content and ε_T is higher than that between diatomite content or asphalt-aggregate ratio and ε_T. The asphalt-aggregate ratio has the highest correlation with the TSR of WRM compared to diatomite content or basalt fibers content and the TSR of WRM. This indicates that the high-temperature performance of WRM is mainly related to the asphalt-aggregate ratio and diatomite content, and the addition of diatomite increases the relative content of the structural asphalt in WRM and thus improves the resistance to permanent deformation at high temperature; the basalt fibers content mainly affects the low-temperature performance of WRM, and the reinforcement effect of basalt fibers can significantly improve the anticracking ability of WRM at low temperature; the water damage resistance of WRM is mainly related to the asphalt-aggregate ratio, and a higher asphalt-aggregate ratio means more WRA to wrap aggregates, which makes it more difficult for external water to penetrate the interface between WRA and aggregates, thus improving the water damage resistance.

For the vibration attenuation of WRM, the correlation degree with ε_r and ε_t of WRM: asphalt-aggregate ratio > basalt fibers content > diatomite content. This reveals that the main material for attenuating vibration in WRM is WRA, followed by basalt fibers and finally diatomite. The improvement of the vibration damping performance of WRM by diatomite and basalt fibers is mainly attributed to the increase of asphalt-aggregate ratio caused by the addition of the two, which enhances the vibration damping performance of WRM. Besides, basalt fibers, as a reinforcement and toughening material, can rapidly spread the internal

stress of the asphalt mixtures, which further improves the vibration attenuation performance of the WRM.

4. Conclusions

In this paper, the pavement performance and vibration attenuation of WRM were reinforced by the diatomite and basalt fibers. The effect of diatomite and basalt fibers content on the pavement performance and vibration attenuation of WRM were analysed by the tests and the GCGA method. The following conclusions can be achieved:

(1) VMA, VFA, and MS of WRM increase with the addition of diatomite and basalt fibers. While VV of WRM decreases with the increase of diatomite content and increases with the increase of basalt fibers content. Besides, the variety of VV and VMA of WRM are closely related to basalt fiber content, while the variety of VFA of WRM is mainly related to diatomite content and WRA content.

(2) Diatomite and basalt fibers can significantly improve the high- and low-temperature performance and water damage resistance of WRM. And the improvement of high-temperature permanent deformation resistance, low-temperature cracking resistance, and water damage resistance of WRM is mainly attributed to diatomite, basalt fibers, and asphalt-aggregate ratio, respectively.

(3) The addition of diatomite and basalt fibers can significantly reinforce the vibration attenuation properties of WRM, and with the increase of the content of diatomite and basalt fibers, the reinforcement is gradually significant. In addition, the basalt fibers are superior to diatomite in improving the vibration attenuation properties of WRM and the tire on the WRM.

(4) The improvement of the vibration damping performance of WRM by diatomite and basalt fibers is

mainly attributed to the increase of WRA content caused by adding diatomite and basalt fibers. And the reinforcement and toughening effect of basalt fibers can further improve the vibration attenuation performance of WRM.

Data Availability

The data used to support the findings of this study are available from the corresponding author upon request.

Conflicts of Interest

The authors declare no conflicts of interest.

Acknowledgments

References

[1] D. Lo Presti, "Recycled tyre rubber modified bitumens for road asphalt mixtures: a literature review," *Construction and Building Materials*, vol. 49, pp. 863–881, 2013.

[2] M. A. Morcillo, M. E. Hidalgo, M. D. Pastrana et al., "LIFE SOUNDLESS: new generation of eco-friendly asphalt with recycled materials," *Environments*, vol. 6, no. 4, p. 48, 2019.

[3] X. Shu and B. Huang, "Recycling of waste tire rubber in asphalt and portland cement concrete: an overview," *Construction and Building Materials*, vol. 67, no. Part B, pp. 217–224, 2014.

[4] M. A. H. Al-Jumaili, "Sustainability of asphalt paving materials containing different waste materials," *International Conference on Materials Engineering and Science*, vol. 454, Article ID 012176, 2018.

[5] R. H. Zhang, J. Liu, J. C. Huang, and Y. Fu, "Rubber modified asphalt mixture properties and mechanical testing," *Applied Mechanics and Materials*, vol. 105–107, pp. 810–817, 2011.

[6] N. S. Mashaan and M. R. Karim, "Evaluation of permanent deformation of CRM-reinforced SMA and its correlation with dynamic stiffness and dynamic creep," *Scientific World Journal*, vol. 2013, Article ID 981637, 7 pages, 2013.

[7] N. S. Mashaan, A. H. Ali, S. Koting, and M. R. Karim, "Dynamic properties and fatigue life of stone mastic asphalt mixtures reinforced with waste tyre rubber," *Advances in Materials Science and Engineering*, vol. 2013, Article ID 319259, 9 pages, 2013.

[8] S. M. Asgharzadeh, J. Sadeghi, P. Peivast, and M. Pedram, "Fatigue properties of crumb rubber asphalt mixtures used in railways," *Construction and Building Materials*, vol. 184, pp. 248–257, 2018.

[9] S. Chen, F. Gong, D. Ge, Z. You, and J. B. Sousa, "Use of reacted and activated rubber in ultra-thin hot mixture asphalt

[10] W. D. Cao, "Study on properties of recycled tire rubber modified asphalt mixtures using dry process," *Construction and Building Materials*, vol. 21, no. 5, pp. 1011–1015, 2007.

[11] C. M. Li, Z. R. Fan, S. P. Wu et al., "Effect of carbon black nanoparticles from the pyrolysis of discarded tires on the performance of asphalt and its mixtures," *Applied Sciences*, vol. 8, no. 4, p. 624, 2018.

[12] X. Zhang, B. Zhang, H. Chen, and D. Kuang, "Feasibility evaluation of preparing asphalt mixture with low-grade aggregate, rubber asphalt and desulphurization gypsum residues," *Materials*, vol. 11, no. 8, p. 1481, 2018.

[13] J. H. Liu, "Fatigue life evaluation of asphalt rubber mixtures using semi-circular bending test," *Advanced Materials Research*, vol. 255–260, pp. 3444–3449, 2011.

[14] A. R. Pasandín and I. Pérez, "Fatigue performance of bituminous mixtures made with recycled concrete aggregates and waste tire rubber," *Construction and Building Materials*, vol. 157, pp. 26–33, 2017.

[15] A. Subhy, D. Lo Presti, and G. Airey, "Evaluation of the fracture performance of different rubberised bitumens based on the essential work of fracture," *Engineering Fracture Mechanics*, vol. 179, pp. 203–212, 2017.

[16] B. V. Kök, M. Yilmaz, and A. Geçkil, "Evaluation of low-temperature and elastic properties of crumb rubber- and SBS-modified bitumen and mixtures," *Journal of Materials in Civil Engineering*, vol. 25, no. 2, pp. 257–265, 2013.

[17] F. Gong, S. Guo, S. Chen, Z. You, Y. Liu, and Q. Dai, "Strength and durability of dry-processed stone matrix asphalt containing cement pre-coated scrap tire rubber particles," *Construction and Building Materials*, vol. 214, pp. 475–483, 2019.

[18] H. B. Liu, L. X. Fu, Y. B. Jiao, H. Liu, and J. Tao, "Short-term aging effect on properties of sustainable pavement asphalts modified by waste rubber and diatomite," *Sustainability*, vol. 9, no. 6, p. 996, 2017.

[19] R. Maharaj, C. Maharaj, and A. Hosein, "Performance of waste polymer modified road paving materials," *Progress in Rubber Plastics and Recycling Technology*, vol. 34, no. 1, pp. 19–33, 2018.

[20] X. Yang, Z. You, D. Perram et al., "Emission analysis of recycled tire rubber modified asphalt in hot and warm mix conditions," *Journal of Hazardous Materials*, vol. 365, pp. 942–951, 2019.

[21] P. Polaczyk, B. Han, B. Huang, X. Jia, and X. Shu, "Evaluation of the hot mix asphalt compactability utilizing the impact compaction method," *Construction and Building Materials*, vol. 187, pp. 131–137, 2018.

[22] T. Real, L. Montalbán, C. Masanet, and J. Real, "New laboratory procedure using a modal approach to obtain vibration attenuation properties of unaged and aged asphalt mixtures," *Proceedings of the Institution of Mechanical Engineers, Part L: Journal of Materials: Design and Applications*, vol. 230, no. 2, pp. 627–639, 2016.

[23] K. P. Biligiri, "Effect of pavement materials' damping properties on tyre/road noise characteristics," *Construction and Building Materials*, vol. 49, pp. 223–232, 2013.

[24] M. Ameri, M. Reza Seif, M. Abbasi, and A. Khavandi Khiavi, "Viscoelastic fatigue resistance of asphalt binders modified with crumb rubber and styrene butadiene polymer," *Petroleum Science and Technology*, vol. 35, no. 1, pp. 30–36, 2017.

[25] S. Aflaki and M. Memarzadeh, "Using two-way ANOVA and hypothesis test in evaluating crumb rubber modification (CRM) agitation effects on rheological properties of bitumen,"

Construction and Building Materials, vol. 25, no. 4, pp. 2094–2106, 2011.

[26] L. Zhang, C. Xing, F. Gao, T.-s. Li, and Y.-q. Tan, "Using DSR and MSCR tests to characterize high temperature performance of different rubber modified asphalt," *Construction and Building Materials*, vol. 127, pp. 466–474, 2016.

[27] Research Institute of Highway Ministry of Transport, "Standard test methods of bitumen and bituminous mixtures for highway engineering," China communications Press, Beijing, China, JTG E20-2011 in Chinese, 2011.

[28] Z. Lv, "Study on road performance and vibration and noise reduction performance of diatomite-basalt fiber compound modified asphalt mixture," MS thesis, Jilin University, Jilin, China, 2019.

[29] Y. Cheng, L. Li, Y. Zhang, Z. Lv, and C. Zhu, "Quantitative analysis of effect and interaction of diatomite and basalt fiber on asphalt performance," *Journal of Materials in Civil Engineering*, vol. 31, no. 12, Article ID 04019306, 2019.

[30] Y. C. Cheng, L. L. Li, P. L. Zhou, Y. Zhang, and H. Liu, "Multi-objective optimization design and test of compound diatomite and basalt fiber asphalt mixture," *Materials*, vol. 12, no. 9, 1461 pages, 2019.

[31] R. Xiong, J. Fang, A. Xu, B. Guan, and Z. Liu, "Laboratory investigation on the brucite fiber reinforced asphalt binder and asphalt concrete," *Construction and Building Materials*, vol. 83, pp. 44–52, 2015.

[32] J. Gao, A. Sha, Y. Huang et al., "Cycling comfort on asphalt pavement: influence of the pavement-tyre interface on vibration," *Journal of Cleaner Production*, vol. 223, pp. 323–341, 2019.

[33] S. J. Hong, S.-W. Park, and S. W. Lee, "Tire-pavement noise prediction using asphalt pavement texture," *KSCE Journal of Civil Engineering*, vol. 22, no. 9, pp. 3358–3362, 2018.

[34] D. Zhang, M. Chen, S. Wu et al., "Analysis of the relationships between waste cooking oil qualities and rejuvenated asphalt properties," *Materials*, vol. 10, no. 5, p. 508, 2017.

[35] Z. Wang, Q. Wang, and T. Ai, "Comparative study on effects of binders and curing ages on properties of cement emulsified asphalt mixture using gray correlation entropy analysis," *Construction and Building Materials*, vol. 54, pp. 615–622, 2014.

[36] J.-c. Du and M.-F. Kuo, "Grey relational-regression analysis for hot mix asphalt design," *Construction and Building Materials*, vol. 25, no. 5, pp. 2627–2634, 2011.

[37] J. Gao, H. Wang, Z. You et al., "Gray relational entropy analysis of high temperature performance of bio-asphalt binder and its mixture," *International Journal of Pavement Research and Technology*, vol. 11, pp. 698–708, 2018.

[38] Y. Zheng, Y. Cai, G. Zhang, and H. Fang, "Fatigue property of basalt fiber-modified asphalt mixture under complicated environment," *Journal of Wuhan University of Technology-Materials Science Edition*, vol. 29, no. 5, pp. 996–1004, 2014.

[39] N. Morova, "Investigation of usability of basalt fibers in hot mix asphalt concrete," *Construction and Building Materials*, vol. 47, pp. 175–180, 2013.

Research Article

Modelling and Characterizing the Adhesion of Parallel-Grooved Interface between Concrete Lining Structure and Geopolymer by Wedge Splitting Method

Zhaopeng Yang,[1] Ya Wei,[2] and Linbing Wang (ORCID)[1,3]

[1]*National Center for Materials Service Safety, University of Science and Technology Beijing, Beijing 100083, China*
[2]*Key Laboratory of Civil Engineering Safety and Durability of China Education Ministry, Department of Civil Engineering, Tsinghua University, Beijing 100084, China*
[3]*Department of Civil and Environmental Engineering, Virginia Tech, Blacksburg, VA 24061, USA*

Correspondence should be addressed to Linbing Wang; wangl@vt.edu

A new method for increasing the interface resistance between geopolymer coating and concrete lining structure without applying the organic binder was suggested in this study. Parallel grooves with different depths and orientations were milled on the top surface of concrete block, and well-blended geopolymer mixture (Na-PSS type geopolymer: Sodium poly-sialate-siloxo) was coated upon the grooved interface. The wedge splitting (WS) experiments were conducted to compare the interface adhesion capacity of specimens with different groove width/depth ratios and groove orientations. The average energy release rate (ERR) was calculated by integrating the P_v-CMOD diagram to quantify the interfacial fracture toughness. To understand the interface strength mechanisms and the fracture mode at the front crack mouth, franc 3D simulation was carried out to segregate the mixed fracture mode to determine the initial pure stress intensity factors (K_I, K_{II}, K_{III}) at the crack mouth. Both the experiments and simulation results indicated that the highest interface fracture toughness was reached by the double diagonal parallel grooves with 0.375 width/depth ratio. These findings put forward a promising attaching method for efficient and reliable passive fire protection coating, with the aim of decreasing the risk of layer delamination in highway tunnels.

1. Introduction

The concrete lining structures in underground tunnels are susceptible to fire hazards due to their large length/width ratio and narrow enclosure space. Damage to the concrete lining structure is the primary reason for rapidly decreasing the safety of a tunnel. A growing body of literature has recognized the importance of passive fire protection coating, which is a relatively efficient and economic method for eliminating this potential threat.

Geopolymer [1] is a man-made two-component stone-like material with excellent fire resistance. Any material that contains silica and alumina could be activated by alkali and polymerized into geopolymer, such as the meta-kaolin, furnace slag, and fly ash. Over the past two decades,

numerous systematic investigations have focused on geo-polymer's thermal conductivity and heat isolation along with the variation of the ingredients [2–4]. Singh et al. [5] assessed a mortar/concrete made with geopolymeric binder and tested its bond strength with aggregate; Cheng and Chiu [6] described a mixture of geopolymer and blast furnace slag and set a 10 mm thick geopolymer panel exposed to 1100°C fire. Rahman and Radford [7] tested the interfacial bond strength of the nanofiber geopolymer and evaluated the pure mode I fracture toughness with different factors. Zhang et al. [8] coated 5 mm thick geopolymer over the structure rect-angular cross-section (RC) beam and compared it with the RC beam strengthened with fiber sheet.

Although most researchers claim that there are no clear delamination phenomena during the fire test for the

geopolymer coating, this may be because their coating was relatively thin (5 mm thickness or lower) in their experiments. To prevent serious fire accidents, the requirement of the thermal barrier coating thickness of common material in the high way tunnels is estimated to be 20–30 mm. Along with the increment of the coating thickness, the failure mode of layered structure may switch from thin film coating (plane stress) to unignorable thickness coating (plane strain), and the chances of delamination can substantially increase. Another problem in previous researcher's tests was that the geopolymer coating and the concrete base were considered as indivisible whole system, and the experiment data is insufficient to characterize the adhesion ability between the geopolymer coating and concrete base. Moreover, these approaches have failed to address the potential delamination threat due to the different coefficient of thermal strain between the concrete (0.003 to 0.006 at 300°C) and geopolymer coating (−0.01 to −0.02 at 250°C) [8, 9].

Currently, to prevent the debonding threat of the thermal barrier coating in concrete lining structures, the organic binders need to be painted underneath the geopolymer coating. However, the bonding strength of epoxy resin or vinyl ester decreases dramatically when the temperature reaches a critical level. Recent evidence suggests that the bond strength of these organic binders remains only 40% of the original value when the temperature reaches around 140°C. As these carbon-based materials have limited reliability in fire attack, the challenge for the geopolymer coating is to increase the interface adhesion ability without utilizing the organic binder to minimize the possibility of delamination.

This study focuses on the quantification of the interfacial adhesion between concrete and geopolymer coating by the wedge splitting (WS) experiments and thoroughly investigates the interfacial fracture resistance of the parallel groove interface with different width/depth ratios and groove orientations. Furthermore, the mixed fracture mode partition was analyzed by the Franc 3D method to compare the different fracture modes at the front crack mouth and to support the experiment results.

2. Wedge Splitting Experiments

2.1. The Substrate Shotcrete Base. The concrete lining structure in the highway tunnel is a multilayer system, and the outermost layer of the concrete lining structure is used to ensure the clear space of the tunnel and acts as a permanent support structure. We chose the concrete block sample with the same grading proportion of the outmost layer structure to quantify the interfacial adhesion ability. Guided by Chinese GB 50086-2015 (Technical Code for Ground Anchorages and Shotcrete Support), the China ISO Standard Sand was selected as the fine aggregate for this experiment. The particle size distribution of the sand is shown in Table 1.

Due to the characteristics of shotcrete construction, when selecting the mix proportion of shotcrete, it is necessary not only to meet the requirements of structure mechanical properties of shotcrete (compressive, tensile, and bonding strength), but also to keep the shrinkage

TABLE 1: The particle size distribution of standard sand.

No.	Mesh size (mm)	Cumulative sieve residue (%)
1	2.0	0.0
2	1.6	7 ± 5
3	1.0	33 ± 5
4	0.5	67 ± 5
5	0.2	87 ± 5
6	0.1	99 ± 1

deformation value of shotcrete minimum. In order to transport the shotcrete in the pipe on the construction set, the amount of aggregate is much less than that in the ordinary concrete, while the amount of sand increases, up to 50%. With high sand ratio, the aggregate total surface area will increase, and more cement slurry will be required to wrap the aggregate surface to meet the requirements of shotcrete strength. The mix proportion of general shotcrete mixture in our experiment is as follows: the weight ratio of cement and sand is 1 : 4~1 : 4.5, the sand ratio is 45%~55%, the water cement ratio is 0.04~0.45, and the dosage of accelerator should be determined by experiment according to the product performance.

For the convenience to fit with the Hydraulic Mechanic Test System (HMTS), the concrete cubic size was chosen as 150 mm * 150 mm * 130 mm, in which the 20 mm height was reserved for the geopolymer coating. All the ingredients are thoroughly mixed plus over 1.5 mins of vibration to ensure an even distribution. A total number of 20 blocks of concrete samples are prepared for the same batch to achieve the consistency for the following test.

2.2. The Aluminosilicate Raw Material. The geopolymer can be synthesized by mixing the meta-kaolin binder, 3% sodium silicate (Na_2SiO_3), and 3% alkaline hydroxide (NaOH) together [11, 12]. Meta-kaolin is an aluminosilicate rich kaolin clay mineral, which was calcined at 700°C for 10 hours and grounded into fine-grained powder (200 mesh). The diameter size for the meta-kaolin particle is less than 10 μm to achieve the maximum reactivity. The composition of the meta-kaolin mineral was shown in Table 2.

The properties of geopolymer may be distinctive due to the molecular structure and the raw materials that have been used. Three types of geopolymer were categorized by varying the Si/Al ratio, as shown in Table 3.

To reach the maximum heat isolation capacity, we chose the Na-PSS type geopolymer. The most important mole ratio for Na-PSS type geopolymer is $3.5 \leq (n(SiO_2)/n(Al_2O_3)) \leq 4$ [12]. For every 100 g of meta-kaolin, 60 g of sodium silicate is required. For each concrete block, the geopolymer coating needs to reach a thickness of 20 mm to meet the fire protection requirements. As the high-reactivity cement, meta-kaolin can be easily dissolved into alkaline solution and breaks down into SiO_2 and AlO_4. The weight ratio of SiO_2 and Al_2O_3 in the meta-kaolin powder was 55% and 44%, respectively.

The sodium silicate (Na_2SiO_3) is white powder and needs to disperse in hot water (45°C–55°C) with sodium hydroxide.

TABLE 2: Compositions of highly active meta-kaolin powder.

SiO$_2$	Al$_2$O$_3$	Fe$_2$O$_3$	TiO$_2$	CaO	MgO	K$_2$O	Na$_2$O	LOI
54.06	43.12	0.76	0.24	0.17	0.06	0.55	0.06	0.98
Activity Index ≥110								

TABLE 3: The Composition of three types of geopolymer [11].

Types of geopolymer	Chemical formula	Theoretical values of three key parameters		
		$n(\text{SiO}_2)/n(\text{Al}_2\text{O}_3)$	$n(\text{NaO})/n(\text{Al}_2\text{O}_3)$	$n(\text{H}_2\text{O})/n(\text{Al}_2\text{O}_3)$
PS	Na$_2$Si$_2$Al$_2$O$_8$ (6 − 7)H$_2$O	2	1	6
PSS	Na$_2$Si$_2$Al$_2$O$_{12}$ (2 − 3)H$_2$O	4	1	3
PSDS	Na$_2$Si$_2$Al$_2$O$_{16}$H$_2$O	6	1	2

After stirring for 5 min with a magnetic stirrer, this warm mixture solution was then poured into the orange meta-kaolin powder. The final ingredient distribution was shown in Table 4.

After the raw materials were thoroughly mixed, the geopolymer paste was poured into the mould with the solid concrete block at the bottom, as shown in Figure 1. To reach the maximum adhesion ability, the contact surface of the concrete block was cleaned by sand paper to remove the dirt. The mould was kept in a humidity- and temperature-controlled chamber. The testing block was then covered with a moist towel to prevent from drying and microcracking on the surface.

It took 7 days before the geopolymer was fully hardened and the plastic moulds were removed. Two steel bars were positioned symmetrically 15 mm from the initial cracking interface and glued upon the top surface of each testing sample with epoxy resin, as shown in Figure 2. The steel bars were designed to be attached to the flange of the load transferring clamps.

2.3. Procedures of Wedge Splitting Test.

The WS [13–17] test is a displacement-driven experiment to quantify the material adhesion ability and the fracture energy of the crack. To get precise results, one principle preassumption is that no energy was dissipated except in the fracture process zone and the average work done is all used for crack propagation. Self-weight of the specimen not affecting the final result is one of the advantages of the WS method compared to others such as the three-point bending, compact tension, and direct stretch methods. Another advantage is that the WS test reduces the impact of the vertical load and effectively increases the stiffness of the testing machine by introducing the clamp structure. In addition, a suitable wedge angle shall moderate the requirement of vertical load and easily transfer it to the horizontal load, which effectively increases the data accuracy of the whole testing system.

The specimen was subjected to a constant rate of displacement during the entire loading process. The loading frame in this experiment was an HMTS with a loading acquisition system. The wedge splitter was contacted to the hydraulic testing machine rigidly and provided the vertical displacement; the loading plates were placed symmetrically at both sides of the initial fracture interface (shown in

TABLE 4: Raw material weight list.

Geopolymer (g)	Sodium silicate (g)	Warm water (g)	Sodium hydroxide (g)
800	500	270	40

Figure 3). The components of the loading transfer clamps included two loading plates and one wedge splitter. Although, theoretically, the tangent wedge angle should be as small as possible, a tangent angle θ of 15° was chosen in this study from a practical perspective. The horizontal force can be acquired by

$$p_h = \frac{P_v}{2 \tan \theta}. \tag{1}$$

The crack mouth opening displacement (CMOD) was recorded simultaneously by a digital extensometer (a linear variable displacement transducer). The extensometer in this experiment was YYJ-5/15-L (manufactured by Ji'nan Li Dong Test Equipment Co., Ltd, China), which can measure the CMOD values with a precision up to 0.001 mm. All specimens were tested under the same vertical displacement control rate at 0.00125 mm/s, which is equivalent to 0.0004 mm/s in the horizontal direction. To ensure that fracture initiated along the interface, the loading point needed to be close to the crack mouth.

As the crack resistance capacity is positively proportional to the energy release rate (ERR), the EER method is ideal for quantifying the adhesion ability of the interface as long as the additional bending has less effect around the crack tip fracture zone and the measured CMOD is close to the real value. The initiation of a crack in the specimen will change the compliance of the test sample, while, in the WS test, such changes in compliance can be successfully avoided. Because of the high stiffness of these sections, the energy required for the geopolymer and concrete sections to undergo elastic change was much higher compared with the interfacial fracture initiation energy.

2.4. Parallel-Grooved Surface with Different Width/Depth Ratios and Groove Orientation.

Grooving [19–21] is one conventional method to enhance the interfacial toughness and prevent the debonding phenomenon. In this study, the parallel grooves were milled vertically onto the concrete top

(a)

(b)

(c)
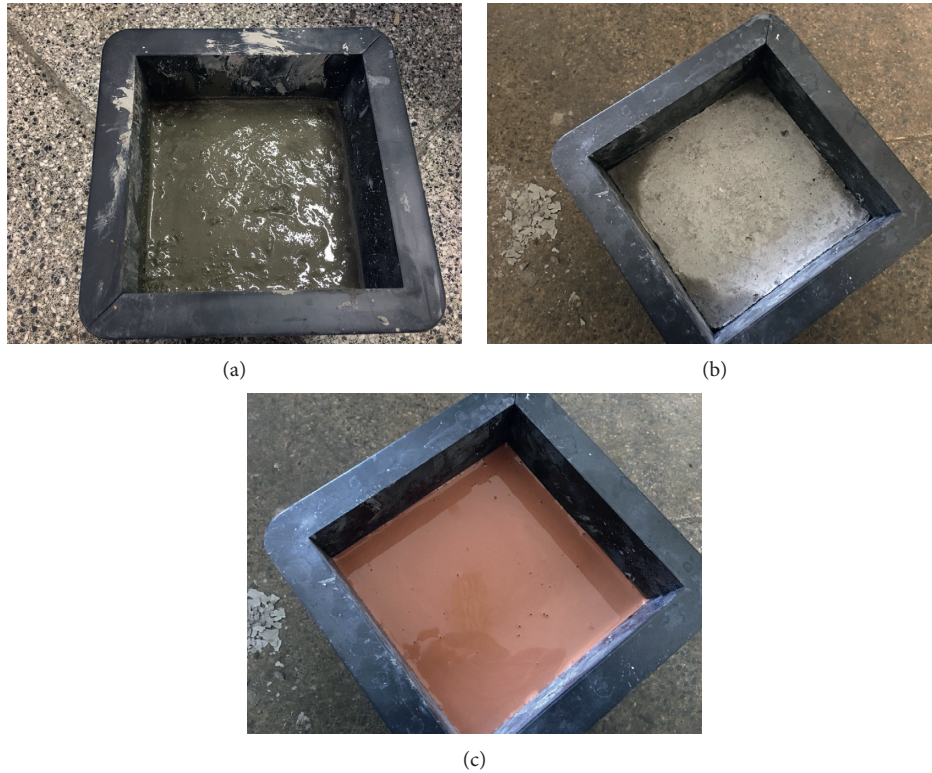
FIGURE 1: Procedure of making the test samples: (a) concrete cement paste; (b) after 28 days curing, the smooth contact surface with dirt removed; (c) pouring the geopolymer binder into the mould.

FIGURE 2: Smooth interface sample glued with two steel bar.

FIGURE 3: The assembled equipment for WS test.

surface before coating with the geopolymer mixture. The parallel grooving was milled with the same 3 mm width and different depths (5 mm, 8 mm), shown in Figure 4. The failure model of the interface fracture and the adhesion ability were compared with those of the control group (smooth surface).

FIGURE 4: Different parallel groove depths and the geopolymer coating: (a) (b) (c) (d) 5 mm depth groove; (e) 5 mm depth parallel groove with geopolymer coating; (f) 8 mm depth parallel groove with geopolymer coating.

The orientation of the parallel grooves is also considered as an impact factor of the interfacial adhesion ability because it changes the fracture mode at the crack front mouth. To evaluate this factor, three more sets of differently orientated grooves were prepared (horizontal, diagonal, and double diagonal). To achieve the consistency of the experiment results, all specimens had the same width/depth ratio (0.375) and the same space between grooves (10 mm), but the orientations of the grooves were different, as shown in Figure 5.

(a)
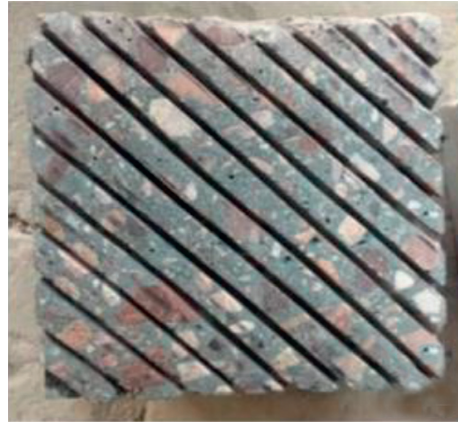
(b)

(c)

(d)
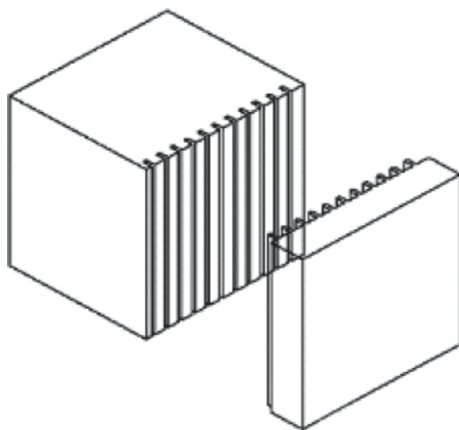
(e)
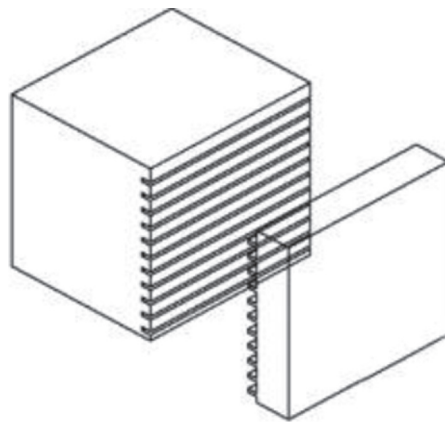
(f)

Figure 5: Continued.

(g)   (h)
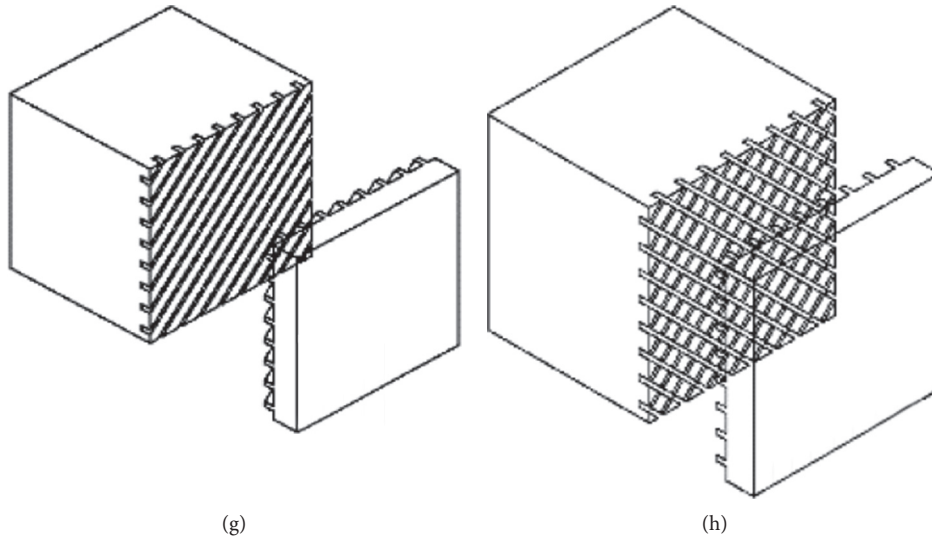
Figure 5: Geometry of the different orientations of grooving: (a) (e) vertical parallel grooves; (b) (f) horizontal parallel grooves; (c) (g) diagonal parallel grooves; (d) (h) double diagonal parallel grooves.

3. WS Test Results

3.1. Smooth Contact Interface. Three unmodified testing samples were prepared to acquire the P_v-CMOD curve for the control group as shown in Figure 6.

From the loading diagram, the fracture propagation process can be divided into three stages: crack initiation, stable expansion, and unstable propagation. For the first stage, the curve was in linear form, and the crack initial point was determined to be the point when the nonlinear decrease change in the load was firstly initiated. The load P_v is equivalent to the external loading plus the self-weight of the load-transmitting plates. The values of $P_{vinital}$ for sample 1 and sample 2 were nearly half of the P_{vmax}. CMOD in the first section for all three samples were only 0.04–0.13 mm, which can be ignored. At the second stable expansion stage, the external load P_v for all three samples jumped from origin to $P_{vinitial}$ and continued to reach P_{vmax} followed by the unstable propagation stage. The curves of sample 1 and sample 3 showed the obvious nonlinear CMOD and slow crack growth. When the CMOD overpassed the critical value, the growth of the crack length was in a stable speed until the final failure occurred. At the third unstable propagation stage, a monotonic decrease was shown in all three samples until the complete failure finally occurred. The energy that was required for the crack initiation ($G_{initial}$) and crack extension ($G_{average}$) can be calculated by integrating the area under the P_h-CMOD curve. However, the direct result from the experiment is the P_v-CMOD, and the integration of the area under the P_v-CMOD curve G_{vo} can be converted to the area under P_h-CMOD curve G_h by formula $G_h = G_{vo}/(2 \tan \theta)$. The final results were shown in Table 5.

The reason why these three test samples have diverse forms of P_v-CMOD curves is that the maximum external load is relatively small (only 0.035 kN on average), so the curves can be easily disturbed by many factors such as the
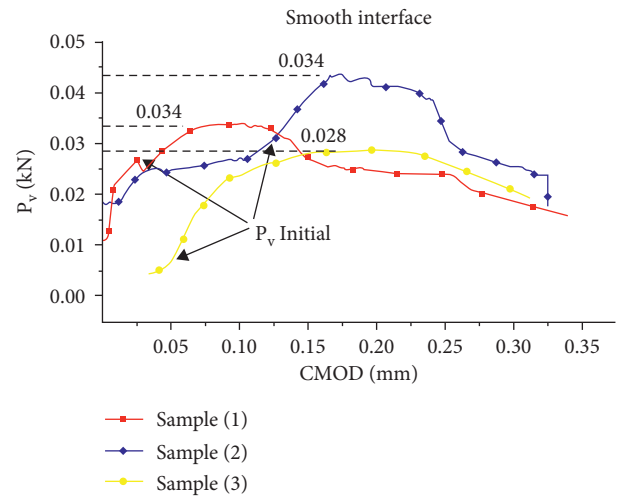
Figure 6: P_v-CMOD curve of the control group with smooth contact interface.

small preexisting fractures. Due to the increments of the compliance of the specimens, the external load will go down as well when the crack length is extended. The crack will not expand until the load exceeds $P_{vinitial}$; the height of the ligament and the crack initial point are not affected by sizes, and there is a stable expansion stage before the final fracture failure. The gradient of the initial stage indicates the resistance of the interface.

3.2. Parallel-Grooved Interface with Different Depth/Width Ratios. The dissymmetric geometry of the geopolymer coating (thickness of the geopolymer is 20 mm, and the groove depth is only 5 mm and 8 mm) was used in this study. As the width W_0 is the same for all specimens, the only difference of these specimens is the width/depth ratios of the

TABLE 5: The WS Test results of the control samples with smooth contact interface.

Specimen	$P_{vinitial}$ (kN)	$P_{hinitial}$ (kN)	P_{vmax} (kN)	P_{hmax} (kN)	CMOD initial (mm)	Crack initial energy (J)	CMOD final (mm)	Average crack energy (J)
Sample 1	0.034	0.063	0.028	0.052	0.02	0.0007	0.34	0.086
Sample 2	0.06	0.111	0.034	0.063	0.005	0.0037	0.33	0.102
Sample 3	0.28	0.522	0.043	0.080	0.004	0.0075	0.32	0.092

grooves. Along with the increment of the depth of the grooves, not only the total contact area between the two materials increased, but also the dominated fracture mode at the interface transferred from mainly pure mode I to a mixed fracture mode. At the bottom edge of the grooving, the transverse stress σ_{xx} in the interface accumulated and became the fracture driving force inside the geopolymer material.

By comparing the 5 mm and 8 mm curve gradients in Figure 7, it was found that the increase in the initial stage of the fracture resistance was distinct. When the depth of the groove increased from 5 mm to 8 mm, the damage mode transformed from a concrete-geopolymer interfacial crack to an interfacial fracture between the geopolymer and concrete surface plus the geopolymer tearing fracture. This is the main reason why the area under the P_v-CMOD in the 8 mm depth curve is much larger than that of the 5 mm depth curve.

As shown in Table 6, both the initial fracture toughness and the cohesive stress increased significantly with the increase of the depths of the grooves. The maximum vertical load increased from 0.022 kN (untreated surface) to 0.3 kN (8 mm depth of grooving), and the CMOD width increased from 0.34 mm to 2.02 mm. These results indicate that the grooved interface successfully enhances the total fracture resistance.

3.3. Parallel-Grooved Interface with Different Orientations. The three different groups of specimens were subjected to the same WS test procedure, and the P_v-CMOD graphs are shown in Figure 8.

Three horizontally grooved samples were tested, but the data of only two samples have been successfully acquired due to the unique failure mode at the edge of the horizontal grooves. By observing the loading graph (Figure 8), the horizontally grooved specimen had linear behavior at the beginning, similar to the vertically grooved specimen. After the initiation of the crack, the load overpassed 0.466 kN and quickly dropped and retained at 0.25 kN for a longer period compared with the vertically grooved samples. As the displacement continued to be applied by the wedge, the load curve moved horizontally as the CMOD increased.

On the other hand, the diagonally parallel grooves reached the highest loading and average ERR among all the specimens. Comparing the $G_{hinital}$ of three categories of grooves, the horizontal and diagonal grooves were at the same levels. The reason for this is that most of the adhesion ability is supplied by the geopolymer strip itself at the interface and the fracture mode is different at the bottom edge of the front crack mouth along with the strip.

4. Test Results Analysis

To explain the WS test results, it is necessary to analyze each case in fracture mechanic perspective. When the fracture propagates along with the interface, the crack resistance capacity is dominated by two terms, the inherent fracture toughness K_{IC}^{ini} and the cohesive fracture toughness after the initial propagation.

$$R(\Delta l) = K_{IC}^{ini}(P_{initial}) + f(w_s, \Delta l, P_{max}, M_t), \qquad (2)$$

where $R(\Delta l)$ is the crack extension resistance; $f(w_s, \Delta l, P_{max}, M_t)$ is the cohesive fracture toughness. From the perspective of a fictitious fracture zone, the value of the cohesive strength $(R(\Delta l))$ is based on the cohesive stress distribution, which is a function of the CMOD width (w_s), the maximum tensile stress, the moment near the crack tip M_t and the crack propagation length (Δl).

Details of external loads were reflected by the terms of SIFs (K_I, K_{II}, K_{III}) with additive properties. The total fracture toughness is not the intrinsic property for geopolymer, which is affected by the load mode and the shape of geometry. For brittle materials like PSS geopolymer, the fracture toughness is different in each pure mode under small-scale yielding assumption. For mode I fractures, the angular component of crack initiated just behind the crack tip will be adjusted once the crack tip was the straight line or the rough curve; but for mode II or III, as the interplane was weaker than the brittle material itself, the angular components of modes II and III were larger than those of pure mode I. This is the main reason why brittle material can bear larger external loads in modes II and III than mode I, and it is known as the "anchoring effect" in the interface mechanics.

Therefore, for any given mixed fracture mode, the near-field solution exhibits an intrinsic spatial invariance of the combination of pure fracture mode. The superposition principle can be used for all linear elastic deformation at any point. For a given loading mode, the SIF corresponding to each load can be added together to get the final SIF term. This principle is very important for the analysis of crack systems subjected to complex loading modes.

4.1. Fracture Mode of Parallel-Grooved Interface with Different Width/Depth Ratios. During the experiments, the debonding damage model of the contact interface can be divided into three types (Figure 9). The first type is total delamination; the second type is mixed damage mode (i.e., the fracture delaminates along the grooves boundary); and the third type is in the plane near and parallel to the

(a)

(b)
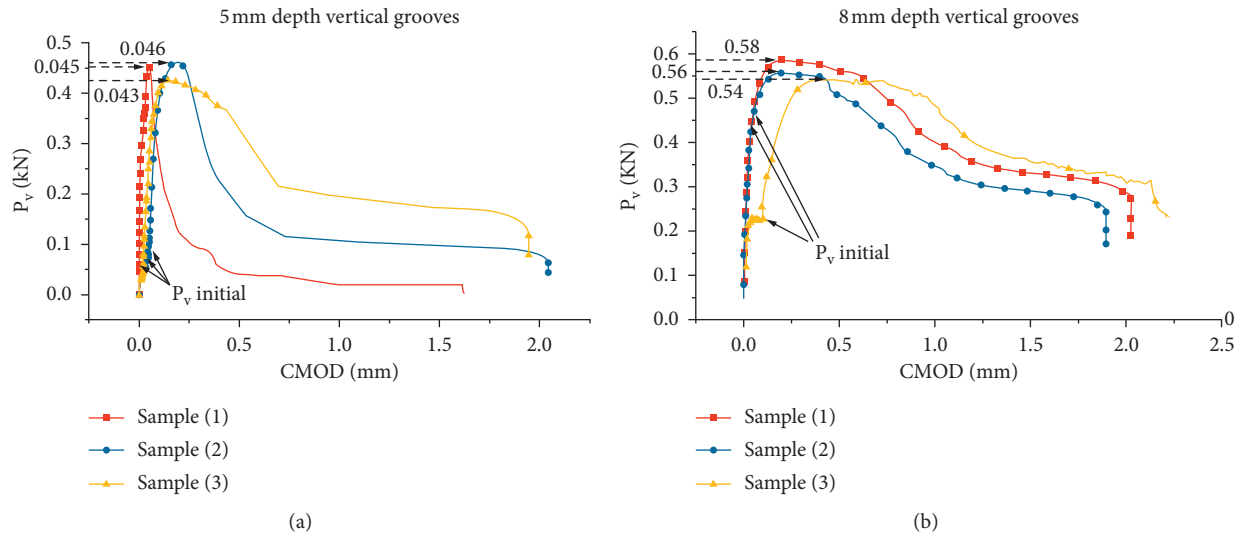
FIGURE 7: P_v-CMOD curve of different vertical parallel grooving depths.

TABLE 6: The comparison of the average ERR and CMOD of difference depths of vertical parallel grooves.

Specimen	$P_{vinitial}$ (kN)	$P_{hinitial}$ (kN)	P_{vmax} (kN)	P_{hmax} (kN)	CMOD initial (mm)	$G_{hinitial}$ (J)	CMOD Final (mm)	$G_{haverage}$ (J)	W/d ratio
5 mm Sample 1	0.064	0.119	0.450	0.840	0.002	0.001	1.600	0.168	0.8
5 mm Sample 2	0.086	0.160	0.460	0.858	0.005	0.002	1.600	0.121	0.8
5 mm Sample 3	0.061	0.114	0.450	0.840	0.005	0.001	2.040	0.358	0.8
8 mm Sample 1	0.450	0.840	0.580	1.082	0.004	0.014	2.020	1.610	0.375
8 mm Sample 2	0.410	0.765	0.560	1.045	0.004	0.013	1.840	1.724	0.375
8 mm Sample 3	0.210	0.392	0.540	1.007	0.01	0.019	2.450	1.564	0.375

(a)

(b)

FIGURE 8: Continued.

8 mm depth double diagonal grooves

(c)
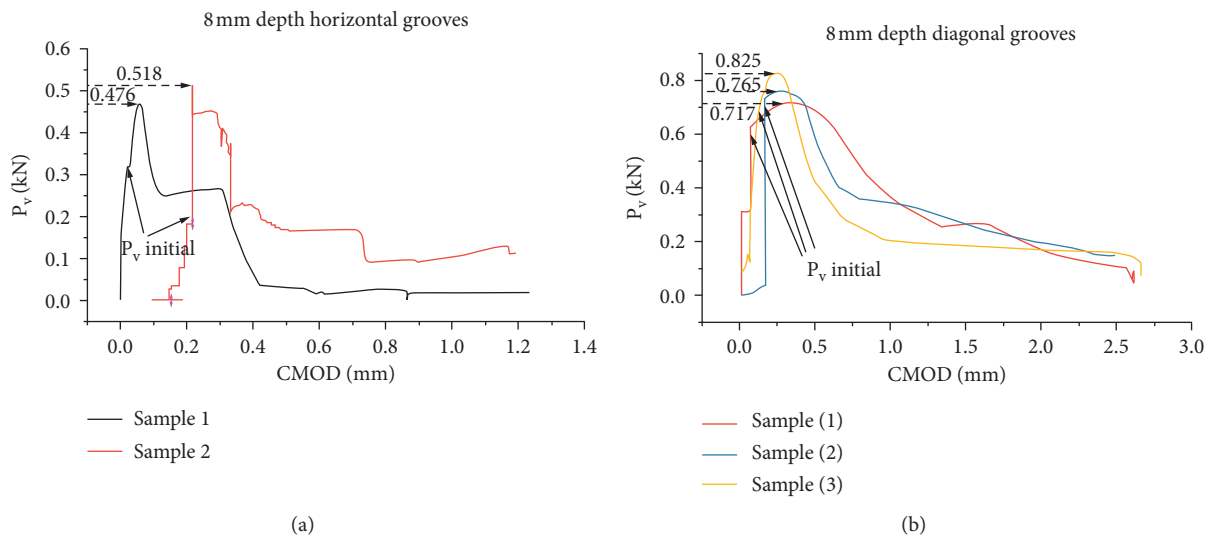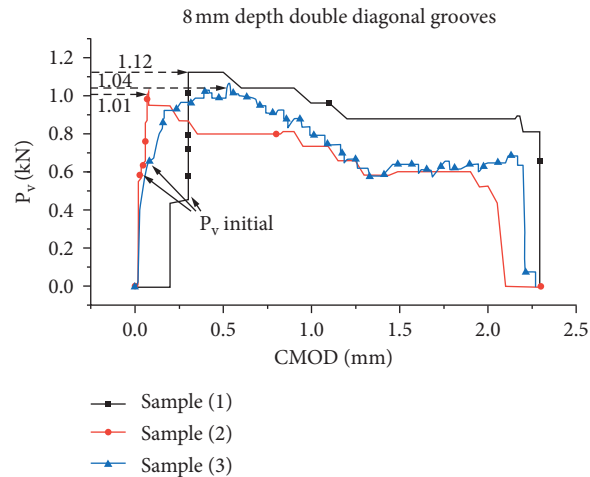
FIGURE 8: P_v-CMOD curve of different grooves orientations.
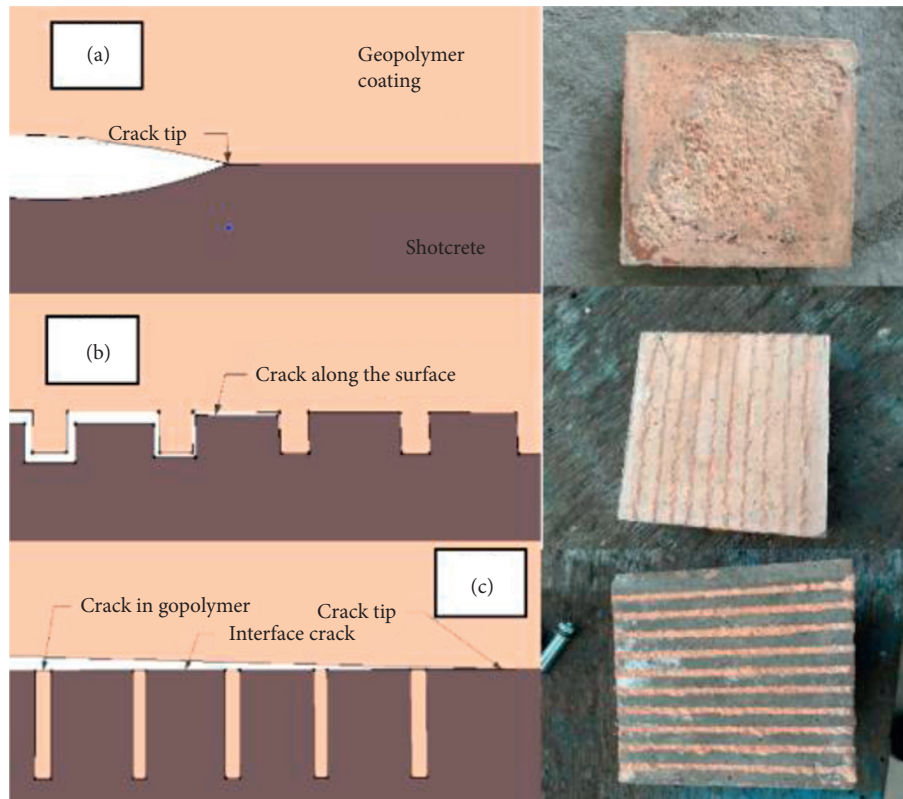
FIGURE 9: Change of the fracture mode along with the decrease of the width/depth ratio: (a) smooth interfacial crack; (b) high width/depth ratio; (c) low width/depth ratio.

interface. After the preresearch, we summarized the cracking conditions in Figure 9.

Unlike the bimaterial surface, the numerical value of fracture toughness can be directly calculated in single material with classical fracture mechanics theory. In this geopolymer and concrete bimaterial body, the fracture model of smooth contact interface is dominated by total

delamination, and the crack is propagated in the plane near and parallel to the interface.

According to Williams [22] and Xu and Reinhardt [23], the singular stress field is universal to the cracked body. Take the stress field directly in front of the crack tip for example; the stress field can take the superposition method for the mixed fracture mode:

$$\sigma_{rr} = \frac{K_{\mathrm{I}}}{\sqrt{2\pi r}} \cos \frac{f_{\theta ij}}{2} \left[1 + \sin^2\left(\frac{f_{\theta ij}}{2}\right) \right]$$
$$+ \frac{K_{\mathrm{II}}}{\sqrt{2\pi r}} \sin \frac{f_{\theta ij}}{2} \left[1 - 3 \sin^2\left(\frac{f_{\theta ij}}{2}\right) \right], \tag{3}$$

where $f_{\theta ij}$ is the function with angular component. Assume the external loading condition is symmetric in the interface plane; the range of the angular component $f_{\theta ij}$ of the SIF for vertical grooves and horizontal grooves varies from $\{0, (\pi/2)\}$. The final SIF was the combination of different local pure SIFs ($K_{\mathrm{I}}, K_{\mathrm{II}}, K_{\mathrm{III}}$) with distinct angular and radial components.

The fracture mode is mixed by mode I (opening mode), mode II (sliding mode), and mode III (tearing mode). The sliding and tearing of the strip occurred for the diagonal direction strips. Along with the change of the fracture's orientations, the predominated fracture mode potentially shifted from mode I into mixed fracture mode. The relationship between ERR and SIFs is

$$G = \frac{1}{E}\left(K_{\mathrm{I}}^2 + K_{\mathrm{II}}^2\right) + \frac{1}{2\mu}K_{\mathrm{III}}^2. \tag{4}$$

This is due to the texture of geopolymer that is amorphous rather than single crystalized. According to Williams Field [13], when the fracture propagates along the dissimilar bimaterial interface, the singular field around the crack tip of the interfacial is not in square root, but at new form:

$$\sigma_{ij}(r, \theta) = \frac{\mathrm{Re}\left[Kr^{i\varepsilon}\right]}{\sqrt{2\pi r}}f_{ij}^{\mathrm{I}}(\theta, \varepsilon) + \frac{IM\left[Kr^{i\varepsilon}\right]}{\sqrt{2\pi r}}f_{ij}^{\mathrm{II}}(\theta, \varepsilon). \tag{5}$$

The total fracture resistance R in the uncracked ligament is the linear elasticity range and can be achieved by combine the different pure mode SIFs ($K_{\mathrm{I}}, K_{\mathrm{II}}, K_{\mathrm{III}}$).

4.2. Fracture Mode of Parallel-Grooved Interface with Different Orientations. When the width/depth ratio reaches the critical value, the stress concentration occurs, and the fracture propagates along the geopolymer strips' bottom side and then kinks off into one of the materials (shown in Figure 10). The point that the crack propagates into the coating layer is the region where the stress concentration at the edge of the grooves occurs. The reduction of stiffness of the geopolymer is accompanied by the crack propagate in the geopolymer coating as the displacement of the wedge continues being applied until the final failure happens. This actually has approved that horizontal orientation of the grooves is not suitable for the contact design as it fails to protect the concrete block, because once the propagation of the interfacial delamination occurs, it is quite easy for the crack to jump into the brittle geopolymer material and join with the vertical edge crack.

The fracture mode at the bottom edge of the strips is in the mixed mode due to the asymmetry of the loading patterns. Although the SIFs ($K_{\mathrm{I}}, K_{\mathrm{II}}, K_{\mathrm{III}}$) are dependent on external boundary conditions, crack geometry, and crack length, the distribution pattern of SIFs around the crack tip is determined by the angular component function, which is independent of the loading conditions and the crack length. From this perspective, the grooves can vary not only in width/depth ratio but also in the pattern of the groove's orientations. To investigate the maximum adhesion ability influenced by the pattern of the grooves, it is necessary to conduct the investigations of the fracture modes at the bottom edge of the geopolymer strips.

5. Mixed Fracture Mode Partition by Franc 3D

The classical definition of fracture behavior depends on both loading conditions (preexisting crack) and properties of the fracture mode. When a specimen loses its symmetry due to the different thicknesses of upper and lower layer structures, the fracture will propagate in the mixed mode. The reason to divide the mixed mode based on the same loading condition is that the fracture is governed by different fracture criteria, and the shear force and friction resistance need to be addressed separately. Among other numerical methods to acquire the partition of the mixed mode fracture, Franc 3D uses the displacement field at the crack tip front and an extrapolation method to calculate all of the pure SIFs () at the same time.

5.1. Building Up the Geometric Model. This simulation does not consider the influence of temperature field, so only the elastic mechanical parameters of materials are set. Young's modulus of 4.1 GPa and Poisson's ratio of 0.21 are identified for the geopolymer. The boundary condition for the bottom plane is fixed, and the displacement for the strip is 5 mm upwards for both models (shown in Figure 11).

After the input document is transferred from ABAQUS into Franc 3D, the initial crack is ready to be inserted into the designated location. The Franc 3D software is powerful to simulate the cracks, and it can generate multicracks, nonplanar cracks, and the cracks with arbitrary shape (Figure 12).

The shape of the crack tip is chosen as half ellipse when the short semiaxis $a = 0.05$ mm and the long semiaxis $c = 0.1$ mm (Figure 13). Step increment is set to 0.1 for both models as this simulation only focuses on the fracture mode partition at the fracture initiation stage. Since Franc 3D is a boundary element analysis system, only the surface and the crack region of the model need to be meshed, and no meshing is needed inside the model.

5.2. Computation of the Partition of SIFs. Franc 3D uses the maximum hoop criterion as the crack propagation criterion. For mode I, the program uses the crack opening displacement (COD) to calculate SIFs; for mode II, it uses the crack sliding displacement (CSD); and for mode III, it uses the crack tearing displacement (CTD). The crack front was discretized into decent amount of points, and the propagation direction of these points was determined by using two-dimensional plane strain equation. According to Franc 3D dialog reference, the expansion size depends on the
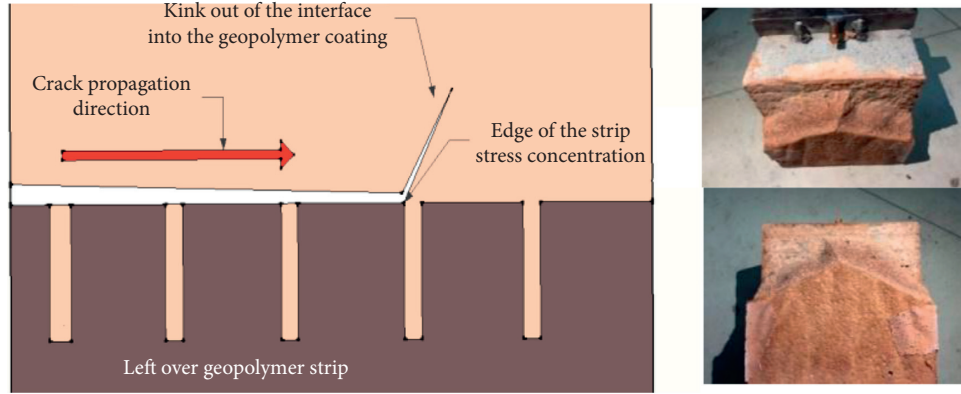
FIGURE 10: Failure mode of horizontal grooves.
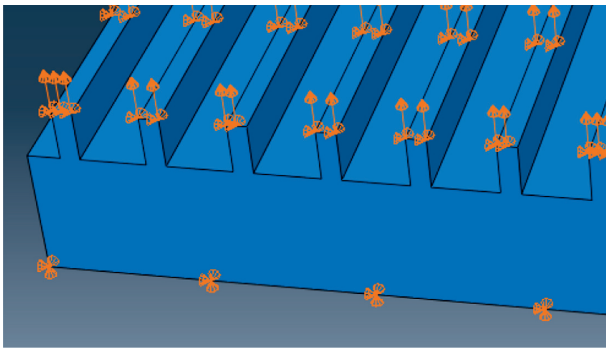
FIGURE 11: Boundary conditions of the vertical parallel-grooved model in ABAQUS.
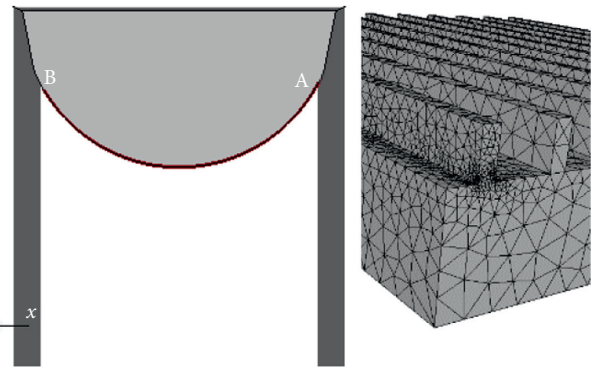
FIGURE 13: Model meshing and crack tip demonstration for both vertical and diagonal grooves.
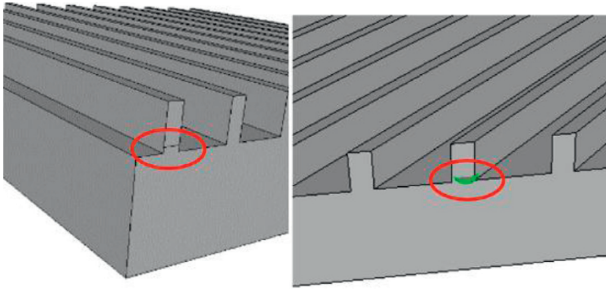
FIGURE 12: Initial cracks at the bottom edge of the geopolymer strips.

corresponding SIF of each point, and the maximum expansion size is identified by the circumstances.

$$\frac{K_{\mathrm{I}}}{e\sqrt{\pi a}} = \frac{1}{E(k)}\left[\sin^2\left(f_{\theta i j}\right) + \left(\frac{a}{c}\right)^2\cos^2\left(f_{\theta i j}\right)\right]^{1/4},$$

$$E(k) = \int_0^{\pi/2}\sqrt{1 - k^2\sin^2\left(f_{\theta i j}\right)}\mathrm{d}\theta, \quad k^2 = \frac{c^2 - a^2}{c^2},$$

(6)

where θ is the angle in $f_{\theta i j}$ of the crack front, and $E(k)$ is the secondary ellipse integral. For the given a and c, the expanded points are connected to form a new crack front mouth. Users can reanalyze the distribution of stress intensity factors at the crack front after propagation. By the

computation of the SIFs $(K_{\mathrm{I}}, K_{\mathrm{II}}, K_{\mathrm{III}})$, the partition of the fracture mode with the normalized distance along the crack front can be achieved.

In Figure 14, the SIF changed with the normalized distance along the crack front (from point B to A, the distance is normalized from 0 to 1). In the vertical grooves, mode I SIF showed the parabolic curve and reached the maximum value at symmetric middle distance, while the mode II and mode III reached relatively low values at the middle distance. On the other hand, the mode I SIF in diagonal grooves monotonically decreased along the normalized crack front, and SIF for mode II and mode III increased from point A to point B. This mixed mode partition process indicates that the vertical parallel grooves are predominated by pure mode I fracture and the diagonal parallel grooves are mainly a combination of mode II and mode III fracture.

From Table 7 we can see clearly that the average energy required and the average ERR of the crack in double diagonal parallel grooves increased nearly 5 times compared with the horizontal grooves, as well as the increased capacity of the crack resistivity. The reason for this phenomenon is that the dominant fracture mode in both the vertical parallel grooves and the double diagonal parallel grooves transferred from mode I to modes II and III. Hence, these WS test results in Table 7 matched with the fracture mode partition in Figure 14.

(a)

(b)

(c)

(d)

(e)

(f)
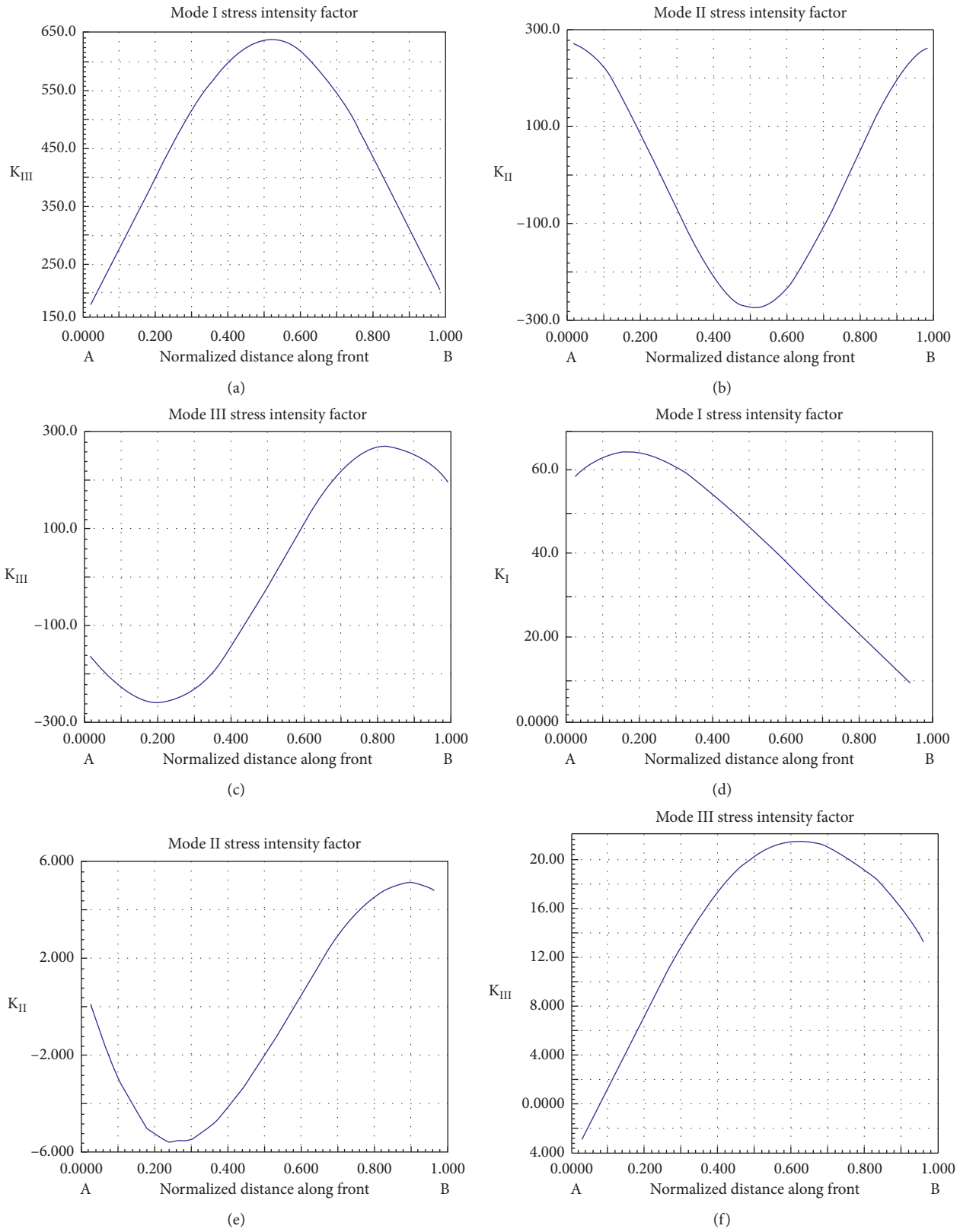
FIGURE 14: Fracture mode partition of pure SIFs for fracture at the edge of vertical parallel grooves (first three) and the fracture at the edge of diagonal parallel grooves (last three).

TABLE 7: Comparison of the average ERR and CMOD widths of different parallel groove orientations.

Specimen	$P_{vinitial}$ (kN)	$P_{hinitial}$ (kN)	P_{vmax} (kN)	P_{hmax} (kN)	CMOD initial (mm)	$G_{hinitial}$ (J)	CMOD final (mm)	$G_{haverage}$ (J)	W/d ratio
Horizontal grooves sample 1	0.320	0.597	0.466	0.869	0.010	0.015	1.220	0.228	0.375
Horizontal grooves sample 2	0.210	0.391	0.518	0.966	0.200	0.011	1.180	0.300	0.375
Vertical grooves sample 1	0.450	0.840	0.580	1.082	0.014	0.004	2.020	0.726	0.375
Vertical grooves sample 2	0.410	0.765	0.560	1.045	0.013	0.003	1.840	0.693	0.375
Vertical grooves sample 3	0.210	0.391	0.540	1.007	0.019	0.019	2.450	0.801	0.375
Diagonal grooves sample 1	0.491	0.916	0.717	1.338	0.004	0.034	2.600	0.931	0.375
Diagonal grooves sample 2	0.411	0.767	0.765	1.427	0.010	0.021	2.500	1.020	0.375
Diagonal grooves sample 3	0.521	0.972	0.825	1.539	0.022	0.032	2.700	1.090	0.375
Double diagonal grooves sample 1	0.570	1.063	1.120	2.090	0.040	0.040	2.400	1.310	0.375
Double diagonal grooves sample 2	0.591	1.103	1.040	1.940	0.003	0.030	2.100	1.423	0.375
Double diagonal grooves sample 3	0.631	1.177	1.010	1.884	0.003	0.101	2.240	1.562	0.375

6. Conclusions

The combination of different angular components for each pure mode has explained the increment of the external applying force successfully. The results of these tests have revealed the following highlights:

(1) The SIFs of ungrooved surface indicate that the adhesion ability of the meta-kaolin alkali-activated geopolymer is not adequate for a coating with an acceptable thickness. Total delamination failure is the main threat for this bimaterial system. The failure mode unveils that the porosity of this brittle material is relatively high. The depths of the remaining hydrated geopolymer are only 0.2–0.5 mm on the top of the concrete, and this is the evidence for the deficit of the interfacial resistance.

(2) The fracture energy to tear up the geopolymer itself is much greater than the fracture initialed along the bimaterial interface due to the different chemical bonds. Double diagonal parallel grooving is a method that can successfully facilitate the mechanical bonding, which increases the fracture resistance as well as the ligament area during the cracking process.

(3) These results are in agreement with previous fracture mechanics theory. However, as a promising fire protection material, geopolymer still needs to be optimized and standardized before the large-scale implementation in tunnel structure.

From this study, we successfully approved the double diagonal grooving with specific W/d ratio as one feasible method to increase the adhesion ability between solid concrete lining structure and fire resistance geopolymer coating. These conclusions lay the ground for future studies of the constitutive failure model at the contact interface of solid concrete and geopolymer bimaterial system. These findings will provide important references to minimize the potential damage to concrete lining structures attacked by fire accidents.

Data Availability

All the data included in this study are available upon request by contact with the corresponding author.

Conflicts of Interest

The authors declare that they have no conflicts of interest.

Acknowledgments

References

[1] A. A. Vrakas and C. Maraveas, "Design of concrete tunnel linings for fire safety," *Structural Engineering International*, vol. 24, no. 3, pp. 319–329, 2014.

[2] K. Sakkas, D. Panias, P. P. Nomikos, and A. I. Sofianos, "Potassium based geopolymer for passive fire protection of concrete tunnels linings," *Tunnelling and Underground Space Technology*, vol. 43, no. 7, pp. 148–156, 2014.

[3] Z.-g. Yan, H.-h. Zhu, and J. W. Ju, "Behavior of reinforced concrete and steel fiber reinforced concrete shield TBM tunnel linings exposed to high temperatures," *Construction and Building Materials*, vol. 38, no. 2, pp. 610–618, 2013.

[4] J. Davidovits, "Geopolymers," *Journal of Thermal Analysis*, vol. 37, no. 8, pp. 1633–1656, 1991.

[5] B. Singh, G. Ishwarya, M. Gupta, and S. K. Bhattacharyya, "Geopolymer concrete: a review of some recent developments," *Construction and Building Materials*, vol. 85, pp. 78–90, 2015.

[6] T. W. Cheng and J. P. Chiu, "Fire-resistant geopolymer produced by granulated blast furnace slag," *Minerals Engineering*, vol. 16, no. 3, pp. 205–210, 2003.

[7] A. S. Rahman and D. W. Radford, "Evaluation of the geopolymer/nanofiber interfacial bond strength and their effects on mode-I fracture toughness of geopolymer matrix at high

temperature," *Composite Interfaces*, vol. 24, no. 8, pp. 817–831, 2017.

[8] Z. H. Zhang, H. J. Zhu, C. H. Zhou, and H. Wang, "Geopolymer from kaolin in China: an overview," *Applied Clay Science*, vol. 119, pp. 31–41, 2016.

[9] J. Temuujin, W. Rickard, M. Lee, and A. van Riessen, "Preparation and thermal properties of fire resistant metakaolin-based geopolymer-type coatings," *Journal of Non-crystalline Solids*, vol. 357, no. 5, pp. 1399–1404, 2011.

[10] W. D. A. Rickard, J. Temuujin, and A. van Riessen, "Thermal analysis of geopolymer pastes synthesised from five fly ashes of variable composition," *Journal of Non-crystalline Solids*, vol. 358, no. 15, pp. 1830–1839, 2012.

[11] J. Davidovits, *Geopolymer Chemistry and Applications*, Geopolymer Institute, Saint-Quentin, France, 3rd edition, 2011.

[12] R. E. Lyon, P. N. Balaguru, A. Foden, U. Sorathia, J. Davidovits, and M. Davidovics, "Fire-resistant aluminosilicate composites," *Fire and Materials*, vol. 21, no. 2, pp. 67–73, 1997.

[13] S. L. Xu, X. F. Zhang, and D. Bu, "Relationship between crack tip opening displacement (CTOD) and crack mouth opening displacement (CMOD) throughtout development of concrete crack," *Engineering Mechanics*, vol. 28, no. 5, pp. 64–70, 2011.

[14] K. Yu and Z. Lu, "Residual crack extension resistance of post-fire wedge-splitting normal strength concrete specimen based on the cohesive force function," *Construction and Building Materials*, vol. 54, no. 3, pp. 270–281, 2014.

[15] E. Brühwiler and F. H. Wittmann, "The wedge splitting test, a new method of performing stable fracture mechanics tests," *Engineering Fracture Mechanics*, vol. 35, no. 1-3, pp. 117–125, 1990.

[16] X. U. Shi-Lang, B. U. Dan, and X. F. Zhang, "Determination of fracture energy of concrete using wedge-splitting test on compact tension specimens," *Journal of Hydraulic Engineering*, vol. 38, no. 6, pp. 683–689, 2007.

[17] S. Xu, Y. Zhao, Z. Wu et al., "Experimental study on the fracture energy of concrete using wedge splitting specimens," *Journal of Hydroelectric Engineering*, vol. 38, no. 6, pp. 683–689, 2007.

[18] D. K. Shetty, A. R. Rosenfield, and W. Duckworth, "Analysis of indentation crack as a wedge-loaded half-penny crack," *Journal of the American Ceramic Society*, vol. 68, no. 2, pp. C65–C67, 2010.

[19] D. Mostofinejad and E. Mahmoudabadi, "Grooving as alternative method of surface preparation to postpone debonding of FRP laminates in concrete beams," *Journal of Composites for Construction*, vol. 14, no. 6, pp. 804–811, 2010.

[20] D. Mostofinejad and M. J. Hajrasouliha, "Effect of concrete strength and groove dimension on performance of grooving method to postpone debonding of frp sheets in strengthened concrete beams," *Iranian Journal of Science & Technology Transactions of Civil Engineering*, vol. 37, no. 2, pp. 219–232, 2013.

[21] H. Sun, S. L. Liu, and X. G. Li, "Test analysis of shear performance on young-old concrete interface between bonded rebar and groove," *Applied Mechanics & Materials*, vol. 438-439, no. 6, pp. 235–239, 2012.

[22] M. L. Williams, "On the stress distribution at the base of a stationary crack," *ASME Journal of Applied Mechanics*, vol. 24, pp. 109–115, 1957.

[23] S. Xu and H. W. Reinhardt, "Determination of double-K criterion for crack propagation in quasi-brittle materials, part I: experimental investigation of crack propagation," *International Journal of Fracture*, vol. 98, no. 2, pp. 111–149, 1999.

Research Article

Micro/Nanoscale Study on the Effect of Aging on the Performance of Crumb Rubber Modified Asphalt

Lan Wang [iD],[1,2] **Yang Liu** [iD],[3] **and Le Zhang** [iD][3]

[1]*Key Laboratory of Civil Engineering Structure and Mechanics, Inner Mongolia University of Technology, Hohhot, China*
[2]*School of Civil Engineering, Inner Mongolia University of Technology, Hohhot, China*
[3]*School of Science, Inner Mongolia University of Technology, Hohhot, China*

Correspondence should be addressed to Lan Wang; wanglan661018@163.com

In order to explore the variation of crumb rubber modified asphalt (CR) before and after aging at the micro- and nanoscales, the molecular dynamics simulation and atomic force microscopy (AFM) asphalt microstructure scanning were carried out on CR before and after aging. The molecular dynamics energy, radial distribution function (RDF), surface microstructure image, roughness, and other test results of the CR before and after aging were compared and analyzed. The results show that the molecular dynamic energy of the CR after aging increases; the asphaltene-asphaltene RDF is decreased after aging; and the AFM surface microstructure images of asphalt before and after aging do not change significantly, but quantitative analysis by roughness theory shows that aging makes the microscopic surface of the CR more uniform and gentle. By analyzing the changes of asphalt properties before and after aging at two scales, it can be found that there is a certain relationship between the properties obtained at different scales. The reasons and mechanisms for the influence of microstructure on aging are obtained by analyzing this relationship.

1. Introduction

There is a certain relationship between the properties of the same material observed at different scales. For asphalt materials, exploring the relationship between the properties at different scales can further obtain the mechanism of the formation and change of macroperformance, which can provide a theoretical basis and feasible ways for further improving the macroperformance of asphalt. The molecular dynamics simulation method is introduced into the field of asphalt research to provide a new scale and method for the research of asphalt materials.

Tang et al. established a three-component model of asphalt through molecular simulation to study the aggregation state of asphalt molecules, but a simple three-component model is difficult to establish a relationship with the macroperformance, which can only be used as a simple analysis [1]. Yue and Ding et al. calculated the interaction between asphalt mixture and rejuvenator by molecular dynamics. The results show that the effect of rejuvenator on

long-term aging asphalt is obvious, and the effect on short-term aging asphalt is limited [2, 3]. Xu and Wang et al. applied molecular dynamics simulation to study the effect of thermal oxygen aging on asphalt and the water damage of asphalt mixture. It is found that aging would reduce the nanoaggregation behavior of asphaltene molecules, reduce the migration rate, and reduce the asphalt and aggregate interface bonding effect [4, 5]. Pan and Tarefder studied the effects of asphalt chemical composition and molecular structure on macroscopic rheological properties and mechanical properties after aging by molecular dynamics. The oxidation functional groups' viscosity of asphalt increases after aging, which leads to the increase of asphalt viscosity, indicating that the hardness of asphalt increases [6]. Yao et al. studied the effect of asphalt aging on the water damage resistance of asphalt mixture by molecular dynamics simulation. The results show that the aging component in asphalt helps to reduce the damage of water to asphalt mixture [7]. Xu et al. established a molecular interface model of asphalt samples and AFM siliceous needle tips. The adhesion

of asphalt at different aging degrees was obtained by AFM test and molecular dynamics simulation. It is found that the adhesion results obtained by the two methods are consistent [8]. Yi used molecular dynamics simulation to study the effect of asphalt aging on the adhesion work of asphalt-aggregate interface. It is believed that aging weakened the aggregation effect of asphalt. When moisture enters the interface between asphalt and aggregate, the interfacial adhesion work decreases, and the decline of aging asphalt is more obvious than that of matrix asphalt [9]. Yongjie Ding et al. studied the changes of functional groups and molecular weight of asphalt before and after aging by liquid chromatography. It is found that the aging effect has little effect on the aliphatic chain, but the aging effect increases the molecular weight of asphalt [10]. Fardin studied the glass transition temperature of SBR modified asphalt by molecular dynamics. It is found that the addition of SBR increases the aggregation of asphaltene molecules and reduces the migration of other component molecules. The macroscopic performance is that the addition of SBR improves the glass transition temperature of asphalt. At the same time, it is observed that the selected molecules follow the relationship between melt viscosity and temperature (VFT) as the behavior function of temperature [11]. Amit Bhasin studied the relationship between the chain length, chain branching, and self-diffusion of asphalt molecules through molecular simulation, so as to understand the nanoscale mechanism of molecular diffusion and self-healing ability [12]. Wang Lan et al. carried out molecular dynamics research on the compatibility between SBR molecules and asphalt, found that the best compatibility state was achieved between asphalt molecules and SBR molecules at 160°C, and studied the compatibility between asphalt molecules and SBR molecules before and after aging under the best compatibility state [13, 14].

For the relationship between multiscale performances, scholars at home and abroad use different test methods to study and analyze asphalt materials. Loeber et al. first discovered the asphaltene molecular gel network using AFM and named it "bee structure" [15]. Alireza Samieadel et al. carried out a multiscale analysis on the behavior of paraffin in asphalt as a warm mixing agent and studied the influence of paraffin on the thermodynamic properties of asphalt by DSC. It is found that the glass transition temperature and viscosity of asphalt decrease with the increase of paraffin concentration. The interaction between asphaltene and paraffin is studied by molecular dynamics simulation, and it is found that the increase of paraffin content leads to the decrease of viscosity. The average size of the asphaltene phase decreases but the number increases, and the diffusion coefficient of paraffin increases about 7 times [16]. Chen Jianhua carried out macroscale analysis on the thixotropic zone of the casting asphalt mixture, such as DSR and rutting test. The aging zone was analyzed by spectroscopy and performance of casting asphalt concrete by using infrared spectroscopy, AFM, and other microscale analysis methods. The thixotropy and serviceability of the casting asphalt concrete were systematically studied. After that, the research results were verified by a full-scale accelerated loading test,

and the correlation among micro-, meso-, macro-, and full-scale indexes was established [17]. Cao Peng and Gong Xiangbing carried out multiscale mechanical analysis and model study on the road surface. The results show that the simulation results of the multiscale unified model have a corroboration relationship with the simulation results of the mesoelement equivalent model, and the mechanism of the micro-meso-macro scale is preliminarily established [18, 19]. Wang Peng et al. explored the genesis of asphalt bee structure through molecular dynamics simulation, studied the contribution of each component to the formation of asphalt colloid, and analyzed the correlation between chemical composition and road performance [20].

Aging is accompanied by the full-life cycle of crumb rubber modified asphalt (CR), so it is necessary to study the aging of CR. Domestic and foreign scholars have used molecular dynamics simulation and cross-scale analysis methods to conduct a variety of research on asphalt materials, but there are few cross-scale studies on crumb rubber modified asphalt aging. Atomic force microscope quantitative nanomechanical model (AFM-QNM) is used to scan the microscale of CR before and after aging, and the change of molecular dynamics energy and radial distribution function of crumb rubber modified asphalt before and after aging are calculated by molecular dynamics simulation. The effects of aging on CR at two scales are analyzed to study the reasons and mechanism of performance change of crumb rubber modified asphalt before and after aging.

2. Test Material

Panjin 90# matrix asphalt and 60 mesh waste crumb rubber were used to prepare crumb rubber modified asphalt by the wet process. The crumb rubber content was 20%, and the aging crumb rubber modified asphalt was prepared by pressure aging test. Three main indexes were tested on the original crumb rubber modified asphalt (O-CR) and aging crumb rubber modified asphalt (A-CR). The results are shown in Table 1. The temperature sensitivity parameters were calculated according to formulas (1) and (2), and the calculation results are shown in Table 2.

$$\lg P = K + AT, \tag{1}$$

$$PI = \frac{20 - 500A}{1 + 50A}, \tag{2}$$

where P is penetration (0.1 mm), K is regression constant, A is temperature sensing coefficient, T is test temperature (°C), and PI is penetration index.

As the temperature coefficient A decreased, the penetration index PI increased, the asphalt temperature sensitivity decreased, and the high-temperature performance of the asphalt improved. The softening point and penetration index of A-CR increased, indicating that its temperature sensitivity was reduced and its high-temperature stability was improved to a certain extent. However, the decrease of ductility and penetration indicated that the main effect of aging was the deterioration of the low-temperature performance of asphalt.

Table 1: Three main indexes test of O-CR and A-CR.

Item	O-CR	A-CR
Penetration (5°C, 100 g, 5 s; 0.1 mm)	11.6	6.3
Penetration (15°C, 100 g, 5 s; 0.1 mm)	30.2	15.6
Penetration (25°C, 100 g, 5 s; 0.1 mm)	73.8	37.5
Ductility (5°C; cm)	16.5	12.3
Softening (°C)	57.3	63.4

Table 2: Temperature sensitivity parameters.

Parameters	A	K	PI	Correlation coefficient R
O-CR	0.0402	0.8681	1.91	0.9998
A-CR	0.0387	0.6078	2.585	0.9999

3. Analysis of Nanometer Energy of CR before and after Aging

In this paper, Panjin 90# matrix asphalt was used to prepare long-term aging asphalt (hereinafter referred to as aging asphalt) according to T0630-2011 pressure aging vessel accelerated asphalt aging test regulations in JTJG E20-2011 "*Standard Test Methods of Bitumen and Bituminous Mixtures for Highway Engineering.*" The four components of asphalt were analyzed according to the regulations of T0618-1993 asphalt chemical component test (four-component method) in JTJG E20—2011 "*Standard Test Methods of Bitumen and Bituminous Mixtures for Highway Engineering.*" During the thermal aging process of asphalt, due to the influence of high-temperature oxidation, the change of its components was mainly manifested as the conversion of the resins in the light components into asphaltenes, which resulted in the decrease of the plasticity and increase of the brittleness of the asphalt in the macroperformance, while the saturate and aromatic content of the asphalt had little change, which made little contribution to the change of the asphalt performance. It can be seen from Table 3 that the mass ratio of four components (m (asphaltene): m (saturate): m (aromatic): m (resin)) before aging was about 1.0 : 2.7 : 3.1 : 3.9, and the content of resin was the largest in matrix asphalt. Therefore, matrix asphalt showed obvious viscosity, high penetration degree, and low softening point. After aging, the mass ratio of four components (m (asphaltene): m (saturate): m (aromatic): m (resin)) of aging asphalt was about 1.0 : 1.0 : 1.0 : 1.1. The asphaltene content increased significantly while the resin content decreased, and the brittleness of asphaltene became the main factor affecting the macroproperties of asphalt.

Some scholars have conducted a large number of studies on the molecular structure of asphaltenes, resins, saturates, and aromatics in asphalt. Asphaltenes are a variety of compounds with aromatic ring groups and short straight chains [21]. Therefore, the highest content of alkane molecules in asphalt is $C_{22}H_{46}$, and $C_{22}H_{46}$ is close to the thermodynamic characteristic temperature of saturation fraction. Therefore, $C_{22}H_{46}$ was selected as the representative molecule of saturation fraction [22, 23]. The resin is a layered molecule composed of various condensed aromatics and alicyclic alkene with various alkyl groups and heteroatoms [24]. The number of aromatic rings and straight chains of the aromatic component is similar to that of 1, 7-dimethyl naphthalene molecules. Therefore 1, 7-dimethyl naphthalene molecules were selected as the representative molecules of the aromatic component [25]. Asphaltenes, saturates, aromatics, and resins in asphalt were represented by known polymer molecules as shown in Figure 1. The matrix asphalt molecular models before and after aging were constructed according to the four-component ratio as shown in Figures 2 and 3.

From the asphalt molecular model before and after aging, the volume of the asphalt molecular group was larger, the content of the benzene ring was more, and the group was more compact as a whole after aging. The relative structure of the original asphalt molecules was looser, and the loose structure led to the weak interaction within the molecular group. When the temperature increased or decreased, the motion state of molecules was more susceptible to the change of external energy, so the original asphalt had higher temperature sensitivity. The closer the molecular group structure was, the higher the energy required for the molecular movement was, so the temperature sensitivity of aging asphalt decreased.

Styrene-butadiene rubber (SBR) is the main component of crumb rubber used in crumb rubber modified asphalt (CR). SBR can significantly improve the temperature sensitivity and viscoelasticity of asphalt, so it plays a major role in asphalt modification. The tire was treated with antiaging treatment during the production process. Therefore, the aging of crumb rubber was not considered in the study of the performance of CR before and after aging. The SBR model was selected to represent the rubber model in this paper. Firstly, random copolymer SBR was constructed. After the energy optimization of SBR monomer model, 50 monomer molecules were polymerized into SBR single-chain molecule. Considering that the main component of waste crumb rubber was SBR, and it had antiaging treatment in the tire production process. Therefore, when studying the properties of CR before and after aging, the aging of crumb rubber was not considered. The molecular model of SBR is shown in Figure 4. The 3D model of SBR was obtained by combining four single-chain molecules of SBR. Then, according to the mass ratio of 20%, the asphalt molecules and SBR molecules were fused to obtain the original crumb rubber modified asphalt molecular model shown in Figure 5. All kinds of molecules were optimized, and the optimization steps and parameters are shown in Table 4.

After optimization, the density of asphalt molecules was stable between 0.95 and approximately g/cm³, which was close to the true density of 90# matrix asphalt at 1.02 g/cm³. The density of SBR molecule was stable between 0.90 and 0.95 g/cm³, which was consistent with the real SBR density of 0.94 g/cm³.

The energy of the Forcite module was calculated for the optimized crumb rubber modified asphalt molecular group, the energy data of the whole process of calculation was processed, and the molecular dynamics energy chart of

TABLE 3: Original matrix asphalt and aging matrix asphalt four components ratio ω/%.

	Original matrix asphalt	Aging matrix asphalt
Asphaltene	9.4	24.6
Saturate	25.2	25
Aromatic	28.8	23.6
Resin	36.6	26.2
Total	100	99.4

(a)

(b)

(c)

(d)
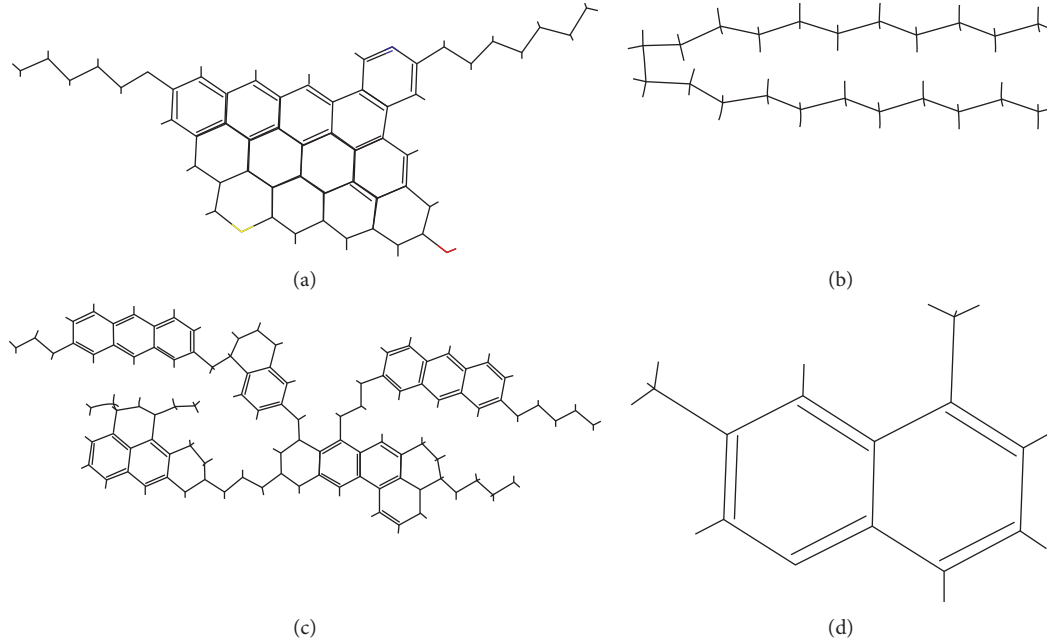
FIGURE 1: Molecular models of asphalt four components. (a) Asphaltene (As). (b) Saturated (S). (c) Resin (R). (d) Aromatic (Ar).

crumb rubber modified asphalt molecular group before and after aging was obtained as shown in Figure 6.

The molecular energy of crumb rubber modified asphalt increased after aging, which was due to the transformation of light small molecules into heavy macromolecules in crumb rubber modified asphalt, which increased the overall molecular weight and then increased the overall dynamic energy of asphalt by 17%.

4. Analysis of RDFs of CR before and after Aging

The radial distribution function $g(r)$ represented the ratio of the probability density of a molecule to the density of a random distribution probability at a distance r around a molecule. The definition of $g(r)$ is shown in the following formula:

$$g_{AB}(r) = \frac{1}{\rho_{AB} 4\pi r^2 \delta r} \frac{\sum_{t=1}^{K} \sum_{j=1}^{N_{AB}} \Delta N_{AB}(r \longrightarrow r + \delta r)}{N_{AB} \times K},$$

(3)

where N_{AB} is the number of A and B atoms in the system, K is the time step, δr is the distance interval width, ΔN_{AB} is the number of B atoms in the range of r to $r + \delta r$ from A atoms, and ρ_{AB} is the system density.

The asphaltene before and after aging was taken as the calculation center with a cut-off radius of 20 Å. The radial distribution functions of each component and crumb powder of CR before and after aging were calculated, respectively. The calculation results are shown in Figure 7.

It can be seen from Figures 7(a) and 7(c) that the aging asphaltene-SBR and asphaltene-resin RDFs are slightly higher than the original asphaltene-SBR and asphaltene-resin RDFs. It can be seen from Figure 7(b) that after aging, the RDF value of asphaltene-asphaltene is significantly lower than that of original asphaltene-asphaltene, indicating that aging weakens the stacking degree between asphaltenes, the distribution of asphaltene in the molecular model is more dispersed, and the aggregation degree is reduced. According to Figures 7(d) and 7(e), RDFs of asphaltene-saturate and asphaltene-aromatic before and after aging, asphaltene-saturate and asphaltene-aromatic basically coincide before and after aging, indicating that aging has no obvious effect on the aggregation of saturate and aromatic in the molecular model.

5. Analysis of CR Microstructure before and after Aging

AFM scanning was carried out to obtain the micrograph of CR before and after aging, as shown in Figure 8.
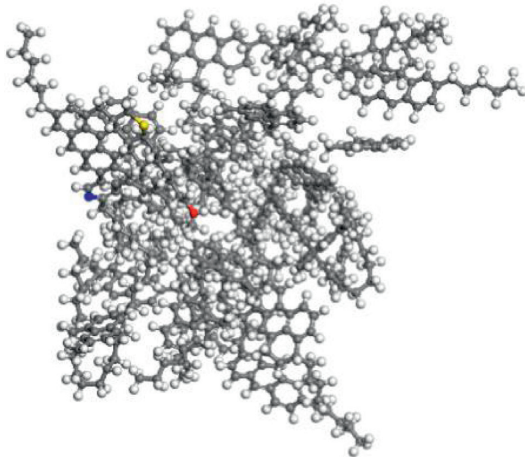
Figure 2: 3D model of the original matrix asphalt.
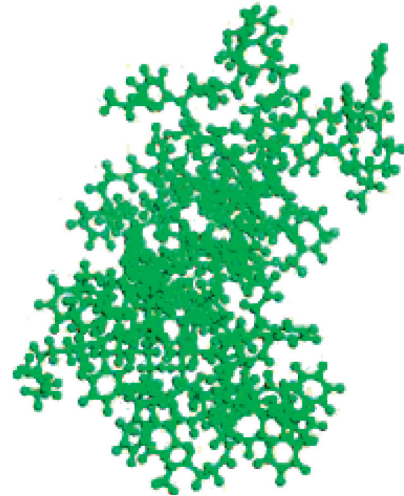
Figure 4: 3D model of SBR.
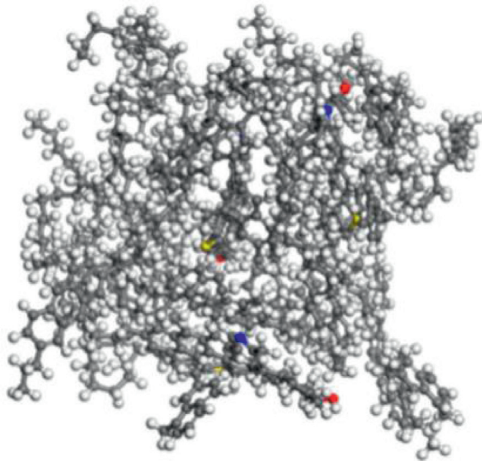
Figure 3: 3D model of aging matrix asphalt.
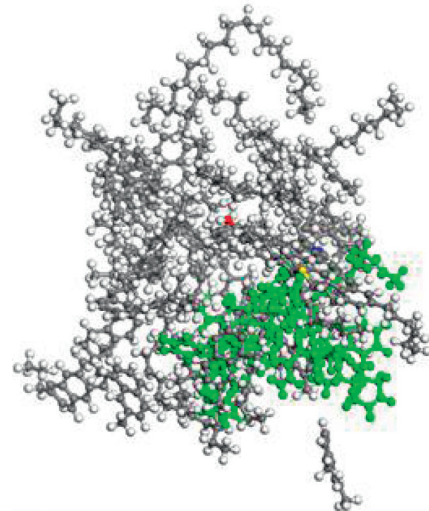
Figure 5: 3D model of original CR.

Table 4: Model optimization steps and parameters.

Steps	Number of steps or time	Forcefield or ensemble
Geometry optimization	10^5	COMPASSII
Anneal	$5^* 10^4$	NPT
Dynamics	200 ps	NPT-298K
	100 ps	NVT-1500K

From the AFM scan image of crumb rubber modified asphalt before and after aging, it can be seen that, unlike matrix asphalt, crumb rubber modified asphalt has no obvious bee structure before and after aging. The addition of crumb rubber caused the microstructure of asphalt to change. Through the observation of three-dimensional images, it is found that although there is no obvious bee structure, the CR still has obvious peak and valley structures. Unlike matrix asphalt, these peaks and valleys were no longer clearly aggregated but were dispersed uniformly and

more finely. These dispersed peaks and valleys formed the black and white speckle structure of crumb rubber modified asphalt in two dimensions. These finely dispersed peaks and valleys formed the black and white speckle structure of crumb rubber modified asphalt in 2D. By analyzing the influence of crumb rubber on the microstructure of asphalt, it can be found that crumb rubber absorbed a large number of light components and wax content in asphalt, which reduced the wax content used to form a bee-shaped structure. At the same time, some long straight chain
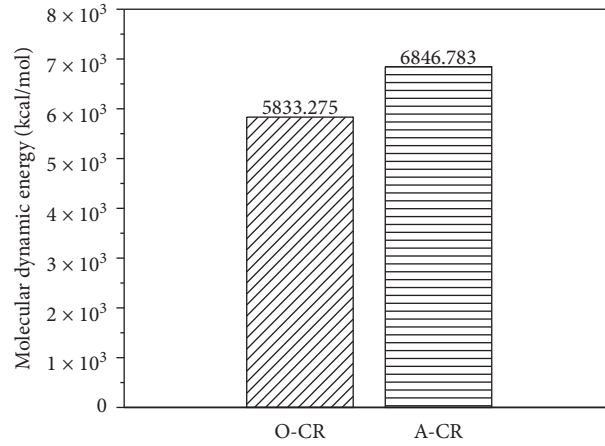
Figure 6: Molecular dynamics energy of O-CR and A-CR.

(a)

(b)

Figure 7: Continued.

(c)

(d)

(e)
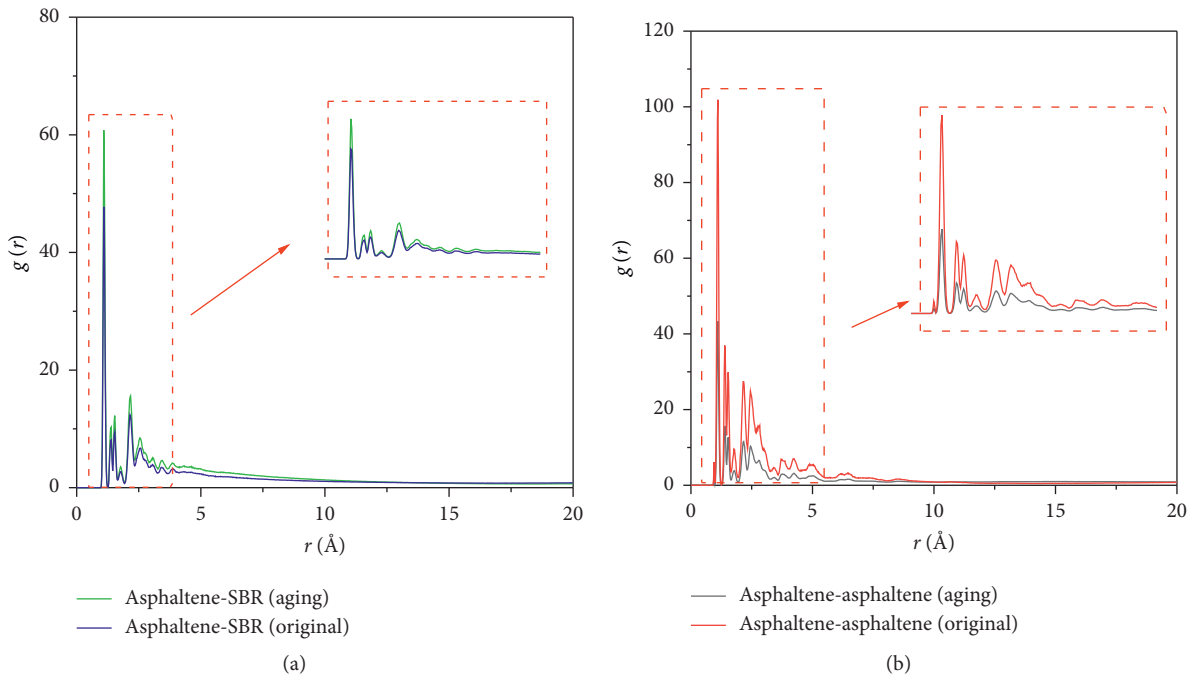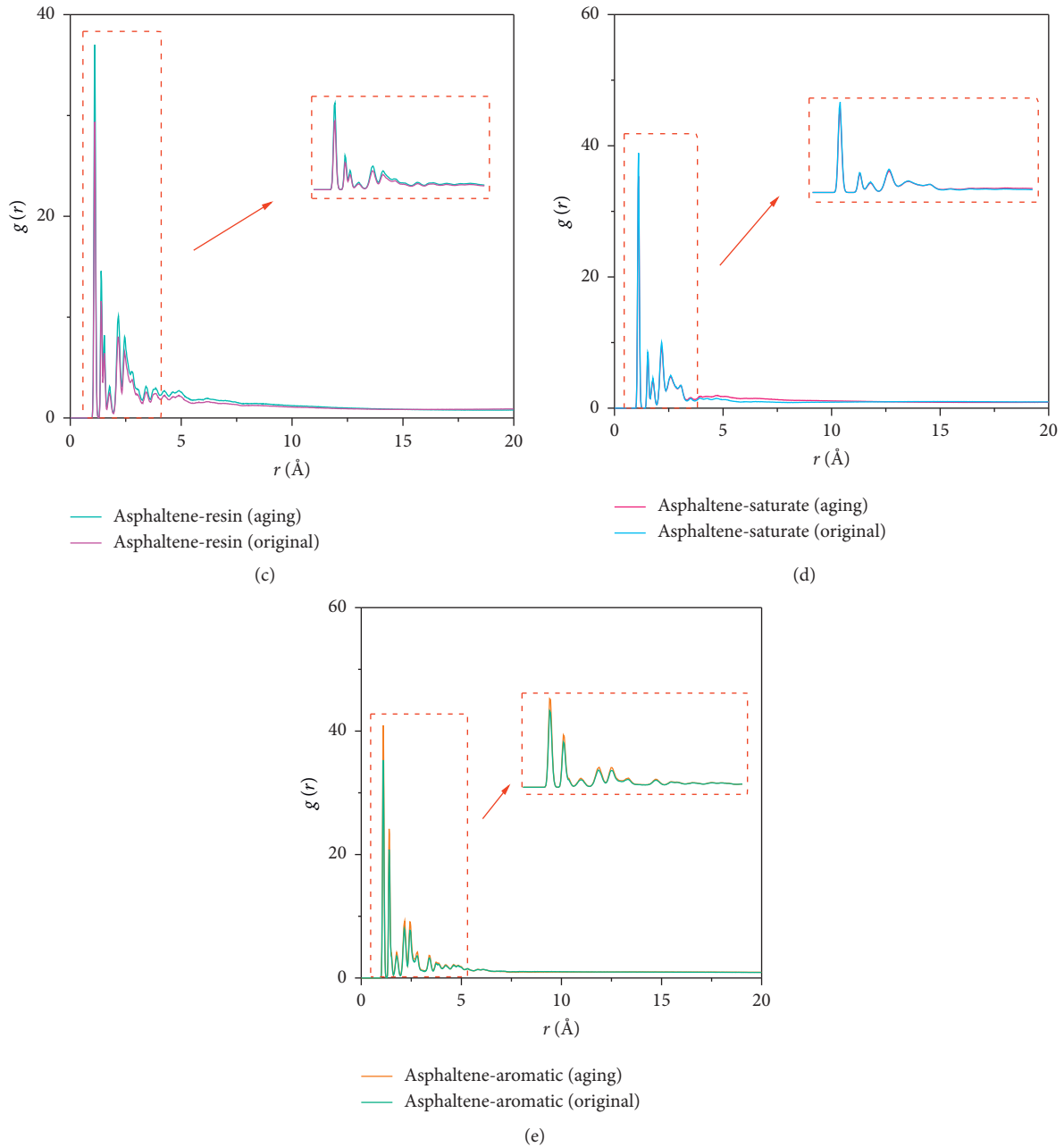
FIGURE 7: Radial distribution function for asphaltene with SBR, resin, saturate, and aromatic pairs in original and aging models. (a) Asphaltene-SBR. (b) Asphaltene-asphaltene. (c) Asphaltene-resin. (d) Asphaltene-saturate. (e) Asphaltene-aromatic.

molecules dissolved by crumb rubber also made asphaltene difficult to agglomerate on a large scale, resulting in asphaltene being more evenly dispersed in asphalt so that it was difficult to form a large bee structure. In terms of colloidal theory, the more uniform the colloidal dispersion is, the better the macroperformance will be, which should also prove the excellent macroperformance of the crumb rubber modified asphalt.

There is no obvious change in the image of the CR before and after aging. The uniformly dispersed asphaltenes and the

long-chain molecules dissolved by the crumb rubber cross-link with each other to form a more stable and uniform internal structure, so the effect of aging on it is reduced.

It was difficult to find the obvious changes of the CR before and after the aging from the morphology map, so more accurate quantitative analysis was needed to explore the microstructure changes of the CR before and after the aging. The surface roughness of the asphalt was analyzed theoretically after the first-order flatten treatment of the image with Nanoscope Analysis.

(a)

(b)

(c)

(d)
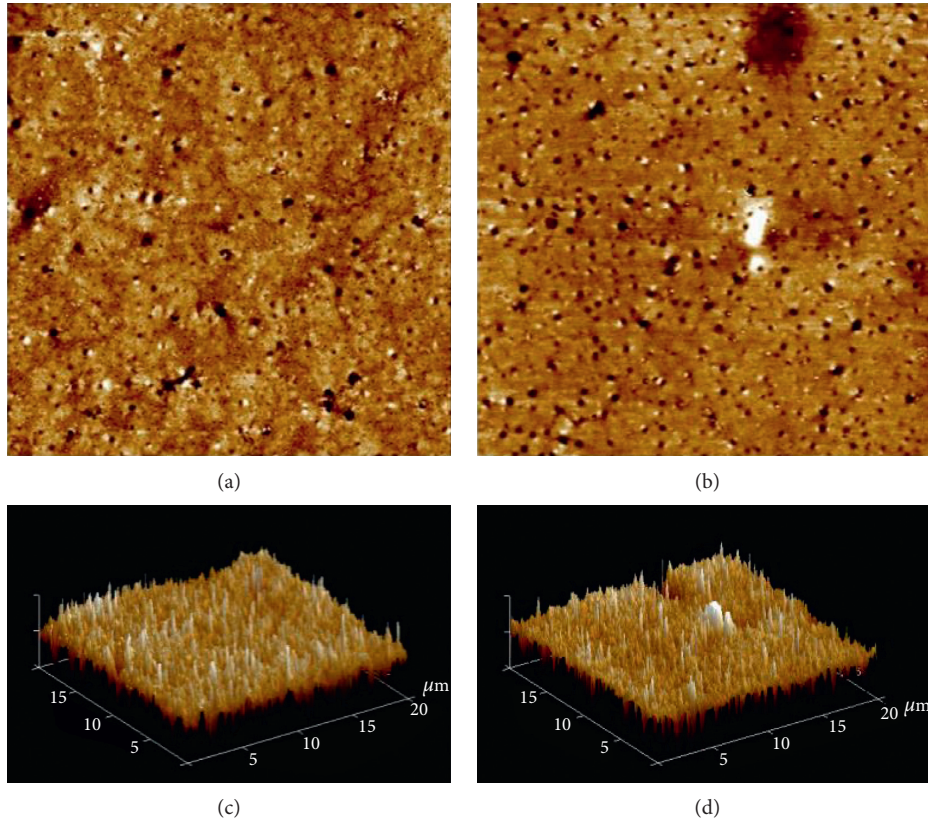
FIGURE 8: 2D and 3D microscopic morphology of O-CR and A-CR.

Root mean square roughness (R_q), surface area difference percentage (ISAD), and peak density (S_{ds}) were selected as the indexes to evaluate the micromorphology of asphalt. In a narrow sense, roughness referred to the height difference between the high and low fluctuation of the observed object surface. Due to the fact that the microstructure of the asphalt surface had slight fluctuation and peak valley intersection, R_q was selected to characterize the surface roughness of the CR before and after aging. The definition of R_q is shown in the following formula:

$$R_q = \sqrt{\frac{\iint [h(x,y) - h_0]^2 dA}{\iint dA}}, \qquad (4)$$

where A is the scanning area, $h(x,y)$ is the shape height function of unit point (x, y), h_0 is the reference height, and $h_0 = \iint h(x,y) dA / \iint dA$.

Surface area difference percentage ISAD referred to the area difference percentage from 3D surface area flattening to 2D surface in the scanning area. ISAD was also a common index in the theoretical analysis of roughness. Through ISAD, the fluctuation degree of microstructure in 3D morphology can be quantitatively analyzed. The calculation formula is shown as

$$\text{ISAD} = \frac{S_{3D} - S_{2D}}{S_{2D}} \times 100\%, \qquad (5)$$

where S_{3D} is 3D surface area and S_{2D} is 2D surface area.

Peak density S_{ds} referred to the number of peaks per unit area. The peak value was defined as the value higher than the adjacent 8 points in the AFM system. In addition, the peak was only used to define the point whose height was 5% higher than the maximum height of the average plane. The peak density was the density of the peaks in the region. The peak density can quantitatively represent the amount and distribution of microstructure in the scanning area. The calculation formula is

$$S_{ds} = \frac{N_{peak}}{A}, \qquad (6)$$

where N_{peak} is the number of maximum height peak structures in the area and A is the area. The results of R_q, ISAD, and S_{ds} are shown in Table 5.

It can be seen from Table 5 that there is a certain change in the surface microstructure of CR before and after aging through quantitative analysis. After aging, the ISAD and S_{ds} of CR surface were decreasing, so it can be known that the number of peak structures and the height of each peak of CR were decreasing, and the comprehensive evaluation index R_q was also decreasing; aging made the microstructure of asphalt more uniform and the surface gentler. Under the influence of aging, the light components, such as aromatics and resins of CR converted to the heavy components, and the proportion of the components of asphalt

Table 5: Surface roughness parameter statistics of O-CR and A-CR.

	R_q (nm)	ISAD (%)	S_{ds} (μm^{-1})
O-CR	2.14	0.0214	2.20
A-CR	1.29	0.0103	1.80

Table 6: Microscale and nanoscale analysis on CR.

Scale	Parameter	Unit	O-CR	A-CR
Microscale	R_q	nm	2.14	1.29
	S_{ds}	μm^{-1}	2.20	1.80
Nanoscale	Energy	kcal/mol	5833.275	6846.783
	RDF(As–as)	—	101.87	43.31

changed, which showed the process of asphalt surface homogenization. The homogenization of asphalt surface resulted in the decrease of the roughness, specific surface area, and peak density of asphalt surface. After aging, the surface of CR was more uniform and flatter than that of the original CR, and the composition and structure were more uniform and stable, which led to its good high-temperature stability.

6. Correlation Analysis of Micro/Nanoproperties of CR before and after Aging

In order to explore the relationship between the structural changes of CR at the microscale and the changes of molecular dynamics energy and radial distribution function at the nanoscale before and after aging and then to explain the changes of the microstructure before and after aging at the molecular scale, the correlation analysis of the variation of nanoenergy, RDF, and microstructure changes was carried out.

It can be seen from Table 6 that the surface of A-CR at the microscale is smoother, the number of peak structures is decreasing, and the height is decreasing. However, after aging, the molecular dynamic energy of CR increased instead. This was due to the increasing proportion of asphaltenes with larger molecular weight after asphalt aging, which led to the increase of the overall molecular weight of asphalt molecules, which increased the molecular dynamic energy. When the energy was higher, the molecular agglomeration was difficult to precipitate, resulting in a reduction in the number and height of peak structures in the micromorphology. After aging, the asphaltene-asphaltene RDF was significantly lower than the original asphaltene-asphaltene RDF, indicating that aging affected the accumulation of asphaltenes and asphaltenes. After aging, the degree of asphaltene aggregation was lower and the distribution was more dispersed. As a result, the peak structure with asphaltene as the core was dispersed in the microstructure, making the asphalt surface structure gentler. Therefore, the dynamic energy and RDF of the crumb rubber modified asphalt molecular group affected the formation of the micromorphology.

7. Conclusions

(1) Aging increases the molecular weight of the asphalt, which leads to an increase in the molecular dynamics energy of the crumb rubber modified asphalt.

(2) After the aging, the peak value of the RDF between asphaltenes is reduced, the asphaltenes are difficult to aggregate, and the asphaltenes are more dispersed in the molecular model.

(3) The surface microstructure of crumb rubber modified asphalt after aging is uniform and gentle. The enhanced high-temperature performance of crumb rubber modified asphalt after aging is related to surface homogenization.

(4) The molecular dynamics energy and radial distribution function of asphalt nanostructure have a certain effect on its microstructure, and there is a certain correlation between different phenomena observed at different scales of the same substance.

Data Availability

The data used to support the findings of this study are available from the corresponding author upon request.

Conflicts of Interest

The authors declare that they have no conflicts of interest regarding this work.

Acknowledgments

References

[1] B. Tang, Y. Ding, H. Zhu et al., "Study on agglomeration variation pattern of asphalt molecules," *China Journal of Highway and Transport*, vol. 26, no. 3, pp. 50–76, 2013.

[2] Y. Xiao, C. Li, M. Wan, X. Zhou, Y. Wang, and S. Wu, "Study of the diffusion of rejuvenators and its effect on aged bitumen binder," *Applied Sciences*, vol. 7, no. 4, p. 397, 2017.

[3] Y. Ding, B. Huang, X. Shu, Y. Zhang, and M. E. Woods, "Use of molecular dynamics to investigate diffusion between virgin and aged asphalt binders," *Fuel*, vol. 174, pp. 267–273, 2016.

[4] G. Xu and H. Wang, "Molecular dynamics study of oxidative aging effect on asphalt binder properties," *Fuel*, vol. 188, pp. 1–10, 2017.

[5] H. Wang, E. Lin, and G. Xu, "Molecular dynamics simulation of asphalt-aggregate interface adhesion strength with moisture effect," *International Journal of Pavement Engineering*, vol. 18, no. 5, pp. 414–423, 2017.

[6] J. Pan and R. A. Tarefder, "Investigation of asphalt aging behaviour due to oxidation using molecular dynamics simulation," *Molecular Simulation*, vol. 42, no. 8, pp. 667–678, 2016.

[7] H. Yao, Q. Dai, and Z. You, "Chemo-physical analysis and molecular dynamics (MD) simulation of moisture susceptibility of nano hydrated lime modified asphalt mixtures," *Construction and Building Materials*, vol. 101, pp. 536–547, 2015.

[8] M. Xu, J. Yi, D. Feng, Y. Huang, and D. Wang, "Analysis of adhesive characteristics of asphalt based on atomic force microscopy and molecular dynamics simulation," *ACS Applied Materials & Interfaces*, vol. 8, no. 19, pp. 12393–12403, 2016.

[9] J. Yi, X. Pang, D. Feng et al., "Studies on surface energy of asphalt and aggregate at different scales and bonding property of asphalt-aggregate system," *Road Materials and Pavement Design*, vol. 19, no. 5, pp. 1102–1125, 2017.

[10] Y. Ding, B. Huang, and X. Shu, "Investigation of functional group distribution of asphalt using liquid chromatography transform and prediction of molecular model," *Fuel*, vol. 227, pp. 300–306, 2018.

[11] K. Fardin and K. Rajesh, "Glass transition and molecular mobility in styrene butadiene rubber modified asphalt," *The Journal of Physical Chemistry B*, vol. 119, pp. 14261–14269, 2015.

[12] B. Amit, A. M. Asce, B. Rammohan, and L. Michael, "Greenfield use of molecular dynamics to investigate self-healing mechanisms in asphalt binders," *Journal of Materials in Civil Engineering*, vol. 23, no. 4, pp. 485–492, 2011.

[13] L. Wang, L. Zhang, and L. I. U. Yang, "Study on compatibility of rubber powder and asphalt in rubber powder modified asphalt by molecular dynamics," *Journal of Building Materials*, vol. 21, no. 4, pp. 689–694, 2018, in Chinese.

[14] L. Wang, L. Z, and L. I. U. Yang, "Moleculahangr dynamics study on compatibility of asphalt and rubber powders before and after aging," *Journal of Building Materials*, vol. 22, no. 3, pp. 474–479, 2019, in Chinese.

[15] L. Loeber, O. Sutton, J. Morel, J.-M. Valleton, and G. Muller, "New direct observations of asphalts and asphalt binders by scanning electron microscopy and atomic force microscopy," *Journal of Microscopy*, vol. 182, no. 1, pp. 32–39, 1996.

[16] S. Alireza, O. Daniel, and H. Elham, "FINI. Multi-scale characterization of the effect of wax on intermolecular interactions in asphalt binder," *Construction and Building Materials*, vol. 157, pp. 1163–1172, 2017.

[17] J. Chen, *The Application and Multi-Scale Research on Thixotropic and Aging Properties of Mixed Asphalt Used in MA*, South China University of Technology, Guangzhou, China, 2015.

[18] P. Cao, *Research on Multiscale Mechanical Analysis Method and Model of Asphalt Pavement*, Harbin Institute of Technology, Harbin, China, 2014.

[19] X. Gong, *Mechanical Behavior within Multi Scales and United Models of Asphalt Pavement Materials*, Harbin Institute of Technology, Harbin, China, 2017.

[20] P. Wang, Z. Dong, Y. Tan et al., "Research on the formation mechanism of bee-like structures in asphalt binders based on molecular simulations," *China Journal of Highway and Transport*, vol. 29, no. 3, pp. 9–16, 2016.

[21] L. Artok, Y. Su, Y. Hirose, M. Hosokawa, S. Murata, and M. Nomura, "Structure and reactivity of petroleum-derived asphaltene," *Energy & Fuels*, vol. 13, no. 2, pp. 287–296, 1999.

[22] D. A. Storm, M. M. Sheu, and M. M. Detar, "Macrostructure of asphaltenes in vacuum residue by small-angle X-ray scattering," *Fuel*, vol. 72, no. 7, pp. 977–981, 1993.

[23] I. DetarSheu, M. Vandenbroucke, A. Y. Huc, M. J. Taylor, and J. L. Faulon, "Preliminary results on molecular modeling of asphaltenes using structure elucidation programs in conjunction with molecular simulation programs," *Energy & Fuels*, vol. 10, no. 1, pp. 97–107, 1996.

[24] D. Wang, Y. Zhao, Y. Pan et al., "Quantum chemical study on the structure of petroleum gums," *Journal of Fuel Chemistry and Technology*, vol. 34, no. 6, pp. 690–694, 2006, in Chinese.

[25] M. Su, H. Zhang, Y. Zhang et al., "Miscibility and mechanical properties of SBS and asphalt blends based on molecular dynamics simulation," *Journal of Chang'An University (Natural Science Edition)*, vol. 37, no. 3, pp. 24–32, 2017, in Chinese.

Research Article

Investigating the Combined Effects of Inherent and Stress-Induced Anisotropy on the Mechanical Behavior of Granular Materials Using Three-Dimensional Discrete Element Method

Xinran Chen, Jinsong Qian ⬥, Lei Zhang, and Jianming Ling

Key Laboratory of Road and Traffic Engineering of the Ministry of Education, Tongji University, 4800 Cao'an Road, Shanghai 201804, China

Correspondence should be addressed to Jinsong Qian; qianjs@tongji.edu.cn

The three-dimensional discrete element method (DEM) was employed to investigate the combined effects of inherent and stress-induced anisotropy of granular materials. The particles were modeled following real particle shapes. Both isotropic and inherently anisotropic specimens were prepared, and then true triaxial numerical tests were conducted using different intermediate principle stress ratios (b). The results indicate that the oriented particles in the anisotropic specimens form strong contacts in their long axis direction in the early stages of shearing, which restrains the contraction of the specimens. As the strain increases, the oriented particles start to rotate and slide, which results in shorter contraction stages and fewer number of interparticle contacts with peak values compared to the isotropic specimens. In addition, the increase in b values aggravates the rotating and sliding of particles in the inherently anisotropic specimens and restrains the contraction of the granular and the increase of contact forces. As a result, the inherent anisotropy reduces the effects of stress-induced anisotropy on the mechanical behavior of granular materials.

1. Introduction

Granular materials are commonly used in the base layers of typical pavement structures. The directional distribution of particles in granular materials significantly affects their mechanical properties [1], which leads to an anisotropic phenomenon. The anisotropy of granular material can be divided into inherent anisotropy and stress-induced anisotropy [2]. Inherent anisotropy is induced by the directional arrangement of particles during compaction or deposition. Stress-induced anisotropy is caused by the nonuniform distribution of external loading, which leads to the rearrangement of the particles [3]. To investigate these two kinds of anisotropy, the long axis orientation (or "bedding angle") of granular particles is widely used for inherent anisotropy analysis, and the intermediate principle stress ratio, denoted by b, which represents the relative magnitude of the intermediate principle stress, is used for stress-induced anisotropy analysis [4, 5].

Several researchers have conducted laboratory tests to study the effect of anisotropy on the mechanical responses of particle assemblies. For example, Guo [6] conducted direct shear tests using specimens with different bedding angles. The results showed that the friction angle of granular materials varies with the orientation of the shear plane relative to the bedding plane. Besides, the degree of anisotropy is affected by particle shapes. Shi et al. [7] investigated the effect of intermediate principle stress on the macroscopic mechanical responses of a coarse-grained soil using true triaxial tests. The results showed that shear strength and intermediate principle strain increase as the b value increases, whereas the minor principle strain decreases. However, some experimental studies have shown uncertain relationships among the angle of shear resistance, b values, and other controversial behavior [8, 9], as laboratory test results can be affected by the initial fabric difference [10, 11], different sample preparation methods [12, 13], different boundary conditions, etc. [14]. In recent years, researchers

used the discrete element method (DEM) [15] to investigate the behavior of granular materials from both macroscopic and microscopic perspectives [16, 17]. The DEM can simulate several test conditions using one specimen and thus avoid the initial fabric difference. Furthermore, microscopic characteristics at the particulate level are easy to obtain and can help to explain the stress and strain evolution during loading [18–20].

Several studies have been undertaken to investigate the anisotropy of soil and granular materials using the DEM. For example, Hosseininia [21] studied the inherent anisotropy of granular soils using a two-dimensional DEM and found that the initial distribution of elongated particles and associated voids vary during shear deformation. Besides, the shear strength and deformability of granular materials are highly dependent on the initial fabric condition. Barreto and O'Sullivan [22] studied the stress-induced anisotropy of soil under a constant mean load using a three-dimensional (3D) DEM. Results showed that the friction coefficient affects the inherent stability of the strong force chains, whereas the intermediate stress ratio affects the lateral support provided to these force chains. Kuhn et al. [23] conducted numerical simulations using a 3D DEM and described the anisotropy of the voids through image analysis and Minkowski tensors. Their results showed that stress-induced anisotropy affects not only the mechanical stress-strain relationship but also the hydraulic properties. Some studies that employed DEM also considered the complex stress path [5, 24] and particle breakage [25, 26]. However, related studies have focused mainly on the effect of different b values on isotropic samples; research into the behavior of inherently anisotropic granular materials under different b values is limited.

In real practice, the granular materials may be inherently anisotropic due to compaction or deposition, and may also work under complex stress states that cause stress-induced anisotropy. Therefore, the combined effects of the two types of anisotropy may affect the mechanical behavior of granular materials simultaneously and thus needs further investigations.

For this purpose, 3D DEM simulations were conducted for this study. Isotropic and inherently anisotropic granular specimens were prepared, and then true triaxial numerical tests were conducted using different b values. Finally, the macroscopic and microscopic responses, including stress-strain characteristics, interparticle contacts, and the anisotropies of contact normal and contact force, were analyzed in detail to address the mechanisms of anisotropy.

2. Numerical Model

2.1. Particle Modeling and Grading.
In DEM simulations, the particle shape can obviously affect the anisotropic properties [3, 6, 27, 28]. Although the use of circular discs (in 2D) or spheres (in 3D) can significantly reduce the calculation time, they can also lead to excessive freedom of the particles and thus a higher degree of rotation and dilation compared with real granular particles [21, 29–31]. Therefore, noncircular/nonspherical particles are widely used and typically are oval or spherical particles made by clusters of bonded circles/

spheres or overlapping rigid clusters [29, 32, 33]. Some researchers have tried another approach that uses convex polygon-shaped particles [34, 35]. The simulation accuracy and computational efficiency of these approaches are of vital importance and are a primary focus of related research.

In this study, the numerical simulations utilized 3D DEM software, Itasca PFC^{3D} (version 5.0). Ten typical shapes of granular particles were considered in the DEM simulations and were modeled in 3D following real particle shapes, as shown in Figure 1(a). Then, based on the bubble pack algorithm proposed by Taghavi [36], the 3D models were filled with different sized balls which partially overlapped each other without generating force to create complex clumps in PFC^{3D}. During the filling process, the largest ball was placed first, followed by decreasingly smaller balls. The distance parameter, which controls the overlap of adjacent balls, and the ratio parameter, which is the ratio of the smallest to the largest ball, both affected the simulation accuracy and calculation efficiency. After several pretests, the distance and ratio parameters were set at 100 and 0.3, respectively. Figure 1(b) presents a comparison of a real particle, the original 3D model, and the PFC^{3D} particle.

In order to simulate an actual granular base that consists of particles of different sizes, a widely used grade was selected for the DEM simulations [31, 37]. In accordance with previous research studies, fine particles were deleted and the particle sizes were adjusted to consider computational efficiency [38, 39], as shown in Figure 2. It should be noted that, the DEM specimen without fine-graded particles may be less dense and more compressible than actual granular material [40]. This simplification would affect the values of some macro-microindexes, but the comparison among different anisotropic conditions would be less affected.

The total number of particles used for the numerical specimens were calculated using the target porosity of 0.33. To avoid the size effect, previous studies suggest that the diameter of the specimen should be at least 10 times larger than the maximum particle size [38, 41]. Therefore, the dimensions of each granular specimen were set to $15^L \times 15^W \times 15^H$ cm^3, and 6,884 particles were used. The ten different particle shapes were randomly distributed. Table 1 lists both the particle sizes and numbers of particles used in this study.

2.2. Specimen Preparation.
Two specimen types were used in DEM simulation, which are the isotropic specimens and inherently anisotropic specimens. Both types of specimens were prepared using the gravitational deposition method [42, 43]. First, a deposition space of $15^L \times 15^W \times 30^H$ cm^3 was created and enclosed by six frictionless rigid walls, and the particles were then generated in the space, as shown in Figure 3. For the isotropic specimens, the long axis of the particles was randomly distributed, whereas for the inherently anisotropic specimens, the long axis of the particles was arranged in the intermediate principle stress (σ_2) direction. During specimen preparation, the particle rotation was fixed to obtain the anticipated anisotropic conditions. Then, the gravity field was introduced using the gravitational forces

(a)

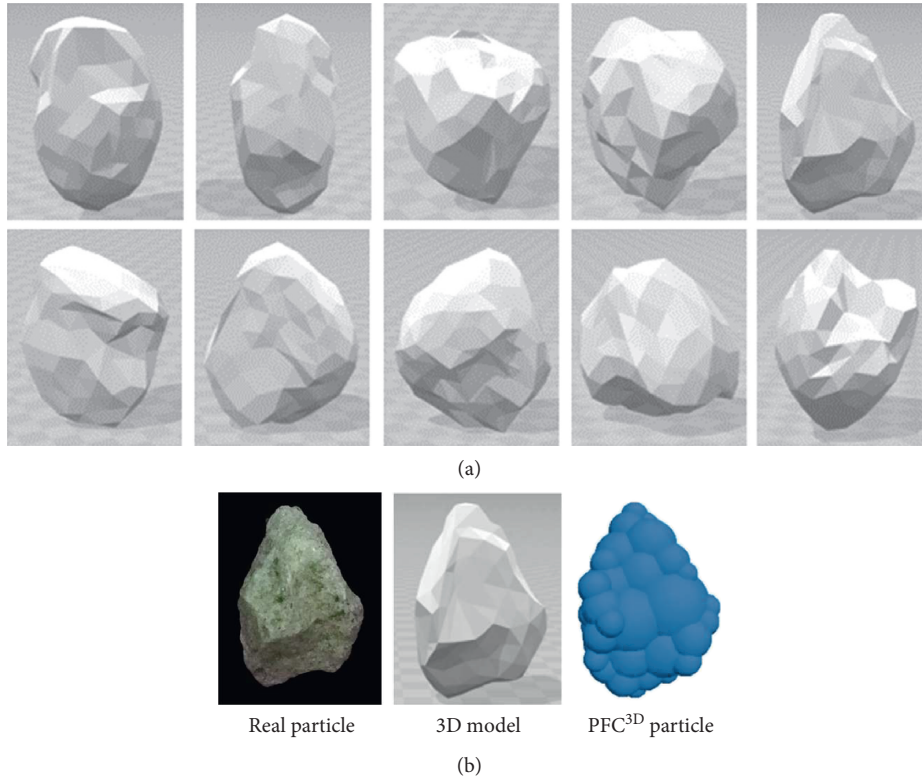Real particle   3D model   PFC^{3D} particle

(b)

FIGURE 1: (a) 3D granular models of different particle shapes and (b) comparison of the real particle, 3D model, and PFC3D particle.
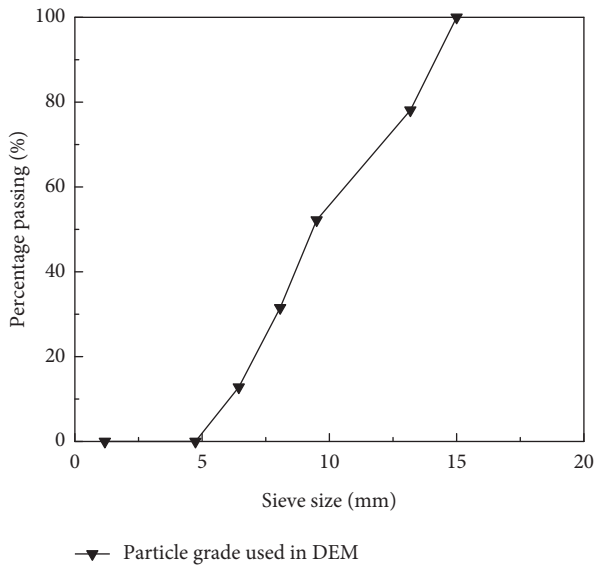

FIGURE 2: Particle size distribution curve used in the DEM simulation.

TABLE 1: Particle size and number of particles for different specimens.

Particle size (mm)	4.75–6.5	6.5–8	8–9.5	9.5–13.25	13.25–15
Number of particles	3925	1346	878	531	204

isotropically compressed by giving the same loading speed to all six rigid walls until the target confining pressure of 100 kPa was reached. Figure 3(e) presents the isotropic and anisotropic specimens after preparation.

The linear contact model [44] was adopted to simulate the interparticle contacts for computational efficiency. In accordance with related studies which also studied the mechanical behavior of granular materials [30, 39, 45, 46], the material parameters were selected for triaxial testing. The stiffness ratio $\kappa*$, effective modulus $E*$ friction coefficient μ, damping constant, and particle density were set at 1.333, 1×10^8 Pa, 0.5, 0.7, and 2.6 g/cm^3, respectively.

2.3. True Triaxial Shearing. The true triaxial tests were conducted using a strain-controlled loading process that was performed by moving the rigid walls of the specimens. As suggested by Andrade et al. [47], increased loading speed increased the calculation efficiency but would affect the mechanical behavior of granular materials due to the dynamic effect. To select a proper loading speed, a sensitivity analysis was conducted using isotropic specimens under five loading speeds ranged from 0.03 m/s to 0.50 m/s, as depicted

applied to all particles in the vertical direction; thus, the particles would be deposited on the bottom boundary of the deposition space. To create a dense specimen and reduce the simulation time during specimen preparation, the particle friction coefficient was temporarily set as zero [5, 29]. At the end of the deposition, a space of $15^L \times 15^W \times 15^H$ cm^3 was chosen as the final specimen size. Finally, the specimen was
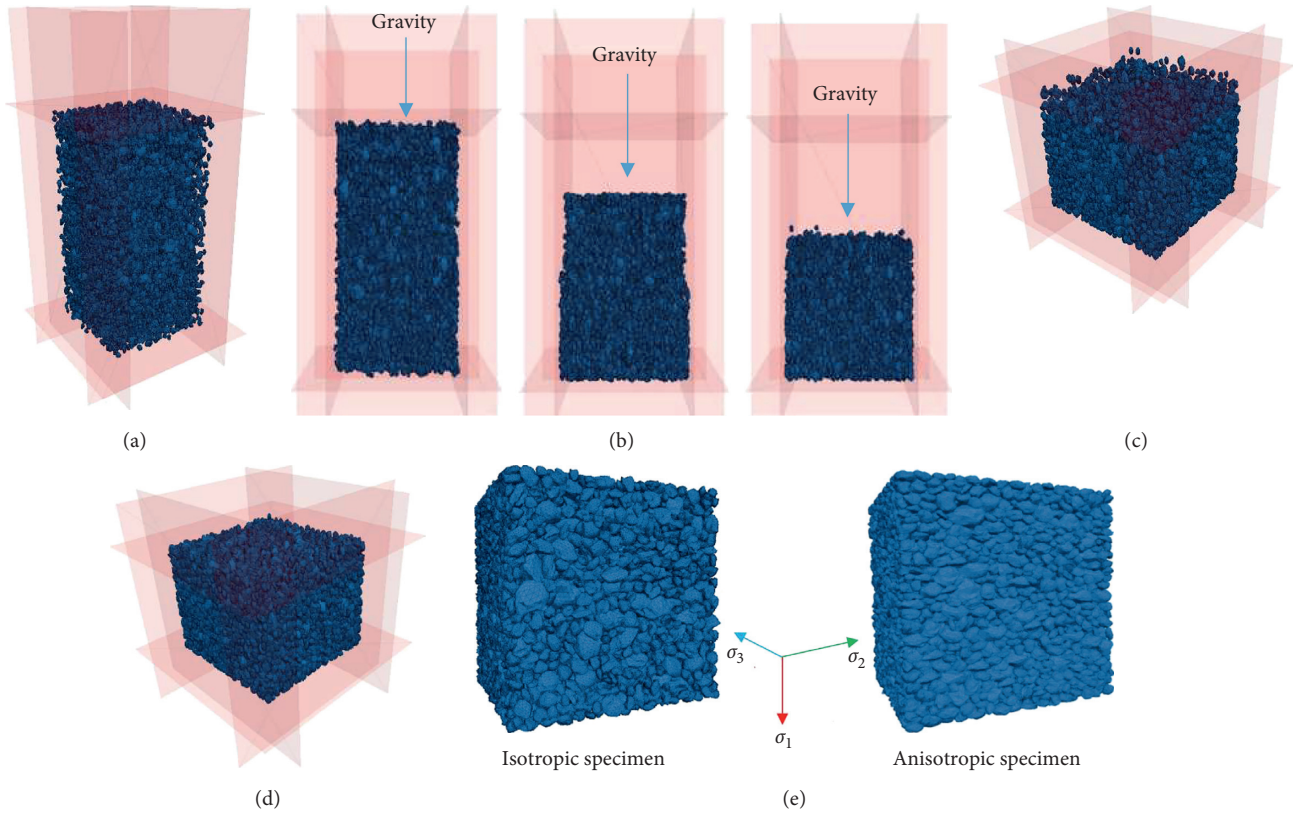
FIGURE 3: The procedure of specimen preparation: (a) particles' generation; (b) gravitational deposition; (c) resizing the walls; (d) isotropic compression; (e) specimens after preparation.

in Figure 4. It can be seen that the porosity, which reflects the volume change of the specimens, changes obviously under high loading speeds. By contrast, the porosity is similar for selected small loading speeds. This indicates that the loading speed had a threshold between quasi-static and dynamic. Thus, the loading speed for this study was set at 0.12 m/s to ensure the loading process was quasi-static.

To simulate stress-induced anisotropy, the intermediate principle stress ratio, b, was induced and is defined as

$$b = \frac{(\sigma_2 - \sigma_3)}{(\sigma_1 - \sigma_3)}, \tag{1}$$

where σ_i ($i = 1, 2, 3$) are the principle stresses. In this paper, the stress and strain indexes take positive values when the granular is compressed.

Five b values ($b = 0.00, 0.25, 0.50, 0.75, 1.00$) were selected for the numerical tests. The test under $b = 0.00$ ($\sigma_2 = \sigma_3$) represents the triaxial compression test, and the test under $b = 1.00$ ($\sigma_1 = \sigma_2$) is the triaxial extension test. The major principle stress σ_1 changes when the top wall moves during testing, so the intermediate principle stress can be calculated using the following equation:

$$\sigma_2 = b(\sigma_1 - \sigma_3) - \sigma_3. \tag{2}$$

The minor principle stress σ_3 was set at 100 kPa for all conditions, and b values were also kept constant during the numerical simulation, so the relationship between σ_1 and σ_2

could be expressed by $d\sigma_2 = b d\sigma_1$. During triaxial shearing, the σ_2 was dynamically adjusted by stress servo-control method to keep equation (2) satisfied.

2.4. Verification of the DEM Simulation. The DEM model was verified by the true triaxial test results conducted by Shi [48]. For the laboratory test, the fine gravel was used with the particle diameter ranged from 2–5 mm. The diameter of the laboratory test specimen is 70 mm × 35 mm × 70 mm, and the loading conditions are the same as the DEM simulation. The long axis of the particles in the laboratory test was randomly distributed, which consists of the isotropic DEM specimen.

The comparison between the laboratory test and the numerical simulation results is depicted in Figure 5. It can be seen that the stress-strain relationship and the peak stress ratio obtained from DEM simulation and laboratory test share the same trend, and the values are similar to each other. Therefore, it can be indicated that the DEM model is reasonable.

3. Numerical Simulation Results

3.1. Macroscopic Analysis: Stress-Strain Characteristics. To evaluate the stress-strain characteristics of granular materials with different initial fabrics and under different b values, several commonly used macroscopic indexes are
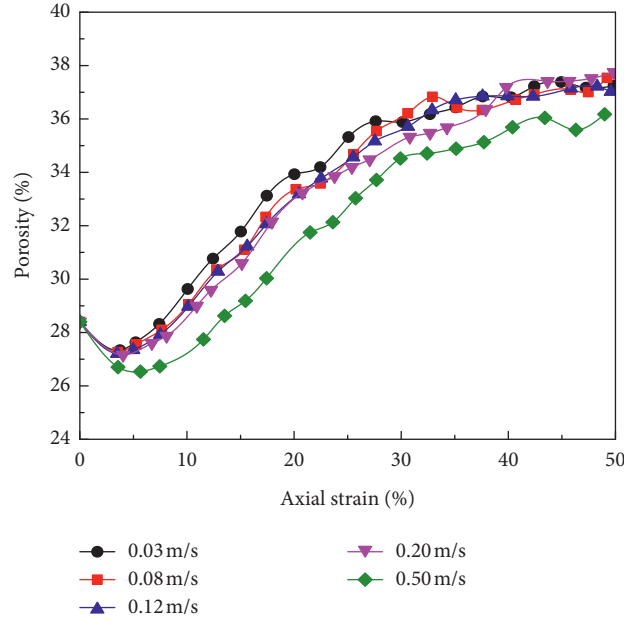
FIGURE 4: The effect of the loading speed sensitivity on the porosity.

(a)

(b)
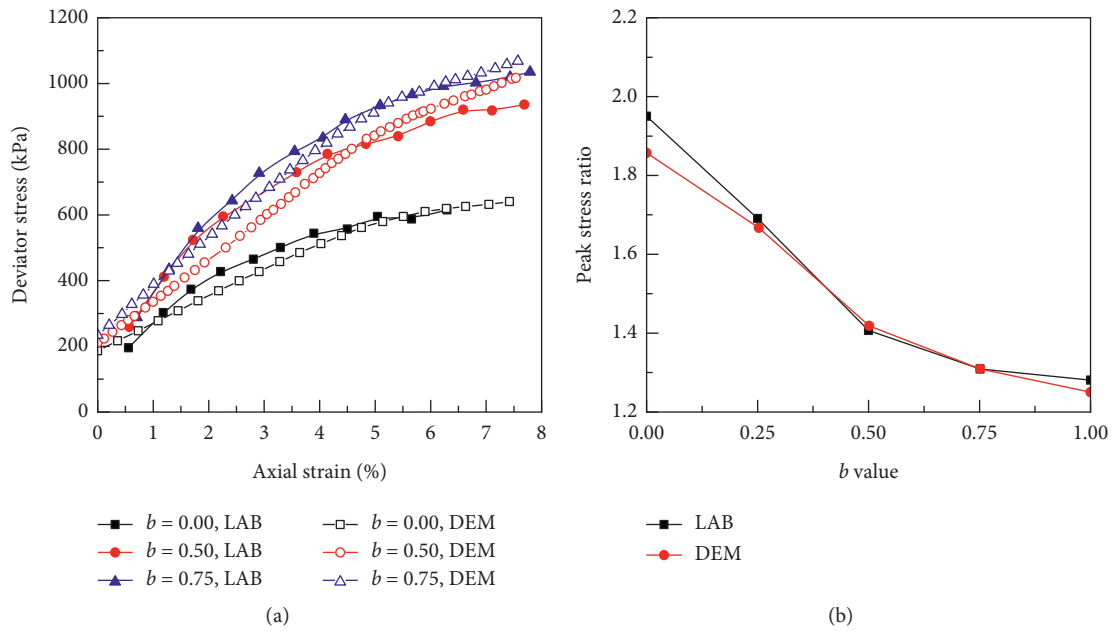
FIGURE 5: Comparison between the DEM model and laboratory tests: (a) the deviator stress; (b) the peak stress ratio.

selected based on the stress and strain in three principle stress directions. The peak internal friction angle (φ_{max}), mean stress (p), shear stress (q), major principle strain (ε_1), and volumetric strain (ε_v) are defined, respectively, as equation (3)–(7) [49]:

$$\sin \varphi_{max} = \frac{(\sigma_1/\sigma_3)_{max} - 1}{(\sigma_1/\sigma_3)_{max} + 1}, \tag{3}$$

$$p = \frac{(\sigma_1 + \sigma_2 + \sigma_3)}{3}, \tag{4}$$

$$q = \sqrt{\left(\frac{1}{2}\right)\left[(\sigma_1 - \sigma_2)^2 + (\sigma_2 - \sigma_3)^2 + (\sigma_1 - \sigma_3)^2\right]}, \quad (5)$$

$$\varepsilon_1 = \ln\left(\frac{H_0}{H}\right), \quad (6)$$

$$\varepsilon_v = \ln\left(\frac{V}{V_0}\right), \quad (7)$$

where H_0 and V_0 are the initial height and volume of the specimen, respectively, and H and V represent the height and volume of the specimen at time t, respectively.

The relationship between φ_{max} and b value is commonly used to investigate of peak strength in true triaxial testing. Figure 6(a) shows that, for both specimen types, φ_{max} increases as the b value increases from 0.00 to 0.75 and then decreases as the b value increases from 0.75 to 1.00. Similar trend was also found by previous studies using laboratory tests [47, 49] and DEM simulations [4, 5, 11]. The peak value of the mean stress (p_{max}) that represents the overall stress level increases as the b value increases for both specimen types, as shown in Figure 6(b). Because all the numerical tests were conducted using the same σ_3 value, the σ_2 value increases as the b value increases and leads to the increase in the mean stress.

Compared to the isotropic specimens, the φ_{max} and p_{max} values for anisotropic specimens are lower at the same b values and change less as the b value increases. This finding indicates that the horizontal alignment of the long axis of the particles reduces the effect of nonuniform stress distribution on the stress behavior of granular materials.

To highlight the effects of the nonuniform distribution of external loading on the stress behavior of the granular materials, the stress ratio, defined as q/p, is introduced. Figure 7 shows that, for the isotropic specimens, the stress ratio deceases as the b value increases, which is consistent with related laboratory test results [50] and numerical simulation results [4, 14]. Also, the stress ratios for both specimen types are similar at the same b values. This finding indicates that the increased proportion of σ_2 results in the decrease of the shear strength of granular materials, and this effect is similar for both isotropic and inherently anisotropic granular specimens.

Figure 8 shows the variation of (ε_v) with the major principle strain ε_1. All specimens exhibit the process from contraction to dilation as ε_1 value increases. For the isotropic specimens, the amount of contraction tends to increase as the b value increases. By contrast, the anisotropic specimens are less contracted than the isotropic specimens for all the selected b values, and their contraction stages end with smaller ε_1 values. This finding indicates that the inherently anisotropic granular materials are less compressible and may dilate earlier than isotropic granular materials and that the effect of b values on strain behavior is reduced.

3.2. *Microscopic Analysis: Contact Characteristics.* In order to illustrate the macroscopic behavior of granular materials at the particle scale, the contact characteristics are analyzed.

The coordination number (CN) is a commonly used index that is directly related to the stability of granular material [4, 51] and is defined as the average number of contacts per particle:

$$CN = \left(\frac{2N_c - N_c^w}{N_p}\right), \quad (8)$$

where CN is the coordination number, N_c is the total number of contacts, N_c^w is the number of contacts between the particle and the wall, and N_p is the total number of particles.

Figure 9 shows the evolution of the CN with the major principle strain. For both specimen types, the CN increases with ε_1 to the peak value and then decreases to a residual value. The peak CNs increase obviously as the b value increases. Compared to the isotropic specimens, the inherently anisotropic specimens have higher initial CNs, lower peak CNs, and smaller ε_1 values that correspond to the peak CNs. Besides, the increase of their peak CNs as b value increases is much smaller than isotropic specimens. This finding indicates that the oriented arrangement of particles in inherently anisotropic specimens form more contacts in the early stage of shearing, and the change of CNs during shearing is less affected by nonuniform stress distribution.

During triaxial testing, the contact sliding typically occurs during the rearrangement of the particles, thus resulting in the permanent deformation of the granular materials. As defined by Gu et al. [39], contact slides when the inequality, shown as equation (9), is satisfied:

$$\frac{|f^t|}{(\mu f^n)} > 0.9999, \quad (9)$$

where f^n and f^t are the normal contact force and tangential contact force, respectively, and μ is the contact friction coefficient.

Figure 10 presents a comparison of the initial and peak sliding contact percentages during triaxial shearing for all specimens. For both specimen types, the initial sliding contact percentages increase as b value increases from 0.00 to 0.25, and decrease as b value increases from 0.25 to 1.00. The peak sliding contact percentages for the isotropic specimens decrease as the b value increases, which is consistent with the DEM simulation results of Mahmud Sazzad et al. [4]. By contrast, the peak sliding contact percentages for the anisotropic specimens decrease as the b value increases from 0.00 to 0.75, then tend to increase as the b value increases from 0.75 to 1.00. Under the same b values, the anisotropic specimens have lower initial sliding contact percentages and higher peak sliding contact percentages compared to the isotropic specimens. This finding indicates that the sliding of contacts is restrained as the b values increase for isotropic specimens. By contrast, the anisotropic specimens restrain contact sliding in the early stages of testing compared with isotropic specimens, but contact sliding occurs more during shearing, especially with high b values.

Both the CNs and the sliding contact percentages can be used to explain the change of volumetric strain (see
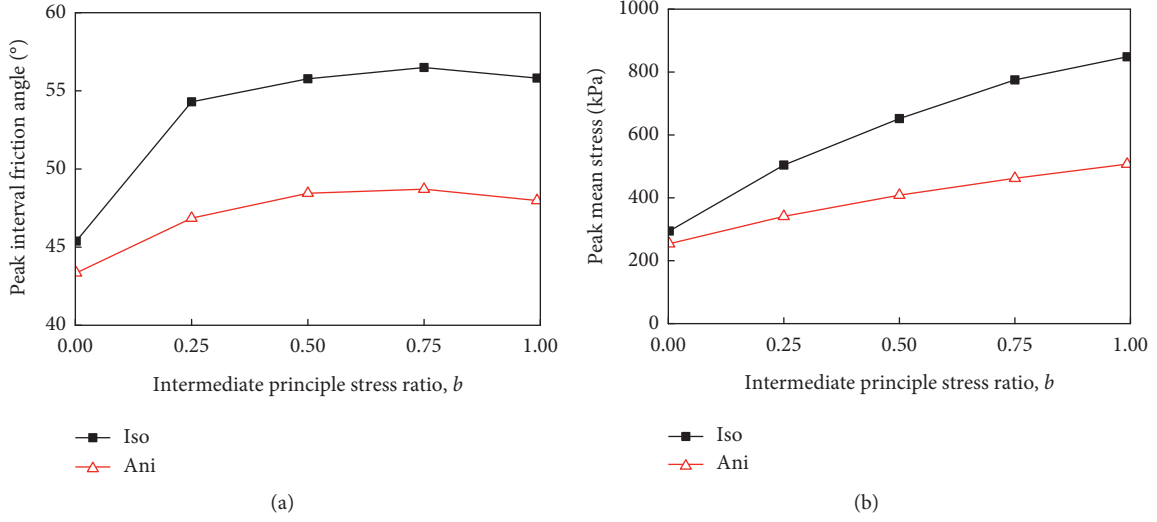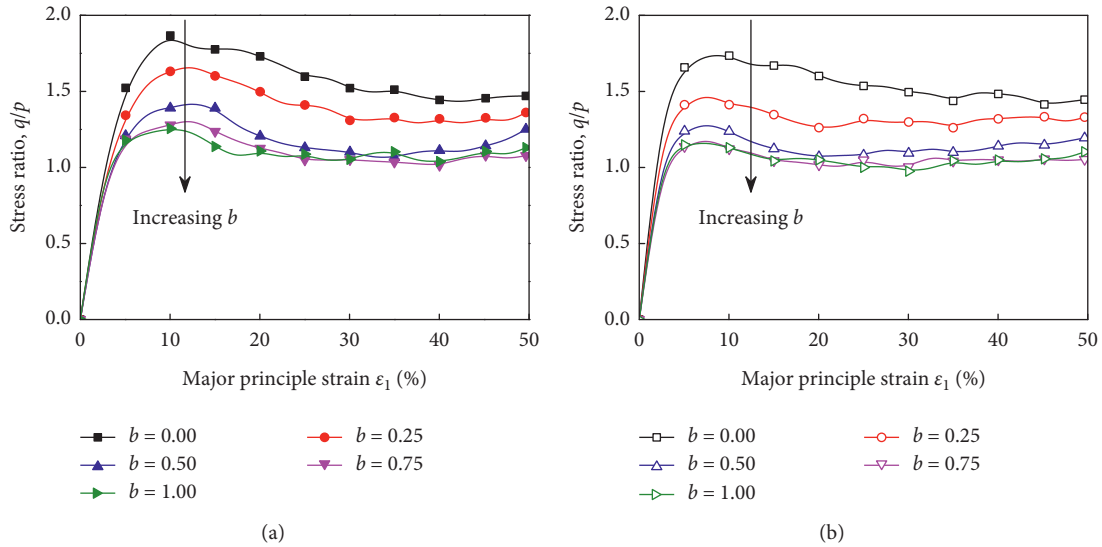
FIGURE 6: Comparison of (a) peak internal friction angle ($\varphi_{\max}$) and (b) peak mean stress ($p_{\max}$).

FIGURE 7: Evolution of stress ratio with the increase of ε_1: (a) isotropic specimens; (b) anisotropic specimens.

Figure 8). During the contraction stage, the particles are squeezed together in close contact with each other, which leads to an increase in the CN value. During the dilation stage, the particles start to rotate and slide, which results in the decrease of CN [51]. The specimen which is contracted mostly also has the largest peak CN and the lowest peak sliding contact percentage.

3.3. Microscopic Analysis: Fabric Tensor and Anisotropy.
The directional distribution of particles, defined as the fabric, plays an important role in the shear behavior of a particle assembly [52–55]. To further investigate the combined effects of inherent and stress-induced anisotropy of granular materials, the contact normal, normal contact force, and tangential contact force are induced.

The directional distribution of the contact normal is usually described by the fabric tensor R_{ij} [56, 57]:

$$R_{ij} = \int_{\Omega} E(\Omega) n_i n_j d\Omega = \left(\frac{1}{N}\right) \sum_{c \in N} n_i n_j, \quad (10)$$

where n_i is the unit contact normal in the i-direction, N is the total number of contacts, and $E(\Omega)$ is the distribution function on the unit sphere Ω and can be calculated by the second-order Fourier expansion as follows [58]:

$$E(\Omega) = \left(\frac{1}{4\pi}\right)\left[1 + \alpha_{ij}^r n_i n_j\right], \quad (11)$$

where α_{ij}^r is the second-order anisotropic tensor and characterizes the fabric anisotropy. This tensor is determined by the deviatoric part of the fabric tensor (R_{ij}') as
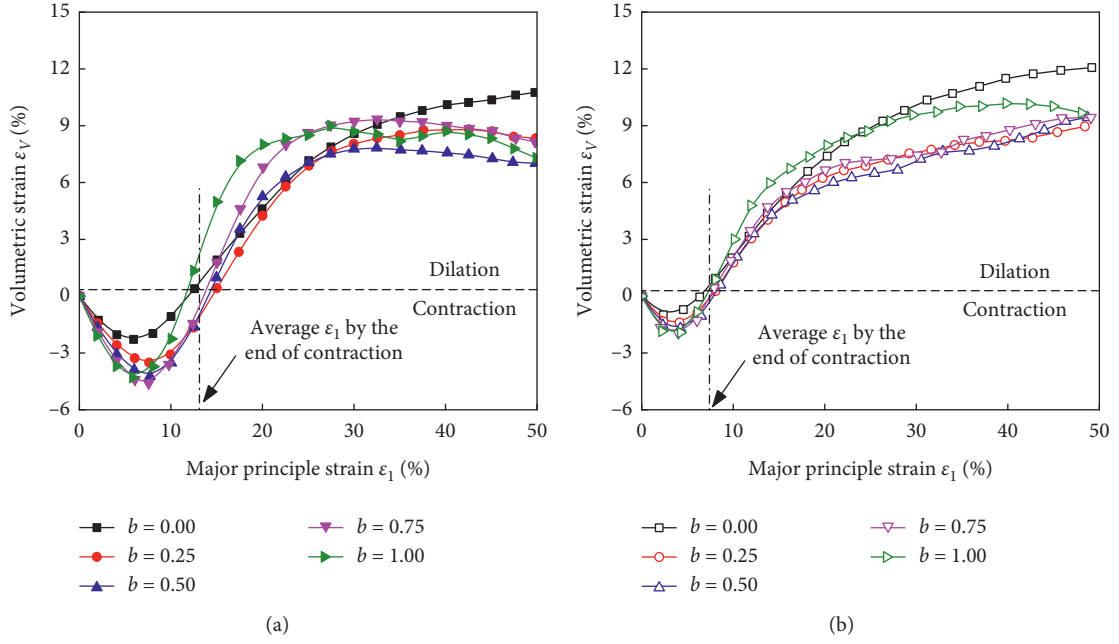
FIGURE 8: Variation of volumetric strain with the increase of ε_1: (a) isotropic specimens; (b) anisotropic specimens.
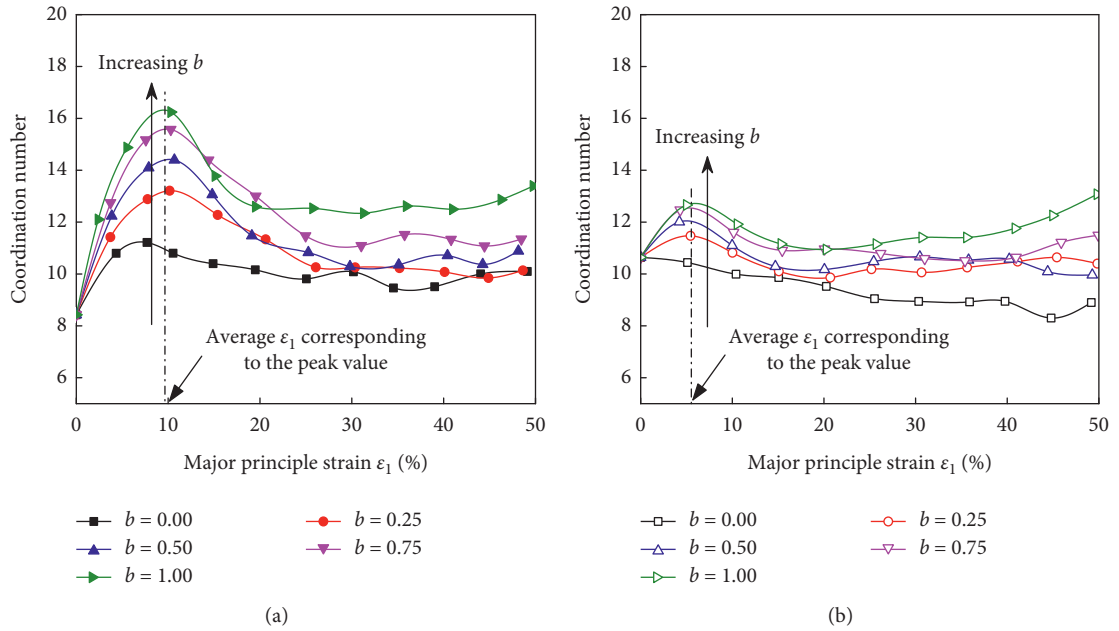
FIGURE 9: Evolution of coordination number with the increase of ε_1: (a) isotropic specimens; (b) anisotropic specimens.

$$\alpha_{ij}^r = \left(\frac{15}{2}\right) R_{ij}'. \tag{12}$$

For normal and tangential contact force, the similar definition is induced, as expressed in equation (13)–(18):

$$F_{ij}^n = \left(\frac{1}{4\pi}\right) \int_\Omega \overline{f}^n(\Omega) n_i n_j \, d\Omega = \sum_{c \in N} \frac{f^n n_i n_j}{N\left(1 + \alpha_{kl}^r n_k n_l\right)}, \tag{13}$$

$$\overline{f}^n(\Omega) = \overline{f}_0^n\left(1 + \alpha_{ij}^n n_i n_j\right), \tag{14}$$
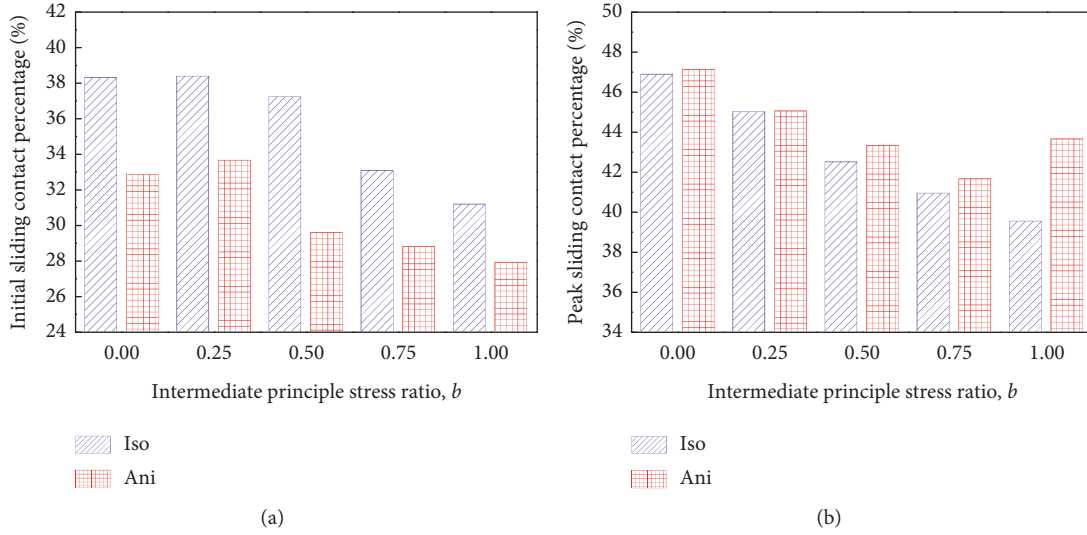
FIGURE 10: Comparison of (a) initial sliding contact percentages and (b) peak sliding contact percentages.

$$\alpha_{ij}^n = \left(\frac{15}{2}\right)\left(\frac{F_{ij}^{n'}}{\overline{f}_0^n}\right), \tag{15}$$

$$F_{ij}^t = \left(\frac{1}{4\pi}\right)\int_\Omega \overline{f}_i^t(\Omega) n_i n_j \mathrm{d}\Omega = \sum_{c\in N} \frac{f^t n_i n_j}{N(1 + \alpha_{kl}^r n_k n_l)}, \tag{16}$$

$$\overline{f}_i^t(\Omega) = \overline{f}_0^n \left[\alpha_{ij}^t n_j - \left(\alpha_{kl}^t n_k n_l\right) n_i\right], \tag{17}$$

$$\alpha_{ij}^t = \left(\frac{5F_{ij}^{t'}}{\overline{f}_0^n}\right), \tag{18}$$

where f^n is the normal contact force, f^t is the tangential contact force, and $\overline{f}_0^n$ is the average normal contact force over all the groups on Ω.

Note that α_{ij}^r, α_{ij}^n, and α_{ij}^t are symmetric and deviatoric, so their second invariants α_r, α_n, and α_t are used to quantify the degree of anisotropy as

$$\alpha_* = \sqrt{\left(\frac{3}{2}\right)\alpha_{ij}^* \alpha_{ij}^*}, \tag{19}$$

where the super and subscript $*$ represents the contact normal r, tangential contact force t, and normal contact force n, respectively.

Figure 11 shows that the α_r, α_n, and α_t values increase at the beginning and then decrease to a residual value as ε_1 value increases. As the b value increases, the initial slope of α_r, shows a small difference, whereas the peak values and residual values decrease obviously. This finding indicates that the contact distribution tends to be more uniform with a higher b value. Besides, the α_n values are about 3 to 4 times higher than the α_t values for all conditions, which suggests that contact force anisotropy is mainly caused by normal contact forces [51].

The initial α_r values for the two specimen types are significantly different. The isotropic specimens have an initial α_r at zero, which means the initial contact distribution is uniform. By contrast, the anisotropic specimens have an initial α_r, at about 1.0, which means the oriented arrangement of particles make the initial contact distribution nonuniform. However, the peak and residual α_r values for two specimen types are similar, which suggests that inherent anisotropy changes the initial contact distribution, but will not obviously affect the extent of contact normal anisotropy during shearing. For α_n and α_t, the values change with different b values for anisotropic specimens is smaller than the isotropic specimens, which suggests that inherent anisotropy significantly reduces the effect of b values on the distribution of contact force of granular materials.

To address the reason for the difference in anisotropy parameters α_r and α_n, between the two specimen types, the principle values corresponding to them are induced. The α_t is not analyzed here because it is much smaller than α_n.

The principle values of the fabric tensor R are used to quantify the cluster extent of contacts in the principle stress directions [14]. R_1, R_2, and R_3 represent the contact clustering extent in the σ_1, σ_2, and σ_3 direction, respectively. As shown in Figure 12, the R principle values show similar trends with the increase of ε_1 for both specimen types. Before the peak of R principle values, R_1 increases, whereas R_3 decreases as ε_1 value increases for all the selected b values. R_2 decreases with the increase of ε_1 when $b < 0.5$ and increases as ε_1 value increases when $b > 0.5$. Such trends are similar to the precious DEM simulation results [11, 14, 22], which also indicates that contacts tend to cluster in the σ_1 direction to carry most of the external load. As the b value increases, the contacts also cluster in the σ_2 direction.

The anisotropic specimens have higher R_3 values and lower R_2 values compared with the isotropic specimens for all selected b values; thus, the contact normal anisotropy α_r for the two specimen types is similar. In addition, for the anisotropic specimens, the R_2 value is lower than the R_3 value under selected small b values, whereas for the isotropic specimens, the relationship is opposite. This finding
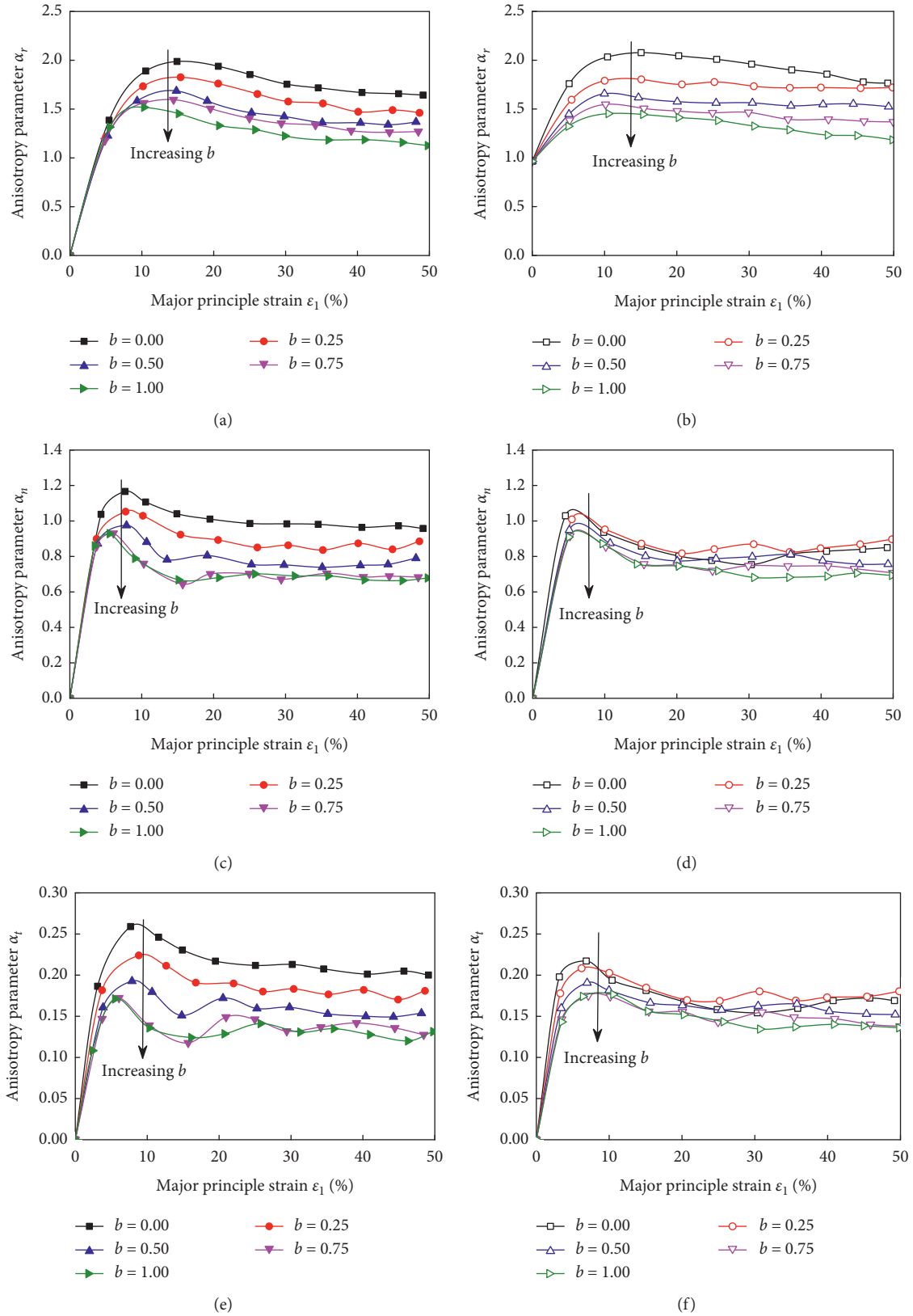
Figure 11: Effects of b values on the anisotropy parameter α_r, α_n, and α_t. (a) α_r Iso, (b) α_r Ani, (c) α_n Iso, (d) α_n Ani, (e) α_t Iso, and (f) α_t Ani.
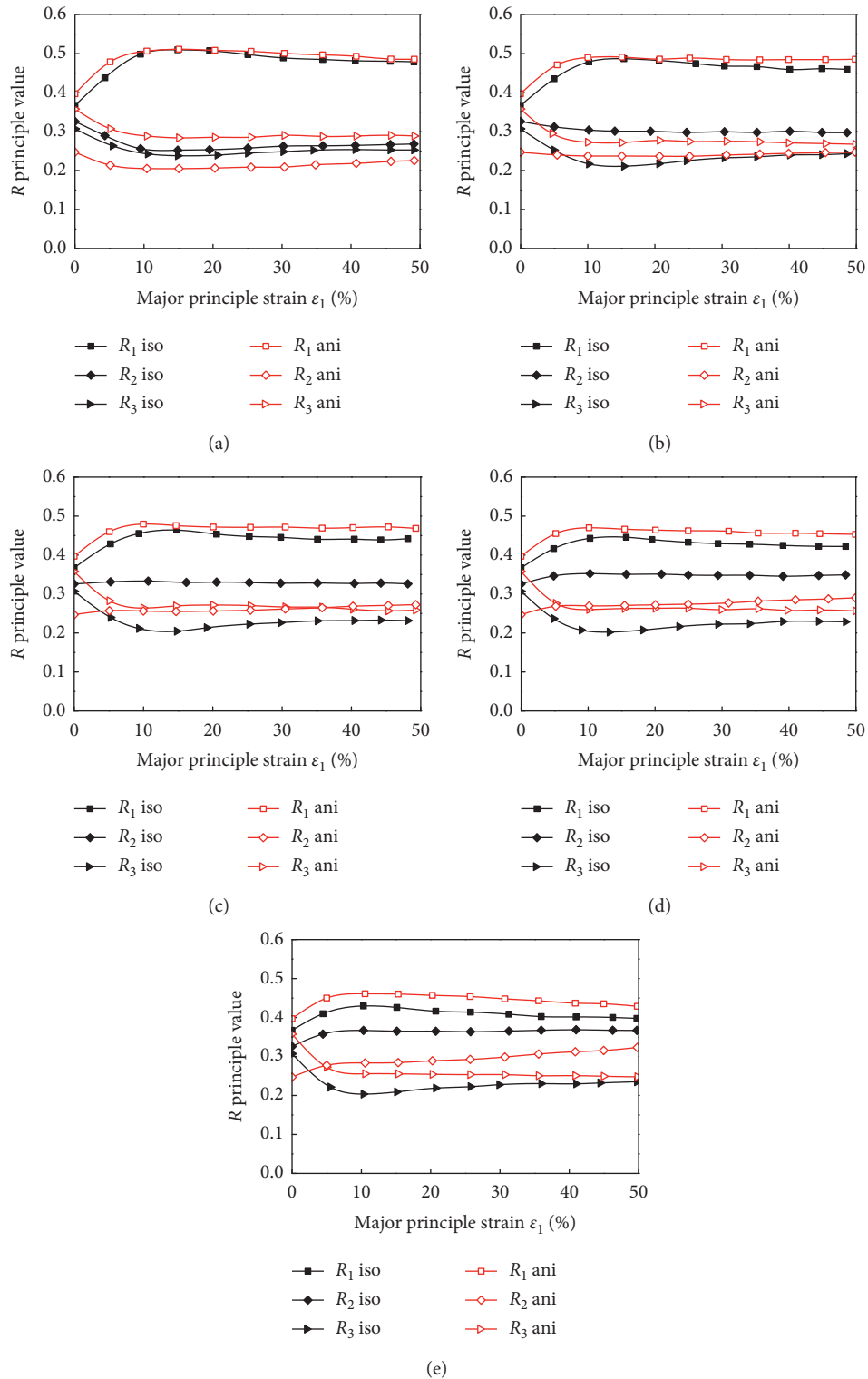
FIGURE 12: Evolution of the R principle values with an increase in b values: (a) $b = 0.00$; (b) $b = 0.25$; (c) $b = 0.50$; (d) $b = 0.75$; (e) $b = 1.00$.

indicates that the inherently anisotropic specimens form less contact in the direction of the long axis orientation of particles during shearing, compared with isotropic specimens.

Figure 13 shows the principle values of the normal contact force tensor Fn (Fn_1, Fn_2, Fn_3). The trends are similar for the three Fn principle changes as the ε_1 increases. As b value increases, all three Fn principle values increase obviously, which leads to the increase of peak internal friction angle and peak mean stress (Figure 6).
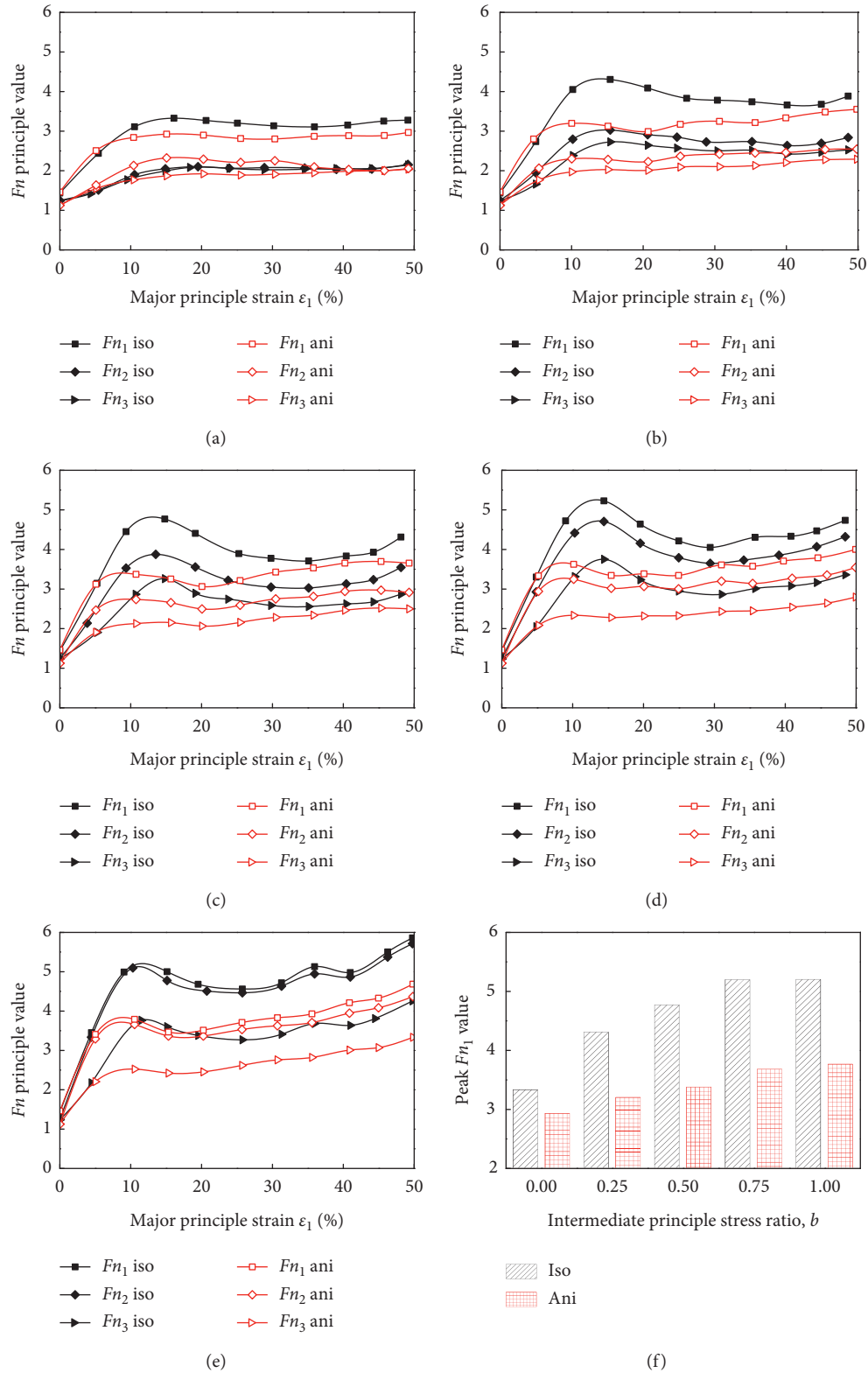
FIGURE 13: Evolution of the Fn principle values with the increase in b values: (a) $b = 0.00$; (b) $b = 0.25$; (c) $b = 0.50$; (d) $b = 0.75$; (e) $b = 1.00$; (f) comparison of peak Fn_1 values.

Compared to the isotropic specimens, the anisotropic specimens have lower principle Fn values (except for Fn_2 when $b = 0$), and the growth rate of contact force for anisotropic specimens is lower as the b value increases, as shown in Figure 13(f). Therefore, the difference in α_n for the anisotropic specimens among different b values is smaller
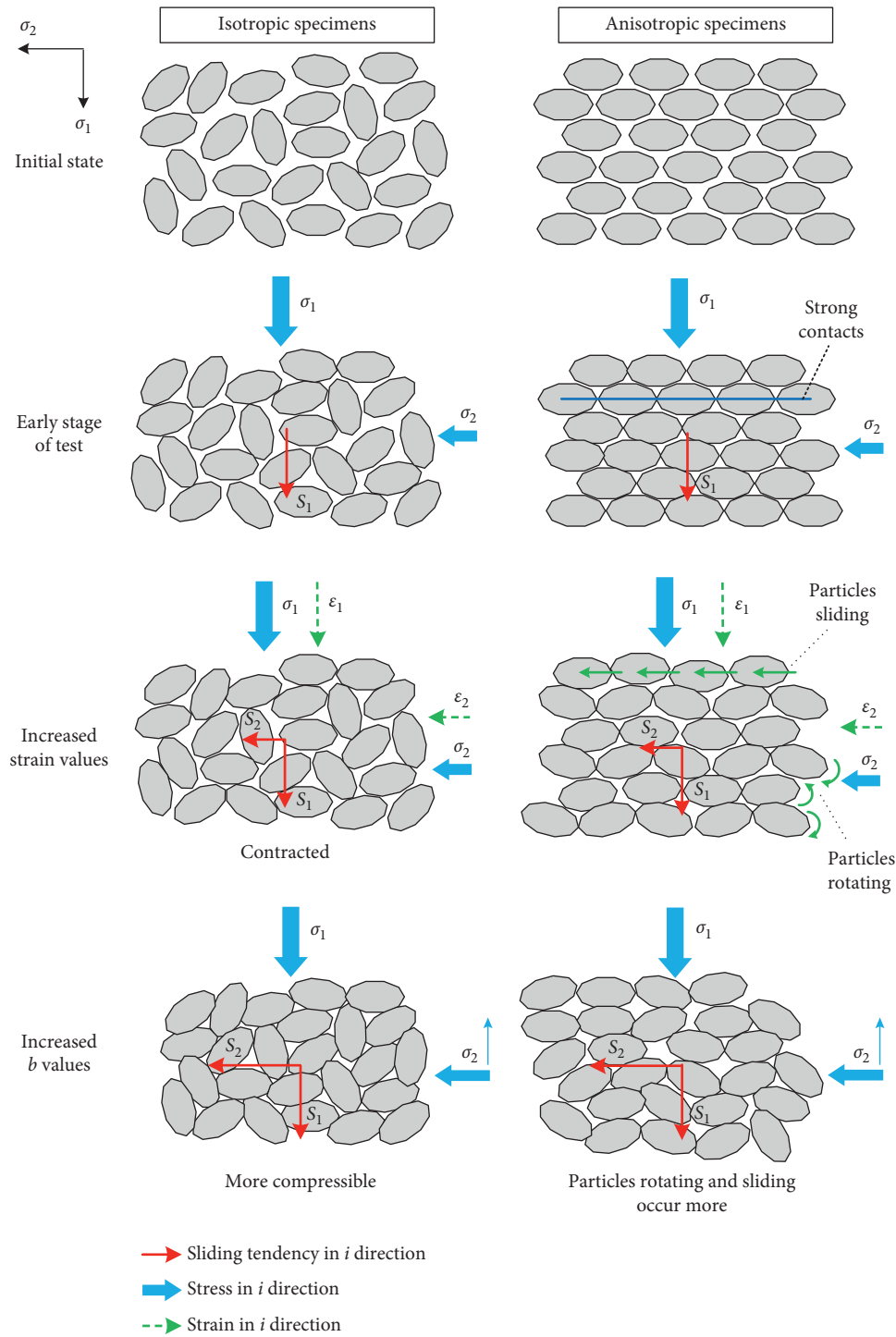
FIGURE 14: Schematics of the combined effects of inherent and stress-induced anisotropy.

(Figure 11), and their peak internal friction angle and peak mean stress are lower than isotropic specimens (Figure 6).

For the anisotropic specimens, the clustering of the contact normal in the σ_2 direction (R_2) is lower than in the σ_3 direction (R_3) for the selected small b values (Figure 12), whereas the clustering of the contact force in the σ_2 direction (Fn_2) is higher than the σ_3 direction (Fn_3), which suggests that the oriented particles form strong contacts in their long

axis direction and thus comprise of a strong force subnetwork [51, 56, 59, 60].

3.4. Discussion of the Combined Effects of Anisotropy.

In summary, the combined effects of inherent anisotropy and stress-induced anisotropy can be illustrated in Figure 14. For selected small b values, the long axis of the particles in the

anisotropic specimens are initially perpendicular to the σ_1 direction to carry most of the external load [21] and resist the sliding tendency in σ_1 direction. Also, these particles form strong contacts in the σ_2 direction, as explained in Section 3.3. Therefore, the anisotropic specimens form a support frame in the early stages of testing, which leads to higher initial CN values and lower initial sliding contact percentages and makes the specimens less compressible compared with isotropic specimens. As the strain value increases, the isotropic specimens are obviously compressed, whereas for the anisotropic specimens, particle rotating and sliding occur due to the increased deformation in the σ_2 direction, which leads to higher peak sliding contact percentages, restrains the increase in the CNs, and shortens the contraction stage.

The increase in b values increases the proportion of σ_2, thus leads to a greater sliding tendency in σ_2 direction. For isotropic specimens, the increase in b values leads to higher peak CNs, restrains the sliding of the contacts, and thus makes the specimens more compressible. For inherently anisotropic specimens, the increased b value significantly aggravates the rotating and sliding of the oriented particles and offsets its compressive effect. Therefore, the anisotropic specimens have higher peak sliding contact percentages and lower growth rate for the coordination number and contact force and are less compressible than the isotropic specimens. As a result, the effect of b values on the mechanical behavior of anisotropic specimens is significantly reduced when combined with the inherently anisotropic condition, compared with isotropic specimens.

4. Conclusion

This paper discussed the results of numerical simulations to investigate the combined effects of inherent and stress-induced anisotropy on the mechanical behavior of granular materials using 3D DEM. The macroscopic stress-strain relationships, microscopic contact characteristics, and anisotropic parameters were analyzed in detail and could be used to provide insights into the mechanism of anisotropy. The following conclusions can be drawn from this study:

(i) The macroscopic and microscopic responses of granular materials are significantly affected by b values. The increase in b values makes isotropic specimens more compressible and leads to lower shear strength at the same stress level, and the directional distribution of contact normal and contact force becomes more uniform.

(ii) Compared with isotropic specimens, the oriented granular particles in inherently anisotropic specimens form a support frame in the early stages of triaxial shearing, and thus make the granular material less compressible. As the strain increases, the oriented particles start to rotate and slide, which result in the redistribution of interparticle contacts and make the granular tend to dilate.

(iii) When applying on the inherently anisotropic specimens, increased b values break the strong

contacts parallel to the long axis of particles, aggravate the rotating and sliding of particles, and offset the compressive effect of b values. Thus, the contraction of granular materials and the increase of shear strength as the b value increases are significantly restrained. As a result, the inherent anisotropy reduces the effects of stress-induced anisotropy on the mechanical behavior of granular materials.

Data Availability

Some of all data, models, or codes used during the study are available from the corresponding author upon request.

Additional Points

Highlights. (i) The combined effects of inherent and stress-induced anisotropy were studied by DEM. (ii) The oriented granular particles form strong contacts but cause a sliding tendency. (iii) The rotating and sliding of oriented particles are aggravated as b values increase. (iv) Inherent anisotropy reduces the effects of b values on macro-microresponses.

Conflicts of Interest

The authors declare that they have no conflicts of interest.

Acknowledgments

References

[1] Y. Qian, S. J. Lee, E. Tutumluer, Y. M. Hashash, and J. Ghaboussi, "Role of initial particle arrangement in ballast mechanical behavior," *International Journal of Geomechanics*, vol. 18, no. 3, Article ID 04017158, 2018.

[2] H. Yang, W.-J. Xu, Q.-C. Sun, and Y. Feng, "Study on the meso-structure development in direct shear tests of a granular material," *Powder Technology*, vol. 314, pp. 129–139, 2017.

[3] J. Zheng and R. D. Hryciw, "Particulate material fabric characterization by rotational haar wavelet transform," *Computers and Geotechnics*, vol. 88, pp. 46–60, 2017.

[4] M. Mahmud Sazzad, K. Suzuki, and A. Modaressi-Farahmand-Razavi, "Macro-micro responses of granular materials under different b values using DEM," *International Journal of Geomechanics*, vol. 12, no. 3, pp. 220–228, 2012.

[5] B. Li, L. Chen, and M. Gutierrez, "Influence of the intermediate principal stress and principal stress direction on the mechanical behavior of cohesionless soils using the discrete element method," *Computers and Geotechnics*, vol. 86, pp. 52–66, 2017.

[6] P. Guo, "Modified direct shear test for anisotropic strength of sand," *Journal of Geotechnical and Geoenvironmental Engineering*, vol. 134, no. 9, pp. 1311–1318, 2008.

[7] W.-c. Shi, J.-g. Zhu, C.-f. Chiu, and H.-l. Liu, "Strength and deformation behaviour of coarse-grained soil by true triaxial tests," *Journal of Central South University of Technology*, vol. 17, no. 5, pp. 1095–1102, 2010.

[8] P. V. Lade and J. M. Duncan, "Cubical triaxial tests on co-hesionless soil," *Journal of Soil Mechanics & Foundations Div*, vol. 99, no. 10, pp. 793–812, 1973.

[9] D. A. Sun, W. Huang, and Y. Yao, "An experimental study of failure and softening in sand under three-dimensional stress condition," *Granular Matter*, vol. 10, no. 3, pp. 187–195, 2008.

[10] P. V. Lade, "Assessment of test data for selection of 3-D failure criterion for sand," *International Journal for Numerical and Analytical Methods in Geomechanics*, vol. 30, no. 4, pp. 307–333, 2006.

[11] W. Zhou, L. Yang, G. Ma, X. Chang, Y. Cheng, and D. Li, "Macro-micro responses of crushable granular materials in simulated true triaxial tests," *Granular Matter*, vol. 17, no. 4, pp. 497–509, 2015.

[12] P. V. Lade and M. M. Kirkgard, "Effects of stress rotation and changes of *b*-values on cross-anisotropic behavior of natural, K0-consolidated soft clay," *Soils and Foundations*, vol. 40, no. 6, pp. 93–105, 2000.

[13] P. V. Lade and N. M. Rodriguez, "Comparison of true triaxial and hollow cylinder tests on cross-anisotropic sand speci-mens," *Geotechnical Testing Journal*, vol. 37, no. 4, pp. 585–596, 2014.

[14] X. Huang, K. J. Hanley, C. O'Sullivan, C. Y. Kwok, and M. A. Wadee, "DEM analysis of the influence of the inter-mediate stress ratio on the critical-state behaviour of granular materials," *Granular Matter*, vol. 16, no. 5, pp. 641–655, 2014.

[15] P. A. Cundall and O. D. L. Strack, "A discrete numerical model for granular assemblies," *Géotechnique*, vol. 29, no. 1, pp. 47–65, 1979.

[16] H. Huang and E. Tutumluer, "Discrete element modeling for fouled railroad ballast," *Construction and Building Materials*, vol. 25, no. 8, pp. 3306–3312, 2011.

[17] E. Tutumluer, Y. Qian, Y. M. Hashash, J. Ghaboussi, and D. D. Davis, "Discrete element modelling of ballasted track deformation behaviour," *International Journal of Rail Transportation*, vol. 1, no. 1-2, pp. 57–73, 2013.

[18] T.-T. Ng, "Macro- and micro-behaviors of granular materials under different sample preparation methods and stress paths," *International Journal of Solids and Structures*, vol. 41, no. 21, pp. 5871–5884, 2004.

[19] M. M. Sazzad and K. Suzuki, "Micromechanical behavior of granular materials with inherent anisotropy under cyclic loading using 2D DEM," *Granular Matter*, vol. 12, no. 6, pp. 597–605, 2010.

[20] O. I. Imole, M. Wojtkowski, V. Magnanimo, and S. Luding, "Micro-macro correlations and anisotropy in granular as-semblies under uniaxial loading and unloading," *Physical Review E*, vol. 89, no. 4, Article ID 042210, 2014.

[21] E. S. Hosseininia, "Investigating the micromechanical evo-lutions within inherently anisotropic granular materials using discrete element method," *Granular Matter*, vol. 14, no. 4, pp. 483–503, 2012.

[22] D. Barreto and C. O'Sullivan, "The influence of inter-particle friction and the intermediate stress ratio on soil response under generalised stress conditions," *Granular Matter*, vol. 14, no. 4, pp. 505–521, 2012.

[23] M. R. Kuhn, W. Sun, and Q. Wang, "Stress-induced an-isotropy in granular materials: fabric, stiffness, and perme-ability," *Acta Geotechnica*, vol. 10, no. 4, pp. 399–419, 2015.

[24] T.-T. Ng, "Shear strength and micro-descriptors of bidisperse ellipsoids under different loading paths," *Mechanics of Ma-terials*, vol. 41, no. 6, pp. 748–763, 2009.

[25] S. Lobo-Guerrero and L. E. Vallejo, "Discrete element method analysis of railtrack ballast degradation during cyclic loading," *Granular Matter*, vol. 8, no. 3-4, pp. 195–204, 2006.

[26] H. A. Carmona, A. V. Guimarães, J. S. Andrade Jr., I. Nikolakopoulos, F. K. Wittel, and H. J. Herrmann, "Fragmentation processes in two-phase materials," *Physical Review E*, vol. 91, no. 1, Article ID 012402, 2015.

[27] Z. Tong, P. Fu, S. Zhou, and Y. F. Dafalias, "Experimental investigation of shear strength of sands with inherent fabric anisotropy," *Acta Geotechnica*, vol. 9, no. 2, pp. 257–275, 2014.

[28] W. J. Xu, G. Y. Liu, and H. Yang, "Study on the mechanical behavior of sands using 3D discrete element method with realistic particle models," *Acta Geotechnica*, vol. 15, no. 10, pp. 2813–2828, 2020.

[29] Z. Mahmood and K. Iwashita, "Influence of inherent an-isotropy on mechanical behavior of granular materials based on DEM simulations," *International Journal for Numerical and Analytical Methods in Geomechanics*, vol. 34, no. 8, pp. 795–819, 2010.

[30] H. Boler, Y. Qian, and E. Tutumluer, "Influence of size and shape properties of railroad ballast on aggregate packing: statistical analysis," *Transportation Research Record: Journal of the Transportation Research Board*, vol. 2448, no. 1, pp. 94–104, 2014.

[31] Y. Xiao, E. Tutumluer, and Y. Qian, "DEM approach for engineering aggregate gradation and shape properties influ-encing mechanical behavior of unbound aggregate materials," in *Geo-Congress 2014: Geo-Characterization and Modeling for Sustainability* pp. 2898–2910, Reston, VA, USA, 2014.

[32] X. Lin and T.-T. Ng, "A three-dimensional discrete element model using arrays of ellipsoids," *Géotechnique*, vol. 47, no. 2, pp. 319–329, 1997.

[33] P. Fu and Y. F. Dafalias, "Study of anisotropic shear strength of granular materials using DEM simulation," *International Journal for Numerical and Analytical Methods in Geo-mechanics*, vol. 35, no. 10, pp. 1098–1126, 2011.

[34] A. A. Mirghasemi, L. Rothenburg, and E. L. Matyas, "Influ-ence of particle shape on engineering properties of assemblies of two-dimensional polygon-shaped particles," *Géotechnique*, vol. 52, no. 3, pp. 209–217, 2002.

[35] A. A. Peña, A. Lizcano, F. Alonso-Marroquin, and H. J. Herrmann, "Biaxial test simulations using a packing of polygonal particles," *International Journal for Numerical and Analytical Methods in Geomechanics*, vol. 32, no. 2, pp. 143–160, 2008.

[36] R. Taghavi, "Automatic clump generation based on mid-sur-face," in *Proceedings of the 2nd International FLAC/DEM Symposium*, pp. 791–797, Melbourne, Australia, February 2011.

[37] X. Bian, H. Huang, E. Tutumluer, and Y. Gao, ""Critical particle size" and ballast gradation studied by discrete element modeling," *Transportation Geotechnics*, vol. 6, pp. 38–44, 2016.

[38] B. S. Kim, S. W. Park, and S. Kato, "DEM simulation of collapse behaviours of unsaturated granular materials under general stress states," *Computers and Geotechnics*, vol. 42, pp. 52–61, 2012.

[39] X. Gu, M. Huang, and J. Qian, "DEM investigation on the evolution of microstructure in granular soils under shearing," *Granular Matter*, vol. 16, no. 1, pp. 91–106, 2014.

[40] N. H. Minh and Y. P. Cheng, "A DEM investigation of the effect of particle-size distribution on one-dimensional com-pression," *Géotechnique*, vol. 63, no. 1, pp. 44–53, 2013.

[41] JGS, *Japanese Standards and Explanations of Laboratory Tests of Geomaterials*, vol. 1, Japanese Geotechnical Society, Tokyo, Japan, 2010.

[42] B. Dai, J. Yang, and X. Luo, "A numerical analysis of the shear behavior of granular soil with fines," *Particuology*, vol. 21, pp. 160–172, 2015.

[43] B. Dai, J. Yang, C. Zhou, and X. Luo, "DEM investigation on the effect of sample preparation on the shear behavior of granular soil," *Particuology*, vol. 25, pp. 111–121, 2016.

[44] Itasca Consulting Group, Inc., *Particle Flow Code in 3 Dimensions (PFC3D) Version 4*, vol. 3, Itasca Consulting Group, Inc., Minneapolis, MN, USA, 2008.

[45] C. Goldenberg and I. Goldhirsch, "Friction enhances elasticity in granular solids," *Nature*, vol. 435, no. 7039, pp. 188–191, 2005.

[46] W. M. Yan and J. Dong, "Effect of particle grading on the response of an idealized granular assemblage," *International Journal of Geomechanics*, vol. 11, no. 4, pp. 276–285, 2011.

[47] J. E. Andrade, Q. Chen, P. H. Le, C. F. Avila, and T. Matthew Evans, "On the rheology of dilative granular media: bridging solid- and fluid-like behavior," *Journal of the Mechanics and Physics of Solids*, vol. 60, no. 6, pp. 1122–1136, 2012.

[48] Shi W., True triaxial tests on coarse-grained soils and study on constitutive model, Dissertation for the doctoral degree, Hohai University, Nanjing, China, 2008, in Chinese.

[49] N. Guo and J. Zhao, "The signature of shear-induced anisotropy in granular media," *Computers and Geotechnics*, vol. 47, pp. 1–15, 2013.

[50] M. U. Ergun, "Evaluation of three-dimensional shear testing," in *Proceedings of the 10th International Conference on Soil Mechanics and Foundation Engineering*, vol. 1, pp. 593–596, Stockholm, Sweden, June 1981.

[51] J. Zhao and N. Guo, "Rotational resistance and shear-induced anisotropy in granular media," *Acta Mechanica Solida Sinica*, vol. 27, no. 1, pp. 1–14, 2014.

[52] S. Nemat-Nasser and Y. Tobita, "Influence of fabric on liquefaction and densification potential of cohesionless sand," *Mechanics of Materials*, vol. 1, no. 1, pp. 43–62, 1982.

[53] F. Alonso-Marroquin, S. Luding, H. J. Herrmann, and I. Vardoulakis, "Role of anisotropy in the elastoplastic response of a polygonal packing," *Physical Review E*, vol. 71, no. 5, Article ID 051304, 2005.

[54] S. Yimsiri and K. Soga, "DEM analysis of soil fabric effects on behaviour of sand," *Géotechnique*, vol. 60, no. 6, pp. 483–495, 2010.

[55] Y. Liu, D. Zhang, S. Wu, and P. Yu, "DEM Investigation on the evolution of fabric under true triaxial conditions in granular materials," *International Journal of Geomechanics*, vol. 20, no. 8, Article ID 04020110, 2020.

[56] L. Rothenburg and R. J. Bathurst, "Analytical study of induced anisotropy in idealized granular materials," *Géotechnique*, vol. 39, no. 4, pp. 601–614, 1989.

[57] T. G. Sitharam, S. V. Dinesh, and N. Shimizu, "Micromechanical modelling of monotonic drained and undrained shear behaviour of granular media using three-dimensional DEM," *International Journal for Numerical and Analytical Methods in Geomechanics*, vol. 26, no. 12, pp. 1167–1189, 2002.

[58] H. Ouadfel and L. Rothenburg, ""Stress-force-fabric" relationship for assemblies of ellipsoids," *Mechanics of Materials*, vol. 33, no. 4, pp. 201–221, 2001.

[59] A. Tordesillas, J. Zhang, and R. Behringer, "Buckling force chains in dense granular assemblies: physical and numerical experiments," *Geomechanics and Geoengineering*, vol. 4, no. 1, pp. 3–16, 2009.

[60] J. Liu, W. Zhou, G. Ma, S. Yang, and X. Chang, "Strong contacts, connectivity and fabric anisotropy in granular materials: a 3D perspective," *Powder Technology*, vol. 366, pp. 747–760, 2020.